Physics of Atomic Nuclei, Vol. 68, No. 12, 2005, pp. 1957–1967. Translated from Yadernaya Fizika, Vol. 68, No. 12, 2005, pp. 2019–2029.

NUCLEI
Experiment

Investigation of the Mechanism of the Reaction ^{10}B(d, $p\gamma$)^{11}B at $E_d =$ 15.3 MeV by the Method of Angular $p\gamma$ Correlations

L. I. Galanina, N. S. Zelenskaya, A. V. Ignatenko, V. M. Lebedev, N. V. Orlova, O. I. Serikov, and A. V. Spassky*

Institute of Nuclear Physics, Moscow State University, Vorob'evy gory, Moscow, 119899 Russia

Received September 15, 2004; in final form, February 8, 2005

Abstract—The results are presented that were obtained by measuring the differential cross sections for the reaction ^{10}B(d, p)^{11}B occurring at $E_d = 15.3$ MeV and leading to the production of a ^{11}B nucleus in the ground state ($3/2^-$) and in the lowest two excited states (the $1/2^-$ state at 2.125 MeV and the $5/2^-$ state at 4.445 MeV). The energy dependence of the differential cross section for this reaction was measured for several proton emission angles in the energy range $E_d = 12$–15.3 MeV. The double-differential cross sections for the reaction ^{10}B(d, $p\gamma$)^{11}B were measured for the $5/2^-$ state of the ^{11}B nucleus at 4.445 MeV, and the angular dependences of the even spin-tensor components of the density matrix were reconstructed on the basis of these data. The angular dependences of the populations of magnetic sublevels are also given. The experimental results in question are compared with their theoretical counterparts obtained under the assumption of various reaction mechanisms (neutron stripping, heavy-particle stripping, and a two-step mechanism that takes into account the delay of interaction). On the basis of this comparison, the deformation parameters of the boron nuclei were found to be $\beta_2(^{10}\mathrm{B}) = -0.55$ and $\beta_2(^{11}\mathrm{B}) = 0.4$.

1. INTRODUCTION

Investigation of mechanisms of direct nuclear reactions on light nuclei is still one of the pressing problems in intermediate-energy nuclear physics. In particular, it is of indisputable interest to study both experimentally and theoretically those features of reactions that are sensitive to manifestations of mechanisms more complicated than the one-step transfer of a nucleon or a group of nucleons.

In [1, 2], it was indicated that some spin-tensor components of the density matrix that were obtained in correlation experiments are highly sensitive to a multistep character of the reaction mechanism and to the structure of nuclear-state wave functions. The first quantitative estimates [3–5] of the contribution from two-step mechanisms featuring the delay of interaction for reactions involving semiheavy ions confirmed that it is important to take them into account.

The present article reports on the application of the angular-correlation method to experimentally studying the reaction ^{10}B(d, $p\gamma$)^{11}B occurring at $E_d =$ 15.3 MeV and leading to the production of a ^{11}B nucleus in the ground ($3/2^-$) state and the lowest two excited states. The angular and energy dependences of the differential cross sections were obtained for these states. For the $5/2^-$ state at 4.445 MeV, we measured the double-differential cross sections and determined the angular dependences of the even spin-tensor components of the density matrix.

Previously, the angular distributions of protons originating from the reaction ^{10}B(d, p_0)^{11}B at energies E_d close to 15 MeV were analyzed in [6–9] within the distorted-wave Born approximation for the neutron-stripping mechanism. This resulted in obtaining a satisfactory description of the shape of the angular distributions for the transition to the ground state of the final nucleus, but the calculated and experimental cross sections differed markedly in magnitude. In studying the transition to the $5/2^-$ excited state at 4.445 MeV, Schiffer *et al.* [9] revealed a serious discrepancy between the calculated and experimental spectroscopic factors and found that the relative amplitudes of oscillations in the angular distribution of protons are poorly described.

Of particular interest is the reaction ^{10}B(d, p_1)^{11}B leading to the production of the final nucleus in the $1/2^-$ state at 2.125 MeV. This state cannot be formed via neutron stripping (at the angular-momentum transfer of $l = 1$); at the same time, it is excited quite intensively in experiments [10, 11], and an increase in the cross section at small angles is observed in the angular distribution of the differential cross section, this being peculiar to a direct process. Available experimental data on this reaction are insufficiently

*e-mail: wg2@anna19.npi.msu.su

informative, and their theoretical interpretation is ambiguous.

A theoretical analysis of the experimental results obtained in the present study made it possible to determine the contribution to the mechanism of the reaction under investigation from processes that are more complicated than neutron stripping and which are associated first with the collective excitation of nonspherical boron nuclei and second with step-by-step cluster transfer (two-step processes), which is a second-order effect in perturbation theory.

2. EXPERIMENTAL PROCEDURE AND PROCEDURE FOR RECONSTRUCTING SPIN-TENSOR COMPONENTS OF THE DENSITY MATRIX

Our experimental investigations were performed with deuterons accelerated to an energy of 15.3 MeV at the cyclotron of the Institute of Nuclear Physics (Moscow State University). A variation of the projectile-particle energy and the formation of the beam spot at the target were implemented with the aid of braking aluminum foils and magnetic quadrupole lenses [12]. The energy spread of the beam was approximately 160 and 350 keV at $E_d = 15.3$ and 12 MeV, respectively.

The protons emitted in the reaction were detected by four silicon semiconductor detectors (the thickness of the sensitive region was between 2 and 3 mm) arranged in same plane—a horizontal or any other plane. The detectors were placed in the scattering chamber of diameter 23 cm at a distance of 75 mm from the target and were fixed on a table, which could be inclined at various angles with respect to the deuteron-beam axis. The position of the table with respect to the horizontal plane (angle φ_γ) could be changed by rotating the table about the axis coinciding with the axis of the accelerated-particle beam. Upon a rotation of the table, the angle θ_p of charged-particle detection remained unchanged for each detector.

The angular and energy dependences of the differential cross sections were measured in an independent experiment by a single semiconductor detector arranged outside the scattering chamber on a horizontal rotating platform. In this case, the protons from the reaction escaped from the scattering chamber through a narrow horizontal slit covered with a thin Mylar window. The angular resolution of the detectors was $\pm 2.5°$ in measuring the double-differential cross sections and $\pm 1°$ in measuring the differential cross section.

The photons were recorded by four BDEG-23 scintillation detectors of angular resolution $\pm 13°$ that were arranged with an interval of 32.5° at four values of the angle θ_γ with respect to the beam axis and were fixed on a horizontal rotating platform outside the scattering chamber. Photon–proton coincidences were detected in the photon-energy range between 2 and 4.5 MeV. This range contained that part of the spectrum which corresponded to the transition of the $5/2^-$ excited state of the final nucleus ^{11}B at 4.445 MeV to the ground state and which was dominant in the total spectrum. The energy calibration of the gamma spectra was performed by using a Pu–Be source. For each value of the angle θ_p, the double-differential cross section was measured at five to nine values of the polar angle θ_γ of photon emission in the range from 20° to 150° and at three values of the azimuthal angle φ_γ of photon emission (180°, 225°, and 270°). Thus, 15 to 27 values of the double-differential cross section were obtained for each value of the proton emission angle θ_p, and the spin-tensor components of the density matrix were determined on the basis of precisely these values by the least squares method (see below). The total exposure time in our experiment was 470 hours. About 8000 coincidences were obtained on average per each value of the angle θ_p, the fraction of random coincidences there being 40%. As a rule, the statistical errors in the measured double-differential cross sections did not exceed 15%.

The energy and time analysis of reaction products was performed with the aid of a measuring and computing complex characterized by a distributed architecture, including several levels of data processing. The first level, which consisted in the analogous treatment of spectrometric information, was implemented on the basis of CAMAC modules and an autonomous processor 131A. The second level ensured a fast digital treatment on the basis of a minicontroller equipped with a Siemens CS167 processor. An ultimate computer-aided filtration of experimental information was performed on the basis of a monitoring code, a control of experimental parameters, and a data treatment in the on-line mode. A more detailed description of the experimental facility and measuring and computing complex is given elsewhere [13–15].

Some typical spectra are presented in Fig. 1. Figure 1*a* displays the "direct" proton spectrum (without coincidences) at $\theta_p = 55°$. The kinematics of the reaction being studied was such that the energy of all three proton groups exceeded the energies of charged particles produced in reactions on possible admixtures. The time spectrum of photon coincidences with the group p_2 is shown in Fig. 1*b* according to data from the time–amplitude converter ($\varphi_\gamma = 270°$, $\theta_\gamma = 52.5°$, $\theta_p = 55°$). The range of the entire spectrum is 500 ns, the duration of the cyclotron-beam pulse being about 10 ns. The true coincidences were calculated by using the difference of the areas under the

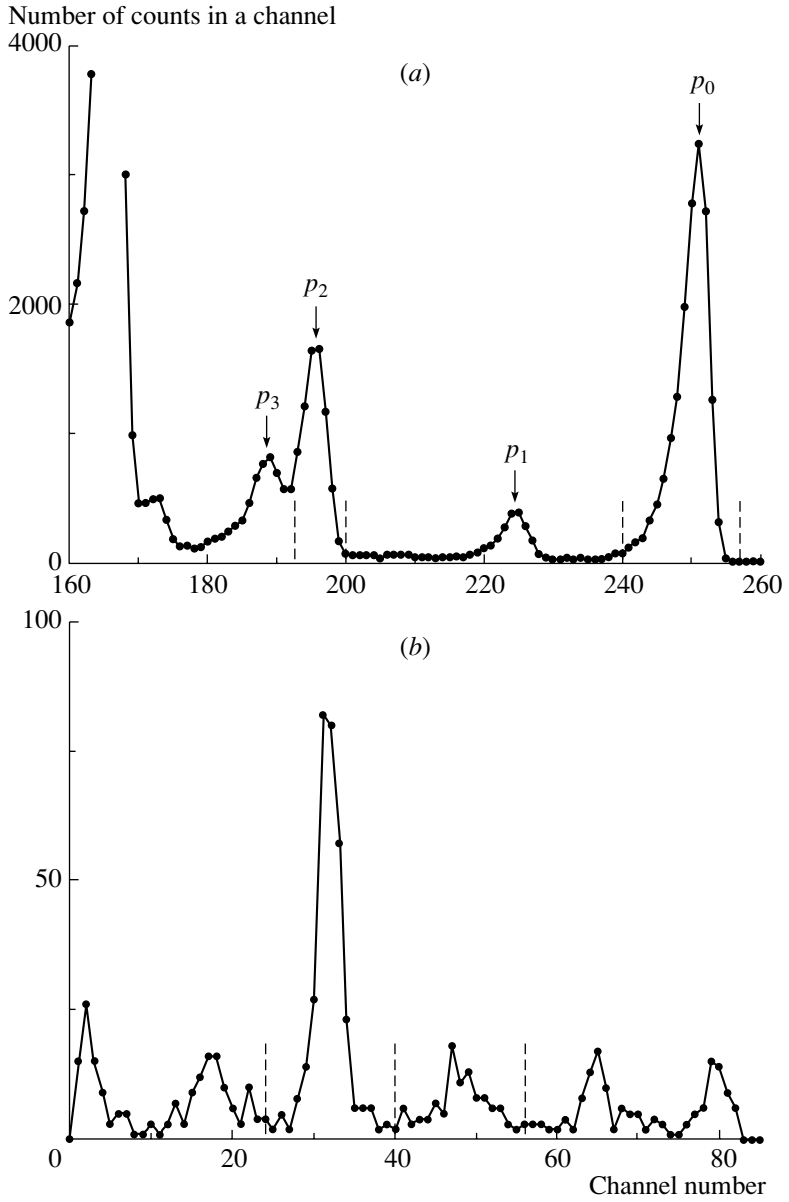

Fig. 1. Spectra for the reaction ^{10}B(d, $p\gamma$)^{11}B at $E_d = 15.3$ MeV and $\theta_p = 55°$ (in the laboratory frame): (a) spectrum of protons without coincidences (the calculated positions of particle groups are indicated here) and (b) time spectrum (from the time–amplitude converter, the converter scale being 500 ns) of photon coincidences with the group p_2 ($\varphi_\gamma = 270°$, $\theta_\gamma = 52.5°$). In Fig. 1b, the large peak represents the sum of true and random coincidences, while the other peaks correspond to random coincidences exclusively. The dashed lines indicate numerical windows used in the analysis of the spectra in the measuring and computing complex.

large peak (which corresponds to the sum of true and random coincidences) and the neighboring peak (random coincidences). The dashed lines in Fig. 1 indicate numerical windows used in the analysis of the spectra in the measuring and computing complex.

For a target, we used a finely dispersed powder of boron enriched in the ^{10}B isotope to 85% and deposited on a thin gold substrate (0.22 mg/cm^2 in thickness). The thickness of the target was estimated by weighing it and was found to be 1.0 ± 0.1 mg/cm^2. The error in determining the target thickness was due primarily to its inhomogeneity over the beam-spot area on the target. The absolute cross-section values were determined to within 15%.

The $5/2^-$(4.445 MeV) $\to$ $3/2^-$(0 MeV) gamma transition in the ^{11}B nucleus is an $M1 + E2$ mixed transition. According to available data, the mixing coefficient (ratio of the reduced matrix elements) $\delta(E2/M1)$ falls between -0.16 and -0.22 [16, 17]. The relative fraction of the $E2$ transition is determined

by δ^2 and is 3 to 5% in the case being considered. In analyzing the angular-correlation function $W(\theta_p; \theta_\gamma, \varphi_\gamma)$, we therefore treated here this transition as a purely magnetic one ($M1$). The angular $p\gamma$ correlation is then defined as [18]

$$W(\theta_p;\theta_\gamma,\varphi_\gamma) = \frac{d^2\sigma}{d\Omega_p d\Omega_\gamma} \quad (1)$$
$$= \frac{1}{\sqrt{4\pi}}\sum_{k\kappa}\frac{1}{\sqrt{2k+1}}\rho_{k\kappa}(\theta_p)Y^*_{k\kappa}(\theta_\gamma,\varphi_\gamma)R_k,$$

where

$$R_k = (-1)^{1+J_f-J_0-k}(2L+1)\sqrt{(2J_f+1)} \quad (2)$$
$$\times \langle L1L-1|k0\rangle W(J_fJ_fLL:kJ_0).$$

In expressions (1) and (2), J_f and J_0 are the spins of, respectively, an excited and the final state of the final nucleus; L is the multipolarity of the gamma transition in question; $\rho_{k\kappa}(\theta_p)$ are spin-tensor components of the density matrix for the nucleus involved [the component $\rho_{00} \equiv d\sigma(\theta_p)/d\Omega$ is the usual differential cross section for the reaction in question], with $k = 0, 2$ ($\mathbf{k} = \mathbf{L} + \mathbf{L} = \mathbf{J}_f + \mathbf{J}_f$) and the projection κ assuming integral values between $-k$ and k; $\langle L1L-1k0\rangle$ and $W(J_fJ_fLL:kJ_0)$ are, respectively, the Clebsch–Gordan and Racah coefficients; and $Y^*_{k\kappa}$ is a spherical harmonic. The maximum rank of spin-tensor components of the density matrix is $k = 2$, since the multipolarity L of the transition in question is equal to unity. From expression (1), it follows that, for each value of the angle θ_p, one can observe experimentally linear combinations of the components $\rho_{k\kappa}(\theta_p)$ rather than the components themselves. Measuring, at several values of the angle θ_γ (for each fixed set of angles θ_p), $W(\theta_p;\theta_\gamma,\varphi_\gamma)$ in various planes with respect to the reaction plane, which are specified by the angle φ_γ, and choosing the number of measurements to be greater than the number of independent spin-tensor components $\rho_{k\kappa}$, we obtain, for determining $\rho_{k\kappa}$, a problem that, in mathematical statistics, is usually referred to as a problem of linear-regression analysis [19]. Standard methods for solving such problems make it possible to evaluate the components $\rho_{k\kappa}(\theta_p)$ and their variances on the basis of the results obtained by measuring angular particle–photon correlations. The errors in the reconstructed values of spin-tensor components are eventually determined by the error matrix that is obtained in solving the overdetermined set of Eqs. (1). In the experiment being discussed, the relative errors in $\rho_{k\kappa}(\theta_p)$ did not fall below 25%, but we will see below that the quality of the experimental data obtained proves to be quite sufficient for drawing specific conclusions on the reaction mechanism.

The details of the method used to reconstruct spin-tensor components of the density matrix on the basis of data on the angular-correlation function $W(\theta_p;\ \theta_\gamma,\ \varphi_\gamma)$ were previously described in [18, 20–22].

3. EXPERIMENTAL RESULTS

The angular dependences of the differential cross sections for the reaction ^{10}B(d, p)^{11}B involving the production of a ^{11}B nucleus in the ground ($3/2^-$) state and in the lowest two excited states (the $1/2^-$ state at 2.125 MeV and the $5/2^-$ state at 4.445 MeV), the respective proton groups being denoted by p_0, p_1, and p_2, are given in Fig. 2. The measured energy dependences of the differential cross section are shown in Fig. 3 for the proton emission angles of $\theta_p = 50°$, 90°, and 160° in the laboratory frame.

The angular dependences of the double-differential cross section for the reaction ^{10}B(d, $p_2\gamma$)^{11}B ($5/2^-$, 4.445 MeV) were measured for 17 values of the angle θ_p in the range between 20° and 160° (in the laboratory frame). On the basis of these double-differential cross sections, we determined the spin-tensor components $\rho_{k\kappa}$ of the density matrix for the ^{11}B($5/2^-$, 4.445 MeV) nucleus. In reconstructing $\rho_{k\kappa}(\theta_p)$, we took into account the finite dimensions of the scintillation detectors. The angular dependences of the components ρ_{20} and ρ_{22} are shown in Fig. 4. The component ρ_{21} proved to carry a small amount of important information. For this reason, it is not given in this figure. The typical value of the confidence level in reconstructing $\rho_{k\kappa}(\theta_p)$ on the basis of angular-correlation functions is 0.01, which demonstrates a satisfactory reliability of the experimental results. All of the components $\rho_{4\kappa}(\theta_p)$ ($\kappa = 0-4$) obtained under the assumption that an $E2$ transition is present proved to be close to zero (within the statistical errors). In order to test our experimental procedure, we additionally derived the spin-tensor components $\rho_{2\kappa}(\theta_p)$ and $\rho_{4\kappa}(\theta_p)$ of the density matrix for the ^{11}B($1/2^-$, 2.125 MeV) nucleus. Within the statistical errors, they proved to be zero, which also confirms the absence of systematic errors in our measurements [in this case, the density matrix must contain only one component, the differential cross section $\rho_{00}(\theta_p)$].

On the basis of the values found for $\rho_{k\kappa}(\theta_p)$, we constructed the angular dependences of the populations $P_{\pm M}(\theta_p)$ of magnetic substates [20] (Fig. 5) for the $5/2^-$ state of the ^{11}B nucleus at 4.445 MeV.

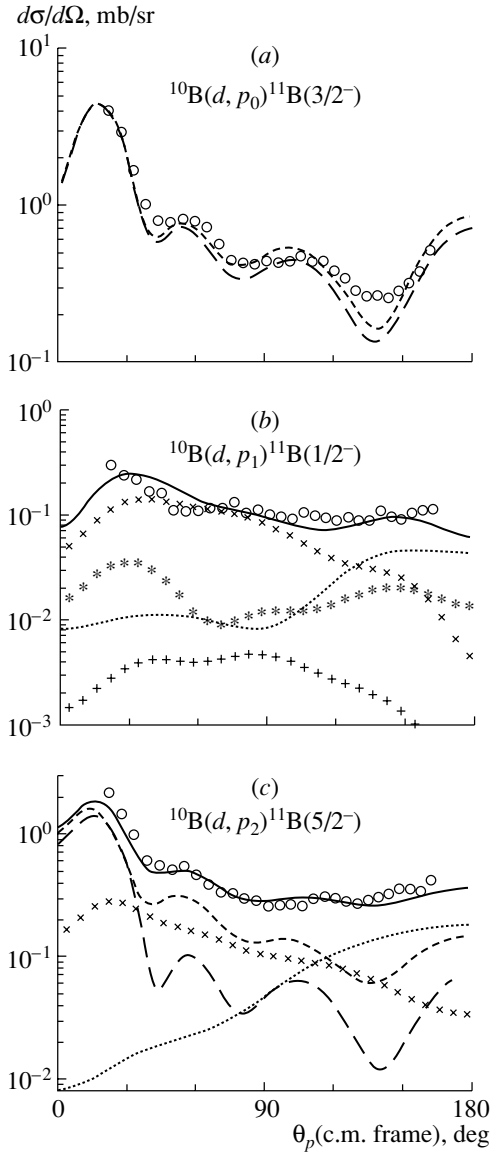

Fig. 2. Angular dependences of the differential cross sections for the reaction $^{10}B(d, p)^{11}B$ occurring at $E_d = 15.3$ MeV and leading to the production of a final nucleus in (*a*) the ground ($3/2^-$) state and the lowest two excited states [(*b*) $1/2^-$ and (*c*) $5/2^-$ states], the respective proton groups being denoted by p_0, p_1, and p_2. The open circles represent experimental results, the statistical errors not being larger than the circle size. The curves correspond to the calculations performed under the assumption of various reaction mechanisms, including (long dashes) the mechanism of neutron stripping according to the coupled-channel Born approximation without allowance for the deformation of the ^{10}B and ^{11}B nuclei, (short dashes) the analogous mechanism according to the coupled-channel Born approximation with optimum values of the deformation parameter [$\beta_2(^{10}B) = -0.55$ and $\beta_2(^{11}B) = 0.4$], and (dotted curve) the mechanism of heavy-particle stripping. For the mechanism that takes into account delay, we present curves (in Figs. 2*b*, 2*c*) corresponding to various states of the intermediate nucleus ^9Be—specifically, for (×) $3/2^-$, (+) $5/2^-$, and (∗) $7/2^-$ states; the solid curve corresponds to the sum of these curves.

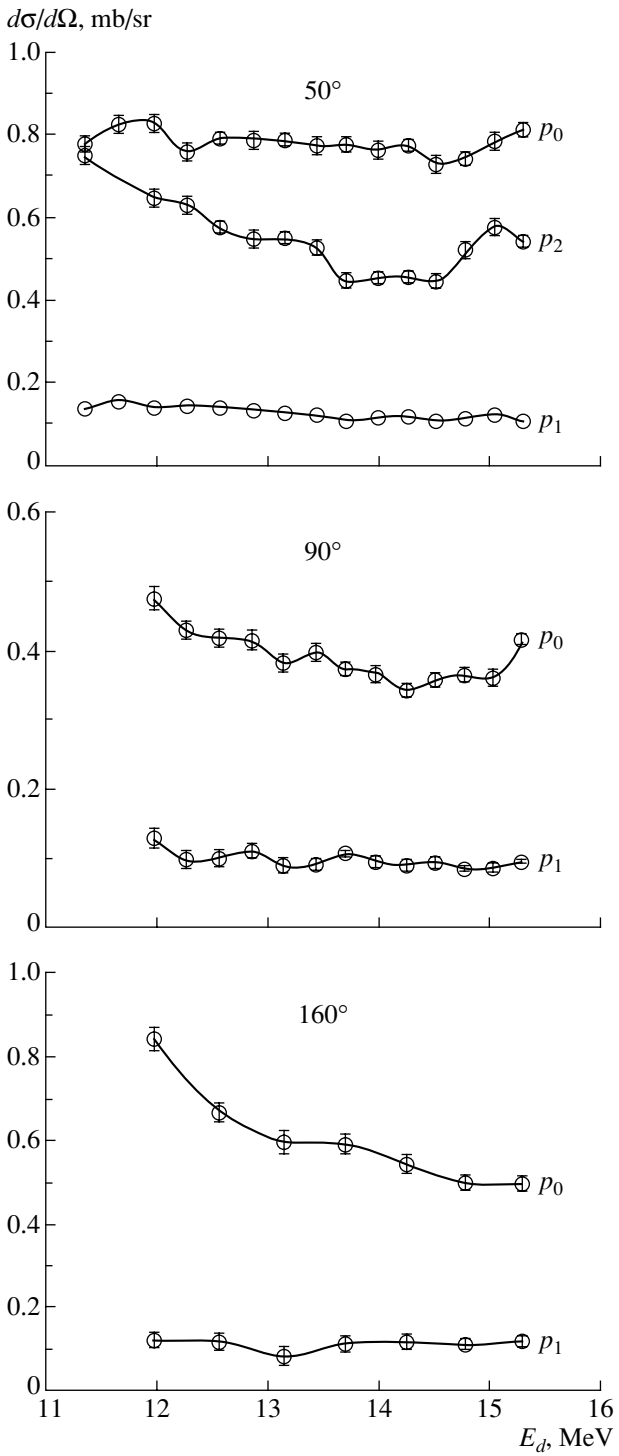

Fig. 3. Experimental energy dependences of the differential cross section for the reaction $^{10}B(d, p)^{11}B$ at three values of the detection angle θ_p (in the laboratory frame). The curves connect experimental points. The proton groups are indicated on the curves.

4. ANALYSIS OF THE RESULTS

We would now like to highlight some special features of our experimental results for the reaction un-

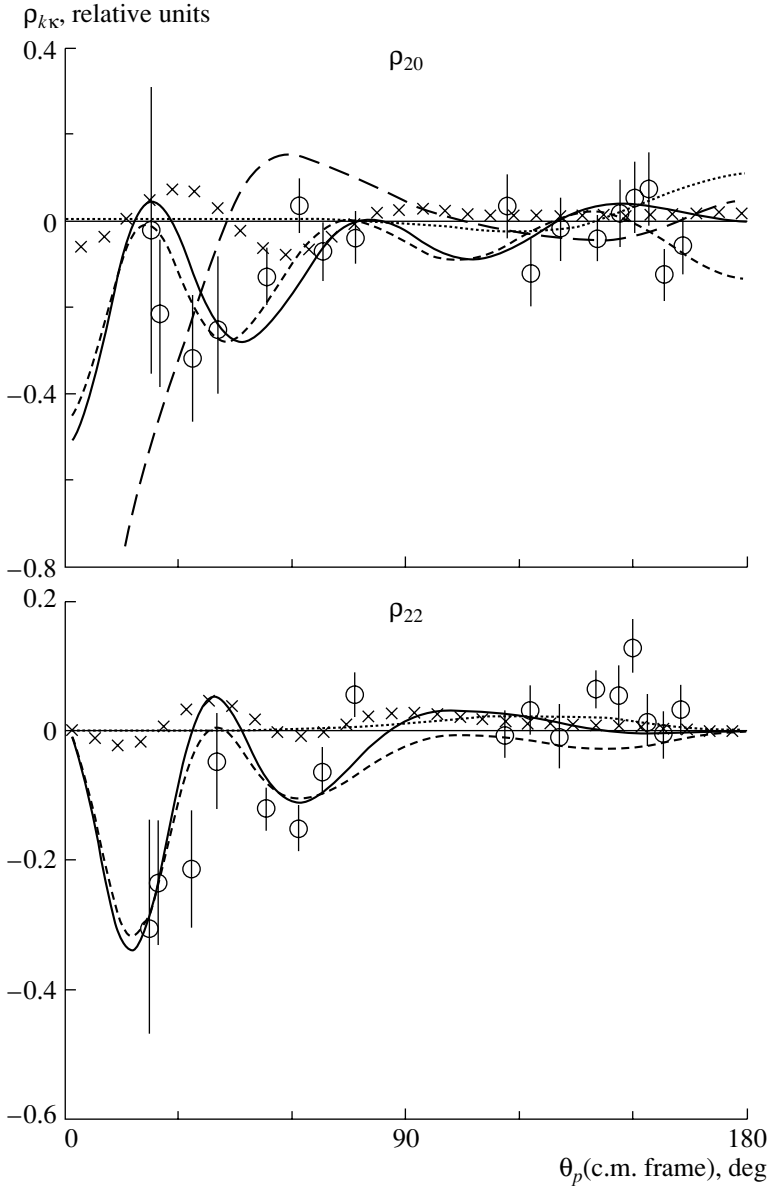

Fig. 4. Angular dependences of the spin-tensor components $\rho_{k\kappa}$ of the density matrix for the $5/2^-$ state of the ^{11}B nucleus at 4.445 MeV. Units along the ordinate are chosen in such a way that the dimensionality of $\rho_{00} \equiv d\sigma/d\Omega$ is mb/sr. The notation for the curves is identical to that in Fig. 2*c*, but long dashes here correspond to the calculation in the coupled-channel Born approximation for the deformation parameter set to $\beta_2(^{10}\mathrm{B}) = 0.55$ and $\beta_2(^{11}\mathrm{B}) = 0.4$.

der study. The angular distribution of protons that correspond to the production of a final nucleus (see Fig. 2*a*) has an oscillating character, which is typical of direct processes. The analogous angular dependences for the groups p_1 and p_2 (see Figs. 2*b*, 2*c*) have a maximum at small angles and a sizable constant component in the remaining angular region. None of the measured excitation functions exhibits pronounced resonance oscillations, and all of them change only slightly with increasing energy (see Fig. 3), this also being peculiar to direct processes.

The angular dependences of the populations $P_{\pm M}(\theta_p)$ at $M = 3/2$ and $M = 5/2$ feature moderate oscillations, which, as is known from [20], are not described by the calculations in the distorted-wave Born approximation under the assumption of the neutron-stripping mechanism and are indicative of the presence of the contribution to the total reaction mechanism from processes different from mere stripping. Figure 5 does not show the population for $M = 3/2$, since it is completely determined by the relation $2P_{\pm 3/2}(\theta_p) = 100\% - 2P_{\pm 1/2}(\theta_p) - 2P_{\pm 5/2}(\theta_p)$.

At the first step, a theoretical analysis of our

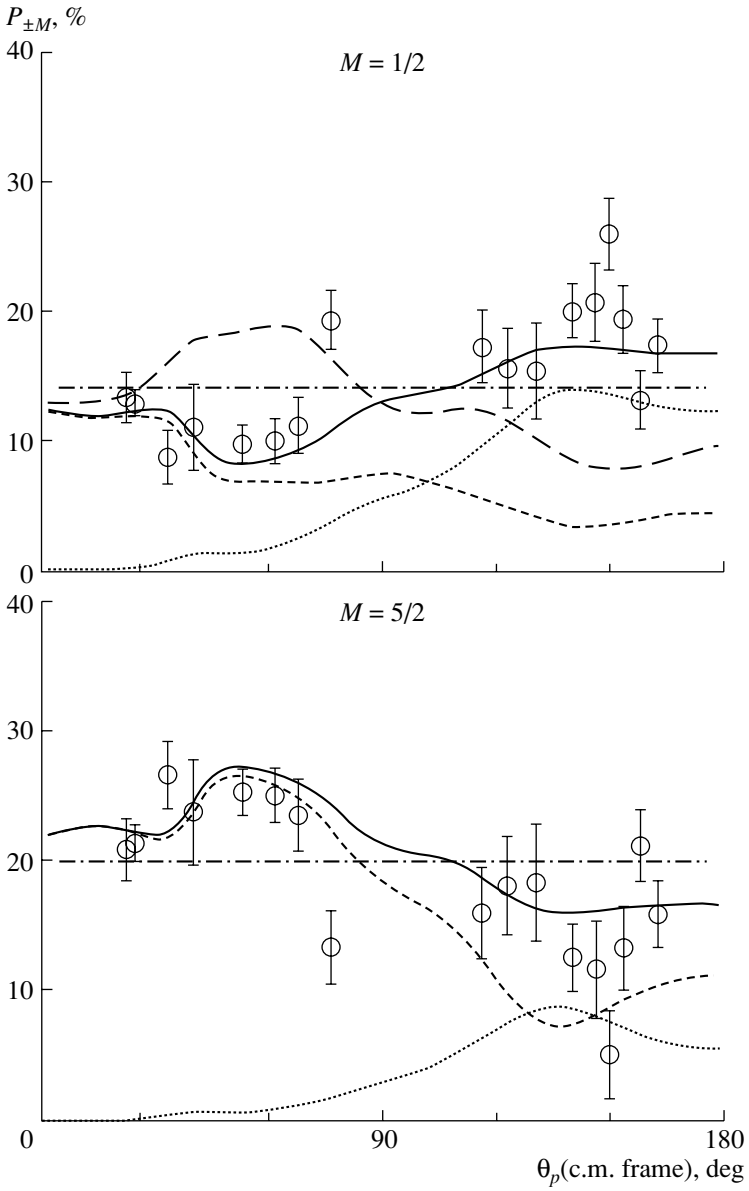

Fig. 5. Angular dependences of the populations of magnetic sublevels of the $5/2^-$ state of the ^{11}B nucleus at 4.445 MeV for various values of the spin projection M. The dash-dotted curve corresponds to the calculation on the basis of the OLYMP-3 code under the assumption of the neutron-stripping mechanism (without allowance for the deformation of the ^{10}B and ^{11}B nuclei). The notation for the remaining curves and points is identical to that in Fig. 4.

experimental data was performed in the finite-range distorted-wave Born approximation by using the OLYMP-3 code [23]. It is well known that, in the first order of perturbation theory, the coupling of only two channels is considered in the numerical realization of the distorted-wave Born approximation. In the case of the reaction ^{10}B(d, $p\gamma$)^{11}B at $E_d = 15.3$ MeV, it can a priori be expected that the entire body of experimental data cannot be described within these approximations.

Indeed, it is usually difficult to interpret theoretically the mechanism of reactions involving ^{10}B. On one hand, the ^{10}B nucleus is in the middle of the $1p$ shell, with the result that there arise significant difficulties in applying traditional models to describing its static properties. By way of example, we indicate that, in the shell model, the wave function for the ground state of the ^{10}B nucleus [24] contains two different components characterized by the same values of the quantum numbers of this model (orbital angular momentum, spin, Young diagram). As a result, a complete description of these components requires introducing additional quantum numbers of the SU_3 scheme. This means that the shell model cannot pro-

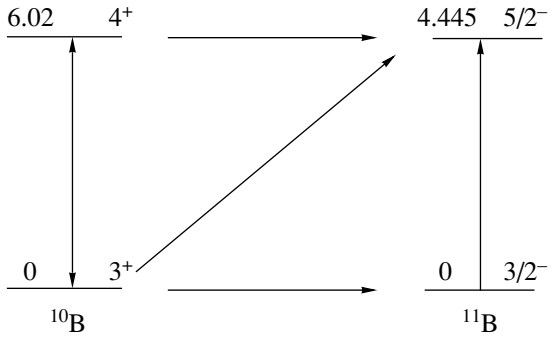

Fig. 6. Scheme of the calculation in the coupled-channel Born approximation for the reaction ^{10}B$(d, p\gamma)^{11}$B. Given in the figure are the energies of the nuclear levels involved (in megaelectronvolts) and their spins and parities. The vertical arrows indicate the coupling of levels in the nuclei, while the remaining arrows show transitions accompanied by particle transfer.

vide correct values of the spectroscopic factors for various channels of ^{10}B decay and that this nucleus features a sizable static deformation in the ground state [25–28]. On the other hand, the total spin J of the ^{10}B nucleus in the ground state is anomalously high ($J = 3$); therefore, the reaction amplitude may receive contributions from many components differing in the transfer of total angular momenta, orbital angular momenta, and spins.

In order to take into account collective excitations of boron nuclei, we employed the coupled-channel method (coupled-channel Born approximation) implemented in the form of the CHUCK code [29], which is adapted to calculating spin-tensor components of the density matrix.

The scheme of the calculations in the coupled-channel Born approximation is shown in Fig. 6. The calculations were performed with allowance for the coupling of the 3^+ state at zero energy and the 4^+ state at 6.02 MeV in the ^{10}B nucleus and the $3/2^-$ state at zero energy and $5/2^-$ state at 4.445 MeV in the final nucleus ^{11}B. The parameter sets used in these calculations for the Woods–Saxon optical potentials are given in the table. The standard values of $r_V = 1.25$ fm and $a_V = 0.65$ fm were taken for the bound-state potentials, and the parameter of the spin–orbit part of the potential was set to $\lambda = 25$. The depths of the bound-state potentials were calculated on the basis of the corresponding values of the binding energy in the system formed by the transferred particle and the nuclear core. For the light vertex ($d \to p + n$), we took the value of $D_0 = 123$ [29], which is typically used in the CHUCK code. For the channel $^{11}\mathrm{B} \to n + ^{10}\mathrm{B}$, the spectroscopic factors were calculated on the basis of the shell model for intermediate coupling [24]. In the calculations based on the CHUCK code, the additional normalization factors for the reaction cross section [and other components $\rho_{k\kappa}(\theta_p)$] were 3.5 for the group p_0 and 3.0 for the group p_2.

Mechanisms that take into account the delay of interaction are second-order corrections to ordinary one-step mechanisms and involve the Green's functions for the intermediate nuclear system that arises in the interaction process. Such mechanisms correspond to quadrangle diagrams. In order to take into account delay processes in the interaction, we employed the method that was proposed in [30] for calculating amplitudes corresponding to quadrangle diagrams and which is based on integral equations of the four-body problem for the (3, 1) channel. In applying this method, it was assumed that cluster transfer in the reaction occurs step by step via two sequential pole mechanisms corresponding to the distorted-wave Born approximation. The QUADRO code originally introduced in [30] and based on the finite-range distorted-wave method was used to estimate quantitatively the contribution of delay processes to the reaction being studied. Specifically, the contribution of the quadrangle mechanism represented by the diagram in Fig. 7*a* was calculated for the reaction ^{10}B$(d, p)^{11}$B. This diagram takes into account processes of second-order smallness in relation to the usual stripping diagram in Fig. 7*b*. It should be noted that these two diagrams are summed coherently. In our calculations, the optical-potential parameters and the geometric parameters of the potentials in the vertex functions were chosen to be identical to their counterparts in the calculations based on the coupled-channel method.

The calculated angular distributions of the differential cross sections for the reaction in question are given in Fig. 2. For the transition to the ground state of the final nucleus (Fig. 2*a*), both the distorted-wave Born approximation (without allowance for the deformation of the nuclei) and the coupled-channel Born approximation provide good agreement with experimental data. The angular distribution obtained in the distorted-wave Born approximation undergoes virtually no changes upon taking into account the finite range of the interaction (the respective results are not shown in Fig. 2*a*).

Since the production of the $1/2^-$ state of the ^{11}B nucleus at 2.125 MeV in the reaction ^{10}B$(d, p_1)^{11}$B via the neutron-stripping mechanism is forbidden by selection rules, the amplitude of this reaction was calculated in the second order of perturbation theory (see Fig. 7*a*). The contribution of the quadrangle mechanism to the angular distribution of protons from the reaction ^{10}B$(d, p_1)^{11}$B$(1/2^-, 2.125$ MeV) is shown in Fig. 2*b* without additional normalizations. In the

Parameters of optical potentials

Channel	V, MeV	r_V, fm	a_V, fm	W, MeV	r_W, fm	a_W, fm	WD, MeV	r_c, fm	References
$^{10}B + d$	63.38	1.5	0.6	7.81	1.5	0.6	13.04*	1.3	[8]
$^{11}B + p$	50.0	1.25	0.4	12.0	1.25	0.4		1.3	[6]

* The surface potential is taken in the form of the derivative of the Woods–Saxon potential. The values of r_{WD} and a_{WD} are identical to those for the imaginary part W of the potential.

calculations, we took into account the $3/2^-$, $5/2^-$, and $7/2^-$ states of the virtual nucleus ^{9}Be at zero energy, 2.429 MeV, and 6.76 MeV, respectively. As can be seen from the figure, the quadrangle mechanism leading to the production of the virtual nucleus ^{9}Be in the $3/2^-$ and $7/2^-$ states plays a dominant role. Together with the pole mechanism of heavy-particle stripping, which corresponds to the diagram in Fig. 7*c*, the above mechanisms provide a satisfactory description of experimental data nearly over the entire angular range.

The calculated angular distributions of the differential cross section for the reaction ^{10}B(d, p_2)^{11}B($5/2^-$, 4.445 MeV) are displayed in Fig. 2*c*. From the figure, one can see that the stripping mechanism that takes into account channel coupling makes a dominant contribution to the production of the final nucleus. In this case, the result changes significantly upon taking into account the deformation of the ^{10}Be nucleus. The contributions coming from the quadrangle mechanism of the production of the virtual nucleus ^{9}B in the $3/2^-$ state and the mechanism of heavy-particle stripping and featuring no additional normalization factors are significant in the region of intermediate and large angles. The contribution of other states of the virtual nucleus ^{9}Be (specifically, the $5/2^-$ and $7/2^-$ states) proved to be much smaller (the corresponding results are not presented in Fig. 2*c*). The total cross section is in satisfactory agreement with the experimental data over the entire angular interval.

The angular dependences of the spin-tensor components of the density matrix for the ^{11}B($5/2^-$, 4.445 MeV) nucleus are shown in Fig. 4 according to calculations performed in the coupled-channel Born approximation for the neutron-stripping mechanism and in the finite-range distorted-wave Born approximation for the mechanism of heavy-particle stripping. The calculated corrections to the spin-tensor components due to the delay mechanism are insignificant and introduce virtually no changes in the angular dependences of these components. The calculated total values of $\rho_{2\kappa}(\theta_p)$ oscillate as functions of θ_p and are in satisfactory agreement with experimental data.

Figure 5 displays the theoretical angular dependences of the populations $P_{\pm M}(\theta_p)$ for the ^{11}B($5/2^-$, 4.445 MeV) nucleus. For the distributions of the populations $P_{\pm M}(\theta_p)$, the calculations under the assumption of the neutron-stripping mechanism that were performed in the finite-range distorted-wave Born approximation without allowance for the deformation of the ^{10,11}B nuclei produce a result that is independent of the angle, this being at odds with the experimental data. In this case, their values are determined by the spectroscopic factor exclusively and are equal to 14, 16, and 20% for, respectively, the $M = \pm 1/2$, $\pm 3/2$, and $\pm 5/2$ substates. In just the same way as in the case of spin-tensor components, the neutron-stripping mechanism treated in the coupled-channel Born approximation and taken together with the mechanism of heavy-particle stripping in the finite-range distorted-wave Born approximation makes it possible to obtain satisfactory agreement with the experimental data over the entire angular range. We emphasize that a complicated angular dependence of the populations arises only upon taking into account the deformation of the nuclei involved in the reaction being studied. The effect of delay mechanisms on the total curve proved to be insignificant, which is explained by their relatively small contribution to the differential cross section for the reaction in question.

A sizable sensitivity of the results of our calculations to the deformation of the nuclei makes it possible to refine the magnitude and the sign of the quadrupole-deformation parameter β_2 for the ^{10}B and ^{11}B nuclei. The analogous sensitivity of some dynamical correlation features to this parameter was previously observed in [1, 2]. It is well known that, in the ^{10}B nucleus, one of the rotational bands is built on the ground state ($K = 3^+$) [31]. According to data available in the literature, the absolute value of the quadrupole-deformation parameter β_2 for the 3^+(0 MeV) $\leftrightarrow$ 4^+(6.02 MeV) coupling of states in this band varies within the broad range from 0.45 [27] to 0.95 [26]. As for the sign of β_2, it has not yet been determined unambiguously. For the ^{11}B nucleus, the parameter β_2 ranges between 0.15 and 0.7 [28, 32].

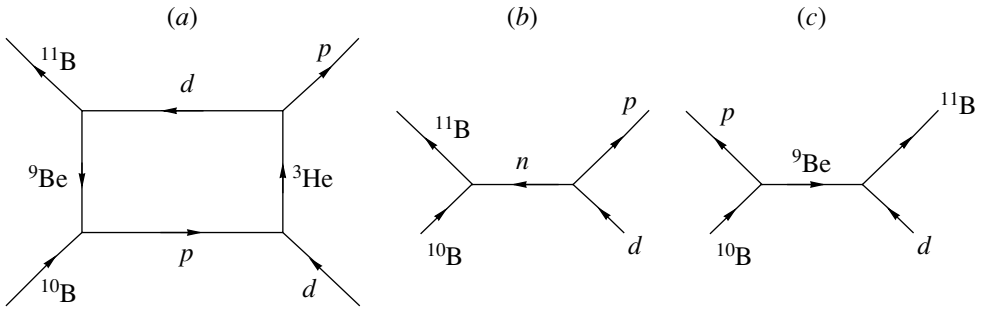

Fig. 7. Diagrams corresponding to the mechanisms of (*a*) step-by-step cluster transfer, (*b*) neutron stripping, and (*c*) heavy-particle stripping.

In order to analyze the correlation features versus the magnitude and sign of the deformation parameter β_2, it was varied from zero to ± 0.8 for both nuclei in the calculations in the coupled-channel Born approximation. It turned out that the dependence of the results of the calculations on the absolute value of β_2 in the output channel is insignificant. A variation in the absolute value of $\beta_2(^{10}\mathrm{B})$ affects substantially the features of the reaction for the transition to the $5/2^-$ level. In particular, the differential cross section calculated for this reaction in the absence of the deformation parameter $\beta_2(^{10}\mathrm{B})$ differs markedly from the experimental differential cross section (see Fig. 2*c*).

As for the sign of the deformation parameter, the bulk of the experimental data is obviously better described at a negative value of $\beta_2(^{10}\mathrm{B})$; at the same time, a positive sign of $\beta_2(^{11}\mathrm{B})$ is merely preferable. The sign of the deformation parameter $\beta_2(^{10}\mathrm{B})$ exhibited the most pronounced effect in describing the component $\rho_{20}(\theta_p)$ and the populations. Figures 4 and 5 display the component ρ_{20} and the populations calculated at $\beta_2(^{10}\mathrm{B}) = 0.55$. One can see that, upon the reversal of the sign of the deformation parameter, the shape of the calculated curves at small angles assumes an antiphase shape. From a comparison of the calculated and experimental features, we found that the deformation parameters of the boron nuclei have the values of $\beta_2(^{10}\mathrm{B}) = -0.55$ and $\beta_2(^{11}\mathrm{B}) = 0.4$. The same value of the parameter β_2 for the ^{10}B nucleus was previously obtained in [25] as an optimal one in analyzing the angular dependences of spin-tensor components for the reaction $^{10}\mathrm{B}(\alpha, d\gamma)^{12}\mathrm{C}$ at $E_\alpha = 25$ MeV.

Here, we do not present the results of calculations based on the assumption that the mechanism of compound-nucleus formation is operative, although such calculations with the aid of the CNCOR code are available [33]. The respective results reveal a symmetric nearly isotropic angular dependence of spin-tensor components (including $d\sigma(\theta_p)/d\Omega$), which contradicts the corresponding experimental dependences even qualitatively.

5. CONCLUSIONS

Our analysis of the angular and energy dependences of the differential cross section for the (d, p) reaction occurring on a ^{10}B nucleus and leading to the production of the $3/2^-$ and $5/2^-$ states of the final nucleus ^{11}B at zero energy and 4.445 MeV, respectively, as well as the analysis of the angular dependences of the spin-tensor components of the density matrix for the $5/2^-$ state of this nucleus at 4.445 MeV, has revealed that neutron stripping is a dominant mechanism of this reaction. In order to obtain an adequate description of experimental data, it is necessary to take into account the collective nature of these states of the participant nuclei and two-step processes associated with delay in the interaction. At large protons emission angles, the contribution of the heavy-particle-stripping mechanism is significant. Allowance for the mechanisms that correspond to quadrangle diagrams provides a natural explanation for a vigorous excitation of the $1/2^-$ state of the final nucleus at 2.125 MeV in the reaction being studied. A comparative analysis of the entire body of experimental and theoretical correlation features has made it possible to determine quite reliably not only the magnitude but also the sign of the quadrupole deformation of the ^{10}B nucleus.

ACKNOWLEDGMENTS

This work was supported by the Russian Foundation for Basic Research (project no. 01-02-16196), the research program Universities of Russia (grant no. 02.02.506), and the Foundation for Support of Leading Scientific Schools (grant no. 1619.2003.2).

REFERENCES

1. N. S. Zelenskaya *et al.*, Yad. Fiz. **64**, 1995 (2001) [Phys. At. Nucl. **64**, 1909 (2001)].
2. V. M. Lebedev, N. V. Orlova, and A. V. Spassky, Yad. Fiz. **61**, 1604 (1998) [Phys. At. Nucl. **61**, 1493 (1998)].
3. N. S. Zelenskaya *et al.*, Yad. Fiz. **13**, 734 (1971) [Sov. J. Nucl. Phys. **13**, 417 (1971)].
4. M. S. Al'vesh *et al.*, Yad. Fiz. **27**, 1431 (1978) [Sov. J. Nucl. Phys. **27**, 755 (1978)].
5. L. I. Galanina *et al.*, Vestn. Mosk. Univ., Ser. 3: Fiz., Astron., No. 4, 24 (2004).
6. W. R. Smith and E. V. Ivash, Phys. Rev. **131**, 304 (1963).
7. B. Zeidman, J. L. Yntema, and G. R. Satchler, in *Proceedings of the Rutherford Jubilee International Conference, Manchester, 1961* (Heywood and Co., London, 1961), p. 515.
8. H. W. Barz *et al.*, Nucl. Phys. **73**, 473 (1965).
9. J. P. Schiffer *et al.*, Phys. Rev. **164**, 1274 (1967).
10. N. T. S. Evans and W. C. Parkinson, Proc. Phys. Soc. London, Sect. A **67**, 684 (1954).
11. O. M. Bilaniuk and J. C. Hensel, Phys. Rev. **120**, 211 (1960).
12. I. B. Teplov *et al.*, Prib. Tekh. Éksp., No. 6, 45 (1965).
13. A. V. Ignatenko *et al.*, Yad. Fiz. **55**, 597 (1992) [Sov. J. Nucl. Phys. **55**, 330 (1992)].
14. N. S. Zelenskaya, V. M. Lebedev, and A. V. Spasskiĭ, Naukoemkie Tekhnologii **4**, 19 (2003).
15. A. V. Ignatenko *et al.*, in *Proceedings of the 49th Conference on Nuclear Spectroscopy and Nuclear Structure, Dubna, 1999* (Petersburg Nucl. Phys. Inst., Russ. Acad. Sci., St. Petersburg, 1999), p. 156.
16. F. Ajzenberg-Selove, Nucl. Phys. A **433**, 1 (1985).
17. R. A. I. Bell, R. D. Gill, B. C. Robertson, *et al.*, Nucl. Phys. A **118**, 481 (1968).
18. H. J. Rose and D. M. Brink, Rev. Mod. Phys. **39**, 306 (1967).
19. Yu. P. Pyt'ev and I. A. Shishmarev, *Course of Probability Theory and Mathematical Statistics for Physicists* (Mosk. Gos. Univ., Moscow, 1983), p. 256.
20. N. S. Zelenskaya and I. B. Teplov, *Properties of Excited Nuclear States and Angular Correlations in Nuclear Reactions* (Énergoatomizdat, Moscow, 1995) [in Russian].
21. A. V. Ignatenko *et al.*, Izv. Akad. Nauk, Ser. Fiz. **58**, 188 (1994).
22. N. S. Zelenskaya and I. B. Teplov, Fiz. Élem. Chastits At. Yadra **18**, 1283 (1987) [Sov. J. Part. Nucl. **18**, 546 (1987)].
23. O. Yu. Balashova, N. S. Zelenskaya, and A. A. Ovchinnikova, *Brief Description of Software Means for the Computers of the Institute of Nuclear Physics at Moscow State University* (Mosk. Gos. Univ., Moscow, 1988), p. 97 [in Russian].
24. A. N. Boyarkina, *Structure of 1p-Shell Nuclei* (Mosk. Gos. Univ., Moscow, 1973) [in Russian].
25. V. M. Lebedev, N. V. Orlova, and A. V. Spasskiĭ, Izv. Akad. Nauk, Ser. Fiz. **65**, 724 (2001).
26. F. Ajzenberg-Selove, Nucl. Phys. A **490**, 1 (1988).
27. M. N. Haraken *et al.*, Nucl. Phys. A **344**, 15 (1980).
28. E. Fabrici *et al.*, Phys. Rev. C **21**, 844 (1980).
29. P. D. Kunz and J. Cejpek, *The Niels Bohr Institute, Comp. Prog. Library, Computer Code CHUCK* (1977) (modified by R.N. Boyd, H. Clement, and E. Sugarbarker for the calculation of angular correlations).
30. L. I. Galanina and N. S. Zelenskaya, Izv. Akad. Nauk, Ser. Fiz. **63**, 47 (1999).
31. D. Kurath, Nucl. Phys. A **317**, 175 (1979).
32. J. F. Cavaignac, S. Jang, and D. H. Worledge, Nucl. Phys. A **243**, 349 (1975).
33. T. L. Belyaeva *et al.*, Comput. Phys. Commun. **73**, 161 (1992).

Translated by A. Isaakyan

Physics of Atomic Nuclei, Vol. 68, No. 12, 2005, pp. 1968–1978. Translated from Yadernaya Fizika, Vol. 68, No. 12, 2005, pp. 2030–2041.

NUCLEI
Theory

Quantum and Thermodynamic Properties of Spontaneous and Low-Energy Induced Fission of Nuclei

S. G. Kadmensky*

Voronezh State University, Universitetskaya pl. 1, Voronezh, 394693 Russia

Received February 14, 2005

Abstract—It is shown that A. Bohr's concept of transition fission states can be matched with the properties of Coriolis interaction if an axisymmetric fissile nucleus near the scission point remains cold despite a nonadiabatic character of nuclear collective deformation motion. The quantum and thermodynamic properties of various stages of binary and ternary fission after the descent of a fissile nucleus from the outer saddle point are studied within quantum-mechanical fission theory. It is shown that two-particle nucleon–nucleon correlations—in particular, superfluid correlations—play an important role in the formation of fission products and in the classification of fission transitions. The distributions of thermalized primary fission fragments with respect to spins and their projections onto the symmetry axis of the fissile nucleus and fission fragments are constructed, these distributions determining the properties of prompt neutrons and gamma rays emitted by these fragments. A new nonevaporation mechanism of third-particle production in ternary fission is proposed. This mechanism involves transitions of third particles from the cluster states of the fissile-nucleus neck to high-energy states under effects of the shake-off type that are due to the nonadiabatic character of nuclear collective deformation motion. © *2005 Pleiades Publishing, Inc.*

1. INTRODUCTION

In [1, 2], a quantum-mechanical theory of spontaneous and low-energy induced binary fission of nuclei was formulated within a conceptual framework based on the time-independent formalism of multiparticle nuclear-reaction theory [3, 4] and on the theory of open Fermi systems [5]. This quantum-mechanical theory employs basic achievements of conventional fission theory [6, 7] and develops the quantum-mechanical concepts introduced in [8–11] in describing the differential cross sections for (n, f) reactions involving thermal and polarized resonance neutrons and P-odd and P-even asymmetries of the angular distributions of products originating from such reactions. By using the concept of a wave function for a fissile nucleus and fission fragments and the concept of partial fission widths and potential fission phase shifts, it became possible to take consistently into account in the fission process not only the laws of baryon-number, charge, energy, and parity conservation but also (for the first time) the law of total-angular-momentum conservation for a fissile nucleus with allowance for both spins and relative orbital angular momenta of fission fragments. Within this theory, it was possible to describe [2, 12] the effect of coupling between physical fission channels on the properties of fission and to validate [2] the mechanism of pumping of high values of relative orbital angular momenta and spins of fission fragments. In analyzing experimental angular distributions of fragments originating from the subthreshold photofission of a group of even–even actinide nuclei, this permitted [13] finding the highest value of $L_m \approx 30$ for the relative orbital angular momentum of fission fragments. This result proved to be in reasonable agreement [2, 13] with fission-fragment-spin values that were extracted from an analysis of experimental data [14] on the multiplicity and multipolarity of prompt photons emitted from fission fragments. A generalization of quantum-mechanical fission theory to the case of ternary fission [15, 2] made it possible to describe P-odd [16], P-even [17], and T-odd [18] asymmetries in the angular distributions of products of binary and ternary nuclear fission induced by polarized cold neutrons.

All of the results discussed above were obtained for spontaneous and low-energy induced fission of nuclei under two assumptions of crucial importance. The first is that, in the fission process, a fissile system remains axisymmetric, which is compatible with an analysis of existing experimental data. The second is that the projection K of the spin J of a fissile nucleus onto its symmetry axis is conserved at all fission stages from the descent of the fissile nucleus from the outer saddle point of its deformation potential. These assumptions are perfectly in accord with the conditions of applicability of A. Bohr's concept [6, 7], within which transition fission states formed at

*e-mail: kadmensky@phys.vsu.ru

the saddle points of the deformation potential [these states are characterized by specific values of the spin J, its projection K onto the symmetry axis of the fissile nucleus, and the parity π and are associated with "cold" states of the fissile nucleus] appear as filters for selecting the most probable values of K and determine the basic properties of partial fission widths and angular distributions of fission fragments.

A significant heating both of a fissile nucleus prior to its disintegration to fission fragments and of fission fragments at early stages of their evolution is the main factor that prevents the conservation of the projection K of the transition-fission-state spin in the fission process. Indeed, the heating of an axisymmetric nucleus to relatively high temperatures gives rise to a dynamical enhancement of Coriolis interaction [19, 20]. The inclusion of this effect leads to a uniform statistical mixing of all possible values of the projection K of the spin J of the nucleus onto its symmetry axis at not overly large values of J. By way of example, we indicate that such a situation is realized for resonance states of a compound nucleus in the first well of the deformation potential that are excited upon resonance-neutron capture by rather heavy nuclei, this manifesting itself in that the projection of the spin of the compound nucleus onto its symmetry axis ceases to be an integral of the motion for Wigner ensembles that characterize the experimental distribution of energy spacings between neighboring neutron resonances [6].

Many fission models [21–24] that provide a reasonable description of mass and charge distributions of fission fragments lead to the idea that a nonadiabatic character of the descent of a fissile nucleus from the outer saddle point causes the heating of this nucleus, with the result that, in the vicinity of its scission point, the temperature reaches a value of $T \approx 1$ MeV, which corresponds to an excitation energy of $E^* \approx 30$ MeV for nuclei of mass number $A \approx 240$ [6]. At so high a temperature, there arise, in a fissile nucleus, complex multiquasiparticle states of high density on the energy scale, which are an ideal object for revealing Coriolis interaction. It was shown in [25] that, owing to uniform statistical mixing of the spin projections onto the symmetry axis for such states of a fissile nucleus in the vicinity of the scission point, the fissile nucleus "forgets" K values that were selected by transition fission states; as a result, all anisotropies (including P-odd, P-even, and T-odd asymmetries) in angular distributions of products originating from binary and ternary nuclear fission disappear completely. Since the existence of such anisotropies for low-energy fission induced by polarized neutrons, photons, and other particles was established reliably in experiments [6, 26], we arrive at the conclusion of crucial importance that the fissile system remains cold at all fission stages starting from the descent of the fissile nucleus from the outer saddle point and ending in the formation of the angular distributions of fission products. This conclusion makes it possible to get a fresh look at the physics of the fission process and on the interplay of the quantum and thermodynamic properties of a fissile system for various stages of this process.

2. STAGE OF THE DESCENT OF A FISSILE NUCLEUS FROM THE OUTER SADDLE POINT

Within the concept that the fission barrier has a two-humped shape [6], we will now consider the low-energy binary fission of an axisymmetric compound nucleus that is characterized by a spin J, a spin projection M onto the z axis in the laboratory frame, a parity π, and other quantum numbers σ and which is formed in the first well of the deformation potential upon the capture of a particle initiating the fission process by a target nucleus. If use is made of the strong-coupling approximation in the generalized shell model [6], the multiparticle shell-model wave function $\Psi_\sigma^{J\pi M}(\tau)$ for the compound nucleus can be represented in the form

$$\Psi_\sigma^{J\pi M}(\tau) = \sum_K a_K^J \Psi_{\sigma K}^{J\pi M}(\tau), \qquad (1)$$

where $\Psi_{\sigma K}^{J\pi M}(\tau)$ is the wave function for the compound-nucleus state characterized by the total set of coordinates τ in the c.m. frame and by a fixed value of the projection K of the spin J of the nucleus onto its symmetry axis and the coefficients a_K^J, which were defined in [16], take into account the Coriolis mixing of the aforementioned spin projections [19, 20].

The evolution of a fissile nucleus up to its disintegration into initial fission fragments can be described in terms of a collective nuclear motion that is associated with the change in nuclear deformation parameters [6], in which case it is assumed that the most probable internal states of product initial fission fragments and the most probable values of their relative coordinates are such that they occur in above-barrier states, where the total energy Q of the relative motion of the fragments in question exceeds the height of the potential barrier, which is formed via the summation of the nuclear and Coulomb potentials of fragment interaction. In describing this collective motion, it is necessary to take into account the formation of transition fission states at the inner and outer saddle points of the deformation potential that correspond to cold states of the fissile nucleus being considered [6].

Let us study the fission stage starting from the descent of the fissile nucleus from the outer saddle point and ending in its disintegration into initial fission fragments. Nonadiabatic effects associated

with the fact that, at final steps of this fission stage, the nucleon system of the fissile nucleus does not have time to undergo rearrangement to equilibrium in accordance with fast variations of its deformation parameters play a very important role for this stage. In describing these effects, it is necessary to take into consideration the above conclusion that, at this stage of the fission process, the fissile nucleus cannot undergo significant heating. This immediately leads to the concept that doorway states that are excited in the fissile nucleus because of a nonadiabatic character of its collective deformation motion and which are characterized by a rather simple (few-quasiparticle) structure and by a rather low density on the energy scale do not have time to transform, within this stage, into complex (multiquasiparticle) states corresponding to a full thermalization of the nuclear excitation energy and possessing a high density on the energy scale. For such doorway states, one can disregard the effect of Coriolis interaction and consider the projections K of the spin J in such states as integrals of the motion. The values of K for the doorway states subjected to analysis will coincide with the values of K for the corresponding transition fission states at the outer saddle point of the deformation potential since the shape of the fissile nucleus preserves axial symmetry in the fission process.

As the compound nucleus reaches the scission point, where it will undergo disintegration into initial fragments, its multiparticle shell wave function (1) reduces to the form [16, 17]

$$\Psi_{\sigma}^{J\pi M} = \sum_{r\nu K} \bar{a}_{\sigma r\nu K}^{J\pi} \Psi_{r\nu K}^{J\pi M}(\tau) \qquad (2)$$
$$= \sum_{tpr\nu K} a_K^J b_{t\sigma K}^{J\pi} c_{ptK}^{J\pi} d_{r\nu pK}^{J\pi} \Psi_{r\nu K}^{J\pi M}(\tau),$$

where the coefficient $\bar{a}_{\sigma r\nu K}^{J\pi}$ is expressed in terms of the coefficient a_K^J appearing in (1) and the coefficients $b_{t\sigma K}^{J\pi}$, $c_{ptK}^{J\pi}$, and $d_{r\nu pK}^{J\pi}$ take into account the dynamics of the transitions of the fissile nucleus from the compound-nucleus states σ in the first well of the deformation potential to a transition fission state t at the inner saddle point of the deformation potential, from the state t to a transition fission state p at the outer saddle point of the deformation potential, and from the state p under the effect of nonadiabatic perturbations to a doorway excited state ν of the fission mode r, the quantum numbers $J\pi K$ being conserved in these transitions. In the case of fission that is highly asymmetric in the masses and charges of nascent fragments, in which case the fission mode r is characterized by large static octupole deformations, one can represent, in the strong-coupling approximation, the shell-model wave function $\Psi_{r\nu K}^{J\pi M}$ for the state ν of the fission mode r as [6]

$$\Psi_{r\nu K}^{J\pi M}(\tau) = \sqrt{\frac{2J+1}{16\pi^2}} i^{(1-\pi)/2} \qquad (3)$$
$$\times \Big\{ \delta_{K,0}\sqrt{2} D_{M0}^J(\omega)\chi_{r\nu s}(\xi) + (1-\delta_{K,0})$$
$$\times \left[D_{MK}^J(\omega)\chi_{r\nu K}(\xi) \right.$$
$$\left. + (-1)^{J+K}\pi D_{M-K}^J(\omega)\chi_{\overline{r\nu K}}(\xi) \right] \Big\},$$

where $D_{MK}^J(\omega)$ is a generalized spherical harmonic depending on the Euler angles $\omega \equiv (\alpha, \beta, \gamma)$ that determine the orientation of the symmetry axes of the fissile nucleus with respect to the axes of the laboratory frame. The intrinsic wave functions $\chi_{r\nu s}(\xi)$, $\chi_{r\nu K}(\xi)$, and $\chi_{\overline{r\nu K}}(\xi)$ for the fissile nucleus are not parity eigenstates and depend on the intrinsic coordinates ξ of the fissile nucleus, the set of quantum numbers $J\pi$ for $K = 0$ being determined by the nuclear-state signature s as $J\pi = 0+, 1-, \ldots$ for $s = 1$ and as $J\pi = 0-, 1+, \ldots$ for $s = -1$. As to the function $\chi_{\overline{r\nu K}}(\xi)$ for $K \neq 0$, it is defined as $\chi_{\overline{r\nu K}}(\xi) = \hat{T}\chi_{r\nu K}(\xi)$, where $\hat{T}$ is the time-inversion operator.

3. STAGE OF INITIAL-FISSION-FRAGMENT EVOLUTION AND OF PRIMARY-FISSION-FRAGMENT FORMATION

Let us consider the fission stage at which initial fission fragments arise after the disintegration of a fissile nucleus. As was shown in [23], these fragments, which are at rather short distances from each other, interact strongly and inelastically and exchange nucleons. This fission stage ends in the formation of primary fission fragments, whose intrinsic wave functions are unaffected by the nuclear and Coulomb potentials of fragment interaction. Therefore, these potentials can be expressed in terms of the real parts of the optical potentials of interaction between these fragments.

In order to describe the fission stage being studied, it is necessary to generalize the projection-operator method formulated in [4, 5] and used in developing the quantum-mechanical theory of fission [1, 2]. This method is based on introducing the mutually orthogonal operators $\hat{P}$ and $\hat{Q}$ ($\hat{P} + \hat{Q} = 1$) that project the fissile-nucleus wave function onto, respectively, the internal (shell) and the external (cluster) region of the configuration space of coordinates τ of the fissile nucleus. Further, the operator $\hat{Q}$ can be represented as the sum of two orthogonal operators $\hat{Q}^{\rm in}$ and $\hat{Q}^{\rm pr}$ that project the fissile-nucleus wave function onto the configuration-space regions $\tau^{\rm in}$ and $\tau^{\rm pr}$ associated,

respectively, with the fission stage at which there occurs the evolution of initial fragments up to the formation of primary fission fragments and fission stages embracing the motion and the rearrangement of primary fragments. With the aid of the methods developed in [1, 2, 4, 5], the fissile-nucleus wave function $\left(\Psi_\sigma^{J\pi M}(\tau)\right)^{\text{in}}$ in the configuration-space region singled out by the projection operator $\hat{Q}^{\text{in}}$ can be represented in the form

$$\left(\Psi_\sigma^{J\pi M}(\tau)\right)^{\text{in}} = \left\langle G^{\text{in}}(\tau,\tau')|H|\Psi_\sigma^{J\pi M}(\tau')\right\rangle, \quad (4)$$

where H is the total Hamiltonian for the fissile nucleus and $G^{\text{in}}(\tau,\tau')$ is the multiparticle Green's function for the fissile system in the configuration-space region τ^{in}. In order to construct the function $G^{\text{in}}(\tau,\tau')$, we introduce the channel function U_α^{JM} describing a fissile-nucleus state in the cluster region, where fission fragments have already been formed, and possessing correct transformation properties with respect to time inversion. Its specific form is

$$U_\alpha^{JM} = \left\{\left\{\Psi_{\sigma_1 K_1}^{J_1\pi_1 M_1}(\omega_1,\xi_1)\Psi_{\sigma_2 K_2}^{J_2\pi_2 M_2}(\omega_2,\xi_2)\right\}_{FM_F} \times i^L Y_{LM_L}(\Omega)\right\}_{JM}, \quad (5)$$

where the braces denote the vector composition of angular momenta and the spherical harmonic $Y_{LM_L}(\Omega)$ depends in the solid angle $\Omega \equiv (\theta,\varphi)$ that specifies the direction of the point-to-point vector between the two fragments (the direction of their relative motion) in the laboratory frame, $\mathbf{R} = \mathbf{R}_{A_1} - \mathbf{R}_{A_2}$, $\mathbf{R}_{A_i}$ being the c.m. coordinate of the ith fragment. The channel index α is defined as $\alpha \equiv c\beta L$, where $c \equiv \pi_1\sigma_1 K_1 \pi_2\sigma_2 K_2$ and $\beta \equiv J_1 J_2 F$. In (5), $\Psi_{\sigma_i K_i}^{J_i\pi_i M_i}(\omega_i,\xi_i)$ is the multiparticle shell-model wave function for the ith fission fragment ($i = 1, 2$) possessing an axisymmetric shape in the absence of odd deformations (including octupole deformations). In the strong-coupling approximation [6], we have

$$\Psi_{\sigma_i K_i}^{J_i\pi_i M_i}(\omega_i,\xi_i) = \sqrt{\frac{2J_i+1}{16\pi^2}}(1+\delta_{K_i,0}(\sqrt{2}-1)) \times \left[D_{M_i K_i}^{J_i}(\omega_i)\chi_{\sigma_i K_i}^{\pi_i}(\xi_i) + (-1)^{J_i+K_i} D_{M_i -K_i}^{J_i}(\omega_i)\chi_{\frac{\pi_i}{\sigma_i K_i}}(\xi_i)\right], \quad (6)$$

where ω_i are the Euler angles that characterize the orientation of the symmetry axes of the fragments with respect to the axes of the laboratory frame; ξ_i is the set of internal coordinates of the ith fragment; and $\chi_{\sigma_i K_i}^{\pi_i}(\xi_i)$ and $\chi_{\frac{\pi_i}{\sigma_i K_i}}(\xi_i)$ are, respectively, the intrinsic wave function for the corresponding fragment and its conjugate counterpart.

By using the transformation of the generalized spherical harmonics $D_{M_i K_i}^{J_i}(\omega_i)$ and the spherical harmonics $Y_{LM_L}(\Omega)$ to the intrinsic coordinate frame of the fissile nucleus and the addition theorem for generalized spherical harmonics, we can represent the channel function U_α^{JM} for the case of $K_1 \neq 0$ and $K_2 \neq 0$ in the form [1]

$$\begin{aligned} U_\alpha^{JM} &= \sqrt{\frac{(2J_1+1)(2J_2+1)}{(16\pi^2)^2}} \\ &\times \sum_{K'K_1'K_2'K_L} C_{FLK_F K_L}^{JK'} C_{J_1 J_2 K_1' K_2'}^{FK_F} D_{MK'}^{J}(\omega) \\ &\times i^L Y_{LK_L}(\Omega')\left\{D_{K_1'K_1}^{J_1}(\omega_1')D_{K_2'K_2}^{J_2}(\omega_2')\chi_{\sigma_1 K_1}^{\pi_1}(\xi_1)\right. \\ &\times \chi_{\sigma_2 K_2}^{\pi_2}(\xi_2) + (-1)^{J_1+K_1} D_{K_1' -K_1}^{J_1}(\omega_1')D_{K_2'K_2}^{J_2}(\omega_2') \\ &\times \chi_{\frac{\pi_1}{\sigma_1 K_1}}(\xi_1)\chi_{\sigma_2 K_2}^{\pi_2}(\xi_2) + (-1)^{J_2+K_2} D_{K_1'K_1}^{J_1}(\omega_1') \\ &\times D_{K_2' -K_2}^{J_2}(\omega_2')\chi_{\sigma_1 K_1}^{\pi_1}(\xi_1)\chi_{\frac{\pi_2}{\sigma_2 K_2}}(\xi_2) \\ &+ (-1)^{J_1+J_2+K_1+K_2} D_{K_1' -K_1}^{J_1}(\omega_1') \\ &\left.\times D_{K_2' -K_2}^{J_2}(\omega_2')\chi_{\frac{\pi_1}{\sigma_1 K_1}}(\xi_1)\chi_{\frac{\pi_2}{\sigma_2 K_2}}(\xi_2)\right\}, \end{aligned} \quad (7)$$

where Ω' is the solid angle of the radius $\mathbf{R}$ and ω_i' stands for the Euler angles that specify the orientation of the symmetry axes of the ith fission fragment with respect to the symmetry axes of the fissile nucleus. Similar expressions can also be obtained for the cases where both values of K_i or one of them is zero.

In constructing the Green's function $G^{\text{in}}(\tau,\tau')$, one must consider that, in the configuration-space region τ^{in}, the fissile nucleus has a compact shape since initial fission fragments interact inelastically at rather short relative distances. By using the methods developed in [2, 12] and the concepts of R-matrix nuclear-reaction theory [3], we can express the Green's function $G^{\text{in}}(\tau,\tau')$ in terms of the regular and irregular solutions to the Schrödinger equation [$f_{nK}^{J\pi M}(\tau)$ and $g_{nK}^{J\pi M}(\tau)$, respectively] for the fissile nucleus in the region τ^{in}. Specifically, we have

$$G^{\text{in}}(\tau,\tau') = B\sum_n g_{nK}^{J\pi M}(\tau_>)f_{nK}^{J\pi M}(\tau_<), \quad (8)$$

where B is a normalization constant and the index $\tau_>$ ($\tau_<$) includes the larger (smaller) of the absolute values of the vectors R and R', which enter into the definition of, respectively, the total sets τ and τ' of coordinates of the fissile nucleus. In turn, the functions

$f_{nK}^{J\pi M}(\tau)$ and $g_{nK}^{J\pi M}(\tau)$ are given by

$$f_{nK}^{J\pi M}(\tau) = \sum_{\alpha} U_{\alpha}^{JM} \frac{f_{\alpha nK}^{J\pi}(R)}{R}, \qquad (9)$$

$$g_{nK}^{J\pi M}(\tau) = \sum_{\alpha} U_{\alpha}^{JM} \frac{g_{\alpha nK}^{J\pi}(R)}{R},$$

where $f_{\alpha nK}^{J\pi}(R)$ and $g_{\alpha nK}^{J\pi}(R)$ are, respectively, the regular and irregular radial form factors that are defined as solutions to coupled radial equations with real boundary conditions corresponding to the appearance of standing waves in a finite range of the coordinate R in the configuration-space region τ^{in}. With the aid of Eq. (2), the fissile-nucleus wave function $(\Psi_{\sigma}^{J\pi M}(\tau))^{\text{in}}$ for the formation of primary fission fragments, which is the final step of the stage being considered, can be represented in the form

$$(\Psi_{\sigma}^{J\pi M}(\tau))^{\text{in}} = \sum_{r\nu nK} \bar{a}_{\sigma r\nu K}^{J\pi} h_{r\nu nK}^{J\pi} g_{nK}^{J\pi M}(\tau), \qquad (10)$$

where the coefficient $h_{r\nu nK}^{J\pi}$ determines the amplitudes for the transition of the fissile nucleus from the prescission configuration $r\nu K$ to the state $f_{nK}^{J\pi}$ of primary fission fragments.

Owing to the fact that the time t_{in} of the fission stage being studied is short, we can deem that the Euler angles ω_i', which appear in Eq. (7) and which specify the orientation of the symmetry axes of primary fission fragments with respect to the symmetry axes of the fissile nucleus, are close to zero. In this case, the projections of the spins J_i of fully developed primary fission fragments onto the symmetry axis of the fissile nucleus (K_i') and onto the fragment symmetry axes (K_i) coincide by virtue of the identity $D_{K_i'K_i}^{J_i}(\omega_i' = 0) = \delta_{K_i',K_i}$ for generalized spherical harmonics. Considering that, in the case where the symmetry axes of fission fragments are aligned with the symmetry axes of the fissile nucleus, the projections K_L of the relative orbital angular momenta L of the fission fragments onto the symmetry axis of the fissile nucleus vanish in view of axial-symmetry conservation for a fissile system in the fission process, one can recast expression (7) for the channel function U_{α}^{JM} into the form

$$U_{\alpha}^{JM} = \sqrt{\frac{(2J_1+1)(2J_2+1)}{(16\pi^2)^2}} C_{FLK_F0}^{JK} i^L Y_{L0}(\Omega') \qquad (11)$$

$$\times D_{MK}^{J}(\omega) \Big\{ C_{J_1J_2K_1K_2}^{FK_F} \chi_{\sigma_1K_1}^{\pi_1}(\xi_1) \chi_{\sigma_2K_2}^{\pi_2}(\xi_2)$$

$$+ (-1)^{J_1+J_2+K_1+K_2} C_{J_1J_2-K_1-K_2}^{FK_F}$$

$$\times \chi_{\overline{\sigma_1}K_1}^{\pi_1}(\xi_1) \chi_{\overline{\sigma_2}K_2}^{\pi_2}(\xi_2) \Big\},$$

where we imply the case of $|K| = K_1 + K_2$.

Although superfluid nucleon–nucleon correlations are strongly suppressed by blocking effects [6] caused by the appearance of excited doorway states in the fission process, these correlations may survive in the fissile nucleus and initial fission fragments if they remain cold within the fission stage being considered. By analogy with alpha and cluster decays of heavy nuclei (see [27] and [28], respectively), one can expect in this case that facilitated fission transitions for which primary fission fragments are formed without breaking Cooper pairs of nucleons occurring in the prescission configuration $r\nu K$ of the fissile nucleus will proceed with the highest probability. It is most likely that initial fission fragments will then exchange nucleons in the form of Cooper pairs rather than in the form of individual nucleons. To some extent, this form of nucleon exchange is similar to the Josephson effect in superconductors. Since Cooper pairs of nucleons have a positive parity and zero projections of their total spin onto the symmetry axis of the fissile nucleus, the relative orbital angular momenta L, parities π_i, spins J_i, and spin projections K_i for primary fission fragments from facilitated fission transitions must have minimum values compatible with manifestations of superfluid correlations and with the laws of conservation of parity π, spin J, and its projection K for a fissile nucleus.

In just the same way as in the case of alpha [27] and cluster [28] decays of nuclei, the probabilities of the formation of initial and primary fission fragments via the rupture of one Cooper pair in the prescission configuration $r\nu K$ of the fissile nucleus (this case corresponds to a first-order-forbidden fission transition) must be reduced in relation to the probability of the formation of the same fragments via the facilitated fission transition. Apparently, the classification of fission transitions according to the order in which they are forbidden makes it possible to explain even–odd effects observed experimentally in [29] in the charge distributions of final fission fragments.

4. STAGE OF THE SEPARATION OF COLD PRIMARY FISSION FRAGMENTS

Primary fragments formed at the final step of the preceding fission stage are in cold states that are, however, strongly nonequilibrium in energy and deformation parameters. We will now study the fission stage within which cold primary fragments move apart. This stage is characterized by a time t_0 that is much shorter than the time it takes for the primary fragments to go over to equilibrium thermalized states. For the condition ensuring the validity of the concept of transition fission states to be met, it is necessary that the angular distributions of primary

fission fragments be fully formed within the time t_0 in order that the subsequent stage involving the thermalization of primary fragments could not change these angular distributions. This is possible if, within the time t_0, primary fission fragments move apart at rather long distances that exceed R_{sc} considerably (where R_{sc} is the distance between the fragments at the scission point), in which case it is legitimate to disregard long-range nonspherical components of the Coulomb potential of interaction between primary fission fragments [2] (these components could change the angular distributions of these fragments at the next fission stage).

As was shown in [1, 2, 11], the real-valued amplitude $\sqrt{\Gamma^{J\pi}_{\sigma K\alpha}}$ of the partial width with respect to fission from the state $\Psi^{J\pi M}_{\sigma K}$ (1) of the compound nucleus and the potential fission phase shift $\delta^{J\pi}_{\alpha}$ can be found from the equation

$$e^{i\delta^{J\pi}_{\alpha}}\sqrt{\Gamma^{J\pi}_{\sigma K\alpha}} = \sqrt{2\pi}\sum_{\alpha'}\sum_{r\nu n}\bar{a}^{J\pi}_{\sigma r\nu K}h^{J\pi}_{r\nu nK} \qquad (12)$$
$$\times\left\langle U^{JM}_{\alpha'}\frac{f^{J\pi(-)}_{\alpha'\alpha}(R)}{R}|H|g^{J\pi M}_{nK}\right\rangle,$$

where the wave function $g^{J\pi M}_{nK}$ and the coefficient $h^{J\pi}_{r\nu nK}$ are given by (10), while the radial form factors $f^{J\pi(-)}_{\alpha'\alpha}(R)$ are found [2, 12] as solutions to coupled radial equations for the case of boundary conditions at large R in the form of diverging spherical waves in channel α and incident spherical waves in channels α'. The fission stage being considered determines completely the amplitudes $\sqrt{\Gamma^{J\pi}_{\sigma K\alpha}}$ and the potential fission phase shifts $\delta^{J\pi}_{\alpha}$, since the overlap integrals appearing in (12) are different from zero in the region of R values in the vicinity of the point R_{pr} at which primary fission fragments are formed, $R \approx R_{pr} \approx R_{sc}$.

For the fission stage being studied, one can make use of the adiabatic approximation [1], which relies on the fact that the relative radial motion of primary fission fragments, which is associated with the change in the absolute value of the vector **R**, is faster than the relative angular and rotational motions of these fragments.

As was shown in [1], only if this approximation is valid are the spherical harmonics $Y_{L0}(\Omega')$, which appear in the channel function (11), coherently mixed, which ensures the emission of primary fission fragments in a direction close to the symmetry axis of the fissile nucleus. This indicates that A. Bohr's formula [6], which was successfully tested [6, 10, 11, 13, 18, 26] in describing the experimental angular distributions and P-odd, P-even, and T-odd correlations in the angular distributions of products originating from induced low-energy fission of nuclei, is approximately valid.

The following conditions must be satisfied for the adiabatic approximation to be applicable. First, it is necessary that, for all open channels c, the kinetic energy $E^{kin}_{c}(R_{pr})$ of the relative motion of primary fragments be much greater than the centrifugal potential

$$\frac{\hbar^2 L(L+1)}{2M_c R^2_{pr}},$$

where M_c is the reduced mass of primary fission fragments in the channel c that is associated with all possible values of the relative orbital angular momentum L of primary fission fragments. If this condition is satisfied, the fission phase shifts $\delta^{J\pi}_{\alpha}$ appear to be independent of L. Second, it is necessary that, for all possible values of the fragment spins J_i, the kinetic energy $E^{kin}_{c}(R_{pr})$ be much greater than the rotational energy of each primary fission fragment,

$$E^{rot}_{i} = \frac{\hbar^2 J_i(J_i+1)}{2\mathcal{J}_i}.$$

Here, $\mathcal{J}_i$ is the moment of inertia of the ith fragment. This condition makes it possible to treat the potential fission phase shifts $\delta^{J\pi}_{\alpha}$ as quantities independent of the spins J_i and the total spin F of primary fission fragments. Finally, it is necessary that, for all possible values of the fragment spins J_i, the time t_0 of the fission stage being considered be much shorter than the spinning periods $t^{rot}_{i} = 2\pi\mathcal{J}_i/(\hbar J_i)$ [6] of primary fission fragments. Owing to this condition, one can deem that the symmetry axes of primary fission fragments are coincident with the symmetry axes of the fissile nucleus and employ expression (11) for the channel functions U^{JM}_{α}.

It was shown in [2] that, in the case where the symmetry axes of primary fission fragments coincide with the symmetry axes of the fissile nucleus, the nonspherical components of the nuclear and Coulomb potentials of the interaction between primary fission fragments depend on the quantity

$$Y_{20}(\Omega') = \sum_{m} D^{(2)}_{m0}(\omega)Y_{2m}(\Omega).$$

It should be noted that its application to the generalized wave function $D^{J}_{MK}(\omega)$ appearing in the definition of the fissile-nucleus wave function does not change the projection K of the spin J of the fissile nucleus onto its symmetry axis. The inclusion of the effect of the aforementioned nonspherical components of the interaction potentials leads to [2] the realization of the mechanism that gives rise to the

pumping of high values of the relative orbital angular momentum L and the spins J_i of primary fission fragments, in which case the maximum values of the relative orbital angular momenta L and the spins J_i of the fragments may become as high as $L_m \approx 30$ and $J_{1m} \approx J_{2m} \leq 12$. In this case, the spins $\mathbf{J}_i$ of primary fission fragments at rather high values of the relative orbital angular momentum L of primary fragments ($L \gg J$) are parallel to each other and are orthogonal to the symmetry axis of the fissile nucleus, this being confirmed by the experiments reported in [17] and devoted to studying the angular distributions of prompt photons emitted by fragments at subsequent fission stages.

If use is made of the above conditions, the partial-fission-width amplitude $\sqrt{\Gamma^{J\pi}_{\sigma K\alpha}}$ (12) can be represented in the form [1, 2]

$$\sqrt{\Gamma^{J\pi}_{\sigma K\alpha}} = \sum_{r\nu n} \bar{a}^{J\pi}_{\sigma r\nu K} h^{J\pi}_{r\nu nK} \sqrt{\Gamma^{J\pi}_{nK\alpha}} \tag{13}$$

$$= \sqrt{\frac{(2J_1+1)(2J_2+1)}{2J+1}} C^{JK}_{FLK0} C^{FK}_{J_1J_2K_1K_2} \times \sqrt{2L+1}\Theta(L_m - L)\Theta(J_{1m} - J_1) \times \Theta(J_{2m} - J_2) p_L \sum_{r\nu n} \bar{a}^{J\pi}_{\sigma r\nu K} h^{J\pi}_{r\nu nK} A_{nKc},$$

where $\sqrt{\Gamma^{J\pi}_{nK\alpha}}$ is the amplitude of the fission width associated with the transition of the fissile nucleus to the state $f^{J\pi}_{nK}$, $\Theta(x)$ is the Heaviside step function, the factor $p_L = [1 + (-1)^L \pi\pi_1\pi_2]/2$ takes into account the parity-conservation law, and the amplitude A_{nKc} is determined by the overlap integrals of the orthogonal radial form factors $f^{J\pi(-)}_{\alpha'\alpha}(R)$ and $g^{J\pi}_{\alpha nK}(R)$ appearing in the definition of the fissile-nucleus wave functions at the fission stage being studied and the stage that precedes it. Taking into account the orthogonality of the intrinsic wave functions for initial fission fragments formed from different prescission states $r\nu n$ of the fissile nucleus and using expressions (1) and (10), we can then represent the total width $\Gamma^{J\pi}_{\sigma}$ of the compound nucleus with respect to fission from the state $\Psi^{J\pi M}_{\sigma}$ (1) in the form

$$\Gamma^{J\pi}_{\sigma} = \sum_K \left|a^J_K\right|^2 \Gamma^{J\pi}_{\sigma K} = \sum_{\alpha K} \left|a^J_K\right|^2 \Gamma^{J\pi}_{\sigma K\alpha} \tag{14}$$

$$= \sum_{Kr\nu n} \left|\bar{a}^{J\pi}_{\sigma r\nu K}\right|^2 \left|h^{J\pi}_{r\nu nK}\right|^2 \Gamma^{J\pi}_{nK}.$$

In turn, the total fission width $\Gamma^{J\pi}_{nK}$ of the fissile-nucleus states described by the wave function $g^{J\pi M}_{nK}$ (9) can be represented in the form

$$\Gamma^{J\pi}_{nK} = \sum_c \Gamma^{J\pi}_{nKc} = \sum_{cJ_1J_2FL} \left(C^{JK}_{FLK0}\right)^2 \left(C^{FK}_{J_1J_2K_1K_2}\right)^2 \times \frac{(2J_1+1)(2J_2+1)(2L+1)}{2J+1} \times \Theta(L_m - L)\Theta(J_{1m} - J_1)\Theta(J_{2m} - J_2) p_L |A_{nKc}|^2. \tag{15}$$

Performing summation over the indices L and F in (15), we can recast the total fission width $\Gamma^{J\pi}_{\sigma}$ (14) into the form

$$\Gamma^{J\pi}_{\sigma} = \sum_{Kr\nu n} \left|\bar{a}^{J\pi}_{\sigma r\nu K}\right|^2 \left|h^{J\pi}_{r\nu nK}\right|^2 \times \sum_{cJ_1J_2} (2J_1+1)(2J_2+1) \times \Theta(J_{1m} - J_1)\Theta(J_{2m} - J_2)|A_{nKc}|^2. \tag{16}$$

This formula determines the character of spin populations of states of primary fission fragments at the final step of the fission stage being studied.

The large-R asymptotic behavior of the wave function describing this fission stage is given by [1, 2]

$$\Psi^{J\pi M}_{\sigma} \to \sum_{K\alpha} \frac{\exp\left[i\left(k_\alpha R - \frac{L\pi}{2}\right)\right]}{R} \times U^{JM}_{\alpha} a^J_K \sqrt{\Gamma^{J\pi}_{\sigma K\alpha}} e^{i\delta^{J\pi}_{\alpha}}, \tag{17}$$

where the channel function U^{JM}_{α} and the partial-fission-width amplitude $\sqrt{\Gamma^{J\pi}_{\sigma K\alpha}}$ are defined in (11) and (13), respectively, and k_α is the wave vector of the relative motion of fission fragments in channel α. Considering that the potential fission phase shifts $\delta^{J\pi}_{\alpha}$ are independent of the indices J_1, J_2, F, and L, we can perform summation over J_1, J_2, and F in (17). Calculating the fission-fragment flux in the direction of the vector $\mathbf{R}$ at large R [1], we obtain the angular distribution $dP^{J\pi M}_{\sigma}(\theta)/d\Omega$ of fission fragments. The result normalized to unity is

$$\frac{dP^{J\pi M}_{\sigma}(\theta)}{d\Omega} = (\Gamma^{J\pi}_{\sigma})^{-1} \sum_K \Gamma^{J\pi}_{\sigma K} \left|a^J_K\right|^2 \frac{2J+1}{16\pi^2} \times \int d\omega \left[\left|D^J_{MK}(\omega)\right|^2 + \left|D^J_{M-K}(\omega)\right|^2\right] F(L_m, \Omega'). \tag{18}$$

The normalized (to unity) angular distribution of fission fragments in terms of the body-frame coordinates of the fissile nucleus, $F(L_m, \Omega')$, has the form

$$F(L_m, \Omega') = \left\{\sum_{L=0}^{L_m} (2L+1) p_L\right\}^{-2} \tag{19}$$

$$\times \left\{ \sum_{L=0}^{L_m} \sqrt{(2L+1)} p_L Y_{L0}(\Omega') \right\}^2 .$$

It approximately corresponds to the escape of fission fragments within a cone whose axis is aligned with symmetry axis of the fissile nucleus and whose apex angle is $\Delta\theta \sim 1/L_m$. In the limit $L_m \to \infty$, expression (18) reduces to A. Bohr's formula [6, 7], which is widely used in describing experimental angular distributions of nuclear-fission fragments.

5. THERMALIZATION OF PRIMARY FISSION FRAGMENTS

The next fission stage is that within which primary fission fragments that arose in cold states that are nonequilibrium in energies and deformation parameters go over to thermalized equilibrium states characterized by temperatures T_i. Since the fissile nucleus remains cold up to the instant of its disintegration into initial fission fragments and since initial and primary fission fragments remain cold within the preceding fission stages, processes that lead to the thermalization of the first and second primary fragments proceed independently. As a result, the temperatures T_i of primary fission fragments can be markedly different.

Since the nonspherical components [2] of the potential of the interaction between primary fragments are negligible within the fission stage being studied, the projections K_i of the fragment spins J_i onto the symmetry axis of the fissile nucleus are integrals of the motion within the thermalization stage and therefore retain their values determined by the preceding stage of fission. Only the projections K_i' of the spins J_i onto the symmetry axes of the fragments change under the effect of Coriolis interaction.

It should be emphasized here that, at the fission stage being considered, the symmetry axes of fission fragments no longer coincide with the symmetry axis of the fissile nucleus, while the channel function U_α^{JM} for thermalized primary fission fragments has the form (7), where the indices K_i and K_i' are interchanged and where the additional factors $\tilde{a}_{K_i'}^{J_i}$, whose squares are normalized to unity and which are determined by the mixing of the projections K_i' in the thermalized states under the effect of Coriolis interaction, are introduced in the summand of the sum over K_i'. Upon substituting these channel functions for the functions U_α^{JM} (11) into (17) and employing Eq. (13), one can obtain the large-R asymptotic behavior of the fissile-nucleus wave function for the fission stage being considered. As might have been expected, the resulting asymptotic expression leads to the angular distribution of thermalized fission fragments that is coincident with the angular distribution (18), which was formed at the preceding stage of fission.

In analyzing the states of the ith axisymmetric thermalized primary fission fragment, we can make use of formulas for the equilibrium nuclear-level density $\rho_T(J_i, K_i')$ on the energy scale in this fragment at fixed values of the fragment spin J_i and its projection K_i' ($K_i' \leq J$) onto the symmetry axis of the fragment at temperature T [6]. Its specific form is

$$\rho_T(J_i, K_i') = \frac{1}{\sqrt{2\pi}} \sigma^{-1} \exp\left\{ -\frac{1}{T} \left[\frac{\hbar^2}{2\mathcal{I}} J_i(J_i+1) + \left(\frac{\hbar^2}{2\mathcal{I}_3} - \frac{\hbar^2}{2\mathcal{I}_i} \right) (K_i')^2 \right] \right\} \rho_T^{\text{int}}, \quad (20)$$

where ρ_T^{int} is the density of intrinsic nuclear states on the energy scale and $\sigma = \hbar^2/(T\mathcal{I}_3)$, $\mathcal{I}$ and $\mathcal{I}_3$ being the effective moments of inertia of the nucleus for rotation about, respectively, an axis orthogonal to the symmetry axis of the nucleus and its symmetry axis. For rather high nuclear temperatures T exceeding the critical temperature T_{cr} ($T_{\text{cr}} \approx 6.8\ A^{-1/2}$ MeV, where A is the mass number of the nucleus), in which case superfluid nucleon–nucleon correlations disappear, the moments of inertia $\mathcal{I}$ and $\mathcal{I}_3$ prove to be close to their rigid-body values [6]. From (20), it follows that, at spin values of $J_i \ll J_0 \equiv \sqrt{2\mathcal{I}T/\hbar^2}$, the nuclear-level density is virtually independent of J_i and K_i', so that, at rather high temperatures T, the inclusion of Coriolis interaction leads to a uniform statistical mixing of possible values of the projections K_i' of these spins. At spin values of $J_i > J_0$, the level density (20) is substantially lower than that in the case of $J_i \ll J_0$, with the result that the mixing effect of Coriolis interaction becomes weaker. In the case where the maximum spins J_{im} of primary fragments [these quantities appear in (16)] exceed considerably J_{0i} owing to the pumping mechanism [2], one can therefore expect that, in thermalized primary fission fragments, there will appear $J_{0i} \ll J_i \leq J_{im}$ states that cannot be affected substantially by the thermalization of fragments, so that the projections K_i' of the spins J_i onto the symmetry axes of fission fragments for these states are hardly mixed by Coriolis interaction and are close to K_i.

6. EMISSION OF PROMPT NEUTRONS AND PHOTONS BY THERMALIZED FISSION FRAGMENTS AND FORMATION OF FINAL FISSION FRAGMENTS

The fission stage following the thermalization of primary fission fragments is that at which these fragments emit prompt neutrons (the characteristic time

is $t_n \geq 10^{-16}$ s) and prompt photons (the characteristic time is $t_\gamma \geq 10^{-12}$ s), whereupon there occurs the formation of final fission fragments in ground or long-lived isomeric states. Since final fragments are neutron-rich, they are involved at the next fission stage (which is not considered here) in beta-decay processes leading to the emergence of delayed neutrons and photons.

At the fission stage being studied, the angular distributions of thermalized primary fission fragments have already been formed, while the kinetic energies of their relative motion are close to the total energy Q_c of the relative motion of these fragments in the fission channel c. Because of high momenta of the fragments, one can expect that the angular distributions of fragments will not change substantially at this fission stage upon the emission of prompt neutrons and photons, which possess rather low energies and, hence, rather low momenta.

In describing the multiplicities and angular and energy distributions of prompt neutrons and photons emitted by thermalized primary fission fragments, it is necessary to take into account not only the relative velocity of these fragments but also some of their other features, such as the excitation energy E_i^* and the spin distributions, which are given by (20). In view of the fact that the projections K_i' of the spins of thermalized primary fragments onto the symmetry axis of the fissile nucleus are much lower than the maximum spins J_{im} of these fragments because of the effect of superfluid correlations at the stage of primary-fission-fragment formation, the fission-fragment spins are approximately orthogonal to the symmetry axis of the fissile nucleus; that is, the spins of the fragments are aligned with respect to the direction along which they move apart and which is nearly coincident with the symmetry axis of the fissile nucleus [12]. This alignment leads to an additional anisotropy in the angular distributions of prompt neutrons emitted by thermalized fragments.

7. STAGES OF TERNARY NUCLEAR FISSION

With the aid of the methods of quantum-mechanical fission theory [2, 15–17], the results obtained above in describing various stages of the low-energy binary fission of nuclei can be generalized to the case of ternary nuclear fission. The statement made in the Introduction that both the fissile nucleus in the region where the products of ternary fission (two rather heavy fragments and a third particle, which is light) are formed and these products at the first stages of their evolution are cold is at odds with a number of ternary-fission models [30–32] relying on the evaporation mechanism of the formation of a third particle and its emission from the neck of a fissile nucleus heated to a rather high temperature. The analysis performed in [16, 17] in order to clarify the nature of P-odd and P-even correlations in the angular distributions of a third particle originating from ternary nuclear fission induced by polarized cold neutrons confirmed the one-step character of the ternary-fission process, in which case a third particle is formed by nucleons of the fissile-nucleus neck rather than by nucleons of one of the nascent fission fragments, predominantly a light one.

The emergence of a third particle leads to a decrease in the kinetic energy of relative motion and in the excitation energy of two ternary-fission fragments in relation to the analogous energies of binary-fission fragments. Also, this leads to some changes in the charge and mass distributions of ternary-fission fragments with respect to the corresponding distributions of binary-fission fragments.

With allowance for these factors, the stages of evolution of ternary-fission fragments are analogous to the stages of binary nuclear fission, which were considered above. In describing the ternary fission of nuclei, attention should therefore be given primarily to the formation of third particles and their subsequent motion.

The concept that the fissile nucleus is cold requires introducing a mechanism of third-particle formation in ternary nuclear fission other than the evaporation mechanism. Such a mechanism was proposed in [33, 34] for the case where a deuteron, a triton, or an alpha particle was considered for a third particle. This mechanism implies that transitions of these particles from surface cluster states of the fissile nucleus to high-energy states of these particles occur under shake-off effects that are due to the nonadiabatic character of the collective deformation motion of the fissile nucleus at the stage of its descent from the outer saddle point. By analogy with binary fission, these high-energy states can be treated as nonthermalized excited cluster states of the fissile nucleus that are doorway states for the emission of third particles in the ternary fission of nuclei. However, the mechanism proposed in [33, 34] calls for a substantial revision, especially in the case where the ternary-fission process involves third particles of structure different from that of deuterons, tritons, and alpha particles. This could be done by changing the ideas of the nature of third-particle states in the fissile nucleus.

It can be conjectured that nucleons forming the fissile-nucleus neck, which is situated between fission prefragments, are rather well separated from nucleons forming the prefragments. With allowance for the fact that the number of nucleons forming the neck is not overly large, the neck can then be considered as an

analog of a light nucleus enriched in neutrons to a considerable extent. It was shown in [35–37] that the spectroscopic factors of deuteron, triton, alpha-particle, and heavier clusters in light nuclei ($A \leq 16$) take values that do not differ markedly from unity and that their form factors are of a volume character. Therefore, the probabilities of the formation of light third particles (we denote by A_3 their atomic weight) in the region of the fissile-nucleus neck are rather high, decreasing substantially only for $A_3 > 20$ third particles, which include nucleons not only from the fissile-nucleus neck but also from fission prefragments. The spectroscopic factors for rather light third particles in ground and low-lying excited states (the latter are filled upon one- and two-nucleon transitions in these particles) take rather close values, this making it possible to explain comparatively high yields obtained in [38] for excited states of ^{5}He, ^{7}He, and ^{8}Li nuclei in the spontaneous ternary fission of ^{252}Cf nuclei.

Since a fissile nucleus is cold within the nonadiabatic segments of its descent from the outer saddle point, superfluid and other two-particle nucleon–nucleon correlations are expected to play an important role, as they do in the binary-fission case, in the formation of ternary-fission fragments and third particles as clusters formed by nucleons of the fissile-nucleus neck. The inclusion of these correlations enables one to explain even–odd charge and mass effects in the yields of third particles for ternary fission of nuclei [39, 40].

If we now take into consideration a shake-off mechanism [33] that is due to the nonadiabatic character of changes in the collective deformation parameters of the fissile nucleus at final stages of its descent from the outer saddle point and which leads to transitions of third particles from bound cluster states of the fissile-nucleus neck to continuum states, there arises the possibility of describing the yields and energy distributions of third particles in ternary nuclear fission with allowance for the time-dependent Coulomb barrier determined as the sum of the Coulomb and nuclear potentials of the interaction between third particles and ternary-fission fragments moving apart.

Taking into account superfluid and other two-particle nucleon–nucleon correlations and the fact that the axial symmetry of a fissile system is conserved in the ternary-fission process, one can arrive at the conclusion that the relative orbital angular momenta l of the third particle and their projections K_l onto the symmetry axis of the fissile nucleus take predominantly zero value. The structure of the nonspherical part of the potential of the interaction between the third particle and ternary-fission fragments [2] leads to the conservation of the projection $K_l = 0$ and to the mechanism that, owing to the focusing character of this potential, gives rise to the pumping of relative orbital angular momenta l of the third particle, as well as to the allied mechanism of pumping [2] of high relative orbital angular momenta L and spins J_i ($i = 1, 2$) of fragments from binary and ternary nuclear fission. By taking the above results into account, one can explain the structure of angular distributions of third particles [15] and the nature of P-odd [16], P-even [17], and T-odd [18] correlations in ternary nuclear fission.

8. CONCLUSIONS

The above analysis performed within quantum-mechanical fission theory in order to explore various stages of low-energy induced binary fission of a compound nucleus that start from its descent from the outer saddle point and which end in the formation of final fission fragments has led to a number of important conclusions.

First, the states of a fissile nucleus and primary fission fragments at the stage of the disintegration of an axisymmetric fissile nucleus and the stages of formation of primary fission fragments and their subsequent motion are excited, but they are cold and strongly nonequilibrium. This makes it possible to disregard the effect of Coriolis interaction, in which case the projections K of the spin J of the fissile nucleus onto its symmetry axis that are formed by transition fission states survive as integrals of the motion.

Second, superfluid nucleon–nucleon correlations have a pronounced effect on the nuclear-fission process owing to the fact that the fissile nucleus and initial and primary fission fragments are cold.

Third, the two primary fission fragments are thermalized independently, which, in general, gives rise to different temperatures of these fragments.

Fourth, the dynamical mechanism of pumping of high values of the relative orbital angular momenta and spins of cold primary fission fragments makes it possible to explain the observed angular distributions of final fragments and the character of the spin and spin-projection populations of states of thermalized primary fission fragments. This is reflected in describing the properties of prompt neutrons and photons emitted by these fragments.

A generalization of these results to the case of ternary nuclear fission has led to the conclusion that the evaporation mechanism of third-particle formation in a hot nucleus is invalid. Instead, the mechanism is operative according to which third particles are formed in volume cluster states of a few-nucleon system corresponding to the fissile-nucleus neck and are emitted from these cluster states to high-energy states under effects of the shake-off type that are due to the nonadiabatic character of the collective

deformation motion of the fissile nucleus at the final steps of its descent from the outer saddle point.

ACKNOWLEDGMENTS

I am grateful to V.E. Bunakov, F. Gönnenwein, and G.A. Petrov for stimulating discussions and L.V. Rodionova for assistance in performing this study.

This work was supported by the Russian Foundation for Basic Research (project no. 03-02-17469) and INTAS (grant no. 03-51-6417).

REFERENCES

1. S. G. Kadmensky, Yad. Fiz. **65**, 1424 (2002) [Phys. At. Nucl. **65**, 1390 (2002)].
2. S. G. Kadmensky, Yad. Fiz. **67**, 167 (2004) [Phys. At. Nucl. **67**, 170 (2004)].
3. M. Goldberger and K. Watson, *Collision Theory* (Wiley, New York, 1964; Mir, Moscow, 1967).
4. K. Wildermuth and Y. C. Tang, *A Unified Theory of the Nucleus* (Vieweg, Braunschweig, 1977; Mir, Moscow, 1980).
5. S. G. Kadmensky, Yad. Fiz. **62**, 236 (1999) [Phys. At. Nucl. **62**, 201 (1999)]; **64**, 478 (2001) [**64**, 423 (2001)].
6. A. Bohr and B. Mottelson, *Nuclear Structure* (Benjamin, New York, 1969, 1974; Mir, Moscow, 1971, 1977), Vols. 1, 2.
7. A. Bohr, in *Proceedings of the International Conference on the Peaceful Uses of Atomic Energy* (New York, 1956), Vol. 2.
8. O. P. Sushkov and V. V. Flambaum, Usp. Fiz. Nauk **136**, 3 (1982) [Sov. Phys. Usp. **25**, 1 (1982)].
9. V. E. Bunakov and V. P. Gudkov, Z. Phys. A **321**, 271 (1985).
10. A. L. Barabanov and W. I. Furman, Z. Phys. A **357**, 411 (1997).
11. W. I. Furman, in *Proceedings of FJ/OM Spring Session* (Geel, Belgium, 1999), p. 248.
12. S. G. Kadmensky, Yad. Fiz. **67**, 2157 (2004) [Phys. At. Nucl. **67**, 2134 (2004)].
13. S. G. Kadmensky and L. V. Rodionova, Yad. Fiz. **66**, 1259 (2003) [Phys. At. Nucl. **66**, 1219 (2003)]; **68**, 1479 (2005).
14. Yu. N. Kopach *et al.*, Phys. Rev. Lett. **82**, 303 (1999).
15. S. G. Kadmensky, Yad. Fiz. **65**, 1833 (2002) [Phys. At. Nucl. **65**, 1785 (2002)].
16. S. G. Kadmensky, Yad. Fiz. **66**, 1739 (2003) [Phys. At. Nucl. **66**, 1691 (2003)].
17. S. G. Kadmensky, Yad. Fiz. **67**, 258 (2004) [Phys. At. Nucl. **67**, 241 (2004)].
18. V. E. Bunakov and S. G. Kadmensky, Yad. Fiz. **66**, 1894 (2003) [Phys. At. Nucl. **66**, 1846 (2003)].
19. S. G. Kadmenskiĭ, V. P. Markushev, and V. I. Furman, Yad. Fiz. **35**, 300 (1982) [Sov. J. Nucl. Phys. **35**, 166 (1982)].
20. S. G. Kadmenskiĭ, V. P. Markushev, Yu. P. Popov, *et al.*, Yad. Fiz. **39**, 7 (1984) [Sov. J. Nucl. Phys. **39**, 4 (1984)].
21. J. R. Nix, Nucl. Phys. A **130**, 241 (1969).
22. M. Brack *et al.*, Rev. Mod. Phys. **44**, 320 (1972).
23. V. A. Rubchenya and S. G. Yavshits, Yad. Fiz. **40**, 649 (1984) [Sov. J. Nucl. Phys. **40**, 416 (1984)].
24. T. M. Schneidman *et al.*, Phys. Rev. C **65**, 064302 (2002).
25. S. G. Kadmensky and L. V. Rodionova, Yad. Fiz. **68**, 1491 (2005).
26. Yu. B. Ostapenko, G. N. Smirenkin, A. S. Soldatov, and Yu. M. Tsipenyuk, Fiz. Élem. Chastits At. Yadra **12**, 1364 (1981) [Sov. J. Part. Nucl. **12**, 545 (1981)].
27. S. G. Kadmensky and W. I. Furman, *Alpha Decay and Related Nuclear Reactions* (Énergoatomizdat, Moscow, 1985) [in Russian].
28. S. G. Kadmenskiĭ *et al.*, Izv. Akad. Nauk SSSR, Ser. Fiz. **50**, 1786 (1986).
29. N. Mollenkopf *et al.*, J. Phys. G **18**, L203 (1992).
30. C. F. Tsang, Phys. Scripta **10A**, 90 (1974).
31. G. V. Val'skiĭ, Yad. Fiz. **24**, 270 (1976) [Sov. J. Nucl. Phys. **24**, 140 (1976)].
32. V. A. Rubchenya, Yad. Fiz. **35**, 576 (1982) [Sov. J. Nucl. Phys. **35**, 334 (1982)].
33. N. Carjan, J. Phys. (Paris) **37**, 1279 (1976).
34. O. Tanimura and T. Fliessbach, Z. Phys. A **328**, 475 (1987).
35. V. G. Neudatchin and Yu. F. Smirnov, *Nucleon Clusters in Light Nuclei* (Nauka, Moscow, 1969).
36. A. G. Val'shin, V. G. Kadmenskiĭ, S. G. Kadmenskiĭ, *et al.*, Yad. Fiz. **33**, 939 (1981) [Sov. J. Nucl. Phys. **33**, 494 (1981)].
37. S. G. Kadmenskiĭ and Yu. M. Chuvil'skiĭ, Yad. Fiz. **38**, 1433 (1983) [Sov. J. Nucl. Phys. **38**, 872 (1983)].
38. M. Mutterer *et al.*, in *Proceedings of the 2nd International Conference on Fission and Neutron-Rich Nuclei, St. Andrews, Sconland, 1999*, p. 98.
39. C. Wagemans *et al.*, Phys. Rev. C **33**, 943 (1986).
40. M. Mutterer and J. P. Theobald, *Dinuclear Decay Modes* (IOP, Bristol, 1996), Chap. 12.

Translated by A. Isaakyan

Physics of Atomic Nuclei, Vol. 68, No. 12, 2005, pp. 1979–1987. Translated from Yadernaya Fizika, Vol. 68, No. 12, 2005, pp. 2042–2050.

NUCLEI
Theory

Searches for Effects of Fundamental-Symmetry Violation in Isomeric Nuclear States

S. D. Kurgalin[1)], I. S. Okunev[2)], T. V. Chuvilskaya[3)], and Yu. M. Tchuvil'sky[3)*]

Received August 27, 2004; in final form, January 14, 2005

Abstract—The results of broad searches for schemes that are convenient for observing effects of time-inversion-invariance violation (T violation) simultaneously with parity violation (PT violation) in electromagnetic transitions in nuclei are presented. The main problems in observing such effects are discussed. A scheme that seems one of the most promising for this and which relies on measuring the linear polarization of gamma radiation accompanying the deexcitation of isomeric states of nuclei that were oriented by a magnetic field at ultralow temperatures is highlighted. © *2005 Pleiades Publishing, Inc.*

INTRODUCTION

Effects associated with the violation of time-inversion invariance (T invariance) or, more precisely, CP-noninvariant effects, which are equivalent to them by virtue of the CPT theorem, have been observed so far only in experiments with K and B mesons. Those measurements led to introducing a T-violating term in the Standard Model Lagrangian or, more specifically, a phase factor $e^{i\delta}$ in the Kobayashi–Maskawa matrix. In the case of $\delta \neq 0$, this generates an imaginary addition to the amplitudes for the mixing of quarks belonging to different generations. Formally, T-noninvariant terms may include P-odd amplitudes in addition to parity-conserving ones. These P-odd amplitudes are responsible for time-inversion-invariance violation accompanied by parity violation (that is, violation of PT invariance). The phase factor in question appears universally in P-even and P-odd amplitudes. It follows that, in all processes, with exception of those that are governed by weak interaction exclusively, in which case parity violation is sizable, PT violation in the Standard Model is suppressed both by the smallness of P-odd amplitudes and by the smallness of the phase δ. As a result, PT-violation effects naturally appear to be extremely small. Therefore, observation of even a very weak PT-noninvariant correlation against the background of strong or electromagnetic (or both strong and electromagnetic) processes would be reliable evidence that it arises owing to effects beyond the Standard Model. It is precisely this circumstance that renders intriguing the problem of searches for PT-violation effects.

Moreover, investigation of the phenomena under discussion in processes not involving strange particles would make it possible to constrain, in relation to what we have on the basis of studying K- and B-meson decays, the set of quark generations contributing to the process being considered, whereby one could remove partly the ambiguity in choosing constants that determine PT violation.

In addition, we note that, if the CPT theorem is valid, knowledge of the constants in the P-, T-, and PT-violating amplitudes determines completely that part in the Lagrangian which violates a fundamental symmetry.

At the present time, the most stringent constraint on the magnitude of PT-violation effects has been obtained on the basis of measuring the electric dipole moment of the neutron: $d_n \leq 0.6 \times 10^{-25} e$ cm, which is equivalent to $d_n/er_n \leq 10^{-12}$. The most precise experiments with atoms and molecules yield, for an upper limit on the nucleon dipole moment, a value that is two to three times higher. If one adopts the natural hypothesis that the main contribution to the amplitudes of PT violation comes from the $N \to N + \pi$ meson–nucleon vertex, there arises the possibility of constraining, on the basis of the aforementioned upper limit, the corresponding constant $g_{PT}^{\Delta T}(\pi)$ as [1, 2]

$$g_{PT}^{\Delta T}(\pi) \leq \begin{cases} 1.4 \times 10^{-11}, & \Delta T = 0, \\ 1.0 \times 10^{-10}, & \Delta T = 1, \\ 1.4 \times 10^{-11}, & \Delta T = 2, \end{cases} \qquad (1)$$

where ΔT stands for the change in the isospin. Thus, the available upper limit on the isovector constant

[1)]Voronezh State University, Universitetskaya pl. 1, Voronezh, 394693 Russia.
[2)]Petersburg Nuclear Physics Institute, Russian Academy of Sciences, Gatchina, 188350 Russia.
[3)]Institute of Nuclear Physics, Moscow State University, Vorob'evy gory, Moscow, 119899 Russia.
[*]E-mail: tchuvl@nucl-th.sinp.msu.ru

appears to be much greater. Taking into account the characteristic value of the main constant that determines the pattern of P-odd effects in nucleon–nucleon interactions, $g_P^{\Delta T=0}(\rho) \sim 10^{-6}$, and the estimate obtained in [3] for the ratio of the kinematical factors in PT- and P-violation effects, $\kappa \sim 10^1$, we can conclude that, for a process characterized by a large contribution from an isovector diagram, a constraint on the PT-noninvariant amplitude at a level of 10^{-3} of the measured P-odd amplitude would supplement substantially information obtained by measuring the electric dipole moment of the neutron and would be an important further step in studying fundamental symmetries of elementary-particle interaction.

Effects of PT violation in nuclear processes have not yet received adequate study even at the level of upper limits. At the same time, the structure of the matrix elements of a PT-violating nucleon–nucleon interaction here may differ substantially from the structure of the diagrams that determine the electric dipole moments of the neutron and atoms. Therefore, it is highly desirable to set, in a nuclear process, even a less stringent constraint on the constant under discussion than its counterpart obtained in measuring the electric dipole moment. It is of importance that the isovector vertex is dominant precisely in nuclear processes since only this vertex generates a volume effect—that is, an effect that grows in direct proportion to the mass of the nucleus involved. Finally, the same enhancement effects are peculiar to nuclear processes accompanied by PT violation as those that are peculiar to processes involving parity violation. Here, it is worthwhile to emphasize that this is the reason why the magnitude of the PT-noninvariant amplitude or an upper limit on it is reliably determined precisely by the ratio of the measured magnitude of a PT-noninvariant effect or an upper limit on it to the P-odd effect measured in the same process (with allowance for the factor $F_{\{J\}}$ that is defined below and which is readily calculable), since this ratio is virtually independent of the properties of the participant nucleus. At the same time, the nuclear P-odd amplitude and the relationship between this and the two-nucleon amplitudes have been studied quite well.

At the present time, three experiments of the type being discussed are known.

First, the PT-noninvariant correlation $a_{PT}((\mathbf{k}_1 \cdot [\mathbf{J} \times \mathbf{k}_2])(\mathbf{J} \cdot \mathbf{k}_2))$, where $\mathbf{k}_1$ and $\mathbf{k}_2$ are the momenta of, respectively, the first and the second photon and $\mathbf{J}$ is the direction of the polarization vector of the sample employed, was studied in [4] on the basis of $\gamma\gamma$ coincidences by using an aligned ^{180m}Hf isomer. The result for the respective correlation coefficient was $a_{PT} = -(0.9 \pm 1.1) \times 10^{-3}$, and the upper limit on the contribution of the PT-noninvariant part of the nuclear-interaction amplitude with respect to the P-odd part was estimated at 0.6 to 0.7. With allowance for the enhancement of the P-odd effect in the Hf nucleus, this corresponds to a constraint on the amplitude of PT-violation in nucleon–nucleon interaction at a level of 10^{-7} with respect to the ordinary nucleon–nucleon amplitude.

Second, $a_{PT}(\boldsymbol{\sigma}_n \cdot [\mathbf{k}_n \times \mathbf{J}])$ (where $\mathbf{k}_n$ is the direction of neutron motion, $\boldsymbol{\sigma}_n$ is the direction of the neutron spin vector, and $\mathbf{J}$ is the direction of the target-nucleus spin vector), which is yet another PT-noninvariant asymmetry, was measured in an experiment where fast polarized neutrons of energy in the range $E_n = 7$–12 MeV traversed a polarized ^{165}Ho target. The results obtained for the coefficient a_{PT} of PT-noninvariant asymmetry were $-(0.9 \pm 2.0) \times 10^{-3}$ for $E_n = 7.1 \pm 0.9$ MeV and $-(0.4 \pm 2.9) \times 10^{-3}$ for $E_n = 11 \pm 0.5$ MeV [5]. The resolution in the neutron energy ranged between 0.5 and 1.0 MeV; in addition, we note that neutron resonances are broad in this energy region. Thus, the effect in question receives contributions from several resonances, with the result that the possible effect is averaged, which reduces its magnitude and appears to be a source of formidable difficulties in deducing, from the respective experimental result, constraints on the amplitude of PT-noninvariant interaction, since the two-level approximation is inapplicable in this case. Irrespective of this, it is obvious that the limit on the ratio of the amplitude in question to the P-odd amplitude—in principle, the respective limit can be obtained from the experiments reported in [5]—is always greater than unity.

Third, the PT-noninvariant correlation $a_{PT}((\mathbf{k}_\gamma \cdot [\mathbf{J} \times \mathbf{e}_\gamma])(\mathbf{J} \cdot \mathbf{e}_\gamma))$, where $\mathbf{k}_\gamma$ is the photon-emission direction, $\mathbf{e}_\gamma$ is the linear-polarization vector of the radiation, and $\mathbf{J}$ is the quantization-axis direction, was studied in [6] by using the hyperfine-structure components of the 23.7-keV line arising in the deexcitation of the ^{119m}Sn isomeric state. The respective experiment was performed with the aid of the Mössbauer procedure, which was used to separate gamma transitions in specific states of nuclear polarization of a ^{119}Sn* excited state. This resulted in obtaining the estimate $a_{PT} = -(0.4 \pm 1.1) \times 10^{-6}$ and, accordingly, a constraint on the ratio of the PT-noninvariant effect to its P-odd counterpart at a level of 4×10^{-2}. At the present time, this is the lowest limit obtained in nuclear processes for PT noninvariance. It should be noted, however, that the parity-violation effect found in [6, 7] by means of the Mössbauer procedure (at a level of 10^{-3}) could not be explained in terms of the generally accepted mechanisms of the enhancement of the P-odd effect.

In this connection, it is required, in all probability, to perform an additional verification of this magnitude of the effect by a more traditional method that has nothing to do with the Mössbauer procedure and, in the case of confirmation, to develop a theoretical scheme for interpreting so unexpected a result.

As to studying PT noninvariance in other processes, we note that the main effort has been mounted to measure the PT-noninvariant correlation $a_{PT}(\boldsymbol{\sigma}_n \cdot [\mathbf{k}_n \times \mathbf{J}])$ corresponding to the rotation of the spin of a polarized neutron that traverses a polarized ^{139}La target. This choice is motivated above all by an extremely large scale of the enhancement of the parity-violation effect here, approximately 10^6. The enhancement of PT-violation effects has the same origin; therefore, its scale is likely to be on the same order of magnitude as the scale of parity violation. In the present case, the dynamical and structural enhancement (see below) provides the possibility of setting a constraint on the PT-noninvariant amplitudes at a level of 10^{-7} eV [8]. Since the characteristic value of the P-odd amplitude at neutron resonances is close to 10^{-3} eV, the scheme being discussed can make it possible in principle to set a constraint on the amplitude of PT-noninvariant interaction at a level of 10^{-4} with respect to the P-odd-interaction amplitude. However, experiments that study the rotation of the spin of a neutron that traverses a polarized target involve a number of serious problems associated with the compensation of spurious effects that are due to pseudomagnetism and P-odd and left–right asymmetries. The problem of polarizing a La sample has not been solved decisively either. Moreover, it is planned to employ a monochromatic beam of polarized resonance neutrons ($E_n = 0.75$ eV), but the beam intensity and the event counting rate for the effect in question would be reduced sharply in this case. Although efforts have been undertaken for more than ten years to develop procedures for the aforementioned measurements with neutron beams and measurements similar to them, no experiment, with the exception to that which was reported in [5], has been performed so far.

In summary, we can state that the upper limit attained to date in nuclear processes for PT-violation effects is rather high, being much poorer than that which was achieved in electric-dipole-moment measurements. Therefore, it is necessary to continue refining measurement procedures and seeking other examples of nuclear processes where PT violation is first enhanced and second convenient for measurement.

SEARCHES FOR PT-VIOLATION EFFECTS IN CORRELATION EXPERIMENTS: ENHANCEMENT EFFECTS

Effects of fundamental-symmetry violation in nuclear processes have been studied predominantly by measuring various correlations between the directions of the momenta and (or) spins of primary particles and reaction products. While a two-vector spin–momentum correlation ($\mathbf{I} \cdot \mathbf{k}$) is peculiar to parity violation, three- and five-vector correlations [$([\mathbf{I}_1 \times \mathbf{k}] \cdot \mathbf{I}_2)$ in the former case and $((\mathbf{k}_2 \cdot [\mathbf{k}_1 \times \mathbf{k}_3])(\mathbf{k}_1 \cdot \mathbf{k}_3)$ and $(\mathbf{k}_1 \cdot [\mathbf{I} \times \mathbf{k}_2])(\mathbf{I} \cdot \mathbf{k}_2))$ in the latter case] are peculiar to PT violation. Here, the photon circular-polarization vector must be axial (that is, a vector of the spin type), while the linear-polarization vector can appear in the correlation in question only through a quadratic form (that is, this vector does not form three-vector correlations).

The correlations being discussed may arise in a wide variety of processes involving the decay and scattering of nuclear particles and in nuclear reactions featuring two or three particles in the final state. The samples used may possess a specific orientation owing to the polarization of the incident beam or may develop it as the result of the preceding stage of the nuclear process. The orientation in question may also be generated by an external magnetic field or be fixed by means of the Mössbauer procedure of an experiment. Even a mere enumeration of all possibilities would consume too much space, so that we prefer here to restrict ourselves to discussing general principles of searches for promising examples of PT-noninvariant correlations.

Since the amplitude of the sought effect is small, the presence of a nuclear enhancement is one of the most important conditions that would make it possible to observe this effect (or to set a low upper limit on its magnitude). It has already been indicated that the same mechanisms are responsible for the enhancement of P- and PT-noninvariant effects; therefore, vast experience accumulated in studying parity-violation processes can readily be extended to PT-noninvariant processes. The schematic form of a typical (nearly universal) expression for the coefficient of a PT-noninvariant correlation in a gamma transition between some nuclear levels (in general, this may also be an alpha or a proton transition) is

$$a_{PT} = F_{\{J\}} \frac{\langle \Psi_f | V_{PT} | \Psi_i \rangle}{\Delta E} \sqrt{\frac{\Gamma_{\text{irreg}}}{\Gamma_{\text{reg}}}}, \qquad (2)$$

where $F_{\{J\}}$ is a coefficient that depends on the spins of primary particles and reaction products. It is the

matrix element in the numerator on the right-hand side of (2)—the amplitude of PT violation—that determines the true scale of the effect. The quantity ΔE is the energy spacing between the state being studied and the closest level that has the same spin and the opposite parity (doublet state) and whose admixture to the state in question due to the PT-noninvariant part of the Lagrangian leads to the violation of invariance. The radicand on the right-hand side of (2) involves the decay width of the level without allowance for the admixture (regular width) and the decay width of the hypothetical level having the same energy and the opposite parity (irregular width). The smallness of ΔE determines the so-called dynamical enhancement of the process, while the smallness of the regular width in relation to its irregular counterpart determines the structural enhancement. Not only does the presence of the enhancement give a chance to record an effect experimentally at a small value of the matrix element, but it also provides the possibility of setting a rather low limit on the amplitude at a sizable value of the error in the measurement of the correlation coefficient on the left-hand side of (2).

The presence of vast statistics is an obvious criterion of the quality of measurements. The statistics in question are determined by the reaction cross section and the potential of an experiment. In this respect, the scheme proposed in the present study differs substantially from schemes that are intended for exploring the phenomenon under discussion in processes generated by neutron beams, in which case the cross section for the resonance process is proportional to Γ_{reg}, while the structural-enhancement condition leads to the conclusion that it is necessary to measure cross sections in the vicinities of p resonances characterized by a small value of Γ_{reg} (this situation is exemplified by the aforementioned study of Masuda [8]) and, hence, to perform an experiment under conditions of a very small cross section, this reducing statistics sharply. As was indicated in [9], the reduction in question annihilates completely the gain in the accuracy of determining the matrix element because of the structural enhancement or even outweighs it. In the scheme presented below and schemes that are similar to it, the initial level of the transition is populated by the preceding gamma cascade, in which case the population cross section is not directly related to the probability of the transition itself; therefore, it is quite profitable here to employ both dynamical and structural enhancement effects.

These considerations underlay the present search.

PT-NONINVARIANT CORRELATION BETWEEN THE DIRECTIONS OF THE INITIAL POLARIZATION AND THE MOMENTUM AND LINEAR POLARIZATION OF THE PHOTON IN A SINGLE GAMMA TRANSITION

From an analysis of all possible schemes of searches for PT violation (these schemes include measurements with beams of various particles and with radioactive sources, methods for obtaining orientations, correlation types, detection methods, and choice of sources or targets), it can be inferred that the scheme that was used in [6] and which is based on the linear polarization of radiation from a polarized radioactive source is the most efficient, along with a few schemes relying on the use of neutron beams (see [8, 10–12]) and one to two schemes beyond the discussion in the present study. At the same time, we believe that, at the present stage of investigations, the cryogenic method for polarizing targets is more reliable than the Mössbauer method and, what is more important, makes it possible to study more promising samples.

The proposed PT-noninvariant correlation has the form $(\mathbf{k}_\gamma \cdot [\mathbf{J} \times \mathbf{e}_\gamma])(\mathbf{J} \cdot \mathbf{e}_\gamma)$, where $\mathbf{k}_\gamma$, $\mathbf{J}$, and $\mathbf{e}_\gamma$ are, respectively, the photon-momentum vector, the vector of initial-state alignment, and the linear-polarization vector of the photon. Expressing this correlation in terms of the Euler angles ϕ, θ, and ψ that determine the coordinate-frame rotation from the laboratory frame (where the z axis coincides with the alignment direction) to the frame specified by the coordinates x', y', and z' where the z' axis is determined by the photon-momentum direction and the x' axis is aligned with the linear-polarization vector, we arrive at [13]

$$W(\theta,\psi) = B_{\lambda=2}(I)\Bigg[A_{\lambda=2}(\gamma,PT)P_{\lambda=2}(\cos\theta) + 2A_{\lambda=2,2}(\gamma,PT)\left\{\frac{(\lambda-2)!}{(\lambda+2)!}\right\}^{1/2} \times P^{(2)}_{\lambda=2}(\cos\theta)\sin(2\psi)\Bigg], \quad (3)$$

where $B_\lambda(I)$ is the parameter of initial-state polarization. Naturally, expression (3) features no dependence on the angle ϕ since this angle determines a rotation in the space of the entire measuring system as a discrete unit. Only the $\lambda = 2$ component of the orientation tensor (alignment) contributes to the effect in which we are interested. The first term in the bracketed expression on the right-hand side of (3) (this term is independent of the direction of the radiation polarization vector) is given for the sake of

generality. Albeit being determined by a PT-violating interaction, this term does not correspond to the correlation being discussed and is of no interest to us since there is no hope for observing an extremely small correction to a nearly identical angular dependence characteristic of the PT-invariant correlation for the process [see Eq. (5) below]. The spin–angular correlation in the second term of the bracketed expression on the right-hand side of (3) is generated only by a PT-noninvariant interaction; therefore, the conditions that must be met to measure it are much less stringent. The respective correlation coefficient has the form

$$A_{\lambda=2,2}(\gamma, PT) = \sum_{L'\pi' L\pi} (-1)^L \hat{L}\hat{L}'\hat{I}\hat{J}(L1L'1|22) \times \begin{Bmatrix} J & L & I \\ J & L' & I \\ 2 & 2 & 0 \end{Bmatrix} \langle J|L'\pi'(PT)|I\rangle \times \langle J|L\pi|I\rangle \Big/ \sum_{L\pi} \langle J|L\pi|I\rangle^2, \quad (4)$$

where the braced factor is a $9j$ coefficient, while the factor in parentheses is a Clebsch–Gordan coefficient. We have also used here the notation $\hat{a} = \sqrt{2a+1}$. The factors in angular brackets are amplitudes of gamma transitions of the system from the initial state $|I\rangle$ to the final state $|J\rangle$. The first of these matrix elements corresponds to the transition of multipolarity $L'\pi'$ whose parity satisfies the condition $\pi' = -\pi$, the phase of this amplitude being shifted by an angle of $\pi/2$ owing to a PT-noninvariant interaction. The product of elements of the Wigner–Racah algebra and the numerical and factorial factors contained in expressions (3) and (4) form a spin factor that is denoted by $F_{\{J\}}$ in Eq. (2).

In almost all of the cases where it is reasonable to seek PT violation, the analysis can be restricted to considering the contribution of the interference between amplitudes of close multiplicities.

The background correlation conserving P and T invariance has the form

$$W(\theta, \psi) = \sum_{\text{even } \lambda} B_\lambda(I)[A_\lambda(\gamma)P_\lambda(\cos\theta) + 2A_{\lambda=2,2}(\gamma)\left\{\frac{(\lambda-2)!}{(\lambda+2)!}\right\}^{1/2} P_\lambda^{(2)}(\cos\theta)\cos 2\psi], \quad (5)$$

where, in contrast to $A_{\lambda,2}(\gamma, PT)$, the quantity $A_{\lambda,2}(\gamma)$ involves parity-conserving matrix elements of electromagnetic transitions ($\pi' = \pi$), a standard phase condition being satisfied. It has already been indicated that the first term in the bracketed expression on the right-hand side of (5) is negligibly distorted by a PT-nonivariant interaction and that the dependence of the second term on the angle ψ is in antiphase with respect to the analogous term in (3). From here, it is obvious that difference measurements of the correlation being discussed are required and that the optimum conditions of searches for this correlation are realized if a Compton scatterer of photons that is sensitive to a linear polarization is arranged in the direction orthogonal to the polarization vector of the sample and if the angle between this polarization vector and the linear-polarization vector of gamma radiation is chosen to be $\psi = \pm\pi/4$ (that is, if the two detectors of the polarimeter are installed in the planes parallel and orthogonal to the polarization vector of the sample).

In order to perform searches for PT violation, it is proposed to study the linear polarization of gamma radiation from a radioactive sample that was oriented by a magnetic field at a low temperature. In this case, the orientation-parameter of the initial state, $B_{\lambda=2}(I)$, has the form [13]

$$B_{\lambda=2}(I) = \sqrt{2I+1}\left(\sum_m e^{-m\beta}\right)^{-1} \times \sum_m (-1)^m (ImI-m|20)e^{-m\beta}, \quad (6)$$

where the quantity

$$\beta = -g\frac{\mu_N B}{kT}, \quad (7)$$

which determines the population of magnetic sublevels m, depends on the magnetic induction B and temperature T; it also involves the respective g factors and the nuclear magneton. Straightforward estimations show that, in order to obtain an alignment at a level of a few tens of percent, it is necessary to cool the sample used to a temperature of 10 to 20 mK and to apply a static magnetic field of strength around a few teslas. There are several operating facilities worldwide that possess such parameters. If there is a ferromagnet or an antiferromagnet composite (compound, alloy, etc.) containing the element being studied, it is possible to relax the requirements on the refrigerator significantly and to increase the degree of alignment.

The proposed scheme of searches for PT-violation effects in nuclear processes has a number of obvious advantages over other approaches. These are the following:

(i) An accelerator or a reactor is only required for obtaining a radionuclide to be studied.

(ii) Possible samples can be chosen among a rather wide range of objects, with the result that

this choice can be optimized in many parameters—in particular, it should be required that the lifetime be reasonable and that a convenient procedure for manufacturing samples be available; however, it is the most important to choose processes where the total enhancement effect is rather great. Herein lies the main advantage of the scheme being discussed over the Mössbauer scheme.

(iii) The range of possible samples becomes still wider upon considering that, in addition to gamma transitions generated by the deexcitation of long-lived isomeric states, one can make use of secondary gamma radiation from radionuclides appearing as beta-decay products. Here, it is worth noting that the use of beta sources leads to various complications, such as depolarization, additional heat release in a sample, and need for more sophisticated theoretical interpretations (in view of this, we do not discuss here such sources), but, under specific conditions, advantages of employing particular isotopes may outweigh these shortcomings.

(iv) In the majority of cases, it is possible to choose an (anti)ferromagnet composite for the element being studied. This makes it possible to achieve a high degree of alignment. At the same time, relatively lenient requirements on temperature increase the cooling output of the facility substantially.

(v) The efficiency of measuring a linear polarization is rather high. In this respect, the proposed scheme is much superior to experimental approaches based on measuring a circular polarization.

(vi) The experimental procedure being discussed does not employ a coincidence scheme, which was used, for example, in [4]. This makes it possible to increase the event counting rate sharply.

(vii) In this approach, the spin factor $F_{\{J\}}$ takes much greater values than in studying cascades in coincidence. The scale of these values is approximately identical to the scale of the spin factors in P-odd correlations in the same processes.

SOME PROMISING EXAMPLES AND POTENTIAL OF THE EXPERIMENT

Within the new scheme considered here, it seems reasonable to explore processes that have already been used in searches for PT-violation effects. First of all, this concerns the decay of an aligned isomeric state ^{180m}Hf (its half-life is 5.5 h). In [4], Murdoch and his coauthors, who employed the method of $\gamma\gamma$ coincidences, measured the PT-noninvariant correlation $(\mathbf{k}_1 \cdot [\mathbf{J} \times \mathbf{k}_2])(\mathbf{J} \cdot \mathbf{k}_2)$ in this decay. The spectrum of the ^{180}Hf nucleus contains a doublet of closely lying opposite-parity states—the 8^- state at 1.142 MeV, which is a K-isomeric state, and the 8^+ state at 1.085 MeV, which belongs to the ground-state rotational band—this leading to the appearance of a dynamical enhancement ($\Delta E = 57$ keV) of P- and PT-violation effects. Moreover, the use of the K-isomeric state, which is characterized by an approximately 14 order of magnitude suppression of the gamma transition from it to the 8^+ level at 57 keV and the 6^+ level at 501 keV of the rotational band, leads to an extremely strong structural enhancement of the violation effects under study owing to a large value of the width ratio in expression (2). Naturally, the matrix element appearing in (2) also decreases strongly. However, this suppression of the PT-violating amplitude is many times smaller than the suppression of the electromagnetic-transition amplitude, since the former is of a two-particle origin. Owing to this, the measured parity violation in the ^{180}Hf nucleus is very large. In the decay of the isomeric state of the Hf nucleus, a very large P-odd asymmetry of $A_\gamma = -(1.66 \pm 0.18) \times 10^{-2}$ was measured by using the 501-keV line [14]. A parity-violation effect of greater magnitude was recorded only in experimentally studying the transmission of polarized resonance neutrons through a ^{139}La sample. Therefore, it is natural to expect a large PT-violation effect as well.

In the scheme being discussed, one can measure both transitions indicated above. Since the cross section for the reaction ^{179}Hf(n,γ)^{180m}Hf is 0.42 b at the thermal point, one does not have to overcome any serious difficulties in obtaining the required isomer. The counting procedure of the experiment imposes the most stringent constraint on the event-counting rate in one polarimeter shoulder, about $10^{5.5}$ events per second. With allowance for the geometry of the scheme for measuring a linear polarization, this corresponds to a sample activity of about 10 mCi; therefore, radiation conditions and the cooling output of the facility used are not of crucial importance. For a relatively short-lived nuclide, an upper limit on the total exposure time can be estimated at about $10^{6.5}$ s. Taking into account the percentage of emitted photons (57 and 14%), one can obtain, in this case, the statistical samples of about $10^{11.5}$ and 10^{11} events for, respectively, the 57- and the 501-keV transitions being discussed. Finally, we note that, according to formulas (3) and (4), the spin factor $F_{\{J\}}$ turns out to be 0.5 and 0.12 for these two transitions. In the case where one measures $\gamma\gamma$ coincidences, the analogous factor takes the value of 0.02. Considering that the polarimeter efficiency is close to unity and that the attainable degree of polarization of a ^{180m}Hf sample is quite high (about 0.5), we can find that, in the transitions being discussed, the correlation of interest can be measured with a statistical error of about 10^{-5} and $10^{-4.3}$, respectively. Thus, we see that, within the

experimental scheme proposed here, the use of the 501-keV line and available research facilities would make it possible to set an upper limit on the PT-violation amplitude at level of about $10^{-2.5}$ with respect to the measured P-odd amplitude, this being far superior to present-day achievements. As to the 57-keV line, the above upper limit can hardly be improved despite better measurement conditions, since, according to the experiment reported in [15], parity violation in the respective transition is an order of magnitude weaker, $P_\gamma = -(2.3 \pm 0.6) \times 10^{-3}$. Nevertheless, an investigation of two transitions in the same experiment is of importance—see the respective argument in the Conclusions. In all probability, the upper limit under study can be reduced further by an order of magnitude upon creating, for an experiment aimed at searches for PT violation, a dedicated facility that would combine a high efficiency of the detector and its short resolution time, the tuning of the polarimeter (owing to filters, scattering angles, and the detector thickness) to a specific photon energy (this would make it possible to apply an integral rather than a counting procedure), a high cooling output of the refrigerator and a small absorption of gamma radiation in its walls, and a circuit that would be able to operate under severe radiation conditions. Thus, the proposed scheme is quite competitive both with respect to measuring the electric dipole moment and with respect to studying the rotation of the spin of a neutron that traverses a polarized ^{139}La target. Moreover, the cost of the facility in question will be much lower than the cost of equipment necessary for measurements within the last two schemes.

At the same time, it cannot be stated that the isomer ^{180m}Hf is optimal for the purpose pursued here. For this reason, we deem it necessary to analyze some more examples of crucial importance.

In the context of the proposed experimental method, the isotope in question is disadvantageous in that it is characterized by a short lifetime and a complicated and hard gamma spectrum. The isotope ^{178}Hf exhibits a similar scheme of levels and transitions (the half-life of the 8^- level at 1.147 MeV is 4.0 s) and, in addition, a higher 16^+ isomeric state at 2.446 MeV (its half-life is 31 yr), which is deexcited through the 8^- level. Unfortunately, the application of this convenient energy-level scheme is hindered by the fact that it is very difficult to obtain the 16^+ isomer of ^{178}Hf. The cross section for the production of this isomer in a thermal-neutron beam is negligible (about 10^{-7} b). The conditions for its production in proton or alpha-particle beams are more favorable, but only rather weak and very expensive sources could be obtained even in those cases.

The isomer ^{119m}Sn, which was already used in the aforementioned experiment, is also a long-lived source. It would be of importance to verify the results of the experiment with this isomer by applying the cryogenic (rather than the Mössbauer) procedure for generating a nuclear polarization. The 23.8-keV line, which is investigated in this case, is the second line of the cascade that deexcites the $11/2^-$ isomeric state at 89.5 keV (its half-life is 293 d). The long lifetime makes it possible to reach an exposure time of about 10^7 s without overcoming serious difficulties, while the absence of other lines in the gamma spectrum (the first transition of the cascade is of a purely conversion character) creates preconditions for employing the integral procedure. Therefore, the constraints on the counting rate are imposed predominantly by radiation conditions and by the cooling output of the refrigerator. Considering that the conversion coefficient for the transition being studied is equal to five, we find that the counting rate attainable at present-day facilities is about $10^{6.5}$ events per second. The cross section for the reaction $^{118}\mathrm{Sn}\,(n, \gamma)^{119m}\mathrm{Sn}$ at the thermal point is not large, 0.004 b, but it is sufficient for obtaining, within the half-life period, the required source of intensity about $10^{-0.5}$ Ci at powerful reactors. Moreover, an efficient production of this radionuclide in the $^{116}\mathrm{Cd} + \alpha$ reaction is possible. Thus, the correlation being discussed can be measured to a precision of about 10^{-6}. It is straightforward to take theoretically into account the depolarization of the sample under study at the first step of the gamma cascade. The depolarization effect is modest. However, the question of the constraint on the matrix element is not quite clear, since a large experimental effect of parity violation, $P_\gamma = -(0.90 \pm 0.13) \times 10^{-3}$ [7], is at odds, as has already been mentioned, with the theoretical estimate that is based on the generally accepted value of the parity-violation amplitude and which is quite small because of an almost complete absence of enhancement effects, about $10^{-5.5}$.

Problems of studying PT violation in the cases where neither P- nor PT-noninvariant effects were measured for a given cascade will be illustrated by considering the following example. Among long-lived isomers, the ^{174}Lu nucleus possesses quite an appropriate doublet pair in the spectrum. The (6^-) isomer of excitation energy 170.8 keV has a lifetime of 142 d. It is deexcited predominantly via the (6^-), 170.8 keV $\rightarrow$ (3^-), 111.8 keV $\rightarrow$ (2^-), 44.7 keV $\rightarrow$ (1^-), 0 keV cascade, the second transition of this cascade being the subject of investigation. The value of the $M1/E2$ ratio suggests that this transition is strongly suppressed. The energy of the (2^+) level, which is the doublet partner of the (2^-) level, is 340.1 keV. The

lifetime of this level has not yet been measured, but the most intense gamma transition from it is precisely $(2^+) \to (3^-)$. Therefore, it is natural to expect that the amplitude of the irregular transition $(3^-) \to (2^+)$ is many times greater than the amplitude of the respective regular transition. A relatively small energy spacing ΔE between the doublet components and a highly probable structural enhancement associated with the smallness of the width Γ_{reg} lead to an expected value of the P-odd effect at a level of about 10^{-4}. The influence of a P-odd admixture of the (3^+) state at 240.8 keV on the magnitude of the effect is insignificant, since measurements reveal that the $E1$ transition $(3^+) \to (2^-)$, which plays the role of the irregular transition in this case, is strongly suppressed. The gamma spectrum of the isomer in question features only two intense lines, which correspond to the last steps of the cascade, the intensity of the background line being greater than the intensity of the line under study by a factor of 1.5. This situation does not present obstacles to the application of the integral scheme. The isomer is vigorously populated in the (α, p), (α, np), $(\alpha, 2np)$, and $(\alpha, 3np)$ reactions on the natural mixture of Yb isotopes, since an alpha particle introduces a high angular momentum in the compound nucleus [16]. In summary, the isomer being discussed is not inferior to and maybe even more promising than ^{119m}Sn. However, spectroscopic tables do not give a hundred percent assurance of the aforementioned spin values for the levels listed above, this rendering the respective scheme not quite reliable. Information about the times of the regular and irregular transitions being discussed is also insufficient. Therefore, the preparation of the main experiment would require spectroscopic measurements (including correlation measurements) that do not have a direct bearing on investigations of fundamental-symmetry violation. Moreover, a preliminary measurement of parity violation is necessary in any case for reliably interpreting results on PT violation, since, in searches for PT violation, the ratio of the upper limit on the amplitude of this violation to the amplitude of P violation is the most informative quantity, as was indicated above. However, this is not a drawback, since measurement of P-odd effects in nuclei is of interest in itself.

We would like to emphasize that the list of promising examples is not exhausted by those that were given above; therefore, more favorable cases can be found in the process of searches.

CONCLUSIONS

The above analysis has led to the conclusion that PT-violation effects in nuclear processes can be measured to a precision at a level of 10^{-3} of the measured magnitude of P violation in the same nucleus. This makes it possible to set a limit on the isovector constant in the PT-violating vertex function at the level reached in measuring the electric dipole moment—that is, at a level of 10^{-10} with respect to strong coupling constants. This conclusion is based on the scheme within which one measures the linear polarization of an oriented source. In all probability, some elements of the scheme can be improved. In this case, there would arise prospects for obtaining experimental results that could compete with or even be superior to their counterparts from measurement of the electric dipole moment rather than supplement them.

It should be noted that, in this (last) case, where the PT-violating correlation is measured at a precision level of 10^{-3} with respect to the P-odd effect in the same process, there arises the problem of final-state PT-invariant interaction—in the specific case being considered, photon interaction with electrons of atomic shells—which can mimic a PT-noninvariant effect. However, Tsinoev *et al.* [6] demonstrated the possibility of tuning away from this spurious effect. Although this possibility is not universal, they showed that one can measure the spurious effect to a fairly high accuracy and, hence, study, in a series of experiments, photon–electron interaction to such an extent that it would be possible to assess, to the required degree of precision, the amplitude mimicking the PT-noninvariant effect and to subtract it from the results of measurements—that is, to separate the actual effect against this background. In order to implement this separation, however, it would be very useful to measure PT-violating correlations and correlations mimicking this effect at least for several nuclear transitions in different nuclei or better in the same nucleus, and this is possible in experiments with the ^{180m}Hf isomer.

ACKNOWLEDGMENTS

We are grateful to S.S. Parzhitsky, Yu.P. Popov, Yu.V. Ryabov, V.G. Tsinoev, and E.A. Cherepanov for their support of this study and stimulating discussions.

This work was supported by the Russian Foundation for Basic Research (project no. 05-02-17461).

REFERENCES

1. P. Herczeg, Hyperfine Interact. **75**, 127 (1992).
2. P. Herczeg, in *Tests of Time Reversal Invariance*, Ed. by N. R. Robertson, C. R. Gould, and J. D. Bowman (World Sci., Singapore, 1987), p. 24.
3. I. S. Towner and A. C. Heyes, Phys. Rev. C **49**, 2391 (1994).
4. T. Murdoch *et al.*, Phys. Lett. B **52B**, 325 (1974).

5. J. P. Soderstrom *et al.*, Phys. Rev. C **38**, 2424 (1988).
6. V. G. Tsinoev *et al.*, Yad. Fiz. **61**, 1357 (1998) [Phys. At. Nucl. **61**, 1255 (1998)].
7. A. V. Baluev *et al.*, Pis'ma Zh. Éksp. Teor. Fiz. **43**, 507 (1986) [JETP Lett. **43**, 656 (1986)].
8. Y. Masuda, in *Time Reversal Invariance and Parity Violation in Neutron Reactions*, Ed. by C. R. Gould, J. D. Bowman, and Yu. P. Popov (World Sci., Singapore, 1993), p. 126.
9. V. E. Bunakov and I. S. Novikov, in *Proceedings of the VI International Seminar on Interaction of Neutrons with Nuclei, Dubna, 1998* (JINR, Dubna, 1998), p. 14.
10. L. Stodolsky, Phys. Lett. B **172**, 5 (1986).
11. V. R. Skoy, Phys. Rev. D **53**, 4070 (1996).
12. V. E. Bunakov *et al.*, Yad. Fiz. **62**, 855 (1999) [Phys. At. Nucl. **62**, 796 (1999)].
13. R. M. Steffen and K. Alder, in *The Electromagnetic Interaction in Nuclear Spectroscopy*, Ed. by W. D. Hamilton (North-Holland, Amsterdam, 1975), p. 505.
14. K. S. Krane *et al.*, Phys. Rev. C **4**, 1906 (1971).
15. E. D. Lipson *et al.*, Phys. Lett. B **35B**, 307 (1971).
16. A. F. Tulinov *et al.*, in *Nuclear Reactions, Proceedings of the First Kiev School on Nuclear Physics, Kiev, 1990* (Naukova Dumka, Kiev, 1991), p. 480.

Translated by A. Isaakyan

Physics of Atomic Nuclei, Vol. 68, No. 12, 2005, pp. 1988–2008. Translated from Yadernaya Fizika, Vol. 68, No. 12, 2005, pp. 2051–2070.

NUCLEI
Theory

On the Electrodisintegration of Nuclei

A. A. Pasitchny[1)*] and O. A. Prygodjuk[2)]

Received February 21, 2005

Abstract—The kinematical dependences of cross sections for the electrodisintegration of nuclei that is induced by high-energy electrons is studied within the shell model of the nucleus. It is proposed to identify the quantum numbers of nuclear shells by a method that involves the subtraction of quasielastic peaks. The effect of Coulomb resonances and quasireal photons on the formation of angular and energy distributions of electrons and protons in $A(e,e'p)(A-1)$ reactions is explored. The phenomenon of quasielastic-peak shift and broadening is interpreted. © *2005 Pleiades Publishing, Inc.*

1. INTRODUCTION: ELECTRODISINTEGRATION OF NUCLEI WITHIN THE SHELL MODEL

At the present time, the shell model of the nucleus is playing the role of a universal model within which one can analyze and systematize [1–3] the results of a wide variety of experiments in nuclear and elementary-particle physics. In view of this, an identification of the shell structure of nuclei in a direct nuclear experiment and an investigation of the applicability range of various shell-model versions are the subject of permanent and unquestionable scientific interest. In solving this problem, researchers place their hope to some extent on experiments aimed at studying proton knockout from nuclei by high-energy electrons in $A(e,e'p)(A-1)$ reactions.

Owing to the weakness of the interaction between electrons and intranuclear nucleons, the exclusive cross section $\sigma_{x\nu l}(\mathbf{k},\mathbf{k}',\mathbf{K})$ for the knockout of an x nucleon ($x=n,p$) from the νl shell of a nucleus can be represented, over a broad kinematical region of $A(e,e'p)(A-1)$ reactions and to a precision sufficient for the purposes of the ensuing analysis, in the factorized form [4–8] ($\hbar=c=1$)

$$\sigma_{x\nu l}(\mathbf{k},\mathbf{k}',\mathbf{K}) \equiv \frac{d^5\sigma_{x\nu l}}{d\varepsilon' d\Omega' d\Omega} = e^4 N_{x\nu l} F_E^2(q_\mu^2) \quad (1)$$
$$\times \frac{4MK}{\mathbf{k}^2} P(\mathbf{k},\mathbf{k}') S_x(\mathbf{k},\mathbf{k}',\mathbf{K}) G_{x\nu l}(\mathbf{q},\mathbf{K}),$$

where e is the electron charge; $M \equiv M_x$ is the nucleon mass; $N_{x\nu l}$ is the number of x nucleons in the νl shell of the nucleus involved; $F_E(q_\mu^2) = (1 + (0.055\ \mathrm{fm}^2) q_\mu^2)^{-2}$ is the form factor of the charge-density distribution in the proton; ε and ε' are the electron energies prior to and after scattering, respectively; $\mathbf{k}$ and $\mathbf{k}'$ are their corresponding momenta;

$$(q_\mu) = (\mathbf{q}, i\omega), \quad \mathbf{q} = \mathbf{k} - \mathbf{k}', \quad \omega = \varepsilon - \varepsilon', \quad (2)$$
$$q_\mu^2 = \mathbf{q}^{\,2} - \omega^2;$$

E and $\mathbf{K}$ are, respectively, the kinetic energy and momentum of the knock-on nucleon;

$$P(\mathbf{k},\mathbf{k}') \equiv P(\theta') = \frac{\mathbf{k}^2 \mathbf{k}'^2}{(q_\mu^2)^2}, \quad (3)$$

$$\theta' \equiv \theta_{\mathbf{k}'}, \quad \theta \equiv \theta_{\mathbf{K}}, \quad \theta_{\mathbf{k}} = 0, \quad \varphi' \equiv \varphi_{\mathbf{k}'} = 0,$$
$$\varphi_{\mathbf{q}} = \pi;$$

$$S_x(\mathbf{k},\mathbf{k}',\mathbf{K}) = \frac{1}{2kk'} \quad (4)$$
$$\times \left\{ \delta_{xp} \left[\left(1 + \frac{\omega}{M} + \frac{\mathbf{q}^2(1-2\gamma_x)}{4M^2} \right) (\varepsilon\varepsilon' + \mathbf{k}\cdot\mathbf{k}') \right.\right.$$
$$- \frac{2}{M} \mathbf{K}\cdot(\varepsilon\mathbf{k}' + \varepsilon'\mathbf{k}) + \frac{q_\mu^2 \mathbf{K}^2 + 4(\mathbf{k}\cdot\mathbf{K})(\mathbf{k}'\cdot\mathbf{K})}{2M^2} \Big]$$
$$\left. + \gamma_x^2 \frac{4[\mathbf{k}\times\mathbf{k}']^2 + (q_\mu^2)^2}{4M^2} \right\}$$

is a dimensionless function of the kinematical vectors $\mathbf{k}$, $\mathbf{k}'$, and $\mathbf{K}$, which reflects the structural features of relativistic-electron interaction with a quasirelativistic nucleon, the quantity γ_x being given by

$$\gamma_x = 1.79\delta_{xp} - 1.91\delta_{xn};$$

and

$$G_{x\nu l}(\mathbf{q},\mathbf{K}) = \frac{1}{(2l+1)(2\pi)^3} \quad (5)$$
$$\times \sum_{m=-l}^{m=l} |\langle \mathbf{K}| \exp(i\mathbf{q}\cdot\mathbf{r}) | x\nu l m\rangle|^2$$

[1)]Bogolyubov Institute for Theoretical Physics, National Academy of Sciences of Ukraine, Metrologichna str. 14-b, 03143 Kyiv, Ukraine.
[2)]National Taras Shevchenko University of Kyiv, Volodymyrska str. 64, 01033 Kyiv, Ukraine.
[*]e-mail: olpa@ukrpost.net

is the distorted momentum distribution, which is determined by the dynamics of the knock-on nucleon in the $|x\nu lm\rangle$ bound state and in the $|\mathbf{K}\rangle$ continuum state. First, we assume that the relativistic-electron energy loss $\omega = \varepsilon - \varepsilon'$ is due exclusively to a single event of electron collision with an individual x nucleon of the νl shell of the nucleus. Part of the energy ω transferred to the nucleon is expended into overcoming the attractive forces holding the nucleon in the bound state within the nucleus and is referred to as the intranuclear-nucleon separation energy $w_{x\nu l}$. In the ensuing calculations, we identify the separation energy $w_{x\nu l}$ ($w_{x\nu l} > 0$) with the binding energy $\varepsilon_{x\nu l}$ ($\varepsilon_{x\nu l} > 0$) of a nucleon in the corresponding nuclear shell in the independent-particle model:

$$w_{x\nu l} = \varepsilon_{x\nu l}. \tag{6}$$

The remainder $\omega - w_{x\nu l}$ is the kinetic energy E of the knock-on nucleon:

$$E = \omega - w_{x\nu l} = \frac{\mathbf{K}^2}{2M}\left(1 - \frac{\mathbf{K}^2}{4M^2}\right). \tag{7}$$

In order to perform more accurate calculations of cross sections for nuclear electrodisintegration, quite involved and cumbersome numerical methods were developed in [9, 10] within the so-called full relativistic model, where the wave functions for nucleons and electrons are determined by numerically integrating the equations of relativistic quantum mechanics for fermions. Over a rather broad kinematical region of nuclear-electrodisintegration processes, the application of this advanced computational procedure to determining the features studied below for $A(e, e'p)(A-1)$ reactions leads [11], in the majority of cases, to some quantitative corrections, which, however, can also be taken into account within the model used here. In the following, emphasis will be placed here on those results for $A(e, e'p)(A-1)$ reactions that can be confirmed by the aforementioned relativistic calculations.

If the energy of knock-on protons is so high that the distortion of nucleon motion in the final state can be disregarded, in which case

$$\psi_{\mathbf{K}}(\mathbf{x}) \to \exp(i\mathbf{K}\cdot\mathbf{x}), \tag{8}$$

then $G_{x\nu l}(\mathbf{q}, \mathbf{K})$ in (5) transforms into the momentum distribution $G^0_{x\nu l}(\mathbf{q} - \mathbf{K})$ of nucleons in the $x\nu l$ shell of the nucleus:

$$G^0_{x\nu l}(\mathbf{q} - \mathbf{K}) = \frac{1}{(2l+1)(2\pi)^3} \tag{9}$$
$$\times \sum_{m=-l}^{m=l} \left| \int \langle \mathbf{x}|\nu lm\rangle \exp(i(\mathbf{q}-\mathbf{K})\cdot\mathbf{x}) d\mathbf{x} \right|^2.$$

From precisely the plane-wave-approximation expression (9), one can readily deduce the idea of employing significant distinctions between the momentum distributions of nucleons in filled nuclear shells to identify the shell structure of light nuclei in $A(e, e'p)(A-1)$ reactions. If, for example, one assumes that the distinction between the separation energies $w_{x\nu l}$ of protons in filled nuclear shells makes it possible to identify protons in an experiment that were knocked out from different shells, then, by studying the cross section (1) as a function of the absolute value $|\varkappa| = |\mathbf{q} - \mathbf{K}|$ of the momentum of an intranuclear nucleon at the instant of its collision with a relativistic electron, we can explore the momentum distribution of protons in different nuclear shells [12].

In experimental investigations of the momentum distributions of protons in shells of medium-mass and heavy nuclei [13], an attempt was made to identify protons knocked out from the outer $2s$ (^{40}Ca nucleus) and $3s$ (^{208}Pb nucleus) shells by using, for this purpose, nonstandard special features of the shape of the momentum distributions of protons in shells whose radial quantum numbers satisfy the condition $\nu \equiv \nu_l > 1$. Since the mean field in which the knock-on proton moves in a heavy nucleus is much stronger than the nuclear field of a light nucleus, it is of interest to study the effect of a strong refraction of the knock-on proton in the final state on the shape of the momentum distributions of protons in individual nuclear shells. Figure 1 shows the cross sections $\sigma_{x\nu l}(\mathbf{k}, \mathbf{k}', \mathbf{K}) = \sigma_{x\nu l}(\varkappa)$ ($\varkappa = |\mathbf{q} - \mathbf{K}|$) for proton knockout from various shells of ^{208}Pb nuclei that is induced by electrons of energy $\varepsilon = 500$ MeV. These cross sections were calculated for the coplanar-orthogonal-kinematics version [14], where the inelastic-electron-scattering angle θ'_0, which is determined from the condition

$$\mathbf{q}^2 = \mathbf{K}^2 \to k^2 + k'^2 - 2kk'\cos\theta'_0 = 2ME + E^2, \tag{10}$$

is fixed and where either the emission angle θ of the knock-on proton or the absolute value of the momentum of the proton in the nucleus, $|\varkappa| = |\mathbf{q} - \mathbf{K}|$, at the instant of the collision between this proton and the electron that knocks it out appears as the argument of the function $\sigma_{x\nu l}(\varkappa)$ (the former is directly related to the latter). The quantity $\varkappa$ can readily be determined from the following sequence of formulas:

$$\cos(\theta_{\mathbf{q}}) = \frac{\mathbf{k}^2 + \mathbf{q}^2 - \mathbf{k}'^2}{2kq}, \tag{11}$$
$$\varkappa = [q^2 + K^2 - 2qK\cos(\theta - \theta_{\mathbf{q}})]^{1/2}$$
$$\times \operatorname{sgn}(\theta - \theta_{\mathbf{q}})|_{q=K} = 2|\mathbf{K}|\sin\frac{\theta - \theta_{\mathbf{q}}}{2}.$$

Here (Fig. 1) and below, the symbols "0" and "d" label results that were obtained in, respectively, the

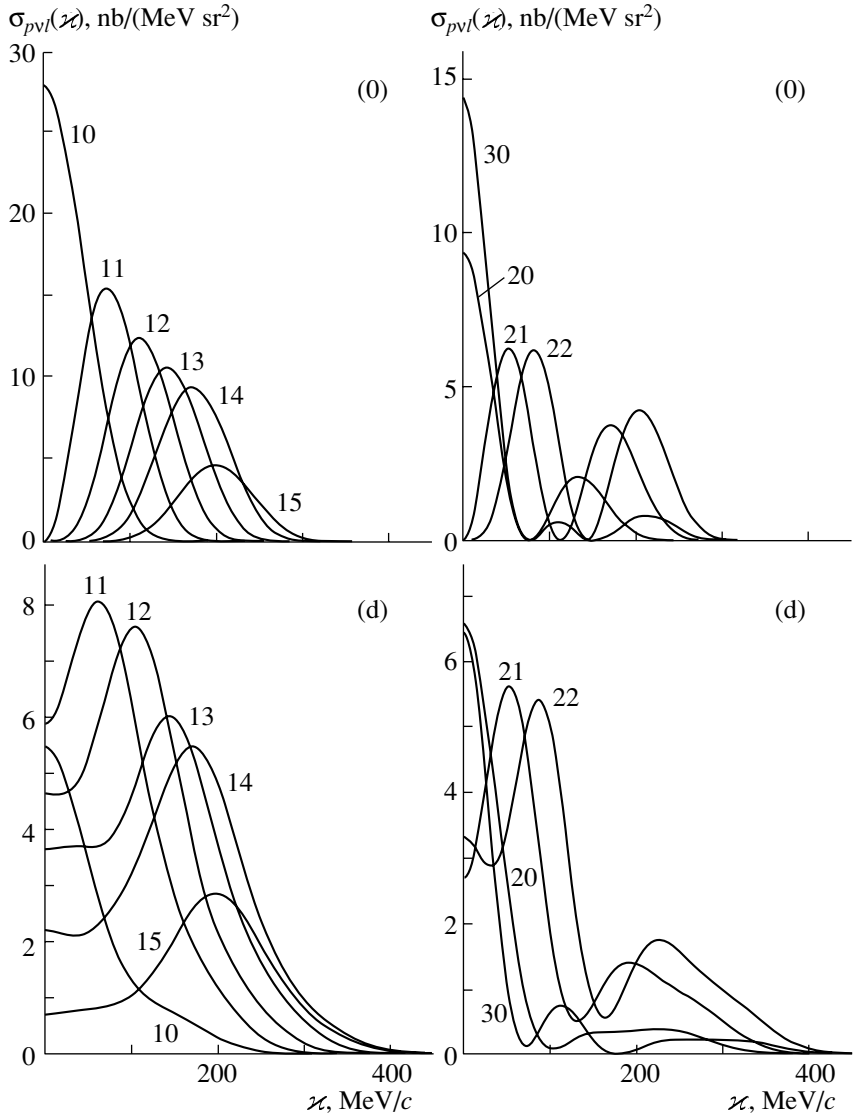

Fig. 1. Exclusive cross sections $\sigma_{p\nu l}(\varkappa)$ for the electrodisintegration of ^{208}Pb nuclei according to calculations in the mode of orthogonal coplanar kinematics [$|\mathbf{q}| = |\mathbf{K}|$, $\varkappa = |\mathbf{K} - \mathbf{q}| = 2K\sin((\theta - \theta_{\mathbf{q}})/2)$] in the (0) plane-wave approximation and (d) with allowance for the final-state interaction of the knock-on proton ($\varepsilon = 500$ MeV, $E = 165$ MeV). The curves representing $\sigma_{p\nu l}(\varkappa)$ are labeled with the quantum numbers νl of the shells from which the proton is knocked out.

plane-wave [see expression (9)] and the impulse [see expression (5)] approximation, the final-state interaction being taken into account in the latter case [12]. The parameters of the Woods–Saxon potential

$$U(r) = \frac{V_{0x}}{1 + \exp(a^{-1}(r - r_0 A^{1/3}))}, \qquad (12)$$

which is used to calculate nucleon wave functions in bound and continuum states, are most frequently chosen to be $V_{0p} \cong 52$, 55, and 58 MeV for, respectively light ($A < 45$), medium-mass, and heavy ($A > 100$) nuclei; $V_{0n} = 45$ MeV; $a = 0.55$ fm; and $r_0 = 1.25$ fm.

From the graphs in Fig. 1, it follows that, in the case of a heavy nucleus, the final-state interaction of the knock-on nucleon with the residual nucleus distorts significantly the shape of the nuclear-electrodisintegration cross section as a function of the proton emission angle in coincidence experiments. It should be noted, however that, as in the case of light nuclei [15, 16], the effect of final-state interaction can in principle be suppressed by means of a special choice of the kinematical conditions of an experiment (for example, by increasing the electron scattering angle in the case of orthogonal kinematics).

We recall that, as a matter of fact, the separation energy $w_{x\nu l}$, which is necessary for removing a nucleon from the $x\nu l$ shell, is a single parameter

according to which one associates, in coincidence experiments, the knock-on proton with the nuclear shell under study, the numerical value of $w_{x\nu l}$ determining directly the kinematical conditions of measurements in coincidence experiments in studying momentum distributions of protons in nuclear shells. For this reason, it is of importance to find additional arguments that would confirm the correctness of determining this significant parameter. Of course, an experimental corroboration of theoretically predicted nonstandard features that manifest themselves in the $A(e,e'p)(A-1)$ cross sections being studied may serve as one of such compelling arguments. For example, agreement between the experimentally measured and the theoretically predicted momentum distributions of protons in the $3s$ shell of the ^{208}Pb nucleus (the number and position of the maxima, the relationship between the cross sections at the points of extrema, and so on) could be interpreted as an unquestionable argument in support of the shell model of the nucleus. Below, we will study some theoretically predicted features of the dynamics of nuclear-electrodisintegration processes and analyze the effect of various factors manifesting themselves in exclusive and inclusive cross sections for nuclear electrodisintegration.

2. QUASIELASTIC PEAKS AND SHELL STRUCTURE OF NUCLEI

The aforementioned experiments (see [13]), in which one fixes the coincidence of an inelastically scattered electron and the proton knocked out by this electron, require painstaking efforts. In view of this, it is of interest to study the potential of inclusive experiments [17] aimed at identifying the shell structure of nuclei and at determining the parameters of the shell model in studying nuclear-electrodisintegration processes. For this purpose, we will study in greater detail the properties of quasielastic peaks—that is, $A(e,e'p)(A-1)$ cross sections $\sigma(\varepsilon',\theta') \equiv \sigma(\omega)$, which determine the energy distribution of electrons at a fixed value of the scattering angle θ' [18, 19]. On the basis of $\sigma_{x\nu l}(\mathbf{k},\mathbf{k}',\mathbf{K})$ (1), we determine, for a subsequent analysis, the cross section $\sigma_{x\nu l}(\varepsilon',\theta')$ for inelastic electron scattering on the nucleons of the $x\nu l$ shell at a fixed value of the scattering angle θ' and the total cross section $\sigma(\omega)$ for scattering on a nucleus (quasielastic peak):

$$\sigma_{x\nu l}(\varepsilon',\theta') \equiv \frac{d^3\sigma_{x\nu l}}{d\varepsilon' d\Omega'} \equiv \sigma_{x\nu l}(\omega) \qquad (13)$$
$$= \int_\Omega \sigma_{x\nu l}(\mathbf{k},\mathbf{k}',\mathbf{K}) d\Omega_{\mathbf{K}},$$

$$\sigma(\varepsilon',\theta') \equiv \sigma(\omega) = \sum_{x\nu l} \sigma_{x\nu l}(\omega).$$

We also introduce some additional quantities used below. These are the cross section $\sigma^u_{x\nu l}(\omega)$ per $x\nu l$ nucleon, the integrated cross section $\sigma^{\rm us}_{x\nu l}(\theta')$ per $x\nu l$ nucleon, and the integrated cross section $\sigma(\theta')$:

$$\sigma^u_{x\nu l}(\omega) = \frac{\sigma_{x\nu l}(\omega)}{N_{x\nu l}}, \qquad (14)$$

$$\sigma^{\rm us}_{x\nu l}(\theta') \equiv \sigma^{\rm us}_{x\nu l} = \int_0^\varepsilon \sigma^u_{x\nu l}(\omega) d\omega,$$

$$\sigma(\theta') = \int_0^\varepsilon \sigma(\omega) d\omega.$$

We will first study special features of the cross sections $\sigma(\omega)$ for as wide a range of light, medium-mass, and heavy nuclei as is possible. With an eye to a comparison of the calculated and measured values of $\sigma(\omega)$, the objects of the investigations and the kinematics of electron scattering are chosen to be identical to those in [18]: $\varepsilon = 500$ MeV and $\theta' = \pi/3$.

By way of example, Fig. 2 shows the cross sections $\sigma(\omega)$ for inelastic electron scattering on ^{24}Mg, ^{59}Ni, ^{119}Sn, and ^{208}Pb nuclei. The solid and dashed curves were calculated in, respectively, the d and the 0 approximation. The Coulomb interaction of knock-on protons with a target nucleus was described in terms of the potential of a uniformly charged ball [its charge and radius being $(Z-1)e$ and $r_0A^{1/3}$, respectively].

In comparing the measured [18] and calculated (Fig. 2, curves *1*) cross sections, we always place emphasis on special features of the shape of the cross sections $\sigma(\omega)$ such as the quasielastic-peak height, the position of the maximum, and the half-width of the peak.

Quasielastic-peak height. Comparing the calculated and the measured quasielastic peaks only in height and paying, for the time being, no attention to other features of the cross sections $\sigma(\omega)$, one can immediately notice that the calculated cross sections exceed somewhat their measured counterparts and that, in the region of heavy nuclei, the relative magnitude of this excess grows monotonically with increasing charge Ze of the target nucleus. In the situation being considered, the magnitude and the character of the above discrepancy between the theoretical and experimental values of $\sigma(\omega)$ suggest invoking the trick proposed in [11] for approximately taking into account the effect of the Coulomb field of the nucleus on the motion of a relativistic electron. The proposed modification of the computational model essentially consists in replacing, in electron plane waves, the

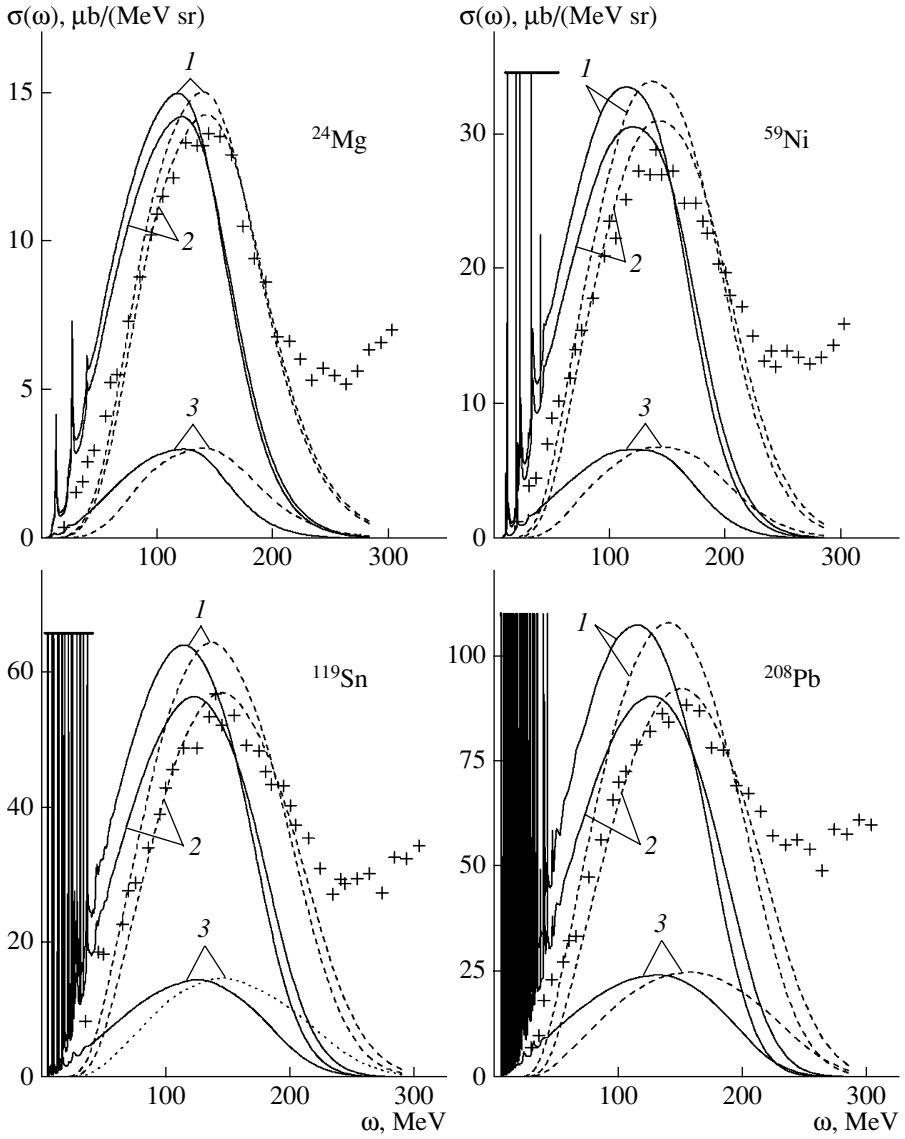

Fig. 2. Inclusive (curves *1, 2*) cross sections $\sigma(\omega)$ for inelastic electron scattering on ^{24}Mg, ^{59}Ni, ^{119}Sn, and ^{208}Pb nuclei versus the energy transfer ω (quasielastic peaks). Curves *1* correspond to the results calculated within the original model specified by Eqs. (1)–(9), while curves *2* take into account the distortion of electron plane waves in accordance with (15) in the initial and final states by the Coulomb field of the nucleus being considered. Curves *3* represent the contribution of the neutron component of the nuclei to the cross section $\sigma(\omega)$ under the following kinematical conditions of scattering: $\varepsilon = 500$ MeV and $\theta' = \pi/3$. In the vicinities of the resonance energies $\omega = \varepsilon_{xvl} - E_{xNL}$, the cross sections $\sigma(\omega)$, which take enormous values in these regions, are cut off for the sake of convenience approximately at the height of the plane-wave quasielastic peak (see Fig. 3 below).

initial and final values of the energy and momenta of scattered electrons by their effective values at the center of the target nucleus according to the scheme

$$\varepsilon = \sqrt{\mathbf{k}^2 + m^2} \to \varepsilon = \sqrt{\mathbf{k}_{\text{eff}}^2 + m^2} \qquad (15)$$
$$-\frac{3Ze^2}{2R} \to \varepsilon_{\text{eff}} = \varepsilon + \frac{3Ze^2}{2R} = \sqrt{\mathbf{k}_{\text{eff}}^2 + m^2};$$

that is, the acceleration by the Coulomb field of the target nucleus results in that the effective momenta (and energies) of the electron immediately prior to ($\mathbf{k}_{\text{eff}}$) and after ($\mathbf{k}'_{\text{eff}}$) the event of a collision with an intranuclear nucleon increase: $k_{\text{eff}} > k$ and $k'_{\text{eff}} > k'$.[3)] Curves *2* in Fig. 2, which were calculated with al-

[3)] A similar empirical trick for approximately taking into account the final-state interaction of a knock-on proton with a nuclear residue by redefining the proton momentum in the plane-wave approximation was applied earlier in [20]. It should also be noted that the trick specified by Eq. (15) is of a low efficiency in interpreting experimental data from [17], in which case the excess of the calculated cross sections over their measured counterparts is much greater.

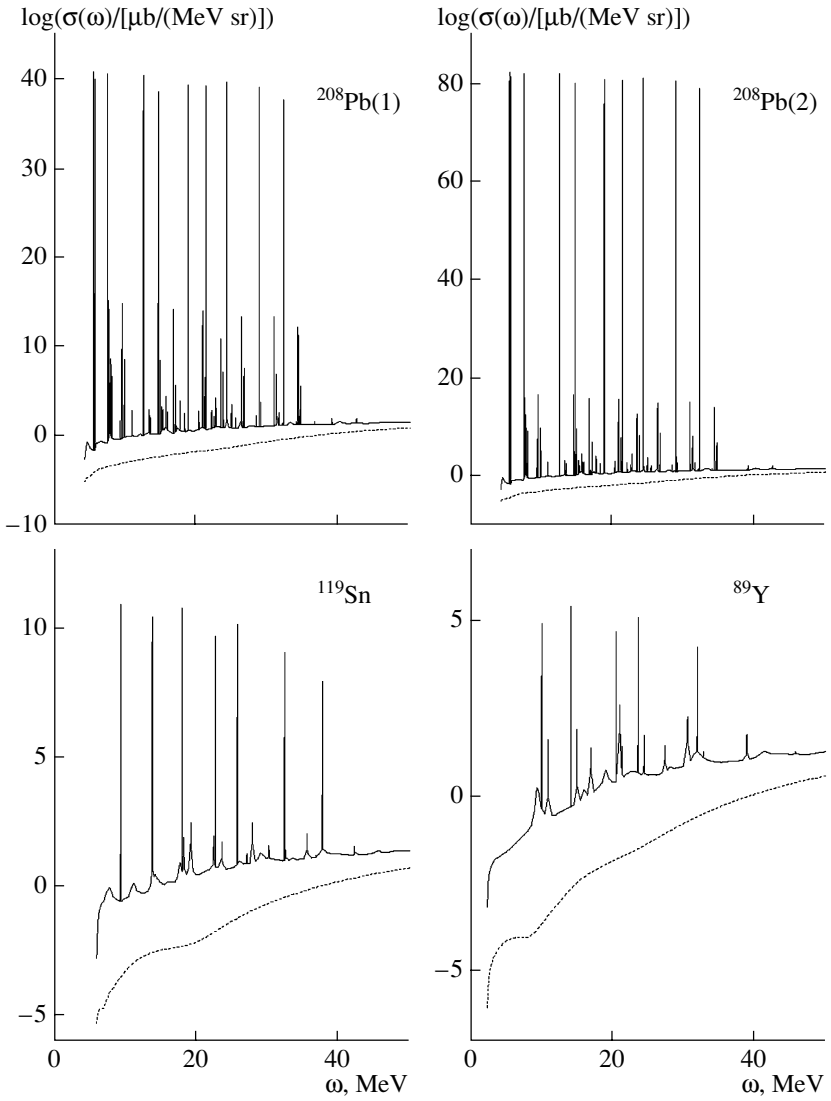

Fig. 3. Resonance structure of the cross sections $\sigma(\omega)$ for inelastic electron scattering ($\varepsilon = 500$ MeV, $\theta' = \pi/3$) on ^{208}Pb, ^{119}Sn, and ^{89}Y nuclei (see main body of the text) versus the energy transfer ω ($\omega \lesssim 60$ MeV). The dotted curves represent the results calculated in the plane-wave approximation, while the solid curves take into account final-state interaction.

lowance for the effect of the Coulomb field of the target nucleus on the dynamics of the scattered electron, describe better the maximum values at the measured quasielastic peaks; curves *3* in the same figure represent the contribution of the neutron component of nuclei to the cross sections $\sigma(\omega)$. We will see below that nuclear-electrodisintegration processes are inevitably accompanied by other phenomena that affect the height, the width, and the position of the quasielastic-peak maximum.

Special features of the resonance spectrum. The presence of sharp resonance peaks [21], which are caused by single-particle resonance states of nucleons in the continuous spectrum, is a feature peculiar to the cross sections $\sigma(\omega)$ calculated with allowance for the final-state interaction of the knock-on nucleon, this being so for almost all (light, medium-mass, and heavy) target nuclei. The majority of the resonance states are single-particle proton states that owe their existence to the concerted effect of attractive nuclear forces and repulsive Coulomb forces; in the case of neutron resonances, whose number is small, centrifugal forces play the role of repulsive forces.[4)]

The heights and half-widths of resonance ($\nu l \rightarrow$

[4)]Coulomb resonances are some kind of analytic continuation of the shell structure of nuclei to the region of the continuous spectrum [21]. In all probability, these resonances are an indispensable attribute of many modifications of the shell model, but, in view of some of the special properties inherent in them (including their elusiveness), one can encounter them only rarely [22] on the graphs of the calculated quasielastic peaks.

Table 1. Integrated cross sections $\sigma^{\rm us}_{p\nu l}(\theta')$ for inelastic electron scattering on a single νl proton of the ^{208}Pb nucleus ($\varepsilon = 500$ MeV, $\theta' = \pi/3$) according to calculations performed (d) with allowance for final-state interaction and (0) in the plane-wave approximation

νl	$\sigma^{\rm us}_{p\nu l}$, 10^2 μb/sr	
	d	0
10	1.039	1.062
11	1.038	1.076
12	1.054	1.056
20	1.050	1.039
13	1.059	1.082
21	1.058	1.109
14	1.072	1.093
22	1.065	1.100
30	1.057	1.081
15	1.097	1.075

NL) peaks are determined by the quantum numbers of the relevant discrete (νl) and resonance (NL) states and, for this reason, are greatly dependent on the parameters of the mean nuclear field in the shell model. For the sake of clarity and convenience of a comparison of the calculated curves, extremely high and sharp resonances in the cross sections $\sigma(\omega)$ in Fig. 2 are deliberately cut off (approximately at the height of the quasielastic peak) and additional information about the properties of $\sigma(\omega)$ in the region of moderate energy transfers is given in Fig. 3 for ^{208}Pb, ^{119}Sn, and ^{89}Y nuclei. In the case of the ^{208}Pb nucleus, the calculations were performed for two values of the depth V_{0p} of the Woods–Saxon potential, $V_{0p} =$ 58.0 MeV(1) and $V_{0p} = 58.4$ MeV(2). From the example of the ^{208}Pb nucleus, it follows that the heights (and half-widths) of resonance peaks in the cross sections for inelastic electron scattering may undergo enormous changes (by several tens of orders of magnitude) even in response to relatively small changes in the potential parameters. Considering, by way of example, the Pb(1) and Pb(2) panels in Fig. 3, we can indicate that, in the former case, the ten (the number of filled proton shells in the ^{208}Pb nucleus) highest vertical lines (resonances) are in fact Lorentzian curves [21] of half-width $\gamma_{p23} \approx 7.1 \times 10^{-42}$ MeV ($E_{23} \approx 0.464$ MeV), but that, in the latter case, which is similar to the former case, these are analogous curves of half-width $\gamma_{p23} \approx 2.1 \times 10^{-83}$ MeV ($E_{23} \approx$ 0.143 MeV). Such nontrivial changes in the properties of Coulomb resonances occur only in the region of modest values of the Coulomb resonance energy E_{NL}. As the depth of the potential well increases further, a continuum resonance state of energy $E_{NL} > 0$ transforms ($NL \to \nu l$) into a discrete bound state of energy $\varepsilon_{\nu l} < 0$.

We note that the exotic values presented in Fig. 3 for the resonance cross sections $\sigma(\omega_{\nu l \to NL})$ do not guarantee a priori an experimental discovery of a Coulomb resonance since an enormous height of the respective resonance peak is usually combined with its anomalously small half-width γ_{pNL}. In a physical experiment, one usually measures the integrated power of one or a few isolated Coulomb resonances:

$$\sigma^{\rm ur}(\omega_{\nu l \to NL}) \equiv \sigma^{\rm ur}_{\nu l \to NL} = \int\limits_{\omega_{\nu l NL}-\delta E}^{\omega_{\nu l NL}+\delta E} \sigma^{u}_{p\nu l}(\omega) d\omega, \tag{16}$$

$$\omega_{\nu l NL} = E_{NL} - \varepsilon_{\nu l}, \qquad \delta E \gg \gamma_{pNL}.$$

Therefore, the possibility of experimentally discovering a Coulomb resonance in studying quasielastic peaks depends greatly on the specific numerical result of integration in (16).[5)] We also note that, in Fig. 3, the observed distinctions between the resonance-peak heights for the ^{208}Pb nucleus (cases 1 and 2) can hardly manifest themselves in measured $\sigma(\omega_{\nu l \to NL})$, since, even if the height of resonance peaks increases by several tens of orders of magnitude, their half-widths γ_{pNL} decrease accordingly: as a result, the integrated [see Eq. (16)] strengths of Coulomb resonances undergo only slight (within a few percent) changes. An answer to the question of whether Coulomb resonances are observable in a physical experiment can be deduced from the data in Table 1, where the integrated cross sections $\sigma^{\rm us}_{p\nu l}$ (14) for inelastic electron scattering are given according to the calculations in the 0 and in the d approximation and the data in Table 2, where the integrated resonance cross sections $\sigma^{\rm ur}_{\nu l \to NL}$ (16), which have the

[5)] Despite the unusual properties of single-particle Coulomb resonances, the proton wave functions in the region of resonance energies in the continuous spectrum are conventional distorted waves $\psi^{(\pm)}_{\mathbf{K}}(\mathbf{r})$—that is, they are solutions to the Schrödinger equation that correspond to a real-valued energy [21]. In order to perform integration in (16), one does not need additional axiomatics associated, for example, with nonstandard properties of states corresponding to complex (according to Gamow) values of energy [23]. In the mathematical aspect, the operation in (16) does not involve technically insuperable difficulties. As the resonance energy E_{NL} approaches the Coulomb barrier height $V^{\rm C}_b$, Coulomb resonances become less sharp, acquiring a width visually observable on the graphs.

Table 2. Integrated cross sections $\sigma^{\mathrm{ur}}_{\nu l\to NL}$ (in μb/sr) per nucleon for inelastic electron scattering ($\varepsilon = 500$ MeV, $\theta' = \pi/3$) accompanied by the excitation of NL Coulomb resonances in the knockout of a proton from the νl shell of the ^{208}Pb nucleus ($\varepsilon = 500$ MeV, $\theta' = \pi/3$)

νl	NL					
	23	16	31	24	32	17
10	3.75×10^{-4}	1.77×10^{-3}	2.40×10^{-4}	2.48×10^{-3}	1.10×10^{-3}	9.41×10^{-3}
11	3.17×10^{-3}	7.50×10^{-3}	1.85×10^{-3}	1.18×10^{-2}	8.46×10^{-3}	3.16×10^{-3}
12	8.03×10^{-3}	4.32×10^{-3}	4.61×10^{-3}	3.45×10^{-3}	9.18×10^{-4}	2.31×10^{-2}
20	1.29×10^{-2}	6.28×10^{-5}	8.20×10^{-3}	6.30×10^{-7}	7.30×10^{-4}	5.57×10^{-2}
13	2.67×10^{-3}	1.57×10^{-2}	3.66×10^{-4}	3.73×10^{-2}	2.74×10^{-2}	1.20×10^{-1}
21	9.47×10^{-4}	4.73×10^{-2}	1.03×10^{-4}	9.30×10^{-2}	5.92×10^{-2}	1.71×10^{-1}
14	2.40×10^{-2}	8.64×10^{-2}	1.88×10^{-2}	1.43×10^{-1}	8.60×10^{-2}	3.51×10^{-1}
22	6.08×10^{-2}	1.51×10^{-1}	4.25×10^{-2}	3.29×10^{-1}	2.61×10^{-1}	2.96×10^{-1}
30	8.40×10^{-2}	1.60×10^{-1}	5.56×10^{-2}	4.32×10^{-1}	3.87×10^{-1}	7.57×10^{-2}
15	8.36×10^{-2}	2.55×10^{-1}	4.46×10^{-2}	2.84×10^{-1}	9.52×10^{-2}	6.57×10^{-1}

same dimensions, are given for the ^{208}Pb nucleus at $\theta' = \pi/3$ and $\varepsilon = 500$ MeV.

From the data presented in Table 1, we deduce that the integrated scattering ability of a single nucleon—that is, its total individual contribution to $\sigma(\omega)$—is virtually independent of the quantum numbers of the shell from which the proton is knocked out.[6)] Relying on this fact, one can conclude that, over a rather wide kinematical region of inelastic-electron-scattering processes, the integrated strength of a quasielastic peak is an invariant quantity within the shell model: $\sigma(\theta') = \mathrm{const}$. This implies, among other things, that the decrease in the height of a peak in response to variations in the parameters of the mean nuclear field is accompanied by its broadening, while the increase in the height of the peak is accompanied by its narrowing. Our numerical calculations revealed that modest relative variations in potential parameters exert virtually no effect on the shape of the quasielastic peak.

An analysis[7)] of the numerical values presented in the tables for $\sigma^{\mathrm{us}}_{p\nu l}$ and $\sigma^{\mathrm{ur}}_{\nu l\to NL}$ makes it possible to predict some of the Coulomb resonance–induced features of the cross sections $\sigma(\omega) \equiv \sigma(\omega, A, Z)$. For a sequence of neighboring nuclei, we now compare in pairs the measured cross sections $\sigma(\omega, A, Z)$ with their counterparts tabulated in [18]. From this comparison, we can readily see that, in the quasielastic-peak region, the following inequality holds as a rule:

$$\sigma(\omega, A, Z) < \sigma(\omega, A', Z'), \quad \forall\{A < A', Z < Z'\}. \tag{17}$$

In the aforementioned measurements, the inequality in (17) is violated only in a few cases and only at moderate values of the energy transfer ω. By way of example, we indicate that, for the pair of ^{208}Pb and ^{181}Ta nuclei, the inequality in (17) is violated at $\omega = 30$, 36, 56, and 60 MeV, while, for ^{181}Ta and ^{119}Sn, it is violated for $\omega = 46$ MeV. Upon taking into account the features of the dynamics of fast-electron-induced nuclear electrodisintegration (phenomenon of quasireal photons) that are studied below and employing the numerical results given in Tables 1 and 2 and in Fig. 2, one can predict a violation of the inequality in (17) in the above regions of the spectra of inelastic electron scattering. The assumption that the inversion of the inequality in (17) in the case of heavy and medium-mass nuclei at modest values of the energy transfer ω occurs more frequently could be verified only by much more thoroughly studying the properties of the electron spectra in the region of low ($\omega \le 60$ MeV) energy transfers. Unfortunately, there are a large number of cases where ellipses appear in [18] precisely in this interval (in all probability, this corresponds to failed measurements).

[6)] This result could be foreseen. Under the kinematical conditions of the scattering process that were specified above, the invariability of $\sigma^{\mathrm{us}}_{p\nu l}$ in response to variations in the quantum numbers νl is in fact a corollary of the normalization condition for the momentum distributions of nucleons in nuclear shells: $\int G_{x\nu l}(\mathbf{q}, \mathbf{K}) d\mathbf{K} = 1$.

[7)] One can easily see that, in the kinematical region being studied, monopole, quadrupole, and octupole transitions, as well as transitions of other multipolarities, can manifest themselves in addition to dipole transitions or even be more noticeable than them, or no transitions are observable there.

Position of the maximum and half-width of the peak. Comparing the positions of the maxima of the calculated and measured quasielastic peaks $\sigma(\omega)$, we can readily see that, at the chosen values of the potential parameters, the plane-wave approximation describes better, at first glance, the position of the maximum of the experimental cross section than the d approximation.

This result, which is somewhat unexpected, is likely to be accidental and is, in the present case, a corollary of some inconsistency in the traditional definition of the limiting transition (8) to the plane-wave approximation. This statement is supported by the calculations of the cross section for the electrodisintegration of a ^{89}Y nucleus that were specially performed for two sets of values for the depths V_{0x} of the Woods–Saxon potential: $V_{0p} = 50$ MeV and $V_{0n} = 45$ MeV (Fig. 4, curves *1*) and $V_{0p} = 70$ MeV and $V_{0n} = 65$ MeV (Fig. 4, curves *2*). On the respective graphs, one can see that, in the d approximation, the positions of the maxima of $\sigma(\omega)$ for the potentials differing significantly in the depths V_{0x} coincide (the effect of orthogonality of the wave functions associated with the discrete and continuous spectra), but that curve *2* calculated in the plane-wave approximation [see Eq. (8)] is shifted rightward sizably with increasing potential depth.[8)] It can readily be guessed that this shift is due to the increase in the binding energies $\varepsilon_{x\nu l}$ of nucleons in nuclear shells with increasing potential depth parameters V_{0x}.

The limiting transition $\psi_{\mathbf{K}}(\mathbf{x}) \to \exp(i\mathbf{K}\cdot\mathbf{x})$ in the continuum region can readily be implemented by setting

$$V_{0x} = 0, \quad (Z-1)e = 0. \tag{18}$$

The orthogonality concept for wave functions [6], which is basic in the theory of quantum-mechanical transitions, suggests that it would be natural to supplement, in realizing the plane-wave approximation specified by Eq. (8), the limiting transition in the continuum region according to (18) with an equivalent operation in the spectrum of bound nucleon states $|x\nu lm\rangle$. The empirical trick specified by (18) is not applicable directly in the case of a discrete spectrum since it annihilates the discrete spectrum itself. Noting that a decrease in the depth parameters V_{0x} of the mean nuclear field ($V_{0x} \to 0$) leads to a decrease in the binding energy of nucleons in nuclear shells ($\varepsilon_{x\nu l} \to 0$), we impose, on all discrete states in the shell model of the nucleus, the requirement $\varepsilon_{x\nu l} = 0$, which is readily implementable in the calculations, and put this requirement in correspondence to the operation specified by (18) in the continuum region. Since $w_{x\nu l} = \varepsilon_{x\nu l}$ [Eq. (6)], one can see, with allowance for (7), that the proposed modification of the plane-wave approximation in the region of the discrete spectrum ultimately reduces to a modification of continuum wave functions by effectively increasing the energy and the momentum of the knock-on nucleon:

$$E = \omega - w_{x\nu l} \to E_{\text{eff}} = \omega, \tag{19}$$

$$E_{\text{eff}} = \frac{\mathbf{K}_{\text{eff}}^2}{2M}\left(1 - \frac{\mathbf{K}_{\text{eff}}{}^2}{4M^2}\right), \quad \psi_{\mathbf{K}}(\mathbf{x}) \to \exp(i\mathbf{K}_{\text{eff}}\cdot\mathbf{x}).$$

Digressing from the above philosophical substantiation of the modification specified by (19) and invoking the concept of orthogonality of the wave functions for the initial and final states, we can say that the proposed improvement of the plane-wave approximation is eventually equivalent to the approximate method for taking into account the final-state interaction of the knock-on nucleon by empirically increasing its momentum in the plane-wave approximation [20].

The cross sections $\sigma(\omega)$ calculated in the approximation specified by (19) are given in Fig. 4 for the above two sets of values for the potential depths V_{0x} (curves $1^{(m)}$ and $2^{(m)}$, respectively). Thus, we see that, if use is made of the improvement of the plane-wave approximation (8) according to (19), the positions of the maxima of the respective four curves in Fig. 4 nearly coincide. Upon redefining the plane-wave approximation in this way, the relative shift of the quasielastic peaks calculated in the 0 and d approximations, which was found previously by many authors [6, 24], disappears, and a resonance [21] character of inelastic electron scattering in the region of moderate energy transfers is in fact the only nontrivial effect introduced in the theory upon taking into account the final-state interaction of the nucleon with a nuclear residue.

Comparing the measured cross sections $\sigma(\omega)$ with their counterparts calculated either in the modified plane-wave approximation [see (19)] or with allowance for the final-state interaction [see (5)], we arrive at the conclusion that, within the computational model being studied, the positions of the maxima of the calculated and measured quasielastic peaks do not agree, the shift $\delta\omega_{\max}$ of these maxima in the region of medium-mass and heavy nuclei being about 20 MeV. Considering the separation energies $w_{x\nu l}$ as model parameters and formally increasing the quantity $w_{x\nu l}$ in (7) by $\delta\omega \approx 20$ MeV, one could match (by means of a fitting procedure) the positions of the extrema of the calculated and measured cross sections and, in passing, identify [in accordance with (6)] increased $w_{x\nu l}$ with the binding energies $\varepsilon_{x\nu l}$ of nucleons in nuclear shells. Within an alternative

[8)] Therefore, the position of the quasielastic-peak maximum in the plane-wave approximation [Eq. (8)] can be described only at specific values of the mean-nuclear-field parameters.

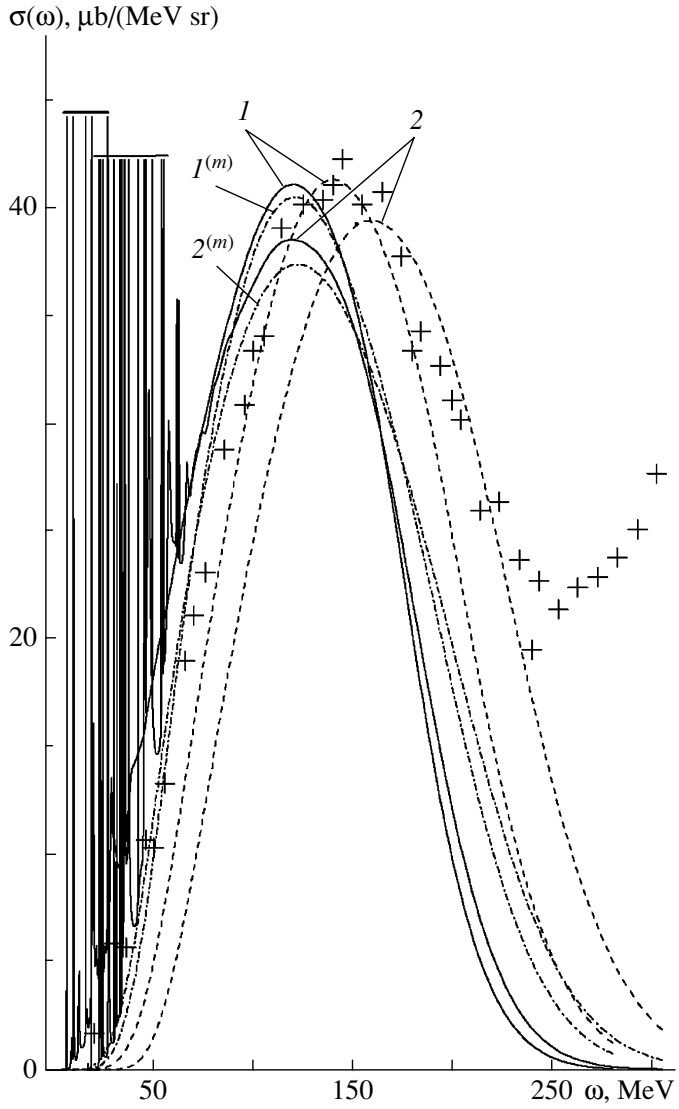

Fig. 4. Inclusive cross sections $\sigma(\omega)$ for inelastic electron scattering on a ^{89}Y nucleus according to calculations for two sets of values for the depth parameter of the Woods–Saxon potential: $V_{0p}^{(1)} = 50$ MeV, $V_{0n}^{(1)} = 45$ MeV (curves *1*, $1^{(m)}$) and $V_{0p}^{(2)} = 70$ MeV, $V_{0n}^{(2)} = 65$ MeV (curves *2*, $2^{(m)}$). The solid, dashed, and dash-dotted curves were calculated, respectively, with allowance for final-state interaction, in the plane-wave approximation [see Eq. (8)], and in the modified plane-wave approximation [see Eq. (19)].

approach, a successful interpretation of the position of the quasielastic-peak maximum could be achieved if, in (7), the binding energies $\varepsilon_{x\nu l}^{\text{expt}}$ determined in various experiments for nucleons in various nuclear shells are substituted for $\varepsilon_{x\nu l}$ (in the case of light nuclei [25], $\varepsilon_{x\nu l}^{\text{expt}} \gg \varepsilon_{x\nu l}$, as a rule). However, the origin of so nontrivial an increase in the nucleon separation energy $w_{x\nu l}$ will remain unclear until the last section of this article.

We will now study the possibility of identifying the shell structure of nuclei and determining the quantum numbers of nuclear shells in experiments devoted to exploring quasielastic peaks. Digressing from the resonance structure of $\sigma(\omega)$ at moderately small ω, one can state that, upon summation of the contributions $\sigma_{x\nu l}(\omega)$ from individual nuclear shells of the same nucleus or, which is equivalent, upon going over from one nucleus to another, a quasielastic peak retains perfectly a regular, without significant special features, bell-like shape in the sequence of calculated cross sections. Since the quasilastic-peak curve of such a simple shape can be successfully interpreted within simpler models (for example, the Fermi gas model [18]), it is hardly possible, in directly

interpreting calculated $\sigma(\omega)$, to prove compellingly the existence of the shell structure on the basis of experimental data and to determine the sequence of quantum numbers of shells that are being filled in nuclei. Nevertheless, we can propose a trick by means of which one can try to determine, from an analysis of experimental results concerning quasielastic peaks, the sequence of quantum numbers of nuclear shells that are being filled.

The proposed trick is essentially based on the fact that the aforementioned gradual filling of the regular bell-like curve of the quasielastic peak is in fact implemented upon summation of the curves $\sigma_{x\nu l}(\omega)$ that represent cross sections for electron scattering on nucleons of the nuclear shell characterized by the quantum numbers νl, which are different in shape, and which are not always regular. In order to illustrate this statement, the cross sections $\sigma^u_{p\nu l}(\omega)$ (14) for inelastic electron scattering on a single proton of the ^{208}Pb nucleus are presented in Fig. 5 versus the quantum numbers νl of the shell from which the proton is knocked out. In our calculations, we used the kinematical parameters of the experiments reported in [18]. From the data in Fig. 5, one can readily deduce that the shape of the resulting curves is obviously sensitive to arguments such as the quantum numbers νl of nuclear shells. For example, the curves $\sigma_{p\nu l}(\omega)$ calculated for shells characterized by quantum numbers $\nu_l > 1$ differ significantly from one another and from the curves corresponding to $\nu_l = 1$. One can identify them even visually by their outward appearance. If, in the total cross sections $\sigma(\omega)$, we can single out the shell contributions $\sigma_{p\nu l}(\omega)$, then there would arise the possibility of identifying the quantum numbers of nuclear shells in studying inelastic electron scattering in $A(e, e'p)(A-1)$ reactions.

On the basis of the earlier established fact that the quantity $\sigma^{\rm us}_{x\nu l}(\theta')$ defined in (14) remains unchanged in response to variations in the quantum numbers νl of nuclear shells, one can readily conjecture, and confirm this conjecture by specific calculations, that the shape and the magnitude of the cross sections $\sigma^u_{x\nu l}(\omega)$ are only weakly sensitive to modest variations in the mean-nuclear-field potential. Since the mean-field parameters for neighboring nuclei are close by assumption, the cross sections (13) as calculated in the quasielastic-peak region by performing summation over the shells common to such nuclei are nearly coincident. Even in the case where the mean-field parameters for two nuclei are markedly different, the character of the possible correction can easily be forecast on the basis of theoretical considerations. If the $(A,\ Z)$ nucleus has filled nucleon shells, then the distinctions between the cross sections (13) for the $(A,\ Z)$ and $(A+\delta A,\ Z+\delta Z)$ nuclei will be due predominantly to extra valence nucleons of the heavier nucleus. Obviously, one can choose pairs of nuclei such that the differences of the cross sections for them would reproduce the distinctive features of $\sigma_{p\nu l}(\varepsilon', \theta')$ for the outer valence (proton) shell of the heavier nucleus. It follows that, by measuring two quasielastic peaks for relatively close nuclei and subtracting one of these measured cross sections from the other, one can associate, by analyzing the shape of the resulting difference, outer nucleons with one nuclear shell or another and, by using the shape of this difference, determine unknown quantum numbers $\nu_x l_x$ of the valence shell. Of particular interest are $\nu \equiv \nu_l > 1$ shells, which occur most frequently in the region of medium-mass and heavy nuclei. One can render such an experiment more informative by concurrently performing similar subtractions for the cross sections corresponding to A and $A - \delta' A$ nuclei as well, in which case the missing valence nucleons have different values of the quantum numbers $\nu'_x l'_x$ and would therefore induce a different (also theoretically predictable) shape of the difference of the cross sections for the pair of nuclei under study. As a matter of fact, the quasielastic-peak subtraction described above is some kind of differentiation of cross sections with respect to a parameter, and its successful application (within various theoretical and experimental modifications) requires that the accuracy achieved in [18] in measuring $\sigma(\omega)$ be significantly improved.

To conclude this section, we would like to note that the nuclear-electrodisintegration cross sections presented in Figs. 2–5 belong to a classical type of cross sections that provide a convenient basis for theoretically predicting the phenomenon of a low-energy nonrelativistic proton confinement. The essence of this phenomenon is that low-energy protons (that is, protons of energy E below the Coulomb barrier height $V_b^{\rm C}$: $E \lesssim V_b^{\rm C}/2$) or other charged clusters knocked out from a heavy nucleus are virtually unobservable. In this statement, it is implied that the energy of the projectile particle is sufficient for the realization of an event in which a proton (cluster) is knocked out from a nucleus and that there are manifestations of a process where the inelastic scattering of a projectile on a nucleus is accompanied by a sufficiently high energy transfer to the nucleus. In the situation being considered, a low-energy proton or charged cluster knocked out from a heavy nucleus cannot be recorded because of the following special features of the nuclear-electrodisintegration process:

(i) The probability of proton transition to a continuum state of energy not equal to a resonance energy is virtually equal to zero—such a transition is suppressed by the Coulomb barrier.

(ii) The probability of proton transition to states of resonance energy is of course significant, but the time

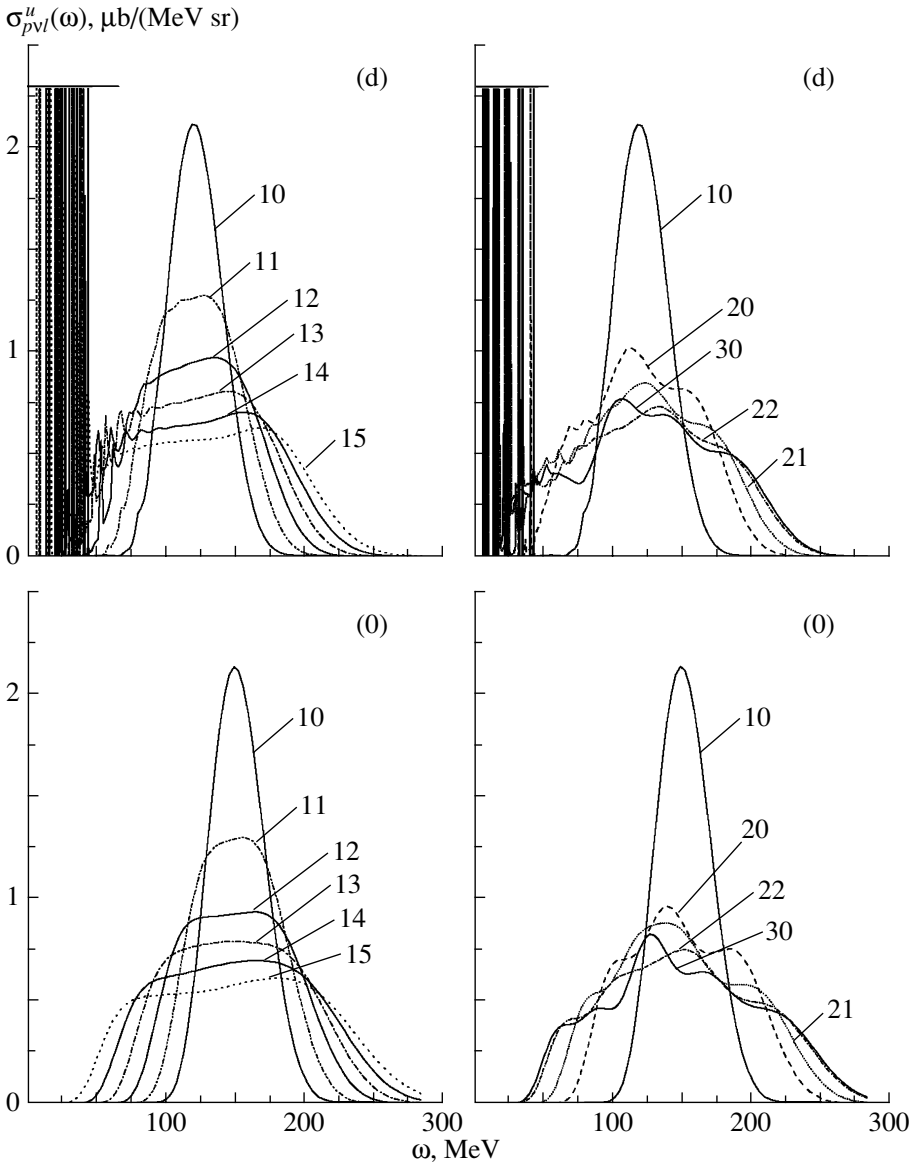

Fig. 5. Cross sections $\sigma^u_{p\nu l}(\omega)$ per nucleon for proton knockout from the νl shell of the ^{208}Pb nucleus according to calculations (0) in the plane-wave approximation and (d) with allowance for the final-state interaction of the knock-on nucleon. The parameters of the Woods–Saxon potential and the kinematical conditions of the scattering process are identical to those for the data in Fig. 2. The curves representing $\sigma^u_{p\nu l}(\omega)$ are labeled with the sets of quantum numbers νl of nuclear shells from which the proton is knocked out.

within which the proton resides within the nucleus in such a state (the resonance lifetime with respect to protonic decay) is so long that, with a much higher probability, the excitation of a Coulomb resonance would eventually result, for example, in an inverse radiative transition of a proton (that is, a transition involving photon emission) to a lower lying stationary (or resonance) level or in a process where the projection of the isospin of the proton involved undergoes inversion induced by nuclear forces and accompanied by neutron emission from the nucleus. The aforementioned processes obviously lead to a nontrivial intrinsic broadening[9)] of Coulomb resonances and to a decrease in their lifetime.

[9)]This kind of Coulomb resonance broadening is impossible in the case where a resonance state of an alpha particle or a heavier charged cluster is the ground state of the nucleus involved. In this case, the concept of Coulomb resonances provides a convenient framework for a consistent quantum-mechanical interpretation of such phenomena as alpha decay and the fission of heavy nuclei [21, 26].

3. ANGULAR DISTRIBUTIONS OF KNOCK-ON PROTONS

Investigation and interpretation of the spectra of inelastic electron scattering (quasielastic peaks) involve some difficulties both in the theoretical and in the experimental aspect. In the theoretical aspect, for example, it is convenient to assume that a quasielastic peak owes its existence to a nuclear-electrodisintegration reaction $A(e,e'p)(A-1)$ exclusively, this implying that, in the kinematical region being studied, one usually disregards processes like meson electroproduction, cluster knockout, and the knockout of a few nucleons. In interpreting experimental data, it is necessary to take into account elastic electron scattering and inelastic electron scattering accompanied by bremsstrahlung, pair production, and so on. In view of the aforesaid, an investigation of nuclear electrodisintegration by means of directly studying the angular and energy distributions of knock-on protons can be considered as a primitive attempt at getting rid of (at least partly) the aforementioned inconveniences.

In the theoretical aspect, it is but of minor interest, at first glance, to study the cross section $\sigma^p_{\nu l}(E,\theta)$ for proton knockout from the νl shell,

$$\sigma^p_{\nu l}(E,\theta) = \int\limits_{\Omega} \sigma_{p\nu l}(\mathbf{k},\mathbf{k}',\mathbf{K})d\Omega', \qquad (20)$$

where $\sigma_{x\nu l}(\mathbf{k},\mathbf{k}',\mathbf{K})$ was defined in (1), and the total cross section $\sigma^{ps}_{\nu l}(E,\theta)$ for proton knockout from a sequence of several filled nuclear shells,

$$\sigma^{ps}_{\nu l}(E,\theta) = \sum_{\nu' l'=(10)}^{\nu' l'=\nu l} \sigma^p_{\nu' l'}(E,\theta), \qquad (21)$$

versus the distribution of knock-on protons with respect to angles and energies.

Indeed, one usually assumes that the main special features of nuclear-electrodisintegration cross sections are associated with the properties of the nucleon momentum distributions $G_{x\nu l}(\mathbf{q},\mathbf{K})$. However, the argument of the function $G^0_{x\nu l}(\mathbf{q}-\mathbf{K}) = G^0_{x\nu l}(\mathbf{k}-\mathbf{k}'-\mathbf{K})$ at fixed $\mathbf{k}$ in the plane-wave approximation, for example, depends symmetrically on the vector arguments $\mathbf{K}$ and $\mathbf{k}'$. Therefore, it would be justifiable to assume that the kinematical dependences of the cross sections $\sigma^p_{\nu l}(E,\theta)$ can hardly develop new qualitative features in relation to the cross sections $\sigma_{p\nu l}(\varepsilon',\theta')$ (13), which were studied above. Upon taking additionally into account the fact that a numerical integration in (20) over the scattered-electron solid angle $d\Omega' \equiv d\Omega_{\mathbf{k}'}$ would be much more involved technically and cumbersome than the analogous integration in (13) over the solid angle $d\Omega_{\mathbf{K}}$, it could easily be foreseen that a natural sense of a priori skepticism prevailed in assessing prospects in this field of investigations into $A(e,e'p)(A-1)$ reactions. However, numerical calculations of the cross sections for proton knockout dispelled completely the above doubts. The most encouraging argument here comes from considering the dimensionless function $P(\mathbf{k},\mathbf{k}')$, which is dependent only on the kinematical parameters $\mathbf{k}$ and $\mathbf{k}'$ of the inelastic-electron-scattering process and which was specially isolated in Eq. (1) [for the definition of this function, see Eq. (3)].

The function $P(\mathbf{k},\mathbf{k}')$ owes its appearance in the cross section (1) to the Fourier component $D_{\mu\nu}(q^2_\lambda) = \delta_{\mu\nu}/(q^2_\lambda)$ of the photon propagator, which is an indispensable and indisputable[10] attribute of the present-day [27, 28] theoretical interpretation of any process induced by the scattering of relativistic electrons on hadrons. For this reason, not only the aforesaid concerns the nuclear-electrodisintegration process, which is considered in the present study, but this also applies indirectly to a much broader range of similar phenomena—for example, meson electroproduction [29].

First, we will list those features of the function $P(\mathbf{k},\mathbf{k}') \equiv P(\theta')$ that one must take into account in choosing an algorithm for integration in (20) over the scattered-electron solid angle $d\Omega'$. In order to obtain simple numerical estimates, we assume that the energies ε and ε' ($\varepsilon > \varepsilon'$) fall within rather wide ranges of values that occur most frequently in actual experiments: $\varepsilon \cong 400-900$ MeV, $\varepsilon' \cong 300-700$ MeV, and $\varepsilon - \varepsilon' \equiv \omega \cong 100-400$ MeV; we also assume that $\varepsilon > \varepsilon'$, $\varepsilon > \omega$, $\varepsilon \sim \varepsilon'$, and $\omega \sim \varepsilon'$. In the kinematical region specified above, the very strong inequalities $\varepsilon \gg m$ and $\varepsilon' \gg m$ are always valid. Therefore, we have

$$\varepsilon = \sqrt{\mathbf{k}^2+m^2} = (k^2+m^2)^{1/2} \qquad (22)$$

$$= k\left(1+\frac{m^2}{2k^2}+O\left(\frac{m^4}{k^4}\right)\right),$$

$$\varepsilon' = \sqrt{\mathbf{k}'^2+m^2} = \left(k'^2+m^2\right)^{1/2} \qquad (23)$$

$$= k'\left(1+\frac{m^2}{2k'^2}+O\left(\frac{m^4}{k'^4}\right)\right).$$

[10] By way of example, we indicate that, in the ten different relativistic generalizations of $\sigma_{x\nu l}(\mathbf{k},\mathbf{k}',\mathbf{K})$ that are presented in [12], the factor $(q^2_\lambda)^{-2}$ is not subjected to a relativistic modification and is present, as it must, in all ten versions in the immutable original form.

Taking into account Eqs. (22) and (23), we can readily find, within the preset accuracy, that

$$(\varepsilon-\varepsilon')^2=(k-k')^2\left(1-\frac{m^2}{kk'}\right), \qquad (24)$$

$$(\mathbf{k}-\mathbf{k}')^2=(k-k')^2+4kk'\sin^2\frac{\theta'}{2};$$

$$q_\mu^2=(\mathbf{k}-\mathbf{k}')^2-(\varepsilon-\varepsilon')^2=4kk'\left(\sin^2\frac{\theta'}{2}+\frac{\lambda^2}{4}\right), \qquad (25)$$

where the dimensionless kinematical parameter λ has the form

$$\lambda=\frac{m(k-k')}{kk'}\cong\frac{m\omega}{\varepsilon\varepsilon'} \qquad (26)$$

and determines [30] the phenomenon of a frontal deceleration of a relativistic electron within a nucleus. Substituting (25) into (3), we obtain

$$P(\theta')=\frac{1}{(4\sin^2(\theta'/2)+\lambda^2)^2}. \qquad (27)$$

In the region of small electron-scattering angles, $\theta'\ll 1$, this reduces to

$$P(\theta')\approx\frac{1}{(\theta'^2+\lambda^2)^2}. \qquad (28)$$

We note that, in the kinematical region considered here, the strong inequalities $\lambda\ll 1$ and $\lambda^2\ll 1$ hold for the dimensionless parameters λ and λ^2. If, for example, $\varepsilon=600$ MeV, $\omega=100$ MeV, and $\varepsilon'=500$ MeV, then $\lambda^2\approx 3\times 10^{-8}$; therefore, $P(0)\approx 1.2\times 10^{15}$, while $P(\theta'=5^\circ=5\pi/180)\approx 1.7\times 10^4$—that is, $P(\theta')$ decreases in magnitude by nearly 11(!) orders over the narrow range $\theta'\in[0;10^{-1}]$.

This property of $P(\theta')$ should be borne in mind in performing integration in (20) and is caused by the strong inequality $q_\mu^2/\omega^2\approx m^2/(\varepsilon\varepsilon')\ll 1$ for $\theta'\ll 1$ (that is, $q_\mu^2/\omega^2\approx 0$ at $\theta'\approx 0$). It is well known [27, 28] that, in the Feynman diagram, the 4-vector q_μ denotes the 4-momentum $(\mathbf{q},i\omega)$ of a virtual photon emitted by the ultrarelativistic electron inelastically scattered by a nucleus. Since the strict equality $q_\mu^2=0$ holds for the 4-momentum of a real photon, we will assume in the following that the knockout of protons from nuclei in inelastic electron scattering at very small angles, $\theta'\ll 1$, is associated with quasireal ($q_\mu^2/\omega^2\approx 0$) virtual photons and accordingly refer to effects induced by inelastic electron scattering in the region $\theta'\ll 1$ as the phenomenon of quasireal photons. Below, we will see that quasireal photons play a nontrivial role in the dynamics of $A(e,e'p)(A-1)$ reactions.

In order to achieve a satisfactory precision of integration with respect to the electron-scattering angle θ' in (20), we represent the respective integrand as a function of θ' in the form of the product $\sigma_{p\nu l}(E,\theta,\theta')=f(E,\theta,\theta')P(\theta')$, where $f(E,\theta,\theta')\equiv f(\theta')$ is a smooth function of the argument θ' in the vicinity of the point $\theta'=0$ and break down the integration interval $(0,\pi)$ into two subintervals $(0,\eta_0)$ and (η_0,π), where $\lambda\ll\eta_0\ll 1$. We then have

$$\sigma_{\nu l}^p(E,\theta)=\int_0^\pi f(\theta')P(\theta')d\Omega' \qquad (29)$$

$$=\int_0^{\eta_0}[f(0)+f'_{\theta'}(0)\theta'+\ldots]P(\theta')d\Omega'$$

$$+\int_{\eta_0}^\pi f(\theta')P(\theta')d\Omega'\equiv\sigma_{\nu l}^{p(1)}(E,\theta,\eta_0)$$

$$+\sigma_{\nu l}^{p(2)}(E,\theta,\eta_0)\equiv I_1(E,\theta,\eta_0)+I_2(E,\theta,\eta_0).$$

The sum of the integrals I_1 and I_2 in (29) is independent of η_0, although each of the terms depends on this parameter. Disregarding the second term in the expansion of $I_1(E,\theta,\eta_0)$ and performing integration over the electron-scattering solid angle $d\Omega'\equiv\sin\theta' d\theta' d\varphi'$, we can state that $I_1\simeq\pi f(0)\lambda^{-2}\left(1+O(\lambda^2/\eta_0^2)\right)\approx\pi f(0)\lambda^{-2}$. It follows that, over a comparatively broad interval of η_0 (in the calculations, the parameter η_0 is $\eta_0=\pi/90$) where the representation $f(\theta')=f(0)+f'_{\theta'}(0)\theta'$ is still valid, the dependence of I_1 (and, hence, of I_2) on this parameter is insignificant. Therefore, the second integral $I_2(E,\theta,\eta_0)\approx\sigma_{\nu l}^p(E,\theta)-\pi f(0)\lambda^{-2}=I_2(E,\theta)$, which can readily be evaluated by standard methods of numerical integration, determines the background of protons that do not originate from the knockout process induced by quasireal virtual photons.

We will now study some aspects of the effect of quasireal photons on the dynamics of the nuclear-electrodisintegration process induced by high-energy electrons. For the example of the $1p$ and $1d$ shells of the ^{40}Ca nucleus, Fig. 6 illustrates the structure of the angular distributions of $E=165$ MeV knock-on protons, in which case $\varepsilon'=\varepsilon-E-\varepsilon_{\nu l}$. In this figure, curves *1* represent the total angular distributions $\sigma_{\nu l}^p(E,\theta)$ of protons knocked out from the aforementioned shells, while curves *2* correspond to the calculations taking no account of protons knocked out by quasireal photons [and including only $\sigma_{\nu l}^{p(2)}(\theta)\equiv$

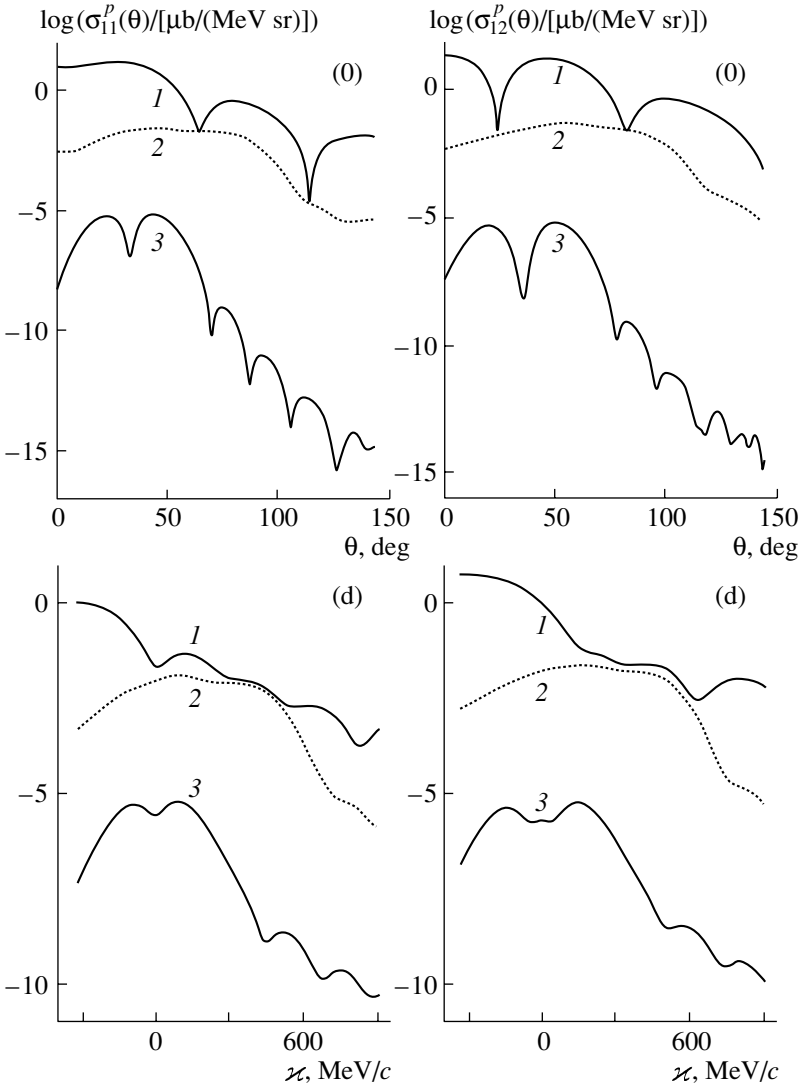

Fig. 6. Angular distributions $\sigma^p_{\nu l}(\theta)$ of protons (curves *1*) knocked out from the $1p$ and $1d$ shells of the ^{40}Ca nucleus in the respective reaction $A(e,e'p)(A-1)$. The energy of knock-on protons is $E = 165$ MeV, while the energy of the scattered electrons is $\varepsilon = 500$ MeV. Curves *2* represent the cross sections $\sigma^{p(2)}_{\nu l}(\theta)$ for proton knockout in inelastic electron scattering at large angles θ' ($\theta' > \eta_0 = \pi/90$), while curves *3* are the cross sections $\sigma^{\mathrm{c}}_{\nu l}(\theta)$ measured experimentally in the coincidence mode. The scale of angles θ (0 approximation) and the scale of momentum transfers $\varkappa$ (d approximation) correspond to each other and transform into each other according to (11).

$I_2(\theta)$]. Finally, curves *3* represent the angular distributions of protons[11)] knocked out from the shells under study by electrons, which are scattered within the solid angle $\Delta\Omega'_0 \sim (\pi/90)^2$. The position of this solid angle is determined by the inequalities

$$\theta'_0 - \Delta\theta' \leqslant \theta' \leqslant \theta'_0 + \Delta\theta',$$

$$\pi - \Delta\varphi' \leqslant \varphi' \leqslant \pi + \Delta\varphi', \quad \Delta\theta' = \Delta\varphi' = \pi/180.$$

The electron-scattering angle θ'_0 and the momentum that the knock-on proton had in the target nucleus are specified here by the coplanar-orthogonal-kinematics conditions (10) and (11). We recall that the angle θ'_0 determines the disposition of the counter of electrons in coincidence experiments aimed at studying the momentum distributions of protons; that is, curve *3* represents the product $\sigma^{\mathrm{c}}_{\nu l}(\theta) = \sigma_{p\nu l}(\mathbf{k},\mathbf{k}',\mathbf{K})\Delta\Omega'_0$, where the quantities $\sigma_{p\nu l}(\mathbf{k},\mathbf{k}',\mathbf{K})$ calculated to a high precision are shown in Fig. 1 versus $\varkappa = |\mathbf{q} - \mathbf{K}|$. From the graphs in Fig. 6, one

[11)] We note that curves *3*, which are subsidiary, were calculated with an a priori poor accuracy (linear approximation) and were intended from the outset for determining a reference scale and for visually monitoring the cumbersome process of our numerical integration over the electron-scattering solid angle $d\Omega'$.

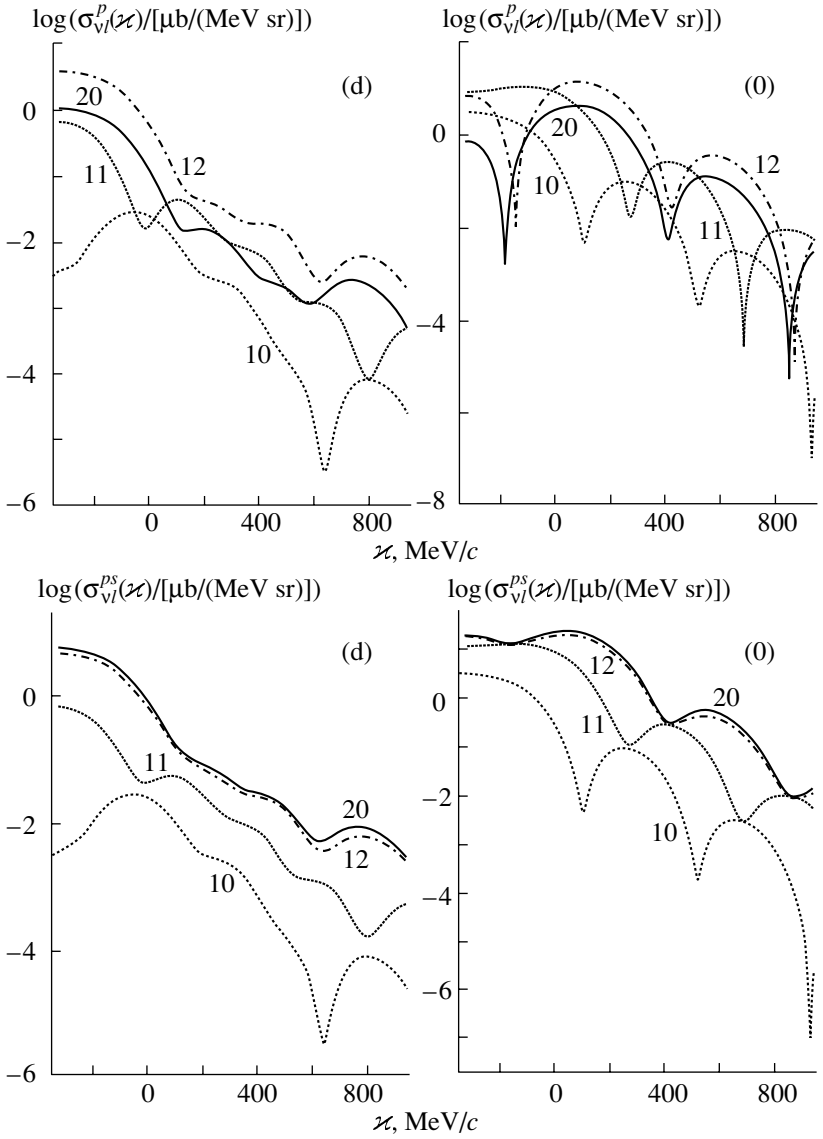

Fig. 7. Angular distributions $\sigma^p_{\nu l}(\theta)$ and total angular distributions $\sigma^{ps}_{\nu l}(\theta)$ of protons knocked out from the $1s$, $1p$, $1d$, and $2s$ shells of the ^{40}Ca nucleus according to calculations (0) in the plane-wave approximation and (d) with allowance for final-state interaction.

can see that the calculated cross sections $\sigma^{\mathrm{c}}_{\nu l}(\theta)$ and $\sigma^p_{\nu l}(\theta)$ differ significantly (by more than five orders of magnitude) in the kinematical region considered here: $\sigma^p_{\nu l}(\theta) \gg \sigma^{\mathrm{c}}_{\nu l}(\theta)$.

Figure 7 shows the calculated angular distributions $\sigma^p_{\nu l}(E,\theta) \equiv \sigma^p_{\nu l}(\theta)$ (20) and the calculated total angular distributions $\sigma^{ps}_{\nu l}(E,\theta) \equiv \sigma^{ps}_{\nu l}(\theta)$ (21) of $E =$ 165 MeV protons ($\varepsilon = 500$ MeV) knocked out from the $1s$, $1p$, $1d$, and $2s$ shells of the ^{40}Ca nucleus. We note that the curves representing the results obtained in the plane-wave approximation for the angular distributions of protons knocked out from the individual nuclear shells have a pronounced oscillating character.

We will now consider manifestations of the phenomenon of quasireal photons in investigations of $A(e,e'p)(A-1)$ reactions, relying on the calculations performed, for example, in the plane-wave approximation (Fig. 6). A comparison of the cross sections $\sigma^{\mathrm{c}}_{\nu l}(\theta)$ (curves *3*) with the proton distributions $\sigma^p_{\nu l}(\theta)$ (curves *1*) will play the main role for the ensuing conclusions. It is precisely the extraordinary excess (by several orders of magnitude) of $\sigma^p_{\nu l}(\theta)$ over $\sigma^{\mathrm{c}}_{\nu l}(\theta)$ [$\sigma^p_{\nu l}(\theta)/\sigma^{\mathrm{c}}_{\nu l}(\theta) \gg 1$] in the kinematical region being studied that is the source of conclusions that are of practical interest in interpreting and planning coincidence experiments for $A(e,e'p)(A-1)$ reactions. In

order to illustrate this statement, we will consider the following example.

We assume that, as a rule, coincidence experiments are conducted at an electron accelerator that operates in the pulsed mode. Suppose that, in a given mode of accelerator operation, the number of electrons in the electron bunch incident to the target is such that, in the $A(e,e'p)(A-1)$ reaction being studied, the analyzer used records (on average) the coincidence of a knock-on proton and the scattered electron in one of 10^4 target-irradiation events. From a comparative analysis of the cross sections $\sigma^{c}_{\nu l}(\theta)$ and $\sigma^{p}_{\nu l}(\theta)$ presented in Fig. 6, it can be deduced that, in the proposed version of investigations, each proton knocked out by an inelastically scattered electron that is recorded at an angle θ'_0 is emitted into the interval of angles θ under study and is accompanied by several (about 10) extra protons knocked out in the same target-irradiation event from neighboring nuclei by other electrons in much more intense inelastic-scattering processes involving quasireal photons. If the experiment in question is performed in such a way that the coincidence scheme records, together with the scattered electron, one of the protons emitted in some direction within the angular range being investigated, then the probability that the coincidence scheme records coincidences of the proton knocked out by a quasireal photon is dominant in the experimental mode under analysis.[12)]

It is obvious that, in the above version of investigations, the proton-momentum-distribution curve *3* transforms in shape into curve *1* (Fig. 6). It should be noted that the total number of detected coincidences is determined by the number of scattered electrons; that is, the area under the correctly (or incorrectly) defined proton-momentum-distribution curve remains invariable. In the example considered above, we will extract, from an experiment, a biased pattern of proton momentum distributions in nuclear shells. In other words, an intense background of protons knocked out in inelastic electron scattering at small angles in the region $\theta' \ll 1$ (phenomenon of quasireal photons) must be taken into account in choosing the mode (accelerator current, pulse duty factor, and so on) and kinematics of coincidence experiments aimed at studying $A(e,e'p)(A-1)$ reactions, since this background may distort substantially the results of experiments devoted to determining the momentum distributions of protons in nuclear shells.

In order to obtain a true curve of the proton momentum distribution in a given shell to an acceptable precision, the number of electrons in the electron bunch incident to the target must be reduced by a factor of 10^2, in which case the coincidence of a scattered electron with a knock-on proton will be observed only once, on average, per 10^6 events of target irradiation with the electron bunch. If the pulse-repetition frequency does not increase concurrently, then the efficiency of the experiment under the aforementioned condition may become so low that a direct investigation of angular distributions of all protons—the connection between these distributions and the shell structure of respective nuclei is illustrated in Figs. 6 and 7—will prove to be much more promising in some cases. As in the case of quasielastic peaks, which was considered above, the problem of determining the quantum numbers of nuclear shells can be solved by subtracting the angular distributions of protons for specially chosen pairs of neighboring nuclei, whereby information about proton dynamics is extracted for various shells of nuclei.

The topic being considered is not exhausted by the above example of the effect of the quasireal-photon phenomenon on the investigation of nuclear-electrodisintegration processes. In the next section, we will address yet another nontrivial aspect introduced by this phenomenon in the dynamics of inelastic electron scattering on nuclei.

4. QUASIREAL PHOTONS AND DYNAMICS OF NUCLEAR ELECTRODISINTEGRATION

By consistently and simultaneously taking into account the aforementioned quasireal-photon and Coulomb resonance phenomena in $A(e,e'p)(A-1)$ reactions, we will be able to trace the dynamics of nuclear-electrodisintegration processes in greater detail—in particular, we will interpret the broadening of the quasielastic peak and the shift of the maximum of $\sigma(\omega)$ to the region of higher energy transfers, an increase in the nucleon separation energy due to the braking of a relativistic electron in the target nucleus, and the related effect of a spurious increase in the proton binding energy in nuclear shells, as well as some other special features of nuclear electrodisintegration. For this, we return to investigating quasielastic peaks and recall the properties of such peaks at small scattering angles ($\theta'_0 \ll 1$).

Both theoretical and experimental investigations [7, 11, 17] indicate that, with decreasing electron-scattering angle θ', the cross section in the quasielastic-peak region increases, while the peak itself is shifted leftward substantially along the energy-transfer scale ω, so that, at small values of the electron-scattering angle ($\theta'_0 \ll 1$), one can in fact observe only the right-hand slope of the quasielastic peak being studied. The quasielastic peak calculated

[12)] We assume that a significant fraction of coincidences between the scattered electron and several knock-on protons may be a distinctive feature of the experiment implemented in this mode of investigations.

in the nonmodified plane-wave approximation according to Eq. (8) is shifted rightward (Fig. 2) with respect to the quasielastic peak calculated with allowance for final-state interaction. As a consequence, proton-knockout cross sections calculated in the plane-wave approximation are dominant on the right-hand slope of quasielastic peaks at small values of the electron-scattering angle θ'; therefore, they will exceed substantially the analogous cross sections (Figs. 6–8) calculated in the d approximation. We note that so significant an excess of the plane-wave cross sections over the cross sections calculated in the d approximation and the discrepancy between the anomalously large plane-wave cross sections (Fig. 8) and experimental data provide a compelling argument in favor taking into account the final-state interaction of the knock-on nucleon with a nuclear residue. We recall that some facets of this interaction can also be taken into account by going over from the standard plane-wave-approximation expression (8) to its modified counterpart (19).

We also note that, if the angle of inelastic electron scattering is very small ($\theta' \ll 1$), even modest variations in the angle θ' lead to sharp changes in the absolute value of the cross section $\sigma(\omega)$, this rendering theoretical and experimental investigations in this kinematical region more involved. It turns out, however, that, from the calculation of $\sigma(\omega)$ at $\theta' = 0$, one can readily deduce valuable information, taking into account the earlier established fact that the cross section $\sigma(\varepsilon', \theta')$ integrated in the region of small θ' over the electron-scattering solid angle $d\Omega'$ [with allowance for (29), integration with respect to $d\Omega'$ for $\theta' \ll 1$ is straightforward] can be identified, to a precision sufficient for drawing the ensuing conclusions, with the total nuclear-electrodisintegration cross section $\sigma^f(\omega)$,

$$\sigma^f_{x\nu l}(\omega) = \int \sigma_{x\nu l}(\varepsilon', \theta') d\Omega', \quad \sigma^f(\omega) = \sum_{x\nu l} \sigma^f_{x\nu l}(\omega), \tag{30}$$

where $\sigma_{x\nu l}(\varepsilon', \theta')$ was defined in (13). By way of example, the graphs of $\sigma^f(\omega)$ for the ^{119}Sn and ^{208}Pb nuclei are given in Fig. 8. From an analysis of the numerical results presented there, we can conclude that the total cross sections for inelastic electron scattering that were calculated in the 0 and d approximations differ substantially in magnitude for the reason indicated above and that, as in Fig. 3, the resonance spectrum in the cross section $\sigma^f(\omega)$ calls for additional refinements.

The integrated contributions $\sigma^{f\,\mathrm{ur}}_{\nu l \to NL}$ per nucleon from various resonance peaks to the cross sections

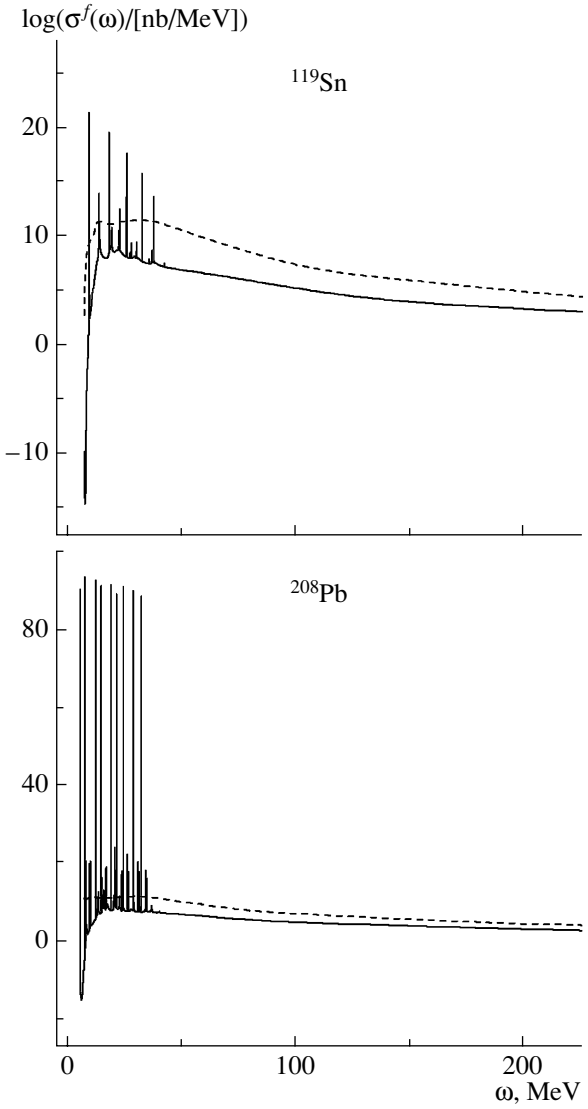

Fig. 8. Total cross sections $\sigma^f(\omega)$ for the electrodisintegration of ^{119}Sn and ^{208}Pb nuclei that is induced by electrons of energy $\varepsilon = 500$ MeV: (dashed curves) results obtained in the plane-wave approximation and (solid curves) results obtained with allowance for final-state interaction.

$\sigma^f_{x\nu l}(\omega_{\nu l \to NL})$,

$$\sigma^{f\,\mathrm{ur}}_{\nu l \to NL} = \frac{1}{N_{x\nu l}} \int\limits_{\omega_{\nu l NL} - \delta E}^{\omega_{\nu l NL} + \delta E} \sigma^f_{x\nu l}(\omega) d\omega \tag{31}$$

$$(\omega_{\nu l NL} = E_{NL} - \varepsilon_{\nu l}, \quad \delta E \gg \gamma_{pNL}),$$

are given in Table 3 for the ^{208}Pb nucleus. It can easily be noticed that the results obtained for $\sigma^{f\,\mathrm{ur}}_{\nu l \to NL}$ in the d approximation for different pairs of the quantum numbers νl and NL are markedly different. The resonance cross sections presented in Table 3 (in contrast to those in Table 2, which is analogous) demonstrate

Table 3. Integrated cross section $\sigma^{f\,\mathrm{ur}}_{\nu l\to NL}$ per nucleon (in barns) for the excitation of NL Coulomb resonances in the inelastic scattering of 500-MeV electrons on ^{208}Pb nuclei

νl	NL					
	23	16	31	24	32	17
10	1.50×10^{-3}	7.14×10^{-8}	1.43×10^{-3}	9.15×10^{-5}	3.82×10^{-4}	3.17×10^{-6}
11	1.62×10^{-2}	3.47×10^{-6}	2.33×10^{-2}	1.19×10^{-3}	1.95×10^{-4}	1.12×10^{-6}
12	7.78×10^{-2}	1.72×10^{-4}	1.97×10^{-2}	1.15×10^{-2}	6.52×10^{-3}	3.69×10^{-5}
20	6.00×10^{-3}	4.84×10^{-9}	1.23×10^{-1}	2.16×10^{-4}	7.12×10^{-3}	7.12×10^{-5}
13	2.39×10^{-1}	8.01×10^{-3}	1.95×10^{-2}	3.75×10^{-2}	1.83×10^{-3}	3.88×10^{-4}
21	2.57×10^{-1}	5.78×10^{-8}	3.59×10^{-1}	5.71×10^{-3}	2.45×10^{-2}	1.19×10^{-4}
14	2.86	4.24×10^{-1}	2.06×10^{-4}	2.25×10^{-1}	8.18×10^{-3}	1.33×10^{-2}
22	3.23×10^{1}	5.90×10^{-7}	6.90	2.65×10^{-1}	1.88×10^{-1}	7.40×10^{-4}
30	1.10×10^{-4}	3.20×10^{-13}	3.83×10^{1}	2.16×10^{-5}	2.25×10^{-1}	1.82×10^{-3}
15	1.35×10^{-2}	4.33×10^{1}	3.77×10^{-8}	2.18	4.79×10^{-4}	5.49×10^{-1}

a crucial role of the $22\to23$, $30\to31$, $15\to16$, and $14\to23$ dipole transitions ($L=l\pm1$, $N_L=\nu_l$, $\nu_l\pm1$) in the braking of ultrarelativistic electrons in the region of the target nucleus. For the example of intranuclear absorption of quasireal photons in the inelastic scattering of high-energy electrons on nuclei, the cross sections $\sigma^{f\,\mathrm{ur}}_{\nu l\to NL}$ in Table 3 show explicitly the phenomenon of a giant dipole resonance.

By making use of the results of our calculations, we will try to predict the fate of an ultrarelativistic electron that penetrates into a target nucleus, knocking out a nucleon from this nucleus. Assuming that the d approximation is valid, we conclude that the electron traverses rather freely only the central part of the nucleus—that is, the region of deep nuclear shells. However, the probability of repeated jumplike electron braking, which is due to the excitation of Coulomb resonances (recall that dipole transitions play a dominant role here), is quite sizable at the periphery of the nucleus, where the quantum numbers of protons belonging to filled shells are close to quantum numbers of Coulomb resonances (neutrons play virtually no part in electron scattering at small angles).

Employing the cross sections for the excitation of Coulomb resonances to obtain standard [31, 32] estimates for the mean free path, the number of collisions, and the energy loss of a relativistic electron within a nucleus, we can state that, prior to and (or) after an event in which a relativistic electron traveling within a nucleus like ^{208}Pb undergoes scattering at a large angle, this electron provokes, with a high probability, several (from one to four) single-particle dipole transitions in the processes of scattering at angles of $\theta'\ll1$, losing an amount of energy in the range $\delta\varepsilon\sim9$–40 MeV. This multiple jumplike braking of an ultrarelativistic electron within a nucleus will cause various effects, including

broadening of the quasielastic peak and, possibly, its lowering to some extent;

a shift of the quasielastic peak to the region of higher energy transfers ω;

the transformation of the separation energy $w_{x\nu l}$ into the spectrum (set) of energies $w^{\lambda}_{x\nu l}$ ($\lambda=1,2,\ldots$) of nucleon separation from the $x\nu l$ shell of a nucleus, whereupon it becomes more difficult to identify the nuclear shell from which a nucleon was knocked out;

a decrease in the effective occupation number of the $3s$ shell due to a high probability of the $3s\to3p$ dipole transition and, hence, a decrease in the cross section for proton knockout from the outer $3s$ shell of the ^{208}Pb nucleus in coincidence experiments.

In comparing theoretical and experimental results, the additional energy loss $\sum\omega_{\nu l\to NL}$ of the electron by the excitation of Coulomb resonances in inelastic scattering at an angle of $\theta'=0$ in the energy-conservation law

$$\varepsilon'=\varepsilon-\left(E+\left(\varepsilon_{x\nu l}+\sum\omega_{\nu l\to NL}\right)\right) \qquad (32)$$

is naturally combined with the binding energy $\varepsilon_{x\nu l}$ of the knock-on proton, this being interpreted as the effect of an increase in the separation energy for nucleons knocked out from nuclear shells:

$$w_{x\nu l}\to w^{\mathrm{incr}}_{x\nu l},\qquad w^{\mathrm{incr}}_{x\nu l}=\varepsilon_{x\nu l}+\sum\omega_{\nu l\to NL}. \qquad (33)$$

But if one assumes that the phenomenon of relativistic-electron braking [second term in Eq. (32)] is unknown, formulas (32) and (33) are naturally treated according to (6) in a simplified form: $\varepsilon_{x\nu l} = w^{\rm incr}_{x\nu l}$; that is, the nucleon binding energy $\varepsilon_{x\nu l}$ in a nucleus is identified with the total separation energy $w^{\rm incr}_{x\nu l}$ for a nucleon knocked out from the $x\nu l$ shell of this nucleus. It comes as no surprise that, even in upper nuclear shells, proton separation energies determined in $A(e,e'p)(A-1)$ reactions traditionally exceed the mean binding energy of protons in corresponding nuclei [25]. Obviously, the frontal deceleration of an ultrarelativistic electron within a nucleus due to the intense dipole transitions of protons to resonance single-particle states of the continuous spectrum may have a nontrivial effect on interpreting and planning experiments devoted to studying $A(e,e'p)(A-1)$ reactions.

An investigation of the second peak in the cross section $\sigma(\omega)$ for deep-inelastic electron scattering on nuclei is one of the most important and interesting results obtained by Williamson *et al.* [11] for $A(e,e'p)(A-1)$ reactions. Those authors treat the appearance of the second peak as a manifestation of the delta-isobar phenomenon in deep-inelastic electron scattering [11]. We note that, in order to confirm this statement, it would be reasonable to rule out preliminarily the possibility that the knockout of two nucleons via $A(e,e'pp)(A-2)$ and $A(e,e'pn)(A-2)$ reactions, where one of the nucleons (proton) is knocked out by a quasireal photon, leads to the emergence of the second quasielastic echo peak in the region of high energy transfers.

5. CONCLUSIONS

From the content of this study, one can conclude that the concerted effect of the quasireal-photon and Coulomb resonance phenomena, which have been studied above, as well as the effect of either phenomenon individually, may introduce new important facets and refinements in our understanding of the dynamics of nuclear-electrodisintegration processes. We believe that, upon consistently taking these phenomena into account, one can avoid spurious discrepancies, incorrect conclusions, exotic hypotheses, and blind alleys in interpreting already performed experiments and in planning new experiments devoted to studying the structure of nuclei in the inelastic scattering of high-energy electrons on nuclei. One can also hope that the effects considered here and the phenomena associated with Coulomb resonances, quasireal photons, and dipole transitions will also manifest themselves in modern relativistic models [9, 10]; we even dare to assume that they would find there a quantitative corroboration and quantitative refinements.

Being guided by an inner voice and basic moral principles, we would like to recall once again in conclusion that it was Professor A.G. Sitenko, Member of the National Academy of Sciences of Ukraine, who was among the authors of one of the first [4] and many other (see, for example, [6, 8]) important studies devoted to exploring the structure of nuclei in $A(e,e'p)(A-1)$ reactions; he also initiated various investigations and lines of investigation in this and other realms of theoretical physics. We dedicate the present study to the blessed memory of this outstanding physicist and striking personality.

REFERENCES

1. A. Bohr and B. R. Mottelson, *Nuclear Structure* (Benjamin, New York, 1969, 1975; Mir, Moscow, 1971, 1977), Vols. 1, 2.
2. J. M. Eisenberg and V. Greiner, *Nuclear Theory* (North-Holland, Amsterdam, London, 1972; Atomizdat, Moscow, 1973–1976).
3. A. S. Davydov, *Theory of the Nucleus* (Fizmatgiz, Moscow, 1958) [in Russian].
4. A. G. Sitenko and V. N. Gur'ev, Zh. Éksp. Teor. Fiz. **39**, 1760 (1960) [Sov. Phys. JETP **12**, 1228 (1961)].
5. V. Devanatan, Ann. Phys. (N.Y.) **43**, 74 (1967).
6. A. G. Sitenko, A. A. Pasichnyĭ, and V. K. Tartakovskiĭ, Yad. Fiz. **12**, 1208 (1970) [Sov. J. Nucl. Phys. **12**, 663 (1971)].
7. A. A. Pasichnyĭ, Ukr. Fiz. Zh. **17**, 1130 (1972).
8. A. I. Akhiezer, A. G. Sitenko, and V. K. Tartakovskii, *Nuclear Electrodynamics* (Naukova Dumka, Kiev, 1989; Springer-Verlag, Berlin, 1994).
9. Yanhe Jin, D. S. Onley, and L. E. Wright, Phys. Rev. C **45**, 1311 (1992).
10. J. M. Udias *et al.*, Phys. Rev. C **48**, 2731 (1993).
11. C. F. Williamson *et al.*, Phys. Rev. C **56**, 1897 (1997).
12. T. de Forest, Jr., Nucl. Phys. A **392**, 232 (1983).
13. L. Lapikas, Nucl. Phys. A **553**, 297 (1993).
14. J. Moygey, Nucl. Phys. A **335**, 35 (1980).
15. A. A. Pasichnyĭ, Yad. Fiz. **46**, 722 (1987) [Sov. J. Nucl. Phys. **46**, 406 (1987)].
16. A. A. Pasichnyĭ, Yad. Fiz. **48**, 694 (1988) [Sov. J. Nucl. Phys. **48**, 444 (1988)].
17. N. G. Afanas'ev *et al.*, Preprint No. 74-7, KhFTI (Kharkov Institute of Physics and Technology, Kharkov, 1974).
18. R. R. Whitney *et al.*, Phys. Rev. C **9**, 2230 (1974).
19. M. Deady *et al.*, Phys. Rev. C **33**, 1897 (1986).
20. A. Watt, Phys. Lett. B **27B**, 190 (1968).
21. A. A. Pasichnyĭ, Yad. Fiz. **54**, 1543 (1991) [Sov. J. Nucl. Phys. **54**, 944 (1991)].
22. M. Zhongyu and F. Dachun, Phys. Rev. C **45**, 811 (1992).
23. D. I. Blokhintsev, *Quantum Mechanics* (Vysshaya Shkola, Moscow, 1963; Reidel, Dordrecht, 1964).

24. A. Yu. Korchin and A. V. Shebeko, Yad. Fiz. **32**, 87 (1980) [Sov. J. Nucl. Phys. **32**, 46 (1980)].
25. L. R. B. Elton and A. Swift, Nucl. Phys. A **94**, 52 (1967).
26. A. A. Pasichnyĭ, Ukr. Fiz. Zh. **38**, 1619 (1993).
27. V. B. Berestetskii, E. M. Lifshitz, and L. P. Pitaevskii, in *Course of Theoretical Physics*, Vol. 4: *Quantum Electrodynamics* (Nauka, Moscow, 1989; Pergamon, Oxford, 1982).
28. A. I. Akhiezer and V. B. Berestetskii, *Quantum Electrodynamics*, 3rd ed. (Nauka, Moscow, 1969; Wiley, New York, 1965).
29. V. G. Neudachin, L. L. Sviridova, and N. P. Yudin, Yad. Fiz. **64**, 1680 (2001) [Phys. At. Nucl. **64**, 1600 (2001)].
30. A. A. Pasichnyĭ, Vestn. Kiev. Univ., Fiz. **1**, 47 (2000).
31. V. V. Balashov, *Quantum Collision Theory* (Mosk. Gos. Univ., Moscow, 1985) [in Russian].
32. S. Sunakawa, *Quantum Scattering Theory* (Iwanami Shoten, 1977; Mir, Moscow, 1979).

Translated by A. Isaakyan

Physics of Atomic Nuclei, Vol. 68, No. 12, 2005, pp. 2009–2021. Translated from Yadernaya Fizika, Vol. 68, No. 12, 2005, pp. 2071–2083.

NUCLEI
Theory

Quantum Non-Markovian Langevin Equations and Transport Coefficients

V. V. Sargsyan[1)], Z. Kanokov[1),2)], G. G. Adamian[1),3)], and N. V. Antonenko[1)]

Received November 3, 2004

Abstract—Quantum diffusion equations featuring explicitly time-dependent transport coefficients are derived from generalized non-Markovian Langevin equations. Generalized fluctuation–dissipation relations and analytic expressions for calculating the friction and diffusion coefficients in nuclear processes are obtained. The asymptotic behavior of the transport coefficients and correlation functions for a damped harmonic oscillator that is linearly coupled in momentum to a heat bath is studied. The coupling to a heat bath in momentum is responsible for the appearance of the diffusion coefficient in coordinate. The problem of regression of correlations in quantum dissipative systems is analyzed . © *2005 Pleiades Publishing, Inc.*

1. INTRODUCTION

The problem of describing open quantum systems arises in considering collective motion in nuclear systems that involves friction. If the collective potential can be approximated by an oscillator, a number of methods developed for a damped quantum oscillator in a quantum-mechanical heat bath [1–9] can be used to derive the respective equations of motion. However, damping in a system was considered with the aid of these methods predominantly in the Markovian limit (instantaneous dissipation, Gaussian delta-correlated fluctuations), and simplifying assumptions on the coupling between the oscillator and the heat bath were used. But if changes in the system being considered are rather fast—this is so, for example, in a collision of heavy ions or in a fissile nucleus immediately prior to disintegration—it is necessary to take additionally into account a nonlocality of dissipation. Investigation of the behavior of a dissipative quantum system beyond the weak-coupling or the high-temperature limit arouses great interest in simple and exactly solvable models [10–15]. In these models, a heat bath is represented by a set of harmonic oscillators whose interaction with the collective subsystem of a harmonic oscillator is realized via a linear coupling between the coordinates. The density of the oscillators and the couplings between a heat bath and the subsystem are chosen in such a way that the equations of motion for mean values take a classical form.

The objective of the present study is to develop a method for determining the time-dependent friction and diffusion coefficients for a collective subsystem in the case of arbitrary temperature and damping. These transport coefficients include non-Markovian effects. As a starting point, we use the Langevin approximation, which is extensively used to describe fluctuation and dissipative effects in macroscopic systems [2, 4]. In kinetic theory, the Langevin method simplifies considerably the calculation of nonequilibrium quantum and thermal fluctuations and provides a clear picture of dynamical processes. It is further verified whether the resulting equations of motion are in accord with the quantum fluctuation–dissipation theorem. From a comparison of the equations of motion for mean values and variances with their classical analogs, we derive expressions for the time-dependent friction and diffusion coefficients. The axiomatic Lindblad approach [16–21] to describing open quantum systems is validated at the microscopic level. The strong-damping limit is considered individually. A dedicated investigation is performed for the case of linear coupling in momentum between the collective subsystem and the heat bath. In the case of this coupling, friction and diffusion in the collective coordinate arise, as was hypothesized earlier, while, in the case of a linear coupling in coordinate—this is the case considered most frequently—there arise only friction and diffusion in momentum.

[1)]Joint Institute for Nuclear Research, Dubna, Moscow oblast, 141980 Russia.
[2)]Uzbek National University, Tashkent, 700174 Republic of Uzbekistan.
[3)]Institute of Nuclear Physics, Uzbek Academy of Sciences, pos. Ulughbek, Tashkent, 702132 Republic of Uzbekistan.

2. QUANTUM NON-MARKOVIAN DYNAMICS

2.1. Generalized Non-Markovian Langevin Equations

We will begin by specifying a microscopic Hamiltonian H for the total system (a heat bath plus a collective subsystem). From this Hamiltonian, we will then derive quantum non-Markovian Langevin equations and time-dependent transport coefficients for the collective subsystem. For nuclear systems, a quantum Hamiltonian was constructed in [22–24]. This Hamiltonian depends directly on a collective coordinate q, the canonically conjugate collective momentum p, and internal degrees of freedom and has the form

$$H = H_c + H_b + H_{cb}, \tag{1}$$

$$H_c = p\frac{1}{2\mu(q)}p + U(q),$$

$$H_b = \sum_\nu \hbar\omega_\nu b_\nu^+ b_\nu,$$

$$H_{cb} = \sum_\nu V_\nu(q)(b_\nu^+ + b_\nu) + i\sum_\nu G_\nu(q,p)(b_\nu^+ - b_\nu).$$

Here, b_ν^+ and b_ν are, respectively, the phonon creation and annihilation operators describing internal excitations of the system that have an energy $\hbar\omega_\nu$ (in order to simplify the notation, the symbols of operators are omitted). The operators H_c and H_b are the Hamiltonians for, respectively, the collective and the internal subsystem. The third term H_{cb} on the right-hand side of Eq. (1) describes the coupling of the collective motion to internal excitations and is a source of dissipative terms in the equations for the operators of collective variables. If, for example, one describes the interaction of nuclei at low energies, the first term in the expression for H_{cb} corresponds to the effect of the mean field of each nucleus on the single-particle motion in the other nucleus, while the second term describes the coupling of the internal-motion current to the collective current. Under the condition $G_\nu(q,p) = \{\tilde{G}_\nu(q), p\}_+ = \tilde{G}_\nu(q)p + p\tilde{G}_\nu(q)$, the Hamiltonian H is invertible in time. Our objective is to derive the Langevin equations for the operators p and q and to solve them analytically.

By using the Hamiltonian in (1), we obtain a set of the quantum Heisenberg equations for the operators associated with the collective and internal motions; that is,

$$\dot{q} = \frac{i}{\hbar}[H,q] = \frac{1}{2}\{\mu^{-1}(q), p\}_+ + i\sum_\nu G'_{\nu,p}(b_\nu^+ - b_\nu), \tag{2}$$

$$\dot{p} = \frac{i}{\hbar}[H,p] = -H'_{c,q}(q,p) - \sum_\nu V'_{\nu,q}(b_\nu^+ + b_\nu) - i\sum_\nu G'_{\nu,q}(b_\nu^+ - b_\nu),$$

$$\dot{b}_\nu^+ = \frac{i}{\hbar}[H,b_\nu^+] = i\omega_\nu b_\nu^+ + \frac{1}{\hbar}(iV_\nu(q) + G_\nu(q,p)),$$

$$\dot{b}_\nu = \frac{i}{\hbar}[H,b_\nu] = -i\omega_\nu b_\nu + \frac{1}{\hbar}(-iV_\nu(q) + G_\nu(q,p)). \tag{3}$$

Here, we use the notation

$$H'_{c,q}(q,p) = \frac{\partial H_c(q,p)}{\partial q}, \quad V'_{\nu,q} = \frac{\partial V_\nu(q(t))}{\partial q},$$

$$G'_{\nu,p} = \frac{\partial G_\nu(q(t),p(t))}{\partial p}, \quad G'_{\nu,q} = \frac{\partial G_\nu(q(t),p(t))}{\partial q}.$$

By substituting into Eqs. (2) the solutions to (3) that have the form

$$b_\nu^+(t) + b_\nu(t) = f_\nu^+(t) + f_\nu(t) - \frac{2V_\nu(q)}{\hbar\omega_\nu} - \frac{i}{\omega_\nu}\int_0^t d\tau[\dot{\Phi}^+(\tau)e^{i\omega_\nu(t-\tau)} - \dot{\Phi}(\tau)e^{-i\omega_\nu(t-\tau)}], \tag{4}$$

$$b_\nu^+(t) - b_\nu(t) = f_\nu^+(t) - f_\nu(t) + \frac{2iG_\nu(q,p)}{\hbar\omega_\nu} - \frac{i}{\omega_\nu}\int_0^t d\tau[\dot{\Phi}^+(\tau)e^{i\omega_\nu(t-\tau)} + \dot{\Phi}(\tau)e^{-i\omega_\nu(t-\tau)}],$$

where

$$f_\nu(t) = [b_\nu(0) + \frac{i}{\omega_\nu}\Phi(0)]e^{-i\omega_\nu t},$$

$$\Phi(t) = \frac{1}{\hbar}[-iV_\nu(q(t)) + G_\nu(q(t),p(t))],$$

we obtain the set of nonlinear integro-differential stochastic equations

$$\dot{q} = \frac{1}{2}\{\tilde{\mu}^{-1}(q), p\}_+ - \frac{1}{2}\int_0^t d\tau\{K_{GV}(t,\tau), \dot{q}(\tau)\}_+ + \frac{1}{2}\int_0^t d\tau\{K_{GG}(t,\tau), \dot{p}(\tau)\}_+ + F_q(t), \tag{5}$$

$$\dot{p} = -\tilde{H}'_{c,q}(q,p) - \frac{1}{2}\int_0^t d\tau\{K_{VV}(t,\tau), \dot{q}(\tau)\}_+ + \frac{1}{2}\int_0^t d\tau\{K_{VG}(t,\tau), \dot{p}(\tau)\}_+ + F_p(t).$$

In deriving Eqs. (5), we have disregarded the following second-order terms in $\hbar$: $[[G'_{\nu,p}(t),\dot{q}(t')],V'_{\nu,q}(t')]$, $[[G'_{\nu,q}(t),\dot{q}(t')],V'_{\nu,q}(t')]$, $[[G'_{\nu,q}(t),\dot{q}(t')],G'_{\nu,q}(t')]$, $[[G'_{\nu,p}(t),\dot{q}(t')],G'_{\nu,q}(t')]$, $[[G'_{\nu,p}(t),\dot{p}(t')],G'_{\nu,p}(t')]$, and $[[G'_{\nu,q}(t),\dot{p}(t')],G'_{\nu,p}(t')]$. In the case of a linear coupling in the coordinate and momentum (V_ν and G_ν are linear functions of q and p, respectively), the equations of motion in (5) are exact.

In (5), the collective Hamiltonian

$$\tilde{H}_c(q,p) = p\frac{1}{2\tilde{\mu}(q)}p + \tilde{U}(q,p)$$

involves a renormalized mass,

$$\tilde{\mu}^{-1}(q(t)) = \mu^{-1}(q(t)) - 2\sum_\nu \frac{[G'_{\nu,p}(t)]^2}{\hbar\omega_\nu},$$

and a renormalized potential energy,

$$\tilde{U}(q(t)) = U(q(t)) - \sum_\nu \frac{[V_\nu(q(t))]^2}{\hbar\omega_\nu}.$$

In the equations of motion (5), the dissipative kernels are isolated in the terms proportional to $\dot{q}$ and $\dot{p}$ [10]:

$$K_{GV}(t,\tau) = \sum_\nu \frac{1}{\hbar\omega_\nu}[\{G'_{\nu,p}(t),V'_{\nu,q}(\tau)\}_+ \times \sin(\omega_\nu[t-\tau]) - \{G'_{\nu,p}(t),G'_{\nu,q}(\tau)\}_+ \times \cos(\omega_\nu[t-\tau])], \quad (6)$$

$$K_{VG}(t,\tau) = -\sum_\nu \frac{1}{\hbar\omega_\nu}[\{G'_{\nu,q}(t),G'_{\nu,p}(\tau)\}_+ \times \cos(\omega_\nu[t-\tau]) + \{V'_{\nu,q}(t),G'_{\nu,p}(\tau)\}_+ \times \sin(\omega_\nu[t-\tau])],$$

$$K_{VV}(t,\tau) = \sum_\nu \frac{1}{\hbar\omega_\nu}[(\{V'_{\nu,q}(t),V'_{\nu,q}(\tau)\}_+ + \{G'_{\nu,q}(t),G'_{\nu,q}(\tau)\}_+)\cos(\omega_\nu[t-\tau]) + (\{V'_{\nu,q}(t),G'_{\nu,q}(\tau)\}_+ - \{G'_{\nu,q}(t),V'_{\nu,q}(\tau)\}_+) \times \sin(\omega_\nu[t-\tau])],$$

$$K_{GG}(t,\tau) = \sum_\nu \frac{1}{\hbar\omega_\nu}\{G'_{\nu,p}(t),G'_{\nu,p}(\tau)\}_+ \times \cos(\omega_\nu[t-\tau]).$$

Since these kernels are independent of the number of phonons, they are also independent of the heat-bath temperature T. Temperature and fluctuations appear in this consideration through the definition of the distribution of initial conditions for the internal system. In Eqs. (5), the operators F_q and F_p,

$$F_q(t) = \sum_\nu F_q^\nu(t) = i\sum_\nu G'_{\nu,p}(t)[f_\nu^+(t) - f_\nu(t)], \quad (7)$$

$$F_p(t) = \sum_\nu F_p^\nu(t) = -\sum_\nu V'_{\nu,q}(t)[f_\nu^+(t) + f_\nu(t)] - i\sum_\nu G'_{\nu,q}(t)[f_\nu^+(t) - f_\nu(t)],$$

play the role of random forces in the coordinate and momentum and depend on $q(t)$, $p(t)$, and initial conditions for the internal subsystem. As usual, the operators $F_q^\nu(t)$ and $F_p^\nu(t)$ are identified in statistical physics with fluctuations because of the uncertainty in the initial conditions for heat-bath operators. In order to determine the statistical properties of these fluctuations, we consider an ensemble of initial states where $q(0)$ and $p(0)$ are preset and where the initial heat-bath operators are taken from a canonical ensemble [10]. In this ensemble, the fluctuations $F_q^\nu(t)$ and $F_p^\nu(t)$ obey a Gaussian distribution and have zero mean values,

$$\langle\langle F_q^\nu(t)\rangle\rangle = \langle\langle F_p^\nu(t)\rangle\rangle = 0, \quad (8)$$

and nonzero second moments. The symbol $\langle\langle\ldots\rangle\rangle$ denotes averaging over heat-bath variables. A Gaussian distribution of random forces corresponds to representing a heat bath by a set of harmonic oscillators [2, 4, 8]. In order to calculate correlation functions for fluctuations, we employ here a heat bath that obeys Bose–Einstein statistics,

$$\langle\langle f_\nu^+(t)f_{\nu'}^+(t')\rangle\rangle = \langle\langle f_\nu(t)f_{\nu'}(t')\rangle\rangle = 0, \quad (9)$$
$$\langle\langle f_\nu^+(t)f_{\nu'}(t')\rangle\rangle = \delta_{\nu,\nu'}n_\nu e^{i\omega_\nu(t-t')},$$
$$\langle\langle f_\nu(t)f_{\nu'}^+(t')\rangle\rangle = \delta_{\nu,\nu'}(n_\nu+1)e^{-i\omega_\nu(t-t')},$$

where $n_\nu = [\exp(\hbar\omega_\nu/T)-1]^{-1}$ stands for the temperature-dependent occupation numbers for phonons.

Thus, we have derived the set of generalized nonlinear Langevin equations (5). The presence of integral terms in the equations of motion means that a non-Markovian system retains memory about the motion along the trajectory preceding the instant t. The second equation in (5) additionally involves a random force, this generating some mathematical difficulties in solving it [2]. An analytic solution can be obtained under the assumption that the functionals $\tilde{\mu}$, $V'_{\nu,q}$, $G'_{\nu,q}$, and $G'_{\nu,p}$ change only slightly within the time interval t. In this case, one can replace

these functionals in Eq. (5) by their mean values and then approximate the renormalized potential by the harmonic-oscillator potential $\tilde{U} = \tilde{\delta}q^2/2$ (or by its inverted counterpart). As a result, one arrives at a set of generalized Langevin equations featuring dissipative kernels that possess memory. In order to solve them, we apply a Laplace transformation $\mathcal{L}$, whereupon we arrive at linear equations for the transforms. Knowing the expressions for the transforms, we derive explicit expressions for the originals; that is,

$$q(t) = A_t q(0) + B_t p(0) \qquad (10)$$
$$+ \int_0^t d\tau [C_\tau F_q(t-\tau) + \tilde{C}_\tau F_p(t-\tau)],$$
$$p(t) = M_t q(0) + N_t p(0)$$
$$+ \int_0^t d\tau [L_\tau F_p(t-\tau) + \tilde{L}_\tau F_q(t-\tau)],$$

where the coefficients have the form

$$A_t = \mathcal{L}^{-1}\left[\frac{s(1+K_{GV}(s))(1-K_{VG}(s)) + (1/\tilde{\mu} + sK_{GG}(s))K_{VV}(s)}{d(s)}\right],$$
$$N_t = \mathcal{L}^{-1}\left[\frac{s(1-K_{VG}(s))(1+K_{GV}(s)) + (\tilde{\delta} + sK_{VV}(s))K_{GG}(s)}{d(s)}\right],$$
$$B_t = \mathcal{L}^{-1}\left[\frac{\tilde{\mu}^{-1}(1-K_{VG}(s))}{d(s)}\right],$$
$$M_t = -\mathcal{L}^{-1}\left[\frac{\tilde{\delta}(1+K_{GV}(s))}{d(s)}\right],$$
$$C_t = \mathcal{L}^{-1}\left[\frac{s(1-K_{VG}(s))}{d(s)}\right],$$
$$L_t = \mathcal{L}^{-1}\left[\frac{s(1+K_{GV}(s))}{d(s)}\right],$$
$$\tilde{C}_t = \mathcal{L}^{-1}\left[\frac{1/\tilde{\mu} + sK_{GG}(s)}{d(s)}\right],$$
$$\tilde{L}_t = -\mathcal{L}^{-1}\left[\frac{\tilde{\delta} + sK_{VV}(s)}{d(s)}\right].$$

Here, $\mathcal{L}^{-1}$ stands for the inverse Laplace transformation and $K_{VV}(s)$, $K_{GG}(s)$, $K_{GV}(s)$, and $K_{VG}(s)$ are the Laplace transforms of the dissipative kernels. The symbols t and τ indicate the time dependence. By using the residue theorem for obtaining the aforementioned originals, the solutions $q(t)$ and $p(t)$ can be expressed in terms of the roots s_i of the equation

$$d(s) \equiv s^2(1+K_{GV}(s))(1-K_{VG}(s)) \qquad (11)$$
$$+ (\tilde{\delta} + sK_{VV}(s))(1/\tilde{\mu} + sK_{GG}(s)) = 0.$$

2.2. Fluctuation–Dissipation Relations

The fluctuation–dissipation relation expresses a macroscopic quantity that describes energy dissipation for a collective subsystem in terms of a microscopic feature describing fluctuations of random forces in the internal subsystem. Thus, this relation expresses the nonequilibrium behavior of a system in terms of equilibrium or quasiequilibrium features. By using the statistical properties (8) and (9) of the random forces (7) and disregarding $O(\hbar)$ terms [this corresponds to disregarding the double commutators in (5)], we obtain the following relations for the symmetrized correlation functions $(k, k' = q, p)$ $\phi^\nu_{kk'}(t,t') = \langle\langle F^\nu_k(t)F^\nu_{k'}(t') + F^\nu_{k'}(t')F^\nu_k(t)\rangle\rangle$ characterizing the random forces:

$$\phi^\nu_{qp}(t,t') = [2n_\nu + 1](-\{G'_{\nu,p}(t), G'_{\nu,q}(t')\}_+ \qquad (12)$$
$$\times \cos(\omega_\nu[t-t']) + \{G'_{\nu,p}(t), V'_{\nu,q}(t')\}_+$$
$$\times \sin(\omega_\nu[t-t'])),$$
$$\phi^\nu_{pq}(t,t') = -[2n_\nu + 1](\{G'_{\nu,q}(t), G'_{\nu,p}(t')\}_+$$
$$\times \cos(\omega_\nu[t-t']) + \{V'_{\nu,q}(t), G'_{\nu,p}(t')\}_+$$
$$\times \sin(\omega_\nu[t-t'])),$$
$$\phi^\nu_{pp}(t,t') = [2n_\nu + 1](\{V'_{\nu,q}(t), V'_{\nu,q}(t')\}_+$$
$$+ \{G'_{\nu,q}(t), G'_{\nu,q}(t')\}_+)\cos(\omega_\nu[t-t'])$$
$$+ (\{V'_{\nu,q}(t), G'_{\nu,q}(t')\}_+ - \{G'_{\nu,q}(t), V'_{\nu,q}(t')\}_+)$$
$$\times \sin(\omega_\nu[t-t'])),$$
$$\phi^\nu_{qq}(t,t') = [2n_\nu + 1]\{G'_{\nu,p}(t), G'_{\nu,p}(t')\}_+$$
$$\times \cos(\omega_\nu[t-t']).$$

The retention of the discarded terms would lead to additional relations. By using Eqs. (6) and (12) and

considering that $2n_\nu + 1 = \coth[\hbar\omega_\nu/(2T)]$, we obtain the quantum fluctuation–dissipation relations

$$\sum_\nu \phi^\nu_{qp}(t,t')\frac{\tanh[\hbar\omega_\nu/(2T)]}{\hbar\omega_\nu} = K_{GV}(t,t'), \quad (13)$$

$$\sum_\nu \phi^\nu_{pq}(t,t')\frac{\tanh[\hbar\omega_\nu/(2T)]}{\hbar\omega_\nu} = K_{VG}(t,t'), \quad (14)$$

$$\sum_\nu \phi^\nu_{pp}(t,t')\frac{\tanh[\hbar\omega_\nu/(2T)]}{\hbar\omega_\nu} = K_{VV}(t,t'), \quad (15)$$

$$\sum_\nu \phi^\nu_{qq}(t,t')\frac{\tanh[\hbar\omega_\nu/(2T)]}{\hbar\omega_\nu} = K_{GG}(t,t'). \quad (16)$$

Thus, the equations of motion for the collective coordinates satisfy the fluctuation–dissipation relations.

Fulfillment of the fluctuation–dissipation relations means that we have correctly defined the dissipative kernels in the non-Markovian dynamical equations of motion. For the simple cases of FC and RWA oscillators, a similar quantum fluctuation–dissipation relation was obtained in [10] and in the studies quoted therein. In the present study, the quantum fluctuation–dissipation theorem is generalized to the case of an arbitrary form of the Hamiltonian term H_{cb}. Quantum fluctuation–dissipation relations differ from their classical counterparts and reduce to them in the limit of high temperature T (or, formally, in the limit $\hbar \to 0$), in which case $\tanh[\hbar\omega_\nu/(2T)] \to 1/(2T)$ in relations (13)–(16). The classical relations contain only temperature fluctuations. Quantum fluctuations are additionally taken into account in relations (13)–(16). Since the equations of motion in (5) for the collective coordinates and momenta are in accord with the fluctuation–dissipation relations, our formalism provides a basis for describing quantum statistical effects of collective motion.

2.3. Transport Coefficients

By using the explicit time dependences of p and q, we can derive their basic properties, such as the mean values $\langle q(t)\rangle$ and $\langle p(t)\rangle$ (first moments),

$$\langle q(t)\rangle = A_t\langle q(0)\rangle + B_t\langle p(0)\rangle, \quad (17)$$
$$\langle p(t)\rangle = M_t\langle q(0)\rangle + N_t\langle p(0)\rangle,$$

and the correlation functions $\sigma_{q_tq_{t'}} = \langle q(t)q(t')\rangle$, $\sigma_{p_tp_{t'}} = \langle p(t)p(t')\rangle$, $\sigma_{q_tp_{t'}} = \langle q(t)p(t')\rangle$, and $\sigma_{p_tq_{t'}} = \langle p(t)q(t')\rangle$,

$$\sigma_{q_tq_{t'}} = A_tA_{t'}\sigma_{q_0q_0} + B_tB_{t'}\sigma_{p_0p_0} \quad (18)$$
$$+ A_tB_{t'}\sigma_{q_0p_0} + B_tA_{t'}\sigma_{p_0q_0} + J_{q_tq_{t'}},$$
$$\sigma_{p_tp_{t'}} = M_tM_{t'}\sigma_{q_0q_0} + N_tN_{t'}\sigma_{p_0p_0} + M_tN_{t'}\sigma_{q_0p_0}$$
$$+ N_tM_{t'}\sigma_{p_0q_0} + J_{p_tp_{t'}},$$
$$\sigma_{q_tp_{t'}} = A_tM_{t'}\sigma_{q_0q_0} + B_tN_{t'}\sigma_{p_0p_0} + A_tN_{t'}\sigma_{q_0p_0}$$
$$+ B_tM_{t'}\sigma_{p_0q_0} + J_{q_tp_{t'}},$$
$$\sigma_{p_tq_{t'}} = M_tA_{t'}\sigma_{q_0q_0} + N_tB_{t'}\sigma_{p_0p_0} + N_tA_{t'}\sigma_{p_0q_0}$$
$$+ M_tB_{t'}\sigma_{q_0p_0} + J_{p_tq_{t'}},$$

where

$$J_{q_tq_{t'}} = \int_0^t\int_0^{t'} d\tau d\tau' \quad (19)$$
$$\times [C_\tau C_{\tau'} I_{qq}(t-\tau, t'-\tau')$$
$$+ C_\tau \tilde{C}_{\tau'} I_{qp}(t-\tau, t'-\tau')$$
$$+ \tilde{C}_\tau C_{\tau'} I_{pq}(t-\tau, t'-\tau')$$
$$+ \tilde{C}_\tau \tilde{C}_{\tau'} I_{pp}(t-\tau, t'-\tau')],$$
$$J_{p_tp_{t'}} = \int_0^t\int_0^{t'} d\tau d\tau' [L_\tau L_{\tau'} I_{pp}(t-\tau, t'-\tau')$$
$$+ L_\tau \tilde{L}_{\tau'} I_{pq}(t-\tau, t'-\tau')$$
$$+ \tilde{L}_\tau L_{\tau'} I_{qp}(t-\tau, t'-\tau')$$
$$+ \tilde{L}_\tau \tilde{L}_{\tau'} I_{qq}(t-\tau, t'-\tau')],$$
$$J_{q_tp_{t'}} = \int_0^t\int_0^{t'} d\tau d\tau' [C_\tau L_{\tau'} I_{qp}(t-\tau, t'-\tau')$$
$$+ \tilde{C}_\tau L_{\tau'} I_{pp}(t-\tau, t'-\tau')$$
$$+ \tilde{C}_\tau \tilde{L}_{\tau'} I_{pq}(t-\tau, t'-\tau')$$
$$+ C_\tau \tilde{L}_{\tau'} I_{qq}(t-\tau, t'-\tau')],$$
$$J_{p_tq_{t'}} = \int_0^t\int_0^{t'} d\tau d\tau' [L_\tau C_{\tau'} I_{pq}(t-\tau, t'-\tau')$$
$$+ \tilde{L}_\tau C_{\tau'} I_{qq}(t-\tau, t'-\tau')$$
$$+ \tilde{L}_\tau \tilde{C}_{\tau'} I_{qp}(t-\tau, t'-\tau')$$
$$+ L_\tau \tilde{C}_{\tau'} I_{pp}(t-\tau, t'-\tau')].$$

The symbol $\langle\ldots\rangle$ in $I_{qq}(t,\tau) = \langle F_q(t)F_q(\tau)\rangle$, $I_{pp}(t,\tau) = \langle F_p(t)F_p(\tau)\rangle$, $I_{pq}(t,\tau) = \langle F_p(t)F_q(\tau)\rangle$, and $I_{qp}(t,\tau) = \langle F_q(t)F_p(\tau)\rangle$ denotes averaging over the entire system.

In order to determine the friction and diffusion coefficients, we consider the equations for the mean values and for the variances with respect to the coordinate, $\sigma_{qq}(t) = \langle q^2(t)\rangle - \langle q(t)\rangle^2 = \sigma_{q_tq_t} - \langle q(t)\rangle^2$; with respect to the momentum, $\sigma_{pp}(t) = \langle p^2(t)\rangle - \langle p(t)\rangle^2 = \sigma_{p_tp_t} - \langle p(t)\rangle^2$; and with respect to the coordinate and momentum, $\sigma_{qp}(t) = \frac{1}{2}\langle p(t)q(t) +$

$q(t)p(t)\rangle - \langle p(t)\rangle\langle q(t)\rangle = \frac{1}{2}(\sigma_{q_tp_t} + \sigma_{p_tq_t}) - \langle p(t)\rangle\langle q(t)\rangle$. Differentiating Eqs. (17) and (18) with respect to time at $t = t'$, we obtain

$$\frac{d}{dt}\langle q(t)\rangle = -\lambda_q(t)\langle q(t)\rangle + \frac{1}{m(t)}\langle p(t)\rangle, \quad (20)$$

$$\frac{d}{dt}\langle p(t)\rangle = -\xi(t)\langle q(t)\rangle - \lambda_p(t)\langle p(t)\rangle,$$

and

$$\dot\sigma_{qq}(t) = -2\lambda_q(t)\sigma_{qq}(t) + \frac{2}{m(t)}\sigma_{qp}(t) + 2D_{qq}(t), \quad (21)$$

$$\dot\sigma_{pp}(t) = -2\lambda_p(t)\sigma_{pp}(t) - 2\xi(t)\sigma_{qp}(t) + 2D_{pp}(t),$$

$$\dot\sigma_{qp}(t) = -[\lambda_p(t) + \lambda_q(t)]\sigma_{qp}(t) - \xi(t)\sigma_{qq}(t) + \frac{1}{m(t)}\sigma_{pp}(t) + 2D_{qp}(t).$$

These equations involve the coefficient of friction in the coordinate,

$$\lambda_q(t) = \frac{\dot A_t N_t - \dot B_t M_t}{B_t M_t - A_t N_t}; \quad (22)$$

the coefficient of friction in the momentum,

$$\lambda_p(t) = \frac{A_t \dot N_t - B_t \dot M_t}{B_t M_t - A_t N_t}; \quad (23)$$

the renormalized inverse mass,

$$1/m(t) = \frac{\dot A_t B_t - \dot B_t A_t}{B_t M_t - A_t N_t}; \quad (24)$$

the renormalized stiffness coefficient,

$$\xi(t) = \frac{\dot M_t N_t - \dot N_t M_t}{B_t M_t - A_t N_t}; \quad (25)$$

the coefficient of diffusion in the coordinate,

$$D_{qq}(t) = \lambda_q(t)J_{q_tq_t} - \frac{1}{2m(t)}(J_{q_tp_t} + J_{p_tq_t}) + \frac{1}{2}\dot J_{q_tq_t}; \quad (26)$$

the coefficient of diffusion in the momentum,

$$D_{pp}(t) = \lambda_p(t)J_{p_tp_t} + \frac{\xi(t)}{2}(J_{q_tp_t} + J_{p_tq_t}) + \frac{1}{2}\dot J_{p_tp_t}; \quad (27)$$

and the coefficient of diffusion in the coordinate and momentum,

$$D_{qp}(t) = \frac{1}{2}\left[\frac{\lambda_p(t) + \lambda_p(t)}{2}(J_{q_tp_t} + J_{p_tq_t}) + \xi(t)J_{q_tq_t} - \frac{1}{m(t)}J_{p_tp_t} + \frac{1}{2}(\dot J_{q_tp_t} + \dot J_{p_tq_t})\right]. \quad (28)$$

Thus, we have derived equations for the first and second moments where the transport coefficients depend explicitly on time, the collective coordinate, and the canonically conjugate momentum. It is the time dependence of the transport coefficients that reflects the fact that non-Markovian processes occur in the system. In the limit $t \to \infty$, the equilibrium diffusion coefficients have the form [$\dot\sigma_{pp} = \dot\sigma_{qq} = \dot\sigma_{qp} = 0$ in (21)]

$$D_{qq}(\infty) = \lambda_q(\infty)\sigma_{qq}(\infty) - \frac{1}{m(\infty)}\sigma_{qp}(\infty), \quad (29)$$

$$D_{pp}(\infty) = \lambda_p(\infty)\sigma_{pp}(\infty) + \xi(\infty)\sigma_{qp}(\infty),$$

$$D_{qp}(\infty) = \frac{1}{2}[(\lambda_p(\infty) + \lambda_q(\infty))\sigma_{qp}(\infty) + \xi(\infty)\sigma_{qq}(\infty) - \frac{1}{m(\infty)}\sigma_{pp}(\infty)].$$

Comparing (26)–(28) with (29), we arrive at the relations $\sigma_{qq}(\infty) = J_{q_\infty q_\infty}$, $\sigma_{pp}(\infty) = J_{p_\infty p_\infty}$, and $\sigma_{qp}(\infty) = \frac{1}{2}(J_{q_\infty p_\infty} + J_{p_\infty q_\infty})$. If $\sigma_{qp}(\infty) = 0$ in (29), the asymptotic diffusion and friction coefficients satisfy the fluctuation–dissipation relations

$$D_{qq}(\infty) = \lambda_q(\infty)\sigma_{qq}(\infty),$$
$$D_{pp}(\infty) = \lambda_p(\infty)\sigma_{pp}(\infty).$$

If all G_ν in (1) are equal to zero, then $\lambda_q(t) = 0$ and $D_{qq}(t) = 0$. Thus, it is the coupling in the momentum p that is responsible for the appearance of the coefficients λ_q and D_{qq} in the stochastic equations.

In order to illustrate our numerical calculations, we set $G_\nu = 0$ and $V_\nu = \alpha_\nu q$ in (1) and replace the sums $\sum_\nu$ by integrals with respect to the heat-bath frequency, taking into account the density of states, $\rho(\omega')$, in the integrand, so that

$$\int_0^\infty d\omega'\rho(\omega')\frac{(\alpha(\omega'))^2}{\hbar\omega'}\ldots = \frac{\alpha^2\gamma^2}{\pi}\int_0^\infty \frac{d\omega'}{\gamma^2 + \omega'^2}\ldots.$$

It is necessary that γ be much greater than ω. We choose ω and α in such a way as to obtain the specific asymptotic values $\xi(\infty) = \mu\tilde\omega^2$ and $\lambda_p(\infty) = \lambda_p$. We consider the case of $\mu = 50m_0$ (m_0 is the nucleon mass) and $\hbar\tilde\omega = 3$ MeV and set $\hbar\gamma = 12$ MeV. The figure shows the coefficients λ_p, D_{pp}, and D_{qp} versus time. The transport coefficients vanish at $t = 0$ and reach asymptotic values within a short time interval. For $t > 0$, the coefficients $\lambda_p(t)$ and $D_{pp}(t)$ are positive; the coefficient D_{qp} is first positive and then becomes negative. The values calculated for the coefficient $D_{pp}(\infty)$ are larger, within a factor of 1.5, than the classical values given by $D^c_{pp} = 0.5\hbar\lambda_p\mu\tilde\omega\coth[\hbar\tilde\omega/(2T)]$, and this fact confirms that

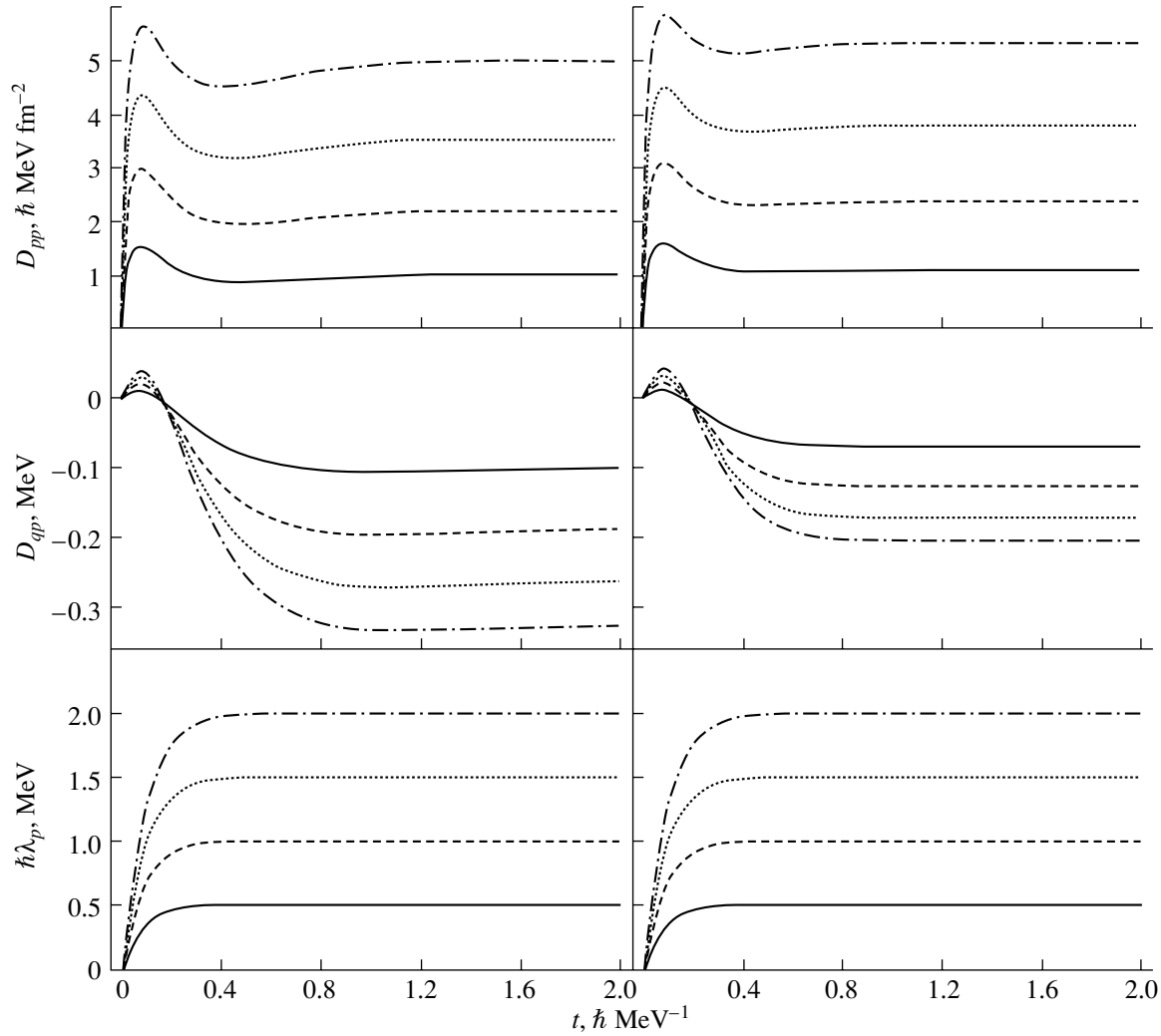

Calculated time dependences of the diffusion and friction coefficients for $\mu = 50m_0$ and $\hbar\tilde{\omega} = 3$ MeV at (left panels) $T = 0.1$ MeV and (right panels) $T = 1$ MeV. The solid, dashed, dotted, and dash-dotted curves represent the results obtained for the cases where the asymptotic values of the friction coefficient are $\hbar\lambda_p = 0.5$, 1.0, 1.5, and 2.0 MeV, respectively.

the calculations were correct and that the parameters were chosen appropriately. We have $D_{pp}(\infty) > D^c_{pp}$ since $D_{qp}(\infty) < 0$ and since $D^c_{qp}(\infty) = 0$ in the classical case.

2.4. Relation to Diffusion Equations

Equations (17) and (21) for the mean values and variances of the collective coordinate and momentum can be obtained from the master equation for the density matrix $\rho(t)$ describing the collective subsystem,

$$\dot{\rho} = -\frac{i}{\hbar}[\tilde{H}_c, \rho] + \frac{i\lambda_q(t)}{2\hbar}[p, \{q, \rho\}_+] \qquad (30)$$
$$- \frac{i\lambda_p(t)}{2\hbar}[q, \{p, \rho\}_+] - \frac{D_{qq}(t)}{\hbar^2}[p, [p, \rho]]$$
$$- \frac{D_{pp}(t)}{\hbar^2}[q, [q, \rho]] + \frac{D_{qp}(t)}{\hbar^2}([p, [q, \rho]] + [q, [p, \rho]]),$$

or from an equation of the Fokker–Planck type for the corresponding Wigner function $W(q, p, t)$,

$$\dot{W} = -\frac{p}{m(t)}\frac{\partial W}{\partial q} + \xi(t)q\frac{\partial W}{\partial p} \qquad (31)$$
$$+ \lambda_p(t)\frac{\partial(pW)}{\partial p} + \lambda_q(t)\frac{\partial(qW)}{\partial q} + D_{qq}(t)\frac{\partial^2 W}{\partial q^2}$$
$$+ D_{pp}(t)\frac{\partial^2 W}{\partial p^2} + 2D_{qp}(t)\frac{\partial^2 W}{\partial q \partial p}.$$

For the case of general coupling, we have assumed here that friction and diffusion depend on t but that they are independent of p and q. In the case of a linear coupling, this assumption is not required because there then exists only a time dependence, which is obtained explicitly. Despite the non-Markovian nature of Eqs. (5), the evolution of ρ and the evolution of W are described by differential equations local in

time. Memory effects lead to the time dependence of the transport coefficients. In general, we have the coefficients of friction and diffusion in the coordinate and in the momentum, this being a consequence of the presence of random forces in q and p. We note that Eqs. (30) and (31) have the same structure as the corresponding phenomenological Lindblad equations featuring constant transport coefficients [16–21].

2.5. Strong-Damping Limit

In the case of large friction, equilibrium with respect to the momentum, $\dot{p} \approx 0$, is reached fast; as a result, the second equation in (5) takes the form

$$0 = -\tilde{\delta} q(t) - \int_0^t d\tau K_{VV}(t,\tau)\dot{q}(\tau) + F_p(t). \quad (32)$$

Solving this equation, we obtain

$$q(t) = A_t q(0) + \int_0^t d\tau \tilde{C}_\tau F_p(t-\tau), \quad (33)$$

where

$$A_t = \int_0^t d\tau K_{VV}(t,\tau)\tilde{C}_\tau,$$
$$\tilde{C}_t = \mathcal{L}^{-1}[\tilde{\delta} + sK_{VV}(s)]^{-1}.$$

By using (33), we obtain the mean value and the variance as functions of time,

$$\langle q(t)\rangle = A_t\langle q(0)\rangle, \quad (34)$$
$$\sigma_{qq}(t) = A_t^2\sigma_{qq}(0) + J_{q_t q_t},$$

where

$$J_{q_t q_t} = \int_0^t\int_0^t d\tau d\tau' \tilde{C}_\tau \tilde{C}_{\tau'} I_{pp}(t-\tau, t-\tau').$$

The differential equations for $\langle q(t)\rangle$ and $\sigma_{qq}(t)$ can be derived from Eqs. (34). As a result, we obtain

$$\langle \dot{q}(t)\rangle = v(t)\langle q(t)\rangle, \quad (35)$$
$$\dot{\sigma}_{qq}(t) = 2v(t)\sigma_{qq}(t) + D_{qq}^{\text{ov}}(t),$$

where the drift $[v(t)]$ and the diffusion $[D_{qq}^{\text{ov}}(t)]$ coefficient have the form

$$v(t) = \dot{A}_t/A_t, \quad (36)$$
$$D_{qq}^{\text{ov}}(t) = -2\frac{\dot{A}_t}{A_t}J_{q_t q_t} + \dot{J}_{q_t q_t}.$$

In the asymptotic limit, we arrive at the fluctuation–dissipation relation $D_{qq}^{\text{ov}}(\infty) = -2v(\infty)\sigma_{qq}(\infty)$.

Equations (35) can be derived from the following differential equation for the distribution $W(q,t)$ of the coordinate:

$$\dot{W} = -v(t)\frac{\partial}{\partial q}(qW) + D_{qq}^{\text{ov}}(t)\frac{\partial^2}{\partial q^2}W. \quad (37)$$

This equation is a quantum analog of the classical Smoluchowski equation for a general coupling of the subsystem to a heat bath. In [25], this equation was obtained by a different method, but only for the FC oscillator. If the transition times for $D_{qq}^{\text{ov}}(t)$ and $v(t)$ are equal to or shorter than the characteristic time $1/\lambda_p(\infty)$ of equilibration in p, the asymptotic expressions for $D_{qq}^{\text{ov}}(\infty)$ and $v(\infty)$ can be used in the calculations to a high accuracy—that is, the time dependence of the transport coefficients can be disregarded.

3. LINEAR COUPLING IN MOMENTUM

As a particular case, we will consider a microscopic Hamiltonian H of the quadratic form for the total system; that is,

$$H_c = \frac{p^2}{2\mu} + \frac{\mu\omega_0^2 q^2}{2} + \frac{\xi_0}{2}(pq+qp), \quad (38)$$
$$H_b = \sum_\nu \left(\frac{p_\nu^2}{2m_\nu} + \frac{m_\nu\omega_\nu^2 q_\nu^2}{2}\right), \quad (39)$$
$$H_{cb} = p\sum_\nu g_\nu p_\nu. \quad (40)$$

Here, H_{cb} describes the interaction between the internal and collective subsystems that is linear in the momenta p and p_ν, the coupling constants being denoted by g_ν. In (38) and (39), μ (m_ν) and ω_0 (ω_ν) are, respectively, the mass and the frequency of the collective (internal) oscillator. With the aid of the parameter ξ_0, one can ensure the translation invariance of the collective subsystem.

By analogy with (5), we obtain the set of the quantum integro-differential stochastic Langevin equations

$$\frac{dq}{dt} = \frac{1}{\tilde{\mu}}p + \xi_0 q + \int_0^t \dot{p}(t')K_{GG}(t-t')dt' + F_q(t), \quad (41)$$
$$\frac{dp}{dt} = -\mu\omega_0^2 q - \xi_0 p,$$

which involve the renormalized collective mass,

$$\frac{1}{\tilde{\mu}} = \frac{1}{\mu} - \sum_\nu m_\nu g_\nu^2; \quad (42)$$

the dissipative kernel of the equation of motion in the coordinate q,

$$K_{GG}(t-t') = \sum_\nu m_\nu g_\nu^2 \cos[\omega_\nu(t-t')]; \quad (43)$$

and the operator of a random force in the coordinate q,

$$F_q(t) = \sum_\nu g_\nu[(p_\nu(0) + m_\nu g_\nu p(0)) \quad (44)$$
$$\times \cos(\omega_\nu t) - q_\nu(0) m_\nu \omega_\nu \sin(\omega_\nu t)].$$

Upon performing the canonical coordinate transformation $p'_\nu = p_\nu + g_\nu m_\nu p$ and $q'_\nu = q_\nu$, we obtain

$$F_q(t) = \sum_\nu F_q^\nu(t) = \sum_\nu g_\nu[p'_\nu(0)\cos(\omega_\nu t) \quad (45)$$
$$- q'_\nu(0) m_\nu \omega_\nu \sin(\omega_\nu t)].$$

We note that this transformation leads to a new total Hamiltonian, where there is no coupling between the collective and internal subsystems and where the frequencies and masses are renormalized. We perform averaging over the internal degrees of freedom with this Hamiltonian. The random-force operator F_q then has a zero first moment and a nonzero second moment. For the symmetrized correlation function $\phi^\nu_{qq}(t,t') = \hbar\omega_\nu m_\nu g_\nu^2 \cos[\omega_\nu(t-t')](2n_\nu + 1)$, we obtain the quantum fluctuation–dissipation relation

$$\sum_\nu \phi^\nu_{qq}(t,t')\frac{1}{\hbar\omega_\nu}\tanh(\hbar\omega_\nu/(2T)) = K_{GG}(t-t'). \quad (46)$$

In order to simplify the ensuing calculations, we replace the sum $\sum_\nu m_\nu g_\nu^2 \ldots$ in the relevant formulas by an integral [10],

$$\int_0^\infty d\omega \rho(\omega) m(\omega)(g(\omega))^2 \ldots = \frac{g_0\gamma^2}{\pi}\int_0^\infty d\omega \frac{d\omega}{\gamma^2+\omega^2}\ldots.$$

Finally, we have

$$K_{GG}(t-t') = g_0\gamma\exp(-\gamma|t-t'|), \quad (47)$$
$$K_{GG}(s) = \frac{g_0\gamma}{s+\gamma}, \quad (48)$$

where γ^{-1} characterizes the dissipation-memory time and $\Gamma = \hbar\gamma$ is the width of internal-subsystem excitations that is due to the couplings to the collective subsystem. In the case of instantaneous dissipation ($\gamma \to \infty$), expression (47) reduces to $K_{GG}(t-t') = 2g_0\delta(t-t')$. This delta-function form of the kernel is frequently used for Markovian processes, but, in some cases, it can lead to a violation of the uncertainty relation [9, 18, 21] at the initial instant.

Solving Eqs. (41), we obtain

$$q(t) = q(0)A_t + p(0)B_t + \int_0^t dt' A_{t'} F_q(t-t'), \quad (49)$$

$$p(t) = q(0)M_t + p(0)N_t + \int_0^t dt' M_{t'} F_q(t-t'),$$

where

$$A_t = \sum_{i=1}^3 A_t^i = \sum_{i=1}^3 \beta_i(s_i+\gamma)(s_i+\xi_0)e^{s_i t}, \quad (50)$$

$$M_t = \sum_{i=1}^3 M_t^i = -\mu\omega_0^2\sum_{i=1}^3 \beta_i(s_i+\gamma)e^{s_i t},$$

$$B_t = \frac{1}{\tilde\mu}\sum_{i=1}^3 \beta_i(s_i+\gamma+(1-\tilde\mu/\mu)\xi_0)e^{s_i t},$$

$$N_t = \sum_{i=1}^3 \beta_i((s_i-\xi_0)(s_i+\gamma)+(1-\mu/\tilde\mu)\omega_0^2)e^{s_i t}.$$

Here, s_i $(i = 1,2,3)$ are the roots of the cubic equation

$$s^3 + \gamma s^2 + (\omega_0^2 - \xi_0^2)s + \gamma\left(\frac{\mu}{\tilde\mu}\omega_0^2 - \xi_0^2\right) = 0, \quad (51)$$

while $\beta_1 = (s_1-s_2)^{-1}(s_1-s_3)^{-1}$, $\beta_2 = (s_2-s_1)^{-1}\times(s_2-s_3)^{-1}$, $\beta_3 = (s_3-s_1)^{-1}(s_3-s_2)^{-1}$, and $1/\tilde\mu = 1/\mu - g_0\gamma$.

For a damped oscillator, the expressions for the transport coefficients can be derived from the general formulas (22)–(28). As a result, we have

$$\xi(t) = \mu\omega_0^2, \quad (52)$$

$$\frac{1}{m(t)} = \frac{1}{\tilde\mu}\frac{\sum_{i,j=1}^3 \beta_i\beta_j(s_i-s_j)^2[(s_i+\gamma)(s_j+\gamma)+\xi_0(1-\frac{\tilde\mu}{\mu})(s_i+s_j+\gamma+\xi_0)]e^{(s_i+s_j)t}}{(\frac{\mu}{\tilde\mu}\omega_0^2-\xi_0^2)\sum_{i,j=1}^3 \beta_i\beta_j(s_i+\gamma)(s_j+\gamma)(s_i-s_j)^2 e^{(s_i+s_j)t}/(s_i s_j)},$$

$$\lambda_p(t) = \xi_0,$$

$$\lambda_q(t) = -\xi_0 - \frac{\sum\limits_{i,j=1}^{3} \beta_i\beta_j(s_i+\gamma)(s_j+\gamma)(s_i+s_j)(s_i-s_j)^2 e^{(s_i+s_j)t}/(s_is_j)}{\sum\limits_{i,j=1}^{3} \beta_i\beta_j(s_i+\gamma)(s_j+\gamma)(s_i-s_j)^2 e^{(s_i+s_j)t}/(s_is_j)},$$

$$D_{pp}(t) = 0,$$

$$D_{qq}(t) = \left(\lambda_q(t) + \frac{1}{2}\frac{d}{dt}\right) J_{q_tq_t} + \frac{1}{m(t)\mu\omega_0^2}\left(\xi_0 + \frac{d}{dt}\right) J_{p_tp_t},$$

$$D_{qp}(t) = \frac{1}{2}\left[\mu\omega_0^2 J_{q_tq_t} - \frac{1}{m(t)\mu\omega_0^2} \times \left(\mu\omega_0^2 + m(t)(\xi_0+\lambda_q(t))\xi_0 + \frac{1}{2}\left[(3\xi_0+\lambda_q(t))\frac{d}{dt} + \frac{d^2}{dt^2}\right]\right) J_{p_tp_t}\right],$$

where

$$J_{q_tq_t} = \frac{\hbar g_0\gamma^2}{\pi}\int\limits_0^\infty d\omega \frac{\omega\coth(\hbar\omega/(2T))}{\gamma^2+\omega^2} \times \sum_{ik} A_t^iA_t^k\varphi_{ik}(s_i,s_k,\omega,t), \tag{53}$$

$$J_{p_tp_t} = \frac{\hbar g_0\gamma^2}{\pi}\int\limits_0^\infty d\omega \frac{\omega\coth(\hbar\omega/(2T))}{\gamma^2+\omega^2} \times \sum_{ik} M_t^iM_t^k\varphi_{ik}(s_i,s_k,\omega,t), \tag{54}$$

$$\frac{1}{2}(J_{p_tq_t} + J_{q_tp_t}) = \frac{\hbar g_0\gamma^2}{\pi} \times \int\limits_0^\infty d\omega \frac{\omega\coth(\hbar\omega/(2T))}{\gamma^2+\omega^2}\sum_{ik} A_t^iM_t^k\varphi_{ik}(s_i,s_k,\omega,t), \tag{55}$$

$$\varphi_{ik} = \int\limits_0^t dt' e^{s_it'}\int\limits_0^t dt'' e^{s_kt''}\cos\left[\omega_\nu(t''-t')\right]. \tag{56}$$

Since $\varphi_{ik}(t=0)=0$ and $\frac{d}{dt}\varphi_{ik}(t=0)=0$, all diffusion coefficients are equal to zero at the initial instant $t=0$; that is, $D_{qq}(t=0) = D_{pp}(t=0) = D_{qp}(t=0) = 0$. It can be shown that, at any instant of time, $D_{pp}(t)=0$ since there is no random force in the momentum in the equations of motion (41).

3.1. Asymptotic Behavior of the Diffusion Coefficients, Friction Coefficients, and Correlation Functions

The roots s_1, s_2, and s_3 of the cubic equation have negative real parts; in addition, two roots, s_1 and s_2, are complex conjugate. At long times, terms proportional to e^{s_3t} can be disregarded in the functions A_t, M_t, B_t, and N_t, since these terms are damped fast. After simple but cumbersome calculations, one can derive the following expressions for the friction and diffusion coefficients in the limit $t\to\infty$:

$$\frac{1}{m(\infty)} = \frac{|s_1|^2}{\mu\omega_0^2 - \tilde{\mu}\xi_0^2} \times \left[1 + \xi_0\left(1 - \frac{\tilde{\mu}}{\mu}\right)\frac{s_1+s_1^*+\gamma+\xi_0}{|s_1+\gamma|^2}\right], \tag{57}$$

$$\lambda_q(\infty) = -\xi_0 - (s_1+s_1^*),$$

$$D_{qq}(\infty) = \lambda_q(\infty)\sigma_{qq}(\infty) + \frac{\xi_0}{m(\infty)\mu\omega_0^2}\sigma_{pp}(\infty),$$

$$D_{qp}(\infty) = \frac{1}{2}\left[\mu\omega_0^2\sigma_{qq}(\infty) - \left(\frac{1}{m(\infty)} + \frac{\xi_0(\xi_0+\lambda_q(\infty))}{\mu\omega_0^2}\right)\sigma_{pp}(\infty)\right].$$

For the renormalized inverse mass, we obtain the simple expression

$$\frac{1}{m(\infty)} = \frac{|s_1|^2}{\mu\omega_0^2} \tag{58}$$

in the case of $\xi_0=0$. From Eqs. (51), (52), and (57), one can see that the collective-energy loss $[\lambda_p(\infty)(t) + \lambda_q(\infty)(t) = 0]$, and the values of the diffusion coefficients vanish if the term $0.5p^2\sum_\nu m_\nu g_\nu^2$, which compensates for the collective-mass renormalization $[m(t) = \mu = \tilde{\mu}]$, is included in the Hamiltonian H_c.

By using Eqs. (18) and (53)–(55), the asymptotic behavior of the variances $\sigma_{pp}(\infty)$, $\sigma_{qq}(\infty)$, and $\sigma_{qp}(\infty)$ appearing in (57) can be expressed in terms of the integrals ($x_n = 2\pi Tn/\hbar$)

$$I = \frac{\hbar g_0\gamma^2}{\pi} \tag{59}$$

$$\times \int_0^\infty \frac{\coth(\hbar\omega/(2T))\omega d\omega}{(s_1^2+\omega^2)(s_2^2+\omega^2)(s_3^2+\omega^2)}$$

$$= \frac{T}{\mu\omega_0^2}\sum_{n=0}^{\infty}\frac{(2-\delta_{n,0})(x_n-\gamma)}{x_n^3-\gamma x_n^2+(\omega_0^2-\xi_0^2)x_n+\gamma(\xi_0^2-\frac{\mu}{\tilde\mu}\omega_0^2)}$$

and

$$\tilde I = \frac{\hbar g_0\gamma^2}{\pi} \tag{60}$$

$$\times \int_0^\infty \frac{\coth(\hbar\omega/(2T))\omega^3 d\omega}{(s_1^2+\omega^2)(s_2^2+\omega^2)(s_3^2+\omega^2)}$$

$$= \frac{T}{\mu\omega_0^2}\sum_{n=0}^{\infty}\frac{(2-\delta_{n,0})(x_n(\omega_0^2-\xi_0^2)+\gamma(\xi_0^2-\frac{\mu}{\tilde\mu}\omega_0^2))}{x_n^3-\gamma x_n^2+(\omega_0^2-\xi_0^2)x_n+\gamma(\xi_0^2-\frac{\mu}{\tilde\mu}\omega_0^2)}$$

as

$$\sigma_{pp}(\infty) = (\mu\omega_0^2)^2 I, \tag{61}$$
$$\sigma_{qq}(\infty) = \xi_0^2 I + \tilde I, \quad \sigma_{qp}(\infty) = -\xi_0\mu\omega_0^2 I.$$

Weak-coupling limit. Disregarding the interaction term H_{cb} and using the collective Hamiltonian in the form (38), we can represent the asymptotic expressions for the variances in the form

$$\sigma_{pp}(\infty) = \frac{\hbar}{2}\frac{\mu\omega_0^2}{(\omega_0^2-\xi_0^2)^{1/2}}\coth(\hbar(\omega_0^2-\xi_0^2)^{1/2}/(2T)), \tag{62}$$

$$\sigma_{qq}(\infty) = \frac{\hbar}{2}\frac{1}{\mu(\omega_0^2-\xi_0^2)^{1/2}}\coth(\hbar(\omega_0^2-\xi_0^2)^{1/2}/(2T)),$$

$$\sigma_{qp}(\infty) = -\frac{\hbar}{2}\frac{\xi_0}{(\omega_0^2-\xi_0^2)^{1/2}}\coth(\hbar(\omega_0^2-\xi_0^2)^{1/2}/(2T)),$$

$$\sigma_{qq}(\infty)\sigma_{pp}(\infty) - \sigma_{qp}^2(\infty)$$
$$= \frac{\hbar^2}{4}\coth^2(\hbar(\omega_0^2-\xi_0^2)^{1/2}/(2T)) \geq \frac{\hbar^2}{4}.$$

Assuming that, in the limit of weak coupling between the collective system and the heat bath, the asymptotic expressions for the variances differ only slightly from those in (62) and employing Eqs. (57), one can obtain asymptotic expressions for the diffusion coefficients. At $\xi_0 = 0$, it follows from these asymptotic expressions that $\lambda_q(\infty) = -(s_1+s_1^*)$, $D_{qq}(\infty) = \frac{\hbar}{2}\lambda_q(\infty)\mu\omega_0\coth(\hbar\omega_0/(2T))$, and $D_{qp}(\infty) = 0$.

High-temperature limit. In the limit $T\to\infty$, the expressions for the integrals I and $\tilde I$ are simplified to become

$$I(T\to\infty) = \frac{T\tilde\mu}{(\mu\omega_0^2-\tilde\mu\xi_0^2)\mu\omega_0^2}, \tag{63}$$
$$\tilde I(T\to\infty) = T/(\mu\omega_0^2). \tag{64}$$

Here, we have taken into account the relations between the roots of the cubic equation (51). It should be noted that expressions (63) and (64) are independent of the parameters g_0 and γ. By using Eqs. (57), (61), (63), and (64), we obtain asymptotic expressions for the diffusion coefficients,

$$D_{qq}(\infty) = \frac{T}{\mu\omega_0^2-\tilde\mu\xi_0^2} \tag{65}$$
$$\times\left(\xi_0\left(\frac{\tilde\mu}{m(\infty)}-1\right)-(s_1+s_1^*)\right),$$
$$D_{qp}(\infty) = \frac{1}{2}\frac{T}{\mu\omega_0^2-\tilde\mu\xi_0^2}$$
$$\times\left(\mu\omega_0^2\left(1-\frac{\tilde\mu}{m(\infty)}\right)+\xi_0\tilde\mu(s_1+s_1^*)\right),$$

and for the variances,

$$\sigma_{pp}(\infty) = \frac{T\tilde\mu\mu\omega_0^2}{\mu\omega_0^2-\tilde\mu\xi_0^2}, \tag{66}$$
$$\sigma_{qq}(\infty) = \frac{T}{\mu\omega_0^2-\tilde\mu\xi_0^2}, \quad \sigma_{qp}(\infty) = -\frac{T\tilde\mu\xi_0}{\mu\omega_0^2-\tilde\mu\xi_0^2}.$$

In the case of $\xi_0 = 0$, we find from (65) that the diffusion coefficients assume the form

$$D_{qq}(\infty) = -(s_1+s_1^*)\frac{1}{\mu\omega_0^2}T, \tag{67}$$
$$D_{pq}(\infty) = \frac{1}{2}\left(1-\frac{\tilde\mu|s_1|^2}{\mu\omega_0^2}\right)T.$$

In the limit of weak coupling and high T, expressions (62) and (66) coincide since $\tilde\mu\approx\mu$ in this case.

Low-temperature limit. Let us now consider the integrals I and $\tilde I$ in the limit $T\to 0$. We have

$$I(T\to 0) = \frac{\hbar}{\pi\mu\omega_0^2}\frac{(s_2^2-s_3^2)\ln s_1+(s_3^2-s_1^2)\ln s_2+(s_1^2-s_2^2)\ln s_3}{(s_1-s_2)(s_1-s_3)(s_2-s_3)}, \tag{68}$$

$$\tilde I(T\to 0) = \frac{\hbar}{\pi\mu\omega_0^2}\frac{s_1^2(s_3^2-s_2^2)\ln s_1+s_2^2(s_1^2-s_3^2)\ln s_2+s_3^2(s_2^2-s_1^2)\ln s_3}{(s_1-s_2)(s_1-s_3)(s_2-s_3)}. \tag{69}$$

In the weak-coupling limit, these expressions are simplified to become

$$I(T\to 0)=\frac{\hbar}{2\mu\omega_0^2}\frac{1}{(\omega_0^2-\xi_0^2)^{1/2}}, \tag{70}$$

$$\tilde{I}(T\to 0)=\frac{\hbar}{2\mu\omega_0^2}(\omega_0^2-\xi_0^2)^{1/2}. \tag{71}$$

Substituting (70) and (71) into (61) and using Eqs. (57), we obtain asymptotic expressions for the diffusion coefficients,

$$D_{qq}(\infty)=\frac{-\hbar}{2\mu\omega_0^2}(s_1+s_1^*)(\omega_0^2-\xi_0^2)^{1/2},$$
$$D_{pq}(\infty)=0, \tag{72}$$

and for the variances,

$$\sigma_{pp}(\infty)=\frac{\hbar\mu\omega_0^2}{2}\frac{1}{(\omega_0^2-\xi_0^2)^{1/2}}, \tag{73}$$
$$\sigma_{qq}(\infty)=\frac{\hbar}{2\mu}\frac{1}{(\omega_0^2-\xi_0^2)^{1/2}},$$
$$\sigma_{qp}(\infty)=-\frac{\hbar}{2}\frac{\xi_0}{(\omega_0^2-\xi_0^2)^{1/2}},$$
$$\sigma_{qq}(\infty)\sigma_{pp}(\infty)-\sigma_{qp}^2(\infty)=\hbar^2/4.$$

It can easily be seen that, in the limit of low T, expressions (62) coincide with expressions (73).

Correlation functions. The asymptotic expressions ($t\gg t'>0$) for the symmetrized correlation functions

$$\sigma^{\rm as}_{q_tq_{t'}}=\frac{\hbar g_0\gamma^2}{\pi} \tag{74}$$
$$\times\int_0^\infty\frac{\coth(\hbar\omega/(2T))\omega(\xi_0^2+\omega^2)\cos[\omega(t-t')]d\omega}{(s_1^2+\omega^2)(s_2^2+\omega^2)(s_3^2+\omega^2)},$$

$$\sigma^{\rm as}_{p_tp_{t'}}=\frac{\hbar g_0\gamma^2\mu^2\omega_0^4}{\pi}$$
$$\times\int_0^\infty\frac{\coth(\hbar\omega/(2T))\omega\cos[\omega(t-t')]d\omega}{(s_1^2+\omega^2)(s_2^2+\omega^2)(s_3^2+\omega^2)}$$

behave differently in the high- and low-temperature limits; that is,

$$\sigma^{\rm as}_{p_tp_{t'}}(T\to 0)\to\frac{-\hbar g_0\gamma^2\mu^2\omega_0^4}{\pi s_1^2s_2^2s_3^2}\frac{1}{(t-t')^2} \tag{75}$$
$$=\frac{-\hbar g_0\tilde{\mu}^2\mu^2\omega_0^4}{(\mu\omega_0^2-\tilde{\mu}\xi_0^2)^2}\frac{1}{(t-t')^2},$$

$$\sigma^{\rm as}_{p_tp_{t'}}(T\to\infty)\to\frac{-T\tilde{\mu}\mu\omega_0^2}{\gamma(\mu\omega_0^2-\tilde{\mu}\xi_0^2)}$$
$$\times\left[\frac{s_2s_3(s_2+s_3)e^{s_1(t-t')}}{(s_2-s_1)(s_3-s_1)}\right.$$
$$+\frac{s_1s_3(s_1+s_3)e^{s_2(t-t')}}{(s_1-s_2)(s_3-s_2)}$$
$$\left.+\frac{s_1s_2(s_1+s_2)e^{s_3(t-t')}}{(s_1-s_3)(s_2-s_3)}\right],$$

$$\sigma^{\rm as}_{q_tq_{t'}}(T\to 0)\to\frac{-\hbar g_0\tilde{\mu}^2\xi_0^2}{(\mu\omega_0^2-\tilde{\mu}\xi_0^2)^2}\frac{1}{(t-t')^2}$$
$$-\frac{i\hbar}{2\mu\omega_0^2}\left[\frac{s_1^2(s_2+s_3)e^{s_1(t-t')}}{(s_2-s_1)(s_3-s_1)}\right.$$
$$+\frac{s_2^2(s_1+s_3)e^{s_2(t-t')}}{(s_1-s_2)(s_3-s_2)}$$
$$\left.+\frac{s_3^2(s_1+s_2)e^{s_3(t-t')}}{(s_1-s_3)(s_2-s_3)}\right],$$

$$\sigma^{\rm as}_{q_tq_{t'}}(T\to\infty)\to\frac{-T\tilde{\mu}\xi_0^2}{\gamma\mu\omega_0^2(\mu\omega_0^2-\tilde{\mu}\xi_0^2)}$$
$$\times\left[\frac{s_2s_3(s_2+s_3)e^{s_1(t-t')}}{(s_2-s_1)(s_3-s_1)}\right.$$
$$+\frac{s_1s_3(s_1+s_3)e^{s_2(t-t')}}{(s_1-s_2)(s_3-s_2)}$$
$$\left.+\frac{s_1s_2(s_1+s_2)e^{s_3(t-t')}}{(s_1-s_3)(s_2-s_3)}\right]$$
$$-\frac{T}{2\mu\omega_0^2}\left[\frac{s_1(s_2+s_3)e^{s_1(t-t')}}{(s_2-s_1)(s_3-s_1)}\right.$$
$$+\frac{s_2(s_1+s_3)e^{s_2(t-t')}}{(s_1-s_2)(s_3-s_2)}$$
$$\left.+\frac{s_3(s_1+s_2)e^{s_2(t-t')}}{(s_1-s_3)(s_2-s_3)}\right].$$

At low temperatures, the correlation functions for an oscillator decrease according to a power law in the limit of long times. This is not observed in the classical limit of high temperatures, where the decay of the correlations is exponential.

4. CONCLUSIONS

Relying on a microscopic Hamiltonian for the total system, we have derived a set of nonlinear Langevin equations for a damped harmonic oscillator under the assumption of a general coupling between the collective and the internal subsystem and have solved these equations analytically. It has been shown that the equations of motion for the collective subsystem satisfy the quantum fluctuation–dissipation relation and the uncertainty relation. On the basis of non-Markovian Langevin equations, we have deduced equations for the first and second moments. These equations are local in time, but they involve transport coefficients depending explicitly on time. Since the

time within which the transport coefficients reach the asymptotic regime is short, non-Markovian effects are not expected to play a significant role in nuclear processes such as fission, fusion, and quasifission. It has been shown that coupling in the coordinate leads to the appearance of λ_p and D_{pp} in the diffusion equation and that coupling in the momentum leads to the appearance of λ_q and D_{qq} there.

In the case of a damped oscillator and a linear coupling in the momentum, we have derived explicit analytic expressions for the coefficients of friction in the coordinate and in the momentum and for the coefficients of diffusion in the coordinate and in the coordinate and momentum and have studied the asymptotic behavior of the correlation functions. At low temperatures, an oscillator is characterized by the decay of the correlations according to a power law in the limit of long times. This is not observed in the classical limit of high temperatures, where the decay of the correlations is exponential.

The nonlinear non-Markovian Langevin equations for an arbitrary potential can be solved analytically within a short time interval by approximating this potential by an oscillator (a harmonic or an inverted one) in the vicinity of the current mean coordinate. Therefore, the analytic formulas obtained here can be used to describe the fluctuation–dissipation dynamics of nuclear processes governed by complicated potentials. The approach developed here is useful in describing the lifetimes of metastable systems, transient processes, and decoherence in quantum systems.

ACKNOWLEDGMENTS

We are grateful to Dr. Yu.V. Pal'chikov for stimulating discussions.

This work was supported in part by the Russian Foundation for Basic Research and by the Deutsche Forschungsgemeinschaft.

REFERENCES

1. A. A. Belavin, B. Ya. Zel'dovich, A. M. Perelomov, and V. S. Popov, Zh. Éksp. Teor. Fiz. **56**, 264 (1969) [Sov. Phys. JETP **29**, 145 (1969)].
2. N. G. van Kampen, *Stochastic Processes in Physics and Chemistry* (North-Holland, Amsterdam, 1981; Vysshaya Shkola, Moscow, 1986).
3. A. O. Caldeira and A. J. Leggett, Physica A **121**, 587 (1983); Ann. Phys. (N.Y.) **149**, 374 (1983).
4. C. W. Gardiner, *Quantum Noise* (Springer, Berlin, 1991).
5. H. J. Carmichael, *An Open System Approach to Quantum Optics* (Springer, Berlin, 1993).
6. Yu. L. Klimontovich, *Statistical Theory of Open Systems* (Yanus, Moscow, 1995; Kluwer, Dordrecht, 1995).
7. D. N. Zubarev, V. G. Morozov, and G. Röpke, *Statistical Mechanics of Nonequilibrium Processes* (Akademie, Berlin, 1997).
8. U. Weiss, *Quantum Dissipative Systems* (World Sci., Singapore, 1999).
9. V. V. Dodonov, O. V. Man'ko, and V. I. Man'ko, J. Russ. Laser Res. **16**, 1 (1995).
10. K. Lindenberg and B. J. West, Phys. Rev. A **30**, 568 (1984).
11. F. Haake and R. Reibold, Phys. Rev. A **32**, 2462 (1985).
12. P. Talkner, Ann. Phys. (N.Y.) **167**, 390 (1986).
13. H. Grabert, P. Schramm, and G.-L. Ingold, Phys. Rep. **168**, 115 (1988).
14. B. L. Hu, J. P. Paz, and Y. Zhang, Phys. Rev. D **45**, 2843 (1992).
15. R. Karrlein and H. Grabert, Phys. Rev. E **55**, 153 (1997).
16. G. Lindblad, Commun. Math. Phys. **48**, 119 (1976); Rep. Math. Phys. **10**, 393 (1976).
17. H. Dekker, Phys. Rep. **80**, 1 (1981).
18. V. V. Dodonov and V. I. Man'ko, in *Proceedings of Lebedev Physical Institute*, Ed. by A. A. Komar (Nova Sci., Commack, New York, 1987), Vol. 167.
19. A. Isar, A. Sandulescu, H. Scutaru, *et al.*, Int. J. Mod. Phys. E **3**, 635 (1994).
20. G. G. Adamian, N. V. Antonenko, and W. Scheid, Phys. Lett. A **244**, 482 (1998); **260**, 39 (1999).
21. Yu. V. Palchikov, G. G. Adamian, N. V. Antonenko, and W. Scheid, J. Phys. A **33**, 4265 (2000); Physica A **316**, 297 (2002).
22. V. G. Zelevinsky, in *Proceedings of the XII Winter School of Leningrad Nuclear Physics Institute* (Leningrad, 1977), p. 53.
23. R. V. Dzholos, S. P. Ivanova, and V. V. Ivanov, Yad. Fiz. **40**, 117 (1984) [Sov. J. Nucl. Phys. **40**, 74 (1984)].
24. S. P. Ivanova and R. V. Jolos, Nucl. Phys. A **530**, 232 (1991).
25. J. Ankerhold, P. Pechukas, and H. Grabert, Phys. Rev. Lett. **87**, 086802 (2001).

Translated by A. Isaakyan

Physics of Atomic Nuclei, Vol. 68, No. 12, 2005, pp. 2022–2033. Translated from Yadernaya Fizika, Vol. 68, No. 12, 2005, pp. 2084–2095.

NUCLEI
Theory

On Solving Nonhomogeneous Bethe–Salpeter Equations

S. S. Semikh*, S. M. Dorkin[1)], M. Beyer[2)], and L. P. Kaptari

Joint Institute for Nuclear Research, Dubna, Moscow oblast, 141980 Russia

Received November 24, 2004

Abstract—A new method for solving nonhomogeneous Bethe–Salpeter equations is developed on the basis of employing expansions of interaction amplitudes and kernels in the basis of four-dimensional spherical harmonics. The method, which is applicable to both scalar and spinor equations, is expounded for the case of the nonhomogeneous Bethe–Salpeter equation for scalar particles in the ladder approximation. The model phase shifts calculated by this method are in good agreement with results published previously.

1. INTRODUCTION

The exclusive electrodisintegration process $D(e,e')pn$ and the quasielastic-nucleon-knockout process $D(p,p')pn$ on a deuteron play a key role in present-day hadron physics in studying, for example, the applicability range of the standard model of the nucleus—that is, a description of nuclear systems and phenomena in terms of nucleon and meson degrees of freedom. In this case, an accurate or, at least, a reliable and self-consistent description of initial and final states of hadron systems would make it possible to deduce comprehensive information not only about interaction mechanisms but also about the validity of model approaches inspired by nonperturbative QCD.

For few-nucleon systems, a satisfactory description of initial and final states is attainable within an effective meson–nucleon theory by using the Schrödinger equation (see [1, 2] and references therein). However, the development of covariant approaches becomes necessary at high energies, in which case the disregard of relativistic effects is less justified, while effects of final-state interaction are still significant. Processes like a low-momentum-transfer charge exchange on a deuteron in the reaction $pD \to n(pp)$ [3], deuteron disintegration leading to the production of a fast proton–proton pair characterized by a low relative momentum [4], and deuteron photo- and electrodisintegration [5–7] exemplify the situation where final-state interaction must be considered in a covariant form. The final states of all of the aforementioned processes feature a correlated nucleon pair (a proton–proton or a proton–neutron one), so that an adequate reaction model cannot be constructed without taking into account the interaction within this pair. While there exist a number of approaches [7–12] to describing an initial state (deuteron), only one self-consistent approach, that of employing solutions to the nonhomogeneous spinor Bethe–Salpeter equation, is appropriate in taking into account final-state interaction. However, the approach in question is not widespread, predominantly because of the computational difficulties that its application entails. One of the possible ways to obtain the Bethe–Salpeter amplitude in a continuum, or the half-off-shell T matrix, consists in applying the single-iteration approximation [13], where the dominant partial-wave component is replaced by its nonrelativistic analog, while P waves are obtained as the first iterations of the dominant component with an interaction kernel. The development of this method resulted in clarifying the origin of relativistic P waves as the contributions of meson-exchange currents [13], and its application in numerical calculations was also successful [3, 4]. However, it is still highly desirable to go beyond this approximate scheme and to obtain the Bethe–Salpeter amplitude as an exact solution to the corresponding equation.

In [14], the nonhomogeneous spinor Bethe–Salpeter equation was solved numerically by using a two-dimensional Gaussian mesh. That series of studies revealed a high potential of the Bethe–Salpeter approach to describing nucleon–nucleon interactions—in particular, processes involving a deuteron. Although there are no grounds to question the correctness of the results obtained in this way, the following two important circumstances are worthy of special note. First, direct calculations demonstrate that an inappropriate choice of two-dimensional integration mesh affects strongly the final results (solution to the equation in question); at the same time, there are no clear-cut criteria for

[1)]Institute of Nuclear Physics, Moscow State University, Vorob'evy gory, Moscow, 119899 Russia.
[2)]Rostock University, Rostock, Germany.
*E-mail: semikh@theor.jinr.ru

choosing a mesh. In other words, there is no single optimum two-dimensional change of variables that would make it possible to go over, in partial-wave Bethe–Salpeter equations, from infinite integration limits to finite ones. However, it is precisely this change of variables that determines the efficiency of an integration mesh, which is traditionally chosen as a Gaussian one in either variable. As a matter of fact, such a change of variables is determined by the trial-and-error method, frequently via a rather cumbersome procedure. Thus, all of the emerging results may become dubious because of an essentially technical problem. Therefore, it is necessary to continue seeking a method for solving Bethe–Salpeter equations such that a smaller degree of arbitrariness would be involved in its application.

The second circumstance that furnishes a motivation for revisiting nonhomogeneous Bethe–Salpeter equations is that their specific solutions that were obtained in [14] for nucleon–nucleon systems and used there have not yet been published—for example, in the form of numerical parametrizations, as was done in [15] for the deuteron Bethe–Salpeter amplitude. At the same time, experimental investigations of reactions leading to the production of interacting nucleon–nucleon pairs (see the examples given above) are being continued, and interest in describing such processes within the Bethe–Salpeter approach, in which case one needs Bethe–Salpeter amplitudes in a continuum, is still rather keen.

In the present article, we propose an efficient method for solving nonhomogeneous Bethe–Salpeter equations that is applicable to scalar and spinor equations involving interaction kernels in the form of the sum of one-boson-exchange terms supplemented with the corresponding form factors. We explain the method in detail for the example of the scalar equation, present some specific solutions, and analyze their structure. Phase shifts calculated within the scalar model are in good agreement with results published previously.

The ensuing exposition is organized as follows. In Section 2, we present the equation to be investigated and formulate basic points of our method for solving it. Section 3 contains details of numerical procedures and an analysis of the resulting numerical solutions. The calculation of phase shifts is described in Section 4. In Section 5, we outline an alternative method and possible ways of further generalizations.

2. EQUATION AND METHOD FOR SOLVING IT

In [16], the expansions of the Bethe–Salpeter vertex function Γ and the interaction kernel V in four-dimensional harmonics were used to formulate a method for solving the homogeneous equation for scalar particles. We have

$$\Gamma(k) = i\int \frac{d^4p}{(2\pi)^4} V(k,p)S(p_1)S(p_2)\Gamma(p), \qquad (1)$$

where $p_{1,2} = P/2 \pm p$, $k = (k_0, \mathbf{k})$, $p = (p_0, \mathbf{p})$ is the relative 4-momentum, and P is the total 4-momentum of the bound state being considered. The particles involved possess masses m and interact via the exchange of a scalar meson, its mass and the corresponding coupling constant being denoted by μ and g, respectively. Therefore, we have

$$S(p) = \frac{1}{p^2 - m^2 + i\varepsilon}, \qquad (2)$$

$$V(k,p) = \frac{g^2}{(k-p)^2 - \mu^2 + i\varepsilon}.$$

The above expansions are introduced upon performing a Wick rotation in (1) and are given by

$$\Gamma(ik_4, \mathbf{k}) = \sum_{nlm} \varphi_l^n(\tilde{k}) Z_{nlm}(\omega_k), \qquad (3)$$

$$V_{\mathrm{E}}(k,p) = -\frac{g^2}{(k-p)_{\mathrm{E}}^2 + \mu^2} \qquad (4)$$

$$= -2\pi^2 \sum_{nlm} \frac{g^2}{n+1} V_n(\tilde{k},\tilde{p}) Z_{nlm}(\omega_k) Z^*_{nlm}(\omega_p),$$

$$V_n(a,b) = \frac{4}{(\Lambda_+ + \Lambda_-)^2}\left(\frac{\Lambda_+ - \Lambda_-}{\Lambda_+ + \Lambda_-}\right)^n, \qquad (5)$$

$$\Lambda_\pm = \sqrt{(a \pm b)^2 + \mu^2},$$

where, by definition, the Euclidean scalar product is $(k-p)_{\mathrm{E}}^2 \equiv k_4 p_4 + (\mathbf{k}, \mathbf{p})$; $\tilde{k} = \sqrt{k_4^2 + \mathbf{k}^2}$ is the four-dimensional absolute value; and $\omega_k = (\chi, \theta, \phi)$ are the angles of the vector $k = (k_4, \mathbf{k})$ in four-dimensional Euclidean space. Here, θ and ϕ are the usual polar and azimuthal angles, while χ is a supplementary angle. The hyperspherical harmonics

$$Z_{nlm}(\chi,\theta,\phi) = X_{nl}(\chi) Y_{lm}(\theta,\phi),$$

$$X_{nl}(\chi) = \sqrt{\frac{2^{2l+1}}{\pi}\frac{(n+1)(n-l)!l!^2}{(n+l+1)!}}\sin^l\chi$$

$$\times C_{n-l}^{l+1}(\cos\chi),$$

are proportional to the product of ordinary spherical harmonics for an orbital angular momentum l and the Gegenbauer polynomials C_{n-l}^{l+1} and satisfy the orthonormalization relation

$$\int_0^{2\pi} d\phi \int_0^{\pi} d\theta \sin\theta \int_0^{\pi} d\chi \sin^2\chi \cdot Z_{klm}(\chi,\theta,\phi)$$

$$\times Z^*_{k'l'm'}(\chi,\theta,\phi) = \delta_{kk'}\delta_{ll'}\delta_{mm'}.$$

In general, the method that was proposed in [16] and which proved to be highly efficient consists in the following. Upon the Wick rotation and the use of the substitutions in (3) and (4), Eq. (1) reduces to an infinite set of one-dimensional integral equations. The integrals involved are transformed into finite sums upon a change of variables and the use of a Gaussian mesh. Since this is a single change of variables, its choice is more straightforward than in the two-dimensional case. At the same time, the basis of hyperspherical harmonics appears to be the most natural for this class of problems, and the series in (3) converges rather fast, so that, in order to obtain a final result, it is sufficient to consider the set of equations for a few (approximately five) first terms of this series.

In the present study, we generalize this method to nonhomogeneous equations. Without changing the notation introduced above, we consider the Bethe–Salpeter equation for scalar particles. We have

$$T(k,q) = V(k,q) + i\int \frac{d^4p}{(2\pi)^4} V(k,p)S(p_1)S(p_2)T(p,q), \tag{6}$$

where $T(k,q)$ is the half-off-shell T matrix describing the scattering of real particles having the 4-momenta $q_{1,2}$. In the c.m. frame, we have

$$s = (q_1+q_2)^2 = (2E_{\hat{p}})^2, \quad E_{\hat{p}} = \sqrt{m^2+\hat{p}^2},$$
$$q = \frac{q_1-q_2}{2} = (0,\mathbf{q}), \quad |\mathbf{q}| = \hat{p};$$

for the Mandelstam variable, we consider the interval

$$(2m)^2 < s < (2m+\mu)^2. \tag{7}$$

For the sake of brevity, we will henceforth omit the 4-momentum q in the arguments of the T matrix, implying that $T(k,q) \equiv T(k)$. Before applying the Wick rotation, it is convenient to introduce a conventional partial-wave expansion in the form

$$T(k_0,\mathbf{k}) = -\frac{2\pi}{k\hat{p}}\sum_{lm} T_l(k_0,k)Y_{lm}(\Omega_k)Y^*_{lm}(\Omega_q). \tag{8}$$

Here and below, we use the notation $|\mathbf{k}| = k$ and $|\mathbf{p}| = p$. As a result, we arrive at the partial-wave equations (see also [17])

$$T_l(k_0,k) = g^2Q_l(k_0,k;0,\hat{p}) - i\int \frac{dp_0dp}{(2\pi)^3} g^2Q_l(k_0,k;p_0,p)S(p_1)S(p_2)T_l(p_0,p), \tag{9}$$

where $Q_l(k_0,k;p_0,p) \equiv Q_l([k^2+p^2+\mu^2-(k_0-p_0)^2-i\varepsilon]/(2kp))$ is a Legendre function of the second kind (see Appendix B). The normalization of the T matrix is fixed by the free term in (9). As a result, we have the following expression for the phase shifts:

$$T_l(0,\hat{p}) = 16\pi\hat{p}\sqrt{s}e^{i\delta_l}\sin\delta_l. \tag{10}$$

The derivation of the normalization factor in (10) is described in detail in Section 4. To pursue our analysis further, we must get rid of the removable singularity at the point $(p_0,p) = (0,\hat{p})$. This can be done by different methods, which lead to the same results (see the respective discussion in Section 5). As a basic method, we use here that which was proposed in [18]. This method amounts to introducing a new unknown function $\varphi_l(k_0,k)$ in the form

$$T_l(k_0,k) \equiv \frac{\varphi_l(k_0,k)}{g^2Q_l(s)}T_l(0,\hat{p}), \tag{11}$$

where, by definition, we have $Q_l(s) \equiv Q_l(0,\hat{p};0,\hat{p})$. From (9), we find that the new function satisfies the equation

$$\varphi_l(k_0,k) = g^2Q_l(k_0,k;0,\hat{p}) - i\int \frac{dp_0dp}{(2\pi)^3} \times \left\{g^2Q_l(k_0,k;p_0,p) - \frac{g^2}{Q_l(s)}Q_l(k_0,k;0,\hat{p}) \times Q_l(0,\hat{p};p_0,p)\right\}S(p_1)S(p_2)\varphi_l(p_0,p). \tag{12}$$

Simultaneously, we obtain the following equation for calculating the phase shifts (for details, see [18, 19]):

$$T_l(0,\hat{p}) = g^2Q_l(s)\left[1 + i\int \frac{dp_0dp}{(2\pi)^3} \times Q_l(0,\hat{p};p_0,p)S(p_1)S(p_2)\frac{\varphi_l(p_0,p)}{Q_l(s)}\right]^{-1}. \tag{13}$$

For the sake of convenience, we introduce the notation

$$\mathcal{K}_l(k_0,k;p_0,p) = g^2Q_l(k_0,k;p_0,p) - \frac{g^2}{Q_l(s)}Q_l(k_0,k;0,\hat{p})Q_l(0,\hat{p};p_0,p),$$
$$S(p_0,p) = S(p_1)S(p_2).$$

The newly defined quantity satisfies the relations

$$\mathcal{K}_l(0,\hat{p};p_0,p) = \mathcal{K}_l(k_0,k;0,\hat{p}) = 0.$$

It can easily be shown that the integrand in (12) is regular at the point $(p_0,p) = (0,\hat{p})$ and that

$$\varphi_l(0,\hat{p}) = g^2Q_l(s). \tag{14}$$

The Wick rotation procedure [20, 21], which must be performed in (12) in order to use expansions of the type in (3) and (4), is not quite trivial. The expression for $S(p_1)S(p_2)$ has four poles in the variable p_0; of these, two,

$$p^0_{1,2} = \mp\left[\frac{\sqrt{s}}{2} - E_p + i\varepsilon\right], \tag{15}$$

can intersect the imaginary axis on the complex plane of p_0 at a specific value of p. It can easily be verified

that this cannot occur for bound states, for which $\sqrt{s} < 2m$, while, for scattering states ($\sqrt{s} > 2m$), the poles given by (15) penetrate, upon intersecting the imaginary axis, into the region bounded by the contour of integration with respect to p_0. The residues of the integrand in (12) at these poles lead to the appearance of additional unknown functions [21], which are denoted below as

$$\tau_l(p) \equiv \varphi_l\left(\frac{\sqrt{s}}{2} - E_p, p\right). \tag{16}$$

The equations for the functions in (16) can be derived in a natural way from (12) at the fixed value $k_0 = k_2^0 \equiv \sqrt{s}/2 - E_k$. Upon performing the Wick rotation ($p_0 \to ip_4$, $k_0 \to ik_4$), we now obtain a set of equations for φ_l and τ_l,

$$\varphi_l(ik_4, k) = g^2 Q_l(ik_4, k; 0, \hat{p}) \tag{17}$$
$$+ \int \frac{dp_4 dp}{(2\pi)^3} \mathcal{K}_l(ik_4, k; ip_4, p) S(ip_4, p) \varphi_l(ip_4, p)$$
$$- \int_0^{\hat{p}} \frac{dp}{8\pi^2} \frac{1}{E_p\sqrt{s}(\sqrt{s} - 2E_p)}$$
$$\times \left[\mathcal{K}_l(ik_4, k; p_2^0, p) + \mathcal{K}_l(ik_4, k; -p_2^0, p)\right] \tau_l(p),$$

$$\tau_l(k) = g^2 Q_l(k_2^0, k; 0, \hat{p}) + \int \frac{dp_4 dp}{2(2\pi)^3} \tag{18}$$
$$\times \left[\mathcal{K}_l(-k_2^0, k; ip_4, p) + \mathcal{K}_l(k_2^0, k; ip_4, p)\right]$$
$$\times S(ip_4, p)\varphi_l(ip_4, p) - \int_0^{\hat{p}} \frac{dp}{8\pi^2} \frac{1}{E_p\sqrt{s}(\sqrt{s} - 2E_p)}$$
$$\times \left[\mathcal{K}_l(k_2^0, k; p_2^0, p) + \mathcal{K}_l(k_2^0, k; -p_2^0, p)\right] \tau_l(p).$$

These equations are real. It should be noted that the function $\varphi_l(k_0, k)$ is always even in k_0—this can easily be proven by using Eq. (12). In deriving Eq. (18), we therefore performed symmetrization with the aid of the obvious identity $\tau_l(k) \equiv [\varphi_l(k_2^0, k) + \varphi_l(-k_2^0, k)]/2$, and this made it possible to obtain the equation in question in an explicitly real form.

Since the equations for different values of the orbital angular momentum l are not coupled to one another, the numerical calculations will be performed below at the values of $l = 0, 1$, which are chosen by way of example. The expansion of the function φ_0 in Gegenbauer polynomials follows from (3) and has the form

$$\varphi_0(ik_4, k) = k\hat{p} \sum_{j=1}^{\infty} g_j(\tilde{k}) X_{2j-2,0}(\chi), \tag{19}$$

where summation is performed over even indices on X since the function in question is even in k_4. By using Eq. (4), we find for Q_0 that (see also [17])

$$Q_0(ik_4, k; ip_4, p) \tag{20}$$
$$= \pi kp \sum_{n=0}^{\infty} \frac{1}{n+1} V_n(\tilde{k}, \tilde{p}) X_{n0}(\chi_k) X_{n0}(\chi_p).$$

By substituting now the expansions in (19) and (20) into (17) and (18), we obtain the required set of equations for the coefficient functions $g_j(\tilde{k})$ and $\tau_0(k)$; that is,

$$g_j(\tilde{k}) = \frac{\pi}{2j-1} g^2 V_{2j-2}(\tilde{k}, \hat{p}) X_{2j-2,0}\left(\frac{\pi}{2}\right) \tag{21}$$
$$+ g^2 \sum_{l=1}^{\infty} \int_0^{\infty} \frac{d\tilde{p}\tilde{p}^3}{8\pi^2} \left[\frac{1}{2j-1} V_{2j-2}(\tilde{k}, \tilde{p}) \right.$$
$$\times S^0_{2j-2,2l-2}(\tilde{p}) - \frac{\hat{p}^2}{2j-1} V_{2j-2}(\tilde{k}, \hat{p})$$
$$\left. \times X_{2j-2,0}\left(\frac{\pi}{2}\right) \frac{1}{Q_0(s)} N_{0,2l-2}(\hat{p}, \tilde{p})\right] g_l(\tilde{p})$$
$$- g^2 \int_0^{\hat{p}} \frac{dp}{8\pi^2} \frac{1}{E_p\sqrt{s}(\sqrt{s} - 2E_p)} \left[\frac{p}{\hat{p}} W_{2j-2,0}(\tilde{k}, p) \right.$$
$$- \frac{2}{Q_0(s)} \frac{\pi}{2j-1} V_{2j-2}(\tilde{k}, \hat{p}) X_{2j-2,0}\left(\frac{\pi}{2}\right)$$
$$\left. \times Q_0(0, \hat{p}; p_2^0, p)\right] \tau_0(p),$$

$$\tau_0(k) = g^2 Q_0(k_2^0, k; 0, \hat{p}) \tag{22}$$
$$+ g^2 \hat{p} \sum_{l=1}^{\infty} \int_0^{\infty} \frac{d\tilde{p}\tilde{p}^3}{(2\pi)^3} \left[kN_{0,2l-2}(k, \tilde{p}) \right.$$
$$\left. - \frac{\hat{p}}{Q_0(s)} Q_0(k_2^0, k; 0, \hat{p}) N_{0,2l-2}(\hat{p}, \tilde{p})\right] g_l(\tilde{p})$$
$$- g^2 \int_0^{\hat{p}} \frac{dp}{8\pi^2} \frac{1}{E_p\sqrt{s}(\sqrt{s} - 2E_p)} \left[kpU_0(k, p) \right.$$
$$\left. - \frac{2}{Q_0(s)} Q_0(k_2^0, k; 0, \hat{p}) Q_0(0, \hat{p}; p_2^0, p)\right] \tau_0(p).$$

The explicit expressions for the partial-wave kernels S, N, W, and U and comments on calculating them are given in Appendix A.

3. CALCULATION OF THE AMPLITUDES

Although the set of Eqs. (21) and (22) seems cumbersome, its numerical analysis does not present serious difficulties and does not require extremely large computer resources. All integrals are single. By choosing an appropriate integration scheme, one can

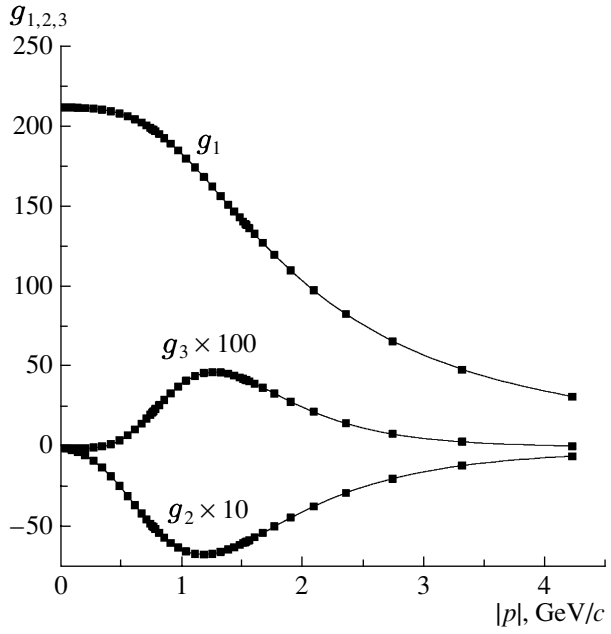

Fig. 1. Functions $g_{1,2,3}$, which are the expansion coefficients in (19) that are specified at the mesh points. The functions g_2 and g_3 are multiplied by 10 and 100, respectively, in view of their smallness. As follows from (21), the functions g_j are dimensionless. The solid lines represent approximations by the functions in (26)–(28).

therefore replace them by finite sums and go over thereby from the set of integral equations to an ordinary set of linear equations. In the present calculations, we employ the following integration procedure: we break down the infinite interval $[0, \infty]$ of $\tilde{p}$ values into three segments and, within each segment, use a specific change of variable that leads to the finite limits, $x \in [-1, 1]$:

(i) $\tilde{p} \in [0, \hat{p}]$, $\tilde{p} = \hat{p}\dfrac{x+1}{2}$;

(ii) $\tilde{p} \in [\hat{p}, 2\hat{p}]$, $\tilde{p} = \hat{p}\dfrac{x+3}{2}$;

(iii) $\tilde{p} \in [2\hat{p}, \infty]$, $\tilde{p} = 2\hat{p} + c_0\dfrac{1+x}{1-x}$, where c_0 is a parameter.[3)]

Upon the change of variable, the Gauss quadrature formulas are applied independently in each of the three intervals. In the direct calculations, it appeared that 16 mesh points ($n = 16$) are sufficient for each interval, since an increase in the number of mesh points beyond this value does not change the results. For each interval, one can choose an individual value of n. In order to ensure the required accuracy over the entire interval specified by (7), it is sufficient to retain only the first five terms of the expansion in (19) ($l_0 = 5$).

The set of linear equations that follows from Eqs. (21) and (22) can be written as

$$X = B + AX, \tag{23}$$

where the column

$$X^T = (\{g_1(\tilde{k}_i)\}_{i=1}^{3n}, \{g_2(\tilde{k}_i)\}_{i=1}^{3n}, \ldots, \{g_{l_0}(\tilde{k}_i)\}_{i=1}^{3n}, \{\tau_0(\tilde{k}_i)\}_{i=1}^{n})$$

represents the sought solution in the form of a set of partial-wave components g_j, $j = 1, 2, \ldots, l_0$, specified on the integration mesh and an additional function τ_0 on its own mesh. The column B is associated with the free terms, while the matrix A can be obtained on the basis of the partial-wave kernels, the Jacobians of the transition to the new variables, and the weights of the Gaussian mesh. It can easily be shown that the dimension of the matrix A is $N \times N$, where $N = n(3l_0 + 1)$ (in the present case, $N = 256$).

We considered two possible methods for solving the set of Eqs. (23). First, it can be represented in the form

$$(A - 1)X = -B$$

and solved as an ordinary set of linear equations. For this, we used the procedure that is based on expanding the matrix A via the Gaussian elimination involving the choice of the leading element and the conditionality estimate [22] and which is known to be quite successful. It turned out that, for systems of the type in question, this method is stable up to values of $N \sim 1000$ (there was no need for testing higher values). The other method employed here to construct the required solution is iterative, in which case there arises, in a natural way, a series of the form

$$X = B + AB + ABAB + ABABAB + \ldots. \tag{24}$$

This series exactly corresponds to the Neumann series [23] for the set of integral Eqs. (21) and (22) and converges to the solution to this set of equations at all values of s from the interval specified by (7). Both methods were used in our calculations, and the results were identical.

For the parameter values

$$\frac{g^2}{4\pi m^2} = 4\pi, \quad m = \mu = 1 \text{ GeV}, \qquad \hat{p} = 0.77 \text{ GeV}/c, \tag{25}$$

Fig. 1 shows the graphs of the functions $g_j(p)$, $j = 1, 2, 3$, appearing in (19). We do not present all of the first five components because the fourth and the fifth one are very small in magnitude. For the same reason, we display the functions g_2 and g_3 multiplied by 10 and 100, respectively. Thus, the series in (19)

[3)] The results of the calculations depend very weakly on the parameter c_0, which can be varied within a broad interval. Here, we set $c_0 = 1$.

converges very fast (as was indicated above), which confirms the efficiency of this expansion.

The values of the functions at the mesh points are shown by the closed boxes in Fig. 1. It should be noted that the curves connecting the points reproduce the results of fitting the parameters in the following functions to the data points:

(i) for $g_1(p)$, $p \equiv \tilde{p}$,

$$F_1(p) = \sum_{j=1}^{4} \frac{a_j^1 p^{2j-2}}{(p^2+b_1^2)^j}; \qquad (26)$$

(ii) for $g_2(p)$,

$$F_2(p) = \frac{p^2}{p^2+b_2^2} \sum_{j=1}^{4} \frac{a_j^2 p^{2j-2}}{(p^2+b_2^2)^j}; \qquad (27)$$

(iii) for $g_3(p)$,

$$F_3(p) = \left[\frac{p^2}{p^2+b_3^2}\right]^2 \sum_{j=1}^{4} \frac{a_j^3 p^{2j-2}}{(p^2+b_3^2)^j}. \qquad (28)$$

The parameter values are presented in the table. The quality of interpolation appears to be so high that this fact deserves a dedicated discussion. The functions presented by formulas (26)–(28) have a very simple analytic form, but, despite this, they reproduce very accurately the resulting components of the solution over the entire interval of $\tilde{p}$. This fact can be considered as a manifestation of the effects of separability in the interaction kernel of the Bethe–Salpeter equation if we take it in the form of one-boson exchange (see [24]). Moreover, the available results suggest that the components of the solutions to the spinor equations in the ladder approximation can also be interpolated by similar expressions to a high degree of precision. Therefore, the functions in (26)–(28) are useful in practical applications as well—for example, they may be helpful for representing results in a compact form.

In order to obtain deeper insights into the structure of the solutions that we obtained, it would be reasonable to consider them globally—that is, to reconstruct, for example, the amplitude φ_0 as a function of two variables, k_4 and k, by summing the series in (19). Figures 2 and 3 show the graphs of the functions $\varphi_0(ik_4,k)/k$ and $\varphi_1(ik_4,k)/k$, respectively—from expressions (8), (11), and (19), it is clear that these are combinations that are proportional to the components of the total T matrix for $l=0$ and 1. Obviously, the behavior of these functions versus k is quite natural—at $k=0$, the amplitude φ_0 takes a constant value, while $\varphi_1 = 0$.

Numerical values of the parameters in formulas (26)–(28) (b_n and a_j^n are given in GeV/c and (GeV/c)^2 units, respectively)

n	b_n	a_1^n	a_2^n	a_3^n	a_4^n
1	0.8807	164.787	166.651	87.412	225.434
2	1.1195	−160.725	−262.017	−730.961	1158.73
3	1.3135	182.945	4872.76	−10705.6	5687.98

4. CALCULATION OF PHASE SHIFTS

As was indicated above, the Bethe–Salpeter amplitude that is a solution to Eq. (6) is the T matrix describing the $2 \to 2$ elastic scattering of real particles. From the methodological point of view, it is very useful to calculate phase shifts for this process. It can easily be shown that, for the above choice of the normalization factors in (2) and (6), the respective matrix element in the c.m. frame has the form

$$\mathcal{M}_{fi} = T(0,\hat{p}). \qquad (29)$$

The calculation of the phase shifts with the aid of the solutions that we obtained is based on Eqs. (10) and (13). By considering the case of $l=0$ as an example, we will first describe a method that can be used to derive relation (10). It is well known that, in terms of the respective phase shift, the partial-wave cross section in the c.m. frame can be represented as

$$\frac{d\sigma_0}{d\Omega^*} = \frac{1}{\hat{p}^2}\sin^2\delta_0. \qquad (30)$$

On the other hand, the cross section for the process $a+b \to a+b$ involving particles of identical masses, $m_a = m_b = m$, can be written as

$$\frac{d\sigma_0}{d\Omega^*} = \frac{1}{64\pi^2 s}|\mathcal{M}_{fi}(l=0)|^2. \qquad (31)$$

From Eqs. (8) and (29), it follows that

$$\mathcal{M}_{fi}(l=0) = -\frac{1}{2\hat{p}^2}T_0(0,\hat{p}). \qquad (32)$$

Taking into account the relation $T_0(0,\hat{p}) = \mathcal{N}e^{i\delta_0} \times \sin\delta_0$ and employing Eqs. (30)–(32), we obtain the required normalization factor:

$$\mathcal{N} = 16\pi\hat{p}\sqrt{s}. \qquad (33)$$

In order to calculate the phase shifts, it is necessary to determine the right-hand side of Eq. (13). Its denominator must be transformed in the same order as Eq. (9)—namely, it is necessary to get rid of the removable singularity at the point $(p_0,p) = (0,\hat{p})$ and to perform a Wick rotation in the integral, whereupon

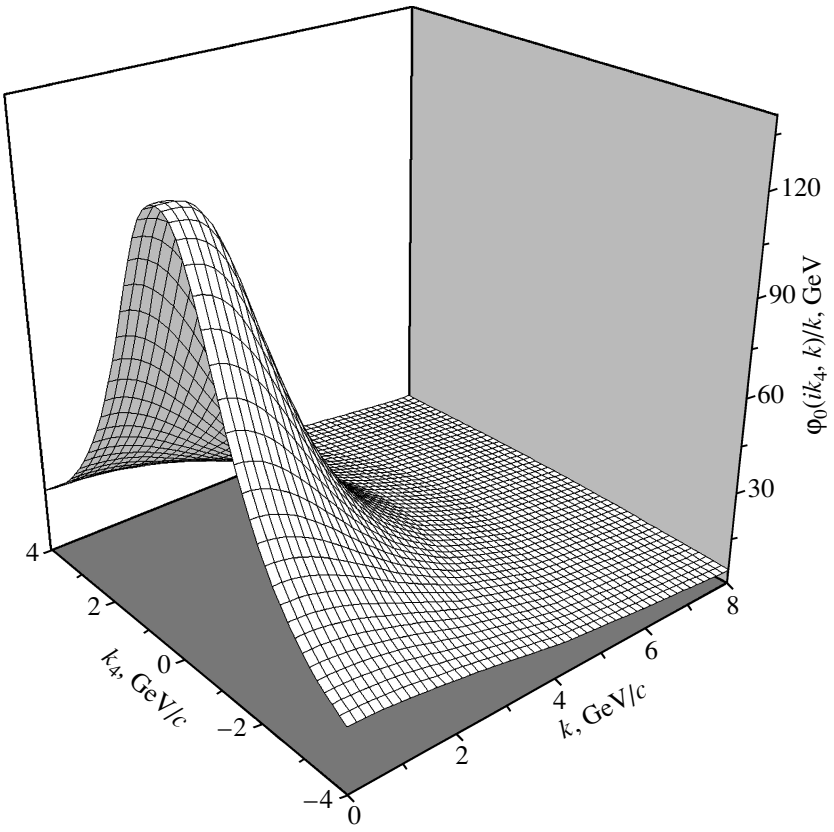

Fig. 2. Graph of the function $\varphi_0(ik_4, k)/k$ at the parameter values in (25).

we can use the solutions obtained in Euclidean space. Let us consider the identical transformation

$$i\int\frac{dp_0dp}{(2\pi)^3}Q_l(0,\hat{p};p_0,p)S(p_0,p)\frac{\varphi_l(p_0,p)}{Q_l(s)} \qquad (34)$$
$$=\frac{i}{Q_l(s)}\int\frac{dp_0dp}{(2\pi)^3}[\varphi_l(p_0,p)-g^2Q_l(0,\hat{p};p_0,p)]$$
$$\times Q_l(0,\hat{p};p_0,p)S(p_0,p)+i\int\frac{dp_0dp}{(2\pi)^3}\frac{g^2}{Q_l(s)}$$
$$\times[Q_l(0,\hat{p};p_0,p)]^2S(p_0,p).$$

It is obvious that a subtraction was performed here under the integral sign, so that the integrand in the first term on the right-hand side of (34) is regular at the point $(p_0,p)=(0,\hat{p})$ [see (14)]. We can now perform a Wick rotation in it and calculate it by using the above solutions. In the case of $l=0$, the result for the first term in (34) takes the form

$$-\frac{\hat{p}^2}{Q_0(s)}\sum_{j=1}^{\infty}\int_0^{\infty}\frac{d\tilde{p}\tilde{p}^3}{(2\pi)^3}\left[g_j(\tilde{p})-\frac{\pi}{2j-1}g^2\right. \qquad (35)$$
$$\left.\times V_{2j-2}(\tilde{p},\hat{p})X_{2j-2,0}\left(\frac{\pi}{2}\right)\right]N_{0,2j-2}(\hat{p},\tilde{p})$$
$$+\frac{1}{Q_0(s)}\int_0^{\hat{p}}\frac{dp}{8\pi^2}\frac{2}{E_p\sqrt{s}(\sqrt{s}-2E_p)}$$
$$\times\left[\tau_0(p)-g^2Q_0(0,\hat{p};p_2^0,p)\right]Q_0(0,\hat{p};p_2^0,p).$$

The last term on the right-hand side of (34) can be calculated directly by using the residues and the discontinuities at the cuts [19]. For $l=0$, the final result is

$$i\int\frac{dp_0dp}{(2\pi)^3}\frac{g^2}{Q_0(s)}[Q_0(0,\hat{p};p_0,p)]^2S(p_0,p) \qquad (36)$$
$$=\frac{g^2}{Q_0(s)}\left[\int_0^{\infty}\frac{dp}{8\pi^2}\left\{\frac{Q_0(0,\hat{p};p_1^0,p)^2}{E_p\sqrt{s}(\sqrt{s}+2E_p)}\right.\right.$$
$$\left.\left.-\int_{x_1(p)}^{x_2(p)}dp_0S(p_0,p)\mathbf{Q}_0[y(p_0,p)]\right\}\right.$$
$$\left.+\text{V.p.}\int_0^{\infty}\frac{dp}{8\pi^2}\frac{Q_0(0,\hat{p};p_2^0,p)^2}{E_p\sqrt{s}(\sqrt{s}-2E_p)}\right]-i\frac{g^2Q_0(s)}{16\pi\hat{p}\sqrt{s}},$$

where the integration limits

$$x_1(p)=-\sqrt{(p+\hat{p})^2+\mu^2},$$

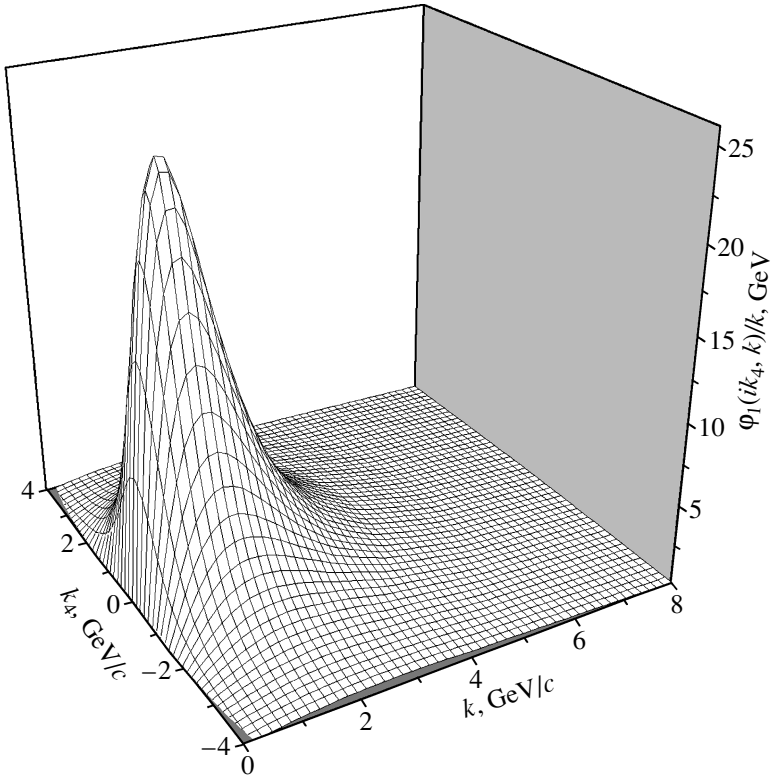

Fig. 3. Graph of the function $\varphi_1(ik_4, k)/k$ at the parameter values in (25).

$$x_2(p) = -\sqrt{(p-\hat{p})^2 + \mu^2}$$

correspond to the cut in the complex plane of p_0 and the argument $y(p_0, p)$ has the form

$$y(p_0, p) = \frac{\hat{p}^2 + p^2 + \mu^2 - p_0^2}{2p\hat{p}}.$$

As to the functions $\mathbf{Q}_l$, the explicit expressions for them are given in Appendix B.

Thus, we see that, in order to determine the denominator in (13), it is necessary to sum expressions (35) and (36) and to add unity to the result. The phase shifts were calculated for the orbital angular momenta of $l = 0, 1$ and s values from the interval specified by (7). The corresponding graphs are given in Figs. 4 and 5. Different curves correspond to different values of the dimensionless parameter λ, which is related to the coupling constant by the equation

$$\frac{g^2}{4\pi m^2} = 4\pi\lambda.$$

Our results are in good agreement with those presented in [18, 19]. It is noteworthy that, according to the Levinson theorem, there are no bound states at $l = 0$ for $\lambda = 0.7$, since the phase shift is zero at the origin. For the values of $\lambda = 1, 3, 5$, there is one bound state, while, for $\lambda = 7$, we have two bound states. It is obvious that, at $l = 1$, there are no bound states for the above values of λ.

5. ON AN ALTERNATIVE APPROACH TO SOLVING THE PROBLEM BEING CONSIDERED

In analyzing Eq. (9), one can use an alternative method for removing the singularity at the point $(p_0, p) = (0, \hat{p})$. This leads to a different scheme for solving the equation in question, and it is reasonable to apply it to test our results. The method is based on an identical construction of the subtraction in the form [25]

$$\begin{aligned} T_l(k_0, k) &= g^2 Q_l(k_0, k; 0, \hat{p}) \\ &- ig^2 \int \frac{dp_0 dp}{(2\pi)^3} \{Q_l(k_0, k; p_0, p) T_l(p_0, p) \\ &- Q_l(k_0, k; 0, \hat{p}) T_l(0, \hat{p})\} S(p_0, p) \\ &- ig^2 Q_l(k_0, k; 0, \hat{p}) T_l(0, \hat{p}) \int \frac{dp_0 dp}{(2\pi)^3} S(p_0, p). \end{aligned} \tag{37}$$

Calculating the integral on the right-hand side of the above equation with the aid of the residue theorem,

$$\int dp_0 dp S(p_0, p) = -\frac{\pi^2}{2\hat{p}\sqrt{s}} + \frac{i\pi}{\hat{p}\sqrt{s}} \ln \frac{2m}{2\hat{p} + \sqrt{s}},$$

and using Eq. (37), we obtain

$$T_l(k_0, k) = g^2 Q_l(k_0, k; 0, \hat{p}) \tag{38}$$

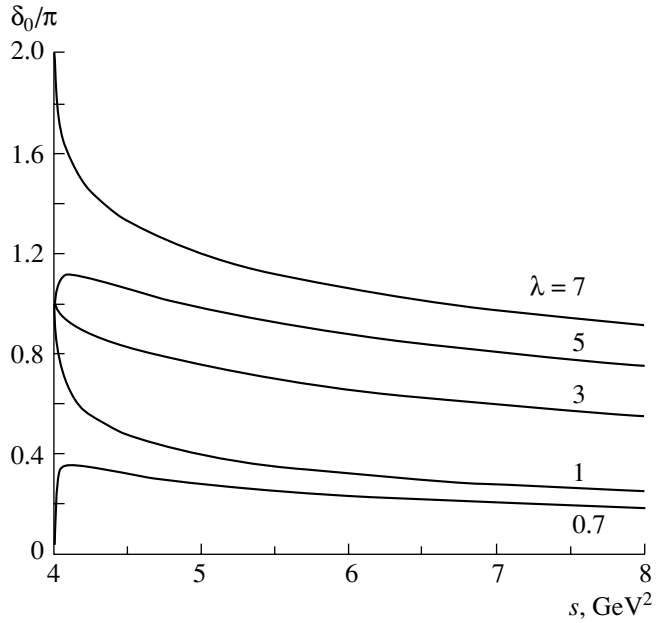

Fig. 4. Phase shifts (in units of π) for $l = 0$ at various values of the coupling constant ($m = \mu = 1$ GeV).

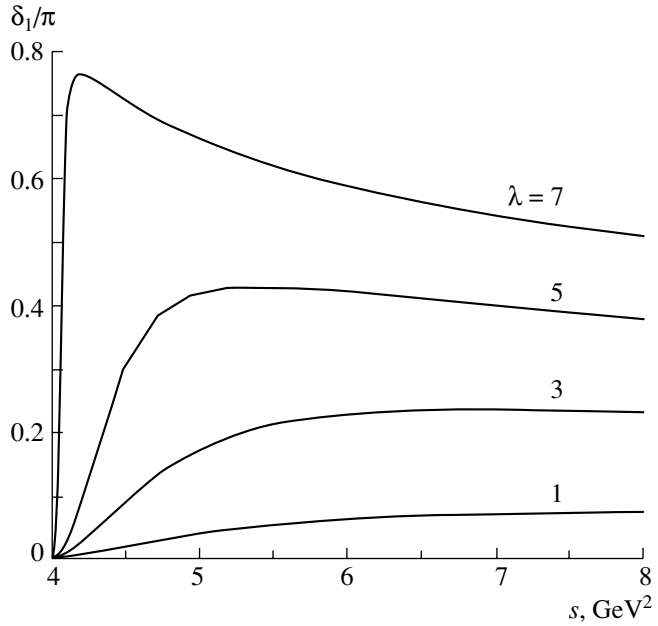

Fig. 5. As in Fig. 4, but for $l = 1$.

$$\times \left\{1 + \frac{i}{16\pi\hat{p}\sqrt{s}} T_l(0,\hat{p})\right\} - ig^2 \int \frac{dp_0 dp}{(2\pi)^3}$$

$$\times \{Q_l(k_0,k;p_0,p)T_l(p_0,p) - Q_l(k_0,k;0,\hat{p})$$

$$\times T_l(0,\hat{p})\}S(p_0,p) + g^2 Q_l(k_0,k;0,\hat{p})$$

$$\times T_l(0,\hat{p}) \frac{1}{8\pi^2\hat{p}\sqrt{s}} \ln\frac{2m}{2\hat{p}+\sqrt{s}}.$$

Further, we redefine the T matrix by introducing the function t via the relation

$$T_l(k_0,k) = \left\{1 + \frac{i}{16\pi\hat{p}\sqrt{s}} T_l(0,\hat{p})\right\} t_l(k_0,k). \quad (39)$$

As a result, we find from (38) that

$$t_l(k_0,k) = g^2 Q_l(k_0,k;0,\hat{p}) \quad (40)$$

$$- ig^2 \int \frac{dp_0 dp}{(2\pi)^3} \{Q_l(k_0,k;p_0,p)t_l(p_0,p)$$

$$- Q_l(k_0, k; 0, \hat{p}) t_l(0, \hat{p})\} S(p_0, p)$$
$$+ g^2 Q_l(k_0, k; 0, \hat{p}) t_l(0, \hat{p}) \frac{1}{8\pi^2 \hat{p}\sqrt{s}} \ln \frac{2m}{2\hat{p} + \sqrt{s}}.$$

It is interesting to note that the normalization factor (33) is obtained directly from relation (39) without additional calculations.

As was done in considering Eq. (12), it is then necessary to perform the Wick rotation, to construct the expansion in hyperspherical harmonics, and to solve the resulting set of equations on a Gaussian mesh. Omitting intermediate calculations, we note that, in this case, it is incorrect to treat the resulting set of equations as a set of linear equations of the form (23). Because of the subtraction scheme applied here, we cannot appropriately construct the leading matrix A of the set since the point $\tilde{p} = \hat{p}$ cannot belong to the integration mesh. In order to find the required solution, we therefore used only the iterative method constructed by analogy with (24). Schematically, the respective iterative process has the form

$$t_l = Q_l + Q_l S Q_l + Q_l S Q_l S Q_l + \ldots, \qquad (41)$$

where appropriate subtractions are implied in accordance with (40), and so on. Within this approach, however, the series in (41) does not always converge, and it is not difficult to understand the reasons for this. First of all, we note that, from relations (10) and (39), it follows that the phase shifts and the functions t_l are related by the equation

$$t_l(0, \hat{p}) = 16\pi \hat{p}\sqrt{s} \tan \delta_l. \qquad (42)$$

Thus, we see that, if the phase shift δ_l approaches $\pi/2$, the solution t_l must increase indefinitely, so that the convergence of the series in (41) becomes ever poorer. In other words, the series in (41) must diverge at those values of the parameters of the problem (coupling constants, particle masses, and the invariant mass $\sqrt{s}$ of the pair) for which the phase shift δ_l becomes equal to or exceeds $\pi/2$, and we can indeed see this in our calculations. Despite these limitations, the method being discussed admits a comparison with that which was described in Section 2. By way of example, we indicate that, at $l = 0$ and $\lambda = 0.7$, the phase shift satisfies the inequality $\delta_0 \leq \pi/2$ (see Fig. 4), and both methods are applicable. The calculations revealed that the results that they produce differ by not more than 0.5% for all values of s in the range specified by (7).

In conclusion, some general comments on the further development of the formalism are in order. In the foregoing, we have considered the scalar Bethe–Salpeter equation in the ladder approximation, assuming that the interaction kernel is generated by one-meson exchange and employing pointlike vertices. A generalization of the method to spinor equations is briefly discussed in [24] and will be the subject of a separate publication. Moreover, a transition to more complicated interaction kernels, such as those that involve form factors of the type (upon the Wick rotation)

$$F[(p-q)^2_{\mathrm{E}}] = \frac{\Lambda^2}{(p-q)^2_{\mathrm{E}} + \Lambda^2},$$

can readily be performed within the methods described above. Indeed, one can prove the validity of the expansion

$$\frac{g^2}{(p-q)^2_{\mathrm{E}} + \mu^2} F[(p-q)^2_{\mathrm{E}}]^2 \qquad (43)$$
$$= 2\pi^2 \sum_{klm} \frac{1}{k+1} \tilde{V}_k(\tilde{p}, \tilde{q}) Z_{klm}(\omega_p) Z^*_{klm}(\omega_q),$$

where

$$\tilde{V}_k(a, b) = 4g^2 \left[\frac{\Lambda^2}{\Lambda^2 - \mu^2}\right]^2 \qquad (44)$$
$$\times \left[\frac{(\Lambda^\mu_+ - \Lambda^\mu_-)^k}{(\Lambda^\mu_+ + \Lambda^\mu_-)^{k+2}} - \frac{(\Lambda^\Lambda_+ - \Lambda^\Lambda_-)^k}{(\Lambda^\Lambda_+ + \Lambda^\Lambda_-)^{k+2}}\right]$$
$$- 4g^2(k+1) \frac{\Lambda^2}{\Lambda^2 - \mu^2} \frac{\Lambda^2}{\Lambda^\Lambda_+ \Lambda^\Lambda_-} \frac{(\Lambda^\Lambda_+ - \Lambda^\Lambda_-)^k}{(\Lambda^\Lambda_+ + \Lambda^\Lambda_-)^{k+2}},$$

$$\Lambda^\mu_\pm = \sqrt{(a \pm b)^2 + \mu^2}, \quad \Lambda^\Lambda_\pm = \sqrt{(a \pm b)^2 + \Lambda^2}.$$

From a comparison of formulas (43) and (44) with formulas (4) and (5), it can be concluded that no radical changes in the methods for constructing solutions are required upon the inclusion of the form factors in the interaction kernel.

6. CONCLUSIONS

A new method for solving nonhomogeneous Bethe–Salpeter equations has been formulated on the basis of expanding the T matrix and the interaction kernel in four-dimensional spherical harmonics. This makes it possible to consider a set of one-dimensional equations instead of a traditional set of two-dimensional integral equations. It has been shown that, if a numerical method is chosen appropriately, the resulting solution converges fast, so that a high precision can be achieved by using only the first four to five equations of this set. The method has been described in detail for the example of scalar particles. We have performed methodological numerical calculations, and a comparison of their results with those that are available from the literature has demonstrated a high

efficiency and accuracy of the method, as well as the possibility of applying it to calculating effects of final-state interaction in deuteron-breakup reactions.

ACKNOWLEDGMENTS

We are grateful to K.Yu. Kazakov for stimulating discussions. S.M. Dorkin and S.S. Semikh gratefully acknowledge the hospitality extended to them by the Group of Elementary Particle Physics at Rostock University (Germany), where part of this study was performed.

This work was supported by grants of the Heisenberg–Landau program of a collaboration between the Joint Institute for Nuclear Research (JINR, Dubna) and Germany and the German Academic Exchange Service (Deutscher Akademischer Austausch Dienst, DAAD).

APPENDIX A

Calculation of Partial-Wave Kernels

Let us discuss the explicit form of the partial-wave kernels S, N, W, and U introduced in (21) and (22) and the procedure for calculating them. The kernel U_l has the simplest form,

$$U_l(k,p) = \frac{1}{kp}\{Q_l(k_2^0,k;p_2^0,p) + Q_l(k_2^0,k;-p_2^0,p)\},$$

where $k_2^0 = \sqrt{s}/2 - E_k$ and $p_2^0 = \sqrt{s}/2 - E_p$ (see above). The kernel $S^l_{k'k}$ can be calculated analytically. The result is

$$S^l_{k'k}(\tilde{p}) = \int_0^\pi d\chi \sin^2\chi \frac{X_{k'l}(\chi)X_{kl}(\chi)}{A^2 + B^2\cos^2\chi} \qquad (A.1)$$

$$= (-1)^l\sqrt{\frac{2}{\pi}}l!\frac{2^{l+1}}{AB}$$

$$\times \sqrt{\frac{(k'+1)(k'-l)!}{(k'+l+1)!}\frac{(k+1)(k-l)!}{(k+l+1)!}}$$

$$\times C^{l+1}_{\min-l}(iz)(-z^2-1)^{(2l+1)/4}Q^{l+1/2}_{\max+1/2}(iz),$$

where max (min) is the maximum (minimum) index of k and k'; $C^{l+1}_{\min-l}(iz)$ is a Gegenbauer polynomial of an imaginary argument; and

$$A = |\tilde{p}^2 - \hat{p}^2|, \quad B = \tilde{p}\sqrt{s}, \quad z = A/B.$$

It should be noted that, as follows from the parity properties of Gegenbauer polynomials, the function $S^l_{k'k}$ does not vanish only in the case where $k + k'$ is an integer. For the values of $l = 0, 1$, we present here the explicit expressions for the Legendre functions of the second kind that appear in (A.1). We have

$$Q^{1/2}_{n+1/2}(z) = i\sqrt{\frac{\pi}{2}}(z^2-1)^{-1/4}(z-\sqrt{z^2-1})^{n+1},$$

$$Q^{3/2}_{n+3/2}(z) = \big[(n+1)zQ^{1/2}_{n+3/2}(z)$$

$$-(n+2)Q^{1/2}_{n+1/2}(z)\big]\frac{1}{\sqrt{z^2-1}}.$$

The partial-wave kernels N and W are given by

$$N_{ml}(k,\tilde{p}) = \int_0^\pi d\chi_p \sin^2\chi_p \frac{1}{2kp} \qquad (A.2)$$

$$\times\{Q_m(k_2^0,k;ip_4,p) + Q_m(-k_2^0,k;ip_4,p)\}$$

$$\times \frac{X_{lm}(\chi_p)}{(\tilde{p}^2-\hat{p}^2)^2 + s\tilde{p}^2\cos^2\chi_p},$$

$$W_{nl}(\tilde{k},p) = \int_0^\pi d\chi_k \sin^2\chi_k X_{nl}(\chi_k)\frac{1}{kp} \qquad (A.3)$$

$$\times\{Q_l(ik_4,k;p_2^0,p) + Q_l(ik_4,k;-p_2^0,p)\},$$

and their calculation is not quite trivial. It can be shown that

$$N_{0,2l-2}(k,\tilde{p}) \qquad (A.4)$$

$$= \sqrt{\frac{\pi}{2}}\sum_{n=1}^\infty \frac{1}{2n-1}V_{2n-2}(|k|,\tilde{p})S^0_{2n-2,2l-2}(\tilde{p})$$

$$\times\left[C^1_{2n-2}\left(-\frac{ik_2^0}{|k|}\right) + C^1_{2n-2}\left(\frac{ik_2^0}{|k|}\right)\right].$$

Here, $|k| = \sqrt{k^2-(k_2^0)^2}$ by definition. Under the condition $k^2 < (k_2^0)^2$, it is a pure imaginary quantity. Similarly, we have

$$W_{2j-2,0}(\tilde{k},p) = \frac{\sqrt{2\pi}}{2j-1}V_{2j-2}(\tilde{k},|p|) \qquad (A.5)$$

$$\times\left[C^1_{2j-2}\left(-\frac{ip_2^0}{|p|}\right) + C^1_{2j-2}\left(\frac{ip_2^0}{|p|}\right)\right].$$

A direct way to verify the correctness of these expressions is the most straightforward—for example, one can calculate numerically the integrals in (A.2) and (A.3) and compare the results with the results of a numerical summation of the series in (A.4) and (A.5). These series converge very fast; therefore, it is preferable to use them in numerical calculations.

APPENDIX B

Legendre Functions

Legendre functions of the second kind $Q_l(y)$ are widely known. They are defined over the whole complex plane of y, with the exception of the cut $-1 < y < 1$ along the real axis. For example, we have

$$Q_0(y) = \frac{1}{2}\ln\frac{y+1}{y-1}, \quad Q_1(y) = \frac{y}{2}\ln\frac{y+1}{y-1} - 1. \tag{A.6}$$

The functions $\mathbf{Q}_l(y)$ appearing in Section 4 are defined at this cut as [26]

$$\mathbf{Q}_l(y) = \frac{1}{2}Q_l(y+i\varepsilon) + \frac{1}{2}Q_l(y-i\varepsilon), \quad -1 < y < 1.$$

Explicitly, we have [compare with (A.6)]

$$\mathbf{Q}_0(y) = \frac{1}{2}\ln\frac{1+y}{1-y}, \quad \mathbf{Q}_1(y) = \frac{y}{2}\ln\frac{1+y}{1-y} - 1.$$

REFERENCES

1. W. Glöckle *et al.*, Phys. Rep. **274**, 107 (1996).
2. A. Kievsky, S. Rosati, and M. Viviani, Nucl. Phys. A **551**, 241 (1993).
3. L. P. Kaptari, B. Kämpfer, S. S. Semikh, and S. M. Dorkin, Eur. Phys. J. A **17**, 119 (2003).
4. L. P. Kaptari, B. Kämpfer, S. S. Semikh, and S. M. Dorkin, Eur. Phys. J. A **19**, 301 (2004).
5. C. Ciofi degli Atti and L. P. Kaptari, nucl-th/0407024; C. Ciofi degli Atti, L. P. Kaptari, and D. Treleani, Phys. Rev. C **63**, 044601 (2001).
6. S. G. Bondarenko, V. V. Burov, M. Beyer, and S. M. Dorkin, nucl-th/9612047.
7. W. N. Polyzou and W. Glöckle, Phys. Rev. C **53**, 3111 (1996).
8. B. D. Keister, Phys. Rev. C **37**, 1765 (1988).
9. F. Gross, Phys. Rev. **186**, 1440 (1969); W. W. Buck and F. Gross, Phys. Rev. C **20**, 2361 (1979); F. Gross, L. W. Van Orden, and K. Holinde, Phys. Rev. C **45**, 2094 (1992).
10. B. Desplanques, V. A. Karmanov, and J. F. Mathiot, Nucl. Phys. A **589**, 697 (1995).
11. L. L. Frankfurt and M. I. Strikman, Phys. Rep. **160**, 235 (1988).
12. C. Ciofi degli Atti, D. Faralli, A. Yu. Umnikov, and L. P. Kaptari, Phys. Rev. C **60**, 034003 (1999).
13. L. P. Kaptari, B. Kämpfer, S. M. Dorkin, and S. S. Semikh, Phys. Rev. C **57**, 1097 (1998); S. G. Bondarenko, V. V. Burov, M. Beyer, and S. M. Dorkin, Phys. Rev. C **58**, 3143 (1998).
14. M. J. Zuilhof and J. A. Tjon, Phys. Rev. C **22**, 2369 (1980), and references therein.
15. A. Yu. Umnikov, Z. Phys. A **357**, 333 (1997).
16. T. Nieuwenhuis and J. A. Tjon, Few-Body Syst. **21**, 167 (1996).
17. S. M. Dorkin, L. P. Kaptar', and S. S. Semikh, Yad. Fiz. **60**, 1784 (1997) [Phys. At. Nucl. **60**, 1629 (1997)].
18. M. J. Levine, J. Wright, and J. A. Tjon, Phys. Rev. **154**, 1433 (1967).
19. M. Fortes and A. D. Jackson, Nucl. Phys. A **175**, 449 (1971).
20. G. C. Wick, Phys. Rev. **96**, 1124 (1954).
21. W. Kemmer and A. Salam, Proc. R. Soc. London, Ser. A **230**, 266 (1955).
22. G. E. Forsythe, M. A. Malcolm, and C. B. Moler, *Computer Methods for Mathematical Computations* (Prentice-Hall, Englewood Cliffs, N.J., 1977; Mir, Moscow, 1980).
23. S. G. Mikhlin, *Lectures on Linear Integral Equations* (Fizmatgiz, Moscow, 1959) [in Russian].
24. S. S. Semikh, S. M. Dorkin, M. Beyer, and L. P. Kaptari, nucl-th/0410076.
25. J. Fleischer and J. A. Tjon, Nucl. Phys. B **84**, 375 (1975).
26. A. Erdelyi, *Higher Transcendental Functions (Bateman Manuscript Project)*, Ed. by A. Erdelyi (McGraw-Hill, New York, 1953; Nauka, Moscow, 1974), Vol. 2.

Translated by A. Isaakyan

Physics of Atomic Nuclei, Vol. 68, No. 12, 2005, pp. 2034–2038. Translated from Yadernaya Fizika, Vol. 68, No. 12, 2005, pp. 2096–2100.

ELEMENTARY PARTICLES AND FIELDS
Experiment

Project of a Large Superconductor Detector Involving Directed Diffusion of Hot Electrons and Microcalorimeter

V. S. Shpinel*

Institute of Nuclear Physics, Moscow State University, Vorob'evy gory, Moscow, 119899 Russia

Received September 21, 2004; in final form, January 18, 2005

Abstract—In recent years, radically new detectors for soft x rays and gamma rays were developed on the basis of superconducting tunnel junctions. These detectors made it possible to attain a very high resolution, but their largest area is overly small for employing them in nuclear spectroscopy. This study is devoted to the problem of designing a superconductor detector whose dimensions are sufficiently large for detecting gamma rays and which is suitable for applications in various fields of science. The detector consists of three units: an absorber, a hot-electron calorimeter, and a tunnel-junction (normal metal–insulator–superconductor) thermometer. The absorber has a multilayer structure consisting of thin superconductor layers arranged in the order of variation of the superconductor energy gap. This structure specifies the direction of hot-electron diffusion. Since quasiparticles diffuse in a specific direction, the diffusion time becomes shorter than that in the case of conventional diffusion. It is necessary that this time be shorter than the time of electron–phonon interaction. Calculations of the diffusion time for the particular structure in question and data from the literature on electron–phonon interaction show that the operating area of the detector can be about 3 to 4 mm^2 and that its thickness can be about 1 mm. These dimensions can be considerably increased in the case of especially pure superconductors. © *2005 Pleiades Publishing, Inc.*

At the present time, work aimed at designing radically new gamma-ray and particle detectors of high resolution and low energy threshold is being performed in many countries. Such detectors are necessary in many fields of science and are based on various physical principles. In particular, resolution that is sufficiently high for detecting soft x and gamma rays (FWHM of about 10 to 20 eV at an energy of about 6 keV) [1] was obtained for a low-temperature detector operating as a microcalorimeter equipped with a thermometer based on a superconducting tunnel junction of the *normal metal–insulator–superconductor* (NIS) type. However, the largest detector area (200×200 μm) attained in a number of experiments is overly small for applications in nuclear spectroscopy.

This study is devoted to the problem of developing a rather large low-temperature detector that would operate as a hot-electron calorimeter, which would be able to detect γ rays of energy up to about 300 keV, and which would be suitable for application in gamma spectroscopy. In such a detector, the photon energy is converted into the thermal energy of so-called hot electrons, which is to be measured. An increase in the detector dimensions leads to an increase in the electron diffusion length and, accordingly, in the diffusion time. However, the diffusion time must not be longer than the time of electron–phonon interaction; otherwise, there would be large heat transfer to the lattice. Another restriction on the detector dimensions is associated with the quasiparticle-recombination time τ_{qp}, which must also exceed the diffusion time τ_{dif}. Because of these restrictions, the detector dimensions cannot be increased beyond some limit. The detector area necessary for our purposes is about several mm^2. The proposed detector has a structure that enables us to obtain directed diffusion, in which case the time of hot-electron propagation becomes shorter than the time of conventional diffusion.

We consider a detector that is formed by an absorber, a calorimeter, and a tunnel NIS junction. The cylindrical absorber consists of a number of layers from different superconducting metals, these layers being arranged top to bottom in order of decrease in the superconducting energy gap (Δ). For example, one can take the following set of superconductors: Nb, Pb, Ta, In, and Ti. A thin normal-metal (for example, Ag) layer, playing the role of a calorimeter and simultaneously serving as a NIS-junction electrode, is deposited on the bottom superconducting layer, which is characterized by the lowest value of Δ. In turn, an insulating barrier I, a superconductor S, and a normal-metal layer for a fast removal of electrons are deposited on the aforementioned normal-metal layer (see Fig. 1*a*).

*e-mail: shpi@pike.pike.ru

1063-7788/05/6812-2034$26.00

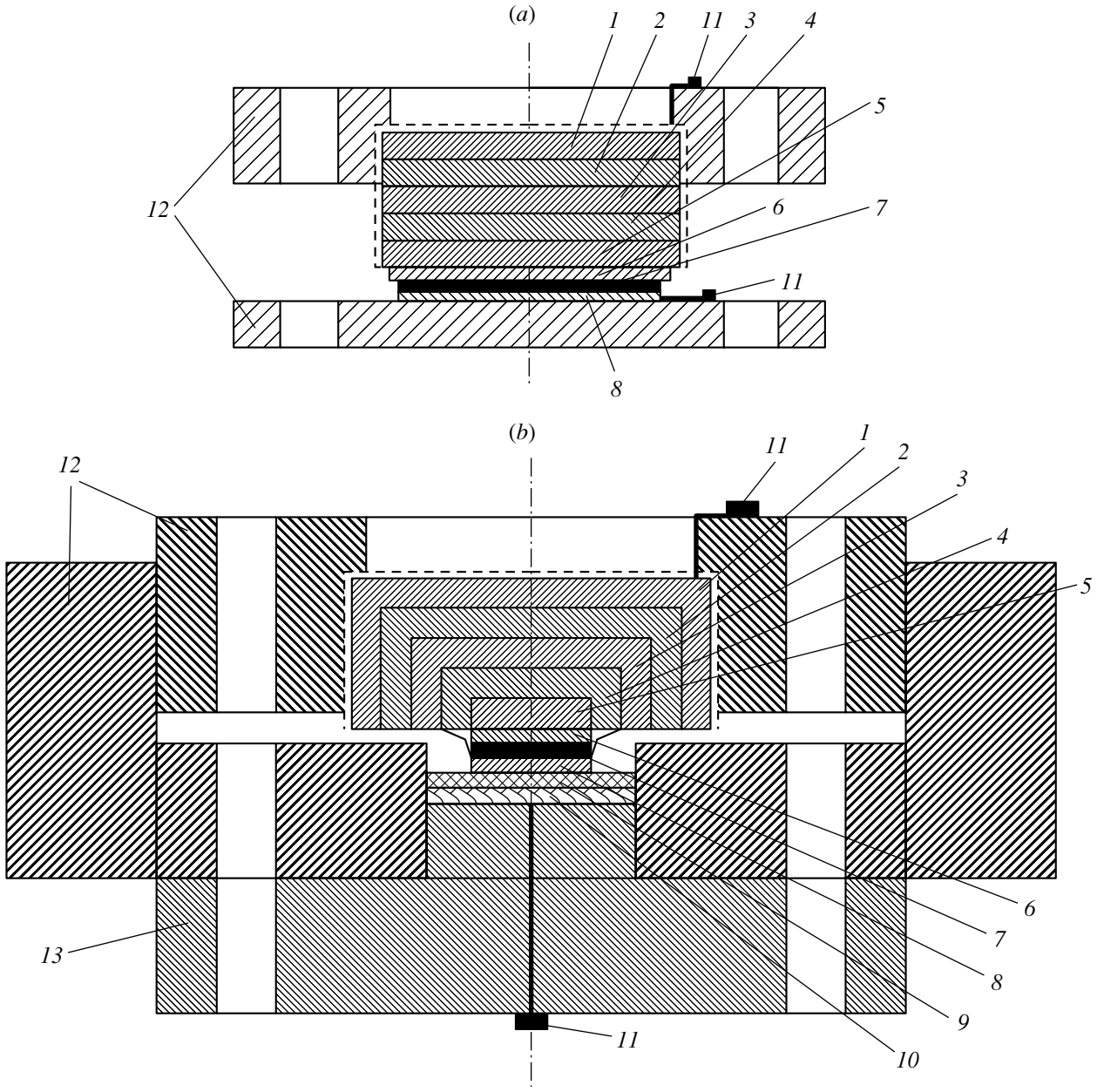

Fig. 1. Schematic view of the detector structure for the cases where absorber layers are in the shape of (*a*) round disks and (*b*) cylindrical glasses inserted into one another: (*1*) Nb, (*2*) Pb, (*3*) Ta, (*4*) In, (*5*) Ti, (*6*) Ag, (*7*) Al_2O_3, (*8*) Al, (*9*) Ag, (*10*) Ag, (*11*) contacts, (*12*) holder with orifices for bolts, and (*13*) clip. The dashed line shows a thin NbN coating for reflecting quasiparticles.

When a photon is absorbed in one of the absorber layers, quasiparticles are excited. They relax within a short time (below 10^{-8} s) to lower lying levels near the boundaries of the superconducting energy gap Δ, and an increased density of hot electrons arises in a small volume. Because of diffusion through the bulk of the layer and in its plane, hot electrons traversing the layer bulk are captured in the next layer, where the value of Δ is lower. This process of diffusion and capture develops in neighboring layers, giving rise to directed diffusion, which terminates upon the capture of hot electrons in the calorimeter. The use of an absorber featuring a multilayer structure enables one to increase its thickness; in addition, the diffusion time τ_{dif} becomes much shorter than the diffusion time in a homogeneous absorber of the same thickness. If the absorber of thickness L involves n layers having the

same thickness and the same diffusion coefficient D, the diffusion time is

$$\tau_{\text{dif}} = \frac{L^2/D}{n};$$

that is, it decreases by the factor n. In the case of absorption in layers lying deeper in the absorber, the diffusion time decreases accordingly. The diffusion time in the layer plane is restricted by the time of diffusion over the bulk of the layer. The cross-sectional area of the hot-electron diffusion flux increases because of diffusion in the plane. However, the process of directed diffusion arises if the mean free path l is much shorter than the layer thickness $\delta = L/n$. If l exceeds δ, no diffusion actually arises because the hot electrons traverse the layer undergoing virtually no collisions; finding their way to the next layer, they cannot return because of Andreev's reflection. In this case, the time within which electrons traverse the absorber is very short, about L/u, where u is the electron velocity at the Fermi surface.

The appearance of hot electrons in the calorimeter leads to the heating of its electron subsystem and to an increase in the stationary tunneling current I through the tunnel junction by the quantity

$$\delta I(T) = \frac{dI}{dT}\delta T(t), \quad \frac{dI}{dT} = \frac{I}{T}\left(\frac{1}{2} + \frac{\Delta - eV}{k_{\text{B}}T}\right)\ldots. \tag{1}$$

The stationary tunnel current through the NIS junction at temperatures $T \ll \Delta$ is given by

$$I(T,V) = \frac{\sqrt{2\pi\Delta k_{\text{B}}T}}{2eR_{\text{j}}}\exp\left\{-\frac{\Delta - eV}{k_{\text{B}}T}\right\}, \tag{2}$$

where the bias V across the junction satisfies the condition $\Delta - eV > k_{\text{B}}T$; R_{j} is the junction resistance in a normal state; T is the normal-electrode (calorimeter) temperature; k_{B} is the Boltzmann constant; and $\delta T(t)$ is the heating- and cooling-induced time-dependent change in the temperature of electrons in the calorimeter,

$$\delta T(t) = \frac{E_\gamma}{c}\left(1 - \exp\left(-\frac{t}{\tau_g}\right)\right)\exp\left(-\frac{t}{\tau_d}\right). \tag{3}$$

Here, E_γ is the absorbed-photon energy; c is the heat capacity of electrons in the calorimeter; and τ_g is a constant that characterizes the rise time for the electron temperature, this time being generally shorter than the hot-electron-diffusion time for the whole calorimeter.

The constant τ_d characterizes the calorimeter-cooling time,

$$\tau_d = c/G,$$

where G is the thermal conductivity between the electrons and their environment. There are two possible mechanisms of the thermal conductivity in question ($G = g_{e-p} + g_t$), that of energy transfer to phonons via electron–phonon interaction (g_{e-p}) and that of electron-energy transfer in the process of tunneling (g_t). The thermal conductivity g_t is equal to the product of the energy transferred by one electron ($\Delta - eV$) and the number of electrons traversing the tunnel barrier per unit time:

$$g_t = \frac{\Delta - eV}{e}\frac{dI}{dT}.$$

As was indicated above, the tunneling time τ_t must be shorter than the time τ_{e-p} of electron–phonon interaction (that is, $g_t > g_{e-p}$). This condition, which is sufficient in the case of microcalorimeters, must be supplemented with the condition that, for a relatively large calorimeter such as that in our case, the hot-electron-diffusion time τ_{dif} must be shorter than the time of electron–phonon interaction ($\tau_{\text{dif}} < \tau_{e-p}$).

In theoretical studies, it was shown that, in the temperature range $T < 1$ K, the strength of electron–phonon interaction in pure metals varies with temperature in proportion to T^4. Further, it was shown that this dependence becomes different in dirty metals, where τ_{e-p} additionally depends on the electron mean free path l [2, 3]. Both T and l dependences change as one goes over from one temperature interval to another. Theoretical formulas for calculating electron–phonon relaxation were obtained in [4], and calculations were performed there for a number of metals by using experimental constants. In particular, the calculations were performed for Cu, and the results were compared with the experimental curve obtained in [5]; the agreement was good. Similar results were obtained for NbC, Al, Au, AuPd, and Nb. From the experimental curve for Cu, it follows that, at $T = 50$ mK, $\tau_{e-p} = 10^{-4}$ s for a film with a diffusion coefficient of $D = 100$ cm^2/s, the calculated value being $\tau_{e-p} = 10^{-3}$ s for $D = 10$ cm^2/s at the same temperature.

In order to estimate the diffusion time in the absorber, we assume that our absorber consists of five layers shaped as disks of radius 1 mm and thickness δ, the diffusion coefficient being D. The diffusion time τ_{dif} for two absorber structures and three values of the diffusion coefficient is presented in the table. These values of τ_{dif} give a lower limit admissible for the time

of electron–phonon interaction in the metals used. It can be conjectured that the values of τ_{e-p} for some of the aforementioned metals for which there are no data are identical to those quoted for Cu. Comparing these values of τ_{e-p} with the values of $\tau_{\rm dif}$ in the table, we can see that the condition $\tau_{e-p} \gg \tau_{\rm dif}$ is satisfied only in very pure films characterized by the diffusion coefficient of $D = 100$ cm^2/s. In other cases where $D \leq 10$ cm^2/s, τ_{e-p} and $\tau_{\rm dif}$ have close values. From here, we conclude that, for creating a detector whose absorber features five layers of thickness $\delta = 0.2$ mm each, it is necessary to use very pure superconductors. Pure superconductors characterized by a high diffusion coefficient D are also necessary for minimizing quasiparticle losses by recombination. The quasiparticle free path associated with the loss by recombination is determined by the quantity $\sqrt{D\tau_{\rm qp}}$, where $\tau_{\rm qp}$ is the mean quasiparticle lifetime. The lower limit on $\tau_{\rm qp}$ can be estimated on the basis of the tunneling time measured in experiments with tunnel NIS junctions. If, for example, one uses the results from [6], such an estimate for Al at $D = 100$ cm^2/s gives the quasiparticle recombination path of $l_{\rm qp} \sim 0.3$ mm, which is commensurate with the absorber-layer thickness δ adopted here. It should be noted that, at the present time, it is possible to obtain samples of high-quality pure single crystals in which the electron mean free path reaches several millimeters (in the purest tungsten and gallium samples, for example, $l \approx 1$ and 2 to 3 cm, respectively, [7]). From the aforesaid, it follows that, if such pure samples are used in a multilayer absorber, the absorber dimensions can be much larger than those mentioned above. In addition, the actual absorber structure must be manufactured with allowance for particular data on the electron–phonon interaction in the metals used and their purity.

For our detector, the cross-sectional area of the hot-electron diffusion flux during the capture in the calorimeter may prove to be smaller than the total calorimeter area. In this case, only a fraction of the electrons are heated, whereupon diffusion extends over the entire calorimeter. If, however, the transparency of the tunnel barrier is reasonably high and if, in addition, the tunneling time is shorter than the diffusion time, the hot electrons can have time to tunnel through it without heating the electrons in the remaining cool section of the calorimeter, with the result that the stationary tunnel current flowing through this section does not change. If the heated section of the calorimeter has the area S' equal to the cross-sectional area of the hot-electron diffusion flux, the jump of a fraction of the stationary tunnel current I' is described by an expression similar to expressions

Values of $\tau_{\rm dif}$ for two absorber structures (n is the number of absorber layers)

n	δ, mm	D, cm^2/s	$\tau_{\rm dif}$, s
10	0.1	1	10^{-3}
10	0.1	10	10^{-4}
10	0.1	100	10^{-5}
5	0.2	1	8×10^{-3}
5	0.2	10	8×10^{-4}
5	0.2	100	8×10^{-5}

(2) and (3),

$$\delta I' \approx \frac{I'}{T}\delta(T') \approx \frac{I'}{T}\frac{\mathrm{E}_\gamma}{c'},$$

where c' is the electron heat capacity in the heated section of the calorimeter. Since the quantities I' and c' vary in just the same way as S', the tunnel-current jump is independent of whether the whole calorimeter or only a section of it is heated.

No difficulties associated with the time of diffusion over the calorimeter are expected to arise at the chosen large area and thickness. However, such a detector also requires manufacturing a tunnel NIS junction of large area, and this can lead to technological difficulties.

For creating a detector featuring a large absorber and a small calorimeter, it is necessary that the diffusion flux of hot electrons could propagate in two orthogonal directions, into the depth of the absorber and along its layers. This can be implemented by replacing the above planar-layer absorber by an absorber consisting of layers shaped as hollow cylinders inserted into one another as in a nesting doll (see Fig. 1*b*). Such a structure can be manufactured by various methods.

It is of interest to investigate the possibility of applying, as the superconducting films of a multilayer absorber, dirty films, for which a long time of electron–phonon interaction was predicted theoretically. This prediction was confirmed experimentally for very thin and dirty superconducting films. In such films, the time of electron–phonon relaxation obeys the T^{-4} dependence and has a record large value of 25 ms in the case of Hf and Ti at 40 mK [4]. The diffusion coefficient in the films is $D = 1.5$ cm^2/s for Hf and $D = 2.5$ cm^2/s for Ti. However, the use of dirty superconductors in a multilayer absorber would lead not only to the desirable weakening of electron–phonon interaction but also to an undesirable increase in the diffusion time. In order to detect current pulses arising in a thermometer based on a NIS

junction, use is usually made of SQUID amplifiers. It should be noted that, in all probability, it will be possible to replace, in the near future, such thermometers by very promising thermoelectric gauges that employ new thermoelectric materials—for example, lanthanum–cerium hexaboride ($La(Ce)B_6$) [8, 9].

In summary, we note that, here, we have proposed a principle that can be used as a basis for creating a low-temperature detector operating as a hot-electron calorimeter and having relatively large dimensions (the operating area is 3 to 4 mm^2, and the thickness is 1 mm) and a gamma-ray-detection efficiency of about 20% for gamma rays of energy 300 keV. The estimate quoted above for the time of hot-electron diffusion and data from the literature on electron–phonon relaxation give sufficient grounds to conclude that such a detector can be realized. The fabrication of an absorber from especially pure superconductors would make it possible to increase considerably the detector dimensions and to extend the range of measured photon energies up to about 1 MeV.

REFERENCES

1. M. Nahum and J. M. Martinis, Appl. Phys. Lett. **66**, 3203 (1955).
2. A. Schmid, Z. Phys. **259**, 421 (1973); J. Rammer and A. Schmid, Phys. Rev. B **34**, 1352 (1986).
3. M. Y. Reizer and A. V. Sergeev, Zh. Éksp. Teor. Fiz. **90**, 1056 (1986) [Sov. Phys. JETP **63**, 616 (1986)]; Int. J. Mod. Phys. B **10**, 635 (1996).
4. B. S. Karasik, A. V. Sergeev, and M. E. Gershenson, in *Proceedings of the 9th International Workshop on Low Temperature Detectors*, Ed. by F. S. Porter *et al.*; AIP Conf. Proc. **605**, 75 (2002).
5. M. L. Roekes, M. R. Freeman, R. S. Germain, *et al.*, Phys. Rev. Lett. **55**, 422 (1985).
6. P. Verhoeve, G. Brammertz, D. Martin, and A. Peacock, in *Proceedings of the 10th International Workshop on Low Temperature Detectors*, Ed. by F. Gatti; Nucl. Instrum. Methods Phys. Res. A **520**, 246 (2004).
7. V. M. Azhazha, A. G. Shepelev, and G. P. Kovtun, Vopr. At. Nauki Tekh., Ser.: Vakuum, Chistye Materialy, Sverkhprovodniki, No. 1, 3 (2002).
8. A. Gulian *et al.*, in *Proceedings of the 10th International Workshop on Low Temperature Detectors*, Ed. by F. Gatti; Nucl. Instrum. Methods Phys. Res. A **520**, 36 (2004).
9. K. Wood *et al.*, in *Proceedings of the 10th International Workshop on Low Temperature Detectors*, Ed. by F. Gatti; Nucl. Instrum. Methods Phys. Res. A **520**, 56 (2004).

Translated by V. Bukhanov

Physics of Atomic Nuclei, Vol. 68, No. 12, 2005, pp. 2039–2046. Translated from Yadernaya Fizika, Vol. 68, No. 12, 2005, pp. 2101–2108.

ELEMENTARY PARTICLES AND FIELDS
Experiment

Yield of ^{8}Be Nuclei Originating from ^{10}B Fragmentation in Photoemulsion at an Energy of 1 GeV per Nucleon

F. G. Lepekhin* **and B. B. Simonov†**

Petersburg Nuclear Physics Institute, Russian Academy of Sciences, Gatchina, 188350 Russia

Received February 9, 2005

Abstract—The fraction of the channel $^{10}\mathrm{B} \to {}^8\mathrm{Be} \to 2\alpha$ is estimated at $(18 \pm 3)\%$. The constants of the distributions with respect to the alpha-particle emission angle and the angle between the alpha-particle momenta are found to be 20.5 ± 0.7 and 31.7 ± 2.0 mrad, respectively. These values agree with the results of the calculations performed prior to our experiment under the assumption of the limiting fragmentation of relativistic nuclei. © *2005 Pleiades Publishing, Inc.*

1. INTRODUCTION

Nuclear photoemulsions irradiated with various light nuclei at the nuclotron of the Laboratory of High Energies at the Joint Institute for Nuclear Research (JINR, Dubna) make it possible to study the cluster structure of these nuclei [1–3]. Our present study, which was performed within the BECQUEREL Collaboration, was aimed at obtaining quantitative features of alpha-cluster formation in the ^{10}B nucleus.

An emulsion chamber irradiated with 10-GeV ^{10}B ions is best suited for this purpose. Because of a rather low momentum of a primary particle, the angles at which relativistic secondary fragments escape from the target are rather large (10–30 mrad). These angles can be measured in photoemulsion to a fairly high precision.

The ^{10}B nucleus has a spin of 3 and positive parity. Within the shell model, its structure is $(1s)^4(1p_{3/2})^6$—that is, four nucleons occupy the $1s$ shell, and the filling of the next shell is not complete since eight nucleons are necessary for closing it [4]. The ^{10}B nucleus can be conventionally considered as $^8\mathrm{Be} + {}^2\mathrm{H}$ or $^8\mathrm{Be} + {}^1\mathrm{H} + n$. Actually, we will see that the probability of observing the respective fragmentation channels is higher than that for any other fragmentation channel. Thus, one can expect that the alpha-particle structure of the ^{10}B nucleus must manifest itself in experiments.

The decay $^8\mathrm{Be} \to 2\alpha$ can proceed only from the 0^+ or 2^+ states. Indeed, it was found in [5] that the 0^+ state is the ground state of the ^{8}Be nucleus and that the spin–parity of the first excited state at 2.9 MeV is 2^+. We can observe the decays in question from precisely these states. Of course, events involving two independently emitted alpha particles that do not form a bound state will also be observed in ^{10}B fragmentation.

This article is organized as follows. A statistical test that can be used to separate these two types of events is considered in Section 2, along with the properties that must be inherent in events of these two types and the number of events expected in our experimental sample. In Section 3, we show how all these quantities can be assessed in the experiment and address the question of whether they are in agreement with the results of the calculation performed in Section 2.

2. LIMITING FRAGMENTATION OF ^{10}B NUCLEI

Experimental data obtained in studying the fragmentation of various relativistic nuclei accelerated to energies of 1 to 200 GeV per nucleon and the fragmentation of target nuclei at various collision energies are in agreement with the concept that the fragment-emission process is fast, so that the nucleus remains cold. Even at relatively low energies of relativistic nuclei, the hypothesis of limiting fragmentation is valid [6].

It is of importance that, although the hypothesis of limiting fragmentation was formulated for hadron–hadron interactions at infinite momentum, it is valid in nucleus–nucleus interactions at a comparatively low momentum per nucleon of the primary nucleus. On the basis of this concept, one can predict not only quantitative features of the angular and momentum distributions of nuclear fragments in nucleus–nucleus interactions for any combinations and any

†Deceased.
*e-mail: lepekhin@pnpi.spb.ru

energies of colliding nuclei but also the fraction of events in which two alpha particles originate from the $^8\mathrm{Be} \to 2\alpha$ channel of ^{10}B fragmentation. To do this, it is necessary to know only the Fermi momentum, which can be determined in experiments aimed at studying electron–nucleus scattering [7]. However, the Fermi momentum was not determined for the ^{10}B nucleus in the experiment reported in [7]. It can be obtained under the assumption that the phase space of the nucleus in the ground state is the product of its geometric volume, which is determined by the nuclear radius $R = r_0 A^{1/3}$, and the volume in momentum space that is determined by the Fermi momentum $P_\mathrm{F} = \sqrt{5}\sigma_0$, where σ_0^2 is the variance of the momentum distribution of nucleons in the ^{10}B nucleus prior to its interaction with a photoemulsion nucleus. In accordance with the Pauli exclusion principle, only four nucleons can occur in each $\hbar$ cell of this volume. It was shown in [8] that $r_0\sigma_0 = 134.4$ MeV/c fm. By using the value of $r_0 = 1.54$ fm, which was established in the experiment aimed at determining the radius of the ^{10}B nucleus and reported in [9], we can find that its Fermi momentum must be 195.2 MeV/c; therefore, the value characterizing the nucleon momentum distribution in the ^{10}B nucleus is $\sigma_0 = 87.3$ MeV/c.

The parabolic Goldhaber law [10] governs the relationship between the variance σ_F^2 of the momentum distribution of any fragment having a mass number A_F and originating from any nucleus of mass number A_0 and the variance σ_0^2 of the momentum distribution of nucleons in this nucleus:

$$\sigma_F^2 = \sigma_0^2 \frac{A_F(A_0 - A_F)}{A_0 - 1}. \qquad (1)$$

Using this law and bearing in mind that

$$P_\perp = A_F P_0 \tan\theta, \qquad (2)$$

where $P_0 = 1.7$ MeV/c is the momentum per nucleon of the ^{10}B nucleus in our experiment, we find that the constant $\sigma(\theta)$, which determines the distribution of alpha-particle emission angles θ, must be 21.0 mrad. This angular distribution must correspond to the Rayleigh distribution at the same value of the constant. The angles θ_{12} between two particles emitted independently in an event must obey a distribution of the same form, but with a variance twice that for single particles.

The angle θ_{12} between the particle tracks in an event must be obtained by sampling a random set governed by the Rayleigh distribution characterized by a constant equal to $\sigma(\theta_{12}) = \sqrt{2}\sigma(\theta) = 29.7$ mrad [11]. The ratio of the mean transverse momentum of particles that is measured in the laboratory frame to that in the c.m. frame of two particles must be equal to $\sqrt{2}$.

In our experiment, the mean angle between the momenta of two independently emitted particles must be

$$\langle\theta_{12}\rangle = \sqrt{\pi/2}\sigma(\theta_{12}) = 37.2 \text{ mrad}. \qquad (3)$$

We determine the emission angles by two angles between the momentum projections onto two planes, the emulsion plane (angle φ) and the plane orthogonal to it (angle α). If two particles are emitted independently in each event and both angles φ and α for each particle are taken at random from a normal distribution of the same variance, then the variance of the sum of these four angles in each event must be equal to four variances of an individual angular distribution. Therefore, we have

$$\sigma(\varphi_1 + \varphi_2 + \alpha_1 + \alpha_2) = 2\sigma(\theta). \qquad (4)$$

The azimuthal asymmetry coefficient A defined as the ratio of the difference of the probabilities of observing angles $\Delta\Psi$ larger or smaller than 90° to their sum,

$$A = \frac{N(\Delta\Psi > 90^\circ) - N(\Delta\Psi < 90^\circ)}{N(\Delta\Psi > 90^\circ) + N(\Delta\Psi < 90^\circ)}, \qquad (5)$$

where $\Delta\Psi$ is the difference of the azimuthal angles of two particles, is the simplest feature of two-particle correlations in the transverse plane. If the particles are emitted independently, this coefficient must be zero. In that case, the distribution of the angles $\Delta\Psi$ between the transverse-momentum vectors of two particles in an event must be uniform. Since the vector sum of the transverse momenta of all particles in each decay event is zero, kinematical correlations in the transverse plane appear necessarily. If an excited system decays to n particles uniformly distributed over the phase space, the azimuthal-asymmetry coefficient A must be equal to $1/(n-1)$ [12]. In ^{10}B nucleus fragmentation, A cannot be zero, because the total number of particles n is not very large.

If ^{8}Be originating from ^{10}B decays to two alpha particles, all differences of the azimuthal angles for two particles must be smaller than 90°. In this case, the azimuthal-asymmetry coefficient A must be close to -1. It is this fact that we are going to verify.

Let us now consider the case where two alpha particles originate from the decay $^8\mathrm{Be} \to 2\alpha$ in our experiment. We assume that the emission of ^{8}Be from a ^{10}B nucleus proceeds as ordinary fragmentation. The transverse momenta of the ^{8}Be nucleus will then obey the Rayleigh distribution whose constant can readily be calculated if the Fermi momentum of the ^{10}B nucleus is known. The longitudinal momentum of the ^{8}Be nucleus undergoes virtually no change and

will be equal to $8P_0 = 13.6$ GeV/c. Hence, we know the direction and the absolute value of the momentum of the nucleus decaying in flight to two alpha particles. The kinetic energy of each alpha particle is 45.96 keV in the rest frame of the decaying nucleus. The angular distribution of the alpha particles is assumed to be isotropic in the rest frame of the decaying ^{8}Be nucleus. We calculate the particle emission angle in the rest frame of the ^{8}Be nucleus by the Monte Carlo method, whereupon we obtain the alpha-particle momentum in the laboratory frame and determine the angle between the particles in each event. Figure 1 shows the distribution of angles between the particle momenta that was simulated in this way. There is a sharp maximum in the probability of observing these angles at $\theta_{12} = 5.45$ mrad because the solid angle of alpha particles emitted in mutually orthogonal directions in the c.m. frame of the decaying nucleus is considerably larger than that of alpha particles emitted along its momentum. The shape of this distribution will remain unchanged with increasing energy of the primary particle, but the limiting angle will become smaller.

Thus, the distributions of angles between the momenta of two alpha particles emitted independently from a ^{10}B nucleus differ markedly in the case where such particles originate from an intermediate ^{8}Be nucleus in the ground state. This is precisely the fact that makes it possible to separate events associated with the channels $^{10}\mathrm{B} \to {}^8\mathrm{Be} \to 2\alpha + \text{all}$ and $^{10}\mathrm{B} \to 2\alpha + \text{all}$. We now consider a procedure that permits estimating the fraction of the channels involving ^{8}Be.

Following the procedure described in [13], we assume that each fragment of charge Z_i and mass number A_i corresponds to a stable or a radioactive isotope whose mass is precisely known. Some amount of energy, ΔE_k, is required for the initial state of the primary ^{10}B nucleus to go over, for some time τ, to the state formed by k fragments in the c.m. frame of this nucleus. This energy will comprise not only the difference of the sum of the rest masses of all fragments and the mass of the primary nucleus but also the sum of the mean kinetic energies of all fragments in their c.m. frame. The mean values of the fragment energies can easily be calculated if the Fermi momentum is known.

The higher the energy ΔE_k, the shorter the lifetime τ of the virtual state, and the longer the lifetime τ, the higher the probability of observing the primary nucleus in the virtual state characterized by the energy deficit ΔE_k.

The theory of dynamical systems [14] provides a rigorous mathematical basis for calculating this probability. This theory proves that, if a sequence of states of the system is invariant under time translations,

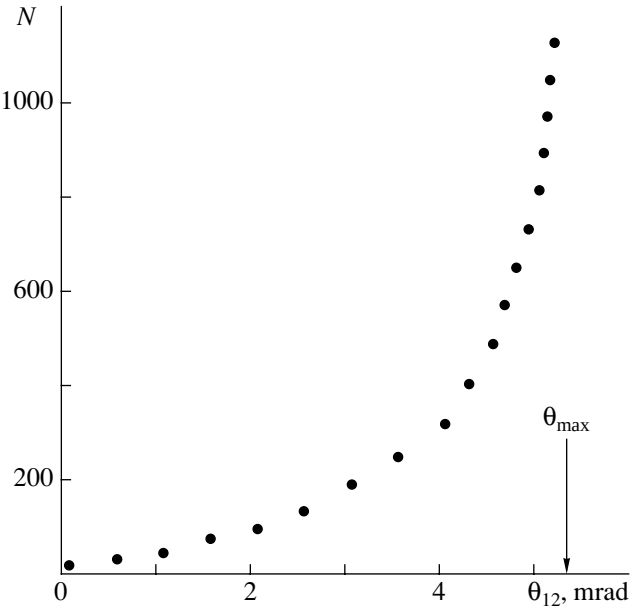

Fig. 1. Distribution with respect to the angle θ_{12} between the alpha-particle tracks in the decay of ^{8}Be originating from a 1.7-GeV/c ^{10}B nucleus according to Monte Carlo simulation for 2500 events, N being the number of events per interval $\theta_{12} = 0.5$ mrad.

then, for a set of these states, one can always introduce an invariant normalized Gibbs measure, which is just the probability of observing this state,

$$W(T, \Delta E_k) = \frac{\exp(-\Delta E_k/T)}{\Xi}. \qquad (6)$$

This is the well-known Gibbs distribution, where $T = \sigma_0^2/m_N$ is the temperature (that is, a value that is proportional to the mean energy of the constituents) and Ξ is the partition function equal to the sum of the expressions in the numerator over all possible k states.

For light nuclei, one can readily list all possible states of the primary nucleus. The number of all possible fragmentation channels is 73 for the ^{10}B nucleus. After a straightforward calculation of the partition function, we determine the absolute probabilities of all fragmentation channels. The nuclear-fragmentation channel $^{10}\mathrm{B} \to {}^4\mathrm{He} + {}^6\mathrm{Li}$ is the most probable (19.73%), and the channel in which there occurs fragmentation to ^{8}Be and a deuteron and which is of interest to us is the next in order of decreasing probability (16.36%). The list of 13 channels in this order is given in Table 1. Naturally, channels involving higher numbers of fragments are less probable. The total probability of ^{8}Be emission from the ^{10}B nucleus is 19.7%.

Table 1. Probabilities W of channels of ^{10}B fragmentation

N	W, %	Fragmentation channel
1	19.73	$^4\mathrm{He} + {}^6\mathrm{Li}$
2	16.36	$^2\mathrm{H} + {}^8\mathrm{Be}$
3	15.29	$p + {}^9\mathrm{Be}$
4	12.19	$n + {}^9\mathrm{B}$
5	8.80	$^5\mathrm{He} + {}^5\mathrm{Li}$
6	4.43	$^2\mathrm{H} + 2{}^4\mathrm{He}$
7	3.83	$^3\mathrm{He} + {}^7\mathrm{Li}$
8	3.43	$^3\mathrm{H} + {}^7\mathrm{Be}$
9	3.37	$n + p + {}^8\mathrm{Be}$
10	3.02	$p + {}^4\mathrm{He} + {}^5\mathrm{He}$
11	2.65	$n + {}^4\mathrm{He} + {}^5\mathrm{Li}$
12	0.91	$n + p + 2{}^4\mathrm{He}$
13	0.76	$^3\mathrm{H} + {}^3\mathrm{He} + {}^4\mathrm{He}$

Thus, the yield of ^{8}Be nuclei from the fragmentation of ^{10}B nuclei must not be small. For the fragmentation of ^{10}B nuclei, a rough estimate of the fraction of events involving two doubly charged particles is 20% of all events in which the sum of the charges of secondary fragments is equal to the charge of the primary nucleus. The fraction of these events among all the events identified by the tracks appeared to be 10% in the experiment reported in [1].

3. DESCRIPTION OF THE EXPERIMENT

In our experiment, an emulsion chamber formed by two emulsion layers 10×20 cm in cross section and 500 μm thick was irradiated along the layer with a beam of 10-GeV ^{10}B ions from the Nuclotron of the Laboratory of High Energies at JINR. Events were sought by means of scanning along tracks. The total length of all portions of scanned primary tracks before inelastic interaction with a photoemulsion nucleus or before the escape from a layer was 243 m. The number of inelastic interactions found along this length was 1823. Thus, the mean range before an interaction event was 13.3 ± 0.3 cm. For 217 events involving doubly charged fragments of a ^{10}B nucleus, the coordinates x, y, and z were measured at eleven points with a step of 100 μm along the x axis for both tracks of the doubly charged fragments and for the primary-particle track. If the mean values of the coordinates are $\langle x\rangle$ and $\langle a\rangle$, where $a = y, z$, then the tangent of the angle $\varepsilon = \varphi$ (at $a = y$) or the tangent of the angle $\varepsilon = \alpha$ (at $a = z$) can be evaluated as

$$\tan\varepsilon = \frac{\langle xa\rangle - \langle x\rangle\langle a\rangle}{\langle x^2\rangle - \langle x\rangle^2}. \quad (7)$$

Having calculated the angles φ and α for a given track, we obtain an estimate of the tangent of the angle θ,

$$\tan\theta = \sqrt{\tan^2\varphi + \tan^2\alpha}. \quad (8)$$

The uncertainty in measuring the angle between the particle momenta was about 1.5 mrad in the range between 3 and 8 mrad. Thus, the accuracy of our measurements in the region of the angles between the alpha-particle momenta that is of interest to us (its width is about 5 mrad), is quite sufficient for establishing the phenomenon of ^{8}Be decay from the ground state to two alpha particles if we assume that precisely events characterized by angles of $\theta_{12} < 8.5$ mrad are associated with this channel.

Although the accuracy of coordinate measurements along the y and z axes is different, the parameters of the distributions with respect to the angles φ and α appeared to be nearly identical. As might have been expected, both distributions agree with the hypothesis that they are samples from a normal distribution whose characteristic constant is calculated by using the radius of the ^{10}B nucleus.

The curve in Fig. 2 represents the expected normal distribution of the particle-emission angles characterized by zero mean value and a standard deviation of 21 mrad, which was calculated from the radius of the ^{10}B nucleus. Also shown in this figure are the empirical distributions of the angles φ and α obtained in the experiment. We emphasize that the curve in Fig. 2 is not a fit to the experimental data on these angles, but that it was obtained prior to the beginning of the experiment.

The sum of the squares of the differences along the vertical direction between the expected and empirical distributions gives the quantity ω^2 (Cramér–von Mises test), which can be used to verify the hypothesis that the empirical distribution agrees with the expected normal distribution. According our data, this hypothesis is acceptable at a 1% confidence level both for φ and for α.

This result agrees perfectly with that obtained in [1], where the experimental value of the mean transverse momentum of product deuterons was 140 ± 10 MeV/c; if it is estimated by using the value of $r_0 = 1.54$ fm, then it must be 145 MeV/c. Evidently, the agreement is good.

Within the event sample being considered, the quantity $c = \varphi_1 + \varphi_2 + \alpha_1 + \alpha_2$ obeys a normal distribution characterized by a standard deviation of

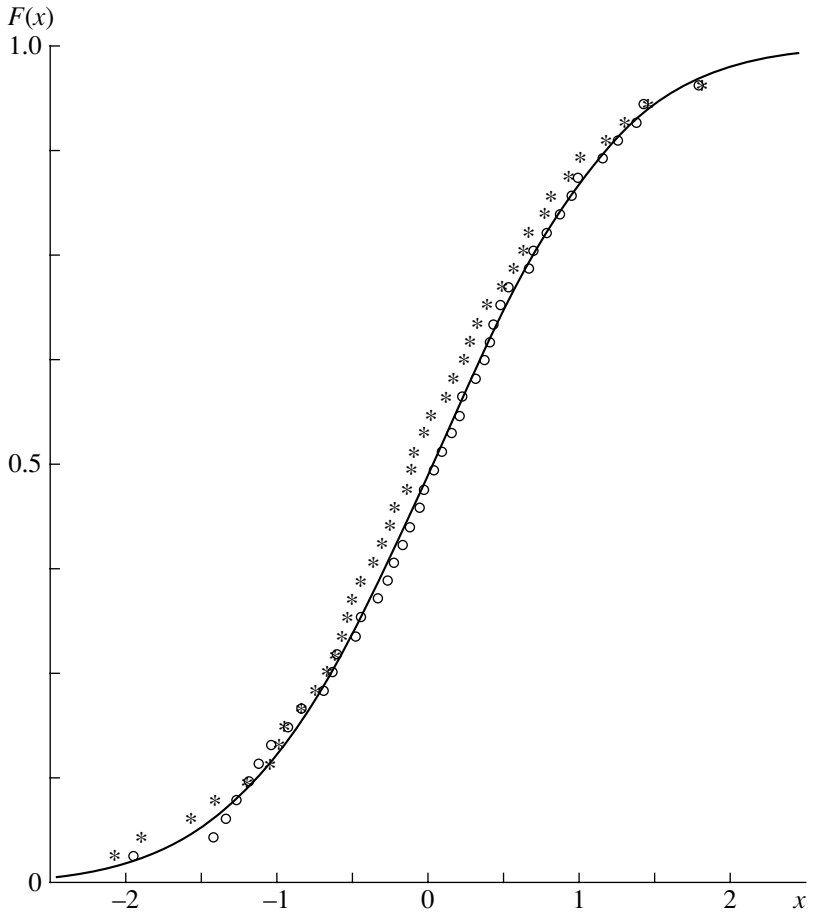

Fig. 2. Expected normal distribution (curve) and empirical distributions of the angles φ (∗) and α (○).

$\sigma_c = 39.7 \pm 2.7$ mrad. Thus, the angular correlations of particles in an event are not observed in the experiment.

Therefore, it is quite natural that the distribution of θ is in good agreement with the hypothesis that it is a sample from a Rayleigh distribution. This means that the distribution of the angles $\theta_{12} = x$ between the momenta of independently emitted alpha particles combined in pairs must correspond to the probability density

$$f(x,\sigma) = \frac{x}{\sigma^2}\exp(-x^2/2\sigma^2) \qquad (9)$$

and the cumulative distribution function

$$F(x,\sigma) = 1 - \exp(-x^2/2\sigma^2). \qquad (10)$$

In order to estimate the parameter σ of this distribution, it is necessary to eliminate from the experiment values of the angle θ_{12} that are smaller than $x_{\min}$ because we seek a small excess due to the $^8\mathrm{Be} \to 2\alpha$ channels over this distribution just within the range of small angles θ_{12}. The angles θ_{12} larger than some value $x_{\max}$ should also be eliminated because rare events of absolutely different nature (for

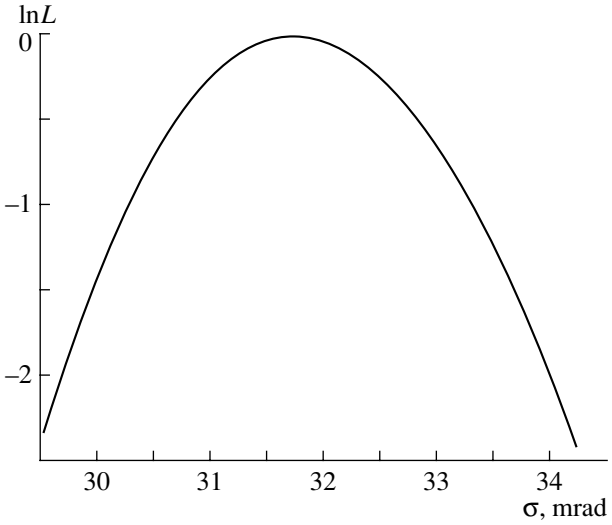

Fig. 3. Logarithm of the likelihood function versus the parameter σ. The horizontal straight line $\ln L = -1$ yields a 68.3% confidence interval for this parameter if the intersection points are projected onto the abscissa.

Table 2. Calculated and experimental values of various quantities characterizing ^{10}B fragmentation

No.	Quantity	Calculation	Experiment
1	$\langle P_\perp \rangle$ (^{2}H) [MeV/c]	145	140 ± 10 [1]
2	$\sigma(\varphi) = \sigma(\alpha)$ [mrad]	21.011	20.5 ± 0.7
3	$\sigma(\mathrm{Rel}, \theta_{12})$ [mrad]	29.714	31.7 ± 2.0
4	$\langle \theta_{12} \rangle$ [mrad]	37.22	34.6 ± 2.2
5	$\sigma(\varphi_1 + \varphi_2 + \alpha_1 + \alpha_2)$ [mrad]	42.0	39.7 ± 2.7
6	$N(\theta_{12} < 8.5$ mrad)	36	33
7	$W(^8\mathrm{Be} \to 2\alpha)$	0.197	0.18 ± 0.03
8	$A(^{10}\mathrm{B} \to 2\alpha)$	0	0.05 ± 0.03
9	$A(^8\mathrm{Be} \to 2\alpha)$	-1.0	-0.96 ± 0.04
10	$\langle \theta_{12} \rangle$ for $\theta_{12} < 8.5$ mrad	6.3	5.6 ± 1.0
11	Kolmogorov coefficient, D	1.63	0.32
12	Kuiper's coefficient, V	2.0	0.88
13	ω^2-test	0.743	0.304

example, the rescattering of final-state particles) may appear in this case. Thus, the likelihood function for the Rayleigh distribution truncated at $x_{\min}$ and $x_{\max}$ is

$$L = \prod_{i=1}^{i=N} f(x_i, \sigma) F(x_{\min}, \sigma)[1 - F(x_{\max}, \sigma)]. \quad (11)$$

In order to estimate the parameter σ, in which we are interested, we must solve a nonlinear equation that arises upon equating the derivative of the logarithm of the above likelihood function to zero. This is achieved by applying the corresponding procedure from the MATHCAD-8 library [15].

Figure 3 shows the logarithm of the likelihood function versus the parameter σ. One can see that, for the sample being considered, L reaches a maximum at $\sigma = 31.7 \pm 2.0$ mrad. With the aid of the data in Fig. 3, one can also assess the confidence interval of the estimate of the parameter. Thus, the experimental estimate of the parameter of the distribution with respect to the angle between the momenta of two particles for the sample where events in which these angles correspond to the decay $^8\mathrm{Be} \to 2\alpha$ are eliminated from consideration is nearly coincident with the expected value of this parameter in the case of two independently emitted particles.

Since we are dealing predominantly with peripheral interactions of incident nuclei with photoemulsion nuclei, the momentum transfer to the incident nucleus as a discrete unit is low. Moreover, the momentum transfer is shared among secondary fragments in accordance with their masses; as a consequence, it is virtually unobservable experimentally.

In our experiment, the azimuthal-asymmetry coefficient is 0.05 ± 0.03 for all events and -0.96 ± 0.04 for events where $\theta_{12} < 8.5$ mrad. This means that there are no correlations between the transverse-momentum directions within the total event sample, but that such correlations are large for events involving the decay $^8\mathrm{Be} \to 2\alpha$.

Finally, 33 events where $\theta_{12} < 8.5$ mrad (instead of 36 events expected theoretically) are observed in our experiment. This means that, in the experiment, the probability of observing a ^{8}Be nucleus in the fragmentation of a ^{10}B nucleus is $(18 \pm 3)\%$, but it is expected to be 19.7% on the basis of the calculation.

If the events observed here for $\theta_{12} < 8.5$ mrad are indeed generated by the channel $^8\mathrm{Be} \to 2\alpha$, then the empirical distribution of these 33 events with respect to angles θ_{12} must be identical to the expected distribution of these angles for this channel. Figure 1 displays the probability density for these angles.

We used three nonparametric criteria of agreement to verify this hypothesis. According to the Kolmogorov test [16], the maximum deviation D of the empirical cumulative distribution from that predicted theoretically cannot exceed 1.63 for the agreement at a 1% confidence level. The value of $D = 0.32$ was found in our experiment.

The second test is based on an analysis of the quantity $V = V^+ - V^-$, which is the difference of the two distribution functions, and is referred to as

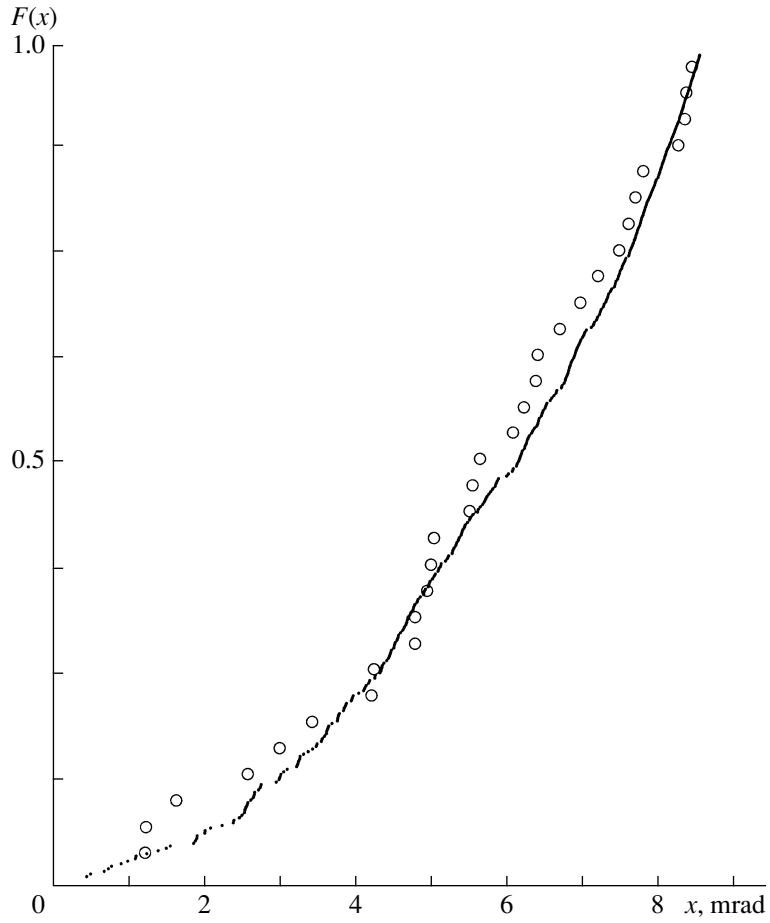

Fig. 4. (○) Empirical distribution $F(x) = F(\theta_{12} < x)$ for 33 angles and (points) expected distribution of the angles θ_{12} for the process $^8\mathrm{Be} \to 2\alpha$.

Kuiper's test [17]; this test is more powerful than the first one, but it is rarely used by experimentalists. Its critical value for the above confidence level is 2.0, but, in our experiment, $V = 0.88$. A similar result was obtained by using the third test mentioned above, the Cramér–von Mises test (see Table 2).

Thus, all three tests do not reject the hypothesis that our 33 events where $\theta_{12} < 8.5$ mrad are due to the process $^8\mathrm{Be} \to 2\alpha$. Figure 4 illustrates the respective result.

4. CONCLUSIONS

The basic results of our study are summarized in Table 2. All predictions obtained a priori have been confirmed experimentally. The yield of ^{8}Be nuclei from the fragmentation of a 10-GeV ^{10}B nucleus is indeed about 2% of all the events found by their tracks in the photoemulsion used or about 20% of those events in which the sum of the secondary-fragment charges is equal to the charge of the incident nucleus.

Events containing two alpha particles from ^{8}Be decay among the products originating from the fragmentation of relativistic nuclei have been revealed for the first time in our experiment. In the fragmentation of carbon and oxygen nuclei with a momentum of 4.1 GeV/c per nucleon to three or four doubly charged fragments [18, 19], the experimentally observed special features of the distributions with respect to the azimuthal angles between the fragment momenta are in good agreement with the calculated fraction of ^{8}Be nuclei among these fragments [20], which is about 30%. It is probable that, in light nuclei having a distinct alpha-particle structure, alpha particles form a Bose condensate and interact resonantly with one another, and this is the reason why we observe a ^{8}Be nucleus. Since the lifetime of this intermediate state is long on the scale of nuclear time, it begins to play an important role in nucleosynthesis in stars as soon as the helium concentration increases upon the burning of hydrogen. In particular, the isotope ^{9}Be, whose concentration in the stars of globular clusters was used in the first experimental determination of the age

of the Milky Way Galaxy [21], is produced via neutron absorption. Thus, experimental data on the yield of ^{8}Be nuclei in the fragmentation of light nuclei can be of use.

Of course, the results presented in Table 2 were obtained under numerous explicit and implicit assumptions; therefore, they can be treated only as indirect evidence. For example, there are grounds to believe that the Fermi momentum of the ^{10}B nucleus and the constant of the momentum distribution of nucleons in this nucleus are 195 MeV/c and about 90 MeV/c, respectively. The nucleus can indeed be treated as a dynamical system, and all general laws of the theory of dynamical systems are applicable to it. As we have seen, this enables us to make predictions, which are supported experimentally.

The theory of dynamical systems incorporates thermodynamic formalism. Therefore, the generally adopted thermodynamic notions such as a nuclear excitation energy and the temperature of an excited nucleus are quite appropriate for a phenomenological description of the fragmentation phenomenon. However, no predictions have been made on the basis of this approach over a number of decades. Further studies of the nuclear-fragmentation process must obviously be devoted to searches for deviations from the predictions based on this simple model of nuclear fragmentation. Having now an outline of the fragmentation process as a whole, we can plunge into the details.

ACKNOWLEDGMENTS

We are grateful to the BECQUEREL Collaboration for irradiating the emulsion and for providing the opportunity to perform our studies. We thank the staff of the Laboratory of High Energies at JINR for high-quality chemical treatment of the emulsion and L.N. Tkach for scanning and measuring events used in our study.

REFERENCES

1. M. I. Adamovich *et al.*, Yad. Fiz. **67**, 533 (2004) [Phys. At. Nucl. **67**, 514 (2004)].
2. V. Bradnova *et al.*, Yad. Fiz. **66**, 1694 (2003) [Phys. At. Nucl. **66**, 1646 (2003)].
3. M. I. Adamovich *et al.*, Fiz. Élem. Chastits At. Yadra **177** (2), 29 (2003).
4. A. S. Davydov, *Theory of the Nucleus* (Fizmatgiz, Moscow, 1958) [in Russian].
5. J. A. Wheeler, Phys. Rev. **59**, 16 (1941).
6. J. Benecke, T. T. Chou, C. N. Yang, and E. Yen, Phys. Rev. **188**, 2159 (1969); R. P. Feynman, *Photon–Hadron Interactions* (Benjamin, Reading, Mass., 1972; Mir, Moscow, 1975).
7. E. J. Moniz *et al.*, Phys. Rev. Lett. **26**, 445 (1971).
8. F. G. Lepekhin, D. M. Seliverstov, and B. B. Simonov, Eur. Phys. J. A **1**, 137 (1998).
9. J. M. Blatt and V. F. Weisskopf, *Theoretical Nuclear Physics* (Wiley, New York, 1952; Inostrannaya Literatura, Moscow, 1954).
10. J. S. Goldhaber, Phys. Lett. B **53B**, 306 (1974).
11. F. G. Lepekhin and B. B. Simonov, Pis'ma Zh. Éksp. Teor. Fiz. **58**, 493 (1993) [JETP Lett. **58**, 493 (1993)].
12. S. A. Azimov *et al.*, *Multiparticle Processes at High Energies* (FAN UzSSR, Tashkent, 1976), p. 120 [in Russian].
13. F. G. Lepekhin, Fiz. Élem. Chastits At. Yadra **112** (3), 25 (2002).
14. Ya. G. Sinaĭ, *Dynamical Systems-2* (VINITI, Moscow, 1985), Vol. 2, p. 306 [in Russian].
15. V. D'yakonov, *MATHCAD 8/2000: Special Handbook* (Piter, St. Petersburg, 2001), p. 582.
16. W. T. Eadie, D. Dryard, F. E. James, *et al.*, *Statistical Methods and Experimental Physics* (North-Holland, Amsterdam, 1971; Atomizdat, Moscow, 1976).
17. K. Mardia, *Statistical Analysis* (Nauka, Moscow, 1978), p. 236.
18. C. V. Belaga *et al.*, Yad. Fiz. **59**, 869 (1996) [Phys. At. Nucl. **59**, 832 (1996)].
19. Almaty–Bucharest–Dubna – Dushanbe – Yerevan – Košice–Moscow–St. Petersburg–Tashkent–Tbilisi Collaboration, Yad. Fiz. **59**, 110 (1996) [Phys. At. Nucl. **59**, 102 (1996)].
20. F. G. Lepekhin, O. V. Levitskaya, and B. B. Simonov, *PNPI Research Report 1998–1999* (Petersburg Nucl. Phys. Inst., Gatchina, 2000), p. 165; Preprint No. 2313, PNPI (Petersburg Nucl. Phys. Inst., Gatchina, 1999).
21. European Southern Observatory, Press Release 20/04; http://www.eso.org/outreach/press-rel/pr-2004/pr-20-04.html.

Translated by E. Kozlovsky

Physics of Atomic Nuclei, Vol. 68, No. 12, 2005, pp. 2047–2060. Translated from Yadernaya Fizika, Vol. 68, No. 12, 2005, pp. 2109–2122.

ELEMENTARY PARTICLES AND FIELDS
Theory

Indirect Methods for Determining Heavy-Neutrino Masses

G. G. Boyarkina and O. M. Boyarkin*

Belarussian State Pedagogical University, Sovetskaya ul. 18, Minsk, 220050 Belarus

Received March 4, 2005

Abstract—Within the two-flavor approximation, equations that relate the oscillation parameters for both light and heavy neutrinos to the Yukawa coupling constants and the vacuum expectation values of the Higgs fields are derived within the left–right model. The contributions from Higgs bosons to the muon anomalous magnetic moment, to the cross sections for lepton-flavor-violating processes, and to the cross sections for low-energy light-neutrino scattering are studied in order to determine the Yukawa coupling constants. It is shown that the heavy-neutrino masses $m_{N_{1,2}}$ can be expressed in terms of only the triplet Yukawa coupling constants and the mass of the gauge boson W_2. Data on direct and inverse muon decay and constraints on the masses of the $\tilde{\delta}^{(-)}$, $\Delta_{1,2}^{(--)}$, and W_2 bosons are used to obtain bounds on $m_{N_{1,2}}$ both in the absence of degeneracy and in the presence of mass degeneracy in the sector of heavy neutrinos. Only in the case of degeneracy are data concerning the explanation of the $(g-2)_\mu$ anomaly used to determine bounds on $m_{N_{1,2}}$. © *2005 Pleiades Publishing, Inc.*

1. INTRODUCTION

Within the standard model of electroweak interactions, the neutrinos are massless Weyl particles, the law of lepton-number conservation being rigorous. However, these statements do not stand up to experimental tests. By way of example, we indicate that, in an experiment with atmospheric neutrinos at SuperKamiokande [1], a significant up–down asymmetry was found in events featuring high-energy muons. In an SNO experiment with solar neutrinos [2], direct evidence was obtained for ν_e transitions to ν_μ and ν_τ. Thus, we have unambiguous indications that the neutrino mass is nonzero and that there is mixing in the lepton sector. These conclusions were corroborated in experiments with terrestrial neutrinos as well, in which case use was made of a well-controlled initial flux. Here, we mean the KamLAND experiment with reactor antineutrinos [3] and the K2K experiment [4], which was the first accelerator long-baseline experiment.

From all of available experimental data, it follows that the neutrino masses are many orders of magnitude lower than the masses of other fundamental fermions, charged leptons and quarks. For example, direct kinematical measurements constrain the neutrino masses from above as (the mass spectrum is assumed to be degenerate) $m_{\nu_e} \approx |m_i| < 2.2$ eV at a 95% C.L. [5]. The cosmological bound on the sum of the masses of all light neutrinos [6], $\sum_i |m_i| < 0.7–2.1$ eV at a 95% C.L., leads to a still more stringent limit on the neutrino masses, $|m_i| < (0.23–0.70)$ eV.

An explanation for so giant a suppression of the neutrino masses is provided by the seesaw mechanism, which is an indispensable element in many Grand Unification theories. Such a theory can be exemplified by a model based on $SO(10)$ symmetry. An interesting facet of the $SO(10)$ model is that it contains the $SU(2)_L \times SU(2)_R \times U(1)_{B-L}$ gauge group (left–right model). Within the left–right model, heavy Majorana neutrinos N_a $(a = e, \mu, \tau)$, which enter into the composition of the right-handed lepton doublet

$$\Psi_{aR} = \begin{pmatrix} N_{aR} \\ l_{aR} \end{pmatrix},$$

are partners in the seesaw mechanism.

Unfortunately, information about heavy neutrinos is scanty at the present time. However, the parameters of the heavy-neutrino sector in the left–right model are not isolated from the remaining part of the model, this making it possible to determine these parameters not only in direct but also in indirect measurements. The objective of the present study is to set constraints on the masses of the heavy neutrinos N_i and on their mixing angles by using available experimental data but without directly detecting N_i.

The ensuing exposition is organized as follows. In the next section, we present necessary information about the left–right model. In Section 3, the $(g-2)_\mu$ anomaly, lepton-flavor-violating processes, and low-energy light-neutrino scattering are considered from

*e-mail: boyarkin@front.ru

the point of view of obtaining bounds on the constant α_H of Higgs bosons coupling to leptons. In Section 4, the values found for α_H are used to set constraints on the parameters of the heavy-neutrino sector. Section 5 contains conclusions and discussion of the results obtained in this study.

2. DESCRIPTION OF THE MODEL

Let us consider the symmetric version of the left–right model ($g_L = g_R$). In the Higgs sector, it contains one bidoublet $\Phi(\frac{1}{2},\frac{1}{2},0)$ and two triplets $\Delta_L(1,0,2)$ and $\Delta_R(0,1,2)$. The Higgs potential is represented by the expression proposed in [7], while the Yukawa Lagrangian describing gauge-invariant interaction in the lepton sector is given by

$$\mathcal{L}_{\rm Y} = -\sum_{a,b}\{h_{ab}\bar{\Psi}_{aL}\Phi\Psi_{bR} + h'_{ab}\bar{\Psi}_{aL}\tilde{\Phi}\Psi_{bR} \quad (1)$$
$$+ if_{ab}[\Psi^T_{aL}C\tau_2(\boldsymbol{\tau}\cdot\boldsymbol{\Delta}_L)\Psi_{bL} + (L\to R)] + \text{conj.}\},$$

where $\tau_{1,2,3}$ are the Pauli matrices, $\tilde{\Phi} = \tau_2\Phi^*\tau_2$, h_{ab} and h'_{ab} are the bidoublet Yukawa coupling constants, and $f_{ab} = f_{ba}$ are the triplet Yukawa coupling constants.

After spontaneous symmetry breaking, 14 Higgs bosons remain in the theory. These are four doubly charged scalars $\Delta^{(\pm\pm)}_{1,2}$, four singly charged scalars $h^{(\pm)}$ and $\tilde{\delta}^{(\pm)}$, four neutral scalars $S_{1,2,3,4}$ (S_1 is the analog of the Standard Model Higgs boson), and two neutral pseudoscalars $P_{1,2}$. The Lagrangians describing Higgs boson interactions with leptons and gauge bosons can be found in [8].

Our further consideration will be based on the equations that relate the neutrino-oscillation parameters to the Yukawa coupling constants and the vacuum expectation values of the neutral components of the Higgs triplets ($v_{L,R}$) and bidoublet ($k_{1,2}$). In the two-flavor approximation, the choice of the basis $\Psi^T = (\nu^T_{aL}, N^T_{aR}, \nu^T_{bL}, N^T_{bR})$ involves representing the neutrino mass matrix in the form

$$\mathcal{M} = \begin{pmatrix} f_{aa}v_L & m^a_D & f_{ab}v_L & M_D \\ m^a_D & f_{aa}v_R & M'_D & f_{ab}v_R \\ f_{ab}v_L & M'_D & f_{bb}v_L & m^b_D \\ M_D & f_{ab}v_R & m^b_D & f_{bb}v_R \end{pmatrix}, \quad (2)$$

where

$$m^a_D = h_{aa}k_1 + h'_{aa}k_2, \quad (3)$$

$$M_D = h_{ab}k_1 + h'_{ab}k_2, \quad M'_D = h_{ba}k_1 + h'_{ba}k_2, \quad (4)$$

and $v_L \ll \max(k_1,k_2) \ll v_R$. Diagonalizing the matrix $\mathcal{M}$, we arrive at the relations [9]

$$\left.\begin{aligned} m^a_D &= c_{\varphi_a}s_{\varphi_a}(c^2_{\theta_N}m_{N_1} + s^2_{\theta_N}m_{N_2} \\ &- c^2_{\theta_\nu}m_{\nu_1} - s^2_{\theta_\nu}m_{\nu_2}), \\ m^b_D &= m^a_D(\varphi_a\to\varphi_b, \theta_{\nu,N}\to\theta_{\nu,N}+\pi/2), \end{aligned}\right\} \quad (5)$$

$$\left.\begin{aligned} M_D &= c_{\varphi_a}s_{\varphi_b}c_{\theta_\nu}s_{\theta_\nu}(m_{\nu_1} - m_{\nu_2}) \\ &+ s_{\varphi_a}c_{\varphi_b}c_{\theta_N}s_{\theta_N}(m_{N_2} - m_{N_1}), \\ M'_D &= M_D(\varphi_a\to\varphi_b), \end{aligned}\right\} \quad (6)$$

$$f_{ab}v_R = s_{\varphi_a}s_{\varphi_b}c_{\theta_\nu}s_{\theta_\nu}(m_{\nu_2} - m_{\nu_1}) \quad (7)$$
$$+ c_{\varphi_a}c_{\varphi_b}c_{\theta_N}s_{\theta_N}(m_{N_2} - m_{N_1}),$$

$$\left.\begin{aligned} f_{aa}v_R &= s^2_{\varphi_a}(c^2_{\theta_\nu}m_{\nu_1} + s^2_{\theta_\nu}m_{\nu_2}) \\ &+ c^2_{\varphi_a}(c^2_{\theta_N}m_{N_1} + s^2_{\theta_N}m_{N_2}), \\ f_{bb}v_R &= f_{aa}v_R(\varphi_a\to\varphi_b, \\ &\theta_{\nu,N}\to\theta_{\nu,N}+\pi/2), \end{aligned}\right\} \quad (8)$$

$$f_{ll'}v_L = f_{ll'}v_R(\varphi_{l,l'}\to\varphi_{l,l'}+\pi/2), \quad (9)$$
$$l,l' = a,b,$$

where φ_a is the mixing angle in the generation a between the light and heavy neutrinos, θ_ν (θ_N) is the mixing angle between the ν_{aL} neutrino and the ν_{bL} neutrino (N_{aR} and N_{bR}), $c_{\varphi_a} = \cos\varphi_a$, $s_{\varphi_a} = \sin\varphi_a$, etc.

3. BOUNDS ON THE MODEL PARAMETERS

3.1. $(g-2)_\mu$ Anomaly

The experiment that is devoted to measuring the anomalous magnetic moment of the muon and which is being performed at the Brookhaven National Laboratory (BNL) is presently one of the most precise experiments in microscopic physics. The latest result obtained for the anomalous magnetic moment of the positively charged muon was based on data accumulated within the year 2000 and is [10]

$$a^{\rm expt}_{\mu^+} = 116\,592\,040(70)(50)\times 10^{-11}\mu_0 \quad \text{(BNL'00)}, \quad (10)$$

where μ_0 is the muon magnetic moment predicted by Dirac theory. At the same time, the value obtained for the anomalous magnetic moment of the negatively

charged muon on the basis of data collected over the year 2001 is [11]

$$a_{\mu^-}^{\rm expt} = 11\,659\,214(8)(3) \times 10^{-10}\mu_0 \quad \text{(BNL'01)}. \tag{11}$$

We can see that the two results in question are virtually coincident, which is in excellent agreement with the CPT theorem. Thus, the present-day averaged value of $a_\mu^{\rm expt}$ is

$$a_\mu^{\rm expt} = 11\,659\,208(6) \times 10^{-10}\mu_0. \tag{12}$$

Both for BNL'00 and for BNL'01, the relative error is 0.7×10^{-6}, which is only two times greater than that which is planned at the final stage of the BNL-E-0821 experiment. It is obvious that, for a comparison of experimental and theoretical data to be successful, it is necessary that the muon anomalous magnetic moment be calculated to the same high degree of precision. First of all, this means that one must take into account the contributions from all sectors of the model used in these calculations. In other words, the expression for the muon anomalous magnetic moment in the Standard Model (or its extension) must involve three terms,

$$a_\mu^{\rm SM} = a_\mu^{\rm QED} + a_\mu^{\rm EW} + a_\mu^{\rm had}, \tag{13}$$

where the QED and electroweak contributions are given by (see [12] and references therein)

$$a_\mu^{\rm QED} = 116\,584\,705.7(2.9) \times 10^{-11}\mu_0, \tag{14}$$
$$a_\mu^{\rm EW} = 152(4) \times 10^{-11}\mu_0.$$

The quantity $a_\mu^{\rm had}$ is determined primarily by the virtual-hadron contributions to the photon propagator in the fourth and sixth orders, the lowest corrections leading to vacuum polarization by hadrons, $a_\mu^{\rm had}$(VP1). As to the sixth-order corrections, they include, in addition to vacuum polarization by hadrons, $a_\mu^{\rm had}$(VP2), the scattering of light by light, $a_\mu^{\rm had}$(LbyL). For $a_\mu^{\rm had}$(LbyL) and $a_\mu^{\rm had}$(VP2), we will employ the results presented in [13] and [14], respectively, while, for $a_\mu^{\rm had}$(VP1), we will take the value obtained on the basis of the latest data of the SMD-2 Collaboration that concern the analysis of the cross section $\sigma_{e^+e^-\to\text{hadrons}}$ [15]. For $a_\mu^{\rm SM}$, we then have

$$a_\mu^{\rm SM} = 11\,659\,181(8) \times 10^{-10}\mu_0. \tag{15}$$

We note that, if only data on τ decay to hadrons are used to determine $a_\mu^{\rm had}$(VP1), then

$$a_\mu^{\rm SM} = 11\,659\,196(8) \times 10^{-10}\mu_0. \tag{16}$$

A comparison of (15) and (16) with the experimental value $a_\mu^{\rm expt}$ (12) shows the disagreement of the theoretical and experimental results at the levels of 2.7σ and 1.4σ, respectively. In [16], $a_\mu^{\rm had}$(VP1) and $a_\mu^{\rm had}$(VP2) were calculated on the basis of almost all data obtained by that time. The resulting value of the muon anomalous magnetic moment is

$$a_\mu^{\rm SM} = 11\,659\,176.3(7.4) \times 10^{-10}\mu_0. \tag{17}$$

A comparison with (12) now leads to the deviation δa_μ equal to 2.8σ.

In the following, we will assume that the deviation δa_μ is due to the contributions from particles not present in the Standard Model. In the left–right model, this may be only Higgs bosons [8]. In studying the $(g-2)_\mu$ anomaly, it is usually assumed that new-physics effects are concealed in electroweak corrections exclusively. In our case, this means that $(a_\mu^{\rm QED} + a_\mu^{\rm had})^{\rm SM} = (a_\mu^{\rm QED} + a_\mu^{\rm had})^{\rm LRM}$, but that $(a_\mu^{\rm EW})^{\rm SM} \neq (a_\mu^{\rm EW})^{\rm LRM}$. Following [11], we assume that the disagreement between the Standard Model predictions and experimental data is at the level of 2.7σ. At a 90% C.L., $\delta a_\mu/\mu_0$ must then lie within the interval

$$42 \times 10^{-11} \le \frac{\delta a_\mu}{\mu_0} \le 398 \times 10^{-11}. \tag{18}$$

First, we assume that the observed value of the muon anomalous magnetic moment is due exclusively to the $h^{(-)}$-boson contribution. For m_h, we have [9]

$$m_h^2 = \alpha(v_R^2 + k_0^2) + \frac{\beta_1^2 k_+^2}{2(\alpha + \rho_1 - \rho_3/2)}, \tag{19}$$

where

$$\alpha = \frac{\alpha_3 k_+^2}{2k_-^2} = \frac{\alpha_3(1+\tan^2\beta)}{2(\tan^2\beta - 1)}, \quad k_0 = \frac{k_-^2}{\sqrt{2}k_+}.$$

Here, α_j, ρ_j, and β_j are constants that appear in the Yukawa potential; $\tan\beta = k_1/k_2$; and $k_\pm = k_1^2 \pm k_2^2$. From (19), it follows that the $h^{(-)}$-boson mass is on the electroweak scale if

$$\alpha \ll 1.$$

We will assume that mixing occurs in the $e\mu$ sector, in which case we set $a = e$ and $b = \mu$ in Eqs. (5)–(9). Feynman diagrams that contribute to the muon anomalous magnetic moment in the one-loop approximation are shown in Fig. 1. Disregarding amplitudes that are proportional to $\sin\xi$ (where ξ is the mixing angle in the sector of charged gauge bosons), we obtain a correction to the muon anomalous magnetic moment in the form

$$\delta a_\mu^{(h)} = \delta a_\mu^{(hh)} + \delta a_\mu^{(Wh)}, \tag{20}$$

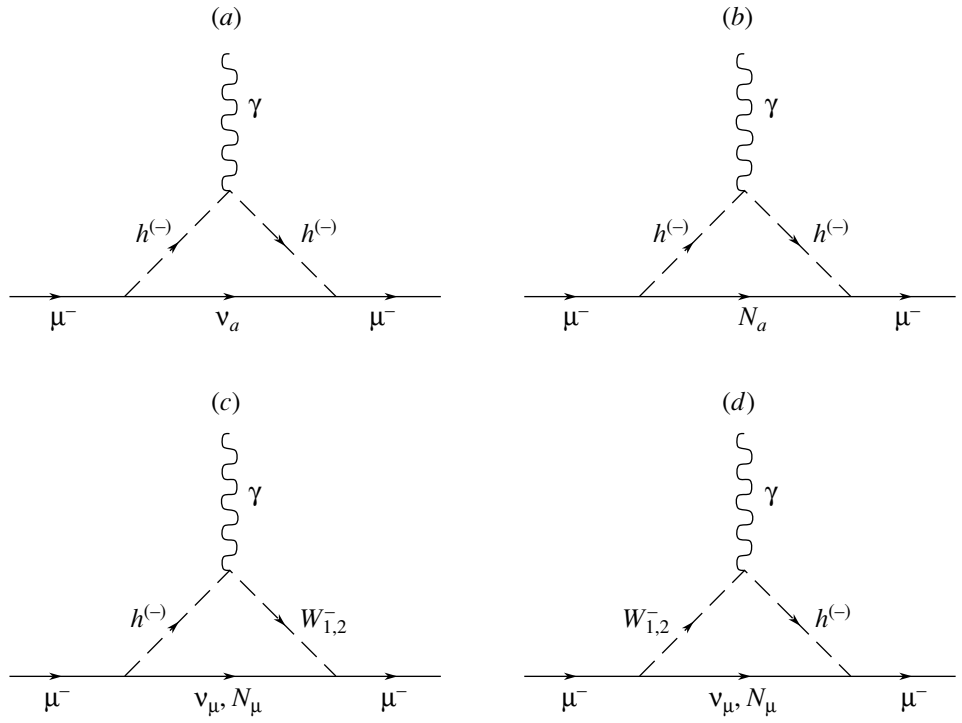

Fig. 1. Feynman diagrams involving $h^{(-)}$ bosons and making a contribution to the muon anomalous magnetic moment in the one-loop approximation.

where

$$\frac{\delta a_\mu^{(hh)}}{\mu_0} = \frac{1}{8\pi^2}\sum_{a=e,\mu}\left(\alpha^2_{\bar\mu N_a h} I^{hh}_{N_a} + \alpha^2_{\bar\mu \nu_a h} I^{hh}_{\nu_a}\right), \quad (21)$$

$$\frac{\delta a_\mu^{(Wh)}}{\mu_0} = \frac{(1-\rho_3/2+\rho_1)(\tan^2\beta-1)m_{W_1}}{16\sqrt{2}\pi^2(1+\tan^2\beta)} \times \left(s_\xi \alpha_{\bar\mu\nu_\mu h} I^{W_1 h} + c_\xi \alpha_{\bar\mu N_\mu h} I^{W_2 h}\right), \quad (22)$$

$$\alpha_{\bar l_a \nu_a h} = \frac{h'_{aa}k_2 - h_{aa}k_1}{2k_+} = \frac{1+\tan^2\beta}{2k_+(1-\tan^2\beta)} \times \left(-\frac{2m_{l_a}\tan\beta}{1+\tan^2\beta} + m_D^a\right), \quad (23)$$

$$\alpha_{\bar l_a N_a h} = \alpha_{\bar l_a \nu_a h}(m_{l_a} \leftrightarrow -m_D^a), \quad (24)$$

$$\alpha_{\bar l_a \nu_b h} = -\frac{M_D}{2k_+}, \quad \alpha_{\bar l_a N_b h} = -\frac{M_D\tan\beta}{k_+(1+\tan^2\beta)}, \quad a \neq b, \quad (25)$$

$$I_i^{hh} = \int_0^1 \frac{m_\mu^2(z^3-z^2)dz}{m_\mu^2 z^2 + (m_h^2 - m_i^2 - m_\mu^2)z + m_i^2}, \quad i = \nu_a, N_a, \quad I_i^{hh} < 0,$$

$$I^{W_1 h} = \frac{m_\mu}{m_{W_1}^2 - m_h^2}\left\{\ln\left(\frac{m_{W_1}^2}{m_h^2}\right) - \left[\int_0^1 \frac{z^2[m_\mu^2(2z-1) + m_{W_1}^2 - m_{\nu_\mu}^2]dz}{m_\mu^2 z^2 + (m_{W_1}^2 - m_{\nu_\mu}^2 - m_\mu^2)z + m_{\nu_\mu}^2} - (m_{W_1} \to m_h)\right]\right\},$$

$$I^{W_2 h} = I^{W_1 h}(m_{W_1} \to m_{W_2}, m_{\nu_\mu} \to m_{N_\mu}), \quad I^{W_k h} > 0.$$

We emphasize that, since the constant $\rho_1 - \rho_3/2$ determines the square of the $\tilde\delta^{(-)}$-boson mass,

$$m_{\tilde\delta}^2 = (\rho_3/2 - \rho_1)v_R^2 - \frac{\beta_1^2 k_+^2}{2(\alpha + \rho_1 - \rho_3/2)}, \quad (26)$$

the inequality $\rho_3/2 - \rho_1 > 0$ must hold. It follows that, if the expressions $1 + \rho_1 - \rho_3/2$ and $\tan^2\beta - 1$ have opposite signs, the contributions of the diagrams in Figs. 1*c* and 1*d* will be negative, which will prevent the explanation of the observed value of the muon anomalous magnetic moment. Thus, one must consider the regions $\tan^2\beta > 1$ and $\tan^2\beta < 1$ for, respectively, positive and negative values of $1 + \rho_1 - \rho_3/2$.

Prior to proceeding to analyze directly the $(g-2)_\mu$ anomaly, we must reduce arbitrariness in the choice of Higgs boson coupling constants. This can be achieved by expressing them in terms of quantities that are presently being studied in experiments. The quantities v_L and v_R, which appear in the coupling constants, present no problems. We can estimate v_L with the aid of ρ, comparing its theoretical value

$$\rho^{\text{theor}} = \frac{m_{Z_1}^2 c_{\theta_W}^2}{m_{W_1}^2} = \frac{1+4x}{1+2x} \tag{27}$$

[$x = (v_L/k_+)^2$, and θ_W is the Weinberg angle] with the experimental value

$$\rho^{\text{expt}} = 1.0107 \pm 0.0006. \tag{28}$$

In order to evaluate v_R, it is sufficient to use the relation

$$v_R = \sqrt{\frac{(m_{W_2}^2 - m_{W_1}^2)\cos 2\xi}{g_L^2}}, \tag{29}$$

which follows from the formulas that determine the masses of charged gauge bosons and their mixing angle. The Higgs boson coupling constants also involve the heavy-neutrino masses $m_{N_{1,2}}$. Although our problem here is to set bounds on precisely these quantities, we have to move in the opposite direction—that is, to assess roughly $m_{N_{1,2}}$ in one way or another and to employ the resulting estimates in determining the respective contribution to the muon anomalous magnetic moment.

For the heavy neutrino N_1, one can employ the bound

$$m_{N_1} > 63\ \text{GeV} \cdot \left(\frac{1.6\ \text{TeV}}{m_{W_2}}\right)^4, \tag{30}$$

which is known from the literature and which was obtained in studying neutrinoless double-beta decay. On the other hand, it follows from relations (8) and (9) that

$$f_{ee} + f_{\mu\mu} = \frac{m_{\nu_1} + m_{\nu_2} + m_{N_1} + m_{N_2}}{v_R + v_L}. \tag{31}$$

It is reasonable to assume that

$$0 < f_{ee} < 1, \quad 0 < f_{\mu\mu} < 1. \tag{32}$$

Considering that $m_{\nu_1},\ m_{\nu_2} \ll m_{N_1},\ m_{N_2}$, we then arrive at the inequality

$$0 < \left\{\frac{m_{N_1} + m_{N_2}}{v_R + v_L}\right\} < 2, \tag{33}$$

which, together with (27), (29), and (30), makes it possible to set bounds on m_{N_2}.

Further, we represent the mixing angles θ_N and $\varphi_{e,\mu}$ as functions of $f_{\mu\mu}$. The use of relations (8) and (9) yields the required formulas

$$s_{\theta_N}^2 = \frac{f_{\mu\mu}(v_R + v_L) - (m_{\nu_1} s_{\theta_\nu}^2 + m_{\nu_2} c_{\theta_\nu}^2) - m_{N_2}}{m_{N_1} - m_{N_2}}, \tag{34}$$

$$\sin(2\varphi_e) = \frac{2\sqrt{f_{ee}^2 v_R v_L - [f_{ee}(v_R + v_L) - m_{\nu_1} c_{\theta_\nu}^2 - m_{\nu_2} s_{\theta_\nu}^2](m_{\nu_1} c_{\theta_\nu}^2 + m_{\nu_2} s_{\theta_\nu}^2)}}{f_{ee}(v_R + v_L) - 2(m_{\nu_1} c_{\theta_\nu}^2 + m_{\nu_2} s_{\theta_\nu}^2)}, \tag{35}$$

$$\sin(2\varphi_\mu) = \sin(2\varphi_e)\,(f_{ee} \to f_{\mu\mu}, \theta_\nu \to \theta_\nu + \pi/2), \tag{36}$$

where, in accordance with experimental data, the parameters of the light-neutrino sector are set to

$$\tan^2\theta_\nu = 0.34, \quad m_{\nu_1} = 0.5\ \text{eV},$$
$$m_{\nu_2} = 0.5 + 7 \times 10^{-2}\ \text{eV}.$$

Thus, we can express the Higgs boson coupling constants in terms of the triplet Yukawa coupling constant $f_{\mu\mu}$ and the quantities $m_{N_{1,2}}$ and $v_{L,R}$. Since we require fulfillment of the condition

$$0 \le \theta_N \le \pi/2, \tag{37}$$

the regions of allowed values of $f_{\mu\mu}$ will be different here for each set of $m_{N_{1,2}}$ and $v_{L,R}$.

Let us assume that m_{W_2} is equal to 0.8 TeV. As to the mixing angle ξ, we henceforth set it to 10^{-2}. We will specify the heavy-neutrino masses and the triplet Yukawa coupling constant $f_{\mu\mu}$. We note that, within this approach, the value of $f_{\mu\mu}$ will affect only the angle θ_N. An analysis then reveals that, as m_h is varied from 100 to 200 GeV, the $h^{(-)}$-boson contribution becomes commensurate with $\delta a_\mu/\mu_0$ only if $\tan\beta$ is close to unity and if v_L is about several gigaelectronvolts.

Let us now proceed to discuss corrections to the muon anomalous magnetic moment that are associated with the neutral Higgs bosons. We note that,

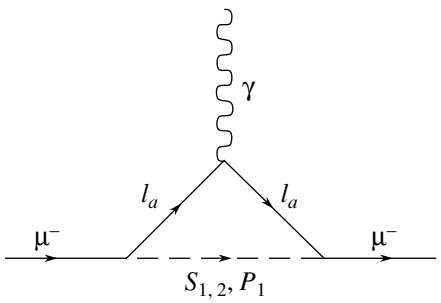

Fig. 2. Feynman diagrams involving neutral Higgs bosons and contributing to the muon anomalous magnetic moment.

since

$$m^2_{S_2} = \frac{\alpha_2 k_+^2}{k_1 k_2} v_R^2 - \frac{4k_1 k_2 k_-^4 [2(2\lambda_2+\lambda_3)k_1 k_2/k_+^2 - \lambda_4]^2}{\alpha_2 k_+^2 v_R^2}, \tag{38}$$

$$m^2_{P_1} = \frac{\alpha_2 k_+^2}{k_1 k_2} v_R^2 + 2k_+^2(\lambda_3 - 2\lambda_2), \tag{39}$$

S_2 and P_1 bosons have close masses. For the masses of these bosons to be on the electroweak scale, not only must we require fulfillment of the condition $\alpha_2 k_+^2/(k_1 k_2) \sim 10^{-2}$, but we must also use, in the quark sector, a Yukawa Lagrangian that does not induce, at the tree level, flavor-violating neutral currents [9].

The correction to the muon anomalous magnetic moment from the diagrams in Fig. 2 is given by

$$\frac{\delta a_\mu^n}{\mu_0} = \frac{1}{8\pi^2}\sum_a \left[\alpha^2_{\bar{\mu} l_a S_1} I^{S_1}_{l_a} + \alpha^2_{\bar{\mu} l_a S_2} I^{S_2}_{l_a} + \alpha^2_{\bar{\mu} l_a P_1} I^{P_1}_{l_a}\right], \tag{40}$$

where

$$I^{S_j}_{l_a} = \int_0^1 \frac{m_\mu[m_\mu(z^2-z^3)+m_{l_a}z^2]dz}{m_\mu^2(z^2-z)+m^2_{S_j}(1-z)+m^2_{l_a}z},$$

$$j = 1,2, \quad I^{S_j}_{l_a} > 0,$$

$$I^{P_1}_{l_a} = \int_0^1 \frac{m_\mu[m_\mu(z^2-z^3)-m_{l_a}z^2]dz}{m_\mu^2(z^2-z)+m^2_{P_1}(1-z)+m^2_{l_a}z},$$

$$I^{P_1}_{l_a} < 0,$$

$$\alpha_{\bar{l}_a l_b S_1} = -\sqrt{2}\alpha_{\bar{l}_a N_b h}, \tag{41}$$

$$\alpha_{\bar{l}_a l_a S_2} = -\frac{h_{aa}k_1 + h'_{aa}k_2}{\sqrt{2}k_+} = -\frac{m_D^a}{\sqrt{2}k_+}, \tag{42}$$

$$\alpha_{\bar{l}_a l_a P_1} = -\frac{h_{aa}k_1 - h'_{aa}k_2}{\sqrt{2}k_+} = \frac{1}{\sqrt{2}k_+(1-\tan^2\beta)}\left[m_D^a(\tan^2\beta+1) - 2m_{l_a}\tan\beta\right], \tag{43}$$

$$\alpha_{\bar{l}_a l_b S_2} = -\frac{h_{ab}k_1 + h'_{ab}k_2}{\sqrt{2}k_+} = \frac{M_D(\tan^2\beta-1)}{\sqrt{2}k_+(\tan^2\beta+1)}, \tag{44}$$

$$a \neq b,$$

$$\alpha_{\bar{l}_a l_b P_1} = -\frac{h_{ab}k_1 - h'_{ab}k_2}{\sqrt{2}k_+} = -\frac{M_D}{\sqrt{2}k_+}, \tag{45}$$

$$a \neq b.$$

Here, the mixing angle in the sector of the S_1 and S_2 bosons has been set to zero.

We will now determine the contributions from each of the neutral Higgs bosons to the muon anomalous magnetic moment. It turns out that only for $\tan\beta$ close to unity can the values of the anomalous magnetic moment within the range in (18) be explained by the contribution from the S_1 boson of mass ranging between 115 and 200 GeV. In this case, there are two regions of $\tan\beta$, $\tan^2\beta > 1$ and $\tan^2\beta < 1$, that ensure agreement between theoretical and experimental results.

As to the S_2 boson, its contribution to the muon anomalous magnetic moment is negligible owing to the smallness of the coupling constants $\alpha_{\bar{\mu} l_a S_2}$. In turn, the contribution from the P_1 boson is negative and, at identical values of variable parameters, is virtually equal in magnitude to the contribution from the S_1 boson. All this gives sufficient grounds to assume that, in a rough approximation, the contributions to the muon anomalous magnetic moment from the S_1, S_2, and P_1 bosons are mutually canceled. Of course, there is yet another case—that of $\tan\beta$ markedly different from unity—where one can disregard the contributions from neutral bosons.

Further, we will discuss the version that explains the observed value of the muon anomalous magnetic moment by the corrections from the $\Delta^{(--)}_{1,2}$ and $\tilde{\delta}^{(-)}$ bosons. From Eq. (26) and from the relations

$$m^2_{\Delta_1} = 2\rho_2 v_R^2 + \frac{\alpha_3 k_-^2}{2} + \frac{k_-^4(\beta_3 k_+^2 + \beta_1 k_1 k_2)^2}{2k_1^4(4\rho_2+\rho_3-2\rho_1)v_R^2}, \tag{46}$$

$$m^2_{\Delta_2} = (\rho_3/2-\rho_1)v_R^2 + \frac{\alpha_3 k_-^2}{2} - \frac{k_-^4(\beta_3 k_+^2 + \beta_1 k_1 k_2)^2}{2k_1^4(4\rho_2+\rho_3-2\rho_1)v_R^2}, \tag{47}$$

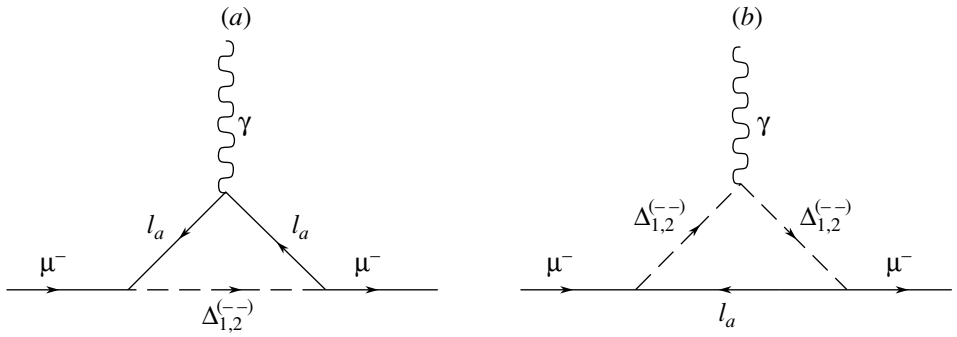

Fig. 3. Diagrams inducing corrections to the muon anomalous magnetic moment from $\Delta^{(--)}_{1,2}$ bosons.

it follows that the masses of the $\Delta^{(--)}_2$ and $\tilde{\delta}^{(-)}$ bosons may be rather close to each other and that, for the masses of all three bosons being considered to be on the electroweak scale, the following conditions must be satisfied:

$$\rho_2 \ll 1, \quad \rho_3/2 - \rho_1 \ll 1. \tag{48}$$

The diagrams inducing corrections to the muon anomalous magnetic moment from the $\Delta^{(--)}_{1,2}$ bosons are depicted in Fig. 3, while the analogous diagrams for the $\tilde{\delta}^{(-)}$ boson are obtained from the diagrams in Fig. 1 upon the substitution $h^{(-)} \to \tilde{\delta}^{(-)}$. As before, we disregard the amplitudes associated with the diagrams proportional to $\sin\xi$, whereupon the dominant contribution to the muon anomalous magnetic moment reduces to the form

$$\frac{\delta a_\mu^{cH}}{\mu_0} = \frac{1}{8\pi^2}\Bigg[4f_{\mu e}^2\sum_{i=1}^{2} I_e^{\Delta_i} + f_{\mu\mu}^2\sum_{i=1}^{2} I_\mu^{\Delta_i} + \sum_{b=e,\mu}\left(\frac{1}{2}f_{\mu b}^2 I_{\nu_b}^{\tilde{\delta}\tilde{\delta}} + \alpha_{\bar{\mu}N_b\tilde{\delta}}^2 I_{N_b}^{\tilde{\delta}\tilde{\delta}}\right) + f_{\mu\mu}\Bigg(-\frac{\beta_1 s_\xi m_{W_1}}{4} I^{W_1\tilde{\delta}} + \frac{\beta_1^2 m_{W_1}^2 c_\xi(\tan^2\beta - 1)}{2\alpha_3 g_L(\tan^2\beta + 1)v_R} I^{W_2\tilde{\delta}}\Bigg)\Bigg], \tag{49}$$

where

$$I_{l_a}^{\Delta_i} = \int_0^1 \left[\frac{2m_\mu^2(z^2 - z^3)}{m_\mu^2(z^2 - z) + m_{\Delta_i}^2 z + m_{l_a}^2(1 - z)} + \frac{m_\mu^2(z^2 - z^3)}{m_\mu^2(z^2 - z) + m_{\Delta_i}^2(1 - z) + m_{l_a}^2 z}\right] dz, \tag{50}$$

$$I_{l_a}^{\Delta_i} > 0, \quad I_i^{\tilde{\delta}\tilde{\delta}} = I_i^{hh}(m_h \to m_{\tilde{\delta}}),$$

$$I^{W_k\tilde{\delta}} = I^{W_k h}(m_h \to m_{\tilde{\delta}}),$$

$$k = 1, 2, \quad \alpha_{\bar{l}_a N_b\tilde{\delta}} = \frac{f_{ab}\beta_1 k_+}{(\alpha_3 k_+^2/k_-^2 + 2\rho_1 - \rho_3)v_R}.$$

Since $I^{W_k\tilde{\delta}} > 0$, the contribution to the muon anomalous magnetic moment from the last two terms on the right-hand side of (49) will also be positive if the coefficients in front of them are positive. From the condition $\alpha > 0$, it follows that

$$\frac{\alpha_3}{\tan^2\beta - 1} > 0;$$

that is, the last term on the right-hand side of (49) is always possible. The coefficient of $I^{W_1\tilde{\delta}}$ is positive under the condition that s_ξ and β_1 have opposite signs.

In our calculations, there now appears the triplet Yukawa coupling constant $f_{e\mu}$. By using relations (7) and (9), we obtain

$$f_{e\mu}^2 v_R v_L \approx \frac{1}{4}\sin(2\varphi_e)\sin(2\varphi_\mu)c_{\theta_N}^2 s_{\theta_N}^2 \times (m_{N_2} - m_{N_1})^2 = \frac{1}{4}\sin(2\varphi_e)\sin(2\varphi_\mu) \times [f_{\mu\mu}(v_R + v_L) - m_{\nu_1}s_{\theta_\nu}^2 - m_{\nu_2}c_{\theta_\nu}^2 - m_{N_2}] \times [f_{ee}(v_R + v_L) - m_{\nu_1}c_{\theta_\nu}^2 - m_{\nu_2}s_{\theta_\nu}^2 - m_{N_2}], \tag{51}$$

where we have assumed that the mass spectrum of light neutrinos is degenerate.

First, we assume that the masses of the $\Delta^{(--)}_2$ and $\tilde{\delta}^{(-)}$ bosons are on the electroweak scale, but that m_{Δ_1} is beyond it. We fix the model parameters as follows:

$$m_{W_2} = 2500\ \text{GeV}, \quad m_{\tilde{\delta}} = 1.2m_{\Delta_2}, \quad \tan\beta = 2.34, \quad \alpha_3 = -\beta_1 = 1.$$

We note that, since, in (49), $\tan\beta$ appears only in the last term, whose contribution to the muon anomalous magnetic moment is negligible, the value of $\tan\beta$ does not play any significant role in the situation

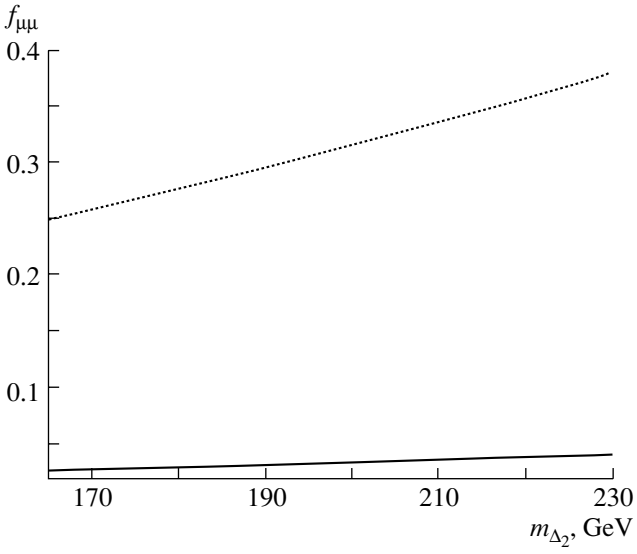

Fig. 4. Curves representing the boundaries of the region of allowed values of $f_{\mu\mu}$ and m_{Δ_2} for the case where the muon anomalous magnetic moment is determined by the contributions from the $\tilde{\delta}^{(-)}$ and $\Delta_2^{(--)}$ bosons.

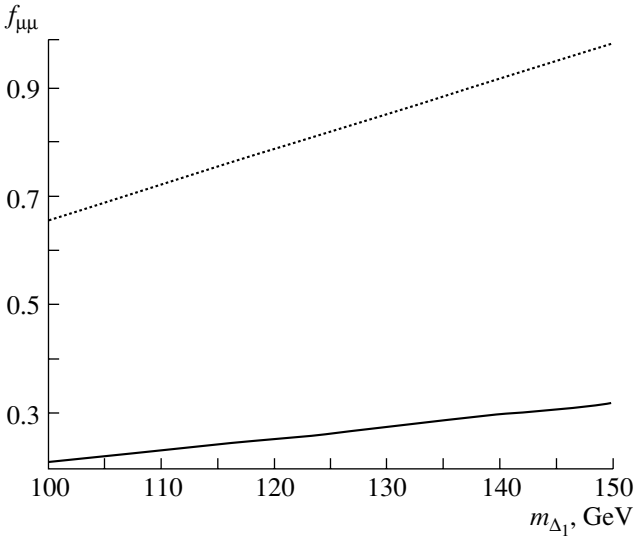

Fig. 5. Curves representing the boundaries of the region of allowed values of $f_{\mu\mu}$ and m_{Δ_1} for the case where the muon anomalous magnetic moment is determined by the contribution from the $\Delta_1^{(--)}$ boson and where the heavy-neutrino masses are degenerate.

being considered. By virtue of relation (31), the triplet Yukawa coupling constant $f_{\mu\mu}$ is determined primarily by v_R and $m_{N_{1,2}}$. Thus, we see that, at fixed v_R, curves of $f_{\mu\mu}(m_{\Delta_2})$ for different values of m_{N_1} and m_{N_2} will correspond to the $\delta a_\mu/\mu_0$ values of 42×10^{-11} and 398×10^{-11} in the $(f_{\mu\mu}, m_{\Delta_2})$ plane.

For the parameters of the left–right model, Fig. 4 illustrates the possible sets explaining the observed value of the muon anomalous magnetic moment by the contributions from $\tilde{\delta}^{(-)}$ and $\Delta_2^{(--)}$ bosons. Here, the solid curve $f_{\mu\mu}(m_{\Delta_2})$ for which $m_{N_1} = 100$ GeV and $m_{N_2} = 160$ GeV corresponds to the maximum value of $\delta a_\mu/\mu_0$, while the dotted curve for which $m_{N_1} = 900$ GeV and $m_{N_2} = 1500$ GeV corresponds to the minimum value of $\delta a_\mu/\mu_0$.

Since, in the case being considered, we have a large number of parameters that determine the muon anomalous magnetic moment, it is impossible to obtain unambiguous information about $f_{\mu\mu}$ and $m_{\tilde{\delta}}$. The situation remains unchanged in the case where the $\tilde{\delta}^{(-)}$-boson contribution is dominant. Information about the model parameters becomes less ambiguous if the masses of $\Delta_2^{(--)}$ and $\tilde{\delta}^{(-)}$ bosons (and of $S_{1,2}$, P_1, and $h^{(-)}$ bosons as well) are high and if m_{Δ_1} is on the electroweak scale. It then follows that the contribution to the muon anomalous magnetic moment will be induced only by the diagrams involving virtual $\Delta_1^{(--)}$ bosons and that the muon anomalous magnetic moment will be a function of the parameters m_{Δ_1}, $f_{\mu\mu}$, and $m_{N_{1,2}}$. In the case of mass degeneracy in the heavy-neutrino sector, the triplet Yukawa coupling constant $f_{e\mu}$ vanishes, with the result that $\delta a_\mu/\mu_0$ becomes independent of $m_{N_{1,2}}$. The solid and dotted curves corresponding to this case that are associated with the $\delta a_\mu/\mu_0$ values of 398×10^{-11} and 42×10^{-11} are shown in Fig. 5.

3.2. Lepton-Flavor-Violating Processes

We will now continue our analysis of bounds on the Higgs boson coupling constants, employing, for this purpose, results of searches for reactions involving the violation of an individual lepton flavor. We consider muon decay through the channel

$$\mu^- \to e^+ e^- e^-. \tag{52}$$

In the left–right model, this process proceeds in the second order of perturbation theory. It is described by the diagrams in Fig. 6. In the case of unpolarized initial- and final-state particles, the decay probability is given by

$$\Gamma_{\mu^- \to e^+ e^- e^-} = \frac{d m_\mu^5}{96(4\pi)^3}, \tag{53}$$

where

$$d = (f_{e\mu} f_{ee})^2 [m_{\Delta_1}^{-4} + m_{\Delta_2}^{-4}]$$

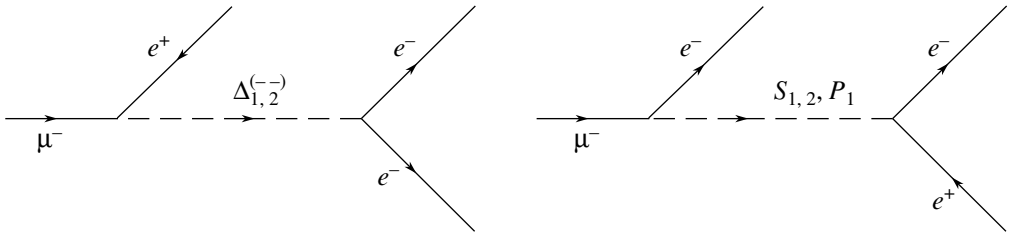

Fig. 6. Feynman diagrams describing muon decay through the channel $\mu^- \to e^+e^-e^-$.

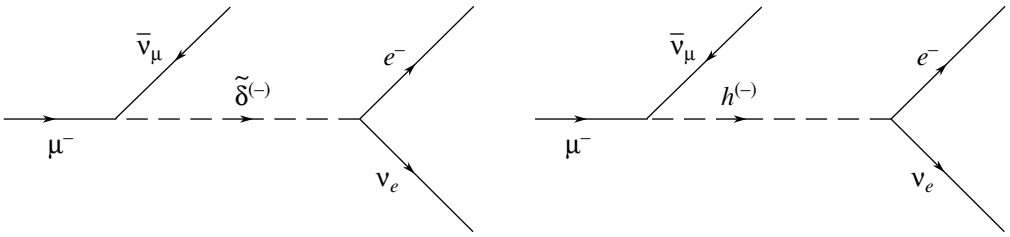

Fig. 7. Feynman diagrams for the process $\mu^- \to e^-\nu_e\bar{\nu}_\mu$.

$$+8\left[\left(\frac{\alpha_{\bar{\mu}eS_1}\alpha_{\bar{e}eS_1}}{m^2_{S_1}}+\frac{\alpha_{\bar{\mu}eS_2}\alpha_{\bar{e}eS_2}}{m^2_{S_2}}\right)^2+\frac{(\alpha_{\bar{\mu}eP_1}\alpha_{\bar{e}eP_1})^2}{m^4_{P_1}}\right]+\left(\frac{\alpha_{\bar{\mu}eS_1}\alpha_{\bar{e}eS_1}}{m^2_{S_1}}+\frac{\alpha_{\bar{\mu}eS_2}\alpha_{\bar{e}eS_2}}{m^2_{S_2}}+\frac{\alpha_{\bar{\mu}eP_1}\alpha_{\bar{e}eP_1}}{m^2_{P_1}}\right)^2.$$

Considering that, according to experimental data, the branching ratio for reaction (52) is constrained as

$$\mathrm{Br}_{\mu^-\to e^+e^-e^-}=\frac{\Gamma_{\mu^-\to e^+e^-e^-}}{\Gamma_{\mu^-\to\,\mathrm{all}}}<10^{-12},$$

we then obtain the inequality

$$\sqrt{d}<6.6\times10^{-11}\ \mathrm{GeV}^{-2}. \tag{54}$$

If one disregards the contributions from neutral Higgs bosons, the inequality in (54) yields an exaggerated bound on the triplet Yukawa coupling constant [17]:

$$f_{e\mu}f_{ee}\sqrt{m^{-4}_{\Delta_1}+m^{-4}_{\Delta_2}}<6.6\times10^{-11}\ \mathrm{GeV}^{-2}. \tag{55}$$

Further, we proceed to analyze the decay

$$\mu^-\to e^-\nu_e\bar{\nu}_\mu. \tag{56}$$

The diagrams corresponding to this process in the second order of perturbation theory are shown in Fig. 7. Assuming that the initial- and final-state particles are not polarized, we arrive at the result

$$\Gamma_{\mu^-\to e^-\nu_e\bar{\nu}_\mu}=\frac{m^5_\mu}{96(2\pi)^3}\times\left[4\frac{\alpha^2_{\bar{e}\nu_eh}\alpha^2_{\bar{\mu}\nu_\mu h}+\alpha^4_{\bar{\mu}\nu_eh}}{m^4_h}+\frac{f^2_{ee}f^2_{\mu\mu}+f^4_{e\mu}}{m^4_{\tilde{\delta}}}\right]. \tag{57}$$

By comparing the result obtained here for the probability of the decay in (56) with the total muon-decay probability

$$\Gamma_{\mu^-\to\mathrm{all}}=\frac{G^2_\Gamma m^5_\mu}{192\pi^3}$$

and taking into account the experimental value

$$\mathrm{Br}_{\mu^-\to e^-\nu_e\bar{\nu}_\mu}<1.2\times10^{-2}, \tag{58}$$

we obtain the inequality

$$4\frac{\alpha^2_{\bar{e}\nu_eh}\alpha^2_{\bar{\mu}\nu_\mu h}+\alpha^4_{\bar{\mu}\nu_eh}}{m^4_h}+\frac{f^2_{ee}f^2_{\mu\mu}+f^4_{e\mu}}{m^4_{\tilde{\delta}}}<0.65\times10^{-11}\ \mathrm{GeV}^{-4}. \tag{59}$$

Since the inequality in (59) does not involve interference terms, it can be used to obtain exaggerated bounds both on the $h^{(-)}$-boson coupling constants $\alpha_{\bar{l}_a\nu_bh}$ and on the $\tilde{\delta}^{(-)}$-boson coupling constants f_{ab}.

We will also discuss muon decay through the channel

$$\mu^-\to e^-\gamma. \tag{60}$$

In analyzing this process, it was found in [17] that

$$\frac{f_{ee}f_{\mu\mu}}{m^2_\Delta}<2\times10^{-10}\ \mathrm{GeV}^{-2}, \tag{61}$$

where m_Δ stands for the mass of the lightest doubly charged Higgs boson. This process proceeds in the third order of perturbation theory. The corresponding

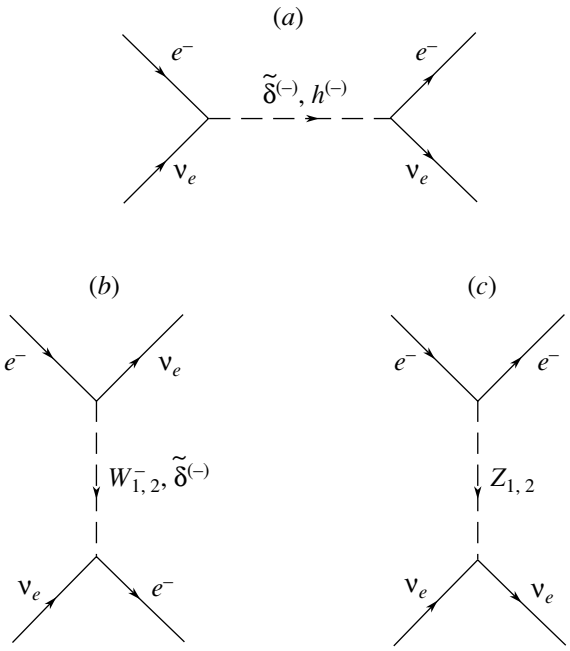

Fig. 8. Feynman diagrams for the process $\nu_e e \to \nu_e e$.

Feynman diagrams can be obtained from the diagrams in Figs. 1–3 by replacing the final-state muon by an electron. Obviously, the authors of [17] took into account only the diagram in Fig. 3*a*. On the other hand, calculations reveal that the amplitudes of the diagrams in Figs. 1–3 have different signs, so that there occurs interference upon squaring them. This in turn means that the boundaries that are determined by the inequality in (61) are quite arbitrary. The same conclusion can be drawn for the boundaries obtained by studying the cross section for Bhabha scattering in [17]:

$$\frac{f_{ee}^2}{m_\Delta^2} < 9.7 \times 10^{-6}\ \mathrm{GeV}^{-2}. \qquad (62)$$

As was shown in [8], the cross section for the process in (60) also receives a contribution from the diagrams involving virtual gauge bosons Z_2 and Higgs bosons S_1, S_2, and P_1. The situation is perfectly analogous for the boundaries found in searches for the muonium–antimuonium transition in [17]:

$$\frac{f_{ee} f_{\mu\mu}}{m_\Delta^2} < 5.8 \times 10^{-5}\ \mathrm{GeV}^{-2}. \qquad (63)$$

In addition to the diagrams involving $\Delta_{1,2}^{(--)}$-boson exchange, there are indeed diagrams involving S_1-, S_2-, and P_1-boson exchanges in that case inclusive [9].

3.3. Low-Energy Neutrino Scattering on Charged Leptons

Let us consider elastic antineutrino scattering on an electron,

$$\bar\nu_e e^- \to \bar\nu_e e^-. \qquad (64)$$

Within the Standard Model, this process proceeds both owing to neutral and owing to charged currents. It is obvious that, in order to establish conclusively the $V-A$ structure of the charged-current Lagrangian $\mathcal{L}_{\bar e \nu_e W}$ and the Lagrangian $\mathcal{L}_{\bar\nu_e \nu_e Z}$ describing neutrino interaction with the Z boson, it is necessary to detect all final-state particles simultaneously. Since present-day experimental techniques give no way to perform such measurements, we cannot state without reservations that the Lagrangians $\mathcal{L}_{\bar e \nu_e W}$ and $\mathcal{L}_{\bar\nu_e \nu_e Z}$ do indeed have a $V-A$ form. In other words, we cannot rule out the possibility that the neutrinos feature interactions beyond the Standard Model (nonstandard interactions).

In searches for nonstandard neutrino interactions in elastic scattering on electrons, one sometimes introduces phenomenological parameters ϵ_{aL} and ϵ_{aR} ($a = e, \mu, \tau$) that characterize the strength of nonstandard interaction with respect to G_F. In this case, the nonstandard neutrino interaction at low energies is described by a contact four-fermion Lagrangian of the form

$$-\mathcal{L}_\mathrm{NSI} = 2\sqrt{2} G_\mathrm{F} \bar\nu_a(x)\gamma_\sigma P_L \nu_a(x) \qquad (65)$$
$$\times [\epsilon_{aR} \bar e(x)\gamma^\sigma P_R e(x) + \epsilon_{aL} \bar e(x)\gamma^\sigma P_L e(x)],$$

where $P_{L,R} = (1 \pm \gamma_5)/2$.

The most precise determination of the cross section for the process

$$\nu_e e \to \nu_e e \qquad (66)$$

was performed by the LSND Collaboration [18]. One of the earliest measurements of the cross section for elastic reactor-antineutrino scattering on electrons [19],

$$\bar\nu_e e^- \to \bar\nu_e e^-, \qquad (67)$$

has so far remained the most precise. An analysis of reactions (66) and (67) in terms of the Lagrangian in (65) yields wide regions for ϵ_{eL} and ϵ_{eR} values at which the strength of nonstandard neutrino interactions may be as high as about two [20].

However, the above parametrization unfortunately is not general. For the example of the left–right model, we will show that it does not cover all possible types of nonstandard neutrino interactions. For the reactions in (66) and (67), both gauge bosons ($Z_{1,2}$ and $W_{1,2}^{(\pm)}$) and Higgs bosons ($h^{(\pm)}, \tilde\delta^{(\pm)}$) may be a source of nonstandard interactions.

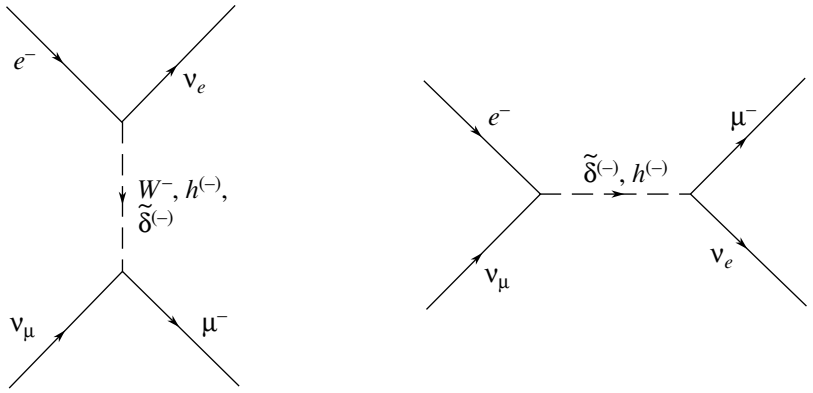

Fig. 9. Feynman diagrams for inverse muon decay.

Within the left–right model, the process in (66) is described by the Feynman diagrams in Fig. 8. The gauge bosons $Z_{1,2}$ induce the following correction to the contact Lagrangian in (65):

$$\Delta\mathcal{L}_{\rm NSI} = \frac{g_L^2}{2\sqrt{\cos(2\theta_{\rm W})}}\left[\frac{\xi}{m_{Z_1}^2} - \frac{1}{m_{Z_2}^2}\right] \times \bar\nu_a(x)\gamma_\sigma\gamma_5\nu_a(x)[\epsilon_{aR}\bar e(x)\gamma_\sigma P_R e(x) + \epsilon_{aL}\bar e(x)\gamma_\sigma P_L e(x)]. \quad (68)$$

In the low-energy limit, the amplitudes corresponding to the diagrams in Fig. 8*a* have the form

$$\mathcal{M}^b = \frac{\alpha^2_{\bar e\nu_e h}}{m_h^2}\bar\nu_e(x)(1-\gamma_5)e(x)\bar e(x)(1+\gamma_5)\nu_e(x), \quad (69)$$

$$\mathcal{M}^c = \frac{f_{ee}^2}{2m_{\tilde\delta^2}}\overline{e^c}(x)(1+\gamma_5)\nu_e(x)\bar\nu_e(x)(1-\gamma_5)e^c(x). \quad (70)$$

Performing the Fierz transformation in (69) and (70), we obtain

$$\mathcal{M}^b + \mathcal{M}^c = \bar\nu_e(x)\gamma_\sigma(1-\gamma_5)\nu_e(x) \times \left[\frac{\alpha^2_{\bar e\nu_e h}}{m_h^2}\bar e(x)\gamma^\sigma(1+\gamma_5)e(x) + \frac{f_{ee}^2}{2m_{\tilde\delta}^2}\overline{e^c}(x)\gamma^\sigma(1+\gamma_5)e^c(x)\right]. \quad (71)$$

Thus, the parametrization in (65) does not cover the case of singly charged Higgs bosons.

A more general parametrization for describing low-energy neutrino scattering on charged leptons was proposed in [21]. With the aid of this parametrization, the amplitude for the process

$$\nu_a l_b \to l_a \nu_b \quad (72)$$

can be represented in the form

$$\mathcal{M} = \frac{4G_{\rm F}}{\sqrt{2}}\sum_{\gamma=S,V,T}\sum_{\lambda,\lambda'=R,L} g^\gamma_{\lambda\lambda'}\langle\bar l_{b\lambda}|\Gamma_\gamma|\nu_{bn}\rangle \times \langle\bar\nu_{am}|\Gamma_\gamma|l_{a\lambda'}\rangle, \quad (73)$$

where the index γ fixes the type of interaction ($\Gamma_S = 1$, $\Gamma_V = \gamma_\mu$, and $\Gamma_T = \sigma_{\mu\nu}/\sqrt{2}$ correspond to scalar, vector, and tensor interactions), the indices λ and λ' specify the helicities of the charged leptons involved, and the indices n and m are those of ν_b and ν_a. Nine complex-valued amplitudes $g^\gamma_{\lambda\lambda'}$ and $G_{\rm F}$ form the set of 19 independent real-valued parameters to be determined experimentally.

If, by convention, the decay

$$\mu^- \to e^-\bar\nu_e\nu_\mu \quad (74)$$

is referred to as muon decay, then the term "inverse muon decay" can be used for the process

$$\nu_\mu e^- \to \mu^-\nu_e. \quad (75)$$

Within the left–right model, where the process in (75) is described by the diagrams in Fig. 9, the following amplitudes are different from zero: g^V_{LL}, g^V_{RR}, g^S_{LL}, and g^S_{RR}. At a 90% C.L., the existing experimental bounds on them are [22]

$$|g^V_{LL}| > 0.96, \quad |g^V_{RR}| < 0.033, \quad |g^S_{LL}| < 0.55, \quad |g^S_{RR}| < 0.066. \quad (76)$$

By using the explicit expression for the inverse-muon-decay matrix element and the inequalities in (76), we obtain (all quantities are taken in GeV^{-2} units)

$$\frac{\alpha_{\bar\nu_e e h}\alpha_{\bar\nu_\mu\mu h}}{m_h^2} < 0.54\times10^{-6}, \quad (77)$$

$$\frac{\alpha^2_{\bar\nu_e\mu h}}{m_h^2} < 0.66\times10^{-6}, \quad (78)$$

$$\frac{f_{ee}f_{\mu\mu}}{m^2_{\tilde{\delta}}} < 0.907 \times 10^{-5}, \quad (79)$$

$$\frac{f^2_{e\mu}}{m^2_{\tilde{\delta}}} < 0.109 \times 10^{-5}. \quad (80)$$

4. PARAMETERS OF HEAVY-NEUTRINO OSCILLATIONS

The results of the preceding section lead to the conclusion that relations (55), (59), and (77)–(80) provide the less ambiguous bounds on the parameters of the Higgs sector. From the point of view of practical applications, the inequalities that involve the triplet Yukawa coupling constants f_{ab} are more convenient since they do not contain $\tan\beta$. Two scenarios are possible if one employs upper bounds in the inequalities presented above. In the first scenario, the $\tilde{\delta}^{(-)}$-boson mass is on the electroweak scale, while the $\Delta^{(--)}_{1,2}$-boson masses are beyond it. From relations (46) and (47), it follows that, in order to render $\Delta^{(--)}_{1,2}$ bosons heavy, it is sufficient to require fulfillment of the conditions

$$\rho_3/2 - \rho_1 \sim 1, \quad \rho_2 \sim 1. \quad (81)$$

However, the $\tilde{\delta}^{(-)}$-boson mass can be made to remain on the electroweak scale only via a fine tuning of the constants that appear in the Higgs potential—that is, only if

$$\frac{\rho_1 - \rho_3/2 + \alpha_3 k^2_+/(2k^2_-)}{\beta^2_1} \approx 10^{-2}. \quad (82)$$

Within this scenario, a simultaneous fulfillment of the equalities in (55) and (79) can be ensured even at rather large values of $f_{e\mu}$.

In the second scenario, both $m_{\tilde{\delta}}$ and m_{Δ_2} are on the electroweak scale (the value of m_{Δ_1} does not play a significant role). From (55), it follows that $f_{e\mu}$ is negligible in this case.

Two roots of Eq. (51) are given by

$$(m_{N_1})_{1,2} = \frac{1}{2}[(f_{ee} + f_{\mu\mu})(v_R + v_L) - (m_{\nu_1} + m_{\nu_2})] \pm \Omega, \quad (83)$$

where

$$\Omega = \sqrt{\frac{1}{4}\left[(f_{ee} + f_{\mu\mu})(v_R + v_L) - m_{\nu_1} - m_{\nu_2}\right]^2 - f_{ee}f_{\mu\mu}(v_R + v_L)^2 + \frac{4f^2_{e\mu}v_R v_L}{\sin(2\varphi_e)\sin(2\varphi_\mu)}}. \quad (84)$$

Combining this expression with Eq. (31), we obtain

$$(m_{N_2})_{1,2} = \frac{1}{2}[(f_{ee} + f_{\mu\mu})(v_R + v_L) - (m_{\nu_1} + m_{\nu_2})] \mp \Omega. \quad (85)$$

At $m_{\nu_1} = m_{\nu_2} \approx 0$, the expression for Ω is simplified significantly to become

$$\Omega = \frac{v_R + v_L}{2}\sqrt{(f_{\mu\mu} + f_{ee})^2 + 4f^2_{e\mu} - 4f_{\mu\mu}f_{ee}}. \quad (86)$$

Thus, we can see that, for m_{N_1} and m_{N_2}, there are two sets of symmetric values, these being determined primarily by the triplet Yukawa coupling constants f_{ab} and the vacuum expectation values $v_{R,L}$. The light-neutrino-induced corrections to $m_{N_{1,2}}$ are as small as a few electronvolts.

We begin by considering the first scenario. Suppose that the mass of the lightest $\Delta^{(--)}$ boson is 10 TeV and that the $\tilde{\delta}^{(-)}$-boson mass is 72 GeV [22]. With the aid of relations (55), (79), and (80), we then obtain the following upper bounds on the triplet Yukawa coupling constants:

$$(f_{e\mu})_{\max} = 0.0748, \quad (f_{ee})_{\max} = 0.0881, \quad (f_{\mu\mu})_{\max} = 0.533. \quad (87)$$

By using (87), we obtain

$$m_{N_1} > 92.4 \text{ GeV}, \quad m_{N_2} < 664.3 \text{ GeV}, \quad m_{N_1} < 92.4 \text{ GeV}, \quad m_{N_2} > 664.3 \text{ GeV}, \quad m_{N_1} + m_{N_2} = 756.7 \text{ GeV}, \quad \varphi_e \approx \varphi_\mu = 0.0103, \quad \theta_N = 0.162 \quad (88)$$

for $m_{W_2} = 800$ GeV and $v_L = 0.13$ GeV and

$$m_{N_1} > 290.1 \text{ GeV}, \quad m_{N_2} < 2085.4 \text{ GeV}, \quad m_{N_1} < 290.1 \text{ GeV}, \quad m_{N_2} > 2085.4 \text{ GeV}, \quad m_{N_1} + m_{N_2} = 2375.5 \text{ GeV}, \quad \varphi_e \approx \varphi_\mu = 0.0058, \quad \theta_N = 0.162 \quad (89)$$

for $m_{W_2} = 2500$ GeV and $v_L = 0.13$ GeV.

In fact, the value of v_L affects only $\varphi_{e,\mu}$. For example, we have $\varphi_{e,\mu} = 0.103\ (0.058)$ at $m_{W_2} = 800$ (2500) GeV and $v_L = 13$ GeV.

We will now proceed to consider the second scenario. This means that we set the masses $m_{\tilde{\delta}}$ and m_{Δ_2} to their lower experimental limits [22, 23]:

$$m_{\tilde{\delta}} > 71.5\ \text{GeV}, \quad m_{\Delta_2} > 98.5\ \text{GeV}.$$

From (7), it follows that, if $f_{e\mu}$ is close to zero, then either $v_L \approx 0$, or the heavy-neutrino masses are quasidegenerate. In the first case, we have

$$\varphi_e = \varphi_\mu = 0, \quad m_{N_1} = f_{ee} v_R, \quad m_{N_2} = f_{\mu\mu} v_R. \tag{90}$$

However, we now have at our disposal only relation (79), from which one can find an upper bound on the product of the triplet Yukawa coupling constants f_{ee} and $f_{\mu\mu}$. Thus, it is impossible at the present time to obtain any piece of information about m_{N_1}, m_{N_2}, and θ_N for this case.

It is obvious that

$$f_{ee} \approx f_{\mu\mu} \tag{91}$$

if the heavy-neutrino masses are quasidegenerate.

We note that no constraints on θ_N can be found in this case. Substituting $m_{\tilde{\delta}} = 72$ GeV into (79), we find an upper bound of 0.215 for $f_{\mu\mu}$. At $v_L = 13$ GeV, we then obtain

$$m_{N_1} < 825.1\ \text{GeV}, \quad \varphi_e \approx \varphi_\mu = 0.058 \tag{92}$$

for $m_{W_2} = 2500$ GeV and

$$m_{N_1} < 264\ \text{GeV}, \quad \varphi_e \approx \varphi_\mu = 0.103 \tag{93}$$

for $m_{W_2} = 800$ GeV.

In the case where the heavy-neutrino masses are quasidegenerate or degenerate, stringent bounds on $f_{\mu\mu}$ can also be obtained from an analysis of the $(g-2)_\mu$ anomaly under the condition that a dominant contribution comes from the $\Delta_1^{(--)}$ boson. We now define the quantity

$$(f_{\mu\mu})_m = \frac{1}{2}\left[(f_{\mu\mu})_{\max} + (f_{\mu\mu})_{\min}\right],$$

where $(f_{\mu\mu})_{\max}$ and $(f_{\mu\mu})_{\min}$ correspond to the dotted and the solid curve in Fig. 5. For the values of the mass m_{Δ_1} that are equal to 105 and 130 GeV, we have $(f_{\mu\mu})_m = 0.4545$ and $(f_{\mu\mu})_m = 0.563$, respectively. If one sets $m_{W_2} = 800$ GeV and $v_L = 13$ GeV, the parameters of the heavy-neutrino sector become

$$m_{N_1} = 559.6\ \text{GeV}, \quad \varphi_e \approx \varphi_\mu = 0.103 \tag{94}$$

for $m_{\Delta_1} = 105$ GeV and

$$m_{N_1} = 693\ \text{GeV}, \quad \varphi_e \approx \varphi_\mu = 0.103 \tag{95}$$

for $m_{\Delta_1} = 130$ GeV.

At $m_{W_2} = 2500$ GeV and $v_L = 13$ GeV, the results are

$$m_{N_1} = 1744.2\ \text{GeV}, \quad \varphi_e \approx \varphi_\mu = 0.058 \tag{96}$$

for $m_{\Delta_1} = 105$ GeV and

$$m_{N_1} = 2160.5\ \text{GeV}, \quad \varphi_e \approx \varphi_\mu = 0.058 \tag{97}$$

for $m_{\Delta_1} = 130$ GeV.

5. CONCLUSIONS

The objective of the present study was to determine the parameters of the sector of heavy neutrinos N_i without detecting them directly. Within the two-flavor approximation, we have derived equations that relate the parameters of oscillations of both light and heavy neutrinos to the Yukawa coupling constants and the vacuum expectation values of the Higgs fields. In turn, the Yukawa coupling constants determine the constants of Higgs boson coupling to leptons. Thus, we see that, in order to determine the Yukawa coupling constants, it is necessary to study processes involving Higgs bosons.

We have considered Higgs boson contributions to the muon anomalous magnetic moment, to the cross sections for lepton-flavor-violating processes, and to the cross sections for low-energy light-neutrino scattering. Our analysis has revealed that, in the majority of situations, one can set bounds on quantities of the type

$$\sum_i \left[A_i \left(\frac{\alpha_{H_i}}{m_{H_i}}\right)^4 + B_i \left(\frac{\alpha'_{H_i}}{m_{H_i}}\right)^4 + C_i \left(\frac{\alpha_{H_i}\alpha'_{H_i}}{m^2_{H_i}}\right)^2 \right],$$

where A_i, B_i, and C_i are constants and α_{H_i} and α'_{H_i} characterize H_i interactions with various leptons. Obviously, it is impossible to deduce, in this way, unambiguous information about only one constant α_{H_i}. However, the situation is more favorable in some cases. For example, it was shown in studying the $(g-2)_\mu$ anomaly that, if the corrections to the muon anomalous magnetic moment are due to diagrams involving virtual $\Delta_1^{(--)}$ bosons and if there is mass degeneracy in the heavy-neutrino sector, the muon anomalous magnetic moment is a function of only two parameters, m_{Δ_1} and $f_{\mu\mu}$. Upper bounds on quantities of the type

$$\alpha^2_{H_i}/m^2_{H_i}$$

can also be obtained by studying low-energy neutrino scattering on charged leptons. Since the constants of $\tilde{\delta}^{(-)}$- and $\Delta_{1,2}^{(--)}$-boson coupling to leptons are

equal, apart from a constant, to the triplet Yukawa coupling constants f_{ee}, $f_{e\mu}$, and $f_{\mu\mu}$, it is the most convenient for practical calculations to use bounds on these constants. On the other hand, it turns out that, within the left–right model, the masses of the neutrinos $N_{1,2}$ can be expressed in terms of only the triplet Yukawa coupling constant and the mass of the gauge boson W_2.

By using data on direct and inverse muon decays and constraints on the masses of the $\tilde{\delta}^{(-)}$, $\Delta_{1,2}^{(--)}$, and W_2 bosons, we have set limits on the heavy-neutrino masses both in the absence and in the presence of degeneracy. Only in the presence of degeneracy have data concerning the explanation of the $(g-2)_\mu$ anomaly been employed to set limits on the mass of the neutrino $N_{1,2}$.

The formalism developed in this study can readily be generalized to the case where all three neutrino flavors are mixed. We would also like to emphasize that the above scheme for estimating the heavy-neutrino masses can be employed in any gauge electroweak theory possessing an extended Higgs sector and involving the seesaw mechanism.

In conclusion, we note that, within the left–right model, the application of the proposed scheme upon directly measuring the W_2-boson mass and three triplet Yukawa constants f_{ee}, $f_{e\mu}$, and $f_{\mu\mu}$ will yield precise values for $m_{N_{1,2}}$. These Yukawa constants can be determined in detecting $\Delta_{1,2}^{(--)}$ bosons in the reactions

$$e^-e^- \to e^-e^-, \mu^-\mu^-, \quad e^-\mu^- \to e^-\mu^-. \qquad (98)$$

Thus, information about heavy neutrinos can be obtained in studying processes not involving them directly. However, the most important point is that charged rather than neutral particles are now becoming the object of investigations, this simplifying the experimental facet of the problem significantly.

REFERENCES

1. SuperKamiokande Collab. (Y. Fukuda *et al.*), Phys. Rev. Lett. **81**, 1562 (1998); **82**, 2644 (1999); S. Fukuda *et al.*, Phys. Rev. Lett. **85**, 3999 (2000).
2. SNO Collab. (Q. R. Ahmad *et al.*), Phys. Rev. Lett. **87**, 071301 (2001); **89**, 011301 (2002); **89**, 011302 (2002).
3. KamLAND Collab. (K. Eguchi *et al.*), Phys. Rev. Lett. **90**, 021802 (2003).
4. K2K Collab. (M. H. Ahn *et al.*), Phys. Rev. Lett. **90**, 041801 (2003).
5. J. Bonn *et al.*, Nucl. Phys. B (Proc. Suppl.) **91**, 273 (2001); V. M. Lobashev *et al.*, Nucl. Phys. B (Proc. Suppl.) **91**, 280 (2001).
6. D. N. Spergel *et al.*, astro-ph/0302209; S. Hannestad, astro-ph/0303076.
7. N. G. Deshpande *et al.*, Phys. Rev. D **44**, 837 (1991).
8. G. G. Boyarkina, O. M. Boyarkin, and V. V. Makhnach, Yad. Fiz. **66**, 306 (2003) [Phys. At. Nucl. **66**, 281 (2003)].
9. G. G. Boyarkina, O. M. Boyarkin, and A. N. Senko, Eur. Phys. J. C **13**, 99 (2000).
10. Muon g-2 Collab. (G. W. Bennet *et al.*), Phys. Rev. Lett. **89**, 101804 (2002); **89**, 129903(E) (2002).
11. Muon g-2 Collab. (G. W. Bennett *et al.*), Phys. Rev. Lett. **92**, 161802 (2004).
12. A. Czarnecki and W. J. Marciano, Phys. Rev. D **64**, 013014 (2001).
13. M. Knecht and A. Nyffeler, Phys. Rev. D **65**, 073034 (2002); M. Hayakawa and T. Kinoshita, Phys. Rev. D **57**, 465 (1998); **66**, 019902(E) (2002).
14. R. Alemany, M. Davier, and A. Höcker, Eur. Phys. J. C **2**, 123 (1998).
15. M. Davier, S. Eidelman, A. Höcker, and Z. Zhang, Eur. Phys. J. C **31**, 503 (2003); S. Ghozzi and F. Jegerlehner, Phys. Lett. B **583**, 222 (2004).
16. K. Hagiwara *et al.*, hep-ph/0312250.
17. M. L. Swartz, Phys. Rev. D **40**, 1521 (1989); R. N. Mohapatra, Phys. Rev. D **46**, 2990 (1992).
18. LSND Collab. (L. B. Auerbach *et al.*), Phys. Rev. D **63**, 112001 (2001).
19. F. Reines, H. S. Gurr, and H. W. Sobel, Phys. Rev. Lett. **37**, 315 (1976).
20. Z. Berezhiani and A. Rossi, hep-ph/0111137.
21. W. Fetscher, H.-J. Gerber, and K. F. Johnson, Phys. Lett. B **173**, 102 (1986).
22. Review of Particle Physics (K. Hagiwara *et al.*), Phys. Rev. D **66**, 010001 (2002).
23. OPAL Collab. (G. Abbiendi *et al.*), hep-ex/0111059.

Translated by A. Isaakyan

Physics of Atomic Nuclei, Vol. 68, No. 12, 2005, pp. 2061–2067. Translated from Yadernaya Fizika, Vol. 68, No. 12, 2005, pp. 2123–2129.

ELEMENTARY PARTICLES AND FIELDS
Theory

Heavy Majorana Neutrinos in Dilepton Production in Deep-Inelastic Lepton–Proton Scattering

A. Ali[1)], A. V. Borisov[*], and D. V. Zhuridov

Moscow State University, Vorob'evy gory, Moscow, 119992 Russia

Received November 10, 2004

Abstract—The cross section for the production of pairs of likely charged leptons in the deep-inelastic processes $e^+p \to \bar{\nu}_e \ell^+ \ell'^+ X$ ($\ell, \ell' = e, \mu, \tau$) induced by the exchange of heavy Majorana neutrinos is calculated. The effect of interference between different neutrino mass eigenstates is studied. The possibilities for observing this effect at future lepton–proton colliders are considered. © *2005 Pleiades Publishing, Inc.*

1. The discovery of oscillations of solar, atmospheric, reactor, and accelerator neutrinos (for an overview, see [1, 2] and references therein to recent experimental results obtained at SNO, SuperKamiokande, KamLAND, some other facilities) showed that neutrinos have nonzero masses whose spectrum is nontrivial. Among other things, this means that there is mixing: neutrinos of specific flavor, ν_ℓ, which appear in the weak charged current, together with the charged leptons $\ell = e, \mu, \tau$, are coherent superpositions of the neutrino mass eigenstates ν_i,

$$\nu_\ell = \sum_i U_{\ell i} \nu_i, \tag{1}$$

the masses of these eigenstates being denoted by m_i. In (1), the coefficients $U_{\ell i}$ are elements of the unitary lepton-mixing matrix (an analog of the quark-mixing matrix).

At the present time, massive effort is devoted to determining the detailed structure of the neutrino mass spectrum and mixing matrix. From oscillation experiments, it is already known that lepton mixing is substantially stronger than quark mixing. However, these experiments cannot yield the absolute mass scale. Only the differences of the squares of the masses (to be more precise, the absolute values of these differences), $\Delta m_{ij}^2 = m_i^2 - m_j^2$, are determined under the assumption that the number of neutrino mass eigenstates ν_i is equal to the number of flavors ν_ℓ (that is, to three).

We use mass ordering in the form $0 \le m_1 < m_2 < m_3$ and two values of the mass scale that describe the oscillations of solar and atmospheric neutrinos and which correspond to the best global three-neutrino fit to experimental data [3]:

$$\Delta m_{21}^2 = \Delta m_{\rm sol}^2 = 7.9 \times 10^{-5}\ {\rm eV}^2, \tag{2}$$
$$\Delta m_{31}^2 = \Delta m_{\rm atm}^2 = 2.3 \times 10^{-3}\ {\rm eV}^2.$$

This leads to a lower bound on the largest neutrino mass:

$$m_3 > \sqrt{\Delta m_{31}^2} \simeq 0.05\ {\rm eV}. \tag{3}$$

Recent cosmological data constrain the sum of the light-neutrino masses (those below approximately 1 MeV) as [4]

$$\sum_i m_i < 0.75\ {\rm eV},$$

which, with allowance for (2), leads to an upper bound on the masses,

$$m_i < 0.25\ {\rm eV} \quad (i = 1, 2, 3). \tag{4}$$

The mass values m_i can in principle be determined from a precise measurement of the spectra of charged particles emitted, together with neutrinos, in weak decays. Measurements of the high-energy part of the tritium beta spectrum are presently the most sensitive to the neutrino mass. However, the individual values of m_i are not resolved because of a very small value of the neutrino-mass difference [see (2)]. As a matter of fact, one determines only the effective electron-neutrino mass [2]

$$m_{\nu_e}^{\rm eff} = \left(\sum_i |U_{ei}|^2 m_i^2 \right)^{1/2}. \tag{5}$$

The most stringent constraint on this quantity was obtained in an experiment that is being performed at the Institute for Nuclear Research (INR, Troitsk) [5]:

$$m_{\nu_e}^{\rm eff} < 2.05\ {\rm eV}. \tag{6}$$

[1)]DESY, Hamburg, Germany.
[*]e-mail: borisov@ave.phys.msu.su

Using the definition in (5) and taking into account the relation $\sum_i |U_{ei}|^2 = 1$, which follows from the unitarity of the mixing matrix, we find a constraint on the lowest neutrino mass:

$$m_1 \leq m_{\nu_e}^{\text{eff}}.$$

In view of (6), it is much more lenient than the cosmological constraint (4).

Charged fermions have Dirac masses, which, in the Standard Model, appear owing to the Yukawa coupling of fermions to the Higgs field. The electrically neutral neutrinos may have either Dirac or Majorana masses [2, 6]. In particle physics, the nature of the neutrino mass is a fundamental problem that has not yet been solved. The Dirac neutrino carries a lepton number that distinguishes it from the antineutrino. In contrast, the Majorana neutrino is a true neutral particle that does not carry any lepton number.

In general, the mass term can be represented in the form of the sum of a Dirac and a left- and a right-handed Majorana term. By diagonalizing the corresponding block mass matrix, one obtains eigenvectors that describe Majorana neutrino mass eigenstates [6–8]. We note that a Dirac neutrino can be represented in terms of a superposition of two Majorana neutrinos of the same mass. From the theoretical point of view, the Majorana neutrinos are therefore preferable to the Dirac neutrinos.

At the present time, neither possibility (Dirac or Majorana neutrinos) contradicts experimental data. From experiments, we know three generations of light neutrinos, each being of two types. In the version of Dirac neutrinos, these are three particles ν_e, ν_μ, and ν_τ, and the corresponding antiparticles $\bar{\nu}_e$, $\bar{\nu}_\mu$, and $\bar{\nu}_\tau$. Each particle has two polarization states, for which it is convenient to choose eigenvectors of the helicity operator $\mathbf{\Sigma} \cdot \mathbf{p}/|\mathbf{p}|$, the doubled spin projection onto the momentum direction. In all, there are 12 neutrino states. Six Majorana neutrinos give the same total number of neutrino polarization states (see below). In the Majorana neutrino pattern, there are neutrinos in two polarization states instead of neutrinos and antineutrinos. It is well known [6] that, for a massless particle, the chiral states (the eigenvectors of the chirality operator, the γ^5 matrix) coincide with the corresponding helicity states. For massive particles, chirality is not conserved, but, in the ultrarelativistic case, the left-handed (right-handed) helicity state virtually coincides with the left-handed (right-handed) chirality state, the admixture of the right-handed (left-handed) chirality state being suppressed by the small ratio of the mass to energy ($m/E \ll 1$). The majority of experiments performed thus far recorded only relativistic (anti)neutrinos in processes induced by weak charged currents. Such currents involve only left-handed chirality components of the neutrino fields; therefore, it is impossible to distinguish, in such experiments, a Dirac neutrino of left-handed helicity from a Majorana neutrino of the same polarization. The cross sections for the analogous processes involving Dirac antineutrinos of right-handed helicity or Majorana neutrinos of the same polarization are suppressed by the factor $(m/E)^2$ with respect to the corresponding cross sections for neutrinos of left-handed helicity.

From (3) and (4), it follows that the neutrino masses are substantially smaller than the masses of charged leptons and quarks. Within the Standard Model, the introduction of right-handed neutrino singlets makes it possible to obtain masses of about 0.1 eV for the Dirac neutrinos only at extremely small (about 10^{-12}) Yukawa coupling constants. Small neutrino masses appear in a rather natural way in extended models (of the Grand Unification type) owing to the seesaw mechanism (see, for example, [7, 8]). The seesaw mechanism is based on the use of a Dirac–Majorana mass term, where the standard Dirac term has a scale m_{D} on the order of the typical charged-lepton or quark mass, while the Majorana term of order $M \gg m_{\text{D}}$ is generated owing to spontaneous symmetry breaking beyond the Standard Model. By diagonalizing the mass term, one obtains mass eigenstates that correspond to Majorana neutrinos of two types: light neutrinos of mass $m_\nu \sim m_{\text{D}}^2/M \ll m_{\text{D}}$ and heavy neutrinos of mass $m_N \sim M$. In the minimal scheme, which involves three known lepton generations, the seesaw mechanism gives three light and three heavy Majorana neutrinos [7]. The total number of polarization states is 12, as in the case of three pairs of light Dirac neutrinos and antineutrinos (see above). In general, the number of both light and heavy neutrinos can exceed three; that is, there can exist sterile neutrinos not directly involved in weak interaction (they do not appear in the standard weak currents).

Thus, we see that, if neutrino masses are generated via the seesaw mechanism, the neutrino mass eigenstates are Majorana particles, in which case at least three heavy Majorana neutrinos must exist along with light neutrinos. There are a large number of seesaw models, where the scale M varies within a broad range from a few TeV to the Grand Unification scale of $M_{\text{GUT}} \sim 10^{16}$ GeV [9].

We emphasize that heavy Majorana neutrinos must decay rather fast; therefore, they cannot affect the cosmological constraint on the sum of the light-neutrino masses [see (4)]. A direct experimental (conservative) lower bound on the mass of heavy Majorana neutrinos is 80.5 GeV [1].

The Dirac and Majorana neutrinos have substantially different properties. By way of example, we indicate that, in contrast to the Dirac neutrinos, the Majorana neutrinos cannot have nonzero electric dipole and magnetic dipole moments. The lepton mixing matrix [see (1)] for the Majorana neutrinos contains a greater number of phases that violate the CP symmetry of the Lagrangian (in the simplest case of three light Majorana neutrinos, there are three phases instead of one for the Dirac neutrinos). The Majorana mass term in the model Lagrangian does not conserve the lepton number, changing it by two units [6]. In contrast to the Dirac neutrinos, the Majorana neutrinos can therefore give rise to a number of lepton-number-violating processes whose searches are one of the important lines in neutrino physics.

Neither neutrino-flavor oscillations nor processes featuring a single external neutrino, like tritium beta decay and tau-lepton or pion decays, are sensitive to the type of the neutrino mass [10]. Processes that are allowed only for the Majorana neutrinos are those where a dilepton (a pair of likely charged leptons) is produced via an intermediate Majorana neutrino, this changing explicitly the lepton number. Since 2001, the observation of one such process, nuclear neutrinoless double-beta decay [6, 11], has been reported by the Heidelberg–Moscow group (see, for example, [12]), but this result has not yet been confirmed by any other group. Rare decays of K, D, D_s, and B mesons like $M^+ \to M'^- \ell^+ \ell'^+$ ($\ell, \ell' = e, \mu, \tau$) are analogs of this process for elementary particles. Constraints on the effective masses of the Majorana neutrinos were obtained in [13] from experimental data for these processes. Dilepton production is also possible in deep-inelastic hadron–hadron and lepton–hadron collisions, such as $pp \to \ell^\pm \ell'^\pm X$ [14, 15], $e^+ p \to \bar{\nu}_e \ell^+ \ell'^+ X$ [16–18], and $\nu_\mu N \to \mu^- \mu^+ \mu^+ X$ [19].

In this study, we analyze the process

$$e^+ p \to \bar{\nu}_e \ell^+ \ell'^+ X \tag{7}$$

under the assumption that it is induced by the exchange of a heavy Majorana neutrino. At high energies considered here, the results will also be valid for the cross-symmetric process

$$\nu_e p \to e \ell^+ \ell'^+ X, \tag{8}$$

because the cross sections for the reactions in (7) and (8) are asymptotically equal to each other. In [18], these processes were considered for the case where the mass spectrum of heavy neutrinos [see Eq. (13) below] is such that only one heavy Majorana neutrino contributes to the cross section over a rather broad range of high energies. Here, we extend the results obtained in [18] to the versions where the mass spectrum features a few heavy Majorana neutrinos, in which case it is necessary to take into account the interference between different mass eigenstates. In addition, we consider the possibility of extracting information about CP-violating phases in the lepton mixing matrix.

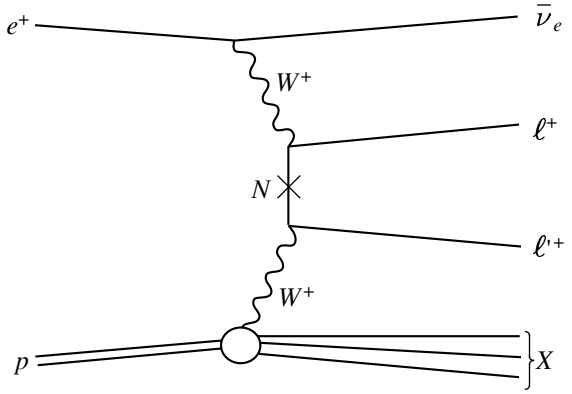

Fig. 1. Feynman diagram for the process in (7).

2. In the leading order in the coupling constant, the amplitude of the process is determined by the sum of two Feynman diagrams. One of these is shown in Fig. 1 (N stands for a heavy Majorana neutrino, and X is a hadron jet), while the other is obtained by means of the interchange of the lepton lines ℓ and ℓ'. We assume that the neutrino of specific flavor is a coherent superposition of the light (n_i) and heavy (N_j) Majorana neutrinos whose masses are m_i and M_j, respectively; that is,

$$\nu_\ell = \sum_i^3 U_{\ell i} n_i + \sum_j u_{\ell j} N_j. \tag{9}$$

We consider the high-energy region

$$\sqrt{s} \gg m_W \tag{10}$$

and calculate the cross section for the process in (7) as in [18] by using the method of equivalent vector bosons (see, for example, [20]) and neglecting quark mixing. The contributions of light (l) and heavy (h) neutrinos to the cross section for the process are then determined by their contributions to the cross section for the subprocess $WW \to \ell\ell'$ [21]:

$$\sigma_l \sim |U_{\ell i} U_{\ell' i}|^2 \left(\frac{m_i}{m_W}\right)^2, \quad m_i \ll m_W,$$

$$\sigma_h \sim |u_{\ell j} u_{\ell' j}|^2 \left(\frac{s}{m_W M_j}\right)^2, \quad M_j \gg \sqrt{s}.$$

The effects of the light and heavy neutrinos compete if

$$\frac{m_i M_j}{s} \sim \frac{|u_{\ell j} u_{\ell' j}|}{|U_{\ell i} U_{\ell' i}|} \equiv k_{\ell\ell'}.$$

We assume that the values of $k_{\ell\ell'}$ are such that, under the conditions

$$m_W \ll \sqrt{s} \sim M_j,$$

the effects from the light neutrinos are small ($k_{\ell\ell'} \gg m_i M_j/s$).

In our numerical calculations, we used the CTEQ6 set of parton distributions [22] and experimental constraints on the absolute values of the elements of the mixing matrix u from the analysis of electroweak processes [23],

$$\sum |u_{ej}|^2 < 6.6 \times 10^{-3}, \qquad (11)$$

$$\sum |u_{\mu j}|^2 < 6.0 \times 10^{-3}, \quad \sum |u_{\tau j}|^2_{\text{eff}} < 3.1 \times 10^{-3},$$

and from data on searches for neutrinoless double-beta decay [21],

$$\left| \sum_j u_{ej}^2 M_j^{-1} \right| < 5 \times 10^{-5}\ \text{TeV}^{-1}, \qquad (12)$$

where, for the tau lepton, we have employed the effective value obtained through the multiplication by the branching ratio $\text{Br}(\tau^- \to \mu^- \bar{\nu}_\mu \nu_\tau) = 0.1737$ [1] for the decay mode convenient for observation. The observability criterion for a collider of luminosity L per year is chosen to be

$$\sigma L \geq 1,$$

which means the detection of at least one event per year.

Let us consider several possible forms of the mass spectrum of heavy Majorana neutrinos.

(i) In the case of an effective singlet,

$$M_1 \ll M_2 < M_3 \ldots, \qquad (13)$$

the main contribution to the amplitude for the process in the energy region

$$m_W \ll \sqrt{s} \ll M_2$$

comes from one heavy Majorana neutrino of mass M_1. In [18], we showed that the observation of the processes in (7) and (8) requires a collider whose properties are substantially superior to those of the future supercollider VLHC [24] ($\sqrt{s} = 6320$ GeV, $L = 1.4\ \text{fb}^{-1}$). For example, the energy of a collider whose luminosity per year is 100 fb^{-1} must exceed 23 TeV; at an energy of 25 TeV, one can observe $\mu\tau$ and $\mu\mu$ processes for M_1 values in the range 1–3 TeV.

(ii) In the effective-doublet case of

$$M_1 \lesssim M_2 \ll M_3 \ldots, \qquad (14)$$

which is similar to the case of a direct hierarchy of the light neutrino masses [2], the contributions to the amplitude from two heavy Majorana neutrinos whose masses are M_1 and M_2 are significant in the energy region

$$m_W \ll \sqrt{s} \ll M_3.$$

In the approximation adopted here, the cross section for the process assumes the form

$$\sigma_2 = \frac{1}{2} C \left(\rho_1^2 f_1 + 2 c_{12} \rho_1 \rho_2 F_{12} + \rho_2^2 f_2 \right), \qquad (15)$$

where the dimensional coefficient in the cross section is

$$C = \frac{G_F^4 m_W^6}{8\pi^5} = 0.80\ \text{fb} \qquad (16)$$

and the mixing parameters are

$$c_{12} = \cos(\phi_1 - \phi_2), \quad \phi_i = \arg(u_{\ell i} u_{\ell' i}), \qquad (17)$$
$$\rho_i = \sqrt{2 - \delta_{\ell\ell'}} |u_{\ell i} u_{\ell' i}|.$$

We have also introduced the dimensionless functions

$$f_i \equiv f(s, M_i) \qquad (18)$$
$$= \left(\frac{M_i}{m_W} \right)^2 \int\limits_{y_0}^1 \frac{dy}{y} \int\limits_y^1 \frac{dx}{x} p(x, xs) h\left(\frac{y}{x} \right) \omega(t_i),$$
$$F_{ij} \equiv F(s, M_i, M_j)$$
$$= \frac{M_i M_j}{m_W^2} \int\limits_{y_0}^1 \frac{dy}{y} \int\limits_y^1 \frac{dx}{x} p(x, xs) h\left(\frac{y}{x} \right) \Omega(t_i, t_j),$$

where $y_0 = 4m_W^2/s$; $t_i = ys/M_i^2$;

$$p(x, Q^2) = x(u + c + t + \bar{d} + \bar{s} + \bar{b})$$

is the distribution of quarks and antiquarks in the proton, which corresponds to the processes in (7) and (8);

$$h(r) = -(1 + r) \ln r - 2(1 - r)$$

is the quantity obtained by multiplying the normalized W-boson emissivity in the quark–lepton system by r; and

$$\Omega(t_1, t_2) = 2 - \frac{1}{t_1 + t_2 + t_1 t_2}$$
$$\times \left[\frac{t_2(t_1^2 - 2t_1 t_2 - 2t_2)}{t_1(t_1 - t_2)} \ln(1 + t_1) \right.$$
$$\left. + \frac{t_1(t_2^2 - 2t_1 t_2 - 2t_1)}{t_2(t_2 - t_1)} \ln(1 + t_2) \right] = \Omega(t_2, t_1),$$
$$\omega(t) = \Omega(t, t) \equiv \lim_{t' \to t} \Omega(t, t')$$
$$= 2 + \frac{1}{1 + t} - \frac{2(3 + 2t)}{t(2 + t)} \ln(1 + t).$$

Formula (15) generalizes the expression obtained for the cross section $\sigma \equiv \sigma_1$ in [18] with allowance for

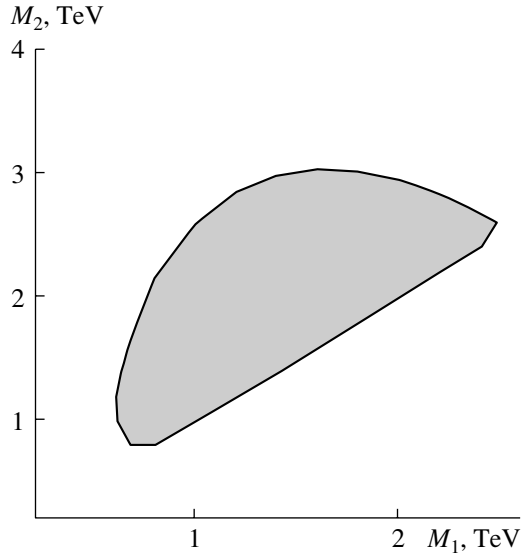

Fig. 2. Mass-parameter region where the process in (7) can be observed at a collider whose parameters are $L = 100\ \text{fb}^{-1}$ and $\sqrt{s} = 25$ TeV.

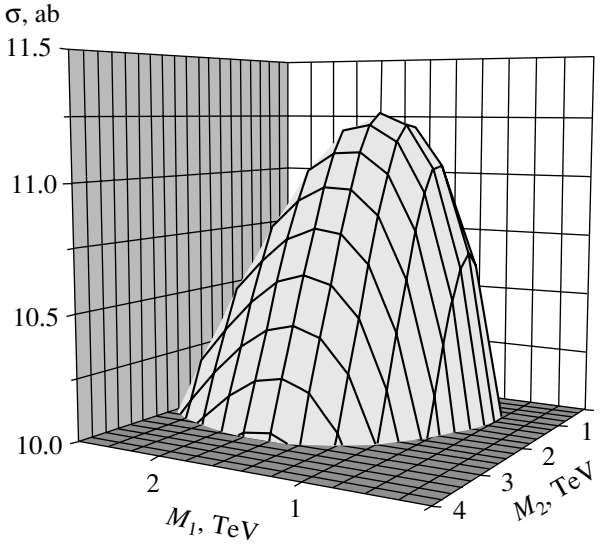

Fig. 3. Cross section for the process in (7) as a function of the masses of heavy Majorana neutrinos.

the contribution from only one heavy Majorana neutrino. The functions f_i correspond to the individual contributions of each heavy Majorana neutrino, while F_{12} allows for their interference; the functions $\omega(t_i)$ and $\Omega(t_1, t_2)$ appearing in (18) describe the analogous contributions to the normalized cross section for the subprocess $W^+W^+ \to \ell^+\ell'^+$ (the cross-symmetric process $e^-e^- \to W^-W^-$ was studied in [25]).

It can easily be shown that the cross section σ_2 at the maximum is equal to the cross section σ_1 for the effectively singlet spectrum. This maximum is reached for the constructive interference ($c_{12} = 1$) in the case of virtually degenerate neutrinos ($M_1 \simeq M_2$), or in the case of the mixing hierarchy [$\rho_1 \gg \rho_2$ ($\rho_1 \ll \rho_2$)], or when both of these cases are realized. In the case of the destructive interference ($c_{12} = -1$), the cross section σ_2 can be negligible (at $\rho_1 = \rho_2$ and $M_1 \simeq M_2$).

In the (M_1, M_2) parameter plane, Fig. 2 displays the region where the process under consideration can be observed at a collider characterized by $L = 100\ \text{fb}^{-1}$ and $\sqrt{s} = 25$ TeV. Here, we consider the $\ell = \ell' = \mu$ process, for which the existing constraints are the most lenient [see (11) and (12)], and choose the mixing-parameter values of $|u_{\mu 1}|^2 = |u_{\mu 2}|^2 = 3 \times 10^{-3}$ and $c_{12} = 1$, which are the most favorable for observation. Figure 3 shows a three-dimensional picture of $\sigma = \sigma_2$ (in attobarns, $1\ \text{ab} = 10^{-18}\ \text{b}$) as a function of the masses M_1 and M_2 (the boundary of the region in Fig. 2 is the section of the surface in Fig. 3 by the horizontal plane $\sigma = 1/L = 10$ ab).

(iii) In the case of an effective triplet,

$$M_1 \lesssim M_2 \lesssim M_3 \ll M_4 \ldots, \tag{19}$$

it is necessary to take into account the contributions from three heavy Majorana neutrinos. It can readily be shown that the expression for the cross section is a generalization of that in (15),

$$\sigma_3 = \frac{1}{2}C[\rho_1^2 f_1 + \rho_2^2 f_2 + \rho_3^2 f_3 \tag{20}$$
$$+ 2c_{12}\rho_1\rho_2 F_{12} + 2c_{13}\rho_1\rho_3 F_{13} + 2c_{23}\rho_2\rho_3 F_{23}],$$

where f_i and F_{ij} are defined in (18) and $c_{ij} = \cos(\phi_i - \phi_j)$, ϕ_i being specified in (17). A further generalization to the case of n neutrinos is obvious.

In the case of an approximate degeneracy, $M_2 \simeq M_3$ (an exact equality is possible if the neutrinos N_2 and N_3 differ in the values of the Majorana phases), the triplet spectrum (19) is effectively similar to the mass spectrum of the light neutrinos, obeying the inverse hierarchy [2]

$$M_1 < M_2 \simeq M_3.$$

From (18), it then follows that $F_{23} \simeq f_2 \simeq f_3$ and $F_{12} \simeq F_{13}$; apart from coefficients, the cross section (20), which takes into account the contributions from three heavy Majorana neutrinos, therefore assumes the form of the cross section (15):

$$\sigma_3 \simeq \frac{1}{2}C[\rho_1^2 f_1 + 2\rho_1(c_{12}\rho_2 + c_{13}\rho_3)F_{12}$$
$$+ (\rho_2^2 + 2c_{23}\rho_2\rho_3 + \rho_3^2)f_2].$$

In the simplest case of an approximate mass degeneracy and equality of the mixing parameters,

$$M_1 \simeq M_2 \simeq M_3, \quad \rho_1 = \rho_2 = \rho_3,$$

expression (20) is significantly simplified to become

$$\sigma_3 \simeq \frac{2}{9}\sigma_1\left(\frac{3}{2}+c_{12}+c_{13}+c_{23}\right),$$

where $\sigma_1 = C\rho_1^2 f_1/2$. At $\phi_1=\phi_2=\phi_3$ ($c_{ij}=1$ for all i and j), the cross section reaches a maximum (constructive interference): $\sigma_3=\sigma_1$. In the case of the destructive interference ($c_{12}+c_{13}+c_{23}=-3/2$, for example, at $\phi_1-\phi_2=\phi_2-\phi_3=2\pi/3$), the cross section is negligible. It can easily be shown that, for an arbitrary number n of heavy Majorana neutrinos, the relation $\sigma_n \le \sigma_1$ holds.

3. The cross sections for the effective-doublet and more complicated spectra carry information about the CP-violating phases of the matrix u in the coefficients c_{ij}. We will try to find out how one can in principle extract this information. It is rather difficult to use the total cross section σ_2 [in the case of the effective-doublet spectrum—see (14) and (15)] to determine all five parameters M_1, M_2, ρ_1, ρ_2, and c_{12}, because it is necessary to measure the cross section at various (at least five) values of the energy $\sqrt{s}$. The differential cross sections contain more detailed information about the process, but one needs vast statistics in order to determine them.

By a standard method (see, for example, Subsection 17.4 in [26]), we obtain the differential cross section for the process with respect to the observed longitudinal rapidities β and β' of the final leptons and their transverse momentum $p_\perp$:

$$\frac{d^3\sigma}{d\beta d\beta' dp_\perp} = \frac{C}{8}\frac{S}{m_W^2 p_\perp \cosh^2 y_*} \times \int\limits_{x_0}^{1}\frac{dx}{x}p(x,xs)R(x,s,\beta,\beta',p_\perp). \quad (21)$$

Here, the coefficient C is identical to that in (16); $x_0 = 4p_\perp^2\cosh^2 y_*/s$;

$$S = \left|\sum_i M_i\rho_i e^{i\phi_i}g_i\right|^2 \quad (22)$$

is the normalized differential cross section for the subprocess $W^+W^+\to\ell^+\ell'^+$ (for an arbitrary mass spectrum of heavy Majorana neutrinos), where

$$g_i = \frac{1-z}{1-z+k_i}+\frac{1+z}{1+z+k_i},$$
$$k_i = \frac{M_i}{2p_\perp^2\cosh^2 y_*},$$
$$z\equiv\cos\theta_* = \tanh y_*,$$

and θ_* is the scattering angle of the leptons ℓ and ℓ' in the c.m. frame of the W-boson pair (the quantities in this frame are labeled with the subscript $*$);

$$R = 1-\sqrt{\hat{x}}\cosh Y+\hat{x},\quad \hat{x}=x_0/x,$$

is the normalized spectrum of W-boson pairs emitted by the quark–positron system in the approximation of high positron and quark energies (well above m_W); and the variables y_* and Y are, respectively, the half-difference and the half-sum of the rapidities β and β'.

Integration of (21) with respect to $p_\perp$ over the interval

$$m_W/\cosh y_* \le p_\perp \le \sqrt{s}/(2\cosh y_*)$$

and then with respect to β and β' between infinite limits yields the total cross section $\sigma(s)$ for the process under consideration.

For the effectively doublet spectrum, we find from (22) that

$$S\equiv S_2 = \frac{1}{m_W^2}(\rho_1^2M_1^2g_1^2 + 2c_{12}\rho_1\rho_2M_1M_2g_1g_2+\rho_2^2M_2^2g_2^2).$$

By fixing $\sqrt{s}$ in (21) (this corresponds to a preset collider energy) and any two of three kinematical variables y_*, Y, and $p_\perp$, we obtain three different functions of one variable and five parameters indicated above. Each of these functions can be used to determine these parameters. The corresponding procedure is similar to that described in detail in [25] for the process $e^-e^-\to W^-W^-$ in the case of two heavy Majorana neutrinos.

The cross sections for all six possible $\ell\ell'$ processes are determined by 20 parameters: M_1, M_2, $\rho_1^{\ell\ell'}$, $\rho_2^{\ell\ell'}$, and $c_{12}^{\ell\ell'}$. Of eighteen parameters $\rho_1^{\ell\ell'}$, $\rho_2^{\ell\ell'}$, and $c_{12}^{\ell\ell'}$, only nine are independent, those for which $\ell=\ell'$ [see (17)]. Provided that these parameters are known, one can determine nine parameters of the mixing matrix

$$||u_{\ell i}|| \equiv \left|\left|r_{\ell i}e^{i\varphi_{\ell i}}\right|\right|,$$

that is, six moduli $r_{\ell 1}$ and $r_{\ell 2}$ of the matrix elements of the first two columns and three phase differences $\Delta\varphi_\ell = \varphi_{\ell 1}-\varphi_{\ell 2}$.

ACKNOWLEDGMENTS

We are grateful to D.V. Peregudov for assistance in performing numerical calculations.

REFERENCES

1. Particle Data Group (S. Eidelman *et al.*), Phys. Lett. B **592**, 1 (2004).
2. S. M. Bilen'kiĭ, Usp. Fiz. Nauk **173**, 1171 (2003) [Phys. Usp. **46**, 1137 (2003)].
3. M. Maltoni, T. Schwetz, M. Tórtola, and J. W. F. Valle, hep-ph/0405172.
4. V. Barger, D. Marfatia, and A. Tregre, Phys. Lett. B **595**, 55 (2004); hep-ph/0312065; S. Hannestad, hep-ph/0404239.
5. V. M. Lobashev, Nucl. Phys. A **719**, 153c (2003).
6. F. Boehm and P. Vogel, *Physics of Massive Neutrinos* (Cambridge Univ. Press, New York, 1987; Mir, Moscow, 1990).
7. B. Kayser, hep-ph/0211134.
8. S. F. King, Rep. Prog. Phys. **67**, 107 (2004); hep-ph/0310204.
9. P. Langacker, Nucl. Phys. B (Proc. Suppl.) **100**, 383 (2001).
10. M. Zrałek, Acta Phys. Pol. B **28**, 2225 (1997); hep-ph/9711506.
11. M. G. Shchepkin, Usp. Fiz. Nauk **143**, 513 (1984) [Sov. Phys. Usp. **27**, 555 (1984)].
12. H. V. Klapdor-Kleingrothaus, I. V. Krivosheina, A. Dietz, and O. Chkvorets, Phys. Lett. B **586**, 198 (2004); hep-ph/0404088.
13. A. Ali, A. V. Borisov, and N. B. Zamorin, Eur. Phys. J. C **21**, 123 (2001).
14. A. Ali, A. V. Borisov, and N. B. Zamorin, in *Proceedings of the Tenth Lomonosov Conference on Elementary Particle Physics "Frontiers of Particle Physics," Moscow, 2001*, Ed. by A. I. Studenikin (World Sci., Singapore, 2003), p. 74.
15. O. Panella, M. Cannoni, C. Carimalo, and Y. N. Srivastava, Phys. Rev. D **65**, 035005 (2002).
16. M. Flanz, W. Rodejohann, and K. Zuber, Phys. Lett. B **473**, 324 (2000); **480**, 418(E) (2000).
17. W. Rodejohann and K. Zuber, Phys. Rev. D **62**, 094017 (2000).
18. A. Ali, A. V. Borisov, and D. V. Zhuridov, Vestn. Mosk. Univ., Ser. 3: Fiz., Astron., No. 1, 15 (2004).
19. M. Flanz, W. Rodejohann, and K. Zuber, Eur. Phys. J. C **16**, 453 (2000).
20. S. Dawson, Nucl. Phys. B **249**, 42 (1985); I. Kuss and H. Spiesberger, Phys. Rev. D **53**, 6078 (1996).
21. G. Bélanger, F. Boudjema, D. London, and H. Nadeau, Phys. Rev. D **53**, 6292 (1996); hep-ph/9508317; D. London, hep-ph/9907419.
22. J. Pumplin, D. R. Stump, J. Huston, *et al.*, J. High Energy Phys., No. 07, 012 (2002); hep-ph/0201195.
23. E. Nardi, E. Roulet, and D. Tommasini, Phys. Lett. B **344**, 225 (1995).
24. M. Blaskiewicz *et al.*, Fermilab Report TM-2158 (2001); F. M. L. de Almeida, Jr., Y. A. Coutinho, J. A. Martins Simões, and M. A. B. do Vale, hep-ph/0201032.
25. C. Greub and P. Minkowski, Int. J. Mod. Phys. A **13**, 2363 (1998); hep-ph/9612340.
26. M. Peskin and D. Schroeder, *An Introduction to Quantum Field Theory* (Addison-Wesley, New York, 1995; NITs RKhD, Izhevsk, 2001).

Translated by M. Kobrinsky

Physics of Atomic Nuclei, Vol. 68, No. 12, 2005, pp. 2068–2080. Translated from Yadernaya Fizika, Vol. 68, No. 12, 2005, pp. 2130–2142.

ELEMENTARY PARTICLES AND FIELDS
Theory

On the Possibility of Observing $a_0^0(980)-f_0(980)$ Mixing in the Reaction $\pi^- p \to \eta\pi^0 n$ on a Polarized Target

N. N. Achasov* **and G. N. Shestakov****

Sobolev Institute of Mathematics, Siberian Division, Russian Academy of Sciences, pr. Akademika Koptyuga 4, Novosibirsk, 630090 Russia

Received September 14, 2004

Abstract—It is shown that the spin asymmetry in the reaction $\pi^- p \to a_0^0(980)n \to (\eta\pi^0)_S n$ is highly sensitive to the mixing of the $a_0^0(980)$ and $f_0(980)$ resonances. At low momentum transfers (namely, in any of the intervals $0 \le -t \le 0.025, \ldots, 0.1\ \mathrm{GeV}^2$), the asymmetry normalized in such a way that it takes values between -1 and 1 must undergo a jump close in magnitude to unity in the region of the $\eta\pi^0$ invariant masses between 0.965 and 1.01 GeV. A large jump of the asymmetry is due exclusively to $a_0^0(980)-f_0(980)$ mixing. A very high resolution in the $\eta\pi^0$ invariant mass is not required for observing the jump of the asymmetry. The energy dependence of the polarization effect is expected to be rather weak; therefore, the polarization effect in question can be studied at any high energy—for example, in the range between 8 and 100 GeV. © *2005 Pleiades Publishing, Inc.*

1. INTRODUCTION

Investigation of the nature of light scalar resonances has become one of the most important problems of nonperturbative QCD. The point is that the clarification of their nature would be of paramount importance for obtaining deeper insights both into confinement physics and into the way in which chiral symmetry is realized in the region of low energies, these two phenomena being the main consequences of QCD in the hadron world. At the present time, it is generally accepted that the already well established lightest scalar resonances have a nontrivial nature. In particular, there are many pieces of evidence in support of the four-quark ($q^2\bar{q}^2$) structure of these states (see, for example, [1] and references therein). A new method for studying the nature of the $a_0(980)$ and $f_0(980)$ resonances in polarization experiments was recently proposed in [2]. The method in question is based on employing the phenomenon of $a_0^0(980)-f_0(980)$ mixing, this phenomenon carrying, among other things, important information about the coupling of these resonances to $K\bar{K}$ channels.

The mixing of the $a_0^0(980)$ and $f_0(980)$ resonances as a threshold phenomenon was predicted theoretically in the late 1970s [3]. In [3a], the cross section for the process $\pi^+\pi^- \to \eta\pi^0$, which is forbidden in G parity, but which can proceed owing to $a_0^0(980)-f_0(980)$ mixing, was calculated for the first time. In addition, some other processes that include the reactions $\pi^\pm N \to \eta\pi^0(N, \Delta)$ and $KN \to [(\eta\pi^0), (\pi^+\pi^-)][\Lambda, \Sigma, \Sigma(1385)]$ on unpolarized targets, the decay $f_1(1285) \to a_0^0(980)\pi^0 \to 3\pi$, and $\bar{p}n$ annihilation at rest via the processes $\bar{p}n \to (\pi^-, \rho^-)f_0(980) \to (\pi^-, \rho^-)\eta\pi^0$ and where one can observe $a_0^0(980)-f_0(980)$ mixing were considered in detail in [3], and the mixing-induced effects of isotopic-invariance violation in the $\eta\pi^0$ and $\pi\pi$ mass spectra and differential cross sections were estimated there.

In recent years, interest in $a_0^0(980)-f_0(980)$ mixing has been rekindled, and the possible manifestations of this phenomenon in various reactions have been hotly debated in the literature [4–19]. For example, it was hypothesized in [8] that data on the central production of the $a_0^0(980)$ resonance in the reaction $pp \to p_s(\eta\pi^0)p_f$ can in principle be interpreted as an argument in favor of $a_0^0(980)-f_0(980)$ mixing. In [11], it was indicated that, within the experimental errors and the model uncertainty in the cross section for $f_0(980)$ production, the results obtained in [8] are compatible with the predictions made in [3b] (1981). In order to confirm this scenario experimentally, it is necessary, however, to rule out the possible effect of secondary Regge trajectories, for which $\eta\pi^0$ production is not forbidden in G parity. This can achieved by performing measurements for the reaction $pp \to p_s(\eta\pi^0)p_f$ at much higher energies.

A qualitatively new proposal concerning searches

*e-mail: achasov@math.nsc.ru
**e-mail: shestako@math.nsc.ru

for the effect of $a_0^0(980)-f_0(980)$ mixing was put forth in [2]. Specifically, it was proposed there to perform measurements for the reaction $\pi^-p \to \eta\pi^0 n$ on a polarized target at a high energy, in which case the very fact that $a_0^0(980)-f_0(980)$ mixing exists can be established straightforwardly and unambiguously by the presence of a large jump in the azimuthal (spin) asymmetry of the cross section for the production of the $\eta\pi^0$ system in the S wave in the vicinity of $K\bar{K}$ thresholds.

In the present study, we consider in greater detail the polarization effect expected in the reaction $\pi^-p \to a_0^0(980)n \to (\eta\pi^0)_S n$ and discuss thoroughly all relevant quantitative estimates (here and below, the index S indicates that we are dealing with the $\eta\pi^0$ system in the state of relative orbital angular momentum $L = 0$—that is, in the S wave). It should be emphasized that the estimates presented here for the magnitude of the polarization effect that must be observed experimentally are model-independent to a considerable extent. Below, it will be shown that the jump in the spin asymmetry is due exclusively to $a_0^0(980)-f_0(980)$ mixing, which violates isotopic invariance, and that the expected polarization effect is quite sizable. Its measure is provided by the characteristic scale of the normalized spin asymmetry, which assumes values in the range between -1 and 1. Our main conclusion is that, on the scale indicated above, the asymmetry in the region of $K\bar{K}$ thresholds must undergo a jump close to unity in magnitude. Further, it is emphasized that a reliable observation of the jump in the asymmetry does not require a resolution in the invariant mass of the $\eta\pi^0$ system as high as that which would be necessary for revealing manifestations of $a_0^0(980)-f_0(980)$ mixing in the mass spectrum of the $\eta\pi^0$ system in an experiment featuring no polarizations. The energy dependence of the polarization effect is expected to be rather weak; therefore, it can be studied at any high energy—for example, in the range between 8 and 100 GeV.

The ensuing exposition is organized as follows. In Section 2, we determine the cross section and asymmetry for the reaction $\pi^-p \to (\eta\pi^0)_S n$ on a polarized target. Section 3 is purely technical. It contains detailed expressions for the amplitudes of the reaction $\pi^-p \to a_0^0(980)n \to (\eta\pi^0)_S n$ at high energies. These amplitudes correspond to the mechanisms of ρ_2, b_1, and π Regge exchanges. The one-pion-exchange mechanism, which violates G parity, owes its existence to $a_0^0(980)-f_0(980)$ mixing. In the same section, we demonstrate the special features of the amplitude for the $a_0^0(980)-f_0(980)$ transition that are of crucial importance for polarization phenomena. In Section 4, we discuss data from experiments performed to date to study the reaction $\pi^-p \to \eta\pi^0 n$ on unpolarized targets and present quantitative estimates of the contributions of the ρ_2- and b_1-exchange mechanisms to the cross section for the production of the $(\eta\pi^0)_S$ system. In Section 5, the polarization effect due to $a_0^0(980)-f_0(980)$ mixing is calculated on the basis of the ρ_2- and π-exchange model. The analogous results obtained on the basis of the ρ_2-, b_1-, and π-exchange model are given in Section 6. The conclusions based on the results presented in those two sections are briefly formulated in Section 7.

2. CROSS SECTION AND ASYMMETRY

Upon taking into account parity conservation, the differential cross section for the reaction $\pi^-p \to (\eta\pi^0)_S n$ on polarized protons at a fixed momentum of the incident negatively charged pion, $P_{\text{lab}}^{\pi^-}$, can be represented in the form

$$d^3\sigma/dtdmd\psi = [d^2\sigma/dtdm + I(t,m)P\cos\psi]/2\pi, \quad (1)$$

where t is the square of the 4-momentum transfer from this pion to the $\eta\pi^0$ system; m is the invariant mass of this system; ψ is the angle between the normal to the plane spanned by the momenta of the negatively charged pion and the $\eta\pi^0$ system and the direction of proton polarization, which is transverse with respect to the axis of the incident-pion beam; P is the degree of this polarization; $d^2\sigma/dtdm = |M_{++}|^2 + |M_{+-}|^2$ is the cross section for the analogous reaction on unpolarized protons, M_{+-} and M_{++} being, respectively, the s-channel helicity amplitude for nucleon-helicity-flip processes and its non-helicity-flip counterpart; and $I(t,m) = 2\text{Im}(M_{++}M_{+-}^*)$ describes the contribution responsible for the azimuthal (spin) asymmetry of the cross section. The dimensionless normalized asymmetry $A(t,m) = I(t,m)/[d^2\sigma/dtdm]$, $-1 \le A(t,m) \le 1$, is determined in terms of the experimentally measurable quantities $I(t,m)$ and $d^2\sigma/dtdm$. The asymmetry associated with some interval of $-t$, $A(-t_1 \le -t \le -t_2, m)$, or with some interval of m, $A(t, m_1 \le m \le m_2)$, is naturally given by the ratio of the corresponding integrals of $I(t,m)$ and $d^2\sigma/dtdm$ with respect to t or m. Here, we will consider exclusively the region around $m \approx 1$ GeV, where, according to available data on the reaction $\pi^-p \to \eta\pi^0 n$ [4, 20–23], the mass spectrum of the $(\eta\pi^0)_S$ system is dominated by the contribution from the production of the $a_0^0(980)$ resonance via the process $\pi^-p \to a_0^0(980)n \to (\eta\pi^0)_S n$.

From G-parity conservation, it follows that, at high energies and low $-t$, the amplitudes M_{+-} and

M_{++} receive contributions from t-channel exchanges characterized by the quantum numbers of, respectively, b_1- and ρ_2 Regge poles [5]. In the following, these amplitudes will be written as $M_{+-}^{b_1}$ and $M_{++}^{\rho_2}$.[1)] If one considers the mixing of $a_0^0(980)$ and $f_0(980)$ resonances, which violates G parity, then, in the reaction $\pi^- p \to (\eta\pi^0)_S n$, the exchange of the pion Regge pole in the t channel becomes possible owing to the process $\pi^- p \to f_0(908)n \to a_0^0(980)n \to (\eta\pi^0)_S n$ [3, 5].[2)] As is well known, the amplitude of pion exchange in the reaction $\pi^- p \to (\pi\pi)_S n$ is great in the region of low $-t$. In addition, we note that both the magnitude and the phase of the amplitude of the $a_0^0(980) - f_0(980)$ transition change very sharply and strongly versus m in the region of $K\bar{K}$ thresholds (see Section 3 below). In the following, we will show that, taken together, all these facts lead to impressive consequences that can readily be detected in polarization experiments owing to the unique possibility of observing, in them, the interference between the amplitudes of ρ_2 and π exchanges.

3. AMPLITUDES OF THE REACTION $\pi^- p \to a_0^0(980)n \to (\eta\pi^0)_S n$

We will make use of the Regge pole model and represent the amplitudes of ρ_2, b_1, and π exchanges in the reaction $\pi^- p \to a_0^0(980)n \to (\eta\pi^0)_S n$ as

$$M_{++}^{\rho_2} = e^{-i\pi\alpha_{\rho_2}(t)/2} e^{\Lambda_{\rho_2} t/2} (s/s_0)^{\alpha_{\rho_2}(0)-1} \quad (2)$$
$$\times\, a_{\rho_2} G_{a_0}(m) [2m^2 \Gamma_{a_0\eta\pi^0}(m)/\pi]^{1/2},$$

$$M_{+-}^{b_1} = ie^{-i\pi\alpha_{b_1}(t)/2} \sqrt{-t} e^{\Lambda_{b_1} t/2} \quad (3)$$
$$\times\, (s/s_0)^{\alpha_{b_1}(0)-1} a_{b_1} G_{a_0}(m) [2m^2 \Gamma_{a_0\eta\pi^0}(m)/\pi]^{1/2},$$

$$M_{+-}^{\pi} = e^{-i\pi\alpha_\pi(t)/2} \frac{\sqrt{-t}}{t - m_\pi^2} e^{\Lambda_\pi (t - m_\pi^2)/2} \quad (4)$$
$$\times\, a_\pi e^{i\delta_B(m)} G_{a_0 f_0}(m)\, [2m^2 \Gamma_{a_0\eta\pi^0}(m)/\pi]^{1/2}.$$

From the outset, we note that, for the pion-exchange amplitude M_{+-}^{π}, which is forbidden by G-parity conservation, there is almost an entire body of information, including its absolute normalization [3, 5, 25, 26]. In expressions (2)–(4), $\alpha_j(t) = \alpha_j(0) + \alpha_j' t$, a_j, and $\Lambda_j/2 = \Lambda_j^0/2 + \alpha_j' \ln(s/s_0)$ are, respectively, the trajectory of the j Regge pole, the residue at this pole, and the slope of the residue [as a guideline, we can take the values of $\alpha_\pi(t) \approx 0.8(t - m_\pi^2)/\mathrm{GeV}^2$, $\alpha_{b_1}(t) \approx -0.21 + 0.8t/\mathrm{GeV}^2$, and $\alpha_{\rho_2}(t) \approx -0.31 + 0.8t/\mathrm{GeV}^2$]; $s \approx 2m_p P_{\mathrm{lab}}^{\pi^-}$; $s_0 = 1\,\mathrm{GeV}^2$; $G_{a_0}(m) = D_{f_0}(m)/[D_{a_0}(m)D_{f_0}(m) - \Pi_{a_0 f_0}^2(m)]$ is the propagator of the $a_0^0(980)$ resonance with allowance for mixing [3]; $G_{a_0 f_0}(m) = \Pi_{a_0 f_0}(m)/[D_{a_0}(m)D_{f_0}(m) - \Pi_{a_0 f_0}^2(m)]$; $\Pi_{a_0 f_0}(m)$ is that off-diagonal element of the polarization operator which describes the amplitude of the $a_0^0(980) - f_0(980)$ transition [3]; $1/D_r(m)$ is the propagator for the nonmixed resonance r of mass m_r [$r = a_0(980), f_0(980)$]; $D_r(m) = m_r^2 - m^2 + \Sigma_{ab}[\mathrm{Re}\Pi_r^{ab}(m_{f_0}) - \Pi_r^{ab}(m)]$ [$ab = \eta\pi^0, K^+K^-, K^0\bar{K}^0$ for $r = a_0(980)$ and $ab = \pi^+\pi^-, \pi^0\pi^0, K^+K^-, K^0\bar{K}^0$ for $r = f_0(980)$]; and $\Pi_r^{ab}(m)$ is that diagonal element of the polarization operator for the resonance r which corresponds to the contribution of the intermediate state ab [25, 26]. For $m \geq m_a + m_b$, the diagonal element has the form

$$\Pi_r^{ab}(m) = \frac{g_{rab}^2}{16\pi}\left[\frac{m_+ m_-}{\pi m^2}\ln\frac{m_b}{m_a} + \rho_{ab}(m)\right.$$
$$\left.\times\left(i - \frac{1}{\pi}\ln\frac{\sqrt{m^2 - m_-^2} + \sqrt{m^2 - m_+^2}}{\sqrt{m^2 - m_-^2} - \sqrt{m^2 - m_+^2}}\right)\right],$$

where g_{rab} is the constant representing the coupling of the resonance r to the ab channel (here, we have $g_{f_0\pi^0\pi^0}^2 = g_{f_0\pi^+\pi^-}^2/2$ for identical neutral pions), $\rho_{ab}(m) = [(m^2 - m_+^2)(m^2 - m_-^2)]^{1/2}/m^2$, $m_\pm = m_a \pm m_b$ ($m_a \geq m_b$), and $\Gamma_{rab}(m) = \mathrm{Im}[\Pi_r^{ab}(m)]/m = g_{rab}^2 \rho_{ab}(m)/16\pi m$ is the $r \to ab$ decay width; if $m_- \leq m \leq m_+$, then $(m^2 - m_+^2)^{1/2}$ must be replaced by $i(m_+^2 - m^2)^{1/2}$. In expression (4), $a_\pi = g_{\pi NN} g_{f_0\pi^+\pi^-}/\sqrt{8\pi s}$ (where $g_{\pi NN}^2/4\pi \approx 14.3$), while $\delta_B(m)$ is the phase (which is smooth and large, about 90° at $m \approx 1$ GeV) of the elastic background accompanying the $f_0(980)$ resonance in the S-wave reaction $\pi\pi \to \pi\pi$ in the $I = 0$ channel (where I is the isospin) [3, 25, 26].

In view of the proximity of the $a_0^0(980)$ and $f_0(980)$ resonances to $K\bar{K}$ thresholds and their strong coupling to $K\bar{K}$ channels, the amplitude of the $a_0^0(980) - f_0(980)$ transition, $\Pi_{a_0 f_0}(m)$, is expected

[1)] The history of the exchange of the ρ_2 Regge pole is described in [5]. We recall that the lowest representative of the ρ_2 Regge trajectory has the quantum numbers $I^G(J^{PC}) = 1^+(2^{--})$ and belongs to the $^3D_2$ family of $q\bar{q}$ states [24].

[2)] This process may also proceed via a_1 exchange. However, estimates obtained on the basis of [25] reveal that, at low $-t$, the amplitude $M_{++}^{a_1}$ is negligible in relation to other contributions.

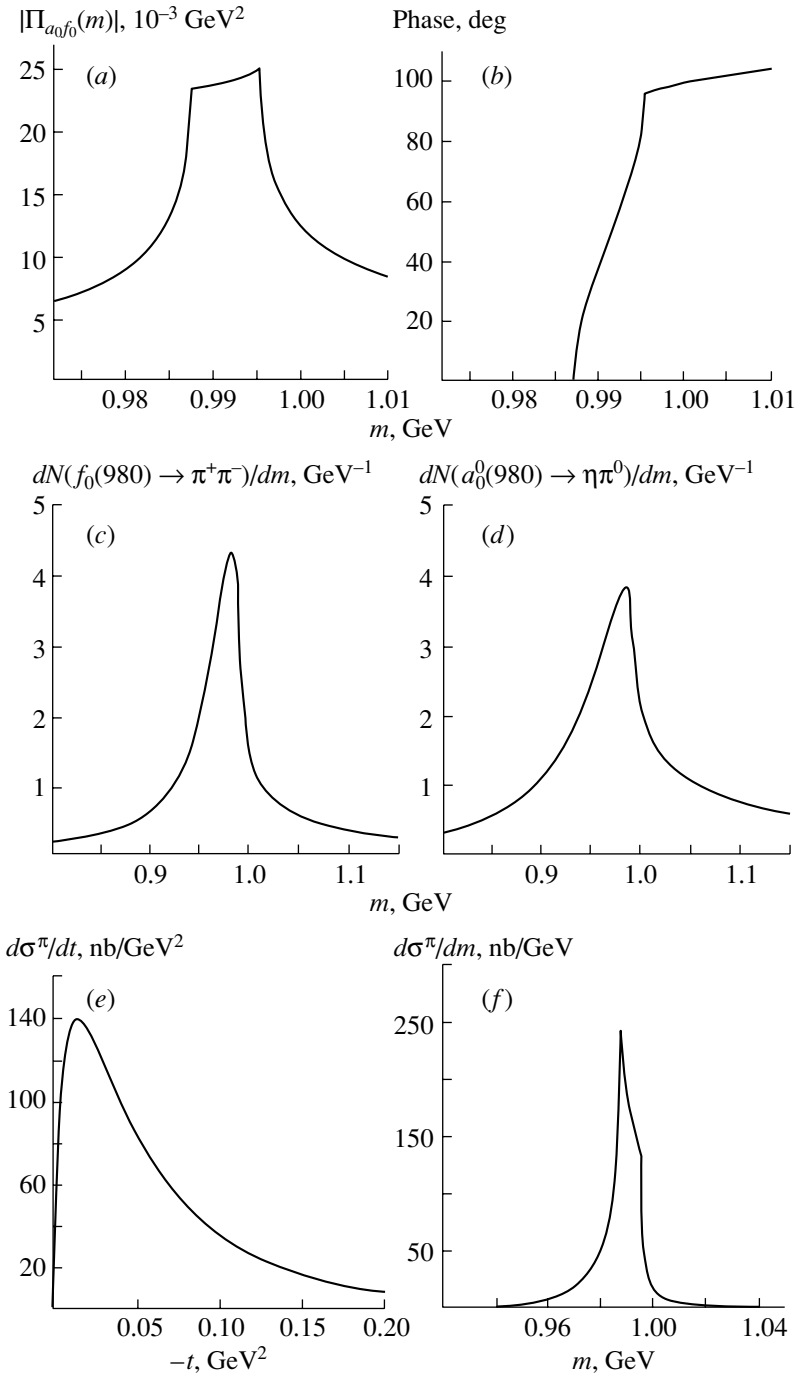

Fig. 1. Example of the (*a*) absolute value and (*b*) phase of the amplitude of the $a_0^0(980)-f_0(980)$ transition [see expression (5)]; (*c*) example of the $\pi^+\pi^-$ mass spectrum corresponding to a single $f_0(980)$ resonance; (*d*) example of the $\eta\pi^0$ mass spectrum corresponding to a single $a_0^0(980)$ resonance; and (*e*, *f*) differential cross sections $d\sigma^\pi/dt$ and $d\sigma^\pi/dm$ for the reaction $\pi^-p \to f_0(980)n \to a_0^0(980)n \to (\eta\pi^0)_S n$ at $P_{\text{lab}}^{\pi^-} = 18.3$ GeV that were calculated for the pion-exchange mechanism and which are associated with the intervals $0.8 \le m \le 1.2$ GeV and $0 \le -t \le 0.025$ GeV^2, respectively.

to receive significant contributions from K^+K^- and $K^0\bar{K}^0$ intermediate states [3]. Evaluating the sum of the $f_0(980) \to K^+K^- \to a_0^0(980)$ and $f_0(980) \to K^0\bar{K}^0 \to a_0^0(980)$ loop diagrams and taking into account isotopic symmetry for the respective coupling constants, one can obtain [3]

$$\Pi_{a_0f_0}(m) = \frac{g_{a_0K^+K^-}g_{f_0K^+K^-}}{16\pi} \qquad (5)$$

$$\times\left[i(\rho_{K^+K^-}(m)-\rho_{K^0\bar{K}^0}(m))-\frac{\rho_{K^+K^-}(m)}{\pi}\right.$$
$$\times\ln\frac{1+\rho_{K^+K^-}(m)}{1-\rho_{K^+K^-}(m)}+\frac{\rho_{K^0\bar{K}^0}(m)}{\pi}$$
$$\left.\times\ln\frac{1+\rho_{K^0\bar{K}^0}(m)}{1-\rho_{K^0\bar{K}^0}(m)}\right],$$

where $m\geq 2m_{K^0}$; in the region $0\leq m\leq 2m_K$, the quantity $\rho_{K\bar{K}}(m)$ must be replaced by $i|\rho_{K\bar{K}}(m)|$. A "resonance-type" behavior of the absolute value and phase of expression (5) is clearly demonstrated in Figs. 1*a* and 1*b*. We note that, in the region of m between K^+K^- and $K^0\bar{K}^0$ thresholds, which has a width of 8 MeV, we have $|\Pi_{a_0f_0}(m)|\approx|g_{a_0K^+K^-}g_{f_0K^+K^-}/16\pi|[(m^2_{K^0}-m^2_{K^+})/m^2_{K^0}]^{1/2}\approx 0.1265|g_{a_0K^+K^-}g_{f_0K^+K^-}/16\pi|$—that is, this quantity is of order $m_K(m^2_{K^0}-m^2_{K^+})^{1/2}\approx\sqrt{\alpha}m^2_K$ [3].[3)] From (4) and (5), it also follows that, in this region, the contribution of the amplitude M^π_{+-} to $d^2\sigma/dtdm$ is controlled predominantly by the products of the ratios of the coupling constants squared; that is, $|M^\pi_{+-}|^2\propto\sigma(\pi^+\pi^-\to\eta\pi^0)\propto(g^2_{f_0K^+K^-}/g^2_{f_0\pi^+\pi^-})\times(g^2_{a_0K^+K^-}/g^2_{a_0\eta\pi^0})$.

In plotting the quantity $|\Pi_{a_0f_0}(m)|$ in Fig. 1*a* and deriving the numerical estimates given below for the polarization effect, we employed the following approximate values for the parameters of the $f_0(980)$ and $a_0(980)$ resonances:

$$m_{f_0}\approx 0.980\ GeV, g^2_{f_0\pi^+\pi^-}/16\pi\approx\frac{2}{3}0.1\ \mathrm{GeV}^2,$$
$$g^2_{f_0K^+K^-}/16\pi\approx\frac{1}{2}0.4\ \mathrm{GeV}^2,$$
$$\delta_B(m)\approx 35.5^\circ+47^\circ m/\mathrm{GeV},$$
$$m_{a_0}\approx 0.9847\ GeV, g^2_{a_0K^+K^-}/16\pi$$
$$\approx g^2_{f_0K^+K^-}/16\pi\approx\frac{1}{2}0.4\ \mathrm{GeV}^2,$$
$$\text{and}\ \ g^2_{a_0\eta\pi^0}/16\pi\approx 0.25\ \mathrm{GeV}^2$$

(see also [3, 24–30]). For the above parameter values, Figs. 1*c* and 1*d* illustrate the $\pi^+\pi^-$ and $\eta\pi^0$ mass spectra $dN(f_0(980)\to\pi^+\pi^-)/dm=2m^2\times\Gamma_{f_0\pi^+\pi^-}(m)/\pi|D_{f_0}(m)|^2$ and $dN(a_0(980)\to\eta\pi^0)/dm=2m^2\Gamma_{a_0\eta\pi^0}(m)/\pi|D_{a_0}(m)|^2$ corresponding to solitary $f_0(980)$ and $a_0(980)$ resonances.[4)] We note that, while $\Gamma_{f_0\pi\pi}(m_{f_0})=\frac{3}{2}\Gamma_{f_0\pi^+\pi^-}(m_{f_0})\approx 98$ MeV and $\Gamma_{a_0\eta\pi^0}(m_{f_0})\approx 166$ MeV, the "apparent" (effective) widths of the corresponding peaks (FWHM values) are approximately equal to 42 and 68 MeV, respectively, owing to the coupling of the resonances to $K\bar{K}$ channels. In turn, Figs. 1*e* and 1*f* give an idea of the absolute values and characteristic shape of the differential cross sections $d\sigma^\pi/dt=\int|M^\pi_{+-}|^2dm$ and $d\sigma^\pi/dm=\int|M^\pi_{+-}|^2dt$ at the momentum of $P^{\pi^-}_{\mathrm{lab}}=18.3$ GeV (that is, at the momentum of incident negatively charged pions at the accelerator of the Brookhaven National Laboratory [4]), in which case $\Lambda_\pi/2\approx 4.5\ \mathrm{GeV}^{-2}$ [31, 32], these cross sections corresponding to the region of integration with respect to m from 0.8 to 1.2 GeV for the former and the region of integration with respect to t from $-0.025\ \mathrm{GeV}^2$ to 0 for the latter. Integrating the cross section $d\sigma^\pi/dt$ shown in Fig. 1*e* with respect to t, we find that the total cross section for the reaction $\pi^-p\to a^0_0(980)n\to(\eta\pi^0)_Sn$ proceeding via the pion-exchange mechanism is $\sigma^\pi\approx 10.9$ nb. On the basis of the previous investigations reported in [3, 5], one can conclude that the value indicated here for the cross section σ^π should be treated as quite a reliable lower bound on it. Thus, one can see that, by using the values given above for the parameters

[3)] The effect that we consider is the only effect of order $\sqrt{m_d-m_u}\sim\sqrt{\alpha}$. As to effects of order $m_d-m_u\sim\alpha$, they are small. Such effects were partly considered in [9] [$a^0_0(980)\to\eta\pi^0\to\pi^0\pi^0\to f_0(980)$]. The quantity $|\Pi_{a_0f_0}(m)|$ for $m<0.95$ GeV and $m>1.05$ GeV gives a clear idea of the magnitude of effects whose order is $m_d-m_u\sim\alpha$ (see Fig. 1*a*). We note that $|\Pi_{\rho^0\omega}(m)|\sim|\Pi_{\pi^0\eta}(m)|\approx 0.0036\ \mathrm{GeV}^2\sim(m_d-m_u)$.

[4)] The simplest line shape shown for a solitary $f_0(980)$ resonance in Fig. 1*c* is distorted in many reactions because of its interference with accompanying background contributions. By way of example, we indicate that, in the region of the $f_0(980)$ resonance, the amplitude of the $I=0$ S wave in the reaction $\pi\pi\to\pi\pi$ has the form $T^0_0=(e^{2i\delta_B(m)}-1)/2i+e^{2i\delta_B(m)}m\Gamma_{f_0\pi\pi}(m)/D_{f_0}(m)$, where the phase $\delta_B(m)$ of a smooth elastic background is close to 90°. Owing to precisely this circumstance, the $f_0(980)$ resonance manifests itself in the corresponding cross section for the process $\pi\pi\to\pi\pi$ as an interference dip rather than a peak. In our case, the amplitude M^π_{+-} involves the amplitude of the reaction $\pi^+\pi^-\to f_0(980)\to K\bar{K}\to a^0_0(980)\to\eta\pi^0$; along with the resonance phase, this amplitude must feature an additional phase of the nonresonance elastic background in the $\pi\pi$ channel. This is the reason why the factor $e^{i\delta_B(m)}$ was introduced in (4). In such situations, this is the simplest (and commonly accepted) method for taking into account nonresonance contributions in accord with the unitarity condition. Since the phase $\delta_B(m)$ is large, it is of paramount importance to take it into account. Nothing is known about the analogous background phase in the $\eta\pi^0$ channel. However, this phase does not play any role in the case being considered, since it is common to all of the amplitudes in (2), (3), and (4). For additional details concerning the aforesaid, the interested reader is referred, for example, to [3, 25–27].

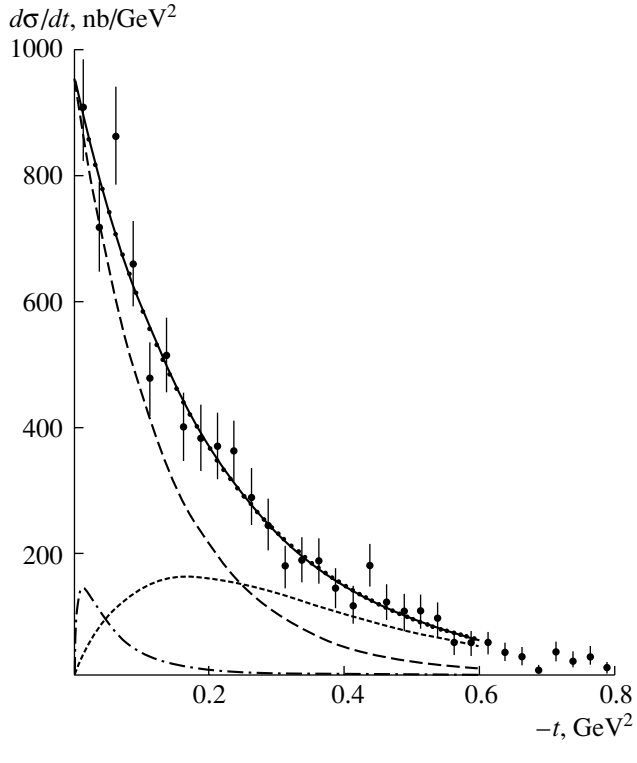

Fig. 2. Differential cross section $d\sigma/dt$ for the reaction $\pi^-p \to a_0^0(980)n \to (\eta\pi^0)_S n$: (points) normalized experimental data from the Brookhaven National Laboratory [4]; (solid curve) fit to these data within the ρ_2-exchange model; (dotted curve, which is nearly coincident with the solid curve) approximation of the data within the model that takes into account ρ_2 and b_1 exchanges, whose possible contributions to $d\sigma/dt$ are represented by long and short dashes, respectively; and (dash-dotted curve) differential cross section $d\sigma^\pi/dt$ corresponding to Fig. 1*e*.

of the $a_0^0(980)$ and $f_0(980)$ resonances, we actually obtain the most conservative estimates of the expected polarization effect. Finally, we emphasize that a sharp change of 90° in the phase of the amplitude $\Pi_{a_0 f_0}(m)$ between $K\bar{K}$ thresholds, this being of crucial importance for polarization phenomena, does not depend on the parameters of the $f_0(980)$ and $a_0^0(980)$ resonances [see Fig. 1*b* and formula (5)].

In order to obtain quantitative estimates for the contributions of the ρ_2- and b_1-exchange mechanisms to the cross section for $(\eta\pi^0)_S$ production and assess thereby the relative contribution of pion exchange, it is necessary to invoke existing experimental data.

4. DATA FROM EXPERIMENTS WITH UNPOLARIZED TARGETS

Experiments devoted to studying the reaction $\pi^-p \to \eta\pi^0 n$ on unpolarized targets were performed at the momenta of $P_{\text{lab}}^{\pi^-} = 18.3$ GeV at the Brookhaven National Laboratory (BNL) [4, 20, 21], 38 GeV at the Institute for High Energy Physics (IHEP, Protvino) [22, 23], 32 GeV at IHEP [23], and 100 GeV at CERN [23]. The resulting situation is quite interesting. The point is that the BNL [4], IHEP [22, 23], and CERN [23] data on dN/dt, which is the quantity obtained by integrating the t distribution of events of the reaction $\pi^-p \to a_0^0(980)n \to (\eta\pi^0)_S n$ with respect to m in the region of the $a_0^0(890)$ peak, formally do not require introducing the b_1-exchange amplitude $M_{+-}^{b_1}$. Within the interval $0 \le -t \le (0.6-0.8)$ GeV^2, all of them admit a very accurate approximation by a simple exponential dependence $C\exp(\Lambda t)$ at $\Lambda \approx 5$ GeV^2 [5, 22, 23], this demonstrating that they can be described by using only the amplitude $M_{++}^{\rho_2}$ [5], which does not vanish for $t \to 0$. For example, the corresponding fit to normalized BNL data [4, 5] on the differential cross section $d\sigma/dt$ for the reaction $\pi^-p \to a_0^0(980)n \to (\eta\pi^0)_S n$ (solid curve in Fig. 2) yields $\chi^2/n.d.f. = 15.75/22$ and $d\sigma/dt = (945.8 \pm 46.3\ \text{nb/GeV}^2)\exp[(4.729 \pm 0.217)t/\text{GeV}^2]$. Here, it is necessary to indicate that the experimental points in Fig. 2 correspond to BNL data on dN/dt at $P_{\text{lab}}^{\pi^-} = 18.3$ GeV [4] that were normalized to the cross section for $a_2^0(1320)$ production in the reaction $\pi^-p \to a_2^0(1320)n$ by following the method used in [5]. According to the estimate obtained in [5], the total cross section σ for the reaction $\pi^-p \to a_0^0(980)n \to (\eta\pi^0)_S n$ at 18.3 GeV is about 200 nb. We refer this value to the region of m between 0.8 and 1.2 GeV and to the entire region $t \le 0$. We note that it agrees well with the analogous estimate presented for σ in [22]. Comparing now the values indicated for σ and $d\sigma/dt$ with σ^π and $d\sigma^\pi/dt$ estimated in the preceding section and associated with pion exchange,[5)] we find that $\sigma^\pi \approx 10.9$ nb is about 5.5% of the total reaction cross section and that $d\sigma^\pi/dt$ at the maximum occurring at $t \approx -0.0149$ GeV^2 is about 139 nb/GeV^2, which is approximately 14.7% of $(d\sigma/dt)|_{t\approx 0}$ (see Fig. 2). However, the most important point here is that, at any value of t, the corresponding value of $d\sigma^\pi/dt$ is due almost completely to a narrow region of m near $K\bar{K}$ thresholds (see Figs. 1*a*, 1*f*), while the value of the "total" $d\sigma/dt$ comes from integration over an m region that is at least an order of magnitude wider (see, for example, Fig. 1*d*). Thus, we can see that, at low $-t$ and m in the vicinity of $K\bar{K}$ thresholds, the pion-exchange contribution can be commensurate

[5)] For the comparison of $d\sigma/dt$ and $d\sigma^\pi/dt$ to be convenient, the curve for $d\sigma^\pi/dt$ given in Fig. 1*e* is reproduced in Fig. 2.

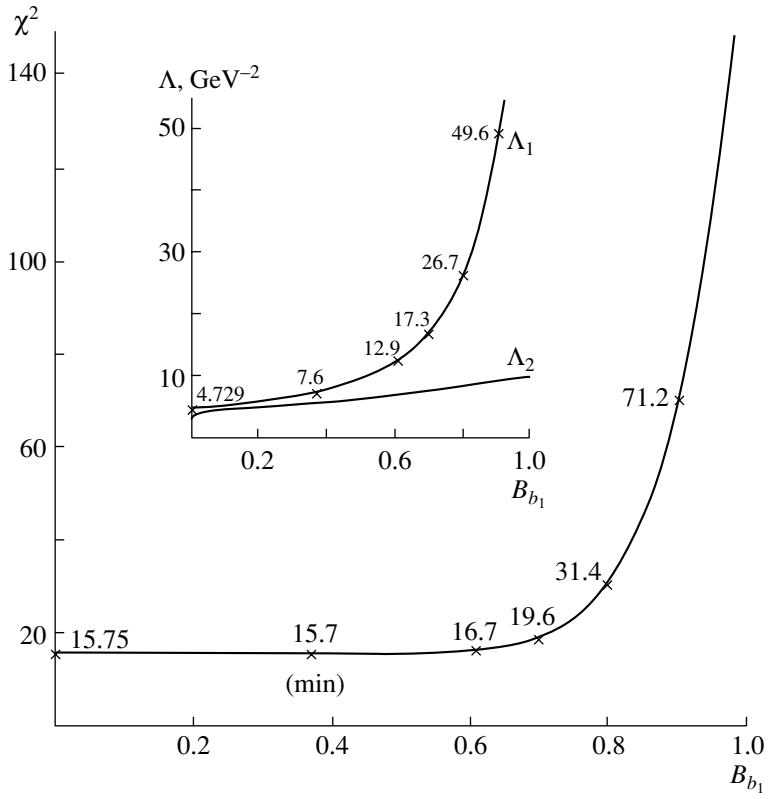

Fig. 3. Values of χ^2, Λ_1, and Λ_2 (the last two are given in the inset) versus B_{b_1} that were obtained by fitting expression (6) to BNL data (see Fig. 2). The χ^2 and Λ_1 values indicated in the figure correspond (from left to right) to $B_{b_1} = 0$, 0.37, 0.61, 0.7, 0.8, and 0.9.

with contribution of ρ_2 exchange, which is the leading one allowed by G parity.

Yet, a good quality of fits to t distributions [4, 22, 23] in terms of the function $C\exp(\Lambda t)$ is not a conclusive argument in favor of discarding the b_1-exchange contribution. In principle, the data from [4, 22, 23] are equally well described by the expression $dN/dt = C_1\exp(\Lambda_1 t) - tC_2\exp(\Lambda_2 t)$ [5, 22], where the first and the second term can be identified with, respectively, the contribution of the amplitude $M_{++}^{\rho_2}$ and the contribution of the amplitude $M_{+-}^{b_1}$ [see Eqs. (2) and (3)]. Figure 2 shows an approximation of the BNL data for the case where the b_1-exchange contribution is not zero. The dotted curve there represents $d\sigma/dt = d\sigma^{\rho_2}/dt + d\sigma^{b_1}/dt$, while long and short dashes show the contributions $d\sigma^{\rho_2}/dt = (958.1\ \text{nb/GeV}^2)\exp(7.6t/\text{GeV}^2)$ and $d\sigma^{b_1}/dt = (-t\times 2486.6[\ \text{nb/GeV}^4])\exp(5.8t/\text{GeV}^2)$, respectively. One can see that the dotted curve is nearly coincident with the solid curve, which corresponds to a fit within the model featuring only ρ_2 exchange. In the present example, b_1 exchange saturates approximately 37% of the integrated cross section. Thus, the χ^2 criterion is insufficient for distinguishing between the two models in question.[6)] Additional information about the model of ρ_2 and b_1 exchanges can be obtained from a fit to the BNL data in terms of the parametrization

$$d\sigma/dt = \sigma[(1-B_{b_1})\Lambda_1 e^{\Lambda_1 t} - tB_{b_1}\Lambda_2^2 e^{\Lambda_2 t}], \quad (6)$$

where $\sigma = 200$ nb, Λ_1 and Λ_2 are adjustable parameters, and B_{b_1} is a fixed b_1-exchange-induced fraction of the integrated cross section. The χ^2, Λ_1, and Λ_2 values obtained in the present study are shown in Fig. 3 versus B_{b_1}. The points indicated on the curves representing χ^2 and Λ_1 correspond (from left to right) to the values of $B_{b_1} = 0$, 0.37, 0.61, 0.7, 0.8, and 0.9. As can be seen from Fig. 3, χ^2 has a broad plateau, remaining virtually constant as B_{b_1} increases from 0 to 0.37;[7)] it increases by unity only when B_{b_1} reaches a value of 0.61. At $B_{b_1} = 0.7$, χ^2 takes a value of about

[6)] We emphasize that only polarization experiments would make it possible to assess unambiguously the contribution of the b_1-exchange amplitude, since only via such experiments would it be possible to perform direct measurements of the interference contribution $\text{Im}(M_{++}M_{+-}^*)$ along with direct measurements of the sum $|M_{++}|^2 + |M_{+-}|^2$.

[7)] The χ^2 functional passes through an "invisible" minimum at $B_{b_1} \approx 0.37$.

19.6 and increases sharply as B_{b_1} grows further. The approximation of the BNL data by expression (6) at $B_{b_1} = 0.7$ is shown in Fig. 4. Formally, this approximation is similar to the approximations presented in Fig. 2 for the cases of (solid curve) $B_{b_1} = 0$ and (dotted curve) $B_{b_1} = 0.37$. The crucial distinction between these examples lies, however, in the values of the slope of Λ_1 for the contribution of ρ_2 exchange. From the inset in Fig. 3, one can see that Λ_1 grows very strongly with increasing B_{b_1}. While a value of $\Lambda_1 \approx 4.729\ \mathrm{GeV}^{-2}$ (at $B_{b_1} = 0$) and a value of $\Lambda_1 \approx 7.6\ \mathrm{GeV}^{-2}$ (at $B_{b_1} = 0.37$) are quite reasonable from the point of view of Regge phenomenology for secondary Regge exchanges, the slope $\Lambda_1 \approx 17.3\ \mathrm{GeV}^{-2}$ (at $B_{b_1} = 0.7$) is absolutely improbable, to say nothing of greater slope values. For the sake of completeness, we nevertheless consider the polarization effect for this case inclusive (see Section 6 below).

5. POLARIZATION EFFECT IN THE MODEL OF ρ_2 AND π EXCHANGES

In view of the aforementioned ambiguity in the information about the b_1-exchange contribution, it is natural to present first of all the theoretical results that the model featuring only the ρ_2 and π-exchange mechanisms yields for the polarization effect induced by $a_0^0(980)-f_0(980)$ mixing.

In Figs. 5*a*, 5*c*, and 5*e* (left panels of the figure), we display, respectively, $d\sigma/dm = \int[|M^{\rho_2}_{++}|^2 + |M^{\pi}_{+-}|^2]dt$ and $d\sigma^{\rho_2}/dm = \int |M^{\rho_2}_{++}|^2 dt$, $I(m) = \int I(t,m)dt = \int 2\mathrm{Im}[M^{\rho_2}_{++}(M^{\pi}_{+-})^*]dt$ at $P^{\pi^-}_{\mathrm{lab}} = 18.3$ GeV (these quantities are given for the interval of $-t$ between 0 and 0.025 GeV^2), and the corresponding asymmetry $A(0 \le -t \le 0.025\ \mathrm{GeV}^2, m)$. Figures 5*b*, 5*d*, and 5*f* (right panels) show the same quantities but for the interval of $-t$ between 0 and 0.2 GeV^2. Here, the values that we substituted into (2) for the parameters of ρ_2 exchange are identical to those in the fit to the BNL data that was discussed above and which is represented by the solid curve in Fig. 2. Since the relative sign of ρ_2 and π exchanges is unknown, $I(m)$ and the asymmetry are determined apart from the sign, which was chosen arbitrarily. We also note that, in the model of ρ_2 and π exchanges, $I(m)$ and the asymmetry for the reaction $\pi^- p \to (\eta\pi^0)_S n$, which is considered here, differ in sign from their counterparts for the reaction $\pi^+ n \to (\eta\pi^0)_S p$, which is related to it by charge symmetry. As follows from the pattern emerging from Fig. 5, the polarization effect induced by the interference between the amplitudes $M^{\rho_2}_{++}$ and M^{π}_{+-} is quite sizable in any of the intervals $0 \le -t \le 0.025, \ldots, 0.2\ \mathrm{GeV}^2$. For its measure, one can take the magnitude of the characteristic jump that the asymmetry undergoes in the region of m between 0.965 and 1.01 GeV. By way of example, we indicate that, in this region, the corresponding difference of the maximum and the minimum value of the asymmetry smoothed because of a finite resolution in m[8)] is approximately 0.95 for the interval $0 \le -t \le 0.025\ \mathrm{GeV}^2$ (see Fig. 5*e*) and is approximately 0.75 for the interval $0 \le -t \le 0.2\ \mathrm{GeV}^2$ (see Fig. 5*f*). Obviously, the jump of the asymmetry is due exclusively to a sharp change of 90° in the phase of the amplitude of $a_0^0(980)-f_0(980)$ mixing between the K^+K^- and $K^0\bar{K}^0$ thresholds

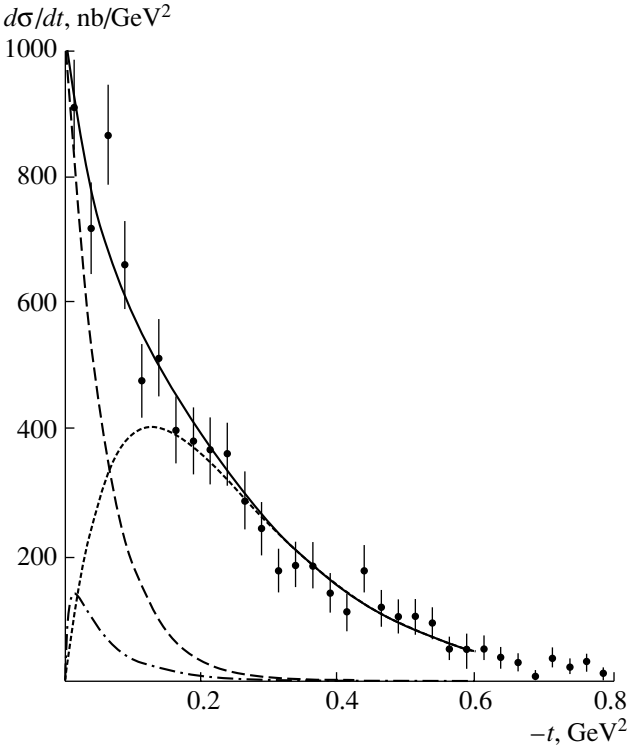

Fig. 4. Differential cross section $d\sigma/dt$ for the reaction $\pi^- p \to a_0^0(908)n \to (\eta\pi^0)_S n$. The displayed experimental data and the dash-dotted curve are identical to those in Fig. 2. The solid curve represents the results obtained by fitting expression (6) at $B_{b_1} = 0.7$ to the data. The contributions of ρ_2 and b_1 exchanges to $d\sigma/dt$ are shown by, respectively, long and short dashes.

[8)] The original quantities $d\sigma/dm$ and $I(m)$ were smoothed by using a Gaussian m distribution of variance 10 MeV. In experiments, one always observes mass distributions that are smoothed owing to a finite resolution of the spectrometers employed. For example, the dotted curves in Fig. 5 can therefore be directly compared with experimental histograms having a step of about 10 MeV in m and a high statistical accuracy. At the present time, it is not very difficult to obtain such high-quality data on $\eta\pi^0$ production in experiments featuring no polarizations [20–23].

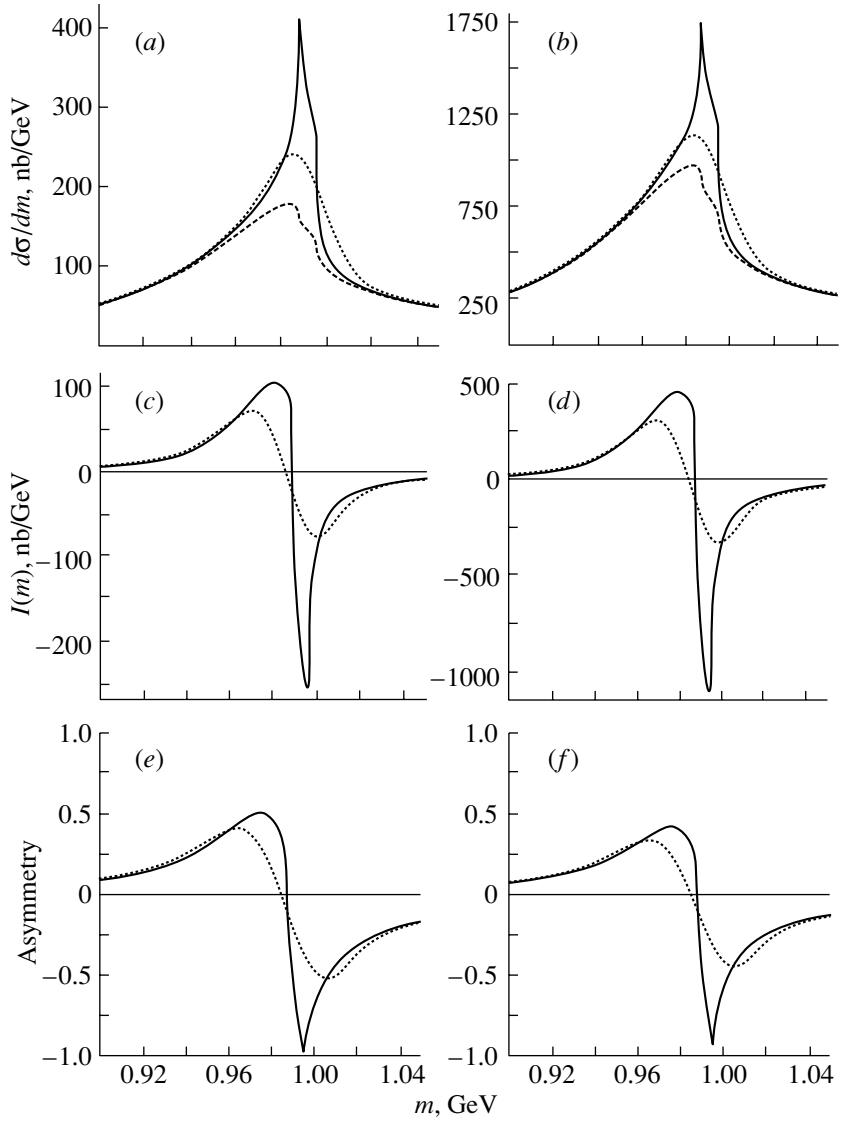

Fig. 5. Manifestation of $a_0^0(980)-f_0(980)$ mixing in the reaction $\pi^- p \to a_0^0(980)n \to (\eta\pi^0)_S n$ on a polarized target at $P_{\rm lab}^{\pi^-} = 18.3$ GeV within the model of ρ_2 and π exchanges. We show respective quantities in the left panels of the figure (Figs. 5*a*, 5*c*, 5*e*) for the interval $0 \le -t \le 0.025$ GeV^2 and in the right panels (Figs. 5*b*, 5*d*, 5*f*) for the interval $0 \le -t \le 0.2$ GeV^2. The solid curves represent $d\sigma/dm$, $I(m)$, and the asymmetry $A(0 \le -t \le -t_2\ \text{GeV}^2, m)$. The dashed curves correspond to the contribution of ρ_2 exchange to $d\sigma/dm$, while the dotted curves show $d\sigma/dm$ and $I(m)$ smoothed by using a Gaussian m distribution of variance 10 MeV and the asymmetry corresponding to them. The sign of $I(m)$ (and, hence, of the asymmetry) is unknown and is chosen arbitrarily.

(see Fig. 1*b*), while its large magnitude is ensured both by a significant absolute value of this amplitude (see Fig. 1*a*) and by a substantial enhancement of its manifestation in this reaction because of the pion-exchange mechanism.

We note that no significant changes in the resulting pattern occur upon refitting the BNL data in Fig. 2 by adding, to the ρ_2-exchange contribution, the fixed pion-exchange contribution shown in the same figure.

6. POLARIZATION EFFECT WITHIN THE MODEL OF ρ_2-, b_1-, and π EXCHANGES

We will now address the question of what can change upon the inclusion of a nonzero b_1-exchange contribution.

First of all, we note that, if the reaction $\pi^- p \to a_0^0(980)n \to (\eta\pi^0)_S n$ were controlled by the ρ_2- and b_1-exchange mechanisms exclusively, a rather tedious pattern would arise for the dependence of $A(t,m)$ on m. At any value of t, the asymmetry in the region of the $a_0^0(980)$ peak would be

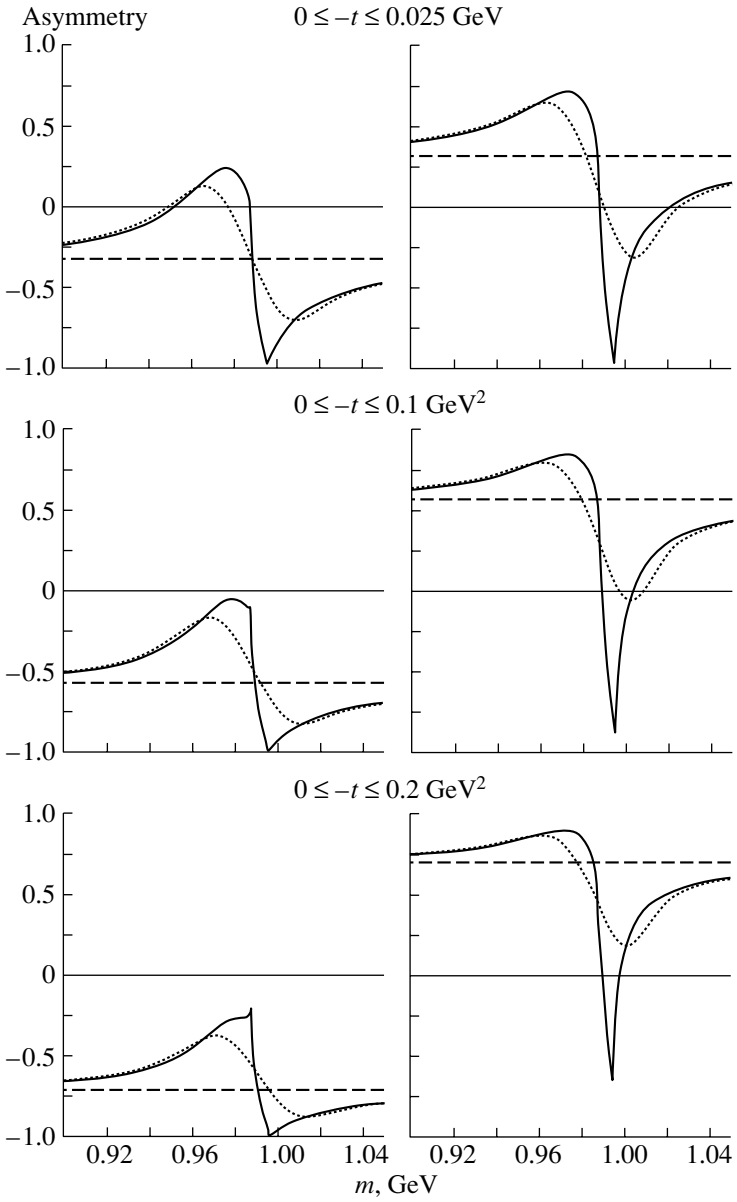

Fig. 6. Asymmetry $A(0 \le -t \le -t_2, m)$ for various intervals of $-t$ in the model of ρ_2, π, and b_1 exchanges (solid curves) without and (dotted curves) with allowance for a Gaussian smearing in m characterized by a variance of 10 MeV. The left and right panels of the figure correspond to different signs of the b_1-exchange amplitude. The dashed lines represent the asymmetry in the model of ρ_2 and b_1 exchanges. The total sign of the asymmetry and the relative sign of the b_1- and π-exchange amplitudes are unknown and are chosen arbitrarily.

independent of m. Indeed, one can see that, in the model of ρ_2 and b_1 exchanges, the complex-valuedness of the product $M_{++}(M_{+-})^*$ is determined exclusively by the Regge signature factors of the amplitudes $M_{++}^{\rho_2}$ and $M_{+-}^{b_1}$ [see Eqs. (2) and (3)]. In the region of the $a_0^0(980)$ peak, the factors that depend resonantly on m would therefore cancel in the asymmetry $A(t,m) = \pm\cos[\pi(\alpha_{\rho_2}(t) - \alpha_{b_1}(t))/2] \times 2|M_{++}^{\rho_2}||M_{+-}^{b_1}|/[|M_{++}^{\rho_2}|^2 + |M_{+-}^{b_1}|^2]$. Here, the symbol $\pm$ implies that the relative sign of ρ_2 and π exchanges is not known. It is clear, however, that, in the presence of the amplitude M_{+-}^{π}, one would expect a totally different pattern: at low values of $-t$, the quantity $A(t,m)$ must change sharply in the region of $K\bar{K}$ thresholds.

We have performed a specific calculation within the model of ρ_2, π, and b_1 exchanges, employing the approximation of the BNL data that was described in Section 4, which is shown in Fig. 2, and which corresponds to approximately 37% contribution of b_1 exchange to the total cross section. The polar-

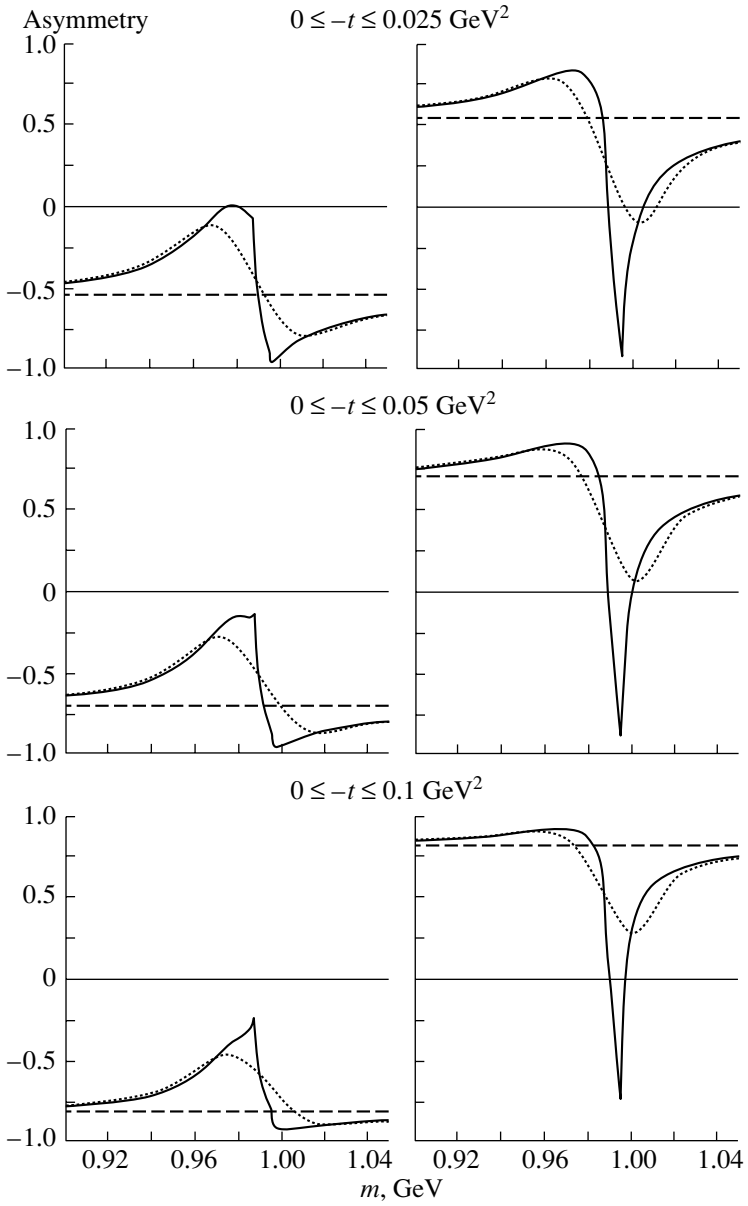

Fig. 7. As in Fig. 6, but for the ρ_2- and b_1-exchange contributions identical to those in Fig. 4.

ization effect corresponding to this example is illustrated in Fig. 6. This figure displays the asymmetry $A(0 \le -t \le -t_2, m)$ for three intervals of $-t$ ($0 \le -t \le 0.025, 0.1, 0.2$ GeV^2) (solid curves) without and (dotted curves) with allowance for a Gaussian smearing in m characterized by a variance of 10 MeV. The left and right panels of Fig. 6 correspond to different signs of the b_1-exchange amplitude. The total sign of the asymmetry is unknown and was chosen arbitrarily, as in the case of the model featuring only ρ_2 and π exchanges. We note that, if, for example, the pattern corresponding to the left (right) panels of Fig. 6 is realized for the reaction $\pi^- p \to (\eta\pi^0)_S n$, then the pattern corresponding to its right (left) panels, where the sign is opposite, must be realized for the reaction $\pi^+ n \to (\eta\pi^0)_S p$, which is related to the above reaction by charge symmetry. From Fig. 6, it can clearly be seen that, owing to an admixture of pion exchange, the asymmetry associated with any of the intervals $0 \le -t \le 0.025, \ldots, 0.1$ GeV^2 undergoes, as before, a jump by a value close to unity in the region of m between 0.965 and 1.01 GeV. However, this jump now occurs with respect to the asymmetry value determined by the interference between the ρ_2- and b_1-exchange contributions rather than with respect to zero value of the asymmetry. Thus, one can see that, taken together, Figs. 5 and 6 give a comprehensive idea of the polarization effect that is induced

by $a_0^0(980)-f_0(980)$ mixing and which is expected in the reaction $\pi^-p \to a_0^0(980)n \to (\eta\pi^0)_S n$. To supplement this pattern, we note that, as follows from Fig. 7, the polarization effect is large at low $-t$ even in the almost improbable case where the b_1-exchange contribution is 70% of the total cross section (see the relevant discussion in Section 4).

A few general comments are in order here. First, we would like to emphasize that a resolution in the invariant mass of the $\eta\pi^0$ system as high as that which would be mandatory for revealing manifestations of $a_0^0(980)-f_0(980)$ mixing in the mass spectrum of the $\eta\pi^0$ system in an experiment featuring no polarizations is not required for reliably detecting the jump of the asymmetry. Indeed, the fine structure that arises in $d\sigma/dm$ owing to $a_0^0(980)-f_0(980)$ mixing is strongly masked because of smearing in m (see Figs. 5*a*, 5*b*); at the same time, a large jump of the asymmetry survives smearing, as can clearly be seen from Figs. 5*e*, 5*f*, 6, and 7. Second, a very weak energy dependence of the polarization effect in question (asymmetry value) is expected in view of the theoretically predicted (and experimentally corroborated!) proximity of the π, ρ_2, and b_1 Regge trajectories. Therefore, an attempt can be made to detect it at any high energy—for example, in the range between 8 and 100 GeV. Even if the simplest Regge model, which is used here, leads to some errors in constructing amplitudes that conserve G parity (for example, in choosing their phases), we are confident that the jump of the spin asymmetry in the reaction $\pi^-p \to a_0^0(980)n \to (\eta\pi^0)_S n$ at the $\eta\pi^0$ invariant mass between the K^+K^- and $K^0\bar{K}^0$ thresholds will inevitably occur owing to a characteristic m dependence of the amplitude for the $a_0^0(980)-f_0(980)$ transition (see Figs. 1*a*, 1*b*), its enhancement caused by the one-pion-exchange mechanism of $f_0(980)$-resonance production, and the fact that the contribution of the amplitude characterized by the quantum numbers of b_1 exchange is suppressed in the region of low $-t$ (see Fig. 2).

7. CONCLUSIONS

Thus, we can conclude that, in the reaction $\pi^-p \to a_0^0(980)n \to (\eta\pi^0)_S n$, the interference between the amplitudes M_{++} and M_{+-}, which is measurable in a polarization experiment, is highly sensitive at low $-t$ to the mixing of the $a_0^0(980)$ and $f_0(980)$ resonances. A jump of the asymmetry in the region of $K\bar{K}$ thresholds is a direct consequence of $a_0^0(980)-f_0(980)$ mixing, and even rather rough experimental indications of the presence of such a jump would suggest the existence of the mixing effect.

At the present time, experimental investigations based on employing polarized beams and targets are gaining momentum. In view of this, we believe that our present analysis is of topical interest. Relevant experiments aimed at studying the reaction $\pi^-p \to \eta\pi^0 n$ on polarized protons can be performed at KEK, BNL, IHEP, CERN (COMPASS), Institute of Theoretical and Experimental Physics (ITEP, Moscow), FNAL, and Institut für Kernphysik (Jülich). The discovery of $a_0^0(980)-f_0(980)$ mixing would open yet another interesting page in studying the nature of the puzzling $a_0^0(980)$ and $f_0(980)$ states. The general idea to use polarization phenomena as an efficient tool for observing $a_0^0(980)-f_0(980)$ mixing—this idea relies on a large change of about 90° in the phase of the amplitude of the $a_0^0(980)-f_0(980)$ transition in the narrow region of m (8 MeV) between the K^+K^- and $K^0\bar{K}^0$ thresholds—can of course be applied to different reactions.

ACKNOWLEDGMENTS

This work was supported in part by the Russian Foundation for Basic Research (project no. 02-02-16061). It was also funded by a Presidential Grant for Support of Leading Scientific Schools (no. 2339.2003.2).

REFERENCES

1. N. N. Achasov, Nucl. Phys. A **728**, 425 (2003); Yad. Fiz. **65**, 573 (2002) [Phys. At. Nucl. **65**, 546 (2002)].
2. N. N. Achasov and G. N. Shestakov, Phys. Rev. Lett. **92**, 182001 (2004).
3. (a) N. N. Achasov, S. A. Devyanin, and G. N. Shestakov, Phys. Lett. B **88B**, 367 (1979); (b) Yad. Fiz. **33**, 1337 (1981) [Sov. J. Nucl. Phys. **33**, 715 (1981)]; Usp. Fiz. Nauk **142**, 361 (1984) [Sov. Phys. Usp. **27**, 161 (1984)].
4. A. R. Dzierba, Frascati Phys. Ser. **4**, 99 (1996).
5. N. N. Achasov and G. N. Shestakov, Phys. Rev. D **56**, 212 (1997); Yad. Fiz. **60**, 1669 (1997) [Phys. At. Nucl. **60**, 1522 (1997)].
6. O. Krehl, R. Rapp, and J. Speth, Phys. Lett. B **390**, 23 (1997).
7. B. Kerbikov and F. Tabakin, Phys. Rev. C **62**, 064601 (2000).
8. F. E. Close and A. Kirk, Phys. Lett. B **489**, 24 (2000).
9. A. E. Kudryavtsev and V. E. Tarasov, Pis'ma Zh. Éksp. Teor. Fiz. **72**, 589 (2000) [JETP Lett. **72**, 410 (2000)].
10. V. Yu. Grishina *et al.*, Phys. Lett. B **521**, 217 (2001).
11. N. N. Achasov and A. V. Kiselev, Phys. Lett. B **534**, 83 (2002).
12. D. Black, M. Harada, and J. Schechter, Phys. Rev. Lett. **88**, 181603 (2002).

13. A. E. Kudryavtsev *et al.*, Phys. Rev. C **66**, 015207 (2002); Yad. Fiz. **66**, 1994 (2003) [Phys. At. Nucl. **66**, 1946 (2003)].
14. M. Buescher *et al.*, hep-ph/0301126.
15. L. A. Kondratyuk *et al.*, Yad. Fiz. **66**, 155 (2003) [Phys. At. Nucl. **66**, 152 (2003)].
16. C. Hanhart, AIP Conf. Proc. **688**, 61 (2003); Phys. Rep. **397**, 155 (2004).
17. C. Amsler and N. A. Törnqvist, Phys. Rep. **389**, 61 (2004).
18. M. Buescher, Acta Phys. Pol. B **35**, 1055 (2004); nucl-ex/0401010.
19. Z.-G. Wang, W.-M. Yang, and S.-L. Wan, hep-ph/0411142v2.
20. S. Teige *et al.*, Phys. Rev. D **59**, 012001 (1999).
21. A. R. Dzierba *et al.*, Phys. Rev. D **67**, 094015 (2003).
22. S. A. Sadovsky (for the GAMS Collab.), AIP Conf. Proc. **432**, 774 (1998).
23. D. Aldi *et al.*, Yad. Fiz. **62**, 462 (1999) [Phys. At. Nucl. **62**, 421 (1999)].
24. Particle Data Group (K. Hagiwara *et al.*), Phys. Rev. D **66**, 010001 (2002).
25. N. N. Achasov and G. N. Shestakov, Phys. Rev. D **58**, 054011 (1998); Yad. Fiz. **62**, 548 (1999) [Phys. At. Nucl. **62**, 505 (1999)].
26. N. N. Achasov, S. A. Devyanin, and G. N. Shestakov, Yad. Fiz. **32**, 1098 (1980) [Sov. J. Nucl. Phys. **32**, 566 (1980)].
27. A. D. Martin, E. N. Ozmutlu, and E. J. Squires, Nucl. Phys. B **121**, 514 (1977).
28. N. N. Achasov, S. A. Devyanin, and G. N. Shestakov, Phys. Lett. B **96B**, 168 (1980); N. N. Achasov and G. N. Shestakov, Z. Phys. C **41**, 309 (1988).
29. N. N. Achasov and V. V. Gubin, Phys. Rev. D **63**, 094007 (2001); Yad. Fiz. **65**, 1566 (2002) [Phys. At. Nucl. **65**, 1528 (2002)]; N. N. Achasov and A. V. Kiselev, Phys. Rev. D **68**, 014006 (2003).
30. P. Colangelo and F. De Fazio, Phys. Lett. B **559**, 49 (2003).
31. J. Gunter *et al.*, Phys. Rev. D **64**, 072003 (2001).
32. N. N. Achasov and G. N. Shestakov, Phys. Rev. D **67**, 114018 (2003).

Translated by A. Isaakyan

Physics of Atomic Nuclei, Vol. 68, No. 12, 2005, pp. 2081–2092. From Yadernaya Fizika, Vol. 68, No. 12, 2005, pp. 2143–2154.

ELEMENTARY PARTICLES AND FIELDS
Theory

Charmed Quark Component of the Photon Wave Function*

V. V. Anisovich, L. G. Dakhno, V. N. Markov, V. A. Nikonov, and A. V. Sarantsev

Petersburg Nuclear Physics Institute, Russian Academy of Sciences, Gatchina, 188350 Russia

Received November 10, 2004; in final form, January 11, 2005

Abstract—We determine the $c\bar{c}$ component of the photon wave function on the basis of (i) the data on the transitions $e^+e^- \to J/\psi(3096), \psi(3686), \psi(4040), \psi(4415)$, (ii) partial widths of the two-photon decays $\eta_{c0}(2979)$, $\chi_{c0}(3415)$, $\chi_{c2}(3556) \to \gamma\gamma$, and (iii) wave functions of the charmonium states obtained by solving the Bethe–Salpeter equation for the $c\bar{c}$ system. Using the obtained $c\bar{c}$ component of the photon wave function, we calculate the $\gamma\gamma$-decay partial widths for radial excitation of the $2S$ state, $\eta_{c0}(3594) \to \gamma\gamma$, and $2P$ states $\chi_{c0}(3849)$, $\chi_{c2}(3950) \to \gamma\gamma$. © *2005 Pleiades Publishing, Inc.*

1. INTRODUCTION

There are a number of processes that can be sensibly treated by introducing the $c\bar{c}$ component of the photon wave function. It is the production of charmonium in the two-photon transitions such as $\gamma^*\gamma^* \to c\bar{c}$ mesons, production of ψ mesons in the e^+e^- annihilation, and production of charmonia in photon–nucleon collisions, $\gamma^* p \to c\bar{c}\,\text{meson} + X$. In the present paper, we determine the $c\bar{c}$ component of the photon wave function, or the transition vertex $\gamma \to c\bar{c}$, following the method developed in [1, 2], where quark–antiquark components were found for the transitions $\gamma \to u\bar{u}, d\bar{d}, s\bar{s}$.

The method of introducing the quark–antiquark photon wave function may be clearly illustrated by considering the $c\bar{c}$-meson $\to \gamma\gamma$ decay. When dealing with the time-ordered processes, which is necessary in the dispersion relation approach or light-cone variable technique, the $c\bar{c}$-meson $\to \gamma\gamma$ decay is a two-step process: first, the emission of photon by a quark (Fig. 1*a*) or antiquark (Fig. 1*b*) and, second, subsequent annihilation $c\bar{c} \to \gamma$.

In [1, 2], the triangle diagrams of Figs. 1*a* and 1*b* were treated in terms of a double-dispersion-relation representation. The double spectral integral cuttings of the diagram in Fig. 1*a* are shown in Fig. 1*c*. In the diagram of Fig. 1*c*, on the left of the first cutting, there is the transition vertex of charmonium, $G_{\text{charm}}(s)$, decaying into a $c\bar{c}$ pair, where s is the quark invariant energy squared. In light-cone variables,

$$s = \frac{m_c^2 + k_\perp^2}{x(1-x)}, \tag{1}$$

where m_c is the mass of c quark and $(x, \mathbf{k}_\perp)$ are the characteristics of one of the quarks (fraction of the momentum along the z axis and transverse component). In the dispersion integral, the left-hand cutting leads to the factor $G_{\text{charm}}/(s - M^2_{\text{charm}})$, where M_{charm} is the charmonium mass, this factor being the wave function of the initial $c\bar{c}$ meson:

$$\frac{G_{\text{charm}}(s)}{s - M^2_{\text{charm}}} = \Psi_{\text{charm}}(s). \tag{2}$$

Likewise, the right-hand cut in Fig. 1*c*, by describing the transition $c\bar{c} \to \gamma$, gives us the factor

$$\frac{1}{s'} e_c, \tag{3}$$

where s' is the invariant energy squared of quarks in the final state and e_c is the c-quark charge.

When we deal with the transition $c\bar{c} \to \gamma$, the interaction of quarks should be specially taken into consideration. The quarks may interact in both the initial (Fig. 2*a*) and final (Fig. 2*b*) states. In fact, the interaction of quarks in the initial state has been accounted for by Eq. (2), because the vertex function G_{charm} (or wave function Ψ_{charm}) is the solution to the Bethe–Salpeter equation—diagrammatically, this equation is shown in Fig. 3*a*. As to quark interaction in the final state, it should be taken into account in addition to the pointlike interaction (3). The diagram shown in Fig. 3*b* stands for the description of quark interaction in the transition $c\bar{c} \to \gamma$, and we approximate it with the sum of the ψ-meson pole terms (see Fig. 3*c*). Accordingly, the factor related to the right-hand cut of Fig. 1*c* is written as follows:

$$\frac{G_{\gamma \to c\bar{c}}(s')}{s'} e_c, \tag{4}$$

where the vertex function $G_{\gamma \to c\bar{c}}(s')$ at $s' \sim 4m_c^2$ is a superposition of vertices of the S-wave ψ mesons (see

*This article was submitted by the authors in English.

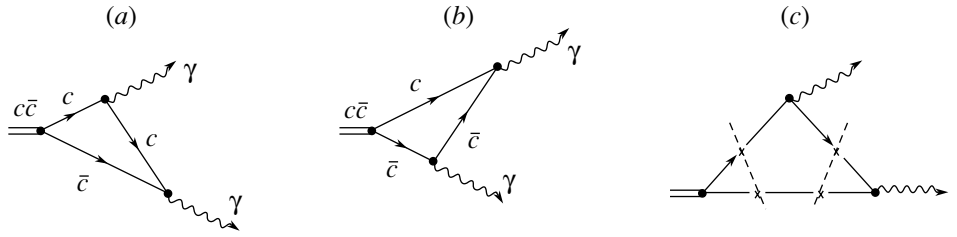

Fig. 1. (a, b) Diagrams for the two-photon decay of $c\bar{c}$ state. (c) Cuttings in the spectral integral representation.

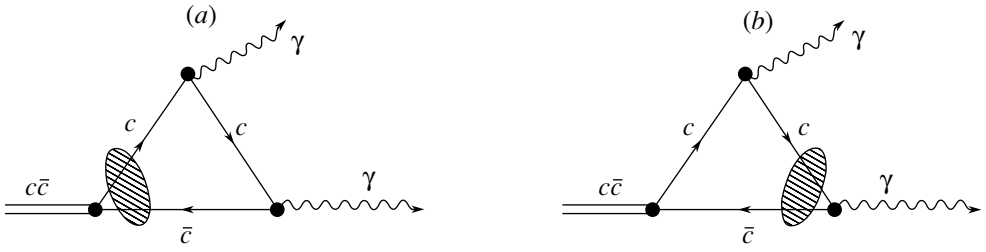

Fig. 2. (a) Initial- and (b) final-state interactions of quarks in the decay diagrams.

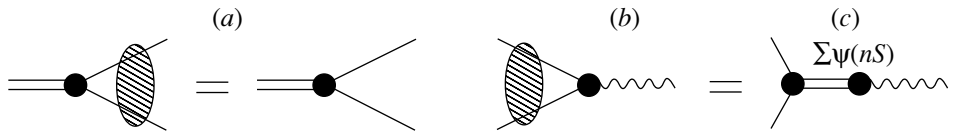

Fig. 3. (a) Graphical representation of the Bethe–Salpeter equation for the $c\bar{c}$ vertex; (b, c) interaction of quarks in the vertex $c\bar{c} \to \gamma$ and its approximation by the sum of transitions $c\bar{c} \to \sum \psi(nS) \to \gamma$.

Fig. 3c):

$$G_{\gamma\to c\bar{c}}(s) \simeq \sum_n C_n G_{\psi(nS)}(s), \qquad s \sim 4m_c^2. \quad (5)$$

Here, n is the radial quantum number of ψ meson and C_n are numerical coefficients—their definition is the task of this paper. At large s, the vertex $c\bar{c} \to \gamma$ is a pointlike one:

$$G_{\gamma\to c\bar{c}}(s) \simeq 1 \qquad \text{at} \quad s > s_0. \quad (6)$$

The parameter s_0 can be determined using the data on e^+e^- annihilation into hadrons: it is defined by the energy range, where the ratio $R(s) = \sigma(e^+e^- \to$ hadrons$)/\sigma(e^+e^- \to \mu^+\mu^-)$ reaches a constant-behavior regime above the threshold of charm production, $R(s) \simeq 10/3$. The data support the value $s_0 \sim 10$–15 GeV^2 [3].

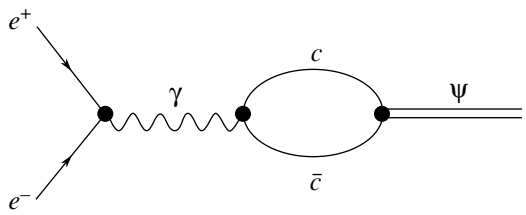

Fig. 4. Quark transition diagram for the process $e^+e^- \to \psi$.

Therefore, to describe the transition $c\bar{c} \to \gamma$, we introduce characteristics, which, similarly to (2), may be called the charmed quark component of the photon wave function:

$$\frac{G_{\gamma\to c\bar{c}}(s)}{s - q^2} = \Psi_{\gamma(q^2)\to c\bar{c}}(s); \quad (7)$$

here, q is the photon four-momentum. Let us emphasize that such a wave function is determined at $s \gtrsim 4m_c^2$.

There exists a reaction which is directly related to the photon wave function. This is the transition $e^+e^- \to \psi(nS)$ (see Fig. 4): here, the loop diagram is defined by the convolution of the meson wave function and the vertex $\gamma \to c\bar{c}$: $\Psi_{nS} \otimes G_{\gamma\to c\bar{c}}$.

Dealing with the $c\bar{c}$ interaction in the transition $\gamma \to c\bar{c}$, we take into consideration the S-wave ψ mesons only, while the contribution of mesons dominated by the D wave, such as $\psi(3770)$ and $\psi(4160)$, is neglected. The error coming from such a neglect can

be evaluated by comparing the ψ-meson production cross sections for S- and D-wave states in the e^+e^- annihilation: it is of the order of 10%. The D-wave admixture into the low-lying 1^{--} mesons is also small: it is of the order of 1% for $J/\psi(1S)$ and $\psi(2S)$ [4].

We perform calculations of two- and three-point loop diagrams in the spectral integration technique. All the equations used, up to trivial substitutions of quark masses and charges, were obtained in [5]. Because of that, in this paper, we present only final expressions accompanied by necessary comments and references.

The main difference between calculations for $\gamma \to c\bar{c}$ and those for $\gamma \to u\bar{u}, d\bar{d}, s\bar{s}$ carried out in [1, 2] consists in our regard towards quark wave functions. In [1, 2], we used phenomenological quark wave functions for π^0, η, η', while for light vector mesons (ρ, ω, ϕ) we assumed the quark wave functions to be similar to analogous pseudoscalar-meson wave functions, with whom they form the lowest 36-plet in terms of $SU(6)$ symmetry. But here, when reconstructing the wave function for the transition $\gamma \to c\bar{c}$, we have applied the charmonium wave functions found from the solution to the Bethe–Salpeter equation [4].

There is a long history of calculation of charmonium states, and now there is a rich collection of results obtained in the framework of the nonrelativistic approaches [6–9] as well as in different variants of the Bethe–Salpeter equation (see [10–13] and references therein). However, one should bear in mind that, in calculations related to quark–antiquark systems, one focuses as a rule on the description of levels (or masses) of the system. Had the potential or its relativistic analog been known, the Bethe–Salpeter equation would undoubtedly provide us with both levels and wave functions. But the problem is that, in fact, our knowledge about the quark–quark interaction in the soft region is rather poor. Therefore, in the reconstruction of quark–antiquark levels, one can obtain a variety of wave functions. Within the spectral integration technique used here, we see that unambiguous determination of interaction is possible in the simultaneous description of both levels and wave functions (see discussion in Section 2.6.3 of [5]). Because of that, by describing the $c\bar{c}$ system, we have used in [4] as an input both the known levels and the known values of radiative transitions $(c\bar{c})_{\text{in}} \to \gamma + (c\bar{c})_{\text{out}}$. These radiative transitions are rather sensitive to wave functions; hence, a comparatively good description of radiation transitions in [4] allows us to believe that the wave functions of lowest $c\bar{c}$ states are determined reliably too.

The paper is organized as follows. In Section 2, we present briefly the information about the spectral-integration Bethe–Salpeter equation, in the framework of which the description of the $c\bar{c}$ systems was performed in [4]. In Section 2, we also give the charmonium wave functions obtained upon the determination of $G_{\gamma\to c\bar{c}}$. In Section 3, we write the formulas for the transition amplitudes $e^+e^- \to \psi$ and $\eta_{c0}, \chi_{c0}, \chi_{c2} \to \gamma\gamma$, which are used in the fit, and present the results for the photon wave function. A brief summary is given in the Conclusion.

2. CHARMONIUM WAVE FUNCTIONS

The spectral integral equation for the quark–antiquark wave function, which can conventionally be called the Bethe–Salpeter equation, is written for a system with the total momentum J, angular momentum L, quark–antiquark spin S, and radial number n. For the $c\bar{c}$ system, it reads

$$\left(s - M^2_{\text{charm}}\right)\widehat{\Psi}^{(S,L,J)}_{(n)\mu_1\ldots\mu_J}(k_\perp) \tag{8}$$
$$= \int\limits_{4m_c^2}^{\infty} \frac{ds'}{\pi} d\Phi_2(P'; k_1', k_2')\widehat{V}\left(s, s', (k_\perp k_\perp')\right)$$
$$\times (\hat{k}_1' + m_c)\widehat{\Psi}^{(S,L,J)}_{(n)\mu_1\ldots\mu_J}(k_\perp')(-\hat{k}_2' + m_c).$$

Here, the quarks are mass-on-shell, $k_1^2 = k_1'^2 = k_2^2 = k_2'^2 = m_c^2$, and the phase space factor in the intermediate state is determined as follows:

$$d\Phi_2(P'; k_1', k_2') = \frac{1}{2}\frac{d^3k_1'}{(2\pi)^3 \cdot 2k_{10}'} \tag{9}$$
$$\times \frac{d^3k_2'}{(2\pi)^3 \cdot 2k_{20}'}(2\pi)^4\delta^{(4)}(P' - k_1' - k_2').$$

We use the following notation:

$$k_\perp = \frac{1}{2}(k_1 - k_2), \quad P = k_1 + k_2, \tag{10}$$
$$k_\perp' = \frac{1}{2}(k_1' - k_2'), \quad P' = k_1' + k_2',$$
$$P^2 = s, \quad P'^2 = s', \quad g^\perp_{\mu\nu} = g_{\mu\nu} - \frac{P_\mu P_\nu}{s},$$
$$g'^\perp_{\mu\nu} = g_{\mu\nu} - \frac{P'_\mu P'_\nu}{s'},$$

so one can write $k_\mu^\perp = k_\nu g^\perp_{\nu\mu}$ and $k_\mu'^\perp = k_\nu' g'^\perp_{\nu\mu}$. In the center-of-mass system, the integration can be rewritten as

$$\int\limits_{4m_c^2}^{\infty} \frac{ds'}{\pi} d\Phi_2(P'; k_1', k_2') \longrightarrow \int \frac{d^3k'}{(2\pi)^3 k_0'}, \tag{11}$$

where k' is the momentum of one of the quarks. The wave function reads

$$\widehat{\Psi}^{(S,L,J)}_{(n)\mu_1\ldots\mu_J}(k_\perp) = Q^{(S,L,J)}_{\mu_1\ldots\mu_J}(k_\perp)\psi^{(S,L,J)}_n(k_\perp^2). \tag{12}$$

Table 1. Parameters of the potential (in GeV)

Type of interaction ($\widehat{O}_I \otimes \widehat{O}_I$)	Solution	a	b	c	$\mu_{\text{sh.r}}$
Scalar (I $\otimes$ I)	I	-1.527	0.170	1.013	0.201
	II	-1.417	0.158	0.883	0.201
Vector ($\gamma_\mu \otimes \gamma_\mu$)	I	-1.539	0	2.133	0.401
	II	-1.540	0	2.130	0.401
Pseudoscalar ($\gamma_5 \otimes \gamma_5$)	I	-3.000	0	0	–
	II	0	0	0	–

Table 2. Measured masses and results of the fit for solutions I and II (in GeV) (boldfaced numbers stand for masses which have been used in the fitting procedure [4])

Solution	n	$\psi(nS)$		$\eta_c(nS)$		$\chi_{c0}(nP)$		$\chi_{c1}(nP)$		$\chi_{c2}(nP)$	
		data	fit	data	fit	data	fit	data	fit	data	fit
I	1	**3.096**	3.1022	**2.979**	2.9776	**3.415**	3.3933	**3.510**	3.4962	**3.556**	3.5676
	2	**3.686**	3.6737	**3.594**	3.6246		3.8485		3.9002		3.9495
	3	4.040	4.0565		4.0225		4.1812		4.2514		4.3046
	4	4.415	4.3960		4.3678		4.5569		4.6709		4.8250
	5		4.8465		4.8233		5.1185		5.1886		5.4758
	6		5.4448		5.4242		5.7510		5.8404		6.2197
II	1	**3.096**	3.1023	**2.979**	2.9772	**3.415**	3.3958	**3.510**	3.4979	**3.556**	3.5687
	2	**3.686**	3.6721	**3.594**	3.6238		3.8447		3.8957		3.9434
	3	4.040	4.0470		4.0139		4.1705		4.2406		4.2976
	4	4.415	4.3801		4.3527		4.5488		4.6605		4.8188
	5		4.8322		4.8090		5.1123		5.1820		5.4669
	6		5.4336		5.4135		5.7460		5.8379		6.1986

Here, $Q^{(S,L,J)}_{\mu_1\ldots\mu_J}(k_\perp)$ is the moment operator for the fermion–antifermion system [14] defined as follows:

$$Q^{(0,J,J)}_{\mu_1\mu_2\ldots\mu_J}(k_\perp) = i\gamma_5 X^{(J)}_{\mu_1\ldots\mu_J}(k_\perp), \qquad (13)$$

$$Q^{(1,J+1,J)}_{\mu_1\ldots\mu_J}(k_\perp) = \gamma^\perp_\alpha X^{(J+1)}_{\mu_1\ldots\mu_J\alpha}(k_\perp),$$

$$Q^{(1,J,J)}_{\mu_1\ldots\mu_J}(k_\perp) = \frac{1}{\sqrt{s}}\varepsilon_{\alpha\nu_1\nu_2\nu_3}\gamma^\perp_\alpha P_{\nu_1} Z^{(J)}_{\nu_2\mu_1\ldots\mu_J,\nu_3}(k_\perp),$$

$$Q^{(1,J-1,J)}_{\mu_1\ldots\mu_J}(k_\perp) = \gamma^\perp_\alpha Z^{(J-1)}_{\mu_1\ldots\mu_J,\alpha}(k_\perp),$$

where

$$X^{(J)}_{\mu_1\ldots\mu_J}(k_\perp) = \frac{(2J-1)!!}{J!} \qquad (14)$$

$$\times \left[k^\perp_{\mu_1} k^\perp_{\mu_2} k^\perp_{\mu_3} k^\perp_{\mu_4} \ldots k^\perp_{\mu_J} - \frac{k^2_\perp}{2J-1} \right.$$

$$\times (g^\perp_{\mu_1\mu_2} k^\perp_{\mu_3} k^\perp_{\mu_4} \ldots k^\perp_{\mu_J}$$

$$+ g^\perp_{\mu_1\mu_3} k^\perp_{\mu_2} k^\perp_{\mu_4} \ldots k^\perp_{\mu_J} + \ldots)$$

$$+ \frac{k^4_\perp}{(2J-1)(2J-3)}$$

$$\times (g^\perp_{\mu_1\mu_2} g^\perp_{\mu_3\mu_4} k^\perp_{\mu_5} k^\perp_{\mu_6} \ldots k^\perp_{\mu_J}$$

$$\left. + g^\perp_{\mu_1\mu_2} g^\perp_{\mu_3\mu_5} k^\perp_{\mu_4} k^\perp_{\mu_6} \ldots k^\perp_{\mu_J} + \ldots) + \ldots \right],$$

$$Z^{(J-1)}_{\mu_1\ldots\mu_J,\alpha}(k_\perp) = \frac{2J-1}{L^2}$$

$$\times \left(\sum_{i=1}^{J} X^{(J-1)}_{\mu_1\ldots\mu_{i-1}\mu_{i+1}\ldots\mu_J}(k_\perp) g^\perp_{\mu_i\alpha} - \frac{2}{2J-1} \right.$$

$$\left. \times \sum_{\substack{i,j=1 \\ i<j}}^{J} g^\perp_{\mu_i\mu_j} X^{(J-1)}_{\mu_1\ldots\mu_{i-1}\mu_{i+1}\ldots\mu_{j-1}\mu_{j+1}\ldots\mu_J\alpha}(k_\perp) \right).$$

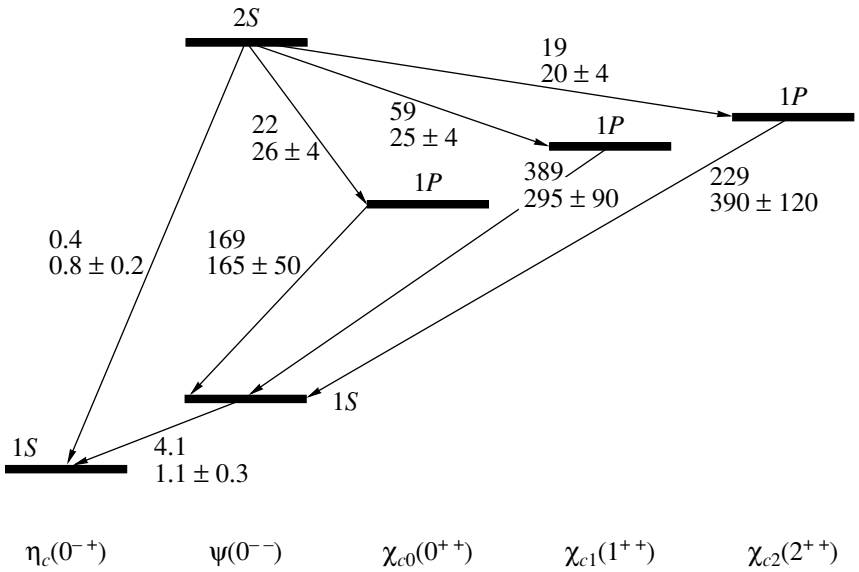

Fig. 5. Radiative decays of the charmonium systems, which were taken into account in the fit [4]. The calculated decay partial widths are shown in keV units (upper numbers) together with experimental data and errors accepted in the fit (lower numbers).

The interaction block can be expanded in a series in a full set of t-channel operators:

$$\widehat{V}\left(s,s',(k_\perp k'_\perp)\right) = \sum_I V_I\left(s,s',(k_\perp k'_\perp)\right)\widehat{O}_I\otimes\widehat{O}_I, \quad \widehat{O}_I = I,\gamma_\mu,i\sigma_{\mu\nu},i\gamma_\mu\gamma_5,\gamma_5. \tag{15}$$

The Bethe–Salpeter equation (8) is written in the momentum representation; it was solved in [4] in the momentum representation as well. Equation (8) allows one to use as an interaction the instantaneous approximation or to take into account retardation effects. In the instantaneous approximation, one has

$$\widehat{V}\left(s,s',(k_\perp k'_\perp)\right)\longrightarrow\widehat{V}(t_\perp), \quad t_\perp = (k_{1\perp}-k'_{1\perp})_\mu(-k_{2\perp}+k'_{2\perp})_\mu. \tag{16}$$

The retardation effects are taken into account when the momentum transfer squared t in the interaction block depends on the time components of quark momenta (for more detail, see Section 2.5 of [5] and the discussion in [13, 15–17]):

$$\widehat{V}\left(s,s',(k_\perp k'_\perp)\right)\longrightarrow\widehat{V}(t), \quad t = (k_1-k'_1)_\mu(-k_2+k'_2)_\mu. \tag{17}$$

The interaction amplitude $\widehat{V}(t)$ was expanded in a series over certain standard interaction blocks, $I_n(t)$, which are singular in the t channel: $\widehat{V}(t) = \sum a_n I_n(t)$. It turned out that, for the fit of the $c\bar{c}$ states, we need only two interaction blocks with the following t dependence:

$$I_0(t) = \frac{8\pi\mu}{(\mu^2-t)^2}, \quad I_1(t) = 8\pi\left(\frac{4\mu^2}{(\mu^2-t)^3}-\frac{1}{(\mu^2-t)^2}\right). \tag{18}$$

It also occurred that the results of the fit depended weakly on whether the t or $t_\perp$ dependence was used below in (19). Because of that, for the sake of simplicity, we present below the results obtained in the instantaneous approximation substituting $t\to t_\perp$ in (19).

Traditionally, the interaction of heavy quarks in the instantaneous approximation is presented in terms of the potential $V(r)$. The form of the potential can be obtained with the Fourier transform of Eq. (18) in the center-of-mass system:

$$t_\perp = -(\mathbf{k}-\mathbf{k}')^2 = -\mathbf{q}^2, \quad I_c^{(N)}(r,\mu) = \int\frac{d^3q}{(2\pi)^3}e^{-i\mathbf{q}\cdot\mathbf{r}}I_N(t_\perp), \tag{19}$$

which gives

$$I_c^{(0)}(r,\mu) = e^{-\mu r}, \qquad I_c^{(1)}(r,\mu) = re^{-\mu r}. \tag{20}$$

The potential used in [4] had the form

$$V(r) = a+br+ce^{-\mu r_{\mathrm{sh.r}}}, \tag{21}$$

where the constant and linear (confinement) terms read

$$a\to aI_c^{(0)}(r,\mu_{\mathrm{const}}\to 0), \quad br\to bI_c^{(1)}(r,\mu_{\mathrm{lin}}\to 0). \tag{22}$$

Table 3. Constants $c_i^{(n)}$ (in GeV) for the wave functions of Eq. (23) in solutions I, II

Solution	i	$J/\psi(1S)$	$\psi(2S)$	$\psi(3S)$	$\psi(4S)$	$\eta_c(1S)$	$\eta_c(2S)$	$\chi_{c0}(1P)$	$\chi_{c0}(2P)$	$\chi_{c2}(1P)$	$\chi_{c2}(2P)$
I	1	8.15	−18.87	43.70	−68.75	−7.064	−17.72	27.17	131.60	−45.15	−144.38
	2	3.01	9.16	−271.18	682.41	0.08171	4.60	−12.77	−480.42	59.15	569.17
	3	−48.02	266.00	465.83	−2356.65	20.748	247.04	−100.08	539.03	141.47	−587.98
	4	76.13	−729.46	−92.87	3873.67	−14.849	−653.28	181.19	−23.55	−432.83	−315.11
	5	−49.16	871.28	−504.13	−3421.29	−22.992	770.56	−120.56	−442.03	481.62	1126.02
	6	9.17	−566.22	587.76	1688.66	41.115	−500.42	23.01	410.77	−286.31	−978.20
	7	4.81	208.18	−286.06	−452.00	−25.682	185.63	11.05	−172.89	96.19	413.89
	8	−2.65	−40.78	66.18	57.34	7.413	−37.01	−6.04	36.23	−17.21	−87.74
	9	0.3712	3.320	−5.948	−2.183	−0.8335	3.094	0.8269	−3.081	1.274	7.454
II	1	8.14	−19.41	45.87	−69.8	−7.061	−18.16	27.79	137.91	−46.32	−151.59
	2	2.86	12.56	−295.78	705.5	0.29980	7.16	−15.64	−520.67	64.72	624.91
	3	−47.50	260.19	559.16	−2482.2	19.754	243.34	−95.29	633.58	132.65	−753.22
	4	75.58	−729.85	−261.10	4172.7	−13.001	−655.51	177.81	−131.97	−428.51	−59.52
	5	−48.97	882.00	−338.96	−3793.5	−24.954	781.02	−120.21	−377.56	484.48	895.03
	6	9.20	−578.49	494.77	1949.0	42.396	−511.22	23.98	393.18	−290.87	−851.60
	7	4.76	214.44	−256.26	−554.9	−26.199	190.89	10.43	−172.64	98.47	372.46
	8	−2.63	−42.31	61.177	78.7	7.527	−38.26	−5.88	37.11	−17.73	−80.30
	9	0.371	3.468	−5.6097	−4.01	−0.84433	3.212	0.8118	−3.211	1.320	6.891

The limits $\mu_{\rm const} \to 0$ and $\mu_{\rm lin} \to 0$ mean that, in the fitting procedure, the parameters $\mu_{\rm const}$ and $\mu_{\rm lin}$ are chosen to be small enough, of the order of 1–10 MeV. It was checked that the solution for the considered states ($n \le 6$) was stable when changing $\mu_{\rm const}$ and $\mu_{\rm lin}$ in this interval, 1–10 MeV. Apart from the potential nonvanishing at large r, we have included in (21) the short-range term $c\exp(-\mu_{\rm sh.r})$, with $\mu_{\rm sh.r} \sim 0.2$–0.6 GeV.

In [4], charmonium wave functions were fitted in the following form:

$$\Psi^{(n)}_{\rm charm}(s) = e^{-\beta k^2} \sum_{i=1}^{9} c_i^{(n)} k^{i-1}. \qquad (23)$$

Recall that k^2 is the relative quark momentum squared, $s = 4m_c^2 + 4k^2$, and n is the radial quantum number; $\beta = 1$ GeV^{-2} for all $c\bar{c}$ states.

Two solutions with two types of t-channel exchanges were used:

solution I : $\quad I \otimes I, \quad \gamma_\mu \otimes \gamma_\mu, \quad \gamma_5 \otimes \gamma_5;$

solution II : $\quad I \otimes I, \quad \gamma_\mu \otimes \gamma_\mu.$

Table 1 displays the obtained values of the potential parameters (a, b, c, $\mu_{\rm sh.r}$) in solutions I and II. In all solutions, we set $m_c = 1.25$ GeV.

The measured masses of the $c\bar{c}$ states and the results of the fit for $n = 1, 2, 3, 4, 5, 6$ are displayed in Table 2.

Figure 5 shows the radiative decay transitions, which were included in the fitting procedure in [4]. One may see the calculated numbers for partial widths and experimental values with errors used in the fit: 20% accuracy was accepted for the transitions $\psi(2S) \to \gamma\chi_{cJ}(1P)$ and 30% for $\chi_{cJ}(1P) \to \gamma\psi(1S)$ (note that slightly smaller errors were obtained in the overall fit of [18]).

The wave function parameters $c_i^{(n)}$ determined in (23) are presented in Table 3 for solutions I and II. Correspondingly, in Figs. 6 and 7, we show the wave functions for $\psi(nS)$ and η_c, χ_{c0}, χ_{c1}, χ_{c2}. Comparing the wave functions depicted in Figs. 6 and 7, one can clearly see that solutions I and II differ insignificantly. We have carried out our calculations with two variants of the interaction in order to make clear that the description of $c\bar{c}$ system does not require

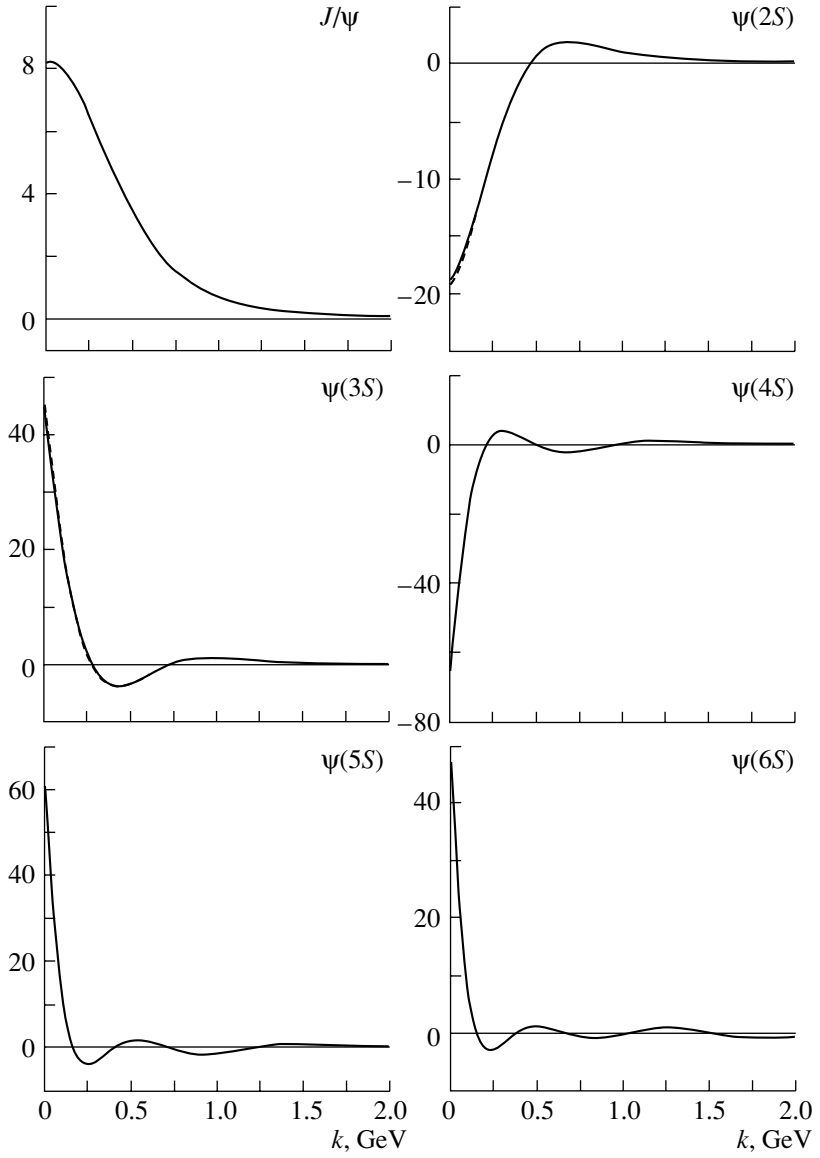

Fig. 6. The $c\bar{c}$ wave functions for $\psi(nS)$. Solid and dashed curves stand for solutions I and II.

a variety of t-channel exchanges and that inclusion of all the versions given by Eq. (15) would only result in the absence of convergence in the fitting procedure. In particular, the considered example of two sorts of interactions demonstrates that the $c\bar{c}$ system does not require instanton-induced forces, which were needed for treating the mass splitting of π, η, η' [19].

3. DETERMINATION OF THE $c\bar{c}$ COMPONENT OF THE PHOTON WAVE FUNCTION

The vertex function of the transition $\gamma \to c\bar{c}$ is represented by the following formula:

$$G_{\gamma\to c\bar{c}}(s) = \sum_{n=1}^{6} C_n G_{\psi(nS)}(s) + \frac{1}{1+\exp[-\beta_\gamma(s-s_0)]}, \qquad (24)$$

where $G_{\psi(nS)}(s) = \Psi_{\psi(nS)}(s)(s - M^2_{\psi(nS)})$ and $M_{\psi(nS)}$ and $\Psi_{\psi(nS)}(s)$ are given in Tables 2 and 3, and C_n, β_γ, and s_0 are parameters to be determined.

3.1. Decay $\psi(nS) \to e^+e^-$

The partial width for the decay $\psi(nS) \to e^+e^-$ reads

$$\Gamma(\psi(nS) \to e^+e^-) = \frac{\pi\alpha^2}{M^5_{\psi(nS)}}\sqrt{\frac{M^2_{\psi(nS)} - 4\mu_e^2}{M^2_{\psi(nS)}}} \qquad (25)$$

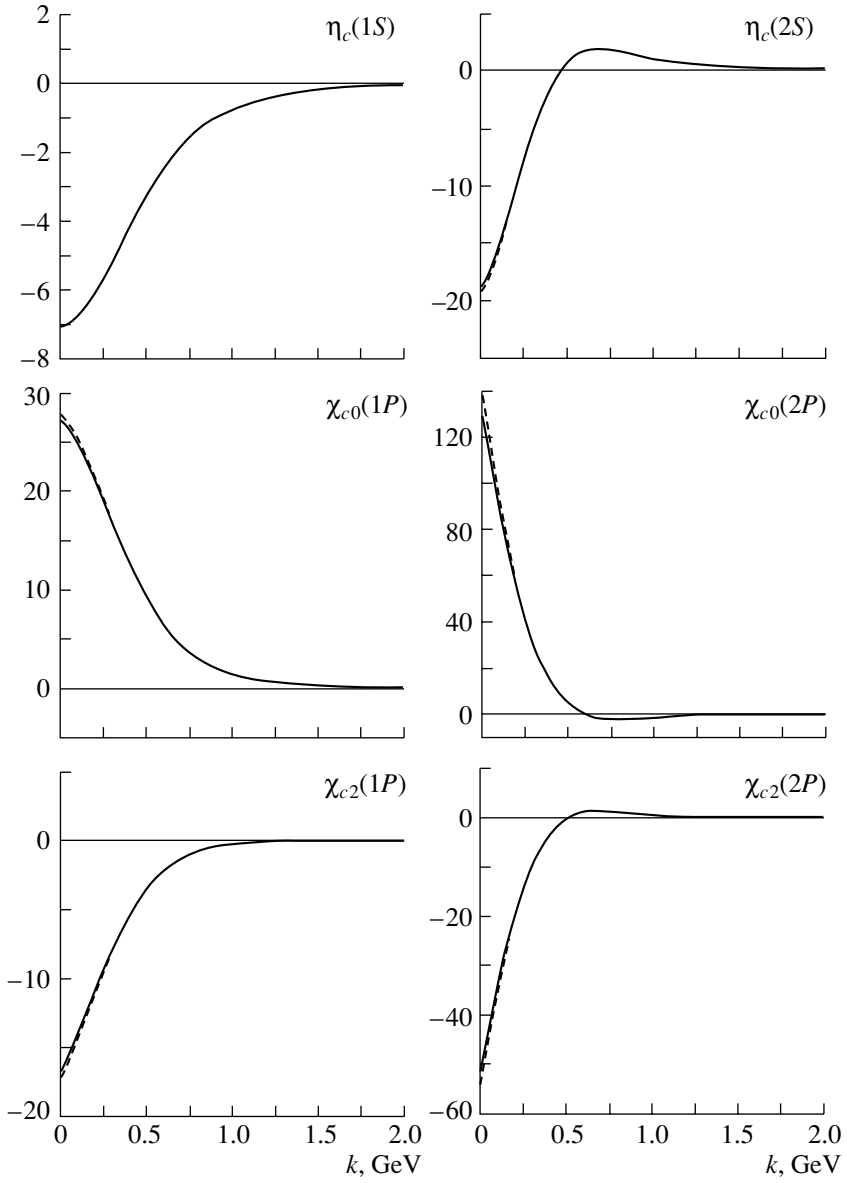

Fig. 7. The $c\bar{c}$ wave functions for $\eta_c(nS)$, $\chi_{c0}(nP)$, and $\chi_{c2}(nP)$. Solid and dashed curves correspond to solutions I and II.

$$\times \left(\frac{8}{3}\mu_e^2 + \frac{4}{3}M^2_{\psi(nS)}\right)\left|F_{\psi(nS)\to e^+e^-}(0)\right|^2,$$

where $\alpha = e^2/4\pi = 1/137$, μ_e is the electron mass, and $M_{\psi(nS)}$ is the charmonium mass. The transition amplitude $F_{\psi(nS)\to e^+e^-}(0)$, being determined by the process of Fig. 4 (see [1]), is equal to

$$F_{\psi(nS)\to e^+e^-}(0) = \frac{2}{3}\sqrt{N_c} \qquad (26)$$
$$\times \int\limits_{4m_c^2}^{\infty} \frac{ds}{16\pi^2}\Psi_{\psi(nS)}(s)G_{\gamma\to c\bar{c}}(s)$$
$$\times \sqrt{1-\frac{4m_c^2}{s}}\left(\frac{8}{3}m_c^2 + \frac{4}{3}s\right).$$

The wave function in (26) is normalized as follows:

$$1 = \int\limits_{4m_c^2}^{\infty} \frac{ds}{16\pi^2}\Psi^2_{\psi(nS)}(s)\sqrt{1-\frac{4m_c^2}{s}}\left(\frac{8}{3}m_c^2 + \frac{4}{3}s\right). \qquad (27)$$

The coefficients $c_i^{(n)}$ given in Table 3 construct the wave functions obeying this normalization constraint.

3.2. Decay $\eta_c(nP) \to \gamma\gamma$

The partial width for the decay $\eta_c \to \gamma\gamma$ reads

$$\Gamma(\eta_c \to \gamma\gamma) = \frac{\pi}{4}\alpha^2 M_{\eta_c}^3 \left|F_{\eta_c\to\gamma\gamma}(0)\right|^2. \qquad (28)$$

The transition amplitude is determined by the processes of Figs. 1*a* and 1*b*; it is equal to [1, 4, 20]

$$F_{\eta_c(nP)\to\gamma\gamma}(0) = \frac{8}{9}\sqrt{N_c}m_c \qquad (29)$$

$$\times \int\limits_{4m_c^2}^{\infty} \frac{ds}{2\pi^2}\Psi_{\eta_c(nP)}(s)\Psi_{\gamma\to c\bar{c}}(s)\ln\frac{\sqrt{s}+\sqrt{s-4m_c^2}}{\sqrt{s}-\sqrt{s-4m_c^2}},$$

where $N_c = 3$. Recall that $\Psi_{\gamma\to c\bar{c}}(s) = G_{\gamma\to c\bar{c}}(s)/s$.

The normalization condition for pseudoscalar charmonium wave functions is as follows:

$$1 = \int\limits_{4m_c^2}^{\infty} \frac{ds}{8\pi^2}\Psi^2_{\eta_c(nP)}(s)\sqrt{1-\frac{4m_c^2}{s}}s. \qquad (30)$$

The coefficients presented in Table 3 give us $\Psi_{\eta_c(nP)}(s)$ obeying (30).

3.3. Decay $\chi_{c0}(nP) \to \gamma\gamma$

The partial width of the decay $\chi_{c0} \to \gamma\gamma$ is equal to

$$\Gamma(\chi_{c0} \to \gamma\gamma) = \frac{\pi\alpha^2}{M_{\chi_{c0}}}\left|F_{\chi_{c0}\to\gamma\gamma}(0)\right|^2, \qquad (31)$$

with the quark transition amplitude (Figs. 1*a*, 1*b*) determined as follows [20, 21]:

$$F_{\chi_{c0(nP)}\to\gamma\gamma}(0) = \frac{8}{9}\sqrt{N_c}m_c \qquad (32)$$

$$\times \int\limits_{4m_c^2}^{\infty} \frac{ds}{4\pi^2}\Psi_{\chi_{c0(nP)}}(s)\Psi_{\gamma\to c\bar{c}}(s)$$

$$\times \left(\sqrt{s(s-4m_c^2)} - 2m_c^2\ln\frac{\sqrt{s}+\sqrt{s-4m_c^2}}{\sqrt{s}-\sqrt{s-4m_c^2}}\right).$$

The normalization condition for the scalar charmonium wave function reads

$$1 = \int\limits_{4m_c^2}^{\infty} \frac{ds}{8\pi^2}\Psi^2_{\chi_{c0(nP)}}(s)\sqrt{1-\frac{4m_c^2}{s}}(s-4m_c^2)m_c^2. \qquad (33)$$

Table 4. Calculated partial widths for nS and nP states vs. experimental data (bold mass numbers stand for the predicted states)

State	Decay	Γ, keV	$\Gamma_{\rm exp}$, keV
$1S$	$J/\psi(3096) \to e^+e^-$	5.444 (I)	5.40 ± 0.22
		5.598 (II)	
$2S$	$\psi(3686) \to e^+e^-$	2.151 (I)	2.14 ± 0.21
		2.210 (II)	
$3S$	$\psi(4040) \to e^+e^-$	0.756 (I)	0.75 ± 0.15
		0.778 (II)	
$4S$	$\psi(4415) \to e^+e^-$	0.462 (I)	0.47 ± 0.10
		0.498 (II)	
$1S$	$\eta_c(2979) \to \gamma\gamma$	6.979 (I)	7.0 ± 1.0
		6.946 (II)	
$2S$	$\eta_c(3594) \to \gamma\gamma$	1.968 (I)	–
		1.034 (II)	
$1P$	$\chi_{c0}(3415) \to \gamma\gamma$	2.572 (I)	2.6 ± 0.5
		2.440 (II)	
$2P$	$\chi_{c0}(\mathbf{3849}) \to \gamma\gamma$	1.159 (I)	–
$3P$	$\chi_{c0}(\mathbf{3845}) \to \gamma\gamma$	1.021 (II)	
$1P$	$\chi_{c2}(3556) \to \gamma\gamma$	1.195 (I)	–
		1.155 (II)	
$2P$	$\chi_{c2}(\mathbf{3950}) \to \gamma\gamma$	2.051 (I)	–
$3P$	$\chi_{c2}(\mathbf{3943}) \to \gamma\gamma$	1.934 (II)	

3.4. Decay $\chi_{c2}(nP) \to \gamma\gamma$

The partial width $\chi_{c2} \to \gamma\gamma$ is defined by two transition amplitudes,

$$\Gamma(\chi_{c2} \to \gamma\gamma) \qquad (34)$$

$$= \frac{4}{5}\frac{\pi\alpha^2}{M_{\chi_{c2}}}\left(\frac{1}{6}\left|F^{(0)}_{\chi_{c2}\to\gamma\gamma}(0)\right|^2 + \left|F^{(2)}_{\chi_{c2}\to\gamma\gamma}(0)\right|^2\right),$$

which are determined by the processes of Figs. 1*a* and 1*b* [20, 22] and for the P-wave quark–antiquark states they read as follows:

$$F^{(i)}_{\chi_{c2}(nP)\to\gamma\gamma}(0) = \frac{8}{9}\sqrt{N_c} \qquad (35)$$

$$\times \int\limits_{4m_c^2}^{\infty} \frac{ds}{16\pi^2}\Psi_{\chi_{c2}(nP)}(s)\Psi_{\gamma\to c\bar{c}}(s)J^{(i)}(s).$$

Here,

$$J^{(0)}(s) = -2\sqrt{s\,(s-4m_c^2)}(12m_c^2+s) \qquad (36)$$

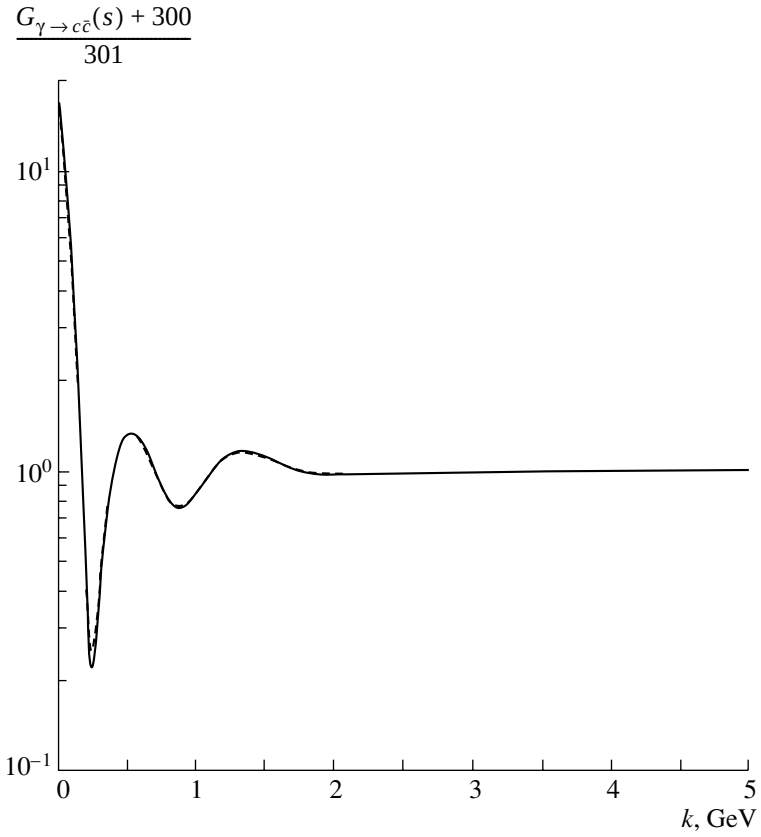

Fig. 8. Vertex $\gamma \to c\bar{c}$. Solid and dashed curves correspond to solutions I and II.

$$+ 4m_c^2(4m_c^2+3s)\ln\frac{s+\sqrt{s\,(s-4m_c^2)}}{s-\sqrt{s\,(s-4m_c^2)}},$$

$$J^{(2)}(s) = \frac{4\sqrt{s\,(s-4m_c^2)}}{3}\left(5m_c^2+s\right)$$

$$- 4m_c^2\left(2m_c^2+s\right)\ln\frac{s+\sqrt{s\,(s-4m_c^2)}}{s-\sqrt{s\,(s-4m_c^2)}}.$$

The normalization condition for the P-wave tensor $c\bar{c}$ system is

$$1 = \int\limits_{4m_c^2}^{\infty}\frac{ds}{16\pi^2}\Psi^2_{\chi_{c2}(nP)}(s)\frac{8}{15}\sqrt{1-\frac{4m_c^2}{s}} \qquad (37)$$

$$\times\ (8m_c^2+3s)(s-4m_c^2).$$

3.5. The Results of the Fit

By fitting the reactions involving the transition $\gamma \to c\bar{c}$, we have determined the parameters C_n, β_γ, and s_0 defined in (24). For solutions I and II, they are as follows (in GeV):

solution I:	solution II:	(38)
$C_1 = -4.945,$	$C_1 = -4.995,$	
$C_2 = -2.893,$	$C_2 = -2.897,$	
$C_3 = -2.191,$	$C_3 = -2.179,$	
$C_4 = -2.300,$	$C_4 = -2.260,$	
$C_5 = -4.264,$	$C_5 = -4.368,$	
$C_6 = -0.690,$	$C_6 = -0.479,$	
$b_\gamma = 0.14,$	$b_\gamma = 0.15,$	
$s_0 = 11.9,$	$s_0 = 22.5.$	

The vertex functions for solutions I and II are shown in Fig. 8; in both solutions, the vertices $G_{\gamma\to c\bar{c}}$ are rather close to each other. The experimental values of partial widths included in the fitting procedure versus those obtained in the fitting procedure are shown in Table 4. There are also predictions made for the two-photon decays of the first radial excitation states: $\eta_c(3594)$, $\chi_0(3847)$, $\chi_2(3947)$.

Let us note that the decay $\chi_{c2}(3556) \to \gamma\gamma$ was not included in the fit because of controversy of the data. In the reaction $p\bar{p} \to \gamma\gamma$, the value $\Gamma(\chi_2(3556) \to \gamma\gamma) = 0.32 \pm 0.080 \pm 0.055$ keV was obtained [23], while in direct measurements, such as e^+e^- annihilation, the width is much larger: $1.02 \pm 0.40 \pm 0.17$ keV [24], $1.76 \pm 0.47 \pm 0.40$ keV [25], $1.08 \pm 0.30 \pm 0.26$ keV [26]. The compilation [27] provides a value close to that of [23]. The value found in

Table 5. Comparison of experimental data [23–27] with our results and calculations of other groups (the values of partial width are in keV)

Decay	Experiment	This work	LS(F) [10]	LS(C) [10]	RM(S) [11]	RM(V) [11]	NR [28]
$\psi(2S) \to \chi_{c0}(1P)\gamma$	26 ± 4	22	31–47	26–31	31	32	19.4
$\psi(2S) \to \chi_{c1}(1P)\gamma$	25 ± 4	59	58–49	63–50	36	48	34.8
$\psi(2S) \to \chi_{c2}(1P)\gamma$	20 ± 4	19	48–47	51–49	60	35	29.3
$\psi(2S) \to \eta_c(1S)\gamma$	0.8 ± 0.2	0.4	11–10	10–13	6	1.3	4.47
$\chi_{c0}(1P) \to J/\psi(1S)\gamma$	165 ± 50	169	130–96	143–110	140	119	147
$\chi_{c1}(1P) \to J/\psi(1S)\gamma$	295 ± 90	389	390–399	426–434	250	230	287
$\chi_{c2}(1P) \to J/\psi(1S)\gamma$	390 ± 120	229	218–195	240–218	270	347	393
$J/\psi(1S) \to \eta_c(1S)\gamma$	1.1 ± 0.3	4.1	1.7–1.3	1.7–1.4	3.35	2.66	1.21
$J/\psi(1S) \to e^+e^-$	5.4 ± 0.22	5.44	5.26	5.26	8.05	9.21	12.2
$\psi(2S) \to e^+e^-$	2.12 ± 0.12	2.15	2.8–2.5	2.9–2.7	4.30	5.87	4.63
$\psi(3S) \to e^+e^-$	0.75 ± 0.15	0.76	2.0–1.6	2.1–1.8	3.05	4.81	3.20
$\psi(4S) \to e^+e^-$	0.47 ± 0.10	0.46	1.4–1.0	1.6–1.3	2.16	3.95	2.41
$\eta_c(1S) \to \gamma\gamma$	7.0 ± 0.9	6.98	6.2–6.3	6.2–6.5	4.2	3.8	19.1
$\chi_{c0}(1P) \to \gamma\gamma$	2.6 ± 0.5	2.57	1.6–1.8	1.5–1.6	–	–	–
$\chi_{c2}(1P) \to \gamma\gamma$	$1.02 \pm 0.40 \pm 0.17$ [24]	1.17	0.3–0.4	0.3–0.4	–	–	–
	$1.76 \pm 0.47 \pm 0.40$ [25]						
	$1.08 \pm 0.30 \pm 0.26$ [26]						
	$0.33 \pm 0.08 \pm 0.06$ [23]						

our fit agrees with data reported by [24–26] and contradicts [23].

4. CONCLUSION

We have carried out calculations of radiative transitions where the $c\bar{c}$ system participates and compared the results with the experiment. The results are given in Table 5. In general, there is a good description of the data. Still, one should point to a disagreement for the following two cases: $\psi(2S) \to \chi_{c1}(1P)\gamma$ and $J/\psi \to \eta_c(1S)\gamma$.

The calculation of partial width $\psi(2S) \to \chi_{c1}(1P)\gamma$ provides us with a value twice as large as the one given in [29, 30]. Such a disagreement may be related to either presumably much higher experimental error [29, 30] or a specific behavior of the wave function of $\chi_{c1}(1P)$ that was not accounted for in [4].

Another discrepancy has been observed for the width of the transition $J/\psi \to \eta_c(1S)\gamma$. This is an $M1$ transition; it is defined by the magnetic moment of the c quark. One possibility to reduce the calculated value of $J/\psi \to \eta_c(1S)\gamma$ consists in increasing the c-quark mass; another one is to take into consideration an anomalous magnetic moment of the c quark. The hypothesis of the existence of an anomalous magnetic moment at light quarks was suggested rather long ago in connection with the description of the decay $\omega \to \pi^0\gamma$ [31] (see also discussion in [32]).

In Table 5, the values of the partial width obtained by other authors are presented.

In [10], the ideology of treating the $c\bar{c}$ system is similar to ours: the charmonium masses were fitted, as well as the widths of radiative transitions. The results obtained in [10] depend on a chosen gauge for gluon exchange interaction—we demonstrate the results obtained for both Feynman (F) and Coulomb (C) gauges; different approaches used in [10] are reflected in the allowed accuracy intervals given in Table 5.

In [11], the $c\bar{c}$ system was studied in terms of scalar (S) and vector (V) confinement forces—both variants are presented in Table 5. For comparison, we give in Table 5 the results obtained in the nonrelativistic (NR) approach to the $c\bar{c}$ system.

It should also be noted that, by describing heavy-quark systems, one may also use schemes where

relativistic effects are taken into account in terms of the v/c expansion (see, e.g., [33] and references therein). Such an approach, which is undoubtedly helpful for the lowest $c\bar{c}$ levels, can face problems with the description of states with masses of about 5 GeV. The purpose of this paper is the elaboration of the method of calculation of the characteristics of highly excited quark–antiquark states for both heavy and light quarks. When one bears in mind such a goal, a full account of the relativism is necessary.

In both relativistic [10, 11] and nonrelativistic [28] approaches, there is a rather large discrepancy between the data and calculated values of $\psi(nS) \to e^+e^-$ (in [10], the width of the transition $J/\psi \to e^+e^-$ was not calculated but fixed). In our opinion, the reason is that, in all the above-mentioned papers, soft interaction of quarks was not accounted for—we mean the processes shown in Figs. 3*b* and 3*c*. In fact, the necessity of taking into consideration the low-energy quark interaction, that is, the vector-meson dominance in the transitions $q\bar{q} \to V \to \gamma$, was understood decades ago, but until now this procedure has not become commonly accepted even for light quarks: see, for example, [34, 35].

ACKNOWLEDGMENTS

We thank A.V. Anisovich, Y.I. Azimov, G.S. Danilov, I.T. Dyatlov, L.N. Lipatov, V.Yu. Petrov, H.R. Petry, and M.G. Ryskin for useful discussions.

This work was supported by the Russian Foundation for Basic Research, project no. 04-02-17091.

REFERENCES

1. V. V. Anisovich, D. I. Melikhov, and V. A. Nikonov, Phys. Rev. D **55**, 2918 (1997).
2. A. V. Anisovich, V. V. Anisovich, L. G. Dakhno, *et al.*, Yad. Fiz. **68**, 1892 (2005); hep-ph/0406320.
3. O. V. Zenin, V. V. Ezhela, S. B. Lugovsky, *et al.*, Report IHEP-2001-25 (2001); hep-ph/0110176.
4. V. V. Anisovich, L. G. Dakhno, V. N. Markov, *et al.*, *Energy Levels and Quark Wave Functions for $b\bar{b}$, $c\bar{c}$, and $q\bar{q}$ Systems in Terms of the Spectral Integral Bethe–Salpeter Equation* (in press).
5. A. V. Anisovich, V. V. Anisovich, V. N. Markov, *et al.*, Yad. Fiz. **67**, 794 (2004) [Phys. At. Nucl. **67**, 773 (2004)].
6. G. Hulth and H. Snellman, Phys. Rev. D **24**, 2978 (1981).
7. S. Godfrey and N. Isgur, Phys. Rev. D **32**, 189 (1985).
8. S. N. Gupta, S. F. Radford, and W. W. Repko, Phys. Rev. D **31**, 160 (1985).
9. W. Lucha, F. Schöberl, and D. Gromes, Phys. Rep. **200**, 127 (1991).
10. J. Linde and H. Snellman, Nucl. Phys. A **619**, 346 (1997).
11. J. Resag and C. R. Münz, Nucl. Phys. A **590**, 735 (1995).
12. P. C. Tiemejer and J. A. Tjon, Phys. Rev. C **49**, 494 (1994).
13. H. Hersbach, Phys. Rev. C **50**, 2562 (1994).
14. A. V. Anisovich, V. V. Anisovich, V. N. Markov, *et al.*, J. Phys. G **28**, 15 (2002).
15. H. Hersbach, Phys. Rev. A **46**, 3657 (1992).
16. F. Gross and J. Milana, Phys. Rev. D **43**, 2401 (1991).
17. K. M. Maung, D. E. Kahana, and J. W. Ng, Phys. Rev. A **46**, 3657 (1992).
18. J. J. Hernandes, S. Navas, and C. Patrignani, Phys. Rev. D **66**, 010001 (2002).
19. G. t'Hooft, Phys. Rev. D **14**, 3432 (1976).
20. A. V. Anisovich, V. V. Anisovich, and V. A. Nikonov, Eur. Phys. J. A **12**, 103 (2001).
21. A. V. Anisovich, V. V. Anisovich, V. N. Markov, and V. A. Nikonov, Yad. Fiz. **65**, 523 (2002) [Phys. At. Nucl. **65**, 497 (2002)].
22. A. V. Anisovich, V. V. Anisovich, M. A. Matveev, and V. A. Nikonov, Yad. Fiz. **66**, 946 (2003) [Phys. At. Nucl. **66**, 914 (2003)].
23. T. A. Armstrong *et al.*, Phys. Rev. Lett. **70**, 2988 (1993).
24. M. Acciari *et al.*, Phys. Lett. B **453**, 73 (1999).
25. K. Ackerstaff *et al.*, Phys. Lett. B **439**, 197 (1998).
26. J. Dominick *et al.*, Phys. Rev. D **50**, 4265 (1994).
27. K. Hagiwara *et al.* (PDG), Phys. Rev. D **66**, 010001 (2002).
28. M. Beyer, U. Bohn, M. G. Huber, *et al.*, Z. Phys. C **55**, 307 (1992).
29. J. Gaiser *et al.*, Phys. Rev. D **34**, 711 (1986).
30. C. J. Biddick *et al.*, Phys. Rev. Lett. **38**, 1324 (1977).
31. I. G. Aznauryan and N. Ter-Isaakyan, Yad. Fiz. **31**, 1680 (1980) [Sov. J. Nucl. Phys. **31**, 871 (1980)].
32. S. B. Gerasimov, hep-ph/0208049; in *FHD Proceedings, Kobe University, Japan, 2002*.
33. D. Ebert, R. N. Faustov, and V. O. Galkin, Phys. Rev. D **67**, 014027 (2003).
34. M. A. DeWitt, H. M. Choi, and C. R. Ji, Phys. Rev. D **68**, 054026 (2003).
35. B.-W. Xiao and B.-Q. Ma, Phys. Rev. D **68**, 034020 (2003).

Physics of Atomic Nuclei, Vol. 68, No. 12, 2005, pp. 2093–2099. From Yadernaya Fizika, Vol. 68, No. 12, 2005, pp. 2155–2161.

ELEMENTARY PARTICLES AND FIELDS
Theory

Baryon-Number Transfer in High-Energy *hp* Collisions*

F. Bopp and **Yu. M. Shabelski**[1)]

Siegen University, Germany

Received February 15, 2005

Abstract—The processes of baryon-number transfer due to string-junction propagation in rapidity is considered. It has a significant effect on the net baryon production in pp collisions at mid-rapidities and an even larger effect in the forward hemisphere in the cases of πp and γp interactions. The results of numerical calculations in the framework of the quark–gluon string model are in reasonable agreement with the data with the same parameter values for different energies. © *2005 Pleiades Publishing, Inc.*

1. INTRODUCTION

The quark–gluon string model (QGSM) and the dual parton model (DPM) are based on the dual topological unitarization (DTU) and describe quite reasonably many features of high-energy production processes, including the inclusive spectra of different secondary hadrons, their multiplicities, KNO distributions, etc., in both hadron–nucleon and hadron–nucleus collisions [1–5]. High-energy interactions are considered as proceeding via the exchange of one or several Pomerons, and all elastic and inelastic processes result from cutting through or between Pomerons [6]. The possibility of exchanging a different number of Pomerons introduces absorptive corrections to the cross sections, which are in agreement with the experimental data on production of hadrons consisting of light quarks. Inclusive spectra of hadrons are related to the corresponding fragmentation functions of quarks and diquarks, which are constructed using the Reggeon counting rules [7].

In the present paper, we discuss the processes connected with the transfer of baryon charge over long rapidity distances. In the string models, baryons are considered as configurations consisting of three strings attached to three valence quarks and connected at a point called a "string junction" (SJ) [8–10]. Thus, SJ has a nonperturbative origin in QCD.

It is very interesting to understand the role of SJ in the dynamics of high-energy hadronic interactions. The important results were obtained in [11]. In this paper, we continue to study this problem. We find a set of model parameters which can describe all experimental data concerning baryon-number transfer. Feynman scaling violation for leading baryons is discussed. We also present a description of new experimental data.

2. INCLUSIVE SPECTRA OF SECONDARY HADRONS IN QGSM

As mentioned above, high-energy hadron–nucleon and hadron–nucleus interactions are considered in the QGSM and in the DPM as proceeding via the

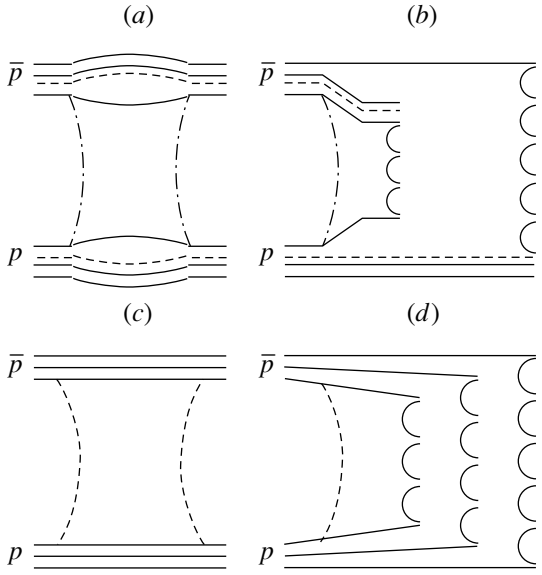

Fig. 1. Cylindrical diagram (dash-dotted curves) corresponding to the one-Pomeron-exchange contribution to (a) elastic $\bar{p}p$ scattering and its cut which determines the contribution to (b) inelastic $\bar{p}p$ cross section (SJ is indicated by a dashed line). The diagram for elastic $\bar{p}p$ scattering with SJ exchange in (c) the t channel and (d) its s-channel discontinuity, which determines the contribution to annihilation $\bar{p}p$ cross section.

*This article was submitted by the authors in English.

[1)]Permanent address: Petersburg Nuclear Physics Institute, Russian Academy of Sciences, Gatchina, 188350 Russia; e-mail: shabelsk@thd.pnpi.spb.ru

**e-mail: Bopp@physik.uni-siegen.de

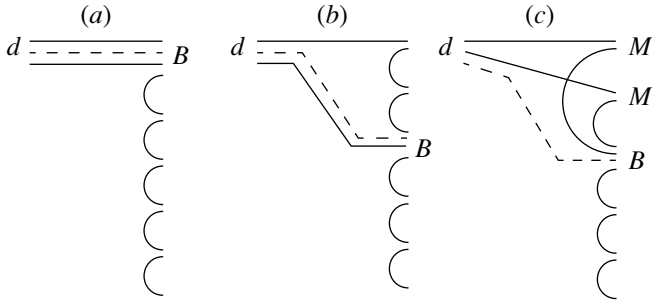

Fig. 2. Three different possibilities of secondary baryon production in pp interactions via diquark d fragmentation: string junction (a) together with two valence quarks and one sea quark, (b) together with one valence quark and two sea quarks, and (c) together with three sea quarks.

exchange of one or several Pomerons. Each Pomeron corresponds to a cylindrical diagram (see Fig. 1a), and thus, when cutting a Pomeron, two showers of secondaries are produced (Fig. 1b). The inclusive spectrum of secondaries is determined by the convolution of diquark, valence-quark, and sea-quark distributions $u(x,n)$ in the incident particles and the fragmentation functions $G(z)$ of quarks and diquarks into secondary hadrons.

The diquark and quark distribution functions depend on the number n of cut Pomerons in the considered diagram. In the following, we use the formalism of the QGSM.

In the case of a nucleon target, the inclusive spectrum of a secondary hadron h has the form [1]

$$\frac{x_E}{\sigma_{\rm inel}}\frac{d\sigma}{dx}=\sum_{n=1}^{\infty}w_n\phi_n^h(x), \qquad (1)$$

where x is the Feynman variable $x_{\rm F}$ and $x_E=2E/\sqrt{s}$.

The functions $\phi_n^h(x)$ determine the contribution of diagrams with n cut Pomerons and w_n is the probability of this process. Here, we neglect the contributions of diffraction–dissociation processes, which are comparatively small in most of the processes considered below. They can be accounted for separately [1, 2].

For pp collisions,

$$\phi_{pp}^h(x)=f_{qq}^h(x_+,n)f_q^h(x_-,n)+f_q^h(x_+,n) \qquad (2)$$
$$\times f_{qq}^h(x_-,n)+2(n-1)f_s^h(x_+,n)f_s^h(x_-,n),$$

$$x_\pm=\frac{1}{2}\left[\sqrt{4m_T^2/s+x^2}\pm x\right], \qquad (3)$$

where the transverse mass of the produced hadron $m_T=\sqrt{m^2+p_T^2}$, and f_{qq}, f_q, and f_s correspond to the contributions of diquarks, valence quarks, and sea quarks, respectively. They are determined by the convolution of the diquark and quark distributions with the fragmentation functions, e.g.,

$$f_q^h(x_+,n)=\int_{x_+}^{1}u_q(x_1,n)G_q^h(x_+/x_1)dx_1. \qquad (4)$$

In the case of a meson beam, the diquark contributions in Eq. (2) should be changed by the contribution of valence antiquarks:

$$\phi_{\pi p}^h(x)=f_{\bar q}^h(x_+,n)f_q^h(x_-,n)+f_q^h(x_+,n) \qquad (5)$$
$$\times f_{qq}^h(x_-,n)+2(n-1)f_s^h(x_+,n)f_s^h(x_-,n).$$

The diquark and quark distributions, as well as the fragmentation functions, are determined from Regge intercepts. Their expressions are given in Appendix 1 of [11]. In the present calculations, we use the same functions with only one exception.

The direct fragmentation of the initial baryon into the secondary one (nucleon or lambda/sigma hyperons) with conservation of the SJ can go via three different processes (Figs. 2a–2c). Obviously, in the case of Ξ production, only two possibilities exist with SJ plus either one valence quark and two sea quarks, or three sea quarks. In the case of production of a secondary baryon having no common quarks with the incident nucleons, only the SJ without valence quarks can contribute (Fig. 2c).

All these contributions are determined by equations similar to Eq. (4) with the corresponding fragmentation functions given by

$$G_{uu}^p=G_{ud}^p=a_Nz^\beta[v_0\varepsilon(1-z)^2 \qquad (6)$$
$$+v_qz^{2-\beta}(1-z)+v_{qq}z^{2.5-\beta}],$$

$$G_{ud}^\Lambda=a_Nz^\beta[v_0\varepsilon(1-z)^2+v_qz^{2-\beta}(1-z) \qquad (7)$$
$$+v_{qq}z^{2.5-\beta}](1-z)^{\Delta\alpha},\qquad G_{uu}^\Lambda=(1-z)G_{ud}^\Lambda,$$

$$G_{d,\rm SJ}^{\Xi^-}=a_Nz^\beta[v_0\varepsilon(1-z)^2+v_qz^{2-\beta}(1-z)] \qquad (8)$$

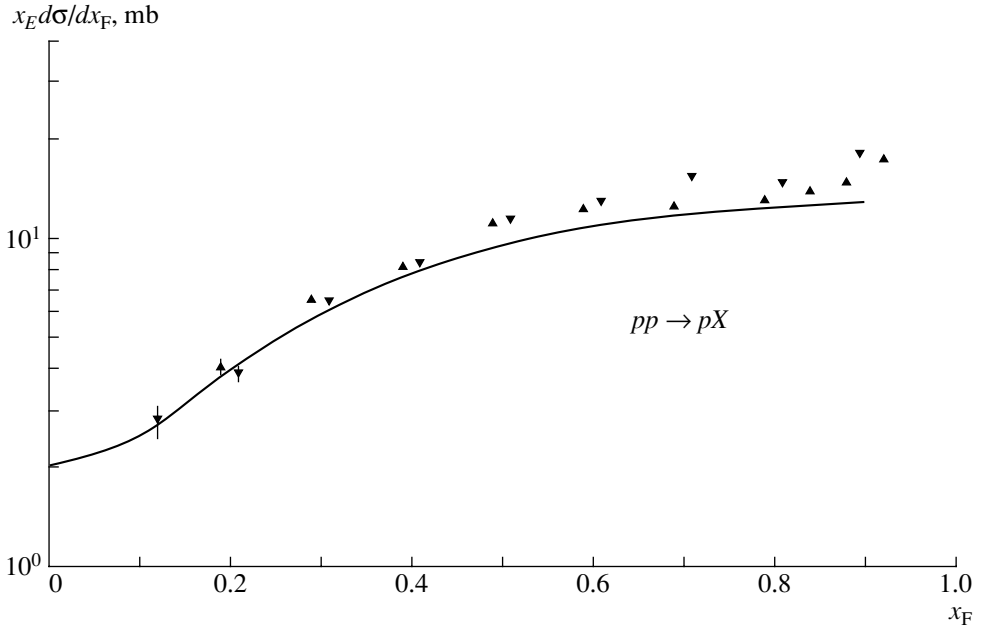

Fig. 3. The spectra of secondary protons in pp collisions at 100 and 175 GeV/c (▲ and ▼) [19] and their description by QGSM.

$$\times (1-z)^{2\Delta\alpha}, \qquad G^{\Xi^-}_{u,\mathrm{SJ}} = (1-z)G^{\Xi^-}_{d,\mathrm{SJ}},$$

$$G^{\Omega}_{\mathrm{SJ}} = a_N v_0 \varepsilon z^{\beta}(1-z)^{2+3\Delta\alpha}. \qquad (9)$$

The factor z^β is really $z^{1-\alpha_{\mathrm{SJ}}}$. As for the factor $z^\beta z^{2-\beta}$ of the second term of Eqs. (6)–(8), it is $2(\alpha_R - \alpha_B)$ [1]. For the third term in Eqs. (6) and (7), we have added an extra factor $z^{1/2}$. The values v_0, v_q, and v_{qq} were taken from [11]; $\Delta\alpha = \alpha_\rho - \alpha_\varphi = 0.5$.

The secondary baryon consists of the SJ together with two valence quarks and one sea quark (Fig. 2*a*), one valence quark and two sea quarks (Fig. 2*b*), or three sea quarks (Fig. 2*c*). The fraction of the incident baryon energy carried by the secondary baryon decreases from Fig. 2*a* to Fig. 2*c*, whereas the mean rapidity gap between the incident and secondary baryon increases. The diagram of Fig. 2*b* has been used for the description of baryon-number transfer in QGSM [1]. It also describes the fast pion production by a diquark.

The probability of finding a comparatively slow SJ in the case of Fig. 2*c* can be estimated from the data on $\bar{p}p$ annihilation into mesons (see Figs. 1*c*, 1*d*). This probability is known experimentally only at comparatively small energies, where it is proportional to $s^{\alpha_{\mathrm{SJ}}-1}$ with $\alpha_{\mathrm{SJ}} \sim 0.5$. However, it has been argued [12] that the annihilation cross section contains a small part which is independent of s, and thus $\alpha_{\mathrm{SJ}} \sim 1$.

The main purpose of this paper is the determination of the contribution of the graph in Fig. 2*c* to the diquark fragmentation function. The magnitude of this contribution is proportional to a coefficient which will be denoted by ε.

Note that SJ (as well as strings) has a nonperturbative origin in QCD and at present it is impossible to determine α_{SJ} from QCD theoretically. Thus, we treat α_{SJ}, ε, and a_N as phenomenological parameters, which should be determined from experimental data with the additional condition of baryon-number conservation.

3. COMPARISON WITH THE DATA

The mechanism of the baryon-charge transfer via SJ without valence quarks (Fig. 2*c*) was accounted for in previous paper [11], where the value $\alpha_{\mathrm{SJ}} = 0.5$ was used. Practically all existing data at comparatively low energies ($\sqrt{s} \sim 15$–30 GeV) were described with the value $\varepsilon = 0.05$. However, the ISR [13] data for the yields of protons and antiprotons separately, as well as their differences, are described quite reasonably by QGSM with $\varepsilon = 0.2$. The same value of $\varepsilon = 0.2$ allows one to describe HERA [14] data on $\bar{p}/p$ asymmetry. This confirms the result [15] that the $\bar{p}/p$ asymmetry measured at HERA can be obtained by simple extrapolation of ISR data. It is necessary to note that the systematic errors in [13] are of the order of 30%, so the value $\varepsilon = 0.05$ cannot be excluded. HERA data are preliminary and have rather large errors. However, now the RHIC data on the $\bar{p}/p$ ratios in pp collisions at $\sqrt{s} = 200$ GeV have appeared [16], and these data are in agreement with HERA data.

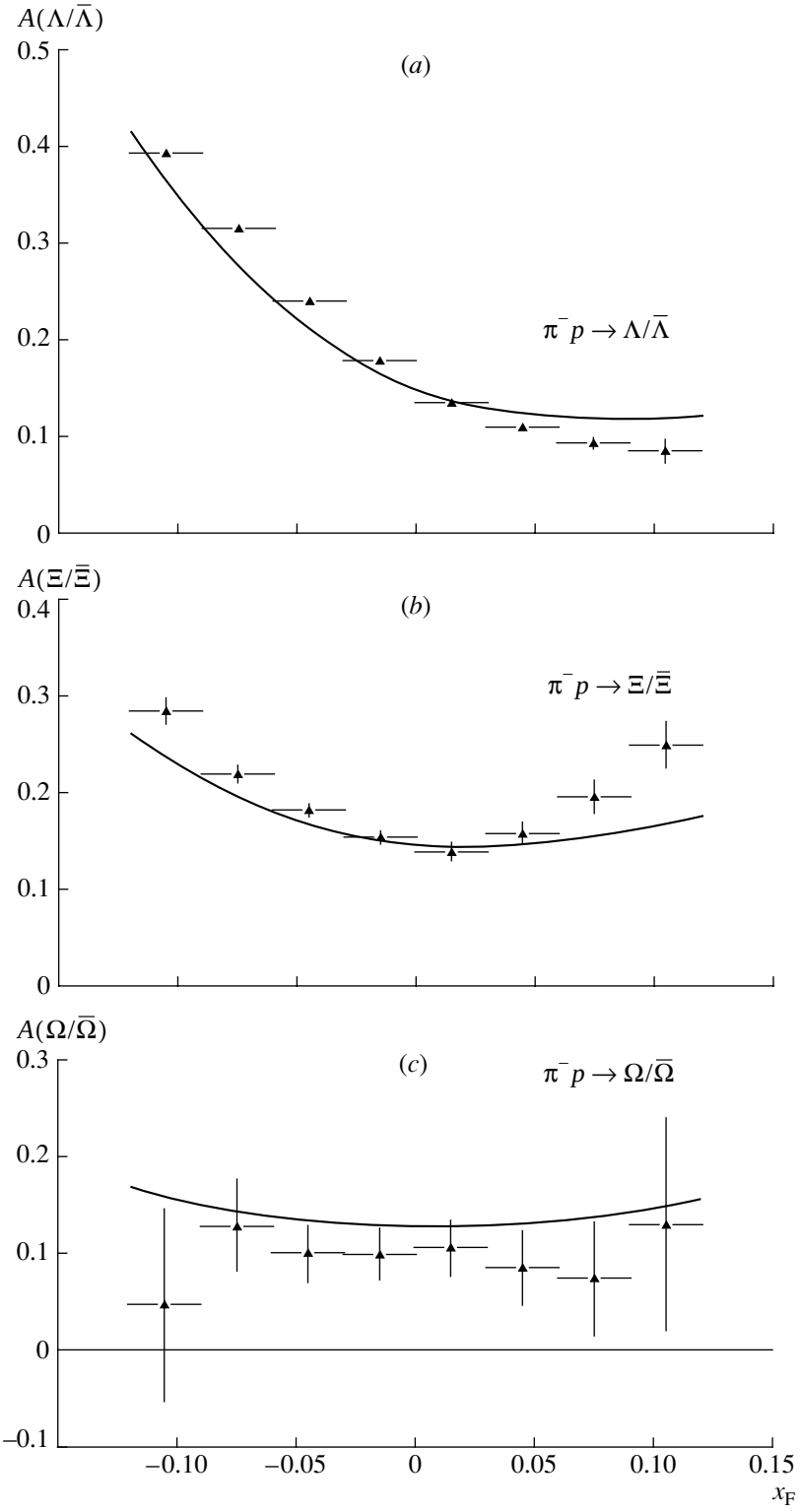

Fig. 4. The asymmetries of secondary (*a*) $\Lambda/\bar{\Lambda}$, (*b*) $\Xi/\bar{\Xi}$, and (*c*) $\Omega/\bar{\Omega}$ in $\pi^- p$ collisions at 500 GeV/c [20] and their description by QGSM.

Some part of the disagreement in the values of the ε parameter at different energies can be connected with phase-space effects. In the process of Fig. 2*c*, as a minimum, two additional mesons M should be produced in one of the strings, which can give an additional suppression [17] of the process of Fig. 2*c* in

comparison with, say, Fig. 2*a*. However, the fourfold difference in the values of the ε parameter obtained in [11] in different energy regions seems to be too large for phase-space suppression.

Another possibility to explain this difference is that the value of the intercept $\alpha_{\rm SJ} = 0.5$ in [11] was taken to be too small. In fact, the SJ contribution to the inclusive cross section of secondary-baryon production at the rapidity distance Δy from the incident particle can be estimated as

$$(1/\sigma)d\sigma_B/dy \sim a_B \varepsilon e^{(\alpha_{\rm SJ}-1)\Delta y}, \qquad (10)$$

$a_B = a_N v_i$. The values of v_i (v_0, v_q, and v_{qq}) determine the relative probabilities for SJ with or without valence quark fragmentation into different baryons. Their quantities were taken from quark combinatorics [11, 18]. So the increase in the effective value of ε with energy, i.e., with Δy, can be considered as a signal to increase the value of $\alpha_{\rm SJ}$.

In the present paper, we found the solution of the problem with the parameters

$$\alpha_{\rm SJ} = 0.9, \qquad \varepsilon = 0.024, \qquad (11)$$
$$a_N = 1.33 \ \text{(low energies)},$$
$$a_N = 1.29 \ \text{(high energies)}.$$

The quality of the description of the experimental data with these parameters is practically the same as in [11]. As an example, we present in Fig. 3 the inclusive spectra of secondary protons in *pp* collisions at lab. energies of 100 and 175 GeV [19].

In Fig. 4, we show the data [20] on the asymmetry of strange baryons produced in π^- interactions[2)] at 500 GeV/c. The asymmetry is determined as

$$A(B/\bar{B}) = \frac{N_B - N_{\bar{B}}}{N_B + N_{\bar{B}}} \qquad (12)$$

for each $x_{\rm F}$ bin.

The theoretical curves for the data on all asymmetries calculated with parameters (11) are in reasonable agreement with the data. Sometimes this agreement is even better than in [11].

In the case of $\Omega/\bar{\Omega}$ production, we predict a nonzero asymmetry in agreement with experimental data. Let us note that such asymmetry is absent, say, in the naive quark model, because Ω and $\bar{\Omega}$ have no valence quarks common with the incident particles.

[2)]These data were obtained from pion interactions on a nuclear target, where different materials were used in a very complicated geometry. We assume that the nuclear effects are small in the asymmetry ratio (12) and compare the pion–nucleus data with calculations for $\pi^- p$ collisions.

The predicted values of the antihyperon/hyperon production asymmetries (13) in γp collisions and $\bar{B}/B$ ratios in *pp* collisions, both at $\sqrt{s} = 200$ GeV

Hyperon	A_B, %	$\bar{B}/B$
$\bar{\Lambda}, \Lambda$	10.8	0.77
$\bar{\Xi}, \Xi$	6.5	0.82
$\bar{\Omega}, \Omega$	12.0	0.81

Preliminary data on $p/\bar{p}$ asymmetry in ep collisions at HERA were presented by the H1 Collaboration [14]. Here, the asymmetry is defined as

$$A_B = 2\frac{N_p - N_{\bar{p}}}{N_p + N_{\bar{p}}}, \qquad (13)$$

i.e., with an additional factor 2 in comparison with Eq. (12). The experimental value of A_B is equal to $(8.0 \pm 1.0 \pm 2.5)\%$ [14] for secondary baryons produced at $x_{\rm F} \sim 0.04$ in the γp c.m. frame. In the QGSM, the hadron structure of the photon is considered as $(\pi^+ + \pi^-)/2$ [21]. Such an approach with parameters (11) leads to the value $A_B = 9.9\%$, in agreement with the data. The experimental value A_B was predicted in [22] using $\alpha_{\rm SJ} = 1$, which is rather close to our choice (11).

The baryon charge transferred to large rapidity distances can be determined by integration of Eq. (10), so it is of the order of

$$\langle n_B \rangle \sim a_B \varepsilon/(1 - \alpha_{\rm SJ}). \qquad (14)$$

It is clear that the value $\alpha_{\rm SJ} = 1$ should be excluded because of the violation of baryon-number conservation at very high energies. At the same time, values of $\alpha_{\rm SJ}$ very close to unity are possible. If the essential part of the initial baryon charge is transferred to large rapidity distances, the altitude of secondary baryon spectra in the proton fragmentation region (large $x_{\rm F}$) should be decreased. This leads to violation [23] of Feynman scaling at very high energies. For example, we predict a decrease in the secondary neutron multiplicity with $x_{\rm F} > 0.28$ from 0.324 to 0.27 for the energy region $\sqrt{s} = 20$–200 GeV. The experimental estimate of this effect [24] is significantly larger, about two times.

The RHIC *pp* data [16] on the ratio of $\bar{p}/p$ at low values of c.m. rapidity also are described reasonably with parameters (11), as one can see in Fig. 5.

Some of our predictions at $\sqrt{s} = 200$ GeV for the antihyperon/hyperon production asymmetries in the γp and $\bar{B}/B$ ratios in *pp* collisions are presented in the table.

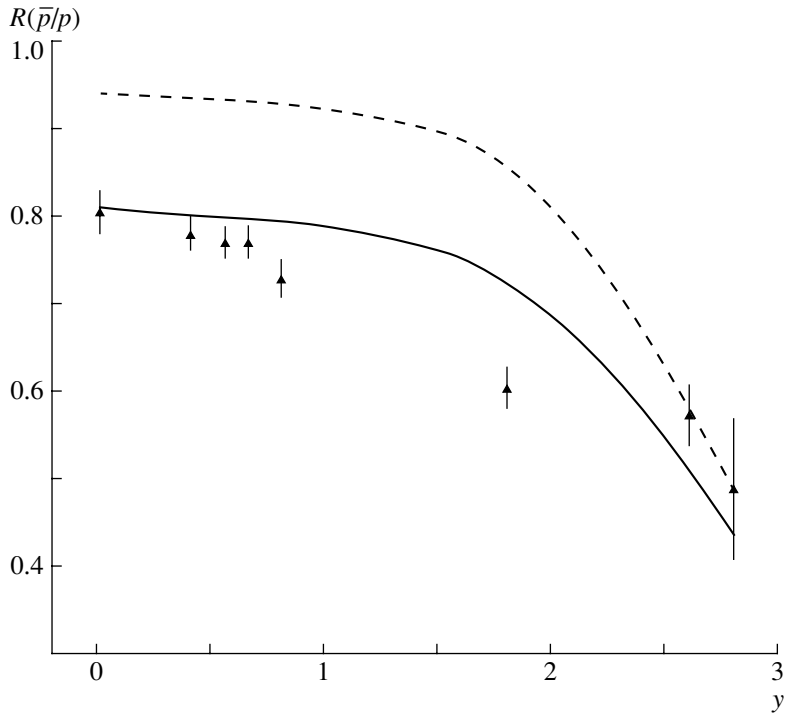

Fig. 5. The ratios of secondary antiproton/proton production in pp interactions at $\sqrt{s} = 200$ GeV (points and solid curve). The calculated result with $\varepsilon = 0$ is shown by the dashed curve.

4. CONCLUSIONS

We presented the role of string-junction diffusion for the baryon charge transfer over large rapidity distances. Without this contribution shown in Fig. 2*c*, the data for hyperon/antihyperon asymmetries (Fig. 4), proton/antiproton asymmetry [14], and $\bar{p}/p$ ratios at RHIC (dashed curve in Fig. 5) are in total disagreement with the data.

It is necessary to note that the value of the ε parameter in (11) was taken from the normalization to one experimental point, the parameter α_{SJ} was found from the energy (or rapidity) dependence of the observed effects, and the value a_N was calculated from the condition of baryon-number conservation. The results of calculations for other processes, which are also sensitive to SJ diffusion of baryon charge, are practically the same as in [11], so we do not present them. It is necessary to note that the existing experimental data are not enough for determination of the SJ parameters with the needed accuracy.

ACKNOWLEDGMENTS

This paper was supported by DFG grant GZ: 436 RUS 113/771/1-2 and, in part, by grants RSGSS-1124.2003.2 and PDD (CP) PST.CLG980287.

REFERENCES

1. A. B. Kaidalov and K. A. Ter-Martirosyan, Yad. Fiz. **39**, 1545 (1984) [Sov. J. Nucl. Phys. **39**, 979 (1984)]; **40**, 211 (1984) [**40**, 135 (1984)]; A. B. Kaidalov and O. I. Piskunova, Yad. Fiz. **41**, 1278 (1985) [Sov. J. Nucl. Phys. **41**, 816 (1985)].
2. A. Capella, U. Sukhatme, C. I. Tan, and J. Tran Thanh Van, Phys. Rep. **236**, 225 (1994); A. Capella and J. Tran Thanh Van, Z. Phys. C **10**, 249 (1981).
3. A. B. Kaidalov, K. A. Ter-Martirosyan, and Yu. M. Shabelski, Yad. Fiz. **43**, 1282 (1986) [Sov. J. Nucl. Phys. **43**, 822 (1986)].
4. Yu. M. Shabelski, Yad. Fiz. **44**, 186 (1986) [Sov. J. Nucl. Phys. **44**, 117 (1986)].
5. Yu. M. Shabelski, Nucl. Phys. B (Proc. Suppl.) **52**, 116 (1997).
6. V. A. Abramovsky, V. N. Gribov, and O. V. Kancheli, Yad. Fiz. **18**, 595 (1973) [Sov. J. Nucl. Phys. **18**, 301 (1973)].
7. A. B. Kaidalov, Yad. Fiz. **45**, 1452 (1987) [Sov. J. Nucl. Phys. **45**, 902 (1987)]; **43**, 1282 (1986) [**43**, 822 (1986)].
8. M. Imachi, S. Otsuki, and F. Toyoda, Prog. Theor. Phys. **54**, 280 (1976); **55**, 551 (1976).
9. G. C. Rossi and G. Veneziano, Nucl. Phys. B **123**, 507 (1977); L. Montanet, G. C. Rossi, and G. Veneziano, Phys. Rep. **63**, 149 (1980).
10. D. Kharzeev, Phys. Lett. B **378**, 238 (1996).
11. G. H. Arakelyan, A. Capella, A. B. Kaidalov, and Yu. M. Shabelski, Eur. Phys. J. C **26**, 81 (2002); hep-ph/0103337.

12. B. Z. Kopeliovich and B. G. Zakharov, Phys. Lett. B **211**, 221 (1988); E. Gotsman and S. Nusinov, Phys. Rev. D **22**, 624 (1980).
13. M. Banner *et al.*, Phys. Lett. B **41B**, 547 (1972); B. Alper *et al.*, Nucl. Phys. B **100**, 237 (1975).
14. C. Adloff *et al.* (H1 Collab.), submitted to *The 29th International Conference on High-Energy Physics ICHEP98, Vancouver, 1998*.
15. F. Bopp, hep-ph/0002190; hep-ph/0007229.
16. B. H. Samset *et al.* (BRAHMS Collab.), submitted to *The Quark Matter 2004 International Conference, Oakland, 2004*.
17. K. A. Ter-Martirosyan and Yu. M. Shabelski, Yad. Fiz. **25**, 403 (1977) [Sov. J. Nucl. Phys. **25**, 217 (1977)]; Yad. Fiz. **25**, 670 (1977) [Sov. J. Nucl. Phys. **25**, 356 (1977)].
18. A. Capella and C.-A. Salgado, Phys. Rev. C **60**, 054906 (1999).
19. A. E. Brenner *et al.*, Phys. Rev. D **26**, 1497 (1982).
20. E. M. Aitala *et al.* (E769 Collab.), hep-ex/0009016; Phys. Lett. B **496**, 9 (2000).
21. V. V. Lugovoi, S. Yu. Sivoklokov, and Yu. M. Shabelski, Yad. Fiz. **58**, 72 (1995) [Phys. At. Nucl. **58**, 67 (1995)].
22. B. Kopeliovich and B. Povh, Z. Phys. C **75**, 693 (1997).
23. Yu. M. Shabelski, Izv. Akad. Nauk SSSR, Ser. Fiz. **50**, 2090 (1986).
24. S. Chekanov *et al.* (ZEUS Collab.), Nucl. Phys. B **637**, 3 (2002).

Physics of Atomic Nuclei, Vol. 68, No. 12, 2005, pp. 2100–2109. Translated from Yadernaya Fizika, Vol. 68, No. 12, 2005, pp. 2162–2171.

ELEMENTARY PARTICLES AND FIELDS
Theory

Effects of Scalar and Pseudoscalar Higgs Bosons in the Process $e^+e^- \to b\bar{b}\nu\bar{\nu}$ at the LEP II Collider

A. A. Likhoded* **and A. E. Chalov**

Institute for High Energy Physics, Protvino, Moscow oblast, 142281 Russia

Received April 19, 2005

Abstract—The possibility of setting constraints on the couplings of the scalar or pseudoscalar Higgs boson to b quarks on the basis of data on the process $e^+e^- \to b\bar{b}\nu\bar{\nu}$ at the LEP II collider is investigated. The mixing of the scalar and the hypothetical pseudoscalar Higgs boson in the $Hb\bar{b}$ vertex is parametrized in the form $\frac{m_b}{v}(a + i\gamma_5 b)$. An analysis of the differential distributions for the process $e^+e^- \to b\bar{b}\nu\bar{\nu}$ reveals that the contribution of the fusion subprocess $WW \to H$ in the channel involving an electron neutrino enhances the sensitivity of data to the parameters under analysis. It is shown that the LEP II data at $\sqrt{s} = 200$ GeV and $\int \mathcal{L}dt = 600$ pb^{-1} per experiment would make it possible to constrain the parameters $\Delta a = a - 1$ and b as follows: $-0.75 \le \Delta a \le 1.4$ at $b = 0$ and free Δa and $-0.97 \le b \le 0.97$ at $\Delta a = 0$ and free b. © *2005 Pleiades Publishing, Inc.*

1. INTRODUCTION

Searches for the Higgs boson and investigation of its properties is one of the most important problems in contemporary elementary-particle physics. In the Standard Model, the Higgs boson is responsible for electroweak-symmetry breaking. In the simplest version of the Standard Model, this symmetry is broken owing to the existence of an electroweak scalar doublet whose interaction potential is ϕ^4. This theory predicts the existence of a neutral Higgs boson whose quantum numbers are $J^{PC} = 0^{++}$. A neutral Higgs boson arises in various extensions of the Standard Model, such as the minimal supersymmetric standard model (MSSM) involving two Higgs doublets (two Higgs doublet model, which is commonly known as 2HDM), three-doublet Weinberg model [1], and models in which electroweak symmetry is broken by new strong interactions. In the last case, there can also exist a pseudoscalar boson [2]. In each scenario, the structure of the Higgs sector provides important information about the respective model. For this reason, it is of particular importance to distinguish between the above scenarios, and this can be achieved by comprehensively studying the CP properties of each predicted scalar or pseudoscalar particle.

Experimental data on the process $e^+e^- \to ZH$ from the LEP collider rule out the existence of the Standard Model Higgs boson having a mass below 114 GeV. There are five physical Higgs particles in the MSSM: a light (h^0) and a heavy (H^0) neutral scalar boson, one CP-odd pseudoscalar boson (A^0), and two charged scalar Higgs bosons ($H^\pm$). Within this model, lower experimental limits on the masses of the lightest scalar particle in the MSSM and the lightest pseudoscalar particle are, respectively, 91 GeV [3] and about 92 GeV [4].

A method for determining the CP nature of the Higgs boson from its decays to fermions or gauge bosons was proposed in [5] and was applied in [6] to Higgs boson production in the process $e^+e^- \to ZH$. It should be noted that experiments at a photon–photon collider offer the most straightforward method for determining the CP properties of the Higgs boson because the use of different polarizations of initial-state photons makes it possible to isolate various CP states [7].

Data on the ZZH coupling constant can be obtained from the angular distributions and threshold behavior of the cross section for the process $e^+e^- \to ZH$. In particular, the CP properties of the Higgs boson can be determined from these data to a fairly high degree of precision [8]. At future hadron colliders, such as LHC, an analysis of the azimuthal-angle distribution of jets produced in the fusion of gauge bosons will provide an efficient tool for studying the CP properties of the HWW vertex [9] and special features of the production of scalar or pseudoscalar Higgs bosons [10]. Data on the Higgs boson coupling to the t quark that are obtained in the process $pp \to t\bar{t}h$ at LHC [11] and in the process $e^+e^- \to t\bar{t}H$ at a future e^+e^- colliders [12] can also be used to determine the CP properties of the Higgs boson.

*e-mail: andre@mx.ihep.su

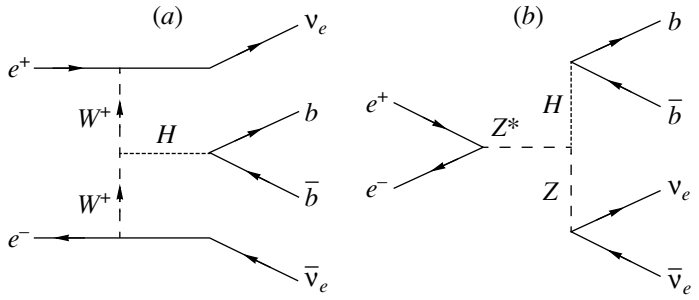

Fig. 1. Feynman diagrams describing Higgs boson production via (*a*) WW fusion and (*b*) the radiative process $Z^* \to ZH$.

The potential of a $\mu^+\mu^-$ collider for investigating the CP transformation properties of Higgs bosons was considered in [13].

In the present study, we address the question of whether it is possible to determine the relative contributions of the scalar and pseudoscalar Higgs bosons to the $Hb\bar{b}$ vertex in the reaction $e^+e^- \to b\bar{b}\nu\bar{\nu}$, relying on the data from the LEP II e^+e^- collider that were obtained at $\sqrt{s} = 200$ GeV and an integrated luminosity of 600 pb^{-1} per experiment. Searches for the resonance production of Higgs bosons in LEP II experiments are based predominantly on the process $e^+e^- \to Z^* \to HZ \to b\bar{b}\mu^+\mu^-(q\bar{q})$, in which case the Higgs boson mass is readily determined if the Z boson is reconstructed by the invariant mass. For this reason, this process is of particular interest in searches for a Higgs resonance. At the LEP II energies, however, a signal from the Higgs boson can also be detected in other reactions, such as $e^+e^- \to b\bar{b}\nu\bar{\nu}$ and $e^+e^- \to b\bar{b}e^+e^-$. Given the magnitude of the cross sections for these processes and the LEP II luminosity, one is able not to only detect them in an experiment but also to investigate the behavior of relevant differential distributions. The distinctive feature of these processes is that the diagrams contributing to their cross sections involve subprocesses of Higgs boson production in the central domain owing to the fusion of vector bosons. This increases substantially the sensitivity of the processes under consideration to anomalous couplings of the Higgs boson. Moreover, the contribution of such subprocesses increases with energy, becoming dominant at the energies of the future linear collider. The program of searches for the Higgs boson and investigation of its properties can be divided into two stages: a direct detection of the Higgs boson produced in the process $e^+e^- \to Z^* \to HZ$ and investigation of its properties in reactions like $e^+e^- \to b\bar{b}\nu\bar{\nu}$ and $e^+e^- \to b\bar{b}e^+e^-$. The latter is the subject of the present study.

The ensuing exposition is organized as follows. In the next section, we consider the interaction of a scalar or a pseudoscalar Higgs boson with fermions within a model-independent approach. An analysis of the process $e^+e^- \to b\bar{b}\nu\bar{\nu}$ is described in Section 3. The last section contains a summary and conclusions.

2. $Hf\bar{f}$ INTERACTION

In possible extensions of the Standard Model that involve additional scalar and pseudoscalar Higgs bosons, the lightest spinless particle can be a superposition of states having no definite parity [14]. Moreover, the coupling constants describing the interaction of the Higgs boson with gauge bosons or fermions are independent parameters in the majority of Standard Model extensions. For the sake of simplicity, we therefore assume in the following that the WWH coupling constants coincide with their counterparts in the Standard Model and parametrize the $Hf\bar{f}$ interaction in a model-independent way as

$$\frac{m_f}{v}(a + i\gamma_5 b), \tag{1}$$

where $v = 246$ GeV and where $a = 1$ and $b = 0$ in the Standard Model. In analyzing the process $e^+e^- \to b\bar{b}\nu\bar{\nu}$, we consider the case where a and b are independent free parameters and the cases where one of these parameters deviates from the respective Standard Model value.

In Monte Carlo simulations of the processes under study, relevant differential distributions are represented as power series in a and b, the coefficients being kinematical factors; that is,

$$\frac{d\sigma}{d\mathcal{O}} = A_0 + a \cdot A_1 + a^2 \cdot A_2 + ab \cdot A_3 + b \cdot A_4 + b^2 \cdot A_5 + \ldots, \tag{2}$$

where $\mathcal{O}$ is an experimentally observable quantity and A_i are purely kinematical factors that are obtained upon squaring the amplitudes and performing integration over the phase space. These kinematical factors are independent of the parameters a and b and are simulated by using the Monte Carlo technique. In the above representation, A_0 is the contribution of

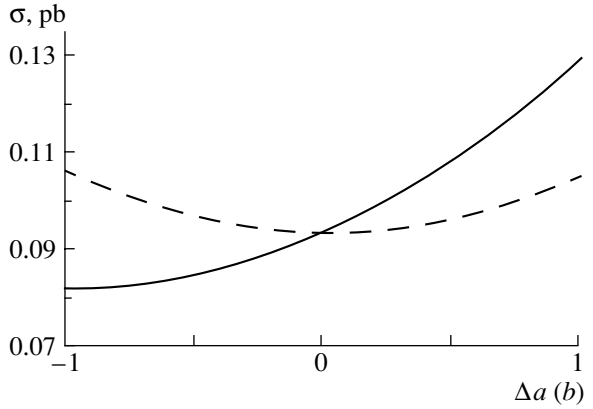

Fig. 2. Total cross section for the reaction $e^+e^- \to b\bar{b}\nu\bar{\nu}$ versus (solid curve) the variation Δa of the parameter a and (dashed curve) the parameter b at the LEP II energies.

the Standard Model diagrams without Higgs bosons, A_1 is the contribution of the interference between the Standard Model diagrams with and without a Higgs boson, and A_2 and A_5 stem from the contribution of the diagrams involving a Higgs boson. In the following, it will be shown that $A_3 = A_4 = 0$ for the processes under study.

In our simulations, we have used, for systematic errors and for the efficiency of b-jet detection, values typical of experiments at LEP II. In our computations, the Higgs boson mass was set to $M_H = 120$ GeV.

3. PROCESS $e^+e^- \to b\bar{b}\nu\bar{\nu}$

Within the Standard Model, the cross section for the process $e^+e^- \to b\bar{b}\nu\bar{\nu}$ receives contributions from the subprocesses involving an electron, a muon, and a tau-lepton neutrino in the final state.

(1) The subprocess $e^+e^- \to b\bar{b}\nu_e\bar{\nu}_e$ is represented by 23 Feynman diagrams: one diagram of Higgs boson production in the fusion reaction $WW \to H$ (Fig. 1a), one diagram of the radiative production of a Higgs boson in the reaction $Z^* \to ZH$ (Fig. 1b), and 21 diagrams of the Standard Model background.

(2) The subprocess $e^+e^- \to b\bar{b}\nu_\mu\bar{\nu}_\mu$ is represented by 11 Feynman diagrams: one diagram of the radiative production of a Higgs boson in the reaction $Z^* \to ZH$ and ten diagrams of the Standard Model background.

(3) The subprocess $e^+e^- \to b\bar{b}\nu_\tau\bar{\nu}_\tau$ is also represented by 11 Feynman diagrams: one diagram of the radiative production of a Higgs boson in the reaction $Z^* \to ZH$ and ten diagrams of the Standard Model background.

At $M_H = 120$ GeV and $\sqrt{s} = 200$ GeV, the total cross section for the reaction $e^+e^- \to b\bar{b}\nu\bar{\nu}$ amounts to about 9.4×10^{-2} pb, the contribution of the subprocess involving an electron neutrino being about 3.6×10^{-2} pb.

Particular attention should be given to the subprocess involving an electron neutrino. At the energies of a future linear collider ($\sqrt{s} = 500$ GeV), the contribution of this subprocess dominates the cross section for the reaction $e^+e^- \to b\bar{b}\nu\bar{\nu}$. The reason is that the contribution of the fusion process $WW \to H$ increases with energy [15, 16]. The sensitivity of the reaction to the $Hb\bar{b}$ coupling constants is also determined primarily by the fusion subprocess $WW \to H$ because the relative contribution of the other signal process, $Z^* \to ZH$, becomes small at high energies. However, the cross sections for the reactions $e^+e^- \to \nu\bar{\nu}W^*W^* \to H\nu\bar{\nu}$ and $e^+e^- \to Z^* \to ZH$ at the LEP II energies are commensurate, so that, at first glance, there is no reason to conclude that one of these subprocesses is dominant. Nevertheless, we will demonstrate that, even at the LEP II energies, the subprocess $e^+e^- \to \nu\bar{\nu}W^*W^* \to H\nu\bar{\nu}$ determines the sensitivity of the reaction $e^+e^- \to b\bar{b}\nu\bar{\nu}$ to the $Hb\bar{b}$ coupling constants.

The sensitivity of the process to a deviation of the parameters of $Hb\bar{b}$ interaction from their Standard Model values can be illustrated by considering the dependence of the total cross section for this reaction on the parameters under consideration. The total cross section for the reaction $e^+e^- \to b\bar{b}\nu\bar{\nu}$ as a function of Δa and b, where $\Delta a = a - 1$, is shown in Fig. 2. The dependence on the parameter b has the form of a parabola whose minimum is at $b = 0$. This fact confirms that the expansion (2) of the cross section involves no linear term in b. The minimum of the parabola representing the dependence on the parameter a (Δa) is shifted to the domain of negative values of Δa, this being indicative of the presence of a linear term in a. Moreover, the sensitivity of the cross section in question increases in the domain of positive values of Δa. In view of this, it is natural to expect that the resulting constraints on the parameter a are more stringent at its positive values [16]. The presence of linear terms in a is explained by the interference between the diagrams involving a Higgs boson and the Standard Model background diagrams. In what is concerned with the parameter b, the situation is totally different because the expression for the vertex involves an imaginary unit as a factor at the parameter b. As a consequence, the interference terms linear in b cancel each other and therefore do not appear in the expression

$$M_i M_j^\dagger + M_j M_i^\dagger.$$

The linear terms in b could in principle appear owing to the antisymmetric tensor $i\epsilon^{ijkl}$ resulting from the

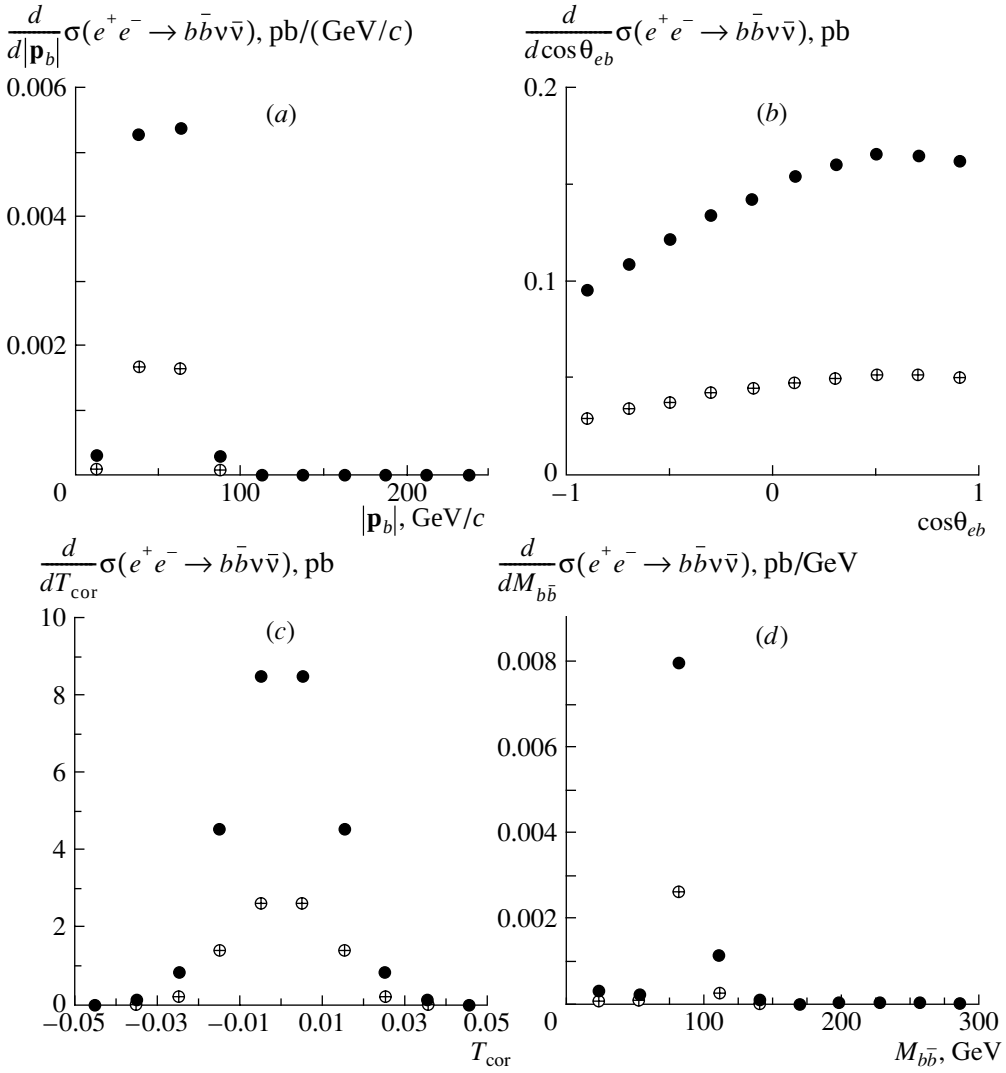

Fig. 3. Differential distributions of the cross section for the process $e^+e^- \to b\bar{b}\nu\bar{\nu}$. Shown are the Standard Model predictions for the distributions with respect to (*a*) the *b*-quark momentum, (*b*) the *b*-quark emission angle, (*c*) $T_{\rm cor}$, and (*d*) the invariant mass of the $b\bar{b}$ pair at $\sqrt{s} = 200$ GeV and $M_H = 120$ GeV. The sum of the contributions of three subprocesses involving ν_e, ν_μ, and ν_τ is shown by closed circles, while the contribution of the only subprocess involving ν_μ is shown by crosses enclosed by circles.

evaluation of the trace $\mathrm{tr}[\gamma_5\gamma_i\gamma_j\gamma_k\gamma_l]$ because this would lead to the cancellation of imaginary parts. However, the number of independent momenta in the case under consideration is not sufficient for constructing such a tensor. For the effect in question to arise, it is necessary, in all probability, to take into account the hadronization or polarization of *b*-quark jets. This explains why $A_3 = A_4 = 0$ in (2).

In studying the process $e^+e^- \to b\bar{b}\nu\bar{\nu}$, we analyze the standard set of experimentally measurable quantities, such as the distributions in the *b*-quark momentum, the *b*-jet emission angle, and the invariant mass of two *b* jets. We also analyze the distribution with respect to the quantity

$$T_{\rm cor} = \frac{1}{(\sqrt{s}/2)^3}\mathbf{p}_e \cdot [\mathbf{p}_b \times \mathbf{p}_{\bar{b}}],$$

which is rather sensitive to possible CP-odd effects in the Higgs sector [15]. The differential distributions for the process $e^+e^- \to b\bar{b}\nu\bar{\nu}$ are demonstrated in Fig. 3 according to Standard Model predictions. The sum of the three subprocesses is shown by closed circles, while the contribution of the muon-neutrino subprocess is shown by crosses enclosed by circles.

In determining the sensitivity of the process to the Higgs boson coupling constants, it is important to know the relative contributions of signal and background diagrams (in the case under consideration,

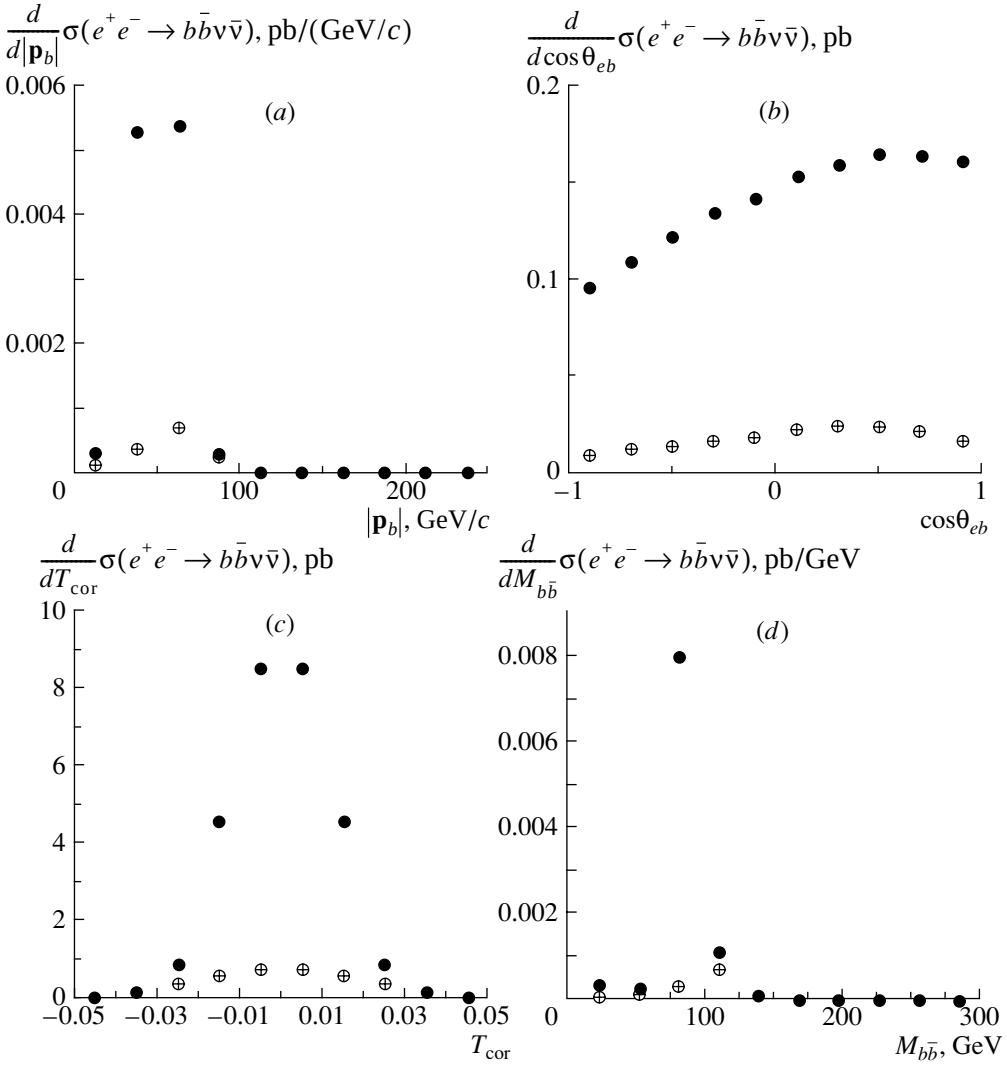

Fig. 4. Differential distributions of the cross section for the process $e^+e^- \to b\bar{b}\nu\bar{\nu}$ with respect to (*a*) the *b*-quark momentum, (*b*) the *b*-quark emission angle, (*c*) $T_{\rm cor}$, and (*d*) the invariant mass of the $b\bar{b}$ pair at $\sqrt{s} = 200$ GeV and $M_H = 120$ GeV. The contributions of all three subprocess (involving three neutrino flavors) are taken into account. Shown are (•) the Standard Model predictions for the contribution of all signal and background diagrams and (⊕) the contribution of the Higgs boson diagrams, including interference diagrams.

these are, respectively, the diagrams involving Higgs bosons and those that do not involve them). The differential distributions with respect to the *b*-quark momentum, the *b*-quark emission angle reckoned from the initial-beam direction, $T_{\rm cor}$, and the invariant mass of the $b\bar{b}$ pair are presented in Fig. 4 for the total contribution of the subprocesses involving ν_e, ν_μ, and ν_τ. The contribution of both signal and background diagrams is shown by closed circles, while the contribution of the Higgs boson diagrams, including the interference diagrams is shown by crosses enclosed by circles. The analogous distributions for the subprocess featuring only a muon neutrino are shown in Fig. 5. From a comparison of Figs. 4 and 5, one can see that the relative contribution of the Higgs boson diagrams for the subprocess involving a muon neutrino is much less than that for the sum of the three subprocesses. This fact confirms the importance of the electron-neutrino subprocess.

The sensitivity of the process to variations in the parameters Δa and b can be illustrated by considering the differential distributions. The distributions of the cross section with respect to the *b*-quark momentum, the *b*-quark emission angle reckoned from the initial-beam direction, $T_{\rm cor}$, and the invariant mass of the $b\bar{b}$ pair are presented in Fig. 6 for the case where all three neutrino flavors are taken into account. The Higgs boson contributions within the Standard Model ($a = 1$, $b = 0$) are shown by closed circles, while the distributions for the case where there is an admixture of

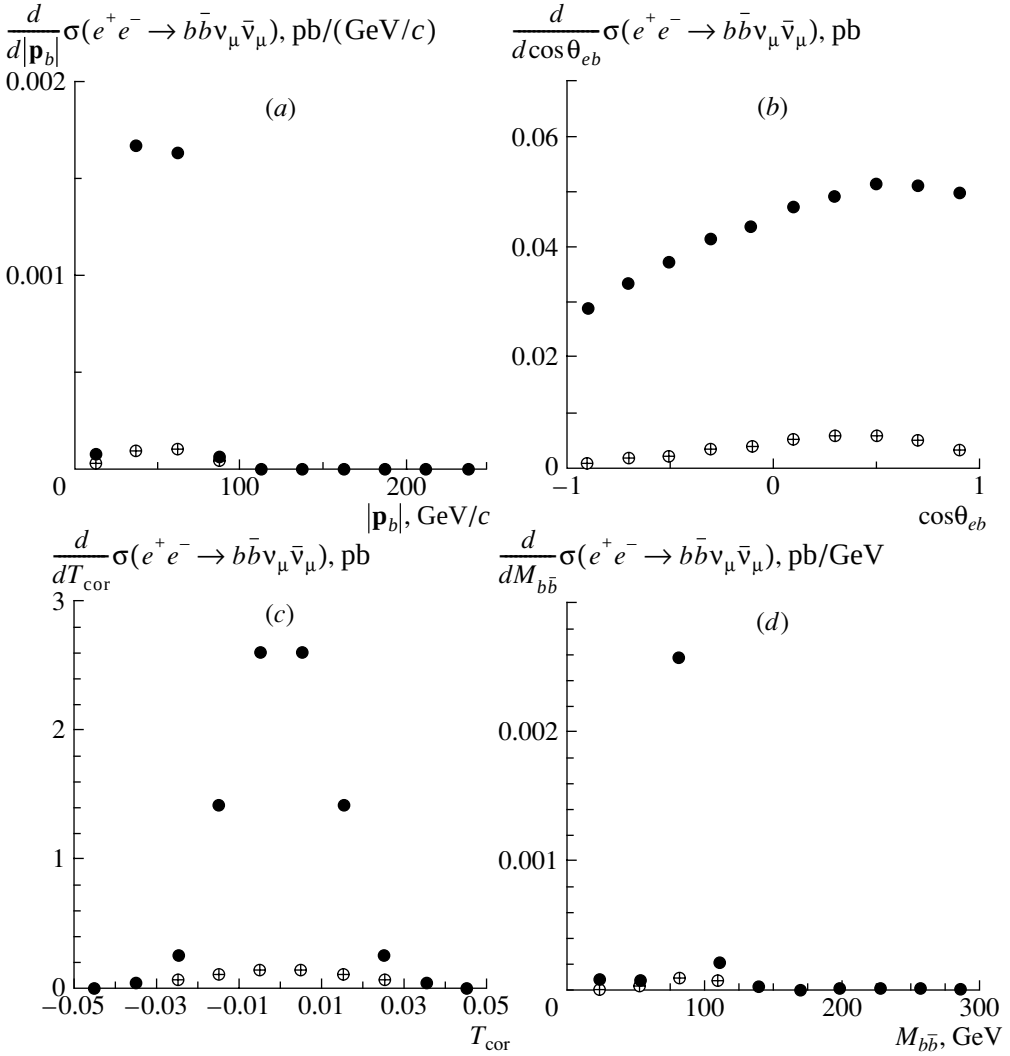

Fig. 5. As in Fig. 4, but for the subprocess $e^+e^- \to b\bar{b}\nu_\mu\bar{\nu}_\mu$.

the pseudoscalar boson ($a = 0.5$, $b = 0.5$) are shown by crosses enclosed by circles. The analogous distributions for the muon-neutrino subprocess alone are shown in Fig. 7. From a comparison of Figs. 6 and 7, one can see that the relative deviation in the muon-neutrino subprocess owing to a variation in the parameters is commensurate with the relative deviation evaluated with allowance for all three subprocesses. However, the relative contribution of the Higgs boson diagrams in the Standard Model is greater for all three channels than for the muon channel.

In order to set limits on the coupling constants a and b, it is important to find observables that are the most sensitive to these parameters. For this purpose, it is advisable to consider the so-called sensitivity function that is defined for each bin of the distribution under study. It is defined as

$$S = \frac{(\sigma_i^{\rm SM} - \sigma_i^{\rm NEW})}{\Delta\sigma_i^{\rm expt}}, \qquad (3)$$

where $\sigma_i^{\rm SM}$ is the value of the distribution within the Standard Model ($a = 1, b = 0$) in the ith bin; $\sigma_i^{\rm NEW}$ is the value of the distribution in the ith bin for the case where either one or both parameters deviate from their Standard Model values; and $\Delta\sigma_i^{\rm expt}$ is the expected value of the experimental error in the ith bin, the procedure for calculating this quantity being given below. Our analysis of the differential distributions for the process $e^+e^- \to b\bar{b}\nu\bar{\nu}$ revealed that the distribution with respect to the b-quark emission angle is the most sensitive to deviations of the parameters a and b from their Standard Model values. The sensitivity function for this distribution is shown in Fig. 8. The effects of new physics are illustrated for the case of $a = 1$ and

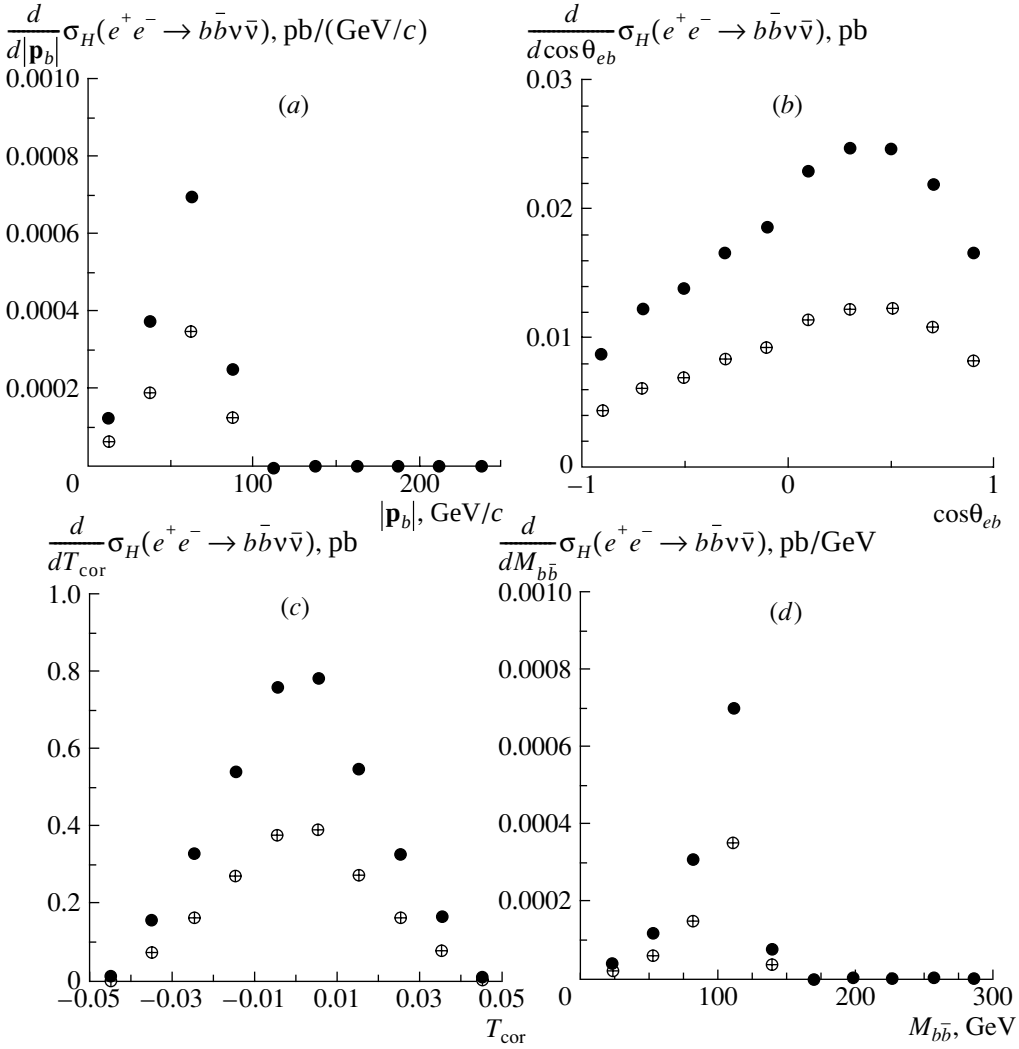

Fig. 6. Differential distributions of the cross section for the process $e^+e^- \to b\bar{b}\nu\bar{\nu}$ with respect to (*a*) the *b*-quark momentum, (*b*) the *b*-quark emission angle, (*c*) $T_{\rm cor}$, and (*d*) the invariant mass of the $b\bar{b}$ pair at $\sqrt{s} = 200$ GeV and $M_H = 120$ GeV. The contributions of all three subprocess (involving all three neutrino flavors) are taken into account. Shown are (•) the Standard Model predictions for the contribution of the Higgs boson diagrams including interference diagrams ($a = 1$, $b = 0$) and (⊕) the contribution of the Higgs boson diagrams in the case where there is an admixture of a pseudoscalar boson ($a = 0.5$, $b = 0.5$).

$b = 0.5$. The experimental error in a bin was evaluated for an integrated luminosity of $\int \mathcal{L}dt = 600$ pb^{-1} per experiment. One can see that the value of S is virtually constant over the entire kinematical domain and is high, whereas the sensitivity function S for the other observables is either small or takes maximum values within a small-sized domain of the phase space.

In order to determine the regions that one can exclude in the plane of the parameters a and b on the basis of LEP II experiments, we use the standard χ^2 criterion. The experimental error $\Delta\sigma_i^{\rm expt}$ is defined as

$$\Delta\sigma_i^{\rm expt} = \sigma_i^{\rm SM}\sqrt{\delta_{\rm syst}^2 + \delta_{\rm stat}^2}, \qquad (4)$$

and the statistical error in a bin of a distribution is given by

$$\delta_{\rm stat} = \frac{1}{\sqrt{\sigma_i^{\rm SM}\varepsilon_{b\bar{b}}\int \mathcal{L}dt}}, \qquad (5)$$

where $\varepsilon_{b\bar{b}}$ is the efficiency of reconstruction of a pair of *b*-quark jets. The analysis performed in [17] revealed that, by using the *b*-trigger algorithm in reconstructing *b*-quark jets, one can obtain an efficiency of $\varepsilon_{b\bar{b}} = 56\%$. The systematic error is determined by the detector resolution, the uncertainty in determining the luminosity, the ambiguity in isolating background processes, etc.

Our analysis of various kinematical distributions for the process under consideration reveals that the most stringent limits on the model parameters come

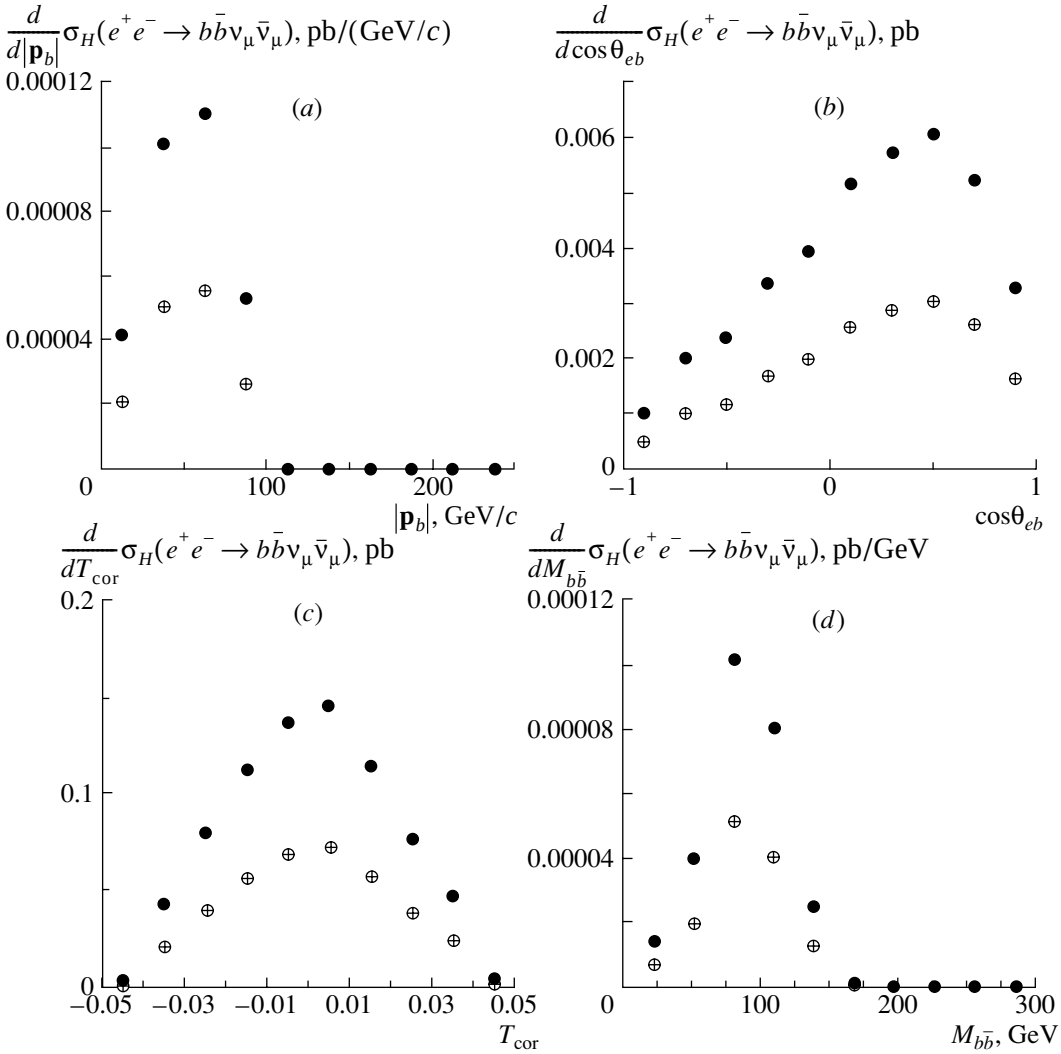

Fig. 7. As in Fig. 6, but for the subprocess $e^+e^- \to b\bar{b}\nu_\mu\bar{\nu}_\mu$.

from the differential distribution with respect to the b-jet emission angle provided that the kinematical domain is partitioned into ten bins, this confirming the conclusions drawn in studying the sensitivity function.

The regions that one can exclude in the Δa–b plane on the basis of the LEP II experiments at $M_H = 120$ GeV, $\sqrt{s} = 200$ GeV, and an integrated luminosity of 600 pb^{-1} per experiment are shown in Fig. 9. In the case where Δa and b are independent parameters, the allowed region at a 95% CL is between the two concentric curves. The allowed domain for the parameter b at $\Delta a = 0$ is bounded by the horizontal lines. The domains between the pairs of the vertical lines in the right and in the left parts in Fig. 9 are the allowed regions for the parameter a at $b = 0$. One can see from Fig. 9 that, in the case where Δa and b are independent parameters, the sensitivity to the parameters Δa and b is rather low throughout the allowed region. For this reason, an individual contribution of one of these parameters can hardly be isolated. By varying one of these parameters, we obtain the respective allowed domain bounded by either the horizontal or the vertical lines. By combining the case where $\Delta a = 0$ and b is a free parameter with the case where $b = 0$ and Δa is a free parameter, we arrive at two disconnected allowed domains labeled with letters A and B in Fig. 9. Domains A and B arise as the intersection of the horizontal band and two vertical bands (in the right and left parts of Fig. 9). Obviously, B is not a physical domain although it is allowed. Considering that the Standard Model describes experimental data well and that effects of new physics will appear as small deviations from Standard Model predictions, we can readily show that domain B shrinks as the luminosity increases and the systematic error decreases or, figuratively speaking, as we attain an ideal experiment. Therefore, the proper allowed region is

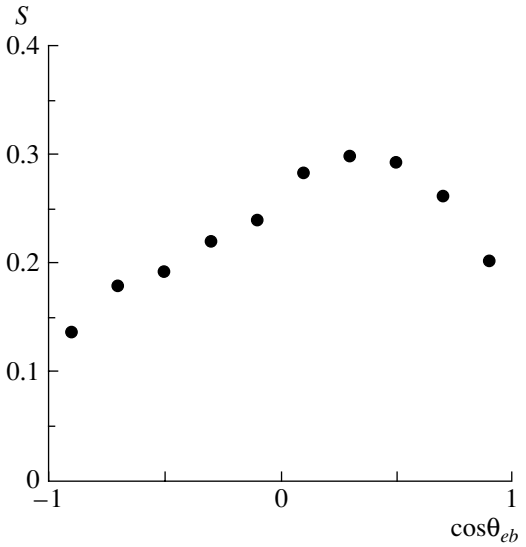

Fig. 8. Sensitivity function S (3) at $a = 1$ and $b = 0.5$ for the distribution with respect to the b-quark emission angle.

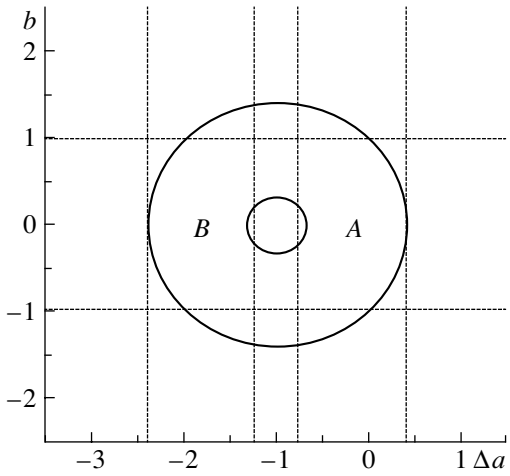

Fig. 9. Domains of allowed values for the parameters Δa and b at $\sqrt{s} = 200$ GeV, the Higgs-boson mass of $M_H = 120$ GeV, and the LEP II integrated luminosity of 600 pb^{-1} per experiment. In the case where the parameters Δa and b are independent, the allowed domain at a 95% CL is between the concentric curves. The allowed domain for the parameter b at $\Delta a = 0$ lies between the horizontal lines, while the allowed domains for the parameter Δa at $b = 0$ are between the vertical lines in the left and the right part of the figure.

localized around the $\Delta a = 0$, $b = 0$ point predicted by the Standard Model. For this reason, only domain A will be taken into consideration in determining the allowed regions for the parameters.

The resulting constraints on the parameters a and b can be represented in the form

$$(0.32)^2 \leq (\Delta a + 1)^2 + b^2 \leq (1.4)^2$$

in the case where a and b are independent parameters,

$$-0.75 \leq \Delta a \leq 1.4$$

in the case where $b = 0$ and Δa is a free parameter (domain A is implied), and

$$-0.97 \leq b \leq 0.97$$

in the case where $\Delta a = 0$ and b is a free parameter. To a high precision these constraints can be extended to values of the Higgs boson mass around $M_H = 120$ GeV by multiplying them by a factor of $(M_H/120\ \text{GeV})^2$.

4. CONCLUSIONS

We have investigated the possibility of detecting a signal from a scalar Higgs boson in LEP II data on the process $e^+e^- \to b\bar{b}\nu\bar{\nu}$. It has been found that the sensitivity of this process to the $Hb\bar{b}$ coupling constants is determined to a considerable extent by the contribution of the fusion subprocess $WW \to H$.

It has been shown that LEP II data on the process $e^+e^- \to b\bar{b}\nu\bar{\nu}$ would either furnish evidence of the existence of a pseudoscalar Higgs boson or make it possible to constrain the allowed region for the couplings of the pseudoscalar Higgs boson to b quarks.

In particular, LEP II data on the process $e^+e^- \to b\bar{b}\nu\bar{\nu}$ at an integrated luminosity of $\int \mathcal{L}dt = 600$ pb^{-1} per experiment and $\sqrt{s} = 200$ GeV would constrain the region allowed for the parameters a and b as

$$(0.32)^2 \leq (\Delta a + 1)^2 + b^2 \leq (1.4)^2$$

for independent parameters a and b, as

$$-0.75 \leq \Delta a \leq 1.4$$

for $b = 0$ and a free parameter Δa, and as

$$-0.97 \leq b \leq 0.97$$

for $\Delta a = 0$ and a free parameter b.

ACKNOWLEDGMENTS

This work was supported in part by the Russian Foundation for Basic Research (project nos. SS-1303.2003.2, 04-02-17530, and 05-02-17098) and the Ministry of the Russian Federation for Higher Education (grant no. E02-3.1-96).

REFERENCES

1. S. Weinberg, Phys. Rev. Lett. **37**, 657 (1976).
2. C. T. Hill and E. H. Simmons, hep-ph/0203079 and references therein.
3. LEP Higgs Working Group, LHWG/2001-03; hep-ex/0107029.
4. LEP Higgs Working Group, LHWG/2001-03; hep-ex/0107030; U. Schwickerath, hep-ph/0205126.
5. J. R. Dell'Aquila and C. A. Nelson, Nucl. Phys. B **320**, 61 (1989); **320**, 86 (1989).
6. B. K. Bullock, K. Hagiwara, and Alan D. Martin, Phys. Lett. B **273**, 501 (1991); Nucl. Phys. B **395**, 499 (1993).
7. B. Grzadkowski and J. F. Gunion, Phys. Lett. B **294**, 361 (1992); M. Krämer, J. Kühn, M. L. Stong, and P. M. Zerwas, Z. Phys. C **64**, 21 (1994); J. F. Gunion and J. G. Kelly, Phys. Lett. B **333**, 110 (1994).
8. K. Hagiwara and M. L. Stong, Z. Phys. C **62**, 99 (1994); D. J. Miller, S. Y. Choi, B. Eberle, *et al.*, Phys. Lett. B **505**, 149 (2001); V. Barger, K. Cheung, A. Djouadi, *et al.*, Phys. Rev. D **49**, 79 (1994); K. Hagiwara, S. Ishihara, J. Kamoshita, and B. A. Kniehl, Eur. Phys. J. C **14**, 457 (2000); T. Han and J. Jiang, Phys. Rev. D **63**, 096007 (2001).
9. T. Plehn, D. Rainwater, and D. Zeppenfeld, Phys. Rev. Lett. **88**, 051801 (2002).
10. B. Field, S. Dawson, and J. Smith, hep-ph/0311199 (2003).
11. J. F. Gunion and J. Pliszka, Phys. Lett. B **444**, 136 (1998).
12. J. F. Gunion, B. Grzadkowski, and X.-G. He, Phys. Rev. Lett. **77**, 5172 (1996).
13. D. Atwood and A. Soni, Phys. Rev. D **52**, 6271 (1995); V. Barger, M. S. Berger, J. F. Gunion, and T. Han, Phys. Rep. **286**, 1 (1997); V. Barger, T. Han, and C.-G. Zhou, Phys. Lett. B **480**, 140 (2000); B. Grzadkowski, J. F. Gunion, and J. Pliszka, Nucl. Phys. B **583**, 49 (2000).
14. B. Grzadkowski and J. F. Gunion, Phys. Lett. B **350**, 218 (1995); B. Grzadkowski, J. F. Gunion, and J. Kalinowski, Phys. Rev. D **60**, 075011 (1999).
15. A. Chalov, A. Likhoded, and R. Rosenfeld, J. Phys. G **29**, 337 (2003).
16. V. Braguta, A. Chalov, A. Likhoded, and R. Rosenfeld, Phys. Rev. Lett. **90**, 241801 (2003).
17. K. Desch and N. Meyer, LC Notes, LC-PHSM-2001-025, http://www.desy.de/lcnotes/2001/025/ww-fus.ps.gz

Translated by R. Rogalyov

Physics of Atomic Nuclei, Vol. 68, No. 12, 2005, pp. 2110–2116. Translated from Yadernaya Fizika, Vol. 68, No. 12, 2005, pp. 2172–2178.

ELEMENTARY PARTICLES AND FIELDS
Theory

Possibilities of Revealing Collective Pion Degrees of Freedom in Nuclei by Means of Quasielastic Pion Knockout by High-Energy Electrons

V. G. Neudatchin, L. L. Sviridova, N. P. Yudin*, and S. N. Yudin

Institute of Nuclear Physics, Moscow State University, Vorob'evy gory, Moscow, 119992 Russia

Received December 8, 2004; in final form, March 9, 2005

Abstract—The kinematics of quasielastic pion knockout by longitudinal virtual photons in the electroproduction process is presented. The possibility of directly investigating pion momentum distributions in specific channels owing to pole-amplitude dominance is considered. It is shown that, taking into account the final-state interaction of the knock-on pion and the nucleus involved, one can reveal the existence of a pion condensate in nuclei, since the momentum distribution of collective pions has a pronounced maximum at a momentum in excess of 0.3 GeV/c and since the excitation spectrum of the final recoil nucleus is concentrated in the low-energy region $E^* \approx K^2/(2AM_N) \leq 1$ MeV. The picture of pion knockout from meson clouds of individual nucleons is totally different. The analogous rho-meson momentum distributions for the process $\rho + \gamma_T^* \to \pi$ are also presented. © *2005 Pleiades Publishing, Inc.*

1. INTRODUCTION

In the 1970s, A.B. Migdal proposed the concept of a pion condensate in nuclei []. Such a condensate may arise owing to a strong interaction of two channels, the *nucleon–nucleon hole* channel and the *delta isobar–nucleon hole* channel. These two channels interact via the absorption and emission of pions. Further investigations revealed that this circumstance leads to noticeable collective effects, the softening of the pion mode and the enrichment of the ground state in pions (a detailed description is given in the monograph of Migdal *et al.* [2]; see also [3]). However, a pion condensate is not formed if collective pions have a fixed momentum k_0 controlled by the dynamics of the nuclear medium. In the aspect of interest here, the softening of the pion mode consists in that, in relation to the intranuclear-motion-averaged pion momentum distribution in a nucleon, the pion momentum distribution in the nucleus develops a new branch, some excess of pions having momenta of about k_0 (according to the estimates presented in [2], k_0 is close to the nucleon Fermi momentum, $p_F > 0.3$ GeV/c). If collective pions are knocked out quasielastically, the recoil entrains the target nucleus as a discrete unit rather than one of its individual nucleons (see below). The problem still attracts attention despite experimental difficulties in unambiguously detecting the aforementioned collective effects. In particular, it was indicated in [4] that the coherent interaction of "virtual pion emitters" may exert a strong effect similar to the effect well known in quantum optics [5]. According to [4], this is expected to result in the existence of a collective pion degree of freedom in nuclei in the form of a pion condensate. The typical feature of this collective branch is that, within the model proposed in [4], the pion mode in question is associated entirely with the excitation of a delta isobar and is characterized by the pion momenta K such that

$$\sqrt{\mathbf{K}^2 + m_\pi^2} = M_\Delta - M_N, \quad K \approx 0.3\ \text{GeV}/c, \quad (1)$$

where M_N and M_Δ are, respectively, the nucleon and delta-isobar masses.

According to the qualitative estimates from [4], the number $n_{i,\text{coll}}$ of collective pions of each type i (π^+, π^-, π^0) per nucleon in an $N = Z$ nucleus can be greater than the corresponding number of pions with momenta $k = (1 \pm 0.1)K$ in the cloud of an individual nucleon (see below). Here, we mean the pion P state in the virtual decay channel $p \to n + \pi$ [6, 7].

Particle–hole states in the even–even nuclei ^{12}C, ^{40}Ca, and ^{208}Pb were studied in relevant (p, n) reactions occurring at intermediate energies and involving polarized particles [8]. For example, the longitudinal response function was measured for the ^{12}C nucleus at a momentum transfer of 1.7 fm^{-1} and an energy transfer of 60 MeV. The experiment showed a considerable enhancement of the 1^+, $T = T_3 = 1$ giant resonance [8], this suggesting the existence of pion degrees of freedom.

The objective of this study is to propose an independent experiment aimed at detecting collective pion degrees of freedom in nuclei by measuring the

*e-mail: yudin@helene.sinp.msu.ru

pion momentum distributions there. In this case, the momentum distribution will have a specific shape corresponding to the component for which the orbital angular momentum of the delocalized pion plane wave in the nucleus is equal to unity. Here, we mean that quasielastic pion knockout from a nucleus by electrons of energy equal to several GeV is studied at an energy resolution of 10 MeV.

Quasielastic knockout of various mesons from a nucleon by high-energy electrons was examined in [6, 7, 9]. Reactions induced by longitudinal and transverse virtual photons can be distinguished experimentally. At values of the virtual-photon 4-momentum squared in the range $Q^2 = 1-3$ $(\mathrm{GeV}/c)^2$, the pole diagrams describing the processes $\pi + \gamma_L^* \to \pi$, $K + \gamma_L^* \to K$, and $\rho + \gamma_T^* \to \pi$ are dominant under the kinematical conditions of quasielastic knockout. This makes it possible to extract, from a coincidence experiment, the momentum distributions of pions, kaons, and rho mesons in various channels like $N \to B + \pi$, which correspond to various states of the final spectator baryon B. In this study, we extend this experience to the case in which a nucleus rather than a nucleon appears as a target.

The ensuing exposition is organized as follows. Section 2 contains some elements of the relativistic formalism for quasielastic-knockout reactions, including constraints on the minimum measurable momentum of a virtual pion (or rho meson) in a nucleus. In Section 3, we discuss final-state pion–nucleus interaction. In Section 4, we present a simple expression for the momentum distribution of collective pions (pion condensate) in the model based on the virtual excitation of a delta isobar and compare this momentum distribution with its counterpart for pions localized in the vicinity of intranuclear nucleons. We assess the extent to which the difference of the two momentum distributions can be smoothed upon taking into account final-state interaction. In the same section, we present the momentum distribution of rho mesons localized in the vicinity of intranuclear nucleons (a measurement of this distribution would correspond to separating the process $\rho + \gamma_T^* \to \pi$). Finally (in Section 5), we outline the advantages of quasielastic knockout $(e, e'\pi)$ over pion photoproduction (γ, π) and another quasielastic-knockout process $(\pi, 2\pi)$.

2. DESCRIPTION OF THE FORMALISM

In the laboratory frame, the differential cross section corresponding to exclusive coincidence experiments studying reactions of the type $T + e \to R + \pi^+ + e'$ has the form $d\sigma^5/dE_{e'}d\Omega_{e'}d\Omega_\pi$ [6, 7] (the notation used is obvious).

Let us introduce the invariant variables $W^2 = (q + p_T)^2$, $Q^2 = -q^2$, and $t = -k^2 = (p_R - p_T)^2$, where q is the virtual-photon 4-momentum; p_T and p_R are the 4-momenta of, respectively, the initial and the final nucleus; and $k = (k_0, \mathbf{k})$ is the virtual-meson 4-momentum in the nucleus (for a virtual pion, we have $k^2 = -\mathbf{k}^2$ to a high accuracy in the case being considered; that is, $k_0 = 0$). By using these variables, we can represent the above cross section as the sum of the longitudinal cross section $d\sigma_L/dt$, the transverse cross section $d\sigma_T/dt$, and the interference terms multiplied by appropriate kinematical factors [6, 7].

In the relativistic pole approximation, which is employed here, the longitudinal cross section for the process $\pi + \gamma_L^* \to \pi$ has the form

$$\frac{d\sigma_L}{dt} = \frac{\alpha}{8}\frac{\overline{|\Psi_T^{R\pi}(\mathbf{k})|^2}}{(k_0 + E_\pi(\mathbf{k}))^2}\frac{1}{|\mathbf{q}^{(\mathrm{c.m.})}|}\frac{1}{W(W^2 - M_T^2)} \times F_\pi^2(Q^2)((k + k')e_{\lambda=0})^2, \quad (2)$$

where α is the fine-structure constant, $\alpha = 1/137$; $\overline{|\Psi_T^{R\pi}(\mathbf{k})|^2}$ is the pion momentum distribution in the nucleus in the virtual-decay channel $N \to N + \pi$; $E_\pi(\mathbf{k}) = \sqrt{\mathbf{k}^2 + m_\pi^2}$; $F_\pi(Q^2)$ is the pion electromagnetic form factor; k' is the emitted-pion 4-momentum; $e_{\lambda=0}$ is the polarization 4-vector of the longitudinal photon;

$$q^{(\mathrm{c.m.})} = \sqrt{Q^2 + \frac{(W^2 - Q^2 - M_T^2)^2}{4W^2}};$$

$((k + k')e_{\lambda=0})^2 = 4(k_0'q_z - q_0k_z')/Q^2$; and the z axis is parallel to the photon momentum.

The spectroscopic factor (the number of pions in the virtual-decay channel $T \to R + \pi$) is calculated as the normalization integral of the wave function with the weight factor $((4\pi)^3 M_T E_\pi(\mathbf{k}) E_R(\mathbf{k}))^{-1/2}$.

The transverse cross section for the process $\rho + \gamma_T^* \to \pi$ has the form [9]

$$\frac{d\sigma_T}{dt} = \overline{|\Psi_T^{R\rho}(\mathbf{k})|}F_{\pi\rho}^2(Q^2)\frac{d\sigma_T^0}{dt}, \quad (3)$$

where $F_{\pi\rho}^2(Q^2)$ is the form factor for the transition $\rho + \gamma_T^* \to \pi$ and $d\sigma_T^0/dt$ is the cross section for the process involving a nucleon and a rho meson taken in the pointlike approximation.

In studying meson knockout from nuclei, it is of importance to know the minimum virtual momentum squared t at given Q^2 and q_0, because, in contrast to the pion momentum distribution in a nucleon, the theoretically predicted pion momentum distribution

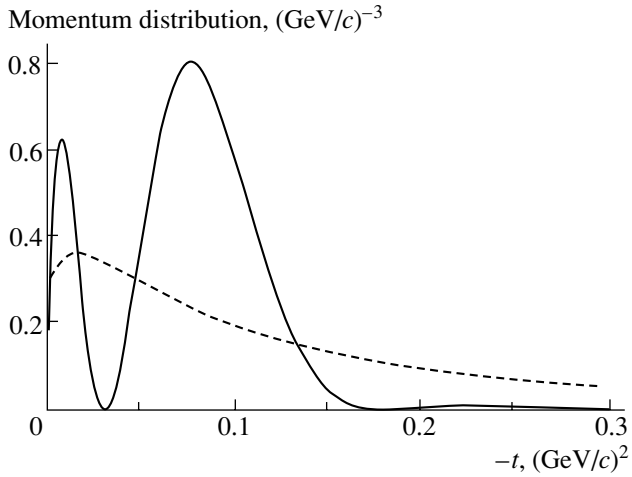

Fig. 1. Pion momentum distributions in a nucleus (per nucleon): (solid curve) momentum distribution of collective pions and (dashed curve) momentum distribution of localized pions.

in a nucleus has pronounced specific features at relatively low values of t. The minimum value of t can be obtained as follows. From the definition $t = -k^2 = -(k' - q)^2$, we obtain an expression for the cosine of the angle between the vectors $\mathbf{q}$ and $\mathbf{k}'$,

$$\cos\theta = \frac{-t - m_\pi^2 + Q^2 + 2q_0(q_0 - t/2M_T)}{2|\mathbf{q}|\sqrt{(q_0 - t/2M_T)^2 - m_\pi^2}}. \quad (4)$$

The condition $|\cos\theta| \le 1$ defines the region of physically valid t. The minimum value of t is given by

$$t_{\min} \approx \left(\sqrt{Q^2 + q_0^2} - q_0\right)^2. \quad (5)$$

It follows that, in order to reach $-t_{\min} = 0.01$ (GeV/c)^2, Q and q_0 must be chosen to be, for example, $Q^2 = 1$ (GeV/c)^2 and $q_0 = 5$ GeV/c.

3. FINAL-STATE INTERACTION

Because of final-state interaction, an experiment aimed at studying quasielastic pion knockout would yield a so-called distorted pion momentum distribution [10, 11]. It can be obtained as follows. The Fourier transform of the pion wave function in the nucleon is given by

$$\Psi_T^{R\pi}(\mathbf{k}) = \Psi_T^{R\pi}(\mathbf{k}', \mathbf{q}) \quad (6)$$
$$= \frac{1}{(2\pi)^{3/2}} \int e^{-i\mathbf{k}\cdot\mathbf{r}} \Psi_T^{R\pi}(\mathbf{r}) d\mathbf{r}$$
$$= \frac{1}{(2\pi)^{3/2}} \int e^{i\mathbf{q}\cdot\mathbf{r}} e^{-i\mathbf{k}'\cdot\mathbf{r}} \Psi_T^{R\pi}(\mathbf{r}) d\mathbf{r}.$$

The plane wave corresponding to a virtual photon, $e^{-i\mathbf{q}\cdot\mathbf{r}}$, is virtually undisturbed by the final spectator nucleus. However, its effect is quite significant for the final pion of asymptotic momentum $\mathbf{k}'$, and it is necessary to use the distorted wave $\Psi^{(-)}(\mathbf{k}', \mathbf{r})$ instead of the plane wave $e^{-i\mathbf{k}'\cdot\mathbf{r}}$. If $\mathbf{k}'$ is sufficiently high (about 1 GeV), one can use the eikonal approximation [12], in which the relevant solution to the Klein–Gordon equation is sought in the form $\Psi^{(-)}(\mathbf{k}', \mathbf{r}) = e^{-ik'z}\varphi(\mathbf{k}', \mathbf{r})$, where the z axis is directed along $\mathbf{k}'$. For the function $\varphi(\mathbf{k}', \mathbf{r})$, we then arrive at the equation

$$i\frac{k'}{E(\mathbf{k}')}\frac{\partial\varphi}{\partial z} = U\varphi. \quad (7)$$

First, we consider a pion–nucleus potential of depth $U = V - iW$. Its localization in the nucleus is formed by the virtual-pion wave function $\Psi_T^{R\pi}(\mathbf{r})$ appearing in the integrand on the right-hand side of (6). This potential demonstrates clearly how the wave function for the pion produced in the medium changes under the impact of final-state interaction. It is assumed that, outside the nucleus, the effect of this potential is zero, since the virtual-pion wave function in the integrand on the right-hand side of (6) vanishes there. Solving Eq. (7), we obtain the distorted wave function

$$\Psi_T^{R\pi}(\mathbf{k}', \mathbf{q}) \quad (8)$$
$$= \frac{1}{(2\pi)^{3/2}} \int e^{i\mathbf{q}\cdot\mathbf{r}} e^{-i(\mathbf{k}' - V\hat{\mathbf{k}}')\cdot\mathbf{r}} e^{-W\hat{\mathbf{k}}'\cdot\mathbf{r}} \Psi_T^{R\pi}(\mathbf{r}) d\mathbf{r}.$$

Thus, the inclusion of the interaction reduces to replacing $\mathbf{k}'$ in (6) by $\mathbf{k}''$,

$$\mathbf{k}'' = \mathbf{k}' - (V + iW)\hat{\mathbf{k}}',$$

where $\hat{\mathbf{k}}' = \mathbf{k}'/|\mathbf{k}'|$.

From a comparison of (6) and (8), we see that allowance for the interaction leads to the shift of the curve leftward (factor $e^{iV\mathbf{k}'\cdot\mathbf{r}}$) and downward approximately by the factor e^{-WR} (R is the radius of the nucleus).

For a finite-range potential, the emitted-pion wave function is written as

$$\Psi^{(-)}(\mathbf{k}', \mathbf{r}) = e^{-i\mathbf{k}'\cdot\mathbf{r}} e^{iS(\mathbf{r})},$$

where

$$S(\mathbf{r}) = -\frac{E(\mathbf{k}')}{k'} \int_z^\infty U(\mathbf{b} + z'\hat{\mathbf{k}}') dz' \quad (9)$$

and $\mathbf{b}$ is the impact parameter.

A square potential well of depth R was used in our calculations. The depth of the well was estimated as follows. In nonrelativistic calculations [13, 14], the final-state interaction was taken in the form

$$U(r) = \frac{2\pi}{m_\pi} f_{\pi N}(0)\rho(r), \quad (10)$$

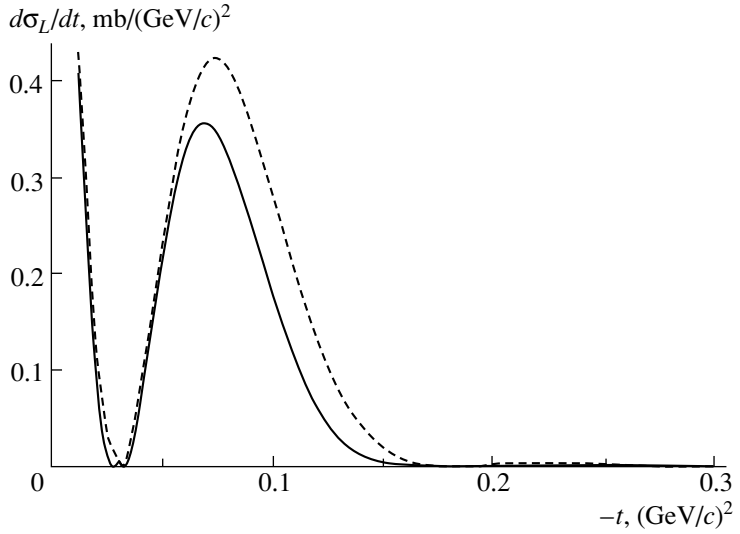

Fig. 2. Calculated longitudinal cross sections for the electroproduction of collective knock-on pions (solid curve) with and (dashed curve) without allowance for final-state interaction [$Q^2 = 1\,(\mathrm{GeV}/c)^2$, $q_0^{(\mathrm{lab})} = 4.86$ GeV/c].

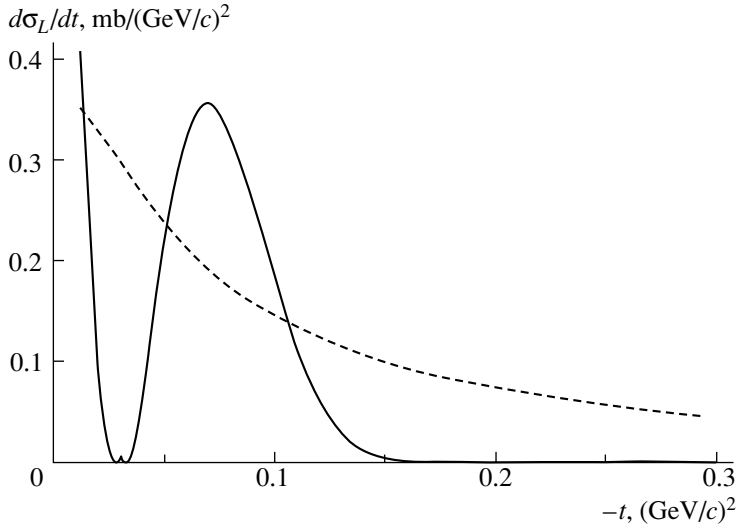

Fig. 3. Longitudinal pion-electroproduction cross section for the cases of (solid curve) collective and (dashed curve) localized pions [$Q^2 = 1\,(\mathrm{GeV}/c)^2$, $q_0^{(\mathrm{lab})} = 4.86$ GeV].

where $f_{\pi N}(0)$ is the amplitude of forward pion–nucleon scattering [15]. The nuclear density $\rho(r)$ is well approximated by the Woods–Saxon form [14]

$$\rho(r) = \rho_0/(1 + \exp\{(r - c)/a\}). \qquad (11)$$

By way of example, we indicate that, for the ^{40}Ca nucleus, the parameters appearing in (11) are $c = 3.55$ and $a = 0.54$. The density ρ_0 takes approximately the same value of 0.17 fm^{-3} in all nuclei. In the relativistic case, the expression $E = E_\pi E_A/(E_\pi + E_A)$ must be substituted for m_π in (10). The amplitude $f_{\pi N}(0)$ is parametrized as [15]

$$f_{\pi N}(0) = \frac{ik'}{4\pi} f_1(1 - if_2). \qquad (12)$$

Momenta of $|\mathbf{k}'| \approx 2$–4 GeV/c are of interest for our examination. At such momenta, $f_1 = 3.3$ fm^{-2} and $f_2 = -0.42$; therefore, we have $V = 22$ MeV and $W = 53$ MeV. This potential was tested by repeating the calculation performed in [16] to determine the differential cross section $d\sigma/d\Omega$ for pion scattering on ^{40}Ca at an energy of 800 MeV and small scattering angles. This calculation relied on the eikonal approximation and involved either a square poten-

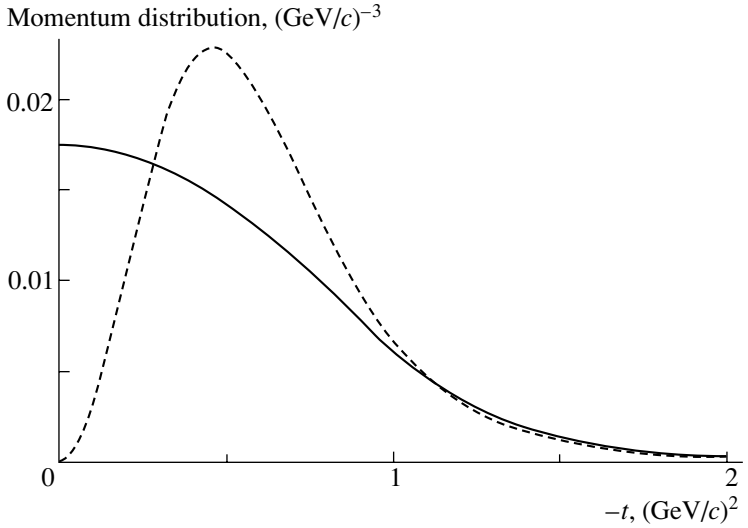

Fig. 4. Rho-meson momentum distribution in (dashed curve) a free nucleon and (solid curve) a nucleus.

tial well or the Woods–Saxon potential. It turned out that the distinction between the results obtained with these potentials is insignificant, either yielding good agreement with experimental data. There are no experimental data for higher energies or for heavier nuclei (this would be closer to the case of $A = 70$ and $|\mathbf{k}'| \approx 2{-}4$ GeV/c examined here).

4. PION AND RHO-MESON MOMENTUM DISTRIBUTIONS IN NUCLEI

The momentum distribution of collective pions in the $A = 70$, $N = Z$ nucleus has the standing-wave form [4]

$$\Phi(r) = cj_1(Kr), \quad r < R, \qquad (13)$$
$$\Phi(r) = 0, \quad r > R.$$

The constant c is normalized to the number of pions per nucleon, $n_{i,\mathrm{coll}} = 0.1$ [4]; that is, $c = 0.027$. The momentum distribution of collective pions is shown in Fig. 1 (solid curve). This distribution has a pronounced maximum at $k = K$; that is, it is close to a standing wave. The localized-pion momentum distribution $\overline{\overline{|\Psi_N^{N\pi}(\mathbf{k})|^2}}$ is also shown in Fig. 1 (dashed curve). It was obtained from the intranuclear-motion-averaged pion momentum distribution in the nucleon [6, 7] $\overline{|\Phi_A^{A-1,N}(\mathbf{p})|^2}$ as

$$\overline{\overline{|\Psi_N^{N\pi}(\mathbf{k})|^2}} \qquad (14)$$
$$= \int \overline{|\Psi_N^{N\pi}(\mathbf{k} + (m_\pi/M_T)\mathbf{p})|^2}\, \overline{|\Phi_A^{A-1,N}(\mathbf{p})|^2} d\mathbf{p}.$$

The momentum distribution $\overline{|\Psi_N^{N\pi}(\mathbf{k})|^2}$ was obtained previously [6, 7] on the basis of experiments devoted to studying pion knockout from a nucleon in quasielastic kinematics [17].

Figure 2 demonstrates the effect of final-state interaction on the cross section for the knockout of collective pions. One can see from (8) that the final-state interaction results in the shift of the wave function to the left and the reduction of its amplitude approximately by the factor e^{-2WR}. However, the inclusion of the interaction does not change the shape of the curves significantly, so that it remains possible to distinguish between the two types of events in question, the knockout of collective pions and the knockout of pions localized at individual intranuclear nucleons.

If collective pions are knocked out, the nucleus involved recoils as a discrete unit, the recoil energy being $E = K^2/(2M_N A) < 1$ MeV for $A = 70{-}80$. In this case, the nucleus is not excited. If a localized pion of the same momentum $k = K$ is knocked out, only one nucleon recoils, with the result that the energy transfer is significant, $E = K^2/(2M_N) = 50$ MeV. Such a nucleon will be emitted by the nucleus with a high probability, and this can be observed in a coincidence experiment that records three particles in the final state, $e' + \pi + p$. If only e' and π are recorded, such an event will appear as that in which the recoil nucleus is excited to an energy of $E = 50$ MeV.

In order to avoid the influence of an intermediate delta isobar in the final-state pion–nucleus interaction, it is necessary that the energy of the final pion not be lower than 1 GeV. Overly high momenta of $k' = 10{-}20$ GeV/c are not appropriate here either, since they correspond to totally different physics [18].

The corresponding cross sections are shown in Fig. 3. One can see that the experimental cross sections in quasielastic kinematics differ markedly in the

cases examined here. The cross section for the knockout of collective pions has a pronounced maximum at $k = K$, while the cross section for the knockout of pions localized at individual nucleons is a monotonically decreasing function. Thus, an experiment devoted to quasielastic pion knockout is a direct way to clarify the character of the pion distribution in a nucleus.

The rho-meson momentum distribution in a nucleus can be determined from the experimental cross section for pion electroproduction [6, 7]. The subprocess $\rho + \gamma_T^* \to \pi$ corresponds to the knockout of virtual rho mesons. Using a formula similar to (10), we have calculated the above momentum distribution from the rho-meson momentum distribution in a nucleon from [9] (see Fig. 4). A deviation of the experimental momentum distribution from this function—an analog of the distinction between the dashed (localized pions) and the solid curve (collective pions) in Fig. 1—would suggest the presence of collective rho mesons in a nucleus.

5. CONCLUSIONS

We have proposed a direct way to study the pion momentum distribution in a nucleus by means of quasielastic pion knockout by high-energy electrons. Similar experiments devoted to pion photoproduction do not serve this purpose, since, in that case, it is impossible to select one dominant diagram, so that it is necessary to sum a large number of diagrams [19].

We have shown that the cross sections for the knockout of collective pions differs markedly from its counterpart for localized pions. The final-state interaction does not blur this distinction. The excitation spectra of the final nucleus are also different in these two cases.

The quasielastic-knockout process $(\pi, 2\pi)$ at similar energies (its experimental investigation began [20], but the energies of knock-on pions are still relatively low) can supplement the aforesaid, since this process is characterized by large cross sections (strong interaction). Investigation of the collective neutral-pion component can also be of interest in this connection, but it is concentrated predominantly in surface layers of nuclei, since high-energy pions are strongly absorbed by a nucleus [21]. This effect, which generates a distorted wave for the initial or the final pion, can complicate the interpretation of experimental data to some extent. However, it can be taken into account (see above) in quantitatively estimating the $(e, e'\pi)$ process, which is much less sensitive to it (one pion wave rather than three).

ACKNOWLEDGMENTS

We are grateful to E.E. Saperstein for enlightening comments.

This work was supported by the Russian Foundation for Basic Research (project no. 00-02-16117).

REFERENCES

1. A. B. Migdal, Zh. Éksp. Teor. Fiz. **61**, 2209 (1971) [Sov. Phys. JETP **34**, 1184 (1971)]; Rev. Mod. Phys. **50**, 107 (1978).
2. A. B. Migdal, D. N. Voskresensky, E. E. Saperstein, and M. A. Troitsky, *Pionic Degrees of Freedom in Nuclear Matter* (Nauka, Moscow, 1991) [in Russian].
3. Yu. B. Ivanov, J. Knoll, H. Van Hees, and D. N. Voskresensky, Yad. Fiz. **64**, 711 (2001) [Phys. At. Nucl. **64**, 652 (2001)].
4. R. Alzetta, G. Liberti, and G. Preparata, Nucl. Phys. A **585**, 307c (1995); R. Alzetta, T. Bubba, R. Le Perra, *et al.*, Nuovo Cimento A **112**, 762 (1999); R. Alzetta, G. Liberti, and G. Preparata, Nuovo Cimento A **112**, 1609 (1999).
5. R. H. Dicke, Phys. Rev. **93**, 99 (1954); A. V. Andreev, V. I. Emelianov, and Yu. A. Il'insky, *Coherent Phenomena in Optics* (Nauka, Moscow, 1988) [in Russian].
6. V. G. Neudatchin, N. P. Yudin, and L. L. Sviridova, Yad. Fiz. **60**, 2020 (1997) [Phys. At. Nucl. **60**, 1848 (1997)]; V. G. Neudatchin, L. L. Sviridova, and N. P. Yudin, Yad. Fiz. **64**, 1680 (2001) [Phys. At. Nucl. **64**, 1600 (2001)].
7. V. G. Neudatchin, I. T. Obukhovsky, L. L. Sviridova, and N. P. Yudin, Nucl. Phys. A **739**, 124 (2004).
8. H. Sakai, Nucl. Phys. A **690**, 66c (2001).
9. N. P. Yudin, L. L. Sviridova, and V. G. Neudatchin, Yad. Fiz. **61**, 1689 (1998) [Phys. At. Nucl. **61**, 1577 (1998)].
10. V. G. Neudatchin, A. A. Sakharuk, V. V. Kurovsky, and Yu. M. Tchuvilsky, Phys. Rev. C **50**, 148 (1994); **51**, 784 (1995).
11. T. Ryckebusch, D. Debruyhe, P. Lava, *et al.*, Nucl. Phys. A **728**, 226 (2003).
12. D. Derbruyhe, T. Ryckebusch, *et al.*, Phys. Rev. C **62**, 024611 (2000); A. De Pace, Phys. Rev. Lett. **75**, 29 (1995).
13. A. Sibirtsev and W. Kassing, Phys. Rev. C **61**, 057601 (2000).
14. M. Alqadi and W. R. Gibbs, Phys. Rev. C **66**, 064604 (2002).
15. M. Mizogushi, K. Sumiyoshi, T. Kajino, and H. Toki, Prog. Theor. Phys. **81**, 1217 (1989).
16. C. M. Chen, D. J. Ernst, and M. B. Johnson, Phys. Rev. C **48**, 841 (1993).
17. C. J. Bebek, C. N. Brown, S. D. Holmes, *et al.*, Phys. Rev. D **17**, 1693 (1978); P. Brauel, T. Canzler, D. Cords, *et al.*, Z. Phys. C **3**, 101 (1979).

18. M. Strikman, Nucl. Phys. A **633–634**, 64c (2000); M. Vanderhaeghen, P. A. M. Guichon, and M. Guidal, Phys. Rev. D **60**, 094017 (1999); Nucl. Phys. A **633–634**, 324c (2000).
19. V. G. Neudatchin, L. L. Sviridova, and N. P. Yudin, Yad. Fiz. **65**, 594 (2002) [Phys. At. Nucl. **65**, 567 (2002)].
20. F. Bonutti, P. Camerini, E. Fragiacomo, *et al.*, Phys. Rev. C **55**, 2999 (1997); B. Slovinski, in *Proceedings of the XIV International Seminar on High Energy Physics Problems, Dubna, Russia, 1998*, Ed. by A. M. Baldin and V. V. Burov (JINR, Dubna, 2000), Vol. II, p. 194.
21. S. Khallaf and A. Ebrahim, Phys. Rev. C **62**, 024603 (2000); S. Jena and S. Swain, Phys. Rev. C **55**, 3015 (1997); M. H. Cha and Y. J. Kim, Phys. Rev. C **54**, 429 (1996).

Translated by E. Baldina

Physics of Atomic Nuclei, Vol. 68, No. 12, 2005, pp. 2117–2123. Translated from Yadernaya Fizika, Vol. 68, No. 12, 2005, pp. 2179–2185.

ELEMENTARY PARTICLES AND FIELDS
Theory

Production of Hadron Resonances in Heavy-Ion Collisions

I. I. Royzen*

Lebedev Institute of Physics, Russian Academy of Sciences, Leninskiĭ pr. 53, Moscow, 119333 Russia

Received March 4, 2005

Abstract— The role of microscopic kinetics in the production of short-lived (broad) hadron resonances from subhadronic nuclear matter is considered. A new approach to calculating the multiplicity of broad meson resonances is proposed. This approach takes explicitly into account the possibility that massive constituent quarks play a decisive role at the last stage of the expansion and cooling of matter produced in the central collisions of relativistic heavy nuclei. The resulting theoretical estimates are compared with available experimental data, and some quantitative and qualitative predictions are made. © *2005 Pleiades Publishing, Inc.*

1. INTRODUCTION

It is well known that measurements of production rates for various particles—photons, leptons, and hadrons—in the central rapidity interval are widely used as a source of information about the dynamics of interaction of relativistic heavy nuclei and about phase states of nuclear matter that arise in such collisions. In particular, such measurements served as a basis for assuming that hadrons and hadron resonances undergo significant modification (reduction of their effective dimensions) in very hot and dense nuclear matter, that the gas of such particles is quasiperfect even at extremely high temperatures [1] up to $T = T_{\rm ch} \simeq 170$–$180$ MeV for SPS/CERN and RHIC/BNL, and that there occurs an early chemical freeze-out [2] at the temperature $T_{\rm ch}$.[1)]

There is also an alternative interpretation [4, 5] that successfully treats available experimental results within the hypothesis [6, 7] that an intermediate (between quark–gluon and hadronic matter) phase preceding hadronization is formed (in the temperature interval $T_c > T > T_H$, where $T_c \geq T_{\rm ch}$ and T_H are, respectively, the chiral-phase-transition and the hadronization temperature; for SPS/CERN and RHIC/BNL, $T_H \simeq 110$–120 MeV). This phase is dominated by valon degrees of freedom,[2)] but pions and kaons in chemical equilibrium with valons are also present there.[3)] The critical comparative analysis of the above approaches in [11] revealed some circumstances in favor of the interpretation in [4, 5]. Briefly, critical arguments against the standard models were as follows: there are no reasons to assume that hadrons "contracted" by a factor of about 20 still preserve their identity; moreover, it is not quite clear what the physical meaning of the early chemical freeze-out is, which, in particular, assumes the long-term (on the nuclear time scale) conservation of the relative content of baryons and antibaryons under conditions of more than tenfold dominance of the former (at the SPS/CERN accelerator), and how the most probable lattice prediction for the deconfinement (and, of course, hadronization) temperature of $T_H \simeq 150$ MeV [12] can be reconciled with the temperature of the early chemical freeze-out, $T_{\rm ch} \simeq 170$–180 MeV, the freeze-out temperature being extracted from a comparison with experimental data obtained at SPS/CERN and RHIC/BNL. However, the alternative model also has a weak point: within QCD, the concept of a valon as a quasiparticle [13]

* e-mail: royzen@lpi.ru

1) The models in question are widely known (see, for example, the review article of Braun-Munzinger *et al.* [3]); therefore, we will hereafter refer to them as standard models.

2) We refer to this approach as an alternative one. The term "valons" [8] is used for the sake of brevity for massive constituent (dynamical) quarks (see, for example, [9, 10]).

3) Here, we mean that, along with valons, pions and kaons, which are the only hadrons whose masses are substantially lower than the sum of the masses of valons that "constitute" them, must also survive in this intermediate ($Q\pi K$) phase [5].

1063-7788/05/6812-2117$26.00

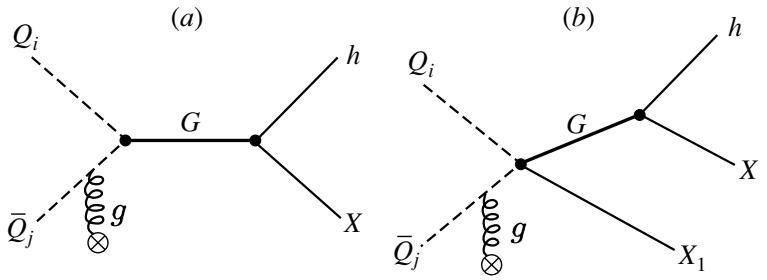

Fig. 1. Mechanisms of formation of (short-lived) resonances in the hadronization process at $T = T_H$. The "redundant" color or angular momentum (or both) are carried away by the gluon g to the medium. If $G = K^{*0}$, then $Q_i = Q_d$, $\bar{Q}_j = \bar{Q}_s$, $h = K^{+,0}$, and $X = \pi^{-,0}$; if $G = \phi$, then $Q_i = Q_s$, $\bar{Q}_j = \bar{Q}_s$, $h = K^+$, and $X = K^-$; etc.

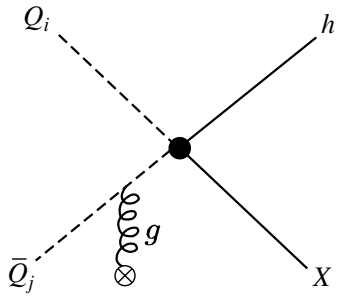

Fig. 2. General hadronization scheme at $T = T_H$ (the notation is identical to that in Fig. 1).

has not yet been formalized, which is likely to be due to its essentially nonperturbative nature.

It has ever become more obvious that the standard models, which are purely thermodynamic, run into significant difficulties in attempts at giving a satisfactory explanation for the observed multiplicities of some short-lived hadron resonances [14, 15] in central heavy-ion collisions (yet, there are presently very few informative measurements of this type). In this connection, two circumstances are worthy of note. The first is obvious—this is the aforementioned question of physical adequacy of the very concept of early chemical freeze-out at very high temperatures.[4)] The second is the question of whether it is necessary to take into account microscopic kinetics and dynamics in the course of hadronization in considering the production rate for some broad resonance (a positive answer to the second question would actually mean that a purely thermodynamic consideration of the process is insufficient).

Within the alternative approach, we propose here a method for estimating, with allowance for microscopic valon kinetics, production rates for broad meson resonances (and phi mesons as well), for which there is presently the most comprehensive experimental information, but which are narrow (as will be seen below) rather than broad resonances. The results obtained on the basis of this method are compared with available experimental data, and some predictions are made.

2. RELATIVE MULTIPLICITY OF SHORT-LIVED MESONS

2.1. Allowance for Microscopic Kinetics

We will first formulate a criterion according to which, in the current context, resonances are considered as narrow or broad ones. We assume that all configurations of final particles corresponding to the decays of a short-lived meson G originate precisely from these decays (that is, the background under the resonance is negligible). In this case, the relative production rate for this resonance and an experimentally observed long-lived hadron h (of the same flavor), which can be produced, in particular, via G-meson decay, is determined by the statistically weighted ratio of the contributions from the sum of diagrams in Fig. 1 and the diagram in Fig. 2. In Figs. 1 and 2, $Q_i\bar{Q}_j$ is the valon–antivalon pair in the corresponding flavor channel, G is a short-lived resonance of mass M_G and width Γ_G, and X stands for all accompanying secondary particles. We consider the resonance G as a broad one if the diagram in Fig. 1*a* is dominant in the total contribution of the diagrams in Figs. 1*a* and 1*b* and as a narrow one in the opposite case.

[4)]Here, is worth noting that this concept was introduced and is used only for describing the production rates for secondary hadrons and that the corresponding temperature has no bearing on phase transitions in nuclear matter, in contrast to other characteristic temperatures, like that of chiral transition and deconfinement (or that of hadronization).

In order to get an idea of the widths in question, we will first derive an explicit expression for the ratio of the contributions of the diagrams in Fig. 1*a* and Fig. 2. Assuming a traditional experiment, we must obviously identify this ratio with the probability that valons are annihilated in states of invariant mass (c.m. pair energy) in the range $M_G - \Gamma_G/2 \le M \le M_G + \Gamma_G/2$. The corresponding probability density is[5)]

$$\frac{dW}{dM^2} = \frac{\int_{-\infty}^{\infty}\Theta(p_1^0)\Theta(p_2^0)\delta[(p_1+p_2)^2 - M^2]\exp(-\sqrt{\mathbf{p}_1^2 + m_{Q_i}^2}/T)\exp(-\sqrt{\mathbf{p}_2^2 + m_{Q_j}^2}/T)d\mathbf{p}_1 d\mathbf{p}_2}{\int_{-\infty}^{\infty}\exp(-\sqrt{\mathbf{p}^2 + m_{Q_i}^2}/T)d\mathbf{p}\int_{-\infty}^{\infty}\exp(-\sqrt{\mathbf{p}^2 + m_{Q_j}^2}/T)d\mathbf{p}}. \quad (1)$$

A direct calculation of the integrals on the right-hand side of (1) yields[6)]

$$\frac{dW}{dM^2} \simeq \frac{[1 + (2 + (m_{Q_i} + m_{Q_j})^2/M^2)T/M]\sqrt{1 - (m_{Q_i} + m_{Q_j})^2/M^2}M^3 K_1(M/T)}{16\pi m_{Q_i}^2 m_{Q_j}^2 T K_2(m_{Q_i}/T)K_2(m_{Q_j}/T)}, \quad (2)$$

where $K_n(z)$ are cylindrical functions of the second kind. For typical values of their arguments ($z \ge 3$), we need to retain only the first term of the asymptotic expansion for $z \gg 1$ [16] in the numerator and two terms in the denominator. It follows that, to a high accuracy, the ratio of the contributions from the diagrams in Figs. 1*a* and 2 assumes the form

$$W(G/h) \simeq \frac{\Gamma_G}{M_G}\frac{[1 + (2 + (m_{Q_i} + m_{Q_j})^2/M_G^2)T/M_G]\sqrt{1 - (m_{Q_i} + m_{Q_j})^2/M_G^2}}{4\sqrt{2\pi}(m_{Q_i}m_{Q_j}T/M_G^3)^{3/2}(1 + (15/8)(T/m_{Q_i}))(1 + (15/8)(T/m_{Q_j}))}e^{(m_{Q_i}+m_{Q_j}-M_G)/T}, \quad (3)$$

where T stands for the hadronization temperature, $T = T_H$.

The contribution of the diagram in Fig. 1*b* is obtained from (1) by substituting the threshold factor $\sqrt{1 - (M_G + m_\pi)^2/M^2}$ [7)] for the delta function in the integrand in the numerator on the right-hand side and performing integration with respect to the mass of the $Q_i\bar{Q}_j$ pair from $M_{\min} = M_G + m_\pi$. Considering that the support of the resulting integral is concentrated within the interval $(1{-}2)T_H$ near the threshold, we can see that the relationship between the contributions of the diagrams in Figs. 1*a* and 1*b* is determined by an effective value of the quantity

$$[1b/1a] \simeq \sqrt{1 - (M_G + m_\pi)^2/M^2}(M/M_G)^{7/2} \times [(1{-}2)T_H/\Gamma_G)]\exp[(M_G - M)/T_H]$$

at $M \simeq M_{\min} + (1{-}2)T_H \simeq M_G + m_\pi + (1{-}2)T_H$. This quantity significantly exceeds unity for the $\phi(1020)$ meson ($T_H/\Gamma_\phi \simeq 25$) and is significantly below unity for the $K^{*0}(892)$, $\rho^0(770)$, $f^0(980)$, and $K_0^*(1430)$ mesons[8)] (the ratio T_H/Γ_G for these mesons ranges between 2.2 and 0.4). Thus, the first meson should preferably be classified with narrow resonances, while the remaining mesons are broad resonances. A more accurate estimation yields

$$[1b/1a] \simeq 2.9,\ 0.22,\ 0.12,\ 0.12,\ 0.027 \quad (4)$$

for the $\phi(1020)$, $K^{*0}(892)$, $\rho^0(770)$, $f^0(980)$, and $K_0^*(1430)$ mesons, respectively.

In the case where $h = \pi$ (that is, we perform a comparison with the pion production rate, as, for example, in considering the relative multiplicities of ρ^0 or f^0 resonances), it is necessary to take into account

[5)] In this calculation, we of course use the perfect-gas approximation and the fact that it is sufficient to calculate this probability in the rest frame of an element dV of the expanding medium, where the valon momentum distribution can be considered to be isotropic.

[6)] In doing this, we neglect corrections of order $(m_{Q_i} - m_{Q_j})^2/(m_{Q_i} + m_{Q_j})^2$, which are within 4% if we restrict our consideration to three flavors—two light and one strange valon whose masses are $m_{Q_{u,d}} \simeq 330$ MeV and $m_{Q_s} \simeq 480$ MeV.

[7)] In the denominator, this factor is always about unity, because the threshold for the production of the corresponding long-lived resonance (in this context, a pion or a kaon) is substantially (at least by about 200 MeV) below the minimum energy of the $Q_i\bar{Q}_j$ pair.

[8)] Here, we have chosen those short-lived mesons for which some preliminary results have already been obtained at the RHIC/BNL accelerator [15] or will soon appear.

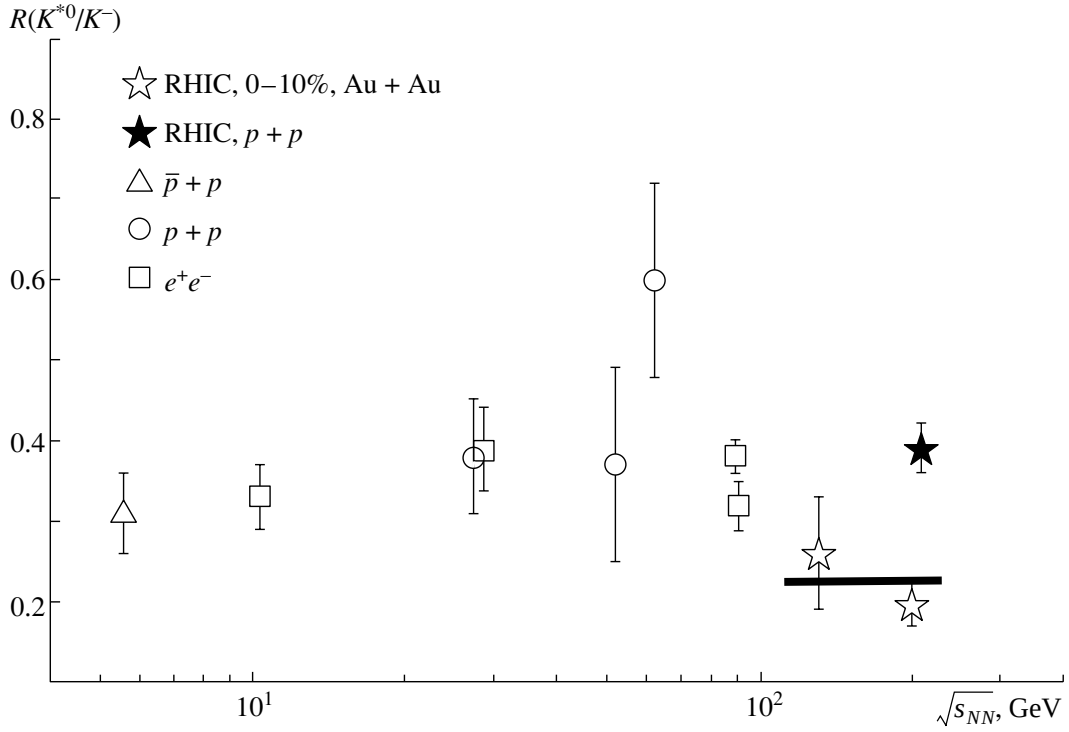

Fig. 3. Expected relative multiplicity of $K^{*0}(892)$ mesons in central heavy-ion collisions at the RHIC/BNL accelerator (thick horizontal segment) according to the present calculation under the assumption of hadron production via valon coalescence [5] (alternative approach) against the background of preliminary data from various experiments [15].

the fact that pions are produced not only in the annihilation of the lightest valons, $Q_q\bar{Q}_q$, $q = u, d$ [this contribution has been completely taken into account in the denominator on the right-hand side of (1)], but also in the production of other (for example, strange) hadrons (see Fig. 1). Since the deficiency of the phase space averaged over the thermal distribution at $T = T_H$ suppresses strongly the production of more than one accompanying pion in each valon-annihilation event, the total number of such pions is close to the total multiplicity of all other hadrons; according to experimental data (see, for example, [3]), this number at the RHIC/BNL energies amounts to about 30% of all observed pions.

Therefore, the quantity

$$R(G/h) \simeq W(G/h)\{1 + [1b/1a]\} \qquad (5)$$

if $h \neq \pi$ or the quantity

$$R(G/h) \simeq 0.7W(G/h)\{1 + [1b/1a]\} \qquad (6)$$

if $h = \pi$, where the right-hand side is determined by expressions (3) and (4), must be compared with experimental data.

2.2. Comparison with Experimental Data

The results of the above theoretical analysis of the production rates for $K^{*0}(892)$ and $\phi(1020)$ mesons [$R(K^{*0}/K^-) \simeq 0.22$ and $R(\phi/K^-) \simeq 0.06$] are displayed in Figs. 3 and 4, respectively, along with preliminary experimental data presented at the International Conference QM2004 [15]. The predicted production rates for the $\rho^0(770)$, $f^0(980)$, and $K_0^*(1430)$ mesons in central nucleus–nucleus collisions at RHIC/BNL are $R(\rho^0/\pi^-) \simeq 0.23$, $R(f^0/\pi^-) \simeq 0.07$, and $R(K_0^*/K^-) \simeq 0.03$.[9)] All of these results and predictions are compiled in the table.

3. DISCUSSION AND CONCLUDING COMMENTS

Although available data on the production of short-lived mesons in central heavy-ion interactions

[9)]For the ρ^0 and f^0 mesons, we took into account the reduction factor of 2/3, which is caused by the fact that the dominating production mechanism for these resonances (Fig. 1*a*) is realized only in two of the four possible types of $Q_{u,d}\bar{Q}_{u,d}$ interactions, while π^- mesons are produced in three of them (the same result is obtained in a more rigorous calculation that employs Clebsch–Gordan coefficients). In addition, we followed the customary format in which one usually presents experimental data, referring the production rates for strange resonances to that for K^- mesons, which is lower than its counterpart for K^+ mesons by about 10% at RHIC/BNL and by factors of 1.85 and 4.5 at SPS/CERN and AGS/BNL, respectively.

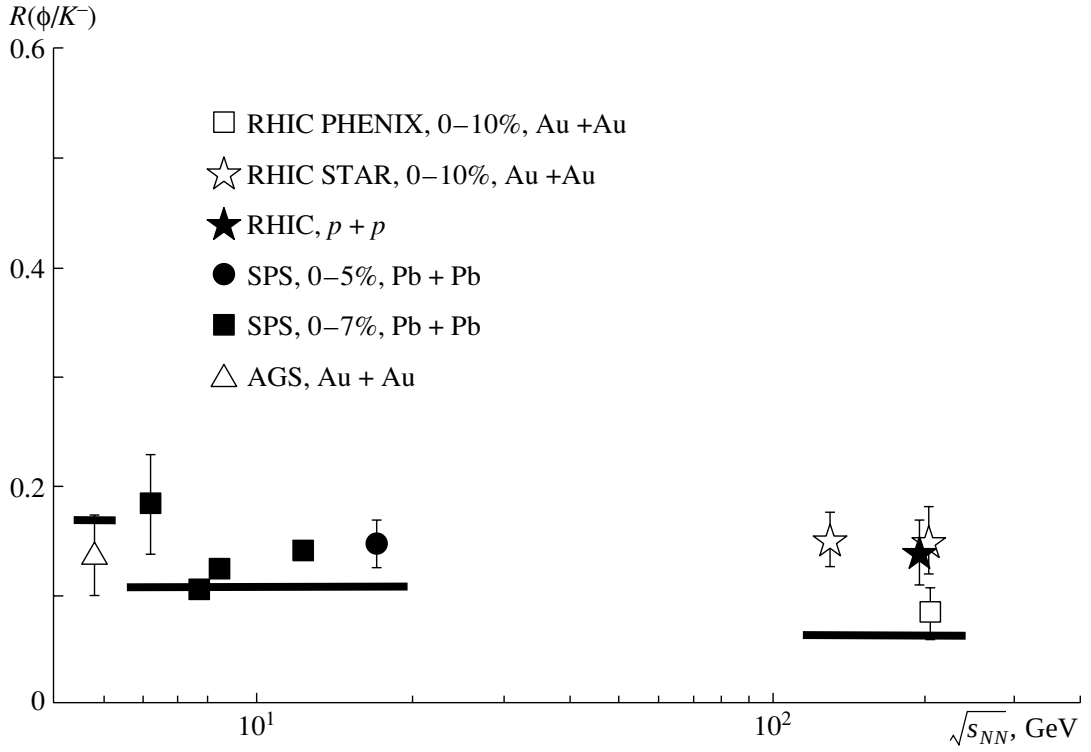

Fig. 4. Expected relative multiplicity of $\phi(1020)$ mesons in central heavy-ion collisions at the RHIC/BNL, SPS/CERN, and AGS/BNL accelerators (thick horizontal segments) according to the present calculation under the assumption of hadron production via valon coalescence [5] (alternative approach) against the background of preliminary data from various experiments [15]. The significance of this comparison for AGS/BNL is doubtful because the data from those measurements were not associated with a specific (central) type of collisions.

are still scanty and are of a low quality, the proposed theoretical approach can boast an obviously good description of the production rate for $K^{*0}(892)$ mesons. In this connection, it is worth emphasizing that the result presented here was obtained within the same conceptual framework as that which earlier provided a successful description [4, 5] of the production of long-lived hadrons and dileptons of low invariant mass without invoking additional assumptions or parameters. At the same time, the situation around $\phi(1020)$ mesons is still ambiguous, because experimental data obtained by two neighboring collaborations at RHIC/BNL (PHENIX and STAR) differ by nearly a factor of 2 (see Fig. 4); this may be due to a relatively small width of the phi meson and accompanying measurement difficulties. Anyway, the theory requires further tests, and there are obviously possibilities for this. In particular, it is necessary to verify the validity of the analogous description (and prediction) of the production rates for short-lived baryon resonances. This requires overcoming specific technical difficulties associated with the convenient (for analysis) representation of the production probability for a given invariant mass of the system consisting of three valons. Unfortunately, the accuracy of available preliminary data [15] for $\Delta^{++}(1232)$ and $\Lambda(1520)$ resonances, which is not higher than 30 to 50%, is most likely insufficient for assessing the aforementioned ratios. The above prediction for the relative production rates $R(\rho^0/\pi^-)$ and $R(f^0/\pi^-)$ in central collisions is more restrictive, especially in the qualitative part. It is natural to expect their significant growth in relation to preliminary RHIC/BNL data for peripheral interactions (about 0.17 and 0.05, respectively—see table), while the experimentally revealed trend in the behavior of the production rates for strange meson resonances, $R(\phi/K^-)$ and $R(K^{*0}/K^-)$, seems the opposite {see [15] for this trend and for the difference already revealed in the experimental behavior of the production rates for usual and strange baryon resonances, $R(\Delta^{++}(1232)/p)$ and $R(\Lambda(1520)/\Lambda)$}.

It is also worth indicating that the problem considered here has another aspect that has not yet been considered. This is the possible role of microscopic dynamics—that is, the resonance structure of the valon-interaction cross section (with maxima at the same points as for final hadrons—see Fig. 1*a*). This structure could manifest itself against

Predictions and some results of the alternative approach along with experimental data (see [15]) on the production of meson resonances in high-energy heavy-ion collisions {the asterisk indicates that the ambiguity in the corresponding measurements can be as large as 100%; the LHC accelerator is mentioned because we can expect there almost the same results (however, the relative strange-resonance production rate can be reduced by 5–10%)}

	SPS		RHIC (LHC?)		
	experiment (central interactions)	theory (only central interactions)	experiment		theory (only central interactions)
			peripheral interactions	central interactions	
$R(\rho^0(770)/\pi^-)$			0.17		0.23
$R(f^0(980)/\pi^-)$			0.05*		0.07
$R(K^{*0}(892)/K^-)$				0.20–0.25	0.22
$R(\varphi(1020)/K^-)$	0.10–018*	0.11	0.11–0.15	0.08–0.14*	0.06
$R(K_0^*(1430)/K^-)$					0.03

the background of their smooth thermal distribution in one way or another that would depend on the lifetime (width) of the resonance (with the result that the shape and the position of the resonance change slightly—see, for example, [17]) and on the relation between this lifetime and the characteristic hadronization time (about 1 fm), because the latter determines the rate of variation of the properties of the medium where the production and a further evolution of the resonance occurs (see, for example, the relevant discussion in [18, 19]).

By and large, the results obtained here within the alternative approach indicate, in the opinion of the present author, that this approach has a high potential for self-consistently describing the observation data on the production of secondary particles, both long- and short-lived ones (for the former, this was demonstrated in [5]), in central heavy-ion collisions.

ACKNOWLEDGMENTS

I am grateful to E.L. Feinberg for the permanent attention to this study and interest in it.

This work was funded by a presidential grant for support of leading scientific schools (no. 1936.2003.2) and was supported by the Russian Foundation for Basic Research (project no. 03-02-16134).

REFERENCES

1. P. Braun-Munzinger, I. Heppe, and J. Stachel, Phys. Lett. B **465**, 15 (1999); P. Braun-Munzinger and J. Stachel, J. Phys. G **28**, 1971 (2002); P. Braun-Munzinger, D. Magestro, K. Redlich, and J. Stachel, Phys. Lett. B **518**, 41 (2001); D. Magestro, J. Phys. G **28**, 1745 (2002) and references therein.
2. J. Cleymans and K. Redlich, Phys. Rev. C **60**, 054908 (1999); Nucl. Phys. A **661**, 379c (1999).
3. P. Braun-Munzinger, K. Redlich, and J. Stachel, nucl-th/0304013.
4. O. D. Chernavskaya, E. L. Feinberg, and I. I. Royzen, Yad. Fiz. **65**, 167 (2002) [Phys. At. Nucl. **65**, 161 (2002)].
5. I. I. Royzen and O. D. Chernavskaya, Yad. Fiz. **66**, 185 (2003) [Phys. At. Nucl. **66**, 182 (2003)].
6. E. L. Feinberg, Preprint No. 197, FIAN (Lebedev Inst. Phys., Russ. Acad. Sci., Moscow, 1989); in *Relativistic Heavy Ion Collisions*, Ed. by L. P. Chernai and D. D. Strottman (World Sci., Singapore, 1991), Chap. 5.
7. O. D. Chernavskaya and E. L. Feinberg, in *Proceedings of the International Conference "Hot Hadronic Matter: Theory and Experiment,"* Ed. by J. Letessier and J. Rafelski (Plenum, New York, 1995); J. Moscow Phys. Soc. **6**, 37 (1996); E. L. Feinberg, in *Proceedings of the 2nd International Sakharov Conference, Moscow, Russia, 1996*, Ed. by I. M. Dremin and A. M. Semikhatov (World Sci., Singapore, 1997), p. 23.
8. R. Hwa, Phys. Rev. D **20**, 2838 (1979).
9. B. L. Ioffe, V. A. Khose, and L. N. Lipatov, *Hard Processes* (Énergoatomizdat, Moscow, 1983; North-Holland, Amsterdam, 1984), Vol. 1.
10. V. V. Anisovich *et al.*, Usp. Fiz. Nauk **144**, 553 (1984) [Sov. Phys. Usp. **27**, 901 (1984)].
11. I. I. Royzen, E. L. Feinberg, and O. D. Chernavskaya, Usp. Fiz. Nauk **174**, 473 (2004) [Phys. Usp. **47**, 427 (2004)].
12. F. Karsch, Nucl. Phys. A **698**, 199c (2002); F. Karsch, A. Peikert, and E. Laermann, Phys. Lett. B **478**, 447 (2000).

13. K. G. Wilson, Phys. Rev. D **10**, 2445 (1974); K. G. Wilson and D. G. Robertson, hep-th/9411007.
14. P. Braun-Munzinger, *Presented at the International Conference: "Quark Matter 2004," Marriott City Center, Oakland, USA, 2004*, and references therein.
15. P. Fachini, *Presented at International Conference "Quark Matter 2004," Marriott City Center, Oakland, USA, 2004*, and references therein.
16. I. S. Gradshteyn and I. M. Ryzhik, *Table of Integrals, Series, and Products* (Fizmatgiz, Moscow, 1962; Academic, New York, 1980).
17. G. Brown and E. Shuryak, Nucl. Phys. A **717**, 322 (2003).
18. I. V. Andreev, Yad. Fiz. **63**, 2080 (2000) [Phys. At. Nucl. **63**, 1988 (2000)]; **66**, 1375 (2003) [**66**, 1335 (2003)].
19. K. G. Boreskov, Doctoral Dissertation in Mathematics and Physics (Institute of Theoretical and Experimental Physics, Moscow, 2004).

Translated by M. Kobrinsky

Physics of Atomic Nuclei, Vol. 68, No. 12, 2005, pp. 2124–2128. From Yadernaya Fizika, Vol. 68, No. 12, 2005, pp. 2186–2190.

ELEMENTARY PARTICLES AND FIELDS
Theory

Production and Decay of Charmed Baryons: Spectra of Muons and Asymmetry between μ^+ and μ^-*

O. I. Piskounova[1)] and N. V. Nikitin[2)]

Received February 18, 2005

Abstract—The calculation of muon spectra from the decay of Λ_c baryons was carried out on the basis of the description of recent data on charmed-baryon production in hadronic interactions. Data are described in the framework of the quark–gluon string model (QGSM) that allows us to consider primary proton interactions of arbitrary high energy. A Monte Carlo code was built for charmed-baryon semileptonic decay in order to obtain the kinematical characteristics of the resulting particles. It is predicted that the charge asymmetry between energy spectra of μ^+ and μ^- in the laboratory system will be clearly seen as the consequence of asymmetry between the spectra of charmed baryons and antibaryons. This extension of the QGSM can be useful to correct the calculations of muon and neutrino spectra in astrophysics.

INTRODUCTION

Charmed-particle decay is an important source of atmospheric muons and neutrinos [1]. We know the characteristics of charmed-hadron production, investigated in recent years by many fixed-target experiments in accelerators [2]. The quark–gluon string model (QGSM) [3] that has been built over the last two decades can reproduce the energy distributions of charmed baryons and mesons in hadronic collisions up to very high energies. These spectra have an interesting behavior in the central region of x_F: the asymmetry between particle and antiparticle distributions shows a narrow dip for charmed baryons, otherwise the charmed meson asymmetry goes down slowly and reaches a nonzero value in the central x_F region, which contradicts the basic QCD theory. In practice, it is not possible to reproduce nonzero asymmetry in the perturbative QCD approach owing to the equal rate of c and $\bar{c}$ production in the perturbative gluon fusion process. These phenomena have found an explanation in recent calculations in the framework of the QGSM [4]. It seems interesting to investigate what sort of peculiarities should be produced by this dip in the spectra of muons and neutrino.

1. PRODUCTION OF CHARMED BARYONS IN pp INTERACTIONS AND QGSM

The inclusive-production cross section of hadrons of type H is written as a sum over n-Pomeron cylinder diagrams:

$$f_1 = x\frac{d\sigma^H}{dx}(s,x) = \int E\frac{d^3\sigma^H}{d^3p}d^2p_\perp = \sum_{n=0}^{\infty}\sigma_n(s)\varphi_n^H(s,x). \quad (1)$$

Here, the function $\varphi_n^H(s,x)$ is a particle distribution in the configuration of n-cut cylinders and σ_n is the probability of this process. The cross sections σ_n depend on the parameter of the supercritical Pomeron Δ_P, which is equal in our model to 0.12 [3]. In the case of Λ_c production in proton fragmentation, the diquark fragmentation plays an important role; this diquark part of the distribution should be written separately. So the distribution for pp collision will include two diquark parts for positive as well as for negative x:

$$\varphi_n^{\Lambda_c}(s,x) = a_f^{\Lambda_c}F_{1qq}^{(n)}(x_+) + a_f^{\Lambda_c}F_{1qq}^{(n)}(x_-) + a_0^{\bar{\Lambda}_c}[F_q^{(n)}(x_+)F_{0qq}^{(n)}(x_-) + F_{0qq}^{(n)}(x_+)F_q^{(n)}(x_-) + 2(n-1)F_{q_{sea}}^{(n)}(x_+)F_{\bar{q}_{sea}}^{(n)}(x_-)], \quad (2)$$

where $F_{1qq}^{(n)}(x_+)$ is the distribution at the leading fragmentation of diquarks, while $F_{0qq}^{(n)}(x_+)$ is the ordinary part of fragmentation written with the central density parameter $a_0^{\bar{\Lambda}_c}$. Obviously, the distribution for $\bar{\Lambda}_c$ does not include the leading fragmentation term.

*This article was submitted by the authors in English.

[1)]Lebedev Institute of Physics, Russian Academy of Sciences, Moscow, Russia; e-mail: piskoun@sci.lebedev.ru

[2)]Institute of Nuclear Physics, Moscow State University, Moscow, Russia; e-mail: nik679@monet.npi.msu.su

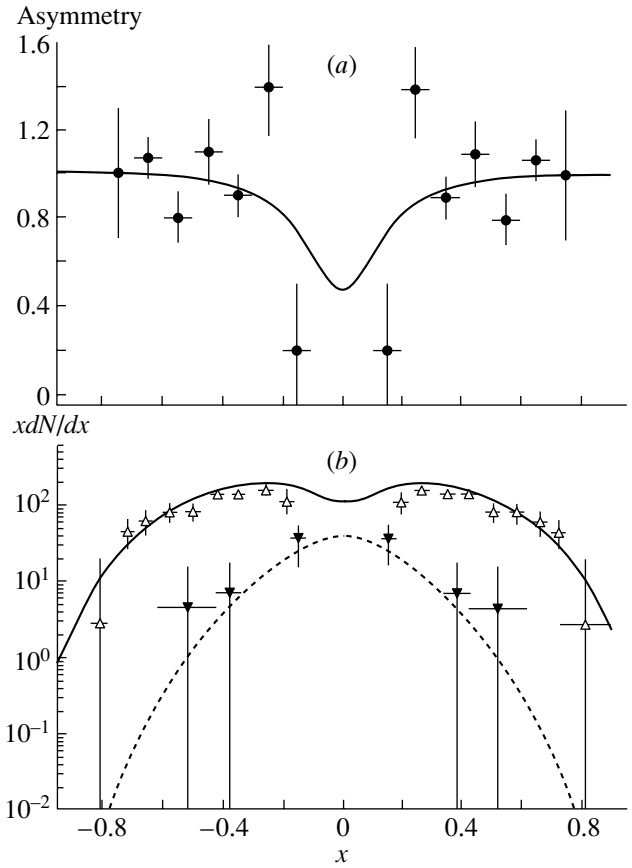

Fig. 1. (a) The asymmetry between Λ_c and $\bar{\Lambda}_c$ spectra obtained for pA collisions in the E781 experiment (•) [9] and the QGSM calculation (solid curve). (b) The distributions of Λ_c (△) and $\bar{\Lambda}_c$ (▼) in E781 for these reactions and QGSM curves: Λ_c (solid) and $\bar{\Lambda}_c$ (dashed).

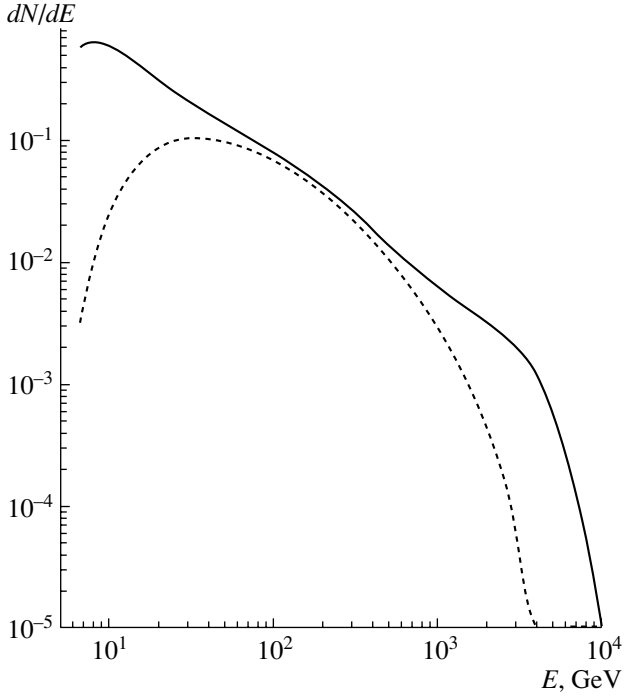

Fig. 2. The distributions of Λ_c (solid curve) and $\bar{\Lambda}_c$ (dashed curve) in the laboratory system, calculated in the QGSM for the energy $E_p = 10^4$ GeV.

The fragmentation functions of diquark and quark chains into charmed baryons or antibaryons are based on the rules written in [5]. The structure functions of quarks in interacting protons have already been described in the previous papers [6–8]. The asymmetry between the spectra of Λ_c and $\bar{\Lambda}_c$ measured in pA collisions at $p_L = 600$ GeV/c [9] is shown in Fig. 1a.

The asymmetry is defined as

$$A(x) = \frac{dN^{\Lambda_c}/dx - dN^{\bar{\Lambda}_c}/dx}{dN^{\Lambda_c}/dx + dN^{\bar{\Lambda}_c}/dx}. \qquad (3)$$

Here, dN^{Λ_c}/dx and $dN^{\bar{\Lambda}_c}/dx$ are the event distributions measured in the experiment [9]. The asymmetry plot has a sharp dip in the central region that is peculiar for baryon production in proton–proton collisions.

The invariant distributions xdN/dx of charmed baryons and antibaryons obtained in proton interactions in the E781 experiment are shown in Fig. 1b with the QGSM curves calculated for proton fragmentation on both sides. It should be mentioned here that usually cosmic protons interact with air nuclei in cosmic-ray physics and the spectra are different. But the dependence on atomic number of target nuclei is important at $y < 0$ and, in addition, it should be canceled in formula (3). Thus, our conclusions about asymmetries are valid for proton–nucleus collisions as well.

2. CHARMED-BARYON/ANTIBARYON SPECTRA IN LABORATORY SYSTEM

The results of accelerator experiment are usually presented in the center-of-mass system (c.m.), which is not accepted in cosmic-ray physics, where the Earth is the only possible laboratory system (lab.) for the measurements. The transformation of spectra at the transition from c.m. to lab. can be done taking into account the invariance of the value $d\sigma/dy = xd\sigma/dx_{\text{c.m.}} = (d\sigma/dy)(y_{\text{lab}} - y_0)_{\text{lab}}$. In this case, we will have an E^{-1} power slope of the spectra in the lab.:

$$d\sigma/dE = (1/E)(xd\sigma/dx) = (1/E)(d\sigma/dy). \qquad (4)$$

This slope should be seen in the energy region corresponding to the central plateau of the distribution in c.m., where $d\sigma/dy = \text{const}$. The transformed baryon and antibaryon spectra are shown in Fig. 2 at the energy of proton interaction $E_p = 10^4$ GeV.

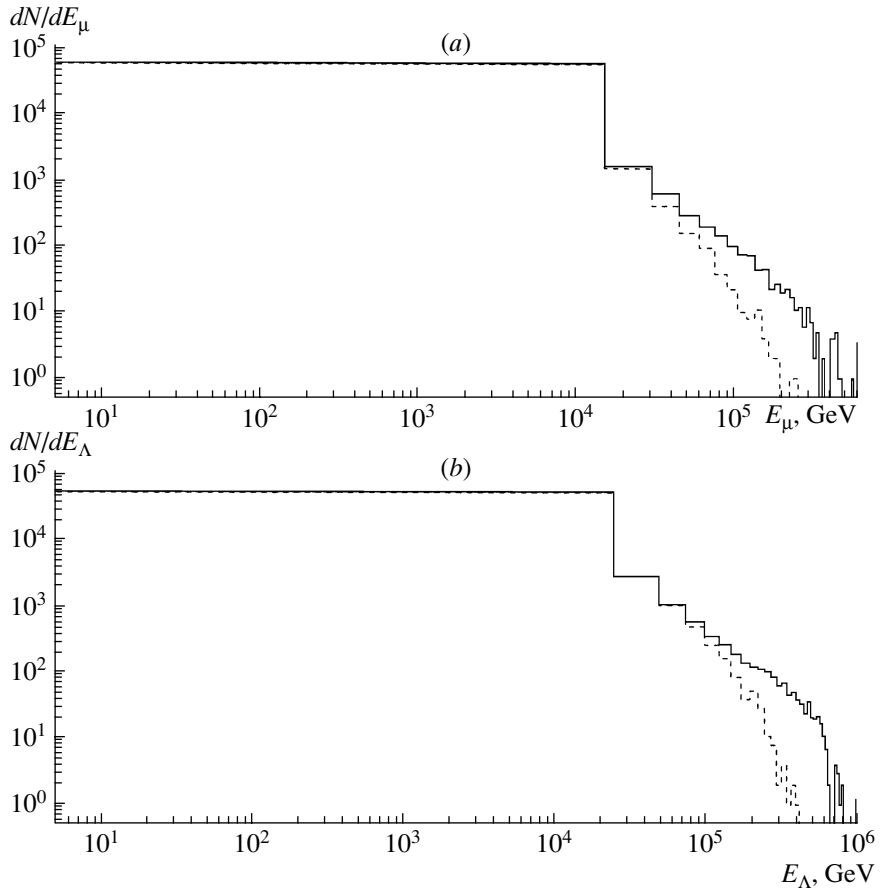

Fig. 3. (*a*) The spectra of μ^+ (solid line) and μ^- (dashed line) calculated at $E_p = 10^5$ GeV. (*b*) The distributions of Λ_c (solid line) and $\bar{\Lambda}_c$ (dashed line) in the QGSM for the energy $E_p = 10^5$ GeV.

This method was already used in the calculation of photon spectra from a monochromatic cosmic proton source [10] and in the estimation of the antiproton/proton ratio [11] in cosmic rays. In Fig. 2, we can see also how the asymmetry between spectra behaves in lab. The dip in asymmetry extends up to energy of the order of $0.1E_p$. Will it be seen in the muon spectra?

3. SPECTRA OF MUONS

In the previous section, we have described the calculations of charmed baryons in lab. Here, we give a brief description of the procedure of the calculation of muon spectra that are generated in semileptonic decays of Λ_c.

It is well known that a rather good approximation to the lepton spectra can be obtained for semileptonic decays of charmed baryons if one takes the probability of these decays to be the same as that for exclusive parton decay $c \to s\mu^+\nu_\mu$, where the c quark possesses the energy and the spectrum of Λ_c.

The decay $c \to s\mu^+\nu_\mu$ has been studied, for example, in [12]. Its differential width is equal to

$$\frac{d^2\Gamma}{d\hat{s}d\hat{t}} = \frac{G_F^2}{16\pi^3} m_c^5 |V_{cs}|^2 \left(1 + \hat{m}_\mu^2 - \hat{t}\right)\left(\hat{t} - \hat{m}_s^2\right), \quad (5)$$

where $\hat{s}$ and $\hat{t}$ are the standard Mandelstam variables, and m_c and m_μ are the masses of quark and muon. Mandelstam variables $\hat{s}, \hat{t}$ have to satisfy the following kinematical restrictions:

$$\hat{m}_\mu^2 \le \hat{s} \le \left(1 - \sqrt{\hat{m}_s^2}\right), \quad \hat{m}_s^2 \le \hat{t} \le \left(1 - \sqrt{\hat{m}_\mu^2}\right). \quad (6)$$

Let us write formula (5) as an expression normalized to the interval 0 to 1 that will be useful in the construction of a Monte Carlo (MC) generator:

$$w(\hat{s}, \hat{t}) = \frac{4}{\left(1 + \hat{m}_\mu^2 - \hat{m}_s^2\right)^2}\left(1 + \hat{m}_\mu^2 - \hat{t}\right)\left(\hat{t} - \hat{m}_s^2\right). \quad (7)$$

The MC procedure for generating muon spectra consists of a few steps. First of all, we consider the

decay $c \to s\mu^+\nu_\mu$ in the rest system of the charmed baryon that is also the rest system of the c quark and get the random pair $\hat{s}, \hat{t}$ from the interval that was written in Eq. (6). This pair is checked with the help of a kinematical function to determine whether it belongs to the physical space of the process (right pair). If the pair is chosen as right, it possesses the weight of Eq. (7). The momenta and energies of the decay products are calculated due to s, t.

Revolution on three axes is applied to the resulting vectors of momenta that are turned with random Euler angles to reach arbitrary positions toward the axes. It helps us to return to the system where Λ_c is moving along the x axis. We neglect here the transverse motion because of the small ratio between transverse and longitudinal momentum.

As a result of the described MC procedure, the table of four-momenta of all products of decay is built, where the data for further analysis can be found.

4. RESULTING PLOTS AND COMPARISONS

In this work, we have the possibility to analyze the Λ_c spectra that can be calculated analytically with the QGSM for arbitrary energy and at the same time to compare these spectra with the muon spectra generated after the decay of charmed baryons. We are interested here in only muon characteristics, but the possibility exists to analyze the neutrino spectra too.

Let us compare the spectra of $\Lambda_c/\bar{\Lambda}_c$ with the spectra of decay products at the energy of initial proton–proton interaction $E_p = 10^6$ GeV. As can be seen from Fig. 3, the asymmetry predicted between the spectra of baryons and antibaryons is clearly reproduced in the spectra of μ^+ and μ^-. The spectra of Λ_c are of the same form as was calculated analytically (see Fig. 2).

The asymmetry between spectra of μ^+ and μ^- that is shown in Fig. 4 is almost equal to zero in the wide region corresponding to the central plateau in the Λ_c-production distribution. It would be interesting to study how this asymmetry is sensitive to the difference in baryon/antibaryon production at high energies that might remain valuable owing to the effect of string-junction transfer, which was not accounted for in our calculations.

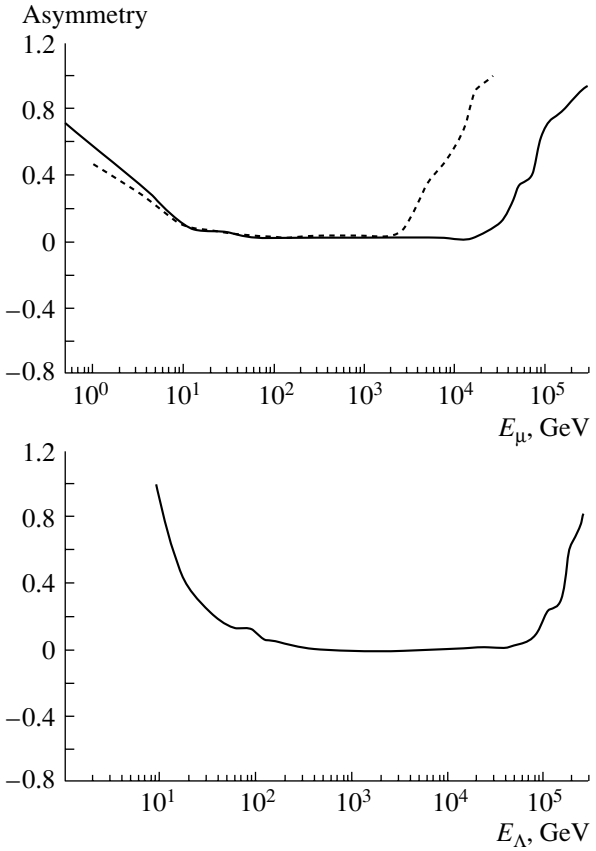

Fig. 4. (a) The asymmetry between spectra of μ^+ and μ^- calculated at $E_p = 10^6$ and 10^5 GeV (solid and dashed curves); (b) the asymmetry between Λ_c and $\bar{\Lambda}_c$ spectra obtained for pp collisions in the QGSM calculation at $E_p = 10^6$ GeV.

SUMMARY

In this paper, we have studied the spectra of muons after the semileptonic decay of charmed baryons produced in hadronic interactions at very high energy. It is assumed that the conclusions from this research are interesting for cosmic-ray physics as well as for high-energy accelerator physics. The asymmetry in production of baryons over antibaryons is caused by the positive baryonic charge of colliding protons. This asymmetry should disappear in the central region with rising interaction energy. The spectra of charmed baryons and antibaryons have been described in the quark–gluon string model with account of quark interaction mechanisms providing the baryon/antibaryon asymmetry. Only the mechanism of string-junction transfer was not yet accounted for in our scheme. Even so, the obvious asymmetry is reproduced on the edges of the spectra of $\Lambda_c/\bar{\Lambda}_c$ in the laboratory system, as was analytically predicted. The knee in the spectra at 0.1 E_p is caused by the form of analytical spectra in the fragmentation region. This very form of spectra in the laboratory system can be a good manifestation of the interaction of monochromatic primary protons. The Monte Carlo generator that was built for the calculation of spectra of products of charmed baryon decays provides the four-momenta of all particles after semileptonic decay. We have analyzed here only muon spectra.

These spectra reproduce the production asymmetry between positive and negative particles, as is seen in the spectra of $\Lambda_c/\bar{\Lambda}_c$. We conclude that muons can be a good instrument to study the baryon production asymmetry in high-energy proton–proton interactions. The estimation of the background from D-meson decays should be done in the same QGSM approach.

ACKNOWLEDGMENTS

We are grateful to Prof. A.B. Kaidalov and Dr. L.V. Volkova for numerous discussions.

One of us (O.I.P.) is supported with a grant from the Russian Foundation for Basic Research (project no. 04-02-16757a), the grant RFBR-DFG 03-02-04026a, and the grant NATO CLG.980335.

REFERENCES

1. F. Halsen *et al.*, Phys. Rev. D **55**, 4475 (1997); EAS-TOP Collab. and MACRO Collab., Astropart. Phys. **20**, 641 (2004); K. Abe *et al.*, Phys. Lett. B **564**, 8 (2003); T. Sanuki *et al.*, Phys. Lett. B **541**, 234 (2002); G. Fiorentini, V. A. Naumov, and F. L. Villante, Phys. Lett. B **510**, 173 (2001).
2. R. Vogt, hep-ph/0412303; in *Proceedings of the Strangeness in Quark Matter, Cape Town, South Africa, 2004*.
3. A. B. Kaidalov and K. A. Ter-Martirosyan, Yad. Fiz. **39**, 1545 (1984) [Sov. J. Nucl. Phys. **39**, 979 (1984)]; **40**, 211 (1984) [**40**, 135 (1984)]; A. B. Kaidalov, Phys. Lett. B **116B**, 459 (1982).
4. A. B. Kaidalov and O. I. Piskounova, Yad. Fiz. **43**, 1545 (1986) [Sov. J. Nucl. Phys. **43**, 994 (1986)]; O. I. Piskounova, Yad. Fiz. **56** (8), 176 (1993) [Phys. At. Nucl. **56**, 1094 (1993)].
5. A. B. Kaidalov, Yad. Fiz. **45**, 1450 (1987) [Sov. J. Nucl. Phys. **45**, 902 (1987)].
6. O. I. Piskounova, Nucl. Phys. B (Proc. Suppl.) **93**, 144 (2001).
7. O. I. Piskounova, Yad. Fiz. **64**, 101 (2001) [Phys. At. Nucl. **64**, 98 (2001)].
8. O. I. Piskounova, in *Proceedings of the DIS', St. Petersburg, Russia, April 2003*.
9. SELEX Collab. (F. G. Garcia *et al.*), Phys. Lett. B **528**, 49 (2002).
10. O. I. Piskounova, Yad. Fiz. **51**, 1332 (1990) [Sov. J. Nucl. Phys. **51**, 846 (1990)].
11. O. I. Piskounova, Yad. Fiz. **47**, 1332 (1988) [Sov. J. Nucl. Phys. **47**, 480 (1988)].
12. V. Novikov *et al.*, Phys. Rev. Lett. **38**, 626 (1977); B. Block, L. Koyrakh, M. Shifman, and A. Vainshtein, Phys. Rev. D **49**, 3356 (1994).

Physics of Atomic Nuclei, Vol. 68, No. 12, 2005, pp. 2129–2138. Translated from Yadernaya Fizika, Vol. 68, No. 12, 2005, pp. 2191–2200.

ELEMENTARY PARTICLES AND FIELDS
Theory

Measurement of the Tensor Analyzing Power for Relativistic-Deuteron Fragmentation as a Means for Studying the Deuteron Structure within Light-Front Dynamics

L. S. Azhgirey*, S. V. Afanasiev, V. N. Zhmyrov, L. S. Zolin, V. I. Ivanov, A. Yu. Isupov, V. P. Ladygin, A. G. Litvinenko, V. F. Peresedov, A. N. Khrenov, and N. P. Yudin[1)]

Joint Institute for Nuclear Research, Dubna, Moscow oblast, 141980 Russia

Received March 15, 2005

Abstract—New data on the vector (A_y) and tensor (A_{yy}) analyzing powers for the reaction ^{9}Be $(d,p)X$ at a primary deuteron momentum of 5 GeV/c for a proton emission angle of 178 mrad are obtained by using the synchrophasotron of the Joint Institute for Nuclear Research (JINR, Dubna). The experimental data on A_{yy} are analyzed within the approach based on light-front dynamics, the relativistic wave function obtained by Karmanov and his colleagues being used for the deuteron. It is shown that, in contrast to what one has from calculations with standard nonrelativistic deuteron wave functions, all relevant data can be explained in this approximation without resort to additional degrees of freedom. © *2005 Pleiades Publishing, Inc.*

1. INTRODUCTION

Measurement of polarization features of the deuteron-fragmentation reaction at intermediate and high energies still remains one of the main tools for studying the deuteron structure and, in a broader context, one of the key problems in relativistic hadron physics. The results of the experiments performed in Saclay [1–4] and in Dubna [5–10] with polarized-deuteron beams cast some doubt on the validity of describing the deuteron structure at short distances with the aid of wave functions obtained on the basis of nonrelativistic wave functions via a kinematical transformation of variables (see, for example, [11, 12]). In particular, this is suggested by following facts.

First of all, we recall that, in the momentum representation, the tensor analyzing power T_{20} for deuteron-fragmentation reactions of the $A(d,p)X$ type has the form $T_{20} \sim w(k)[\sqrt{8}u(k) - w(k)]$, where $u(k)$ and $w(k)$ are the wave functions for, respectively, the S- and D-wave states of the deuteron in momentum space and k is the internal nucleon momentum in the deuteron (in the light-front frame). For the standard deuteron wave functions, the analyzing power T_{20} as a function of k is expected to change sign at $k \sim 0.5$ GeV/c, but this is not observed experimentally [7].

Further, we note that, within the impulse approximation, the momentum dependence of the analyzing power T_{20} is completely determined by the deuteron wave function in momentum space. This function depends only on k, but it was shown experimentally in [10] that, for the pion-free deuteron breakup $dp \to ppn$ in the kinematical region close to that of elastic dp scattering into the backward hemisphere in the c.m. frame, the tensor analyzing power T_{20} depends not only on k but also on the initial deuteron momentum. This gives reasons to hypothesize that, in addition to k, a new variable is required for adequately describing the bound state of two nucleons.

Finally, the results obtained in [13, 14] by measuring the tensor analyzing power A_{yy} for the process where relativistic-deuteron fragmentation on nuclei is accompanied by the emission of high-transverse-momentum protons also favor this hypothesis. From those results, it follows that, at fixed longitudinal momenta of product protons, the tensor analyzing power A_{yy} depends greatly on their transverse momentum; in addition, it turns out that the quantities A_{yy} for fixed values of k display a pronounced dependence on the angle between the vectors $\mathbf{k}$ and $\mathbf{n}$, the latter being a unit normal to the light-front surface. All of these facts do not fit in the traditional theoretical schemes used to describe polarization observables of $A(d,p)X$ reactions.

Of course, the aforementioned features may be attributed to various factors. For example, it can be assumed that an overly simple (pole) mechanism was used to explain experimental data. However, there are serious reasons to believe that this mechanism is

[1)]Institute of Nuclear Physics, Moscow State University, Vorob'evy gory, Moscow, 119899 Russia.
*E-mail: azhgirey@jinr.ru

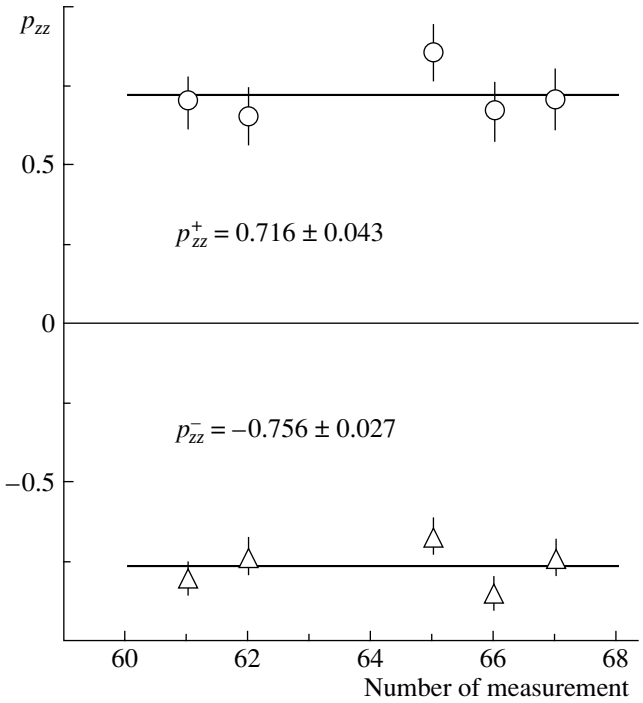

Fig. 1. Tensor polarization of the deuteron beam in the experiment.

quite efficient in describing the processes being considered [15]. For example, it was shown in [16] that the main special features of experimental data on the tensor analyzing power for the relativistic-deuteron fragmentation on nuclei that is accompanied by the emission of high-transverse-momentum protons can be explained on the basis of the simple pole mechanism within light-front dynamics [17] by using the relativistic deuteron wave function derived in [18]. In view of this result, we deem it reasonable to assume that, in describing experimental data obtained with polarized-deuteron beams, it is the most important to take correctly into account the relativistic features of the reaction being studied rather than to perform a refined analysis of the reaction mechanism.

These features can be taken into account by various methods. However, we decided on the approach developed by Karmanov *et al.* [18–20], because it is necessary to introduce a new variable for describing the relativistic deuteron. Within this approach, the relativistic deuteron is described in terms of a more general wave function than that in the nonrelativistic case—that is, a wave function that depends on two momenta, the longitudinal and the transverse one. In the nonrelativistic limit, these components reduce to the modulus of the momentum, with the result that the nonrelativistic wave function depends on a single nontrivial variable. In the relativistic case, there arises a new relation between the longitudinal and transverse components of the momentum characterizing the intranuclear motion of nucleons [18–20], and this relation differs from the relation that is dictated by the superposition of the S and D waves in the nonrelativistic deuteron wave functions.

In this article, we present the results of new measurements of the vector and tensor analyzing powers (A_y and A_{yy}, respectively) for inclusive deuteron fragmentation in the reaction $^9\mathrm{Be}(d,p)X$ at an initial deuteron momentum of 5 GeV/c and a secondary-proton emission angle of 178 mrad in the laboratory frame. These measurements were performed in order to compare their results with the results of the calculations relying on light-front dynamics and employing various deuteron wave functions.

In order to increase the data-accumulation rate, the present experiment was performed with a beryllium target. We note, however, that, in measuring the momentum spectra of protons emitted at angles of 103, 139, and 157 mrad in the laboratory frame in the fragmentation of 9-GeV/c deuterons on hydrogen, deuteron, and carbon targets, it was shown [21] that the shape of the high-momentum sections of the proton spectra is everywhere (with the exception of a segment about ± 80 MeV/c in width around the maxima of the spectra) independent of the atomic number of the target; it is determined exclusively by the deuteron structure and the mechanism of deuteron–nucleon interaction. The same conclusion was also drawn from data on deuteron breakup at 0° [5]. As to the results obtained by measuring the tensor analyzing

power T_{20} for deuteron breakup at 0° [2, 6, 7], they showed that the systematic distinction between the data for hydrogen and nuclear targets does not exceed 20%. Therefore, multiple scattering is modest, so that nuclear targets are also appropriate for extracting information about the deuteron structure.

2. DESCRIPTION OF THE EXPERIMENT

The experiment was performed with a polarized-deuteron beam extracted from the synchrophasotron of the Joint Institute for Nuclear Research (JINR, Dubna). The SFERA setup used in this experiment was described elsewhere [14, 22, 23]. Here, we will dwell only on the basic points of our experimental procedure.

A beam of tensorially polarized deuterons that was characterized by a momentum of 5 GeV/c, a duration of 0.5 s, and an intensity of 5×10^8 particles per accelerator spill was incident to a beryllium target 16 cm thick. The beam intensity was monitored by an ionization chamber arranged in front of the target and by two telescopes of scintillation counters. The position of the beam and its dimensions at specific loci of the ion guide were checked within each pulse by the equipment of the slow-extraction system. The dimensions of the beam at the target position were $\sigma_x \sim 0.4$ cm and $\sigma_y \sim 0.9$ cm in, respectively, the horizontal and the vertical direction.

Polarized deuterons were produced by the POLARIS ion source [24]. The spin quantization axis was orthogonal to the plane containing the mean orbit of the beam in the accelerator. The sign of the beam polarization was reversed regularly from one accelerator pulse to another. The tensor polarization of the beam was determined on the basis of measurements of asymmetry in the emission of protons with momentum $p_p \sim \frac{2}{3}p_d$ at zero angle in the $A(d,p)X$ reactions [25]. The tensor-polarization values obtained in the experiment were $p_{zz}^+ = 0.716 \pm 0.043$ and $p_{zz}^- = -0.756 \pm 0.027$ for, respectively, positively and negatively directed beam polarizations. The results obtained by measuring the tensor component of the deuteron-beam polarization are shown in Fig. 1.

The vector polarization of the beam was continuously monitored in the course of the experiment by measuring asymmetry in quasielastic proton–proton scattering on a thin polyethylene target inserted in the beam. The values of the vector polarization were obtained by using the results of asymmetry measurements in the scattering of 2.5-GeV/c protons at an angle of 14°. The analyzing power of the polarimeter was taken to be 0.235 [26]. The vector polarization of the beam was $p_z^+ = 0.173 \pm 0.008$ and $p_z^- = 0.177 \pm 0.008$ for, respectively, the positive and the negative direction of beam polarization. The results of monitoring the vector component of deuteron-beam polarization are presented in Fig. 2.

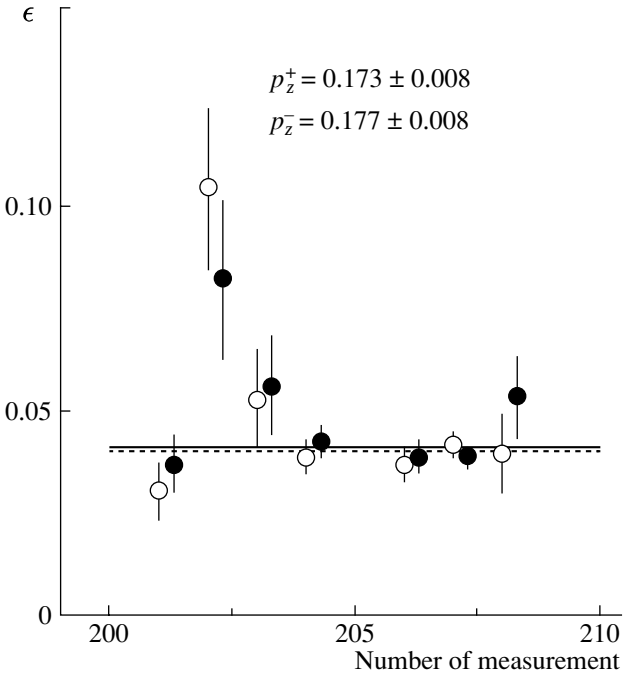

Fig. 2. Asymmetry ϵ in measuring the vector component of deuteron-beam polarization in the course of the experiment (the open and closed circles correspond to the positive and negative directions of polarization, and the dashed and solid curves represent the mean asymmetry values corresponding to them).

The data to be analyzed were obtained for four values of the secondary-particle momentum in the range between 2.7 and 3.6 GeV/c. The transverse momenta of recorded protons ranged between 0.49 and 0.65 GeV/c. By means of magnetic elements, secondary particles emitted from the target at an angle of 178 mrad were transported to the detecting equipment. The momentum and angular acceptances of the setup were determined via a Monte Carlo simulation with allowance for the parameters of the incident deuteron beam; nuclear interactions and multiple scattering in the target, air, windows, and detectors; the energy losses of primary and secondary particles; and so on. The momentum acceptance for secondary protons at four values of their momentum is shown in Fig. 3 according to the results of this simulation. The momentum and polar-angle acceptances were $\Delta p/p \sim \pm 2\%$ and ± 18 mrad, respectively.

Along with secondary protons, our equipment recorded inelastically scattered deuterons. The recorded particles were identified via data processing in an off-line mode upon performing the experiment.

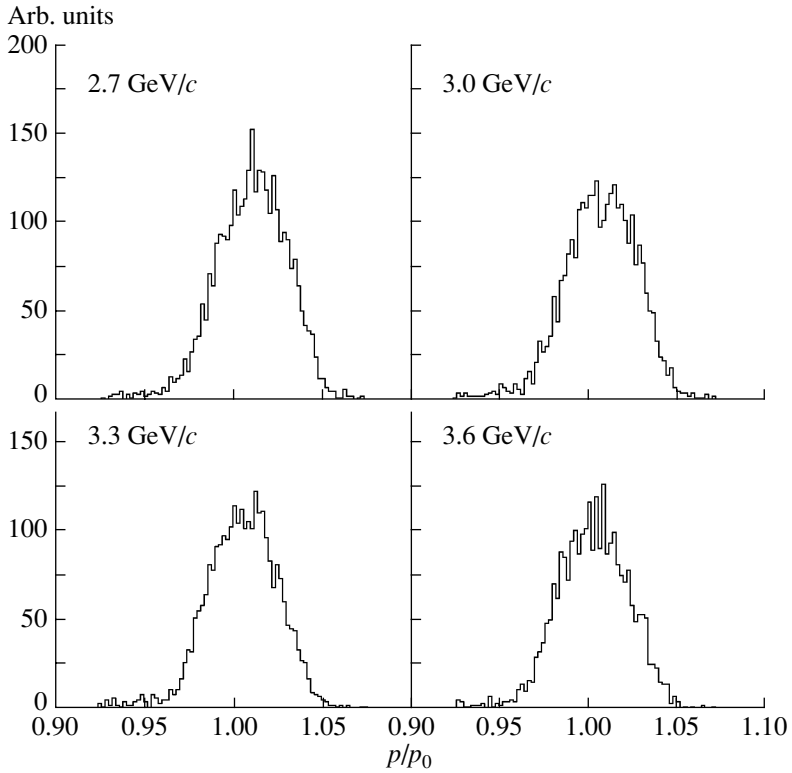

Fig. 3. Momentum acceptances for detecting secondary protons of momentum 2.7, 3.0, 3.3, and 3.6 GeV/c according to a Monte Carlo simulation.

This was done on the basis of the results of two independent measurements of the time of flight over the base of length about 28 m. The resolution in the time of flight was better than 0.2 ns (1σ). The background of inelastically scattered deuterons at 2.7 GeV/c was negligible, but it became more pronounced with increasing secondary-particle momentum. In data processing, we took into consideration only those events for which the results of both time-of-flight measurements met the chosen selection criteria. The correlations between the time-of-flight spectra obtained at four values of the secondary-particle momentum are shown in Fig. 4. They demonstrate a complete separation of secondary protons and deuterons.

The tensor analyzing power A_{yy} and the vector analyzing power A_y were calculated on the basis of the numbers n^+, n^-, and n^0 of protons recorded for the different beam polarization states at the same beam intensity. This was done by using the expressions

$$A_{yy} = 2\frac{p_z^-(n^+/n^0 - 1) - p_z^+(n^-/n^0 - 1)}{p_z^- p_{zz}^+ - p_z^+ p_{zz}^-}, \quad (1)$$

$$A_y = -\frac{2}{3}\frac{p_{zz}^-(n^+/n^0 - 1) - p_{zz}^+(n^-/n^0 - 1)}{p_z^- p_{zz}^+ - p_z^+ p_{zz}^-}.$$

Our experimental results for the tensor and vector analyzing powers are compiled in the table. The secondary-proton momenta, the values of the FWHM Δp for the momentum acceptance, and the values of the transverse momentum p_T and of the longitudinal-momentum fraction x according to the Monte Carlo simulation are also given there. Because of the energy loss in the target, the mean momentum of the primary deuteron beam was 4.977 GeV/c. It should be noted that, because of nuclear-interaction and multiple-scattering effects, the values of p_T differ from those that follow from the expression $p_T = p\sin\theta$ ($\theta = 178$ mrad). The errors quoted in the table are purely statistical; the possible systematic errors are estimated at about 5%.

3. THEORETICAL BACKGROUND

The expressions for calculating the tensor analyzing power for $A(d,p)X$ reactions were derived in [16] on the basis of the light-front-dynamics formalism, and various aspects of this approach were also discussed there. However, we believe that a brief discussion of its aspects concerning the analysis of new data is appropriate.

The mechanism of deuteron fragmentation, (d,p), can be represented by the Feynman diagrams in

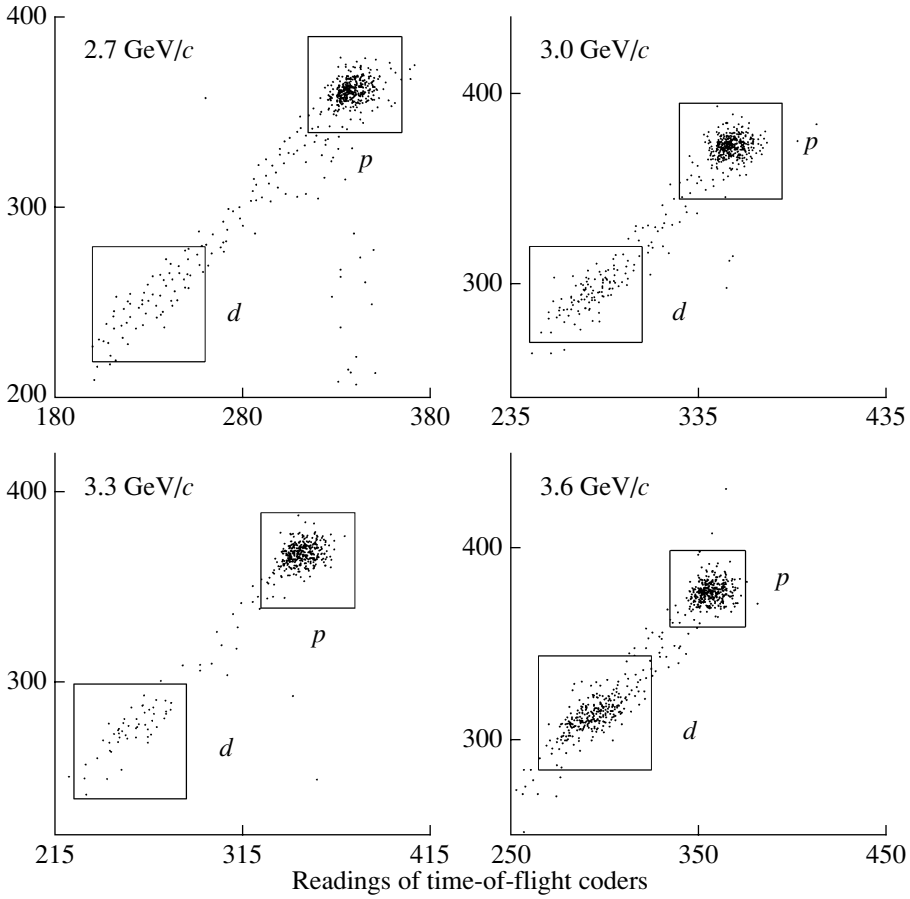

Fig. 4. Correlations between two independent measurements of the time of flight of particles for four momentum values (readings of the time-of-flight coders are plotted along the axes in arbitrary units).

Fig. 5. Here, d is the incident deuteron, p is the target proton, p_1 is the detected proton, b is a virtual (off-shell) nucleon, and p_2 and p_3 are nucleons. Apart from nucleons, one or a few pions can be produced in the lower vertices. The diagram in Fig. 5a corresponds to the case where one proton from the stripping reaction is detected and where neutron–proton scattering occurs in the lower vertex. In the diagrams in Figs. 5b and 5c, the lower vertices correspond to exchange neutron–proton and elastic proton–proton scattering.

The analyzing power $T_{\kappa q}$ for (d,p) reactions is given by the standard expression

$$T_{\kappa q} = \frac{\int d\tau \mathrm{tr}\{\mathcal{M}\cdot t_{\kappa q}\cdot \mathcal{M}^\dagger\}}{\int d\tau \mathrm{tr}\{\mathcal{M}\cdot \mathcal{M}^\dagger\}}. \qquad (2)$$

Here, $d\tau$ is a phase-space element; the operator $t_{\kappa q}$ is determined by the relation

$$\langle m|t_{\kappa q}|m'\rangle = (-1)^{1-m}\langle 1m1-m'|\kappa q\rangle,$$

where $\langle 1m1-m'|\kappa q\rangle$ is a Clebsch–Gordan coefficient; $\mathcal{M}$ is the reaction amplitude, while $\mathcal{M}^\dagger$ is its Hermitian conjugate counterpart; and the symbol tr denotes summation over the diagonal elements of the spin matrices.

Within light-front dynamics, the amplitude for the reaction $^1\mathrm{H}(d,p)X$ can be represented in the form

$$\mathcal{M} = \frac{\mathcal{M}(d\to p_1 b)}{(1-x)(M_d^2 - M^2(k))}\mathcal{M}(bp\to p_2p_3), \qquad (3)$$

where $\mathcal{M}(d\to p_1 b)$ is the amplitude describing deuteron breakup into the spectator proton p_1 and the off-shell particle b, while $\mathcal{M}(bp\to p_2p_3)$ is the amplitude for the reaction $bp\to p_2p_3$ (in the case of the diagram in Fig. 5a, an obvious change in the indices being made for the diagrams in Figs. 5b and 5c). The ratio

$$\psi(x,p_{1T}) = \frac{\mathcal{M}(d\to p_1 b)}{M_d^2 - M^2(k)} \qquad (4)$$

is nothing but the deuteron wave function in the (b,N) channel. In (4), p_{1T} is the p_1 component orthogonal to the z axis, while M_d is the deuteron mass. The light-front variables $p_T \equiv p_{1T}$ and x (the

Tensor analyzing power A_{yy} and vector analyzing power A_y for the reaction $^9\mathrm{Be}(d,p)X$ at an initial deuteron momentum of 4.977 GeV/c and at a proton emission angle of 178 mrad (here, p is the proton momentum in laboratory frame, Δp is the FWHM value for the momentum acceptance, and x and p_T are light-front variables; only the statistical errors are quoted)

p, GeV/c	Δp, GeV/c	x	p_T, GeV/c	$A_{yy} \pm \Delta A_{yy}$	$A_y \pm \Delta A_y$
2.728	0.058	0.537	0.490	0.030 ± 0.029	0.130 ± 0.041
3.021	0.062	0.591	0.544	0.158 ± 0.060	0.202 ± 0.048
3.315	0.067	0.646	0.597	0.081 ± 0.034	0.001 ± 0.048
3.610	0.072	0.701	0.651	0.133 ± 0.048	0.480 ± 0.067

deuteron-longitudinal-momentum fraction carried away by the proton in the infinite-momentum frame [27, 28]) are given by

$$x = \frac{E_p + p_L}{E_d + p_d}, \quad k = \sqrt{\frac{m_p^2 + \mathbf{p}_T^2}{4x(1-x)} - m_p^2}, \quad (5)$$

where E_d and p_d are the energy and the momentum of the incident deuteron, E_p and p_L are the proton energy and the longitudinal component of the momentum $\mathbf{p}_1$, and m_p is the nucleon mass. The quantity $M^2(k)$ is given by

$$M^2(k) = \frac{m_p^2 + p_{1T}^2}{x} + \frac{b^2 + p_{1T}^2}{1-x}, \quad (6)$$

where b^2 is the square of the invariant mass of the exchanged particle.

In [21], the general features of the spectra of protons originating from (d,p) reactions induced by unpolarized deuterons of initial momentum 9 GeV/c and having transverse momenta between 0.5 and 1 GeV/c were satisfactorily reproduced within light-front dynamics on the basis of the diagram in Fig. 5. In those calculations, the deuteron wave function was derived from the nonrelativistic wave function with the aid of a kinematical transformation from the variables of instant-form dynamics to the light-front variables. However, attempts at describing, within the same approach, the tensor analyzing power A_{yy} for the reaction $^{12}\mathrm{C}(d,p)X$ at an initial deuteron momentum of 9 GeV/c and a proton emission angle of 85 mrad proved to be futile [13]. It seems that a simple kinematical transition from the nonrelativistic deuteron wave function to the wave function within light-front dynamics takes no account of important features of the spin structure of the relativistic deuteron.

In [18], the relativistic deuteron wave function was derived within light-front dynamics. It can be expressed in terms of six functions $f_1, \ldots, f_6$ that are invariant under rotations and which depend on two scalar variables k and $z = \cos(\widehat{\mathbf{k}\,\mathbf{n}})$ determining the deuteron state. Its specific form is

$$\begin{aligned}\psi(\mathbf{k},\mathbf{n}) &= \frac{1}{\sqrt{2}}\boldsymbol{\sigma} f_1 + \frac{1}{2}\left[\frac{3}{k^2}\mathbf{k}(\mathbf{k}\cdot\boldsymbol{\sigma}) - \boldsymbol{\sigma}\right] f_2 \quad (7)\\ &+ \frac{1}{2}\big[3\mathbf{n}(\mathbf{n}\cdot\boldsymbol{\sigma}) - \boldsymbol{\sigma}\big] f_3 + \frac{1}{2k}\big[3\mathbf{k}(\mathbf{n}\cdot\boldsymbol{\sigma})\\ &+ 3\mathbf{n}(\mathbf{k}\cdot\boldsymbol{\sigma}) - 2\boldsymbol{\sigma}(\mathbf{k}\cdot\mathbf{n})\big] f_4 + \sqrt{\frac{3}{2}}\frac{i}{k}[\mathbf{k}\times\mathbf{n}] f_5\\ &+ \frac{\sqrt{3}}{2k}\big[[\mathbf{k}\times\mathbf{n}]\times\boldsymbol{\sigma}\big] f_6,\end{aligned}$$

where $\mathbf{k}$ is the nucleon momentum in the c.m. frame, $\mathbf{n}$ is a unit normal to the light-front plane, and $\boldsymbol{\sigma}$ are the Pauli matrices. The variable k was defined above, and

$$(\mathbf{n}\cdot\mathbf{k}) = \left(\frac{1}{2} - x\right)\sqrt{\frac{m_p^2 + \mathbf{p}_T^2}{x(1-x)}}. \quad (8)$$

As in [11, 15], the z axis is chosen to be antiparallel to the deuteron-beam axis, in which case $\mathbf{n} = (0,0,-1)$.

The final expression for the analyzing power has the form

$$\begin{aligned}T_{2q}\left(\frac{p_{10}d\sigma}{d\mathbf{p}_1}\right)_0 &= \frac{1}{2(2\pi)^3} \quad (9)\\ \times\Bigg\{&\frac{I(b,p)}{I(d,p)(1-x)^2}\rho_0(2,q)\sigma(bp\to p_2X)\\ &+ \int\frac{dyd\mathbf{p}_{2T}}{2y(1-y)}\frac{I(b,p)}{(1-y)I(d,p)}\rho_0(2,q)\\ &\times\frac{p_{20}d\sigma(bp\to p_2X)}{d\mathbf{p}_2}\left[1 + \mathbf{P}\langle\sigma\rangle\right]\Bigg\},\end{aligned}$$

where $I(b,p)$ and $I(d,p)$ are the invariant fluxes of the corresponding particles; $\langle\sigma\rangle$ is the vector analyzing power for nucleon–nucleon scattering; $\sigma(bp\to p_2X)$ is the total cross section for nucleon–nucleon scattering (it is independent of polarization); and $\mathbf{P}$

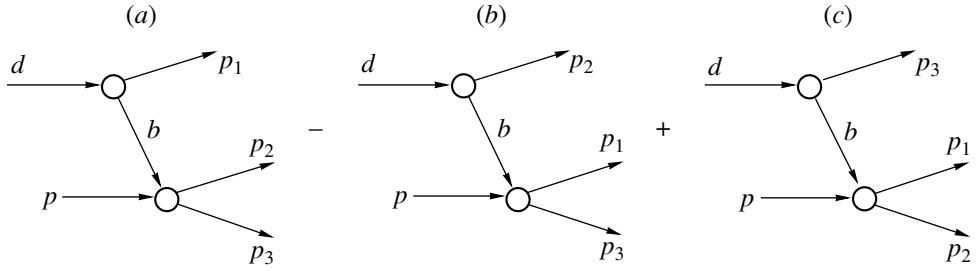

Fig. 5. Feynman diagrams for deuteron fragmentation on protons.

is the nucleon polarization vector in the deuteron, the nucleon polarization being characterized by the indices (κ, q),

$$\mathbf{P} = \frac{\mathrm{tr}\{\boldsymbol{\sigma}\rho(\kappa,q)\}}{\rho_0(\kappa,q)}. \tag{10}$$

The first term in the braced expression on the right-hand side of (9) corresponds to the detection of a spectator proton (diagram in Fig. 5*a*), while the second term corresponds to the detection of a proton originating from nucleon scattering on a target proton (diagrams in Figs. 5*b* and 5*c*). For an unpolarized beam, the invariant differential cross section appearing in (9) is given by

$$\left(\frac{p_{10}d\sigma}{d\mathbf{p}_1}\right)_0 = \frac{1}{2(2\pi)^3} \tag{11}$$
$$\times\left\{\frac{I(b,p)}{I(d,p)(1-x)^2}\rho_0\sigma(bp\to p_2X)\right.$$
$$+\int\frac{dyd\mathbf{p}_{2T}}{2y(1-y)}\frac{I(b,p)}{(1-y)I(d,p)}$$
$$\left.\times\,\rho_0\frac{p_{20}d\sigma(bp\to p_2X)}{d\mathbf{p}_2}\right\},$$

where

$$\rho_0 = 3[f_1^2+f_2^2+f_3^2+f_2f_3(3z^2-1) \tag{12}$$
$$+4f_4(f_2+f_3)z+f_4^2(z^2+3)+(f_5^2+f_6^2)(1-z^2)].$$

Upon introducing the density matrix in the spin space of the nucleon b for deuteron polarization characterized by the indices (κ, q),

$$\rho_{\mu\mu'}(\kappa,q) = \sum_{\nu,M,M'}\psi_M(\nu,\mu)(-1)^{1-M'} \tag{13}$$
$$\times\langle 1M1-M'|\kappa q\rangle\psi^*_{M'}(\nu,\mu') = \rho(\kappa,q)$$
$$= \frac{1}{2}\rho_0(\kappa,q)(1+\mathbf{P}\cdot\boldsymbol{\sigma}),$$

the traces of the density matrices can be calculated by using the relations

$$\rho_0(\kappa,q) = \mathrm{tr}\{\rho(\kappa,q)\} = \sum\psi_M(\nu,\mu) \tag{14}$$
$$\times\langle 1M1-M'|\kappa q\rangle\psi^*_{M'}(\nu,\mu').$$

The expressions for the traces of the density matrices $\rho_0(2,0)$ and $\rho_0(2,2)$ are rather cumbersome; they are presented in [16] and in the Appendix. The density matrix $\rho_0(y,y)$ necessary for calculating the tensor analyzing power A_{yy} can be derived from the relation

$$\rho_0(y,y) = -\frac{1}{\sqrt{2}}\rho_0(2,0)-\sqrt{3}\rho_0(2,2).$$

4. COMPARISON OF THEORETICAL AND EXPERIMENTAL RESULTS

It should be emphasized that the calculation of the tensor analyzing power by formula (9) does not involve free parameters. The invariant differential cross sections $p_{20}d\sigma(bp\to p_2X)/d\mathbf{p}_2$ for the processes occurring in the lower vertices of the pole diagrams in Fig. 5 and the invariant functions $f_1,...,f_6$ appear here as input data. The contributions of the elastic and inelastic processes $pp\to pp$, $np\to pn$, $Np\to p\Delta$, and $Np\to pN\pi$ (up to the $N\pi$ invariant mass of 1.5 GeV/c^2) in the lower vertices of the pole diagrams were taken into account in accordance with the parametrizations proposed in [29]. In addition, it should be borne in mind that particle b is off the mass shell. The virtuality of particle b was taken into account in the calculations through the use of analytic continuations of the parametrizations of $d\sigma(s',t')/dt'$ to $s'=(b+p)^2$ and $t'=(b-p_1)^2$ for $b^2\neq m^2$. The $f_i(k,z)$ values necessary for the calculations were obtained by means of a spline interpolation between the values tabulated in [18].

In Fig. 6, the results of the calculations for the tensor analyzing power A_{yy} in the reaction where the fragmentation of 5-GeV/c deuterons on beryllium nuclei is accompanied by the emission of protons at an angle of 178 mrad are contrasted against our experimental data. One can see that the results of the calculations with Karmanov's wave function agree rather well with the experimental data, but that the curves calculated by using the standard deuteron wave functions corresponding to the Paris

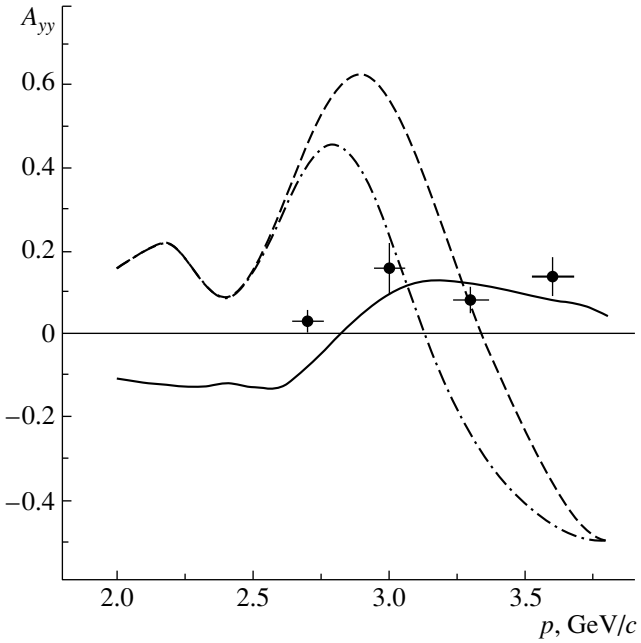

Fig. 6. Tensor analyzing power A_{yy} for the reaction $^9\mathrm{Be}(d,p)X$ at an initial deuteron momentum of 5 GeV/c and a proton-emission angle of 178 mrad as a function of the proton momentum. The points represent experimental data. The curves correspond to the calculations performed with the deuteron wave functions for (dash-dotted curve) the Paris potential [30] and (dashed curve) the Bonn charge-dependent potential [31] and (solid curve) with the relativistic deuteron wave function from [18].

potential [30] and the Bonn charge-dependent potential [31] are in sharp contradiction with the experimental data, changing sign at a proton momentum of about 3.2 GeV/c. In this connection, we note that the calculations performed in [16] within the approach described here led to a qualitative description of the data on the tensor analyzing power A_{yy} for the reaction $^9\mathrm{Be}(d,p)X$ at an initial deuteron momentum of 4.5 GeV/c and a proton emission angle of 85 mrad and to satisfactory agreement with the analogous data for the reaction $^{12}\mathrm{C}(d,p)X$ at 9 GeV/c. The new data obtained in the present study provide an additional piece of evidence in favor of the approach proposed in [16].

Finally, we will touch upon the question of why the disagreement between the theoretical description and the experimental data on T_{20} is considerably smaller in the case of elastic electron–deuteron scattering (see, for example, [32]) than in the case of elastic dp scattering [10] and in the case of inclusive deuteron breakup on nuclei [14] if they are analyzed in the impulse approximation. Of course, this difference stems from the inapplicability of the impulse approximation to describing hadronic reactions involving accelerated deuterons. In our opinion, a transition to the infinite-momentum frame is a key point in the approach that we use, this giving rise to the dependence of the deuteron wave function on an additional nontrivial variable and making it possible to take effectively into account reaction mechanisms beyond the impulse approximation.

5. CONCLUSIONS

The basic results of this study are as follows.

New experimental data on the vector analyzing power A_y and the tensor analyzing power A_{yy} for the reaction $^9\mathrm{Be}(d,p)X$ at an initial deuteron momentum of 5 GeV/c and a proton emission angle of 178 mrad have been obtained. The calculation of the tensor analyzing power for (d,p) reactions within light-front dynamics on the basis of the relativistic deuteron wave function derived by Carbonell and Karmanov [18] has led to results that are in good agreement with our new experimental data. On the other hand, the results of the calculations with the nonrelativistic deuteron wave functions are in sharp contradiction with the experimental data.

The new data favor the point of view [16] that the relation between the longitudinal and transverse components of the internal momentum in a moving deuteron differs significantly from the relation that holds in the nonrelativistic case. It seems that the relativization method proposed in [20] reflects this relation correctly, at least, up to $p_T \sim 0.7$ GeV/c.

It turns out, quite unexpectedly, that, up to short internucleon distances corresponding to internucleon momenta of $k \sim 0.5$–0.8 GeV/c, the deuteron can be treated within light-front dynamics as a two-nucleon system, as was indicated in [21]. In the deuteron-fragmentation process, relativistic effects come into play at rather low energies, and it is the use of light-front dynamics that makes it possible to take these effects into account in the simplest way.

ACKNOWLEDGMENTS

We are grateful to the personnel of the accelerator complex at the Laboratory of High Energies (JINR) and to the team of the POLARIS polarized-deuteron source for providing good conditions for performing our experiment.

This work was supported in part by the Russian Foundation for Basic Research (project no. 03-02-16224).

APPENDIX

The traces $\rho_0(\kappa, q)$ of the density matrices for the analyzing powers T_{20} and T_{22} are given by [16]

$$\rho_0(2,0) = \frac{1}{\sqrt{6}}(\psi\psi^\dagger - 3\psi_z\psi_z) \qquad \text{(A.1)}$$

$$= -3f_3^2 - 12f_3f_4z + 3f_2^2z^2 - 12f_4^2z^2 - 6f_2^2z^4$$
$$- 1.5f_2^2(1-z^2) - 4.5f_4^2(1-z^2) + 3f_5^2(1-z^2)$$
$$- 15.5885f_4f_6(1-z^2) - 1.5f_6^2(1-z^2)$$
$$- 3f_2^2z^2(1-z^2) + 3f_2^2(1-z^2)^2 - 8.48528f_1f_3$$
$$- 16.9706f_1f_4z - 4.24264f_1f_2z^2$$
$$- 4.24264f_1f_2z^4 + 2.12132f_1f_2(1-z^2)$$
$$- 2.12132f_1f_2z^2(1-z^2)$$
$$+ 2.12132f_1f_2(1-z^2)^2 - 6f_2f_3z^4 - 12f_2f_4z^5$$
$$+ 4.5f_2f_3(1-z^2) + 4.5f_2f_4z(1-z^2)$$
$$- 7.79423f_2f_6z(1-z^2) - 7.5f_2f_3z^2(1-z^2)$$
$$- 19.5f_2f_4z^3(1-z^2) - 7.79423f_2f_6z^3(1-z^2)$$
$$- 1.5f_2f_3(1-z^2)^2 - 7.5f_2f_4z(1-z^2)^2$$
$$- 7.79423f_2f_6z(1-z^2)^2;$$

$$\rho_0(2,2) = \frac{1}{2}(\psi_x\psi_x^\dagger - \psi_y\psi_y^\dagger) \qquad \text{(A.2)}$$

$$= 1.06066f_1f_2(1-z^2) - 0.75f_2^2(1-z^2)$$
$$+ 2.25f_4^2(1-z^2) - 1.5f_5^2(1-z^2)$$
$$- 2.59808f_4f_6(1-z^2) + 0.75f_6^2(1-z^2)$$
$$+ 1.06066f_1f_2z^2(1-z^2) + 1.5f_2^2z^2(1-z^2)$$
$$+ 1.06066f_1f_2(1-z^2)^2 + 1.5f_2^2(1-z^2)^2$$
$$- 0.75f_2f_3(1-z^2) + 0.75f_2f_4z(1-z^2)$$
$$- 1.29904f_2f_6z(1-z^2) - 0.75f_2f_3z^2(1-z^2)$$
$$+ 0.75f_2f_4z^3(1-z^2) - 1.29904f_2f_6z^3(1-z^2)$$
$$- 0.75f_2f_3(1-z^2)^2 + 0.75f_2f_4z(1-z^2)^2$$
$$- 1.29904f_2f_6z(1-z^2)^2.$$

REFERENCES

1. J. Arvieux *et al.*, Phys. Rev. Lett. **50**, 19 (1983); Nucl. Phys. A **431**, 613 (1984).
2. C. F. Perdrisat *et al.*, Phys. Rev. Lett. **59**, 2840 (1987); V. Punjabi *et al.*, Phys. Rev. C **39**, 608 (1989).
3. E. Cheung *et al.*, Phys. Lett. B **284**, 210 (1992).
4. V. Punjabi *et al.*, Phys. Lett. B **350**, 178 (1995).
5. V. G. Ableev *et al.*, Pis'ma Zh. Éksp. Teor. Fiz. **47**, 558 (1988) [JETP Lett. **47**, 649 (1988)]; Kratk. Soobshch. OIYaI, No. 4[43]-90, 5 (1990).
6. T. Aono *et al.*, Phys. Rev. Lett. **74**, 4997 (1995).
7. L. S. Azhgirey *et al.*, Phys. Lett. B **387**, 37 (1996).
8. A. A. Nomofilov *et al.*, Phys. Lett. B **325**, 327 (1994).
9. B. Kuehn *et al.*, Phys. Lett. B **334**, 298 (1994); L. S. Azhgirey *et al.*, Kratk. Soobshch. OIYaI, No. 3[77]-96, 23 (1996).
10. L. S. Azhgirey *et al.*, Phys. Lett. B **391**, 22 (1997); Yad. Fiz. **61**, 494 (1998) [Phys. At. Nucl. **61**, 432 (1998)].
11. L. S. Azhgirey and N. P. Yudin, Yad. Fiz. **57**, 160 (1994) [Phys. At. Nucl. **57**, 151 (1994)].
12. C. E. Carlson, J. R. Hiller, and R. J. Holt, Annu. Rev. Nucl. Part. Sci. **47**, 395 (1997).
13. S. V. Afanasiev *et al.*, Phys. Lett. B **434**, 21 (1998).
14. V. P. Ladygin *et al.*, Few-Body Syst. **32**, 127 (2002); L. S. Azhgirey *et al.*, Yad. Fiz. **66**, 719 (2003) [Phys. At. Nucl. **66**, 690 (2003)].
15. L. S. Azhgirey and N. P. Yudin, nucl-th/0212033.
16. L. S. Azhgirey and N. P. Yudin, Yad. Fiz. **68**, 163 (2005) [Phys. At. Nucl. **68**, 160 (2005)]; nucl-th/0311052.
17. P. A. M. Dirac, Rev. Mod. Phys. **21**, 392 (1949).
18. J. Carbonell and V. A. Karmanov, Nucl. Phys. A **581**, 625 (1995).
19. V. A. Karmanov and A. V. Smirnov, Nucl. Phys. A **575**, 520 (1994).
20. J. Carbonell *et al.*, Phys. Rep. **300**, 215 (1998).
21. L. S. Azhgirey *et al.*, Nucl. Phys. A **528**, 621 (1991); L. S. Azhgireĭ *et al.*, Yad. Fiz. **46**, 1134 (1987) [Sov. J. Nucl. Phys. **46**, 661 (1987)]; **53**, 1591 (1991) [**53**, 977 (1991)].
22. L. S. Azhgirey *et al.*, Yad. Fiz. **62**, 1796 (1999) [Phys. At. Nucl. **62**, 1673 (1999)].
23. V. P. Ladygin *et al.*, Eur. Phys. J. A **8**, 409 (2000).
24. N. G. Anishchenko *et al.*, in *Proceedings of 5th International Symposium on High Energy Spin Physics, Brookhaven, 1982*; AIP Conf. Proc. **95**, 445 (1983).

25. L. S. Zolin *et al.*, Kratk. Soobshch. OIYaI, No. 2[88]-98, 27 (1998).
26. L. S. Azhgirey *et al.*, Prib. Tekh. Éksp., No. 1, 51 (1997) [Instrum. Exp. Tech., No. 1, 43 (1997)]; Nucl. Instrum. Methods Phys. Res. A **497**, 340 (2003).
27. I. A. Schmidt and R. Blankenbecler, Phys. Rev. D **15**, 3321 (1977).
28. Ch.-Y. Wong and R. Blankenbecler, Phys. Rev. C **22**, 2433 (1980).
29. L. S. Azhgireĭ, S. V. Razin, and N. P. Yudin, Yad. Fiz. **46**, 1657 (1987) [Sov. J. Nucl. Phys. **46**, 988 (1987)].
30. M. Lacombe *et al.*, Phys. Lett. B **101B**, 139 (1981).
31. R. Machleidt, Phys. Rev. C **63**, 024001 (2001).
32. R. Gilman and F. Gross, nucl-th/0111015.

Translated by A. Isaakyan

Physics of Atomic Nuclei, Vol. 68, No. 12, 2005, p. 2139. Translated from Yadernaya Fizika, Vol. 68, No. 12, 2005, p. 2201.

OBITUARY

Leonid Grigor'evich Landsberg
December 23, 1930–September 13, 2005

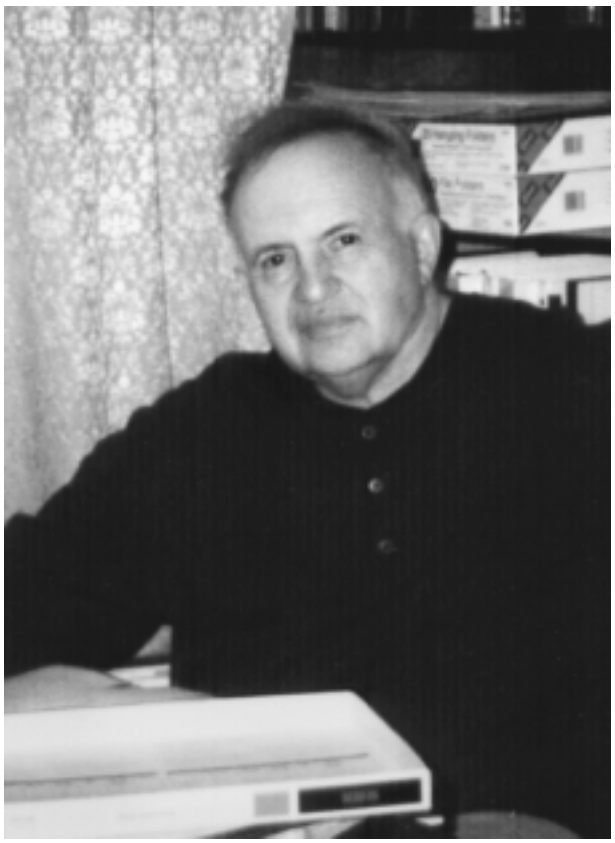

Russian science suffers a heavy blow.

On September 13, 2005, Professor Leonid Grigor'evich Landsberg, eminent scientist, outstanding experimental physicist, head of a laboratory at the Institute for High Energy Physics (IHEP, Protvino), and Honored Scientist of the Russian Federation, passed away after a serious and long illness. He was a man who lived for science and gave it all his remarkable talent and fiery temperament.

After graduating from Moscow State University with honors in 1954, Landsberg began his scientific activity at the Institute of Theoretical and Experimental Physics (ITEP, Moscow) under the supervision of Academician A.I. Alikhanov. In 1963, he obtained his candidate's degree in physics and mathematics. In 1966, Landsberg moved to IHEP, where he headed the Laboratory of Experimental Physics for almost 40 years.

Landsberg never interrupted his scientific collaboration with ITEP. In 1973, he obtained a doctorate degree in physics and mathematics. In 1976, he was nominated a professor in experimental physics.

Landsberg was a man of inexhaustible inquisitiveness and cherished interest in a wide variety of topics. In particular, he was involved in searches for antimatter, heavy quasistable leptons, and free quarks and in investigations of elastic $\pi^- p$, $K^- p$, and $\bar{p}p$ scattering and deep-inelastic scattering of pions and muons on nucleons. Landsberg also sought rare muon and kaon decays and studied radiative decays of light mesons and hyperons, electromagnetic transition form factors of neutral mesons, and the production of J/ψ particles and charmed baryons. Searches for exotic mesons and baryons were also the subject of his studies. He headed work on the creation of the widely known facilities LEPTON and SPHINX and directly participated in this work. Also, Landsberg was deeply involved in the international experiments SELEX, CKM, E949, and KAMI.

Landsberg had great stamina and courage. Despite serious illness, he continued working on the article devoted to rare kaon decays to the extremes; the final version of this article was submitted for publication in *Physics of Atomic Nuclei* on the day of his death.

Landsberg is the author of more than 200 scientific studies. Two series of his investigations were included in the USSR Public Register of Scientific Discoveries. Many of his scientific results were renowned worldwide. In 1996, Landsberg was a recipient of the Main Prize of the MAIK "Nauka/Interperiodica" competition for the best scientific study. His disciples include a corresponding member of the Russian Academy of Sciences and many doctors and candidates of sciences.

The personnel of IHEP and ITEP mourn the untimely death of the brilliant physicist, generous personality, and kind and considerate friend and condole with his family and relatives.

Physics of Atomic Nuclei, Vol. 68, No. 12, 2005, pp. 2140–2146. Translated from Yadernaya Fizika, Vol. 68, No. 12, 2005, pp. 2202–2208.

FUTURE PUBLICATIONS

Observation of Multiparton Interactions in Proton–Nucleus Collisions at an Energy of 70 GeV

V. V. Abramov, A. A. Volkov, P. I. Goncharov, A. V. Korablev, Yu. P. Korneev, A. V. Kostritskii, A. N. Krinitsyn, V. I. Kryshkin, A. A. Markov, V. V. Talov, and L. K. Turchanovich

The production of noncoplanar hadron pairs in proton–nucleus interactions was studied experimentally for the case where the transverse momenta of product particles is in excess of 1 GeV/c. The values obtained for the exponent in the A dependence for noncoplanar hadron pairs are substantially greater than those for coplanar pairs. This nuclear-mass-number dependence for the production of hadron pairs can be explained by the contribution of multiparton interactions in proton–nucleus collisions.

Majorana Neutrinos in Rare Meson Decays

A. Ali, A. V. Borisov, and M. V. Sidorova

The rare meson decays $K^+ \to \pi^-\ell^+\ell'^+$ and $D^+ \to K^-\ell^+\ell'^+$ ($\ell, \ell' = e, \mu$), which are induced by Majorana neutrino exchange and which do not conserve the lepton number, are considered. The effects of the meson structure are taken into account on the basis of the Gaussian model for the respective Bethe–Salpeter amplitudes. It is shown that existing direct experimental constraints on the decay branching ratios are overly lenient and therefore give no way to set realistic limits on effective Majorana masses. On the basis of the constraints on the lepton-mixing parameters and neutrino masses from precision measurements of electroweak processes, neutrino-oscillation experiments, searches for neutrinoless double-beta decay of nuclei, and cosmological data, indirect constraints on the branching ratios for the decays in question are obtained and found to be much more stringent than the above direct constraints.

Resonances in the $\omega\omega$ System

D. V. Amelin, D. V. Bagg, Yu. G. Gavrilov, Yu. P. Guz, V. A. Dorofeev, R. I. Dzhelyadin, A. M. Zaitsev, A. V. Zenin, A. V. Ivashin, I. A. Kachaev, V. V. Kabachenko, A. N. Karyukhin, A. N. Kohoplyannikov, V. F. Konstantinov, V. V. Kostyukhin, V. D. Matveev, V. I. Nikolaenko, A. P. Ostankov, B. F. Polyakov, D. I. Ryabchikov, A. A. Solodkov, A. V. Solodkov, O. V. Solov'yanov, E. A. Starchenko, A. B. Fenyuk, and Yu. A. Khokhlov

The results of a partial-wave analysis of the reaction $\pi^- p \to \omega\omega n$ observed with the aid of the VES facility at the Institute for High Energy Physics (IHEP, Protvino) are presented. The behavior of the $J^{PC} = 2^{++}$ amplitudes in the $\omega\omega$ system is described by using the $f_2(1565)$ resonance of mass $M = 1.590 \pm 0.010$ GeV and width $\Gamma = 0.140 \pm 0.011$ GeV and the $f_2(1910)$ resonance of mass $M = 1.890 \pm 0.010$ GeV and width $\Gamma = 0.165 \pm 0.019$ GeV. The decay $f_4(2050) \to \omega\omega$ is observed, the respective parameters being $M = 1.960 \pm 0.015$ GeV and $\Gamma = 0.290 \pm 0.020$ GeV.

Nuclear Effects in the Production of Lepton Pairs in Hadron–Nucleus Collisions

Ya. A. Berdnikov, M. E. Zavatsky, V. T. Kim, V. F. Kosmach, M. M. Ryzhinsky, and V. M. Samsonov

The results of experimental investigations of muon-pair production via the Drell–Yan process in pBe and pW collisions at 800 GeV on a target at rest are analyzed. The ratios of the inclusive differential cross sections for the production of lepton pairs are calculated. It is shown that agreement between the results of the calculations and experimental data is improved upon taking into account multiple soft rescatterings of an incident-hadron quark within the target nucleus.

1063-7788/05/6812-2140$26.00

Role of the Parton Charges and Masses in the Exclusive Production of Meson Pairs in Photon–Photon Collisions

A. V. Berezhnoy and A. K. Likhoded

Within the QCD parton model, the exclusive production of kaon pairs in photon–photon collisions is analyzed under the kinematical conditions of the BELLE experiment. The differential cross section for this process is studied as a function of the parton masses and charges and the form of the kaon wave function.

Investigation of Special Features of the Neutron and Proton Shell Structure of the $^{90-96}$Zr Isotopes

O. V. Bespalova, I. N. Boboshin, V. V. Varlamov, T. A. Ermakova, B. S. Ishkhanov, E. A. Romanovskii, T. I. Spasskaya, and T. P. Timokhina

The neutron and proton single-particle energies and the occupation probabilities for the valence states of the even–even isotopes ^{90,92,94,96}Zr are determined by matching data on nucleon-stripping and nucleon-pickup reactions on the same nucleus. The data obtained in this way suggest the magicity of the number $N = 56$ for $Z = 40$. The single-particle energies of all bound neutron and proton states in the ^{90,92,94,96}Zr nuclei were described within the experimental errors on the basis of the dispersive optical model.

Calculation of the Nuclear Vertex Constant (Asymptotic Normalization Factor) for the Virtual Decay ^{6}Li $\to \alpha + d$ on the Basis of the Three-Body Model and the Application of the Result to Describing the Astrophysical Nuclear Reaction $d(\alpha,\gamma)^6$Li at Ultralow Energies

L. D. Blokhintsev, S. B. Igamov, M. M. Nishonov, and R. Yarmukhamedov

Within the (α, n, p) three-body model, the s-wave $^6\mathrm{Li} \to \alpha + d$ vertex constant G_{01} and the asymptotic factor C_{01} for the wave function describing the ^{6}Li nucleus in the $\alpha + d$ channel (these two quantities are proportional to each other) are calculated by solving Faddeev equations for various sets of nucleon–nucleon and αN potentials. The resulting values of G_{01} and C_{01} are used to calculate the astrophysical factor $S(E)$ for the radiative-capture reaction $d(\alpha,\gamma)^6$Li at energies in the range $E = 0$–600 keV. The calculated values of G_{01} and C_{01} appear to be sensitive to the form of the pair potentials used. It is shown that, upon correctly taking into account the contributions of the $E2$ and $E1$ multipolarities, the values of $S(E)$ in the region $E < 150$ keV are determined primarily by the values of C_{01} and of ^{6}Li binding energy in the $\alpha + d$ channel.

Asymmetry of Angular Distributions of Products of "Direct + Semidirect" Photoneutron Reactions in the Region of an Isovector Giant Quadrupole Resonance

M. L. Gorelik, B. A. Tulupov, and M. G. Urin

A semimicroscopic approach based on the random-phase approximation taking exactly into account a single-particle continuum and on a phenomenological description of the fragmentation effect is used to describe basic properties of an isovector giant quadrupole resonance. The same approach is employed to perform a quantitative analysis of the asymmetry in the angular distributions of products of "direct + semidirect" photoneutron reactions in the region of such a resonance. The results of the calculations performed for the target nucleus ^{208}Pb are compared with available experimental data.

Excited States of ^{176}Hf

E. P. Grigoriev

The properties of the excited levels of the even–even deformed nucleus ^{176}Hf are analyzed on the basis of available experimental data on ^{176}Ta decay. Thirty-nine new states are included in the energy-level diagram of the ^{176}Hf nucleus. The deexcitation of a number of known levels is supplemented with new transitions.

New levels are included in three rotational bands, and the $K_i = 0_4^+$ band is identified. The 2470.95-keV level is considered as a two-phonon quadrupole–octupole state. A strong interplay of states belonging to different bands is indicated. The Coriolis interaction is calculated for pairs of $K^\pi = 0^-$ and 1^-, 0^+ and 2^+, and 2^+ and 3^+ bands. The interaction parameters are found. It is shown that the sets of positive- and negative-parity states are related by $E1$ transitions characterized by large hindrance factors.

Multipole Mixtures in Gamma Transitions of ^{154}Sm from the $(n, n'\gamma)$ Reaction

A. M. Demidov, L. I. Govor, V. A. Kurkin, and I. V. Mikhailov

The angular distributions of photons from the reaction $^{154}\mathrm{Sm}(n, n'\gamma)$ is measured with respect to the beam of fast reactor neutrons. The known diagram of energy levels and gamma transitions in the ^{154}Sm nucleus is supplemented. The multipole-mixing ratios δ are found for many gamma transitions.

Nuclear-Level Densities in the Vicinity of $Z = 50$ from the Evaporated-Neutron Spectra in (p, n) Reactions

B. V. Zhuravlev, A. A. Lychagin, and N. N. Titarenko

Excitation functions, spectra, and angular distributions of neutrons from the (p, n) reactions on the isotopes ^{116}Sn, ^{118}Sn, ^{122}Sn, and ^{124}Sn were measured in the proton-energy range 7–11 MeV. The measurements were performed by the time-of-flight method with the aid of the fast-neutron spectrometer over the base of the rechargeable pulsed accelerator EGP-15 of the Institute of Physics and Power Engineering (Obninsk). A high resolution (about 0.6 ns/m) and stability of the spectrometer in the time of flight made it possible to identify reliably low-lying levels along with the continuum section of neutron spectra. The data obtained in this way were analyzed on the basis of the statistical equilibrium and preequilibrium models of nuclear reactions. The calculations were performed with the aid of the precise Hauser–Feshbach formalism of statistical theory. The nuclear-level densities in the isotopes ^{116}Sb, ^{118}Sb, ^{122}Sb, and ^{124}Sb were determined, along with their energy dependences and model parameters. In the excitation-energy range 0–2 MeV, the energy dependences of the nuclear-level densities exhibit a structure that is associated with the nonuniformities of the spectrum of single-particle states near filled shells. The isotopic dependence of the nuclear-level density is discovered and explained. It is also shown that the data obtained here for the nuclear-level density differ markedly from the predictions of model systematics of nuclear-level densities.

On the Contribution of a Chiral Scalar to the Cross Sections for the Reactions $pp \to pp\pi^+\pi^-$ and $pn \to pn\pi^+\pi^-$ near the Threshold

D. A. Zaikin and I. I. Osipchuk

A simple estimate of the cross sections for the reactions $pp \to pp\pi^+\pi^-$ and $pn \to pn\pi^+\pi^-$ is given with allowance for the contribution of a nonlinear chiral scalar field. The reaction amplitudes are calculated in the threshold approximation. The final-state interaction of nucleons is taken into account in calculating the cross sections in question. A comparison of the results of the calculations with experimental data leads to the conclusion that the contribution of the chiral scalar to the cross sections for reactions under consideration is quite sizable.

QCD Sum Rules for $g_{\eta\Lambda\Lambda}$ and $g_{\pi\Lambda\Sigma}$

V. S. Zamiralov, A. Özpineci, and S. B. Yakovlev

New relations between the Borel QCD sum rules for the Σ^0- and Λ-hyperon strong coupling constants are derived. It is shown that, using the sum rules for $g_{\mathcal{M}\Sigma\Sigma}$, $\mathcal{M} = \pi^0, \eta$, as a starting point, one can directly obtain the corresponding sum rules for the coupling constants $g_{\eta\Lambda\Lambda}$ and $g_{\pi\Lambda\Sigma}$. The values of these constants are calculated in a specific parameter region.

Vector Analyzing Power in π^{+7}Li Scattering in the Region of the Δ_{33} Resonance

E. T. Ibraeva, M. A. Zhusupov, A. Yu. Zaikin, and O. Imambekov

Within the Glauber diffraction theory, the vector analyzing power iT_{11} is calculated at three energies of positively charged pions: 134, 164, and 194 MeV. These energy values lie in the region of the Δ_{33} resonance in $\pi^{\pm}N$ interaction, the resonance maximum being at 180 MeV. The calculation of iT_{11} was performed with several model ^{7}Li wave functions, including αt-cluster and shell-model ones. The properties of π^{+7}Li scattering are found to be sensitive to the structural features of the target nucleus. A comparison of the results of the calculations with experimental data shows that the wave functions in question and the potentials used to calculate them are quite appropriate.

Resonance Conversion as the Main Channel of the Decay of the 3.5-eV Isomer in ^{229m}Th

F. F. Karpeshin and M. B. Trzhaskovskaya

On the basis of calculations performed within the relativistic multiconfiguration Dirac–Fock method, it is shown that the probability of the decay of the 3.5-eV nuclear level in the ^{229m}Th isomer via resonance conversion exceeds the probability of its direct radiative decay at least by a factor of about 600. The possibility of experimentally observing delayed soft photons or alpha particles in the decay of this isomer is discussed.

Deficit of the Calculated Muon Flux at Sea Level for $E_\mu \gtrsim 100$ GeV: Analysis of Possible Reasons

A. A. Lagutin A. G. Tyumentsev, and A. V. Yushkov

The reasons why the deficit of the calculated muon flux for $E_\mu \gtrsim 100$ GeV arises if use is made of data from direct measurements of the spectra of primary cosmic rays and present-day nuclear-interaction models are considered. It is shown that this problem may stem from significantly underestimating the primary-nucleon flux in balloon experiments employing the technique of emulsion chambers. This procedure relies on an extrapolation of accelerator data; therefore, it is necessary to estimate, on the basis of various Reggeon models of hadron interactions, the systematic error introduced by this circumstance in the results of the measurements. Such an analysis would make it possible to refine the behavior of the spectra of primary cosmic rays, to reduce the methodological part of the error in the calculation of the fluxes of secondary cosmic rays in the atmosphere, and to draw more precise conclusions on the flaws in present-day interaction models without invoking new accelerator data.

Spectrum of Muons at Sea Level in the Energy Range 1–10 TeV according to Data from Underground Experiments

A. A. Lagutin and A. V. Yushkov

Within a conjugate approach, the properties of the muon component in various types of rock and in water are calculated with allowance for fluctuations of energy losses in all muon-interaction processes. The behavior of the muon spectrum at sea level is established on the basis of a comparison of the muon-absorption curves obtained in this way and experimental data from underground facilities. It is shown that the deficit of the calculated muon flux obtained with the aid of data from direct measurements of the spectra of primary nuclei and Reggeon models of nuclear interactions is not less than 50% in the energy range 1–10 TeV.

Polarization in Quasielastic $(p, 2p)$ Scattering on a ^{4}He Nucleus at an Energy of 1 GeV

O. V. Miklukho, G. M. Amal'skii, V. A. Andreev, S. L. Belostotskii, D. O. Veretennikov, Yu. V. Elkin, A. A. Zhdanov, A. A. Izotov, A. Yu. Kiselev, A. I. Kovalev, L. M. Kochenda, M. P. Levchenko, A. N. Prokof'ev, D. A. Prokof'ev, V. Yu. Trautman, V. A. Trofimov, S. I. Trush, O. Ya. Fedorov, A. V. Shvedchikov, T. Noro, Kh. Sakaguchi, and K. Khatanaka

The polarization of secondary protons from the $(p, 2p)$ reaction on a ^{4}He nucleus at a projectile-proton energy of 1 GeV was measured in a kinematically complete experiment. By using a two-arm magnetic spectrometer, two secondary protons were detected in coincidence at unequal scattering angles of $\Theta_1 = 18°–24.21°$ and $\Theta_2 = 53.22°$ over a broad range of residual-nucleus momentum K_B between zero and

150 MeV/c. It was found that the polarization of either secondary proton is less than the polarization in elastic proton–proton scattering. The magnitude of this difference is determined by the mean binding energy of the S-wave proton rather than by the mean effective nuclear density. The results are presented that were obtained by measuring polarization in the quasielastic and elastic scattering of 1-GeV photons on a ^{4}He nucleus in the angular range $\Theta_1 = 18^\circ - 24.21^\circ$.

Role of Antisymmetrization in Describing the Excitation of the $1^+, T = 1$ Level in the ^{12}C Nucleus by Polarized Protons

M. S. Onegin

Inelastic polarized-proton scattering involving the excitation of the $1^+, T = 1$ level at 15.11 MeV in the ^{12}C nucleus is described within the distorted-wave method. The effect of completely or approximately taking into account the antisymmetrization of the wave function for the *incident proton–intranuclear nucleons* system on various observables, including the differential reaction cross section, the analyzing power, the difference of the polarization and analyzing power, and the depolarization parameter, is analyzed. The difference of the polarization and the analyzing power in the case of the excitation of anomalous-parity levels is shown to be highly sensitive to taking into account the above antisymmetrization. The reason for a large value of this difference for the level being studied and the sensitivity of this value to the parameters of the effective nucleon–nucleon interaction used are analyzed.

Effective-Range Function for Doublet *nd* Scattering from an Analysis of Present-Day Data

Yu. V. Orlov and L. I. Nikitina

The parameters of the generalized effective-range function $K(k^2)$ having a pole are found from the results of the calculation of the S-wave phase shift $\delta(E)$ for doublet nd scattering and the triton binding energy on the basis of Faddeev equations and within the N/D method. The convergence of the expansion of $K(k^2)$ in powers of the momentum is studied. The binding energy of the virtual triton and the residues of the scattering amplitudes at the poles corresponding to the bound and virtual states are calculated. Correlations between the binding energies of the bound and virtual states of the triton, on one hand, and the doublet scattering length for nd interaction, on the other hand, are considered. The function $K(k^2)$ is also calculated for a two-body model featuring various potentials.

Doublet Coulomb–Nucleus Scattering Length and Other Parameters of the Effective-Range Function for *pd* Scattering from an Analysis of Present-Day Data

Yu. V. Orlov and Yu. P. Orevkov

Parameters of the effective-range function $K(k^2)$ having a pole are found from the results that are obtained by calculating the S-wave phase shifts for doublet pd scattering and the binding energies of three-nucleon nuclei on the basis of Faddeev equations and within the N/D method and which are known from the literature. The convergence of the expansion of $K(k^2)$ in powers of the momentum is studied. The energy of the pd resonance corresponding to the virtual state of the triton is calculated.

Effect of β Decay to Bound States in Ionized Atoms on the Delayed-Neutron Fraction

A. A. Rukhadze, L. I. Urutskoev, and D. V. Filippov

The ionization of an atom leads to an appearance of an additional channel of beta decay to a bound state of an electron. It is shown that, for nuclei that are products of uranium fission and which are emitters of delayed neutrons, the fraction of delayed neutrons increases upon taking into account the additional channel of beta decay to bound states.

Effect of Octupole Interactions on the Behavior of Negative-Parity States at Low Spins

A. S. Sitdikov, R. Kh. Safarov, and Ya. Kvasil

At low spins, the energies of negative-parity levels built on two-particle states exhibit a nonlinear behavior as functions of the core-rotation energy. This is due to the incompleteness of the alignment process. This behavior of negative-parity levels at low spins is satisfactorily described upon the inclusion of octupole–octupole interactions, as is demonstrated for the example of the even–even isotopes $^{162-168}$Hf by applying the rotational model that takes into account the Coriolis mixing of states.

Reaction $\gamma p \to \eta'(958)p$ and Polarization of Recoil Protons

V. A. Tryasuchev

On the basis of the isobar model extended with allowance for the t channel, the cross section for and the single-polarization features of the reaction $\gamma p \to \eta' p$ are calculated up to incident-photon energies of 5 GeV by invoking two poorly studied resonances, $S_{11}(1978)$ and $P_{13}(2080)$. In order to reduce the ambiguities in choosing these resonances and their parameters that make it possible to reproduce the experimental differential cross sections, it is proposed to measure the polarization of recoil protons in the reaction being considered.

Observation of the Tensor Glueball

V. V. Anisovich, M. A. Matveev, J. Nyiri, and A. V. Sarantsev

In the reactions $p\bar{p} \to \pi^0\pi^0, \eta\eta, \eta\eta'$, there are four relatively narrow resonances $f_2(1920)$, and $f_2(2020)$ $f_2(2240)$, $f_2(2300)$ and a broad one $f_2(2000)$ in the mass region 1990–2400 MeV. In the framework of quark combinatorics, we carry out an analysis of the decay constants for all five resonances. It is shown that the relations for the decay constants corresponding to the broad resonance $f_2(2000) \to \pi^0, \pi^0, \eta\eta, \eta\eta'$ are the same as those corresponding to a glueball. An additional argument in favor of the glueball nature of $f_2(2000)$ is the fact that $f_2(1920)$, $f_2(2020)$, $f_2(2240)$, and $f_2(2300)$ fit well the $q\bar{q}$ trajectories in the (n, M^2) plane (where n is the radial quantum number), while the broad $f_2(2000)$ resonance turns out to be an unnecessary extra state for these trajectories.

LHC Prospects in Searches for Neutral Scalars in $pp \to \gamma\gamma + jet$

S. V. Demidov and D. S. Gorbunov

At hadron colliders, the $\gamma\gamma + jet$ channel provides a larger signal-to-background ratio in comparison with inclusive $\gamma\gamma$ channel in hunting for scalars uncharged under the SM gauge group. By using NLO results for the SM Higgs boson production and corresponding background, we estimate LHC prospects in searches for radion and sgoldstino in $\gamma\gamma + jet$ channel. Three-body final-state kinematics allows for refined cuts. We have found that this channel could be comparable with $\gamma\gamma$ channel in searches for new physics.

$a_0^+(980)$-Resonance Production in the Reaction $pp \to d\pi^+\eta$ Close to the $K\bar{K}$ Threshold

P. V. Fedorets, M. Büscher, V. P. Chernyshev, S. N. Dymov, V. Yu. Grishina, C. Hanhart, M. Hartmann, V. Hejny, V. Kleber, H. R. Koch, L. A. Kondratyuk, V. P. Koptev, A. E. Kudryavtsev, P. Kulessa, S. I. Merzliakov, S. M. Mikirtychiants, V. E. Nekipelov, H. Ohm, R. Schleichert, H. Ströher, V. E. Tarasov, K.-H. Watzlawik, and I. Zychor

The reaction $pp \to d\pi^+\eta$ has been measured at a beam energy of $T_p = 2.65$ GeV ($p_p = 3.46$ Gev/c) using the ANKE spectrometer at COSY-Jülich. The missing-mass distribution of the detected $d\pi^+$ pairs exhibits a peak around the η mass on top of a strong background of multipion $pp \to d\pi^+(n\pi)$ events. The differential cross section $d^4\sigma/d\Omega_d d\Omega_{\pi^+} dp_d dp_{\pi^+}$ for the reaction $pp \to d\pi^+\eta$ has been determined model independently for two regions of phase space. Employing a dynamical model for the a_0^+ production allows one then to deduce a total cross section of $\sigma(pp \to da_0^+ \to d\pi^+\eta) = 1.1 \pm 0.3_{\text{stat}} \pm 0.7_{\text{syst}}$ μb for the production of $\pi^+\eta$ via the scalar

$a_0^+(980)$ resonance and $\sigma(pp \to d\pi^+\eta) = 3.5 \pm 0.3_{\text{stat}} \pm 1.0_{\text{syst}}$ μb for the nonresonant production. Using the same model as for the interpretation of recent results from ANKE for the reaction $pp \to dK^+\bar{K}^0$, the ratio of the total cross sections is $\sigma(pp \to d(K^+\bar{K}^0)_{L=0})/\sigma(pp \to da_0^+ \to d\pi^+\eta) = 0.029 \pm 0.008_{\text{stat}} \pm 0.009_{\text{syst}}$, which is in agreement with branching ratios in the literature.

Analytic Calculation of Field-Strength Correlators

Yu. A. Simonov

Field correlators are expressed using background field formalism through the gluelump Green's functions. The latter are obtained in the path integral and Hamiltonian formalism. As a result, the behavior of field correlators is obtained at small and large distances for both perturbative and nonperturbative parts. The latter decay exponentially at large distances and are finite at $x = 0$, in agreement with OPE and lattice data.